NASA Conference Publication 2432

Proceedings of the Circulation-Control Workshop 1986

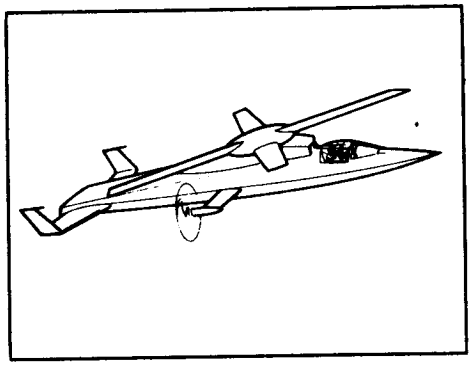

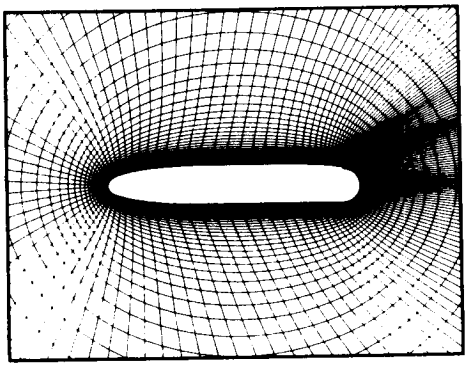

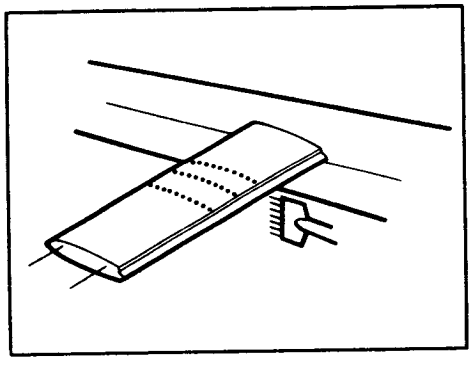

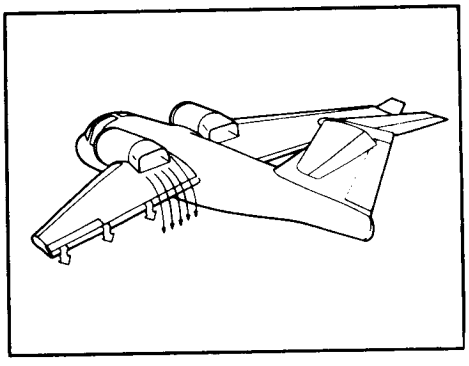

Proceedings of a workshop held at
NASA Ames Research Center
Moffett Field, California
February 19-21, 1986

ORIGINAL CONTAINS
COLOR ILLUSTRATIONS

NASA

NASA Conference Publication 2432

Proceedings of the Circulation-Control Workshop 1986

Compiled by
Jack N. Nielsen
Ames Research Center
Moffett Field, California

Proceedings of a workshop held at
NASA Ames Research Center
Moffett Field, California
February 19–21, 1986

National Aeronautics
and Space Administration

**Scientific and Technical
Information Branch**

1987

TABLE OF CONTENTS

CIRCULATION CONTROL WORKSHOP

SESSION THREE:
CIRCULATION-CONTROL AIRFOIL AND
WING EXPERIMENTS

SESSION FOUR:
CIRCULATION-CONTROL ROTOR THEORY

SESSION FIVE:
X-WING TECHNOLOGY

SESSION SIX:
FIXED-WING TECHNOLOGY AND OTHER CONCEPTS

SESSION SEVEN: CIRCULATION-CONTROL RESEARCH PLANNING

INTRODUCTION

This document is a collection of unclassified papers presented at the Circulation-Control Workshop at NASA Ames Research Center on February 19-21, 1986. Representatives of academia, industry, and government participated in the workshop. Of the papers presented, 25 are published here. The other papers are either proprietary, classified, or limited in distribution. All papers included are listed in the table of contents. The excellent response to the workshop reflects the growing interest in the potential application of circulation-control airfoils to both rotorcraft and fixed-wing aircraft.

The workshop consisted of seven sessions, one of which was classified and another of which addressed future research needs. The other sessions covered viscosity and turbulence, circulation-control airfoil theory, circulation-control airfoil and wing experiments, circulation-control rotor theory, fixed-wing technology and other concepts.

The success of the workshop can be contributed in a large measure to the authors of the papers who were kind enough to take the time to prepare their papers and participate in the workshop.

Much credit must be given to the chairpersons of the seven sessions for the excellent way in which the technical program was accomplished. Particular thanks are due to James Biggers of DTNSRDC for the survey on which the last session was based and for his general advice and help on all aspects of the workshop.

Dr. Kenneth Rosen and Sikorsky Aircraft are both to be thanked for their warm support of the workshop and their extensive contributions to it. Mr. Dennis Riddle of NASA Ames deserves special credit for his job as Administrative Chairman, in which capacity he supervised the arrangements for the workshop.

The unclassified sessions were videotaped and the originals are on file at NASA Ames Research Center. If you want to purchase a copy of all or part of the proceedings, contact Dennis Riddle, Mail Stop 237-3, NASA Ames Research Center, Moffett Field, CA 94035 for more details.

The papers in this publication have not been edited by NASA in the interest of early publication.

ORGANIZING COMMITTEE

General Chairman

Dr. Jack N. Nielsen, Chief Scientist
NASA Ames Research Center

Administrative Chairman

Dennis Riddle, NASA Ames Research Center

Session Chairpersons

Session One

Dr. Sanford Davis, NASA Ames Research Center

Session Two

Jane Abramson, Department of the Navy, David Taylor Naval Ship Research and Development Center

Session Three

Ernest Rogers, Department of the Navy, David Taylor Naval Ship Research and Development Center

Session Four

Dr. Wayne Johnson, NASA Ames Research Center

Session Five

Dr. Kenneth Rosen, Sikorsky Aircraft

(Part of Session Five included the presentation of classified papers which are not included in this publication)

Session Six

Robert Engler, Lockheed-Georgia Company

Session Seven

James Biggers, Department of the Navy, David Taylor Naval Ship Research and Development Center

Viscosity and Turbulence

NAVIER-STOKES CALCULATIONS AND TURBULENCE MODELING IN THE TRAILING EDGE REGION OF A CIRCULATION CONTROL AIRFOIL

by

John R. Viegas and Morris W. Rubesin
NASA Ames Research Center

and

Robert W. MacCormack*
Stanford University

Circulation Control Workshop
NASA Ames Research Center
February 19-21, 1986

*Support provided by NASA Ames Research Center, through Joint Research Interchange No. NCA2-40.

Introduction

The accurate prediction of turbulent flows over curved surfaces in general and over the trailing edge region of circulation control airfoils in particular will require the coupled efforts of turbulence modelers, numerical analysts and experimentalists. In this paper the purpose of our research program in this area will be described (see Fig. 1). Then, the influence on turbulence modeling of the flow characteristics over a typical circulation control wing will be discussed. Next, the scope of this effort to study turbulence in the trailing edge region of a circulation control airfoil will be presented. This will be followed by a brief overview of the computation scheme, including the grid, governing equations, numerical method, boundary conditions and turbulence models applied to date. Then, examples of applications of two algebraic eddy viscosity models (and variants thereof) to the trailing edge region of a circulation control airfoil will be presented. The results from the calculations will be summarized, and conclusions drawn based on the examples. Finally, the future directions of the program will be outlined.

Objective

The overall objective of this research program, summarized in Fig. 2, is to develop an improved turbulence model to permit accurate computation of the flow fields about circulation control wings over a range of flight conditions and trailing edge configurations.

The approach is both computational and experimental. Numerical solutions of flow over circulation control airfoils for various geometries and turbulence models will be used to test, develop and improve the turbulence models for these flows. The experimental program will perform companion experiments over these same flow conditions/geometries to measure turbulence quantities needed to understand these complex flows. The measured results will be used to guide and verify the turbulence modeling over a range of Mach numbers and for various trailing edge configurations.

The present paper will only address the computational part of this program.

Modeling Aspects

The flow about the trailing edge region of a circulation control wing presents a challenging environment to turbulence modelers. Some of the important modeling aspects under these flow conditions, as summarized in Fig. 3, are:

1. The flow is three-dimensional due to the wing having a finite aspect ratio and to being yawed relative to the mean motion.

2. The flow within the boundary layer of a yawed wing experiences large changes in the angles of skewing, (Spaid and Keener, 1986.)

3. Compressibility effects occur in transonic flow regimes and in underexpanded jets. Current Navier-Stokes solvers handle these effects quite well.

4. Multiple streams with different turbulence intensity and length scales merge at the jet and separation points. This requires significant modification to current mixing length models in these regions.

5. The flows experience extreme streamwise curvature way beyond conditions on which usual curvature corrections are based.

6. The flows can experience large regions of separation. Predicting the location of the separation point and the extent of separation correctly is a critical test of a turbulence model. These are also important parameters in the description of the performance of a circulation control airfoil. Unfortunately most turbulence models have difficulty in regimes of large separation.

Current Activities

Current activities have stressed development of a two-dimensional numerical code to permit testing a variety of existing turbulence models and to accept new models likely to be required. This code solves the Reynolds-averaged Navier-Stokes equations in the trailing edge region of a circulation control airfoil. The computational domain is confined to the trailing edge region of the airfoil to emphasize those aspects of this region on the turbulence model (see above) and to allow for high resolution with relatively few mesh points. This latter feature may be very important when complex turbulence models, that are costly in computer time, are tested and developed.

To date only algebraic models of turbulence have been incorporated in the code. These are the well known models developed by Baldwin and Lomax (Baldwin-Lomax, 1978) and by Cebeci and Smith (Cebeci-Smith, 1974). These models, plus modifications, will be shown later.

Computational Domain

For this workshop, the code was used to calculate the flow in the trailing edge region of circulation control wing experiment that was performed at NASA Ames Research Center.

This experiment was the result of a cooperative effort between McDonnell-Douglas and Ames and is reported in another paper of this workshop (Spaid and Keener, 1986). It was chosen for computation because it provided an opportunity for easy access to the experimentors. This wing had a 10 inch chord and was swept back 45°. The case chosen for calculation purposes was one in which the free stream Mach number and the jet pressure ratio were 0.426 and 1.4, respectively.

The sketch on the left side of Fig. 4 shows a typical circulation control wing yawed relative to the mean flow. Shown also is a plane parallel to the mean flow as it crosses the wing. Experimental evidence shows that in the Spaid-Keener experiment the resultant velocity vector in the boundary layer on the top wing surface turned (or skewed) inboard to become nearly parallel to the jet at the surface. In anticipation of eventually obtaining data in the future for an unyawed wing, it was decided to perform the two-dimensional calculations in a plane containing the mean jet velocity vector. It was felt that for such a two-dimensional calculation it would be more important to work in the characteristic plane of the jet and the near-wall flow on the top surface than in the mean flow plane. This satisfied the primary purpose of this work, namely, to test the numerical behavior and the simple turbulence models of the code with typical geometrical and flow parameters. For this limited objective the free stream Mach number and jet pressure are not altered from their swept wing values.

The sketch on the right hand side of figure 4 shows the computational domain in relation to a cross section of the wing. The plane of the figure is normal to the trailing edge of the wing. The wing chord is about 10 inches long and the radius of the computational domain is about 2 feet in length. The vertical boundary for the incoming flow at the top of the airfoil is located at the jet slot. The vertical boundary at the bottom of the airfoil is located at X/C = 0.899, a point where experimental data was available.

The far field grid used in the calculations is shown in Fig. 5. It extends two feet from the body (about 50 tip radii). The outer boundary is circular for the most part. The circles are offset from the center of radius for the trailing edge to provide a vertical location for boundary conditions at the inflow boundaries. The grid spacing stretches exponentially away from the body. A very fine grid is used next to the body to resolve the region where viscous effects are important. The dark region next to the body represents the compressed scales of the fine mesh region which are not resolvable on the scale of this figure. The dark vertical stripe results from the extension of the fine scales, in the flow direction adjacent to the surface, vertically whereas the remainder of the grid is extended radially. The distances on this and subsequent figures are given in feet.

A magnified view of the grid, to show the near field, is presented in Fig. 6. On the scale of this figure the dark vertical stripe on Fig. 5 is seen to blend smoothly with the grid surrounding the trailing edge at the body. Again, the dark band near the surface represents grid spacings that still cannot be resolved at this scale. A total of 61 grid points were used normal to the surface and 65 grid points were used in the circumferential direction.

Computational Method

The computational method is summarized in Fig. 7. The governing equations are the Reynolds-averaged (or mass-averaged) Navier-Stokes equations. They are written here in conservation law form in two-dimensions. In this equation, U represents the conserved quantities: the density, momentum per unit volume in the x and y directions and the total energy per unit volume, and F and G are flux vectors associated with U in the x and y directions, respectively. The flux vectors contain the viscous stresses and the heat flux. These in turn are functions of the molecular and eddy viscosities. The value of the eddy viscosity used in the calculations will depend on the turbulence model employed. The calculations to be shown later will compare results obtained from some algebraic models for the eddy viscosity.

The numerical method employed is the latest implicit finite volume method of MacCormack (MacCormack, 1985). This is a stable, efficient, second order (in space) algorithm that utilizes flux splitting to take advantage of the direction information travels and is built around MacCormack's basic explicit second order accurate method (MacCormack, 1969).

No-slip and adiabatic boundary conditions are used at the surface of the trailing edge. Subsonic boundary conditions based on the method of characteristics are used at all the flow boundaries. At the inflow boundaries the total pressure, total temperature and the flow angle are specified. At the outflow boundary only the static pressure needs to be specified.

It was found that the specification of these boundary conditions for this subsonic flow problem was surprisingly critical to the results obtained. The flow boundary conditions are shown explicitly on Fig. 8. Experimental values of p_t and T_t, taken from Spaid and Keener's data, were used where available at both inflow boundaries. Unfortunately these quantities were measured only in the boundary close to the body, both at the jet and at the X/C = 0.899 inflow station at the bottom of the trailing edge. It was assumed that T_t was a constant across the entire inflow boundaries. At these boundaries it was assumed that P_t varied linearly from the measured value at the edge of the boundary layer to

$p_{t\infty}$ at about 0.1 ft. off the body and remained constant for further distances.

The flow angle, $\tan^{-1}(v/u)$, is also needed at the inflow boundaries, but was not available. Therefore, this angle had to be approximated. At the top surface the flow angle is varied linearly from being parallel to the body at the surface to a value of zero at about 2 chords off of the surface. In the jet the flow angle is parallel to the top and bottom jet walls and varies linearly in between. The inflow angle off of the bottom surface was initially treated in the same manner as that off the top surface. However, in preliminary calculations these inflow angles were found to yield an unsatisfactory static pressure distribution at the inflow boundaries and the separation point moved to the bottom inflow boundary. For these calculations the static pressure at the outflow boundary was taken to be the tunnel static pressure. It was found that the location of the separation point could be moved toward the jet and the exit static pressure distributions on the inflow boundary made to agree better with the experimental results by varying the static pressure vertically from $\mathcal{P}_{\infty}$ at the top of the outflow boundary to 0.98 $\mathcal{P}_{\infty}$ at the bottom of the outflow boundary. It was also found that with the boundary conditions fixed, at values that gave reasonable results, that the results were sensitive to the distance that the outflow boundary was placed from the surface. Control volume radii of 2 ft and 3 ft were tried. Not having experimental evidence to guide either the choice of the inflow angle or the value of the outflow static pressure as a function of position it was decided to fix the static pressure at the outflow boundary to the nominal tunnel static pressure and to locate this boundary 2 feet (2.4 chords) off of the surface. It was also decided to vary the inflow angle along the lower inflow boundary as indicated by the short arrows on Fig. 8. At the top of this boundary the flow angle is parallel to the surface. A linear variation was assumed from this upwash angle to a downwash angle of equal magnitude at a distant equal to 25% of chord below the body. Beyond this, the inflow angle was varied linearly to zero at 1 foot from the body and remained zero for the remaining distance. This tailoring of the inflow angle was done for a single turbulence model and yielded reasonable results. These boundary conditions remained fixed for all other turbulence models tested.

Since the results are indeed sensitive to the boundary conditions, it is apparent that to perform meaningful comparisons of turbulence models with experiment, measurements of flow field parameters need to be made in the boundary regions of the computational domain.

In the jet the total temperature was taken to be equal to the nominal total temperature of the tunnel and the total pressure was determined by matching the mass flow rate of the

experiment and assuming fully developed turbulent channel flow.

The computation is initiated by assuming no flow and a total pressure equal to the maximum P_t in the jet exists throughout the domain except for the exit boundary where the nominal tunnel static pressure is specified. From this the flow relaxes smoothly to a steady state.

Turbulence Models

Two basic algebraic eddy viscosity models were used in the calculations for this workshop. They are the well known Cebeci-Smith model and the more recent, but also well known Baldwin-Lomax model. Both are two layer models for the turbulence. Expressions for inner and outer regions of the boundary layer for both of these models are outlined on Fig. 9 . The Cebeci-Smith (C.S.) model is often inappropriate for complex flows because of great uncertainty in defining the boundary layer thickness δ and the displacement thickness δ^*. The Baldwin-Lomax (B.L.) model avoids this ambiguity by defining a length scale based on the location of the maximum of the velocity-function, F, of the vorticity, . For some complex flows the B.L. will also be inappropriate because F may have multiple maxima.

In the present calculations these two models were applied either without or with modifications.

The modifications to the B.L. model were as follows:

1. The history of the jet was included by evaluating the eddy viscosity at the exit plane of the jet using fully established channel flow relationships and length scales relative to the nearest wall. This jet-plane eddy viscosity was then blended with the local eddy viscosity through an exponential damping function W. The W was selected to vanish at X/C = 1.

2. The effect of curvature was included through the use of Bradshaw's curvature relation (Bradshaw, 1969). This relation is based on Bradshaw's analogy between streamline curvature and buoyancy. The R is the Richardson number.

3. To establish the effect of the intermittancy factor, I_{BL}, on the results, solutions were also obtained with I_{BL} set to unity. This was done to assure that the turbulence in the jet-free stream shear layer winded not be damped artificially through I_{BL}.

The boundary layer thickness used in the C.S. model was taken to be the distance normal to the surface where the velocity parallel to the surface was a maximum. For some parts of the trailing edge region the velocity increases monotonically with this distance and becomes unrealistically large. To avoid this the C.S. model was modified by not allowing to grow larger than 10 times the experimental value at the input boundary of the lower surface.

Results

The next seven figures show computation results obtained when these various turbulence models/modifications were applied to the trailing edge region of a circulation control airfoil under the conditions outlined earlier.

Fig. 10 shows a far field view of particle paths for one of the calculations. This is a typical result. Particle paths agree with streamlines in steady state flow. Here they represent the trajectory of particles selected at every fifth grid point along the inflow boundary. The dark band merely shows the coalescence of many particles that were selected close to the body.

In Fig. 11 a near field view of particle paths are presented for calculations based on the unmodified B. L. model and on this model with modifications for jet history, curvature and combined history and curvature. In these near field figures particle baths were initiated from every other grid point along the inflow boundary. All the results look similar overall. There is, however, evidence of a slight movement of the separation point toward the jet entrance when curvature or jet history effects are included in the turbulence model. This effect is more pronounced when the jet history and curvature terms are both included in the calculations.

The next two Figures (12 and 13) show the corresponding velocity vectors for each of the preceding particle path results. The length of the vectors shown here are proportional to the magnitude of the velocity. The vectors are placed at every third point circumferentially and every other point normal to the body. In spite of the small scale, the jet flow and flow above the jet lip are shown as distinct at the top inflow boundary. These two flows are seen to merge as fluid moves away from the jet. The jet also becomes less pronounced as it gives up its momentum to the mean flow. Also apparent on these figures is the merging of the flows from the top and bottom surface of the airfoil. All the velocity plots look similar and on close inspection reveal the separation points. The turbulence model with modifications for jet history and curvature is seen to predict separation to occur closest to the jet.

Figure 14 shows results obtained, for the same flow as in the previous figures, when the turbulence model is changed to the Cebeci-Smith model. In this figure particle paths and velocity vectors are shown for the unmodified and modified (δ limit) versions of the C.S. model discussed earlier. Both cases give similar results but the limit on has had the effect of moving the separation point closer to the jet. The velocity vectors for the two cases reveal differences that correspond to those seen between particle path comparisons.

The two basic turbulence models used in this study are compared in the next two figures. Figure 15, composed of the top half of Fig. 12 and the bottom half of Fig. 14, compares particle paths and velocity vectors for the B.L. and C.S. turbulence models. This comparison reveals that the basic flow patterns are considerably different for the two models. The location of the separation point is much closer to the jet for the C.S. than for the B.L. model. This is illustrated by the particle paths and the velocity vectors where the jet for the C.S. model is seen to leave the surface early and a reversed region profile is clearly visible below the jet about 45 degrees from the inlet line. Thus, this figure illustrates that the results obtained for this flow are very sensitive to the generic turbulence model used in the calculations.

To complete the comparisons of basic turbulence models and their modifications, the pressure distributions about the trailing edge are shown in Fig. 16. This comparison illustrates that there is not much difference between results obtained with the unmodified B.L. model and the B.L. model with jet history and curvature included. It also shows that large differences can occur between results obtained when the C.S. model is used in place of the B.L. model for fixed boundary conditions consistent with the latter model.

The differences in results between the two models (C.S. and B.L.) cannot be used to favor one over the other. They merely show that calculations for flow in the trailing edge region of a circulation control airfoil, with a single numerical scheme and fixed boundary conditions, are sensitive to the choice of the turbulence model. Recall that the boundary conditions were tailored to give reasonable results when the B.L. model was used in the calculations. Also, the results obtained with the B.L. model were very sensitive to the tailoring. Had the boundary conditions been tailored for the C.S. model the results shown on Fig. 16 would perhaps be very different.

Summary and Future Directions

In summary, a new, efficient, implicit algorithm for solving the two-dimensional Reynolds-averaged Navier-Stokes equations, with algebraic models of turbulence, has been

adapted to solve the trailing edge region of a circulation control airfoil.

The boundary conditions used at the entrance and exit regions of the entire control volume were found to be critically important. In future modeling experiments, it is critical that measurements of enough information be obtained to enable computations to have reliable and completely unambiguous boundary conditions.

Once boundary conditions were fixed, the numerical results were very dependent on the choice of the basic algebraic eddy viscosity model. Once a generic model had been chosen, however, results obtained from it were found to be insensitive to the modifications for streamwise curvature, jet history, itermittancy and outer length scales employed here.

In the future it is planned to incorporate higher order turbulence models into the code. These will include two-equation eddy viscosity models and, if needed, full stress transport models (HaMinh, et al, 1985). For efficiency some wall function development probably will be required (Viegas and Rubesin, 1985). The experimental data base for this modeling activity will include several boundary layer experiments with curved surfaces, and experiments in the vicinity of the trailing edge of circulation control airfoils, such as those of Novak and Cornelius (Novak and Cornelius, 1986). In addition, experiments such as the mean flow measurements of Spaid and Keener (Spaid and Keener, 1986) will be used to verify the results. It is also planned to interact with experimentalists here at NASA and elsewhere. Comparison calculations for various turbulence models would be done for these experiments and others as they become available. Eventually, the code could be extended to three-dimensions to study problems of real yawed wings.

References

Baldwin, B. and Lomax, H.: Thin-Layer Approximation and Algebraic Model for Separated Turbulent Flows, AIAA Paper No. 78-257, 1978.

Bradshaw, P.: The Analogy between Streamline Curvature and Buoyancy in Turbulent Shear Flow, J. Fluid Mech. Vol. 36, p. 177, 1969.

Cebeci, T. and Smith, A.M.O.: Analysis of Turbulent Boundary Layers, Academic Press, 1974, pp. 211-257.

HaMinh, H., Rubesin, M. W., Vandromme, D., and Viegas, J. R.: On the Use of Second Order Closure Modelling for the Prediction of Turbulent Boundary Layer/Shock Wave Interactions: Physical and Numerical Aspects, International Symposium on Computational Fluid Dynamics - Tokyo, Tokyo, Japan, Sept. 1985.

MacCormack, R. W.: The Effect of Viscosity in Hypervelocity Impact Cratering, AIAA Paper No. 69-354, 1969.

MacCormack, R. W.: Current Status of Numerical Solutions of the Navier-Stokes Equations, AIAA Paper No. 85-0032, 1985.

Novak, C. J. and Cornelius, K. C.: An LDV Investigation of a Circulation Control Airfoil Flowfield, AIAA Paper No. 86-0503, 1986.

Spaid, F. W. and Keener, E. R.: Boundary Layer and Wake Measurements on a Swept, Circulation-Control Wing, Circulation Control Workshop, NASA CP 2432, 1986. (Paper 11 of this compilation.)

Viegas, J. R. and Rubesin, M. W.: On the Use of Wall Functions as Boundary Conditions for Two-Dimensional Separated Compressible Flows, AIAA Paper No. 85-0180, 1985.

- Objective
- Identify turbulent modeling aspects
- Describe scope of current activities
- Briefly describe computation scheme
  - * Grid
  - * Governing equations
  - * Numerical method
  - * Turbulence models
- Examples--Applications of algebraic eddy viscosity models to the trailing edge of a circulation control wing
- Conclusions based on examples
- Future directions of research program

Fig. 1.- Purpose of the research program into turbulent flow prediction for circulation control airfoils.

To develop an improved turbulence model to permit the accurate computation of the flow fields about circulation control wings over a range of flight conditions and trailing edge configurations.

- Computations
- Experiments

Fig. 2.- Overall objective of research program.

- Three dimensionality
- Skewing effects
- Compressibility
- Merging of multiple streams
- Extreme streamwise curvature
- Separation

Fig. 3.- Modeling aspects of circulation control wings.

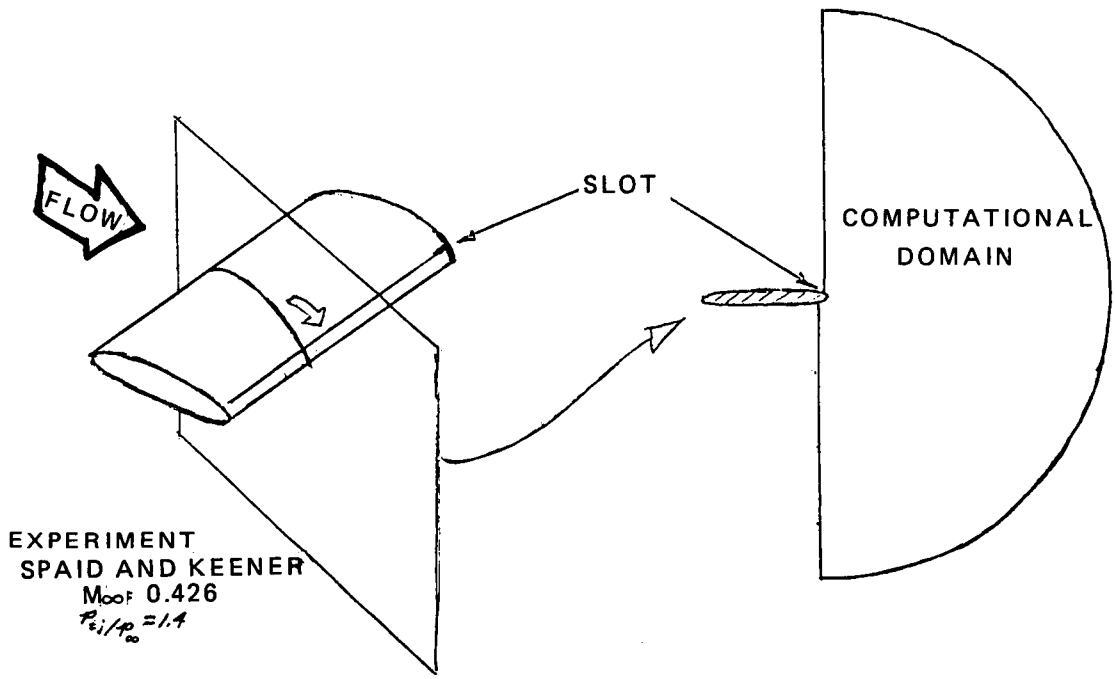

Fig. 4.- Computational domain for the trailing edge region of a circulation control wing.

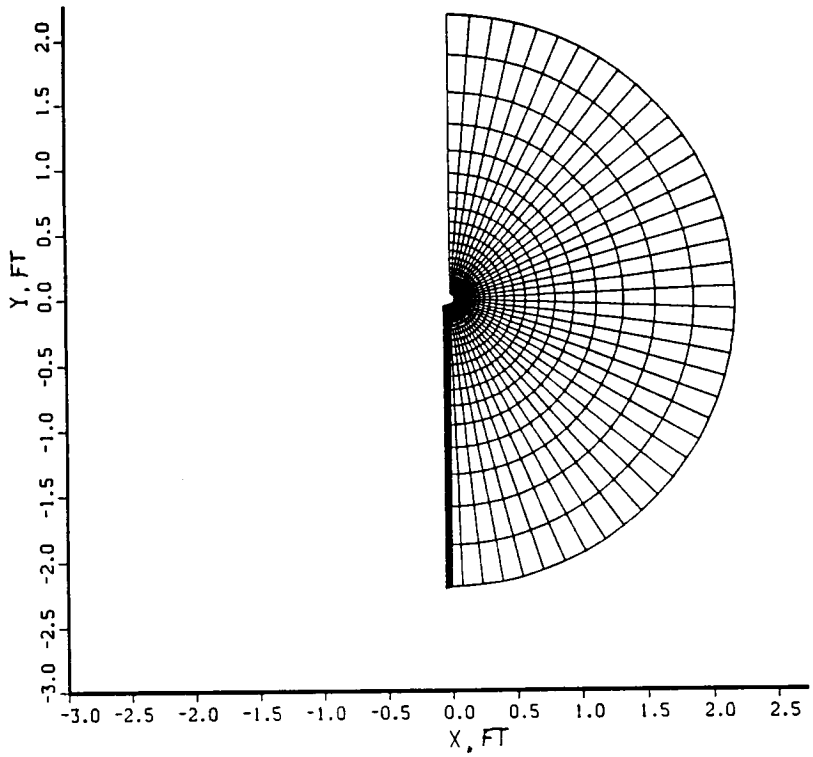

Fig. 5.- Far field grid used in the flow calculations.

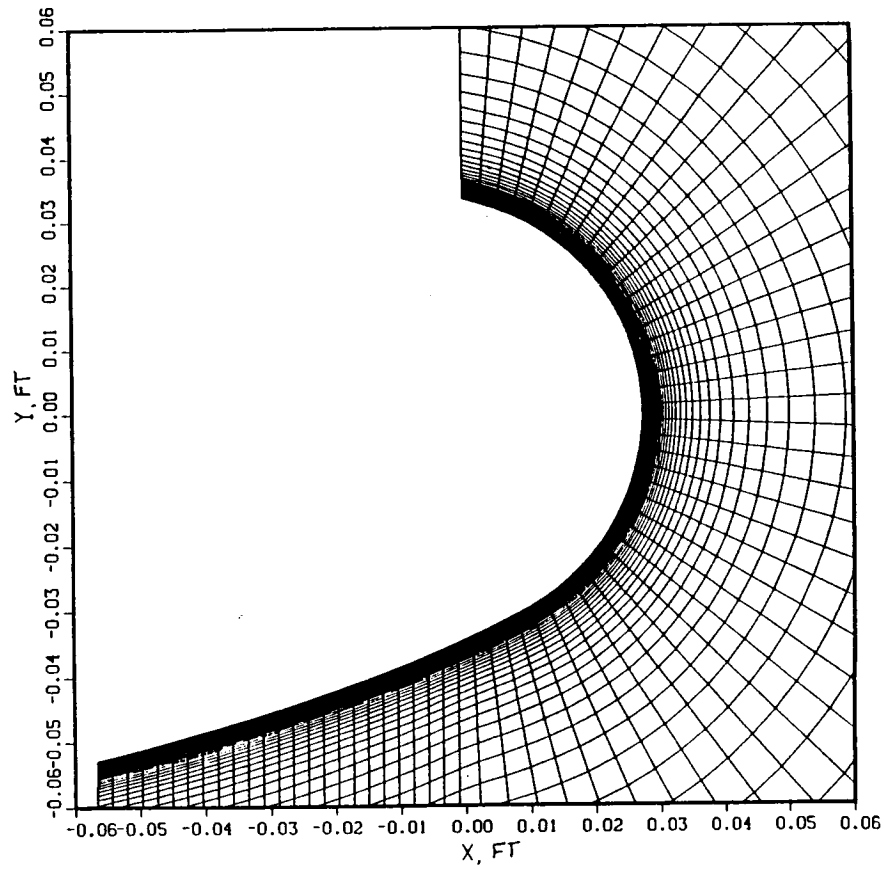

Fig. 6.- Magnified view of the grid showing the near field.

Governing Eqs. (Mass averaged Navier-Stokes equations)

$$\frac{\partial U}{\partial t} + \frac{\partial F}{\partial x} + \frac{\partial G}{\partial y} = 0$$

$$U = [\rho, \rho u, \rho v, \rho e]^T$$

F, G : flux vectors

$$F = \begin{bmatrix} \rho u \\ \rho u^2 + \tau_{xx} \\ \rho uv - \tau_{xy} \\ u(\rho e + \tau_{xx}) - v\tau_{xy} + q_x \end{bmatrix}$$

$$e = c_v T + (u^2+v^2)/2$$

$$\tau_x = p - 2(\mu+\mu_t)\left(\frac{\partial u}{\partial x} + \tfrac{1}{3} \operatorname{div} u\right)$$

$$\tau_{xy} = (\mu+\mu_t)\left(\frac{\partial u}{\partial y} + \frac{\partial v}{\partial x}\right)$$

$$q_x = -K_T \frac{\partial T}{\partial x}$$

Numerical Method.

MacCormack : Implicit Finite Volume Method — 1985

Basic Algorithm: Second order accurate explicit method

Options: Implicit (including boundary conditions)
Flux Splitting
First or Second order accurate in Space, first order in time.

Boundary Conditions:

Surface : No slip, adiabatic

Inflow: (Top and Bottom) Method of Characteristics
p_t, T_t, $\theta = v/u$, given

Outflow: Method of Characteristics p (static) given

Fig. 7.- Summary of computational method.

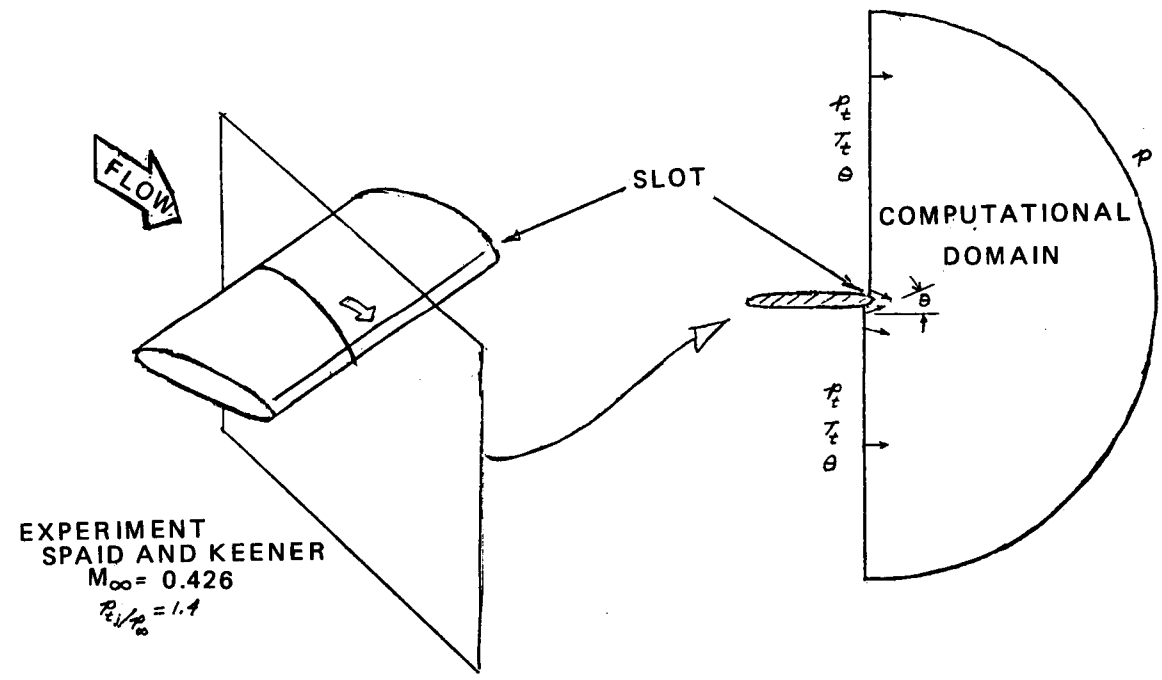

Fig. 8.- Computational domain for the trailing-edge region of a circulation control wing showing boundary conditions.

	Cebeci–Smith	Baldwin–Lomax
Inner region:	$\mu_{t_i} = \rho \ell^2 \left\lvert \frac{\partial u}{\partial y} + \frac{\partial v}{\partial x} \right\rvert$	$\mu_{t_i} = \rho \ell^2 \lvert \omega \rvert$
Outer region:	$\mu_{t_o} = \bar{K} \rho u_e \delta^* / I$ I, I_{BL}, intermittency factors $u^2_{diff} = V^2_{max} - V^2_{min}$	the smaller of $\mu_{t_o} = \bar{K} \rho C_{cp} F_{max} y_{max} / I_{BL}$ or $\mu_{t_o} = \bar{K} \rho C_{cp} C_{WK} \frac{y_{max} u^2_{diff}}{F_{max} I_{BL}}$ $F = y/\omega \lvert (1 - \exp(-y/A)) \rvert$

Modifications:

- History of jet — $\mu_{t_i} = \mu_{t_j} W + \mu_{t_l} (1 - W)$
- Effect of curvature — $\mu_{t_{C_i}} = \mu_{t_i} S^2 \qquad S = (1 + \beta R)^{-1}$
- Limit tests on δ
- Eliminate intermittancy

Fig. 9.- Expressions of inner and outer regions/for both models.

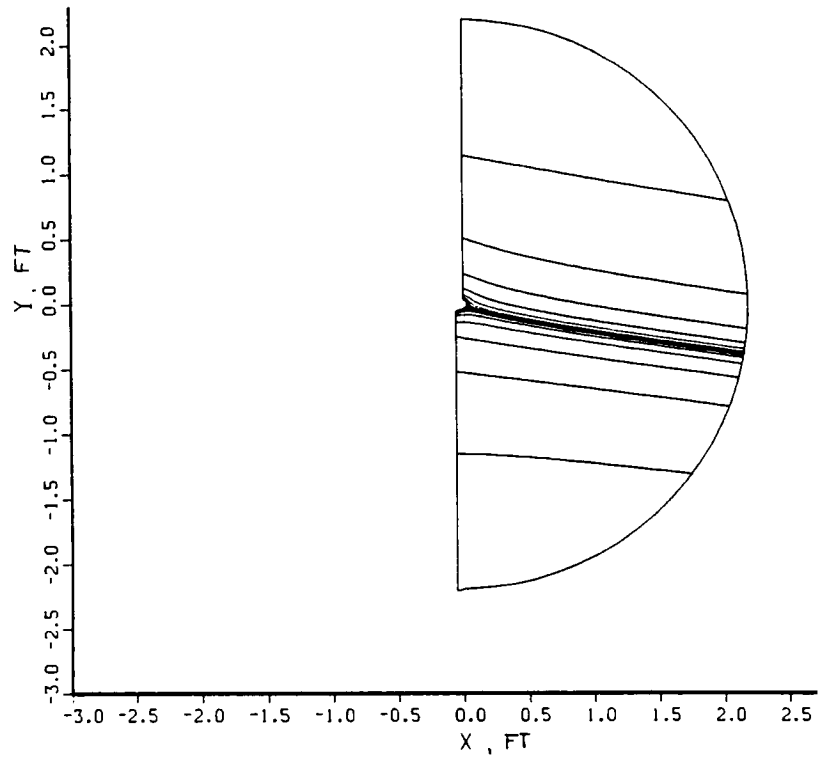

Fig. 10.- Example of far field view of particle path.

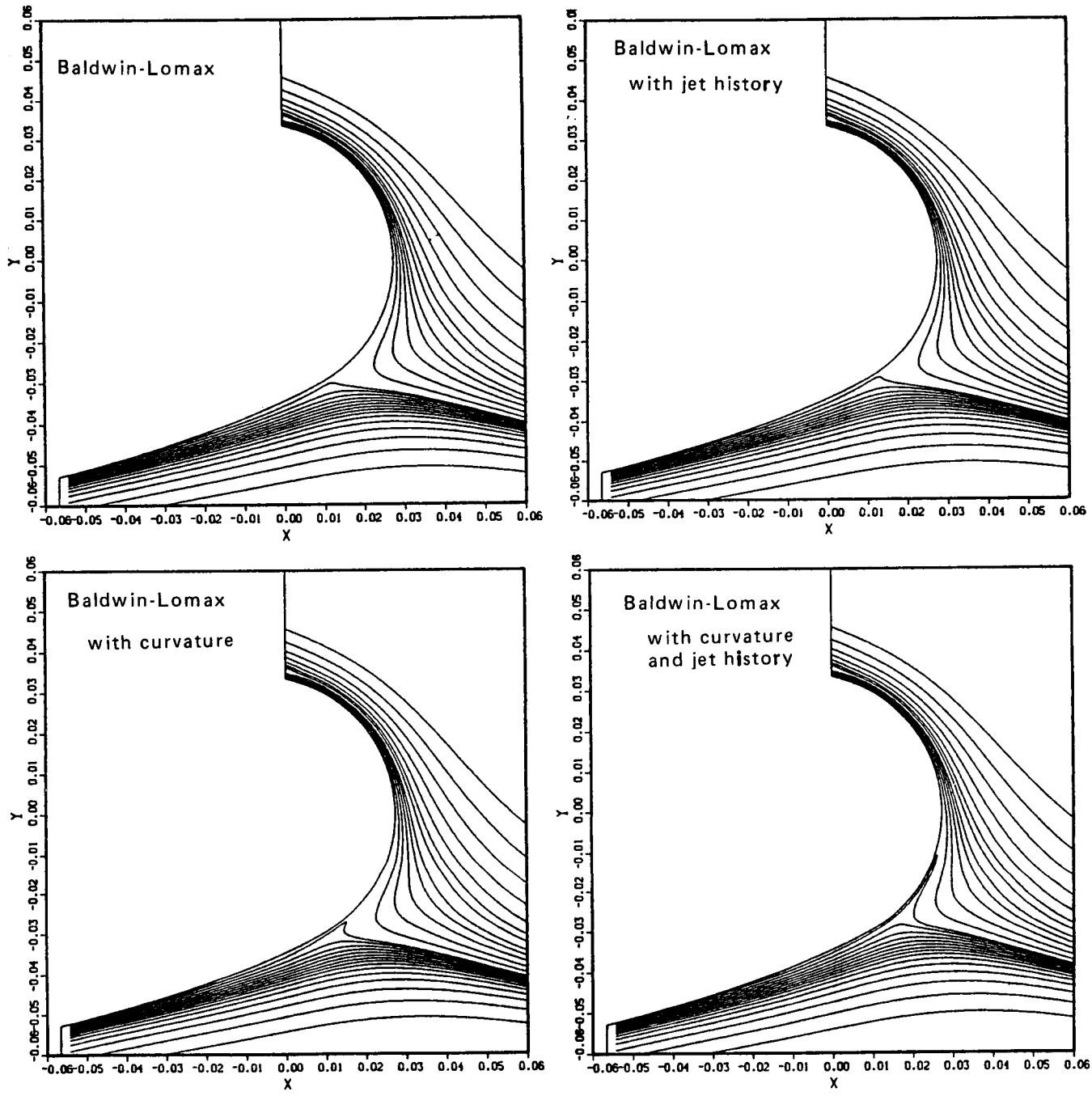

Fig. 11.- Near field view of particle paths for calculations based on Baldwin-Lomax model.

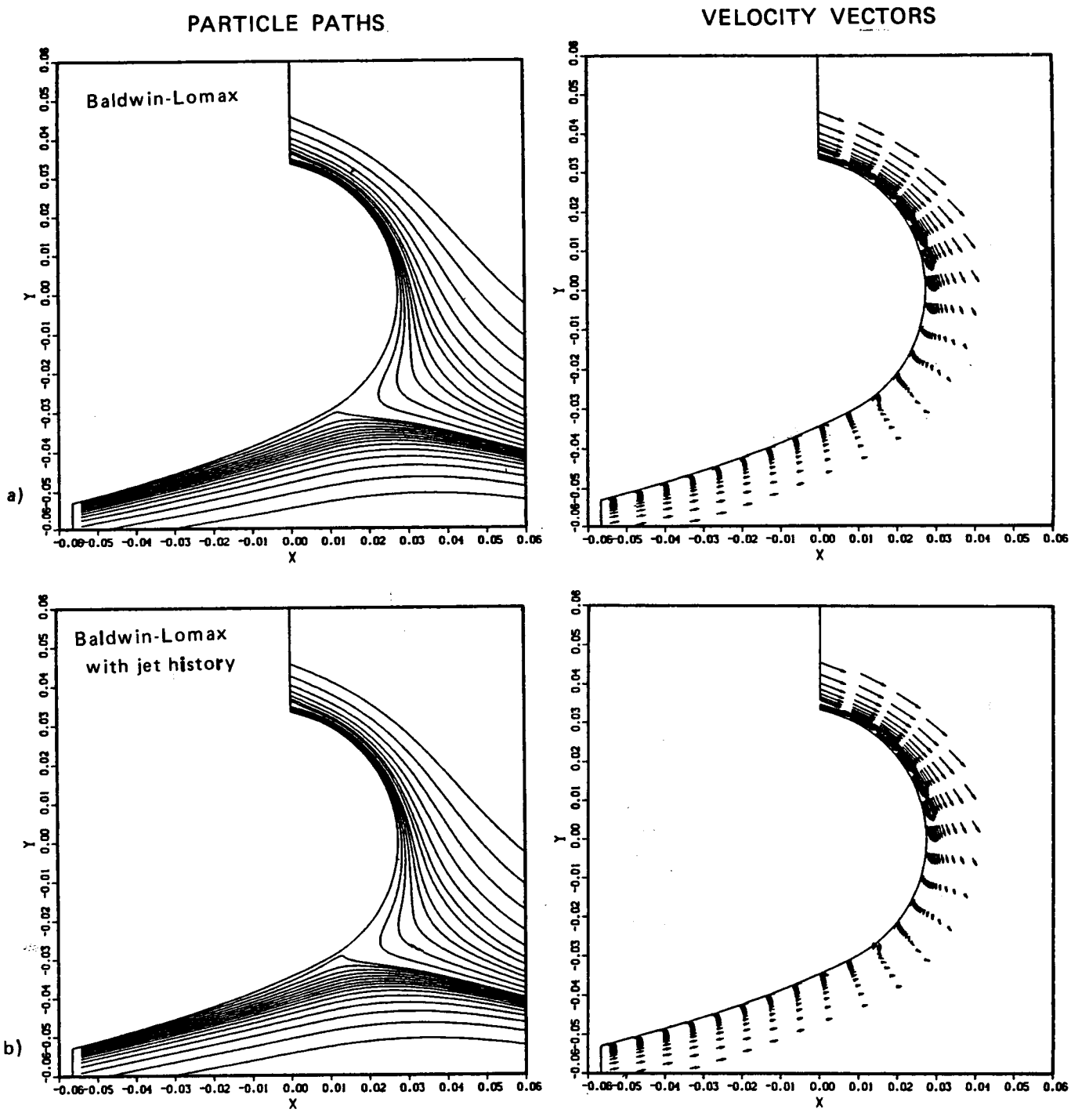

Fig. 12.- Particle paths and corresponding velocity vectors. a) Baldwin-Lomax model; b) Baldwin-Lomax model with jet history.

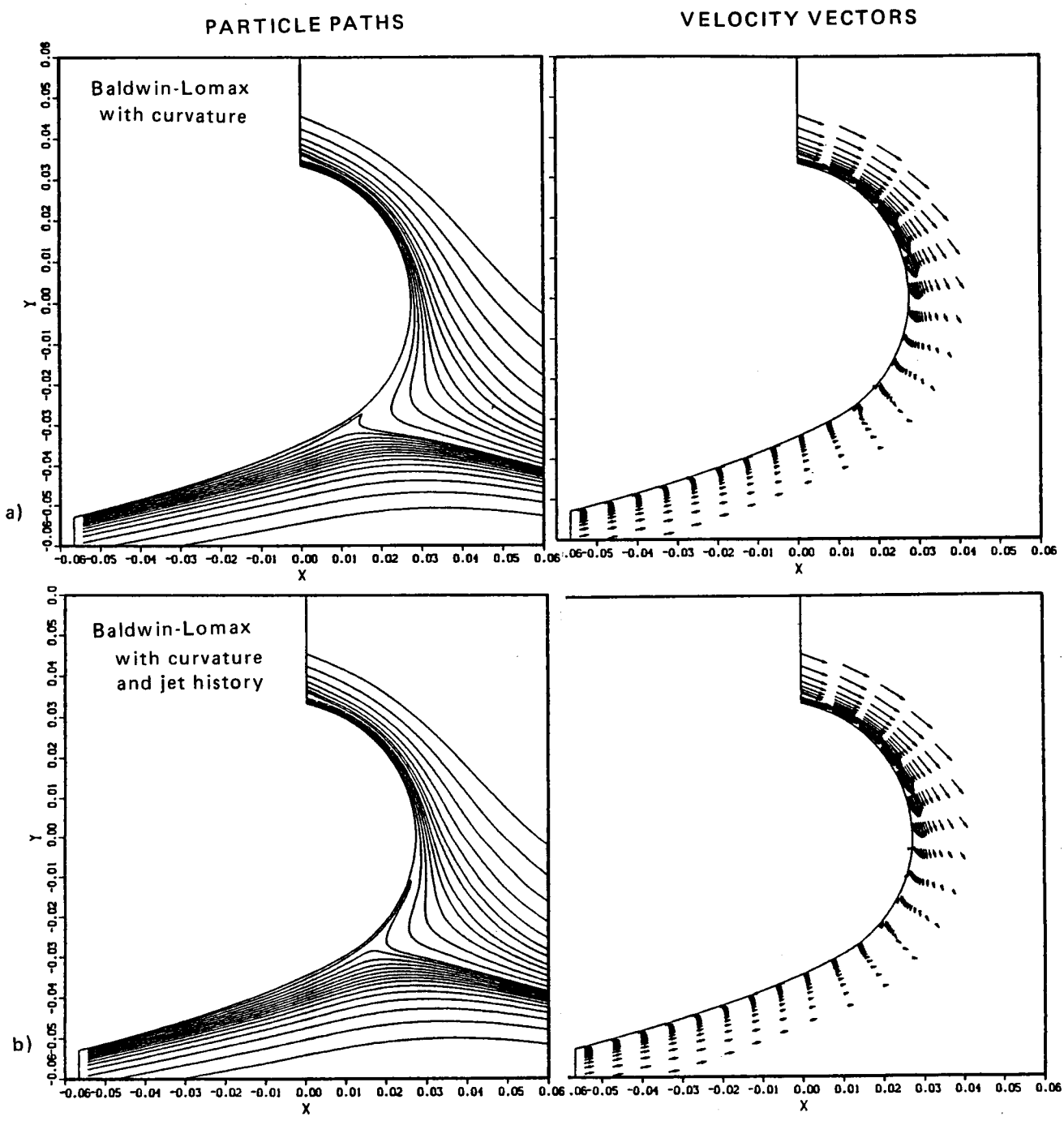

Fig. 13.- Particle paths and corresponding velocity vectors. a) Baldwin-Lomax with curvature; b) Baldwin-Lomax with curvature and jet history.

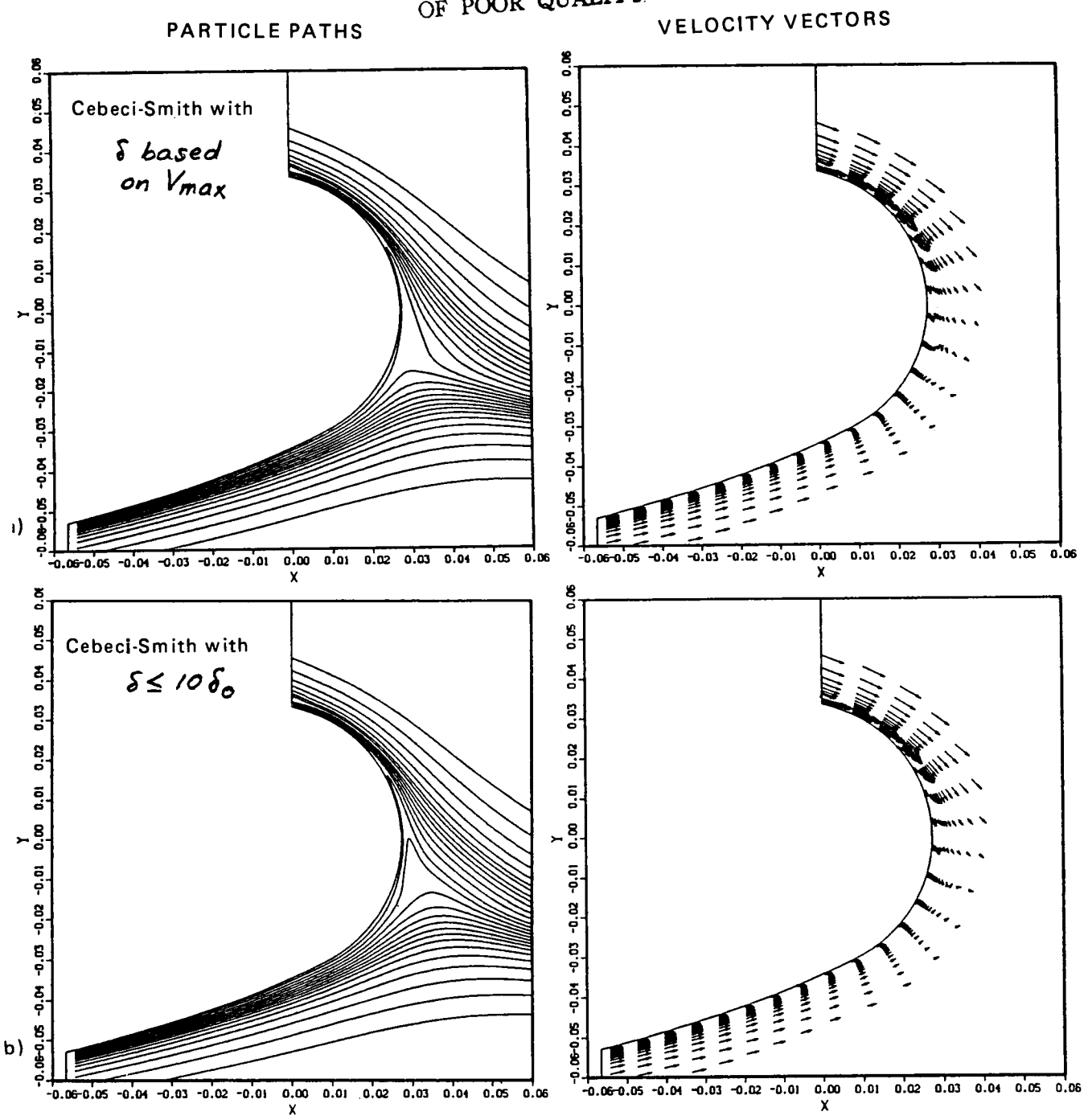

Fig. 14.- Particle paths and corresponding velocity vectors using the Cebeci-Smith model. a) δ based on V_{max}; b) $\delta \leq 10\ \delta_o$

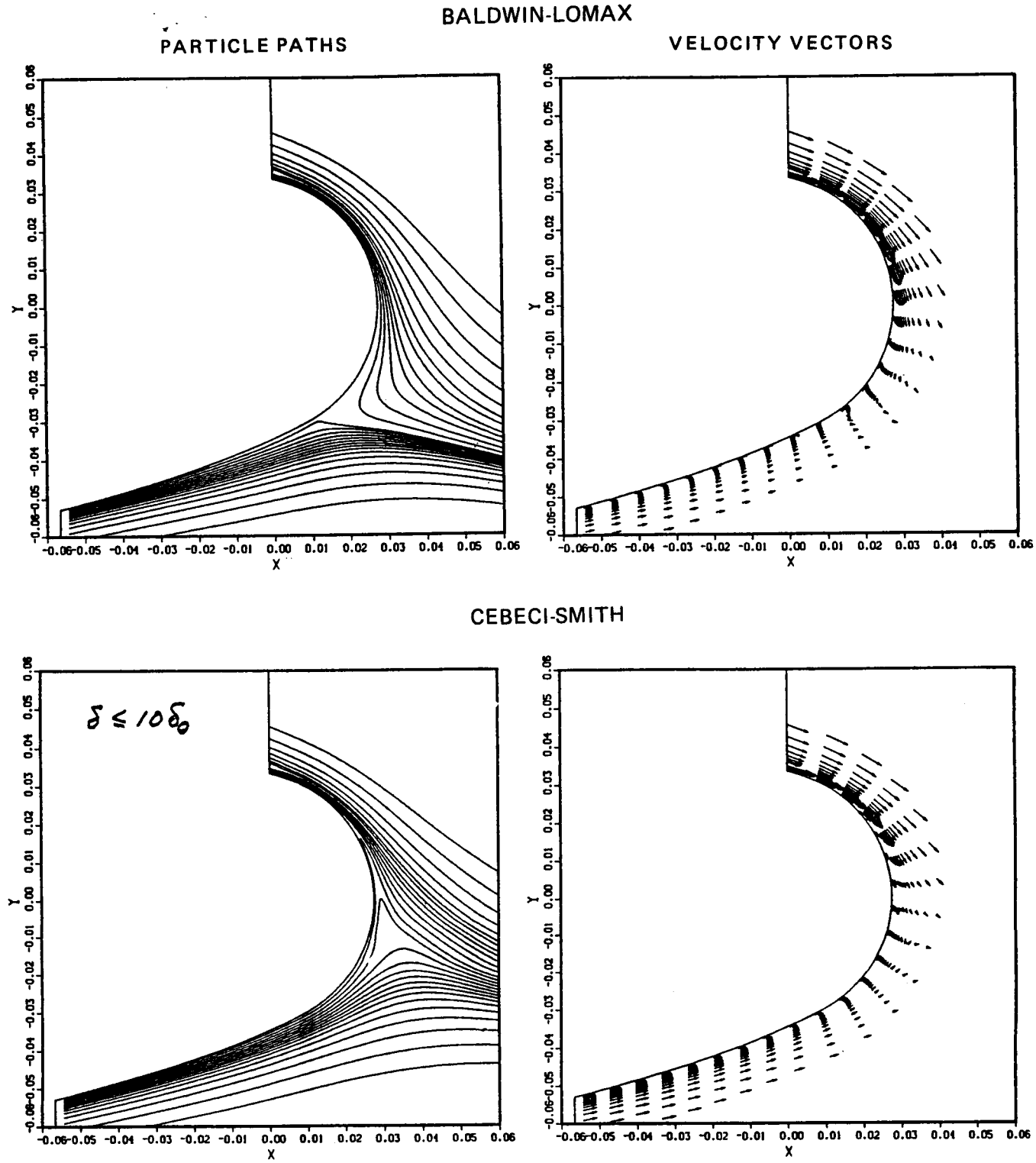

Fig. 15.- Comparison of near region flow fields obtained using Baldwin-Lomax and Cebeci-Smith models.

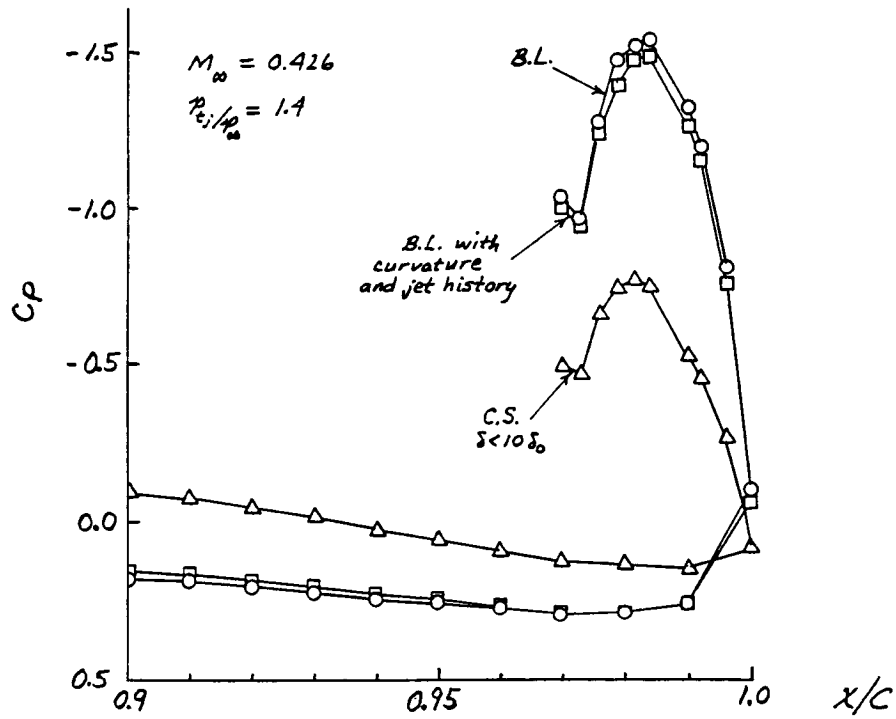

Fig. 16.- Comparison of both models based on pressure distribution about the trailing edge.

WALL JET ANALYSIS FOR CIRCULATION CONTROL AERODYNAMICS, PART I: FUNDAMENTAL CFD AND TURBULENCE MODELING CONCEPTS*

S.M. Dash, B.J. York and N. Sinha
Science Applications International Corporation
Princeton, New Jersey

and

F.A. Dvorak
Analytical Methods, Inc.
Redmond, Washington

ABSTRACT

In Part I of this paper, an overview of parabolic and PNS methodology developed to treat highly curved sub and supersonic wall jets is presented. The fundamental data base to which these models have been applied is discussed in detail. The analysis of strong curvature effects has been found to require a semi-elliptic extension of the parabolic modeling to account for turbulent contributions ($\overline{v'v'}$) to the normal pressure variation, as well as an extension to the turbulence models utilized, to account for the highly enhanced mixing rates observed in situations with large convex curvature. A non-iterative, pressure-split procedure is shown to extend parabolic models to account for such normal pressure variations in an efficient manner, requiring minimal additional run time over a standard parabolic approach. Curvature corrections to a $k\varepsilon$ two-equation turbulence model are reviewed and their general applicability is assessed. For complex flows, the use of algebraic or full Reynolds stress turbulence models may be required, but the $k\varepsilon$ corrections utilized have been adequate for all fundamental cases thus far explored. For strong blowing situations, a supersonic/underexpanded wall jet structure develops with a complex multiple shock cell internal wave structure. A new PNS approach is presented to solve this problem which extends parabolic methodology via the addition of a characteristic-based wave solver. Applications of this approach to analyze the interaction of wave and turbulence processes in wall jets are presented. The present uncertainty in dealing with compressibility effects in supersonic problems

---

* Presented at Circulation Control Workshop, NASA/Ames Research Center, February 18 - 20, 1986. Work supported by David Taylor R&D Center and NASA/Ames.

is pointed out as a problem area for which no data exists. The unification of the parabolic, pressure-split and PNS wave solving capabilities into the wall jet computer code, WJET, is discussed. This code has served as a research tool for studying the effects of various parameters on wall jet structure, and includes advanced turbulence models with curvature and compressibility effects. In Part II of this paper, the steps taken towards incorporating WJET into a zonal component model for analyzing circulation control airfoils is presented.

INTRODUCTION

A zonal model (Figure 1) for the engineering analysis of circulation control airfoil performance (TRACON) was developed by Dvorak and coworkers under David Taylor R&D Center (DTRDC) support[1,2]. TRACON is comprised of separate components which analyze the external potential flow (Jameson's FL06 model), the airfoil boundary layer (Cohen and Reshotko/Green, laminar/turbulent integral models), and the wall jet (Dvorak's finite difference model[3]).

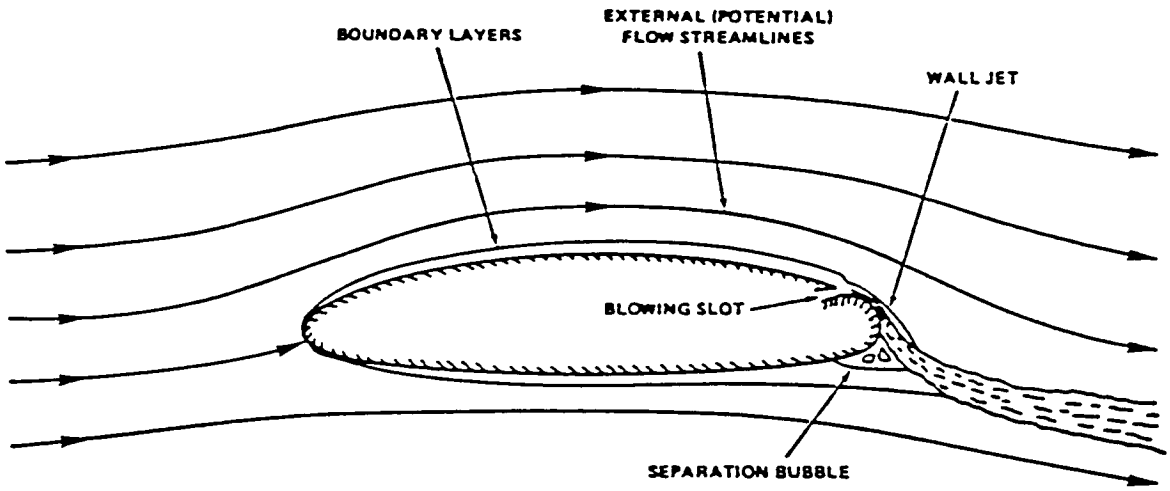

FIGURE 1. Zonal Approach for CC Airfoil Analysis.

While TRACON was demonstrated to perform quite well for a variety of cases, limitations in its ability to deal with very large curvature and/or strong blowing were encountered. These limitations were associated with the modeling assumptions in the TRACON wall jet component which include:

(1) a parabolic approach does not solve the normal momentum equation across the viscous wall jet, hence - ΔC_p is not predicted and has to be estimated from inviscid considerations;

(2) a parabolic approach which does not treat the supersonic wave/shock structure occurring in underexpanded wall jets at high rates of blowing;

(3) a weakly interactive, displacement-thickness based viscous/inviscid coupling approach which becomes inadequate for strongly interactive situations associated with large curvature and/or strong blowing; and,

(4) an algebraic eddy viscosity turbulence model which does not handle lag effects associated with significant pressure gradients.

To remedy these limitations, a new wall jet model, WJET, was developed by Dash and coworkers (under DTRDC support), which employed advanced numerical procedures and utilized a two-equation turbulence model. The first version of this model[4,5] solved the higher order parabolic curved wall jet equations utilizing a conventional implicit algorithm. This model provided for a formal solution of the viscous normal momentum equation to yield ΔC_p across the jet, and, employed a hybrid (inner VanDriest/outer kε) two-equation turbulence model with curvature correction terms. An improved version of WJET[6,7] utilized a subsonic pressure-split approach which solved the semi-elliptic coupled continuity and normal momentum equations across the jet in a non-iterative manner, and, provided for direct coupling of the wall jet with a potential external flow solver, eliminating the requirement for weakly interactive displacement thickness based coupling. The final version of WJET developed under DTRDC support[8,9], extended the parabolic/pressure-split methodology to provide PNS spatial marching capabilities in supersonic flow regions. A new implicit/explicit approach was utilized which employs an upwind finite difference representation of viscous-characteristic methodology to solve the wall jet wave field.

In concurrent work initiated in 1984 under NASA/Ames support, the methodology was formulated[10] and is now being made operational, to incorporate WJET into the TRACON code, replacing the existing wall jet component. This effort is being performed jointly by Dvorak and coworkers (at AMI) and Dash and coworkers (at SAIC). Progress towards this end is discussed in Part II of this paper[11].

In Part I of this paper, a brief overview of the features and capabilities of WJET, and, its application to various simple cases will

be discussed. WJET has been used on a stand alone basis to analyze a variety of basic wall jet data which has led to a greater understanding of the dominant influence of turbulence modeling on our ability to simulate wall jet flowfields. On highly curved convex surfaces, conventional two-equation models grossly underestimate the jet growth and the mixing that occurs, and curvature correction terms are required to properly simulate the flowfield. At supersonic velocities, free jet data indicate that compressibility effects can markedly reduce jet growth and mixing, as will be discussed. A good data base to isolate the influence of compressibility effects on wall jets is not available, which leads to some uncertainty in our ability to treat circulation control airfoil problems, but a much larger uncertainty in other higher speed problems (i.e., tangential injection problems in supersonic combustors, slot cooling problems for hypersonic vehicles, etc.).

OVERVIEW OF WJET MODEL

Mean Flow and Turbulence Model Equations

WJET solves the higher order curved boundary layer equations listed in Table 1. The equations are cast in surface-oriented s,n coordinates (Figure 2) and include a tracer species equation for ϕ (ϕ = 1 in unmixed jet, = 0 in airstream) to delineate the jet/air mixing region. A classical Boussinesq approximation is utilized to relate turbulent stress terms to mean flow gradients, with the parabolized stress terms retained listed in Table 2. Turbulence closure is achieved using the two-equation kε model with standard coefficients (C_μ = 0.09, C_1 = 1.43, C_2 = 1.92, σ_k = 1.0, σ_ε = 1.3). The turbulent transport equations for k and ε are listed in Table 3.

To extend the high Reynolds number kε turbulence model to the wall, a variety of techniques are available ranging from simple wall function approaches to the use of low Re extensions of the kε model. A review of these techniques from both a pragmatic and computational viewpoint (see ref. 5) has led to our use of a classical VanDriest mixing length formulation with damped law of the wall, as routinely employed in two layer algebraic turbulent model formulations (i.e., this comprises the inner layer component in the popular Cebeci-Smith and Baldwin-Lomax two layer formulations). Coupling between the inner (near wall) mixing length formulation and the outer kε formulation is set to occur at y^+ = 50. The values of k and ε at the matching point are determined via the requirement that the mixing length and kε turbulent viscosities match and that the turbulence is in a state of equilibrium. This yields lower boundary conditions for k and ε at the matching point. An analogous ML/kε coupling procedure has been developed by Arora et.al[12] for application to a variety of turbulent boundary layer problems. The inner/outer coupling relations are listed in Table 3 along with a schematic of the coupling procedure. Results obtained are relatively

TABLE 1 – Governing Equations

Continuity

$$\frac{\partial}{\partial s}(\rho U) + \frac{\partial}{\partial n}(h\rho V) = 0$$

Streamwise Momentum

$$\frac{\partial}{\partial s}(\rho U^2) + \frac{\partial}{\partial n}(h\rho UV) - K\rho UV + \frac{\partial P}{\partial s} =$$

$$\frac{\partial}{\partial n}\left(h\left[\tau s_n - \rho\overline{u'v'}\right]\right) - K(\tau s_n - \rho\overline{u'v'})$$

Normal Momentum

$$\frac{\partial}{\partial S}(\rho UV) + \frac{\partial}{\partial n}(h\rho V^2) + K\rho U^2 + h\frac{\partial P}{\partial n} =$$

$$\frac{\partial}{\partial n}\left(h\left[\tau_{nn} - \rho\overline{v'v'}\right]\right) + K(\tau_{ss} - \rho\overline{u'u'})$$

Energy

$$\frac{\partial}{\partial s}(\rho UH) + \frac{\partial}{\partial n}(h\rho VH) = \frac{\partial}{\partial n}\left(h\left[\frac{\mu}{P_r}\frac{\partial}{\partial n}(H)\right] - \frac{1}{2}Q^2\right.$$

$$\left. - \rho\overline{H'v'} + \overline{(\tau_{sn} + \tau'_{sn})(U + u')} + \overline{(\tau_{nn} + \tau'_{nn})(V + v')}\right)$$

Species Continuity

$$\frac{\partial}{\partial S}(\rho U\phi) + \frac{\partial}{\partial n}(h\rho V\phi) = \frac{\partial}{\partial n}\left(h\left[\frac{\mu}{P_r}\frac{\partial\phi}{\partial n}\right] - \rho\overline{\phi'v'}\right)$$

TABLE 2 – Parabolized Stress Terms

Using a Boussinesq type approximation

$$-\rho\overline{u_i'u_j'} = -\frac{2}{3}\rho k\,\delta_{ij} + \mu_t\left[\left(\frac{\partial U_i}{\partial X_j} + \frac{\partial U_j}{\partial X_i}\right) - \frac{2}{3}\,\mathrm{div}\,\bar{V}\right]$$

(where the turbulent kinetic energy $k = u_i'u_i'/2$), the parabolized turbulent stress terms in curvilinear surface-oriented coordinates take the following form:

$$-\rho\overline{u'v'} = \mu_t\left(\frac{\partial U}{\partial n} + \frac{KU}{h}\right)$$

$$-\rho\overline{u'u'} = -\frac{2}{3}\rho k - \frac{\mu_t}{h}\left[2KV + \frac{2}{3}\frac{\partial}{\partial n}(hV)\right]$$

$$-\rho\overline{v'v'} = -\frac{2}{3}\rho k + \mu_t\left[2\frac{\partial v}{\partial n} - \frac{2}{3h}\frac{\partial}{\partial n}(hV)\right]$$

The turbulent transport of a scalar variable, α, is expressed by

$$-\rho\overline{\alpha'v'} = \frac{\mu_t}{\sigma_\alpha}\frac{\partial \alpha}{\partial n}$$

For both H and ϕ, σ_α is taken to be the turbulent Prandtl number, P_{r_t}.

TABLE 3 – Turbulent Transport Equations and Inner (ML) / Outer (kε) Coupling

$$\rho U \frac{\partial k}{\partial s} + h\rho V \frac{\partial k}{\partial n} = \frac{\partial}{\partial n}\left[\frac{h\mu_{eff}}{\sigma_k}\frac{\partial k}{\partial n}\right] + \underline{P} - \rho\varepsilon$$

$$\rho U \frac{\partial \varepsilon}{\partial s} + h\rho V \frac{\partial \varepsilon}{\partial n} = \frac{\partial}{\partial n}\left[\frac{h\mu_{eff}}{\sigma_\varepsilon}\frac{\partial \varepsilon}{\partial n}\right] + \frac{\varepsilon}{k}\left(C_1\underline{P} - C_2\rho\varepsilon\right)$$

where the production term, $\underline{P}$, is given by

$$\underline{P} = \mu_t \left(\frac{\partial U}{\partial n} + \frac{KU}{h}\right)^2$$

$$k_{I*} = L^2_{I*} \left|\partial u/\partial n\right|^2_{I*}/C_\mu^{1/2}$$

$$\varepsilon_{I*} = C_\mu^{3/4} k_{I*}^{3/2}/L_{I*}$$

$$\mu_t = \rho L^2 \left|\frac{\partial u}{\partial n}\right|$$

$$L = \kappa n \left[1 - \exp(y^+/A)\right]$$

$\kappa = .41$ and $A = 27$

$$y^+ = n \tau_s^{1/2} \rho^{1/2}/\mu_l$$

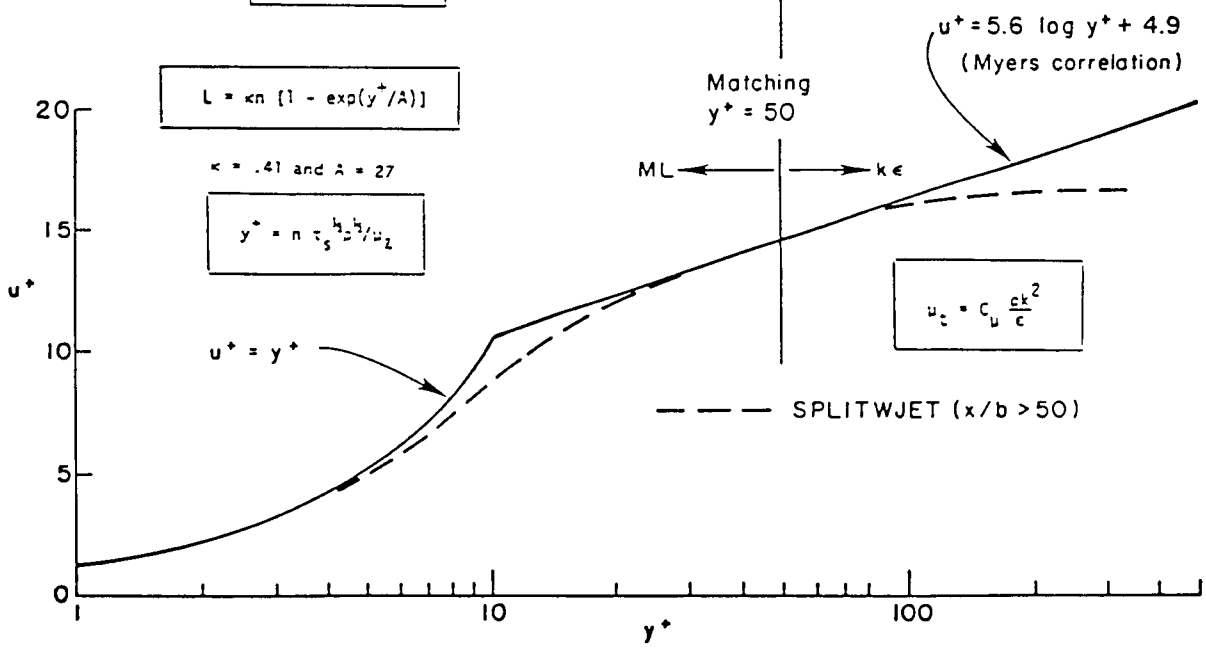

insensitive to the value of y^+ utilized for the coupling as long as it nominally remains in the log region (viz., $20 \sim y^+ \sim 100$).

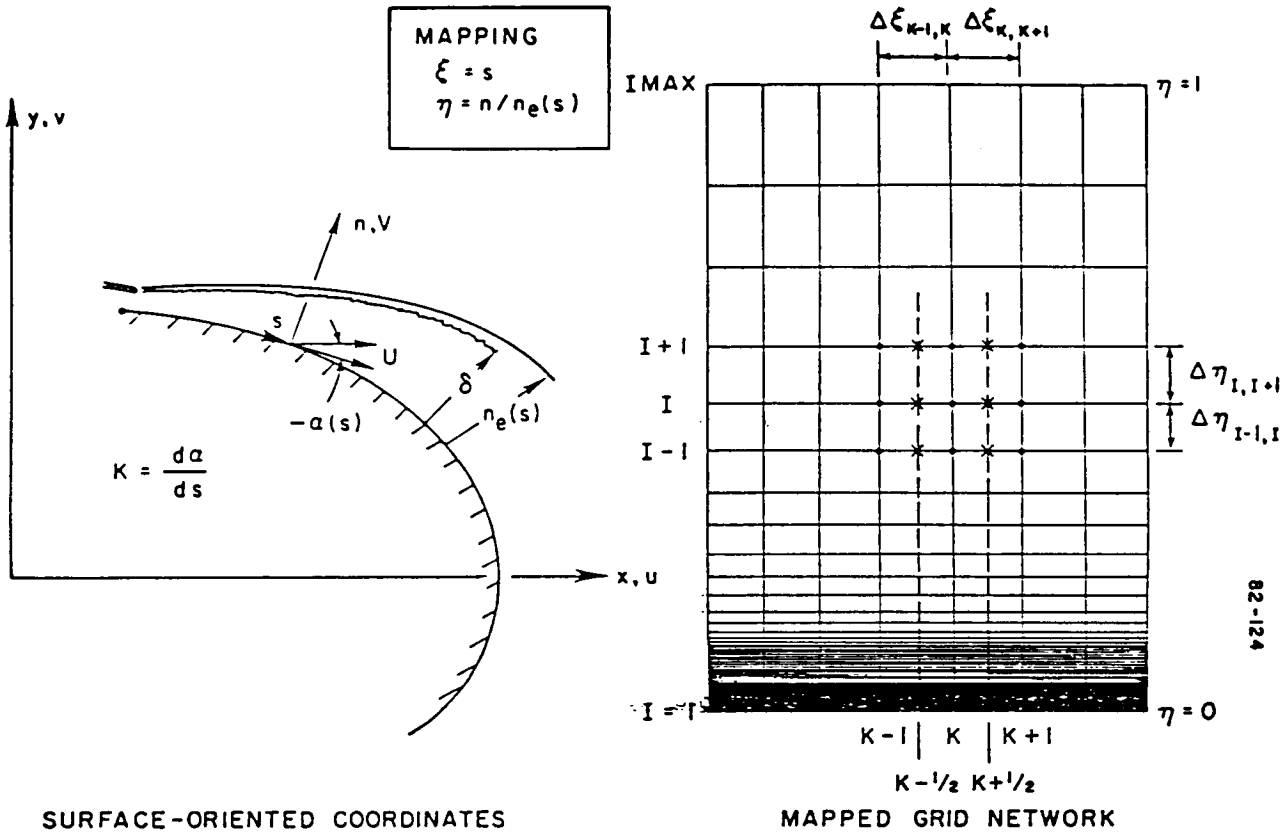

FIGURE 2. Surface-Oriented Grid Nomenclature and Mapped/Stretched Grid Utilized.

While both the mean flow and turbulence model equations contain a number of curvature terms arising from the transformation to curvilinear, surface-oriented coordinates, numerous investigators have demonstrated that additional, curvature corrections terms are required to account for the strong effects of curvature on wall jet turbulence structure. The analogy drawn by Bradshaw[13] between curvature and buoyancy has been utilized by most investigators as the basis for heuristic corrections to algebraic or two-equation turbulence models. Defining the curvature parameter, $s = -KU/(\partial U/\partial n)$, a curvature correction to the ML formulation is given by:

$$L = \frac{L_o(1-\alpha s)}{(1-s)} \tag{1}$$

where L_o is the planar length scale value, while α is a constant, $(5 < \alpha < 10)^o$. This treatment has been implemented for curved wall jets by Foloyan and Whitelaw[14] who utilized a complete (inner/outer) mixing length formulation. For the present near wall use of the mixing length formulation, this correction will only be required in situations with very large curvature. For problems with small to moderate curvature, the near wall region correction to L_o is negligible.

Launder and coworkers[15] have developed a curvature correction for the $k\varepsilon$ model which utilizes a single empirical coefficient, C_c. The curvature correction is proportional to a Richardson number, Ri_c, based on the turbulence time scale. In their formulation, the local Richardson number is given by:

$$Ri = -KU \left(\frac{k}{\varepsilon}\right)^2 \frac{\partial U}{\partial n} \tag{2}$$

and the C_2 coefficient of the ε equation is modified as follows:

$$C_2 = 1.92\ (1 - C_c Ri) \tag{3}$$

Values of C_c of about 0.2 have yielded optimal predictions for a variety of curved boundary layer flows as described in reference 15.

An analogous type of curvature correction for the $k\varepsilon$ model has been developed by Hah and Lakshminarayana at Penn State[16]. They have modified the C_1 coefficient of the ε equation as follows:

$$C_1 = 1.43\ (1 + C_c Ri) \tag{4}$$

We have implemented the Penn State correction using the Launder definition of Ri in our model.

At supersonic wall jet velocities, a compressibility correction analogous to that of Dash, et.al.[17] for free shear layers, may be required. Here, a factor whose magnitude varies from 1.00 at M = 1 to 0.25 for large Mach numbers is used to multiply the C_μ coefficient of the $k\varepsilon$ model. This correction factor is an empirical expression derived from experimental free shear layer observations and is calculated as follows:

$$f_{cc} = 0.25 + 0.75/\{1.0+\exp[24.73(M_\tau-0.2)]\} \quad (5)$$

where M_τ is the Mach number characterizing the fluctuating velocity field, (e.g., $k^{1/2}$ divided by the local speed of sound).

For free shear layers, M_τ is evaluated at the position of maximum k at each station. Its adaptation to supersonic wall jets would entail utilizing the value of k at the position of maximum velocity and incorporating a transverse dependence to smoothly reduce the correction in the 'boundary layer' portion of the wall jet (below the peak velocity point). Data exhibiting the dependence of mixing on the wall jet Mach number is not presently available to derive a correlation analogous to that of equation (5) for wall jet flows.

NUMERICAL PROCEDURES

Splitting of Solution into Parabolic and Elliptic/Hyperbolic Components

The approach taken in WJET involves combining:

(1) a parabolic solution of the streamwise momentum, energy, species parameter, and turbulence model equations with the streamwise pressure gradient term, $\partial P/\partial s$ (s,n) specified - this solution yields the variation of U, H, ϕ, k and ε;

(2) an elliptic/pressure-split solution of the coupled continuity and normal momentum equations in subsonic regions which yields the variation of pressure and normal velocity across the wall jet; and,

(3) a hyperbolic/upwind characteristic-based solution of the coupled continuity and normal momentum equations in supersonic regions which yields the local pressure and flow angle.

These three solution procedures are unified in the WJET code to provide generalized spatial marching capabilities for a broad category of wall jet problems.

Parabolic Analysis

The WJET parabolic algorithm integrates the U momentum, H, ϕ, k and ε equations (Table 1) in mapped rectangular coordinates (Figure 2). The mapped, vectorized equations take the form:

$$\rho U \frac{\partial f}{\partial \xi} + b(hcV - \frac{a}{b}\rho U)\frac{\partial f}{\partial \eta} = b^2 \frac{\partial}{\partial \eta}\left[\frac{h\mu_{eff}}{\sigma_f}\frac{\partial f}{\partial \eta}\right] + g_f \qquad (6)$$

where:

$$f = [\ U,\ H,\ \phi,\ k \text{ and } \varepsilon\ ]^T$$

a and b are mapping parameters, and g_f is the source term. The equations are spatially integrated using an upwind/implicit algorithm. A fixed number of grid points are distributed between the wall ($\eta = 0$) and outer viscous boundary ($\eta = 1$) whose growth is obtained via adaptive methodology keyed to the edge gradients. The distribution of grid points, $\eta(I)$, remains invariant throughout the calculation and the stretching utilized can be arbitrarily stipulated, or specified using built in grid distribution parameters. The equations are solved in an uncoupled manner (the source terms are solved explicitly) and the difference equations then take standard tridiagonal form. Complete details of the parabolic algorithm are available in references 4 and 5.

Pressure-Split Subsonic Cross-Flow Analysis

To analyze subsonic wall jets with large curvature, a pressure-splitting approach analogous to that of Bradshaw and coworkers[18,19] is utilized. In the pressure-splitting procedure, the global pressure field, $P^*(s,n)$, utilized to evaluate $\partial P/\partial s$ in the streamwise momentum equation, must be stipulated. This is initially estimated to be the inviscid pressure field prevailing in the region occupied by the wall jet. In the pressure-splitting approximation, the parabolic equations are integrated with $\partial P/\partial s$ obtained from $P^*(s,n)$. However, the pressure field is revised in the course of the spatial integration by solving the coupled continuity and normal momentum equations across the jet with the inviscid pressure prevailing at the edge of the jet serving as an outer boundary condition. Global convergence in regions of strong curvature is obtained by repeating the calculation with the revised pressure field until the imposed and upgraded pressures are effectively the same.

By manipulations described in references 6 and 7, the continuity equation (in mapped coordinates) can be written in terms of pressure, P, and normal velocity, v, yielding:

$$\gamma\,(a+\bar{V}/U)\frac{\partial P}{\partial \eta} + (\gamma-1)\,\rho\, V \frac{\partial V}{\partial \xi} + \left[\frac{\rho b h C^2}{U} + (\gamma-1)\frac{\rho V \bar{V}}{U}\right]\frac{\partial V}{\partial \eta} = g_p \qquad (7)$$

where the source term, g_p, is listed below:

$$g_p = \rho b C^2 \frac{\partial}{\partial \eta}\left(\frac{a}{b}\right) + K \rho C^2 \frac{V}{U} - \left[\frac{\rho C^2}{U} + (\gamma-1)\rho U\right] \frac{\partial U}{\partial \xi}$$

$$+\left[\frac{\rho a C^2}{U} - (\gamma-1)\rho \tilde{V}\right] \frac{\partial U}{\partial \eta} + (\gamma-1)\rho \left[\frac{\partial H}{\partial \xi} + \frac{\tilde{V}}{U}\frac{\partial H}{\partial \eta}\right]$$

$$- \gamma \frac{\partial P^*}{\partial s} + \frac{\rho C^2}{b}\frac{\partial b}{\partial \xi}$$

Note that g_p contains partial derivatives of U and H (which are evaluated a priori as part of the parabolic solution) and also contains the prescribed streamwise pressure gradient term. The normal momentum equation given below (g_v represents turbulent stress terms - see Table 2):

$$\rho U \frac{\partial V}{\partial \xi} + \rho \tilde{V} \frac{\partial V}{\partial \eta} + bh \frac{\partial P}{\partial \eta} + K \rho U^2 = g_v \qquad (8)$$

is solved with the continuity equation in a coupled manner to yield the variation of P and v across the wall jet (see references 6 and 7 for details).

Figure 3 illustrates results obtained using this pressure-split approach to analyze the simple case of a curved wall jet issuing into still air. Shown are the wall jet geometry, maximum velocity decay (contrasted to the variation for a flat wall), induced entrainment (also contrasted to the flat wall variation), surface pressure variation (utilizing viscous and inviscid forms of the normal momentum equation) and a decomposition of terms in the normal momentum equations showing their individual contributions to ΔC_p across the wall jet. Note that the very significant contribution of turbulent stress terms (specifically $\overline{v'v'}$) to the ΔC_p across the jet. Complete details of this case are provided in references 6 and 7.

Upwind Characteristic-Based Supersonic Wave Solver Analysis

To analyze supersonic regions of underexpanded wall jets, a characteristic-based procedure is employed to locally evaluate the wave field (e.g., to obtain pressures and flow angles at each grid point). The approach taken involves a 'modern' formulation of viscous-characteristic methodology originally developed about 20 years ago[20,21]. The viscous-characteristics approach involves manipulating the continuity and normal momentum equations to obtain characteristic relations of the form:

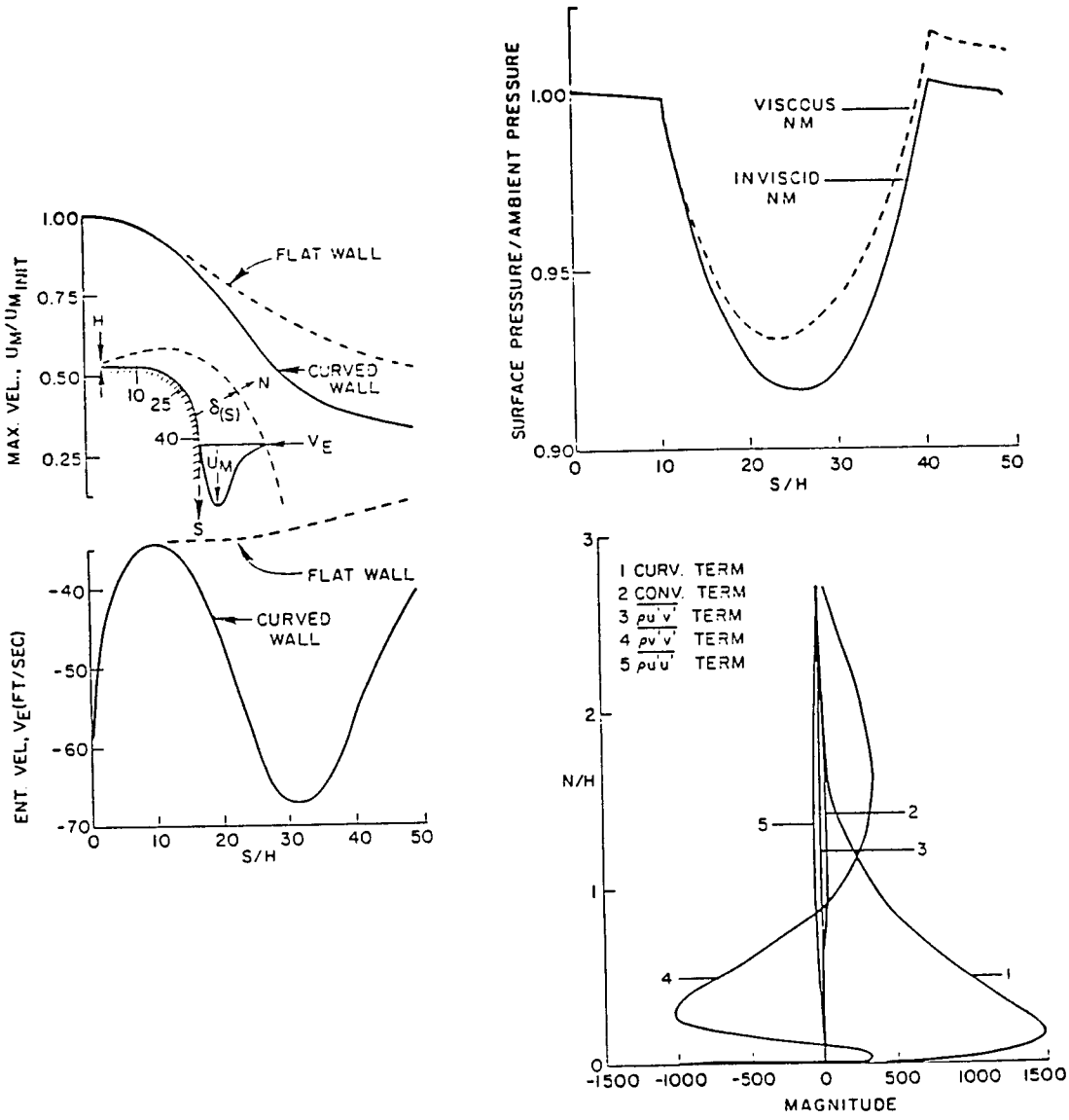

FIGURE 3. Pressure-Split Analysis of Curved Wall Jet Issuing into Still Air.

$$\frac{\sin\mu\cos\mu}{\gamma}\,d\ln p \pm d\theta = \frac{-J\sin\theta\sin\mu}{r}\,d\lambda^{\pm} + \tilde{F}^{\pm}d\lambda^{\pm} \qquad (9)$$

where the source term, $\tilde{F}$, contains the viscous stress terms, and diffusive transport terms, appearing on the r.h.s. of the streamwise momentum (F_u), normal momentum (F_v), and energy (F_H) equations. The source term, $\tilde{F}$, is given by:

$$\tilde{F}^{\pm} = A(F_u+F_v) + BF_H \qquad (10)$$

where:

$$A = -[(1+(\gamma-1)M^2)\sin\mu\cos\theta \pm \cos\mu\sin\theta]/(\gamma PM^2)$$

and:

$$B = -(\gamma-1)\sin\mu/(\gamma PQ)$$

The nomenclature for the characteristic equations is exhibited in Figure 4.

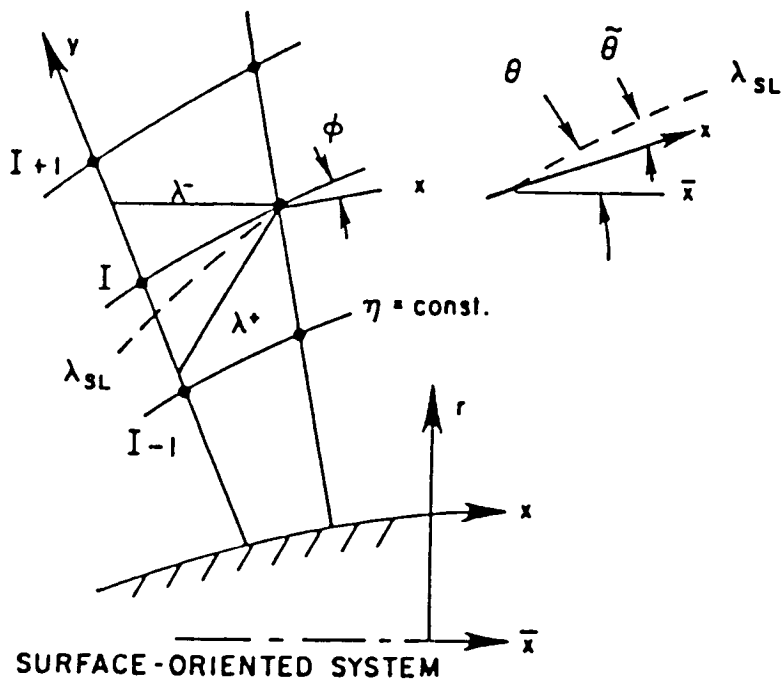

FIGURE 4. Nomenclature for Characteristic Equations.

In earlier applications of this approach, inverse characteristic methodology was utilized which was extremely cumbersome. The new approach developed[8,9] involves representing total derivatives along characteristics as a combination of streamwise and normal partial derivatives in a mapped (ξ,η) computational space. The normal derivatives are evaluated at the known station using an upwind formulation keyed to the λ^- characteristic direction. With the manipulations described in references 8 and 9, the pressure at grid point I at $\xi + \Delta\xi$ can be evaluated as a function of the pressures and flow angles at grid points I-1, I and I+1 at station ξ. This new formulation is summarized in Table 4. In present applications of WJET, the coupled parabolic/hyperbolic solution is performed in the following three step sequence:

(1) Prediction of wave field (P,θ) at $\xi + \Delta\xi$ solving pressure equation and comparable flow angle equation (Table 4) using coefficients evaluated at ξ at characteristic intersection points, and, viscous terms, F_u, F_v and F_H evaluated at ξ at grid points I.

(2) Solution of parabolic system of equations (eq. 6) yielding f at $\xi + \Delta\xi$. Pressure gradients 'prescribed' in accordance with wave field solution of step (1).

(3) Correction of wave field at $\xi + \Delta\xi$ using coefficients averaged along characteristics and, values of F_u, F_v and F_H which are evaluated at $\xi + \Delta\xi$ if the parabolic algorithm of Step (2) is fully implicit; or, are averaged across the integration step if a Crank-Nicolson parabolic procedure is utilized.

The formulation was first checked out in the inviscid limit for weak shock-capturing capabilities and produced results comparable to those of the SCIPPY code (explicit MacCormack algorithm) as exhibited in Figure 5 (see ref. 8 for details). For strong shock waves in inviscid regions, artificial viscosity must be introduced to stabilize the shock calculation and to generate entropy. The approach taken parallels that utilized in Beam and Warming based PNS algorithms and is described in reference 22.

The wave solver formulation was then checked out for supersonic viscous/inviscid jet interaction problems by comparing WJET predictions with those of the well tested SCIPVIS PNS jet mixing model (see refs. 23 - 26). These comparisons are described in references 8, 22 and 27. A typical comparison is exhibited in Figure 6 showing the interaction of an expansion fan with a free turbulent shear layer.

TABLE 4 - Characteristic-Based Upwind Formulation for Determining Local Pressures in Supersonic Flow Regions

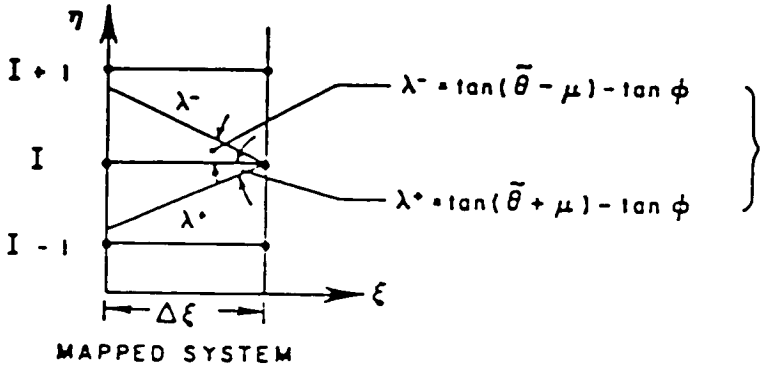

$$\left.\frac{d}{dx}\right|_{\lambda^{\pm}} = \frac{\partial}{\partial \xi} + \lambda^{\pm}\frac{\partial}{\partial \eta}$$

Pressure-Wave Solver Equations in Mapped Coordinates

$$\left.\frac{d}{dx}\right|_{\lambda^{\pm}} = \frac{\partial}{\partial \xi} + \lambda^{\pm}\frac{\partial}{\partial \eta}$$

$$C\left[\frac{\partial \ln p}{\partial \xi} + \lambda^{\pm} b \frac{\partial \ln p}{\partial \eta}\right] \pm \left[\frac{\partial \theta}{\partial \xi} + \lambda^{\pm} b \frac{\partial \theta}{\partial \eta}\right] = F^{\pm}$$

$$C = \frac{\sin u \cos u}{\gamma}$$

$$F^{\pm} = \tilde{F}^{\pm}/\cos(\theta \pm \mu)$$

$$\bar{p}_I = a_1 p_{I+1} + a_2 p_I + a_3 p_{I-1} + a_4 \theta_{I+1} + a_5 \theta_I + a_6 \theta_{I-1} + \bar{F}_I$$

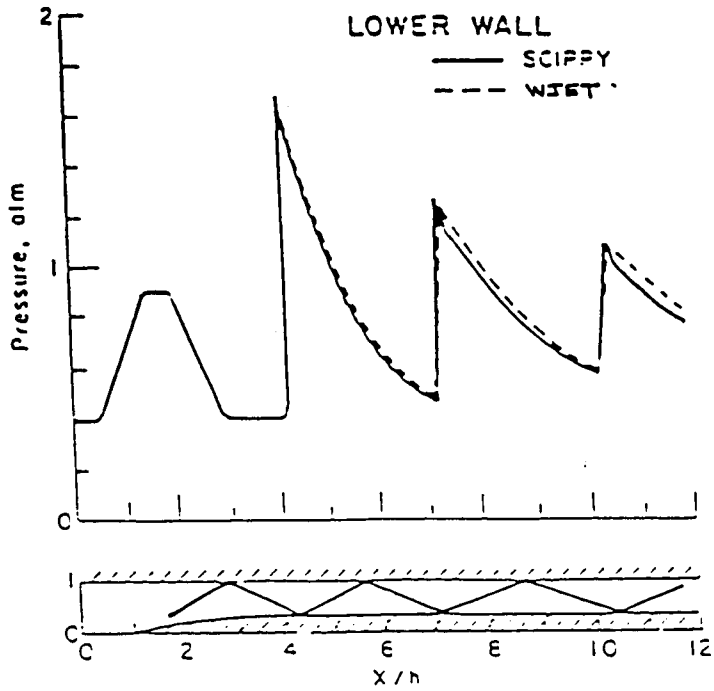

FIGURE 5. Comparison of WJET Wave Solver and SCIPPY Shock-Capturing Predictions.

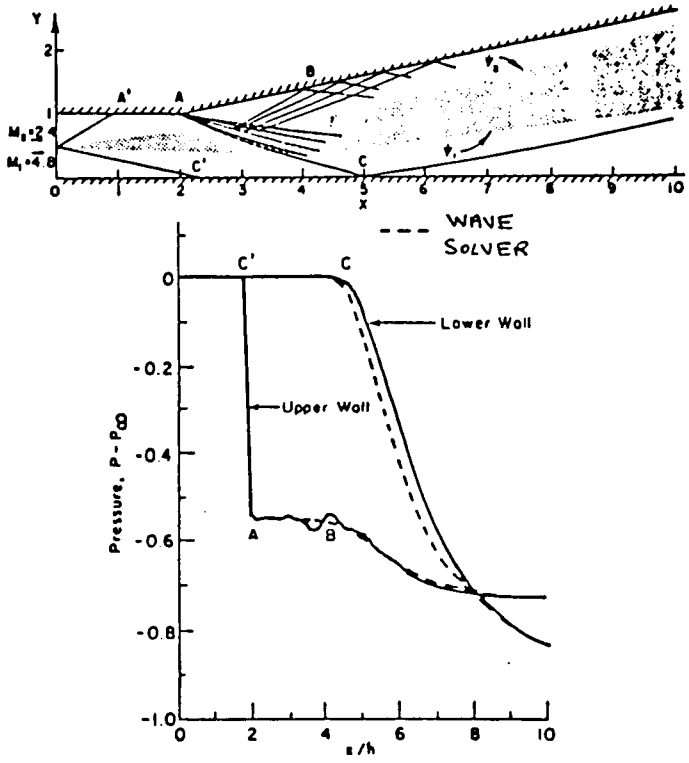

FIGURE 6. Comparison of Wave/Shear Layer Interactions; SCIPVIS (——) Versus Wave Solver (----) Predictions.

Unified Parabolic/Pressure-Split/Wave Solver Model

The WJET code unifies the three solution procedures described above, providing for PNS-based spatial marching capabilities comparable to those developed for free jet problems (see Table 5 and refs. 23 - 26). Referring to Figure 7, the wall jet problem is more complicated than the corresponding free jet problem since subsonic/supersonic coupling is required at both inner (I_1^*) and outer (I_2^*) sonic lines.

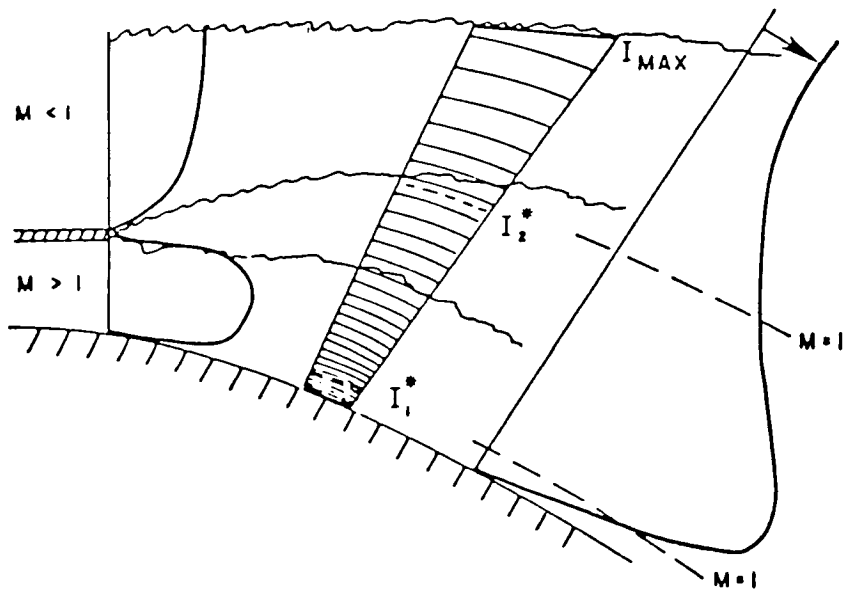

FIGURE 7. Flow Segmentation for Underexpanded Wall Jet Problem.

For free jets, a data base exists for underexpanded problems (see, e.g., ref. 28) which has been utilized for detailed verification[23,25,26]. Figure 8 exhibits predicted wave/mixing layer structure of mildly underexpanded Mach 2 free jet issuing into still air, and, comparisons of predicted and measured turbulent intensities, u'u' (u'u' = 2gk where k is the predicted turbulent kinetic energy and g is an isotropy parameter used to related k to u'u'; g = 2/3 represents the isotropic situation and appears to best correlate with the measurements). Figure 9 exhibits comparisons of the predicted pressure variations (axis and off axis) with the data. The comparisons exhibited here (and the additional comparisons described in refs. 23, 25, 26 and 28) are quite good and were obtained using the kW turbulence model.

TABLE 5 – Aspects of PNS Approach for Free Jets

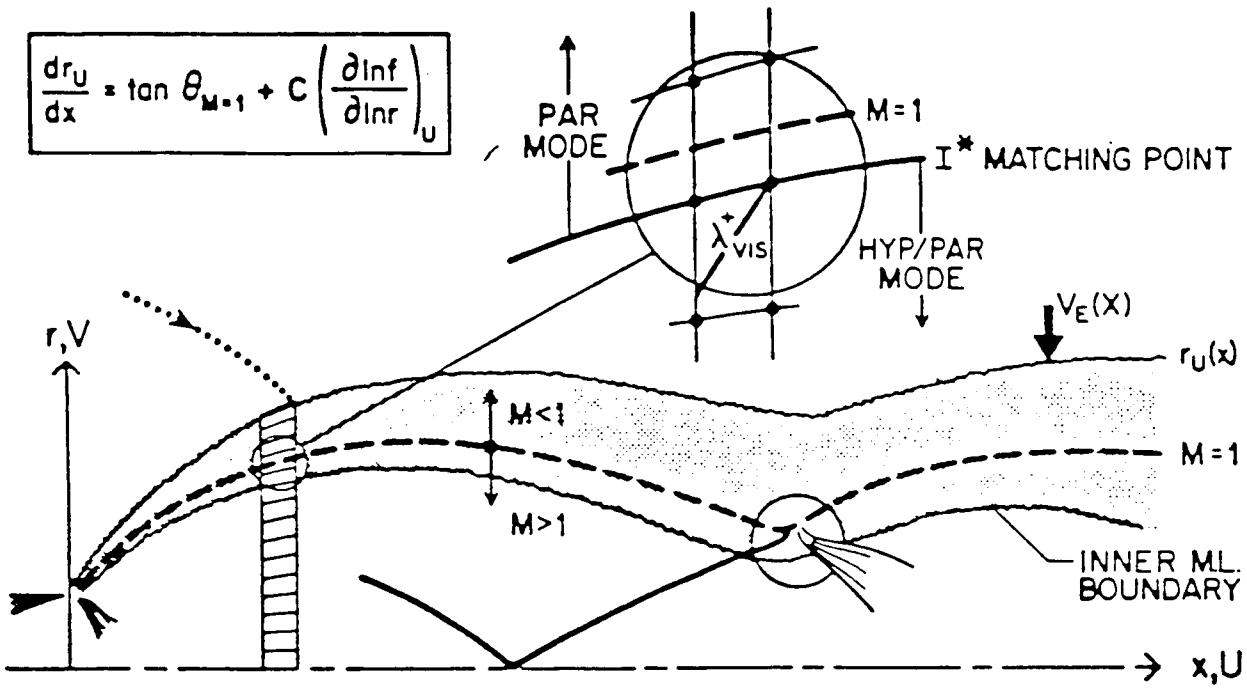

- Shock-Capturing PNS Solution in Supersonic Mixing Regions
- Pressure-Split Approximation in Subsonic Mixing Regions
- Subsonic/Supersonic Coupling at Viscous Sonic Lines
- Use of Compressibility Corrected Two-Equation Turbulence Models
- Solution in Mapped Coordinates Encompassing Viscous/ Inviscid Jet
- Direct-Coupling with External Flow Solution at Outer Viscous Boundary

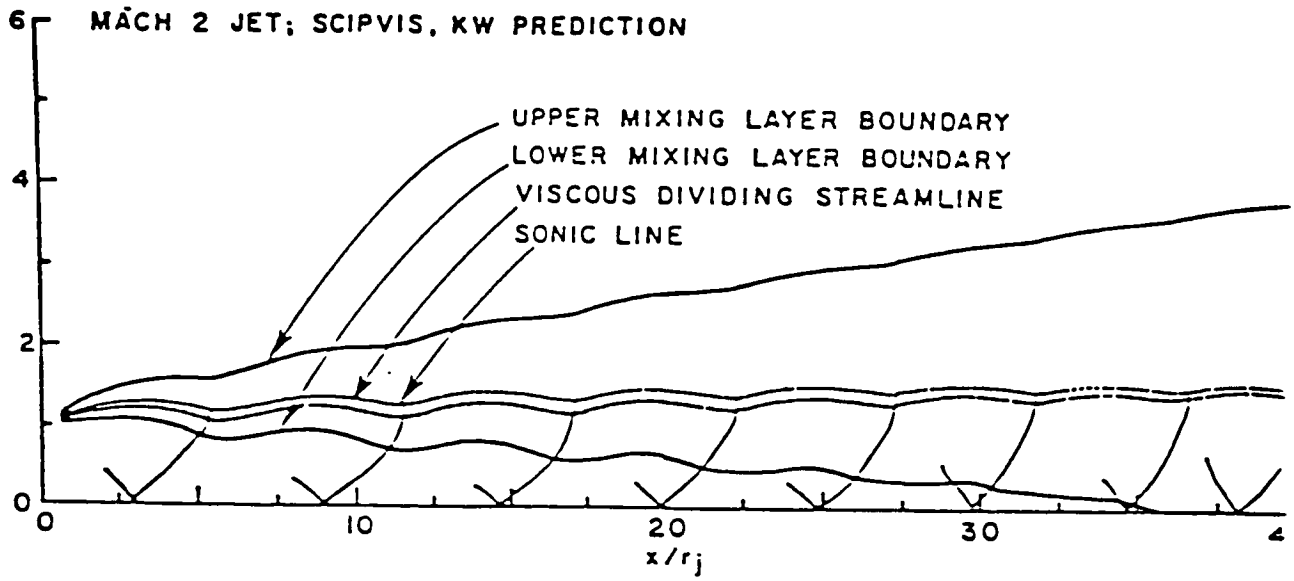

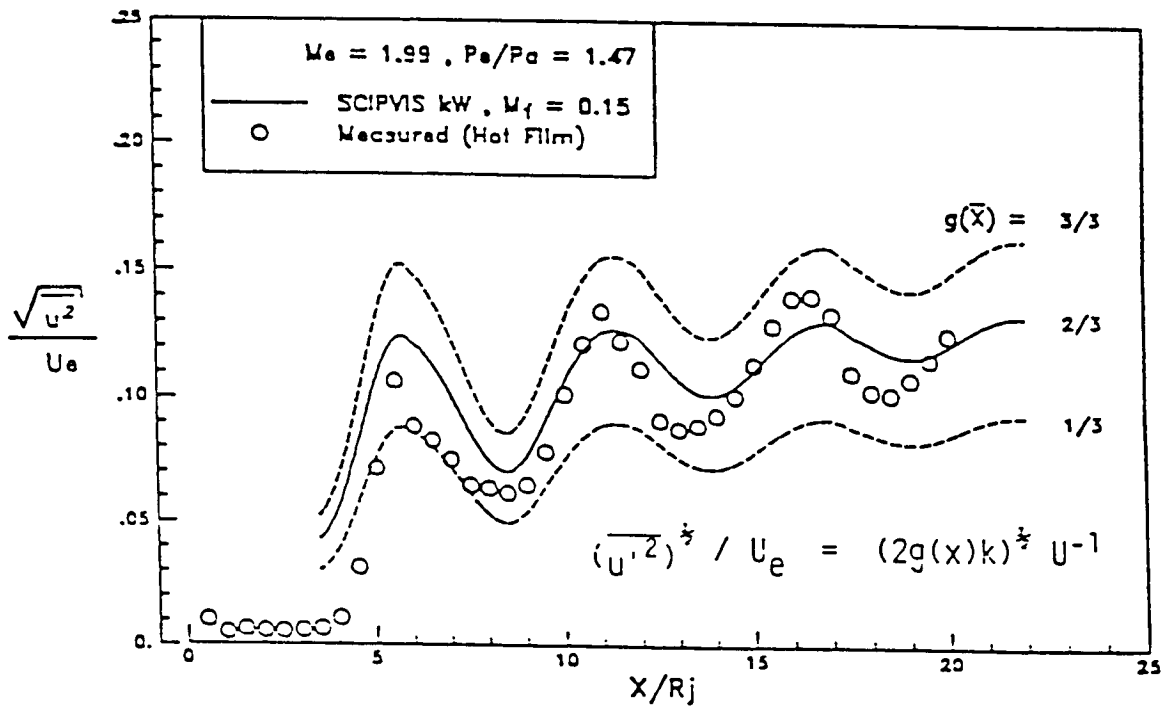

FIGURE 8. Predicted Wave/Mixing Layer Structure of Underexpanded Mach 2 Free Jet and Comparisons of Turbulent Intensity with Data.

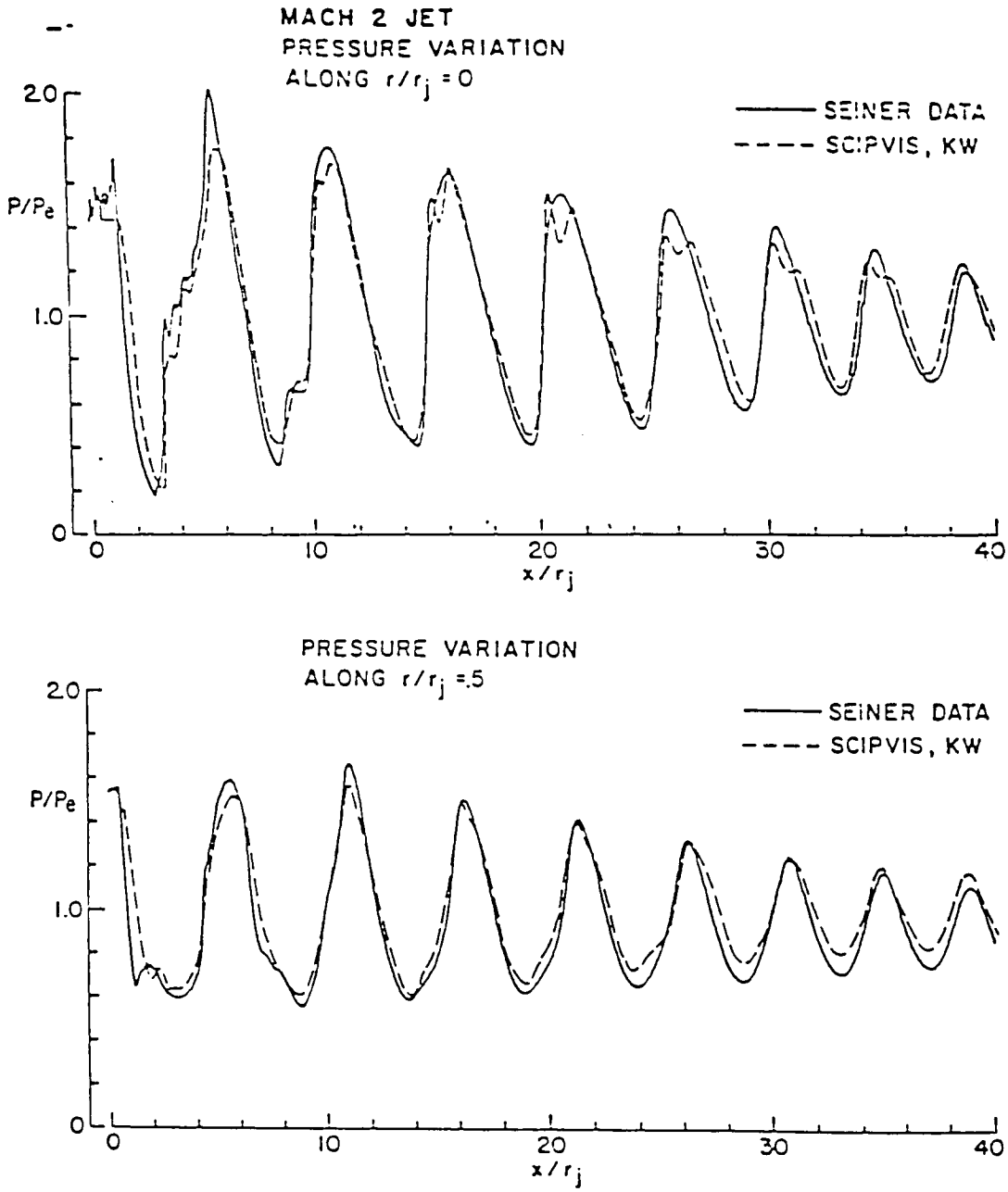

FIGURE 9. Comparison of Predicted and Measured Streamwise Pressure Variations; kW Model Solution.

Results with a standard $k\varepsilon$ model exhibit too fast a rate of mixing as would be expected from earlier comparisons with simple (balanced pressure) shear layer and jet data at supersonic velocities. The issue of compressibility effects in supersonic free turbulent shear layers has been addressed from a pragmatic viewpoint (see refs. 17, 29 - 31) and two-equation turbulence models are now available[32] which can adequately analyze the rather broad base of 'fundamental' high speed free shear layer/jet data and also, some non-fundamental situations with significant wave structure, as exhibited above.

Preliminary calculations made with WJET for an underexpanded curved wall jet are exhibited in Figures 10 through 12. Figure 10 exhibits the overall geometry and predicted streamwise variations of principal jet surfaces (viz., inner/outer shear layer boundaries where ϕ = 0.95/0.05, jet half radius, outer sonic line, and outer/adaptive computational boundary) in physical (x,y) and surface-oriented coordinates. Figure 11 exhibits the variation of wall pressure and skin friction coefficient - note the rapid response of skin friction to the wave field (the details of the interactive procedure for analyzing the near wall subsonic portion of the wall jet are described in refs. 8 and 9). Figure 12 exhibits predicted profiles of pressure and Mach number across the jet. Also shown is the normal grid distribution which is highly stretched in the near wall region (viz., from wall to position of velocity maximum - typically, y^+ of second grid point is ~ 1 and the same number of grid points span the near wall region and the outer region), and, equally spaced in the outer region (from maximum velocity position to outer boundary).

Unfortunately, adequate data to validate underexpanded wall jet solutions and thus resolve turbulence issues regarding compressibility effects, etc., is not presently available, and, hence, no such comparisons with data are exhibited in this article. The high speed wall jet data base available has recently been reviewed (under programs geared towards high speed film cooling and tangential injection in supersonic combustors). No data has been identified as suitable for turbulence model validation due to lack of key measurements (e.g., detailed initial profiles, turbulence levels, etc.). These issues are described in references 33 and 34.

Coupling Procedures for Wall Jet and External Potential Flow

To incorporate the wall jet code in a zonal approach for analyzing circulation control airfoils, a variety of coupling techniques were reviewed as discussed in references 4 and 5. Figure 13 schematizes coupling procedures available for subsonic wall jets. The displacement-thickness coupling approach overlaps the inviscid and viscous solutions and utilizes standard boundary layer concepts which break down for thick, highly curved viscous layers where the normal pressure variation is significant. The direct pressure-split coupling approach introduced

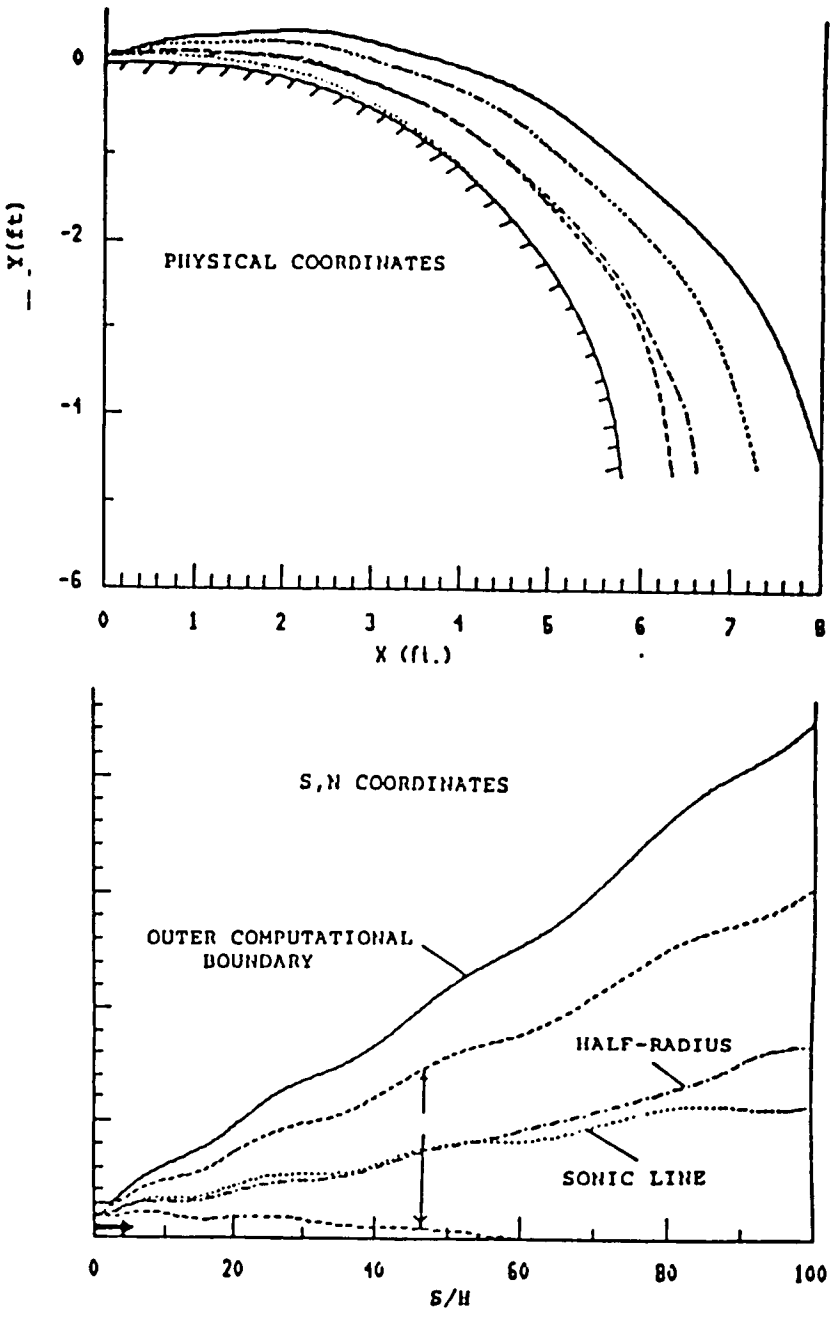

FIGURE 10. Predicted Features of Curved Underexpanded Wall Jet Issuing into Still Air.

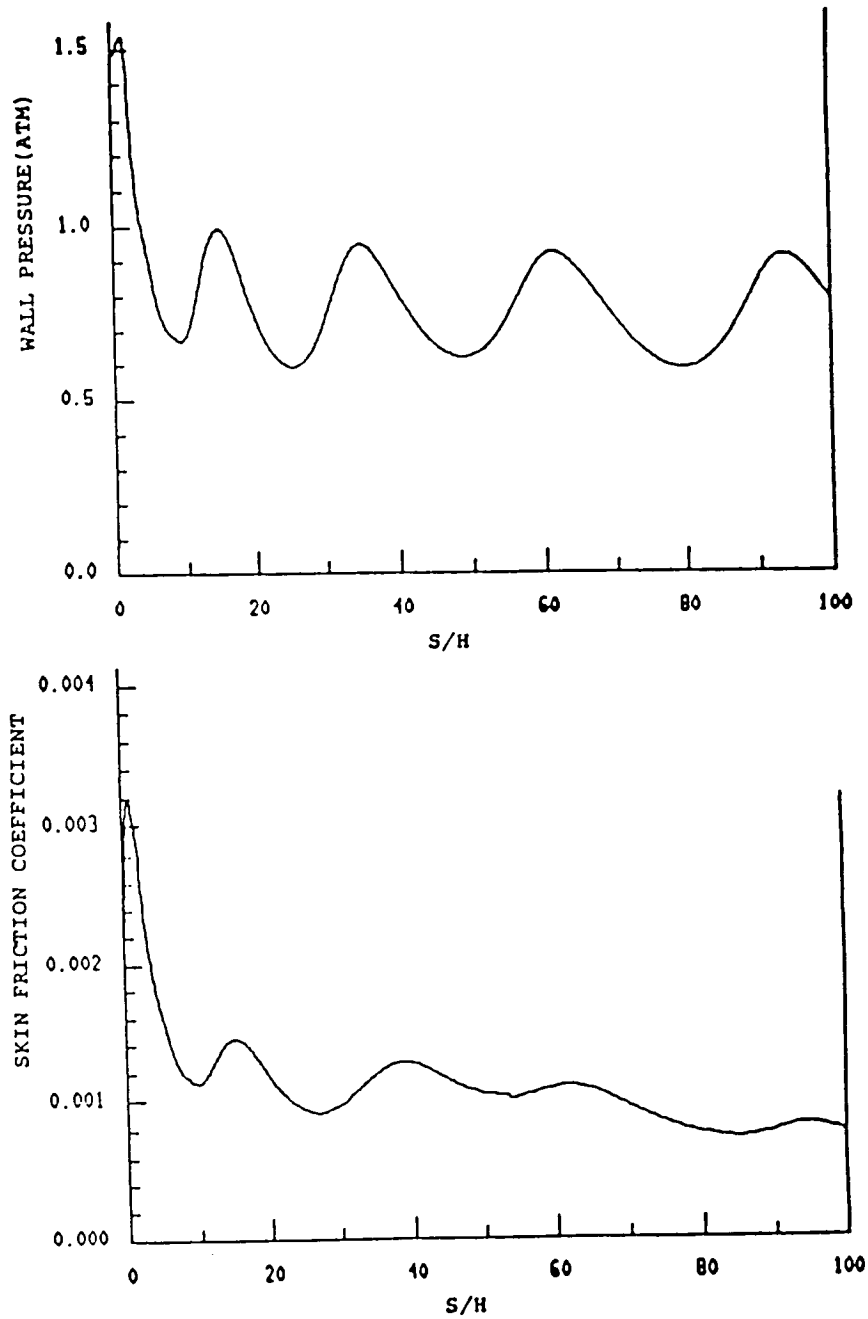

FIGURE 11. Predicted Wall Pressure and Skin Friction Variation for Curved Underexpanded Wall Jet Issuing into Still Air.

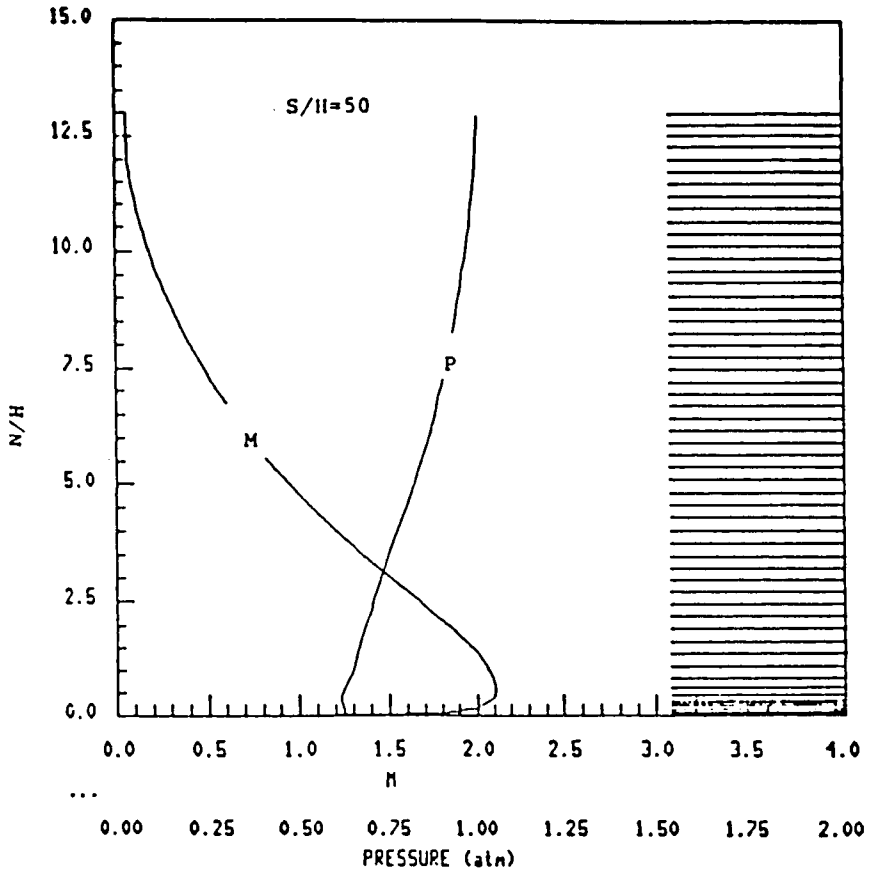

FIGURE 12. Pressure and Mach Number Profiles at Position Fifty Slot Heights Downstream of Slot.

by Bradshaw and coworkers[18,19] couples the viscous and inviscid solutions at the jet viscous boundary, and the pressure field within the jet is determined by the pressure-splitting methodology described above which directly accounts for the contribution of stress/diffusive terms. Details of this coupling methodology for wall jets are described in references 6 and 7. Velocity-split coupling also directly involves a complete overlap of viscous and inviscid solutions, but here, the coupling is intimate and can account for separated flow regions. Applications of this approach to nozzle afterbody problems have been quite successful (see refs. 37 and 38) and results comparable to full NS results have been achieved in a fraction of the run time.

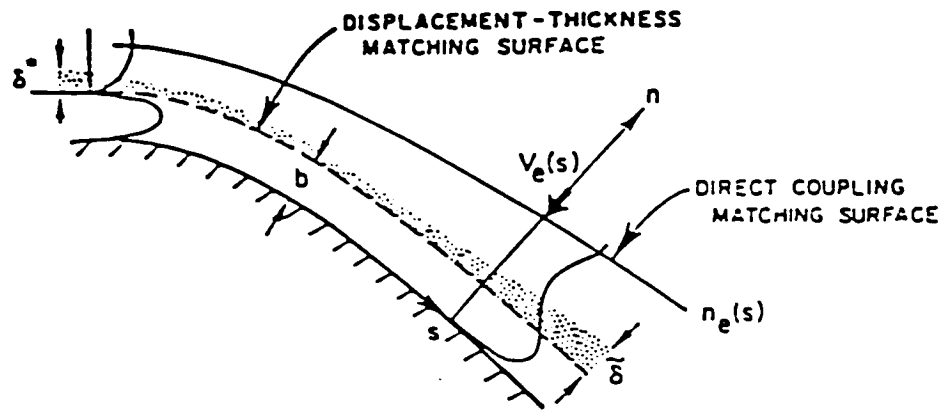

• DISPLACEMENT-THICKNESS COUPLING

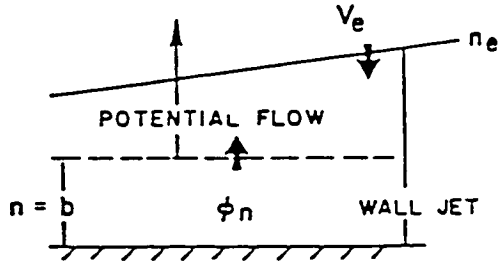

COUPLING

WALL JET		POTENTIAL FLOW
V_e along n_e	—	ϕ_n along n = b
$\frac{\partial P}{\partial s}, U_e, T_e$	—	P_b, U_b, T_b

• DIRECT PRESSURE-SPLIT COUPLING

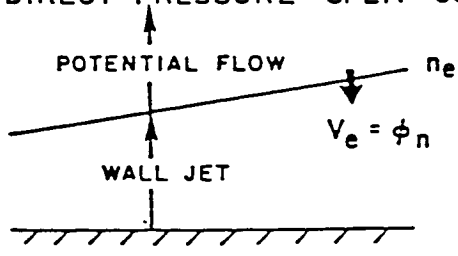

COUPLING

- As Above but Match along n_e
- P(s, n) in Jet from Normal-Momentum via Several Iterative Sweeps for Given P_e

VELOCITY-SPLIT COUPLING

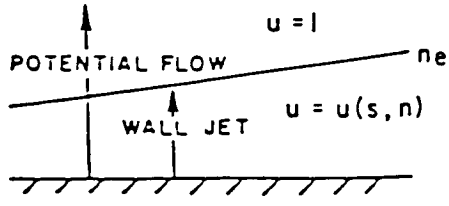

COUPLING

$U/U_E = u(1 + \phi_s)$

$V/U_E = \phi_n$

- Solutions Overlap
- Solve ϕ Equation with u(s, n) Prescribed
- Solve Wall Jet Equations with ϕ Prescribed

FIGURE 13. Coupling Procedures for Subsonic Wall Jet.

For supersonic wall jets, the viscous/inviscid coupling requirements become more complex and no coupling methodology has as yet been made operational. For supersonic free jets, the overlaid viscous/inviscid coupling approach of Dash, et.al.[39], which employs displacement-thickness coupling concepts[40] (Figure 14) has been successful in studies geared toward nozzle afterbody drag predictions[41]. The RAXJET zonal component model (which is based on this methodology) employs components (Figure 15) analogous to those utilized in the TRACON CC airfoil code. The extension of the overlaid coupling approach to wall jets was investigated by Dash[42] but found not to be a viable method (see references 4 and 5).

Recently, the direct-coupling approach for supersonic free jets has been made operational[43] utilizing a free jet version of WJET (the SPLITP model[27]) coupled to the VSAERO panel method potential solver[44]. The work (supported by AFWAL) is geared towards developing interactive methodology for VSTOL jets (Figure 16). Typical predictions are exhibited in Figures 17 and 18. Figure 17 depicts the direct-coupling boundary comprised of the nacelle surface and paneled jet boundary, $\tilde{y}_B$, which lies close to the outer jet computational boundary. Also exhibited is the source distribution, ϕ_n, applied along $\tilde{y}_B$, which combines the effects of jet entrainment (suction) and jet blockage (underexpansion - shock effects). Figure 18 depicts the predicted pressure variation along the coupling boundary $\tilde{y}_B$. In the first pass iteration, the jet is represented as a solid sting and the pressure is given by $C_p^{(1)}$. In subsequent iterations, the coupled effects of jet entrainment and blockage are evident in the pressure variation. See references 29, 43 and 45 for further details of this methodology. Progress towards using advanced coupling concepts for incorporating WJET into the TRACON CC code[12], is described in Part II of this paper[11].

ANALYSIS OF FUNDAMENTAL DATA

The data analyzed by WJET are limited to situations for which WJET can operate on a stand alone basis. Hence, the cases involve rather fundamental situations and primarily reflect upon the ability of the turbulence model incorporated in WJET. The analysis of wall jets in realistic CC airfoil flowfields requires coupling of WJET with TRACON[11]. Most of the cases analyzed have already been described in refs. 4 and 5 and only a very brief overview will be provided here.

Planar Wall Jet Issuing Into Still Air

For this simplest of all wall jet cases, the overall jet growth parameters (viz., half radius and locus of maximum velocity) predicted using the hybrid $k\varepsilon$/VanDriest turbulence model are in reasonable agreement with the data (see Figure 19), and, in better agreement than

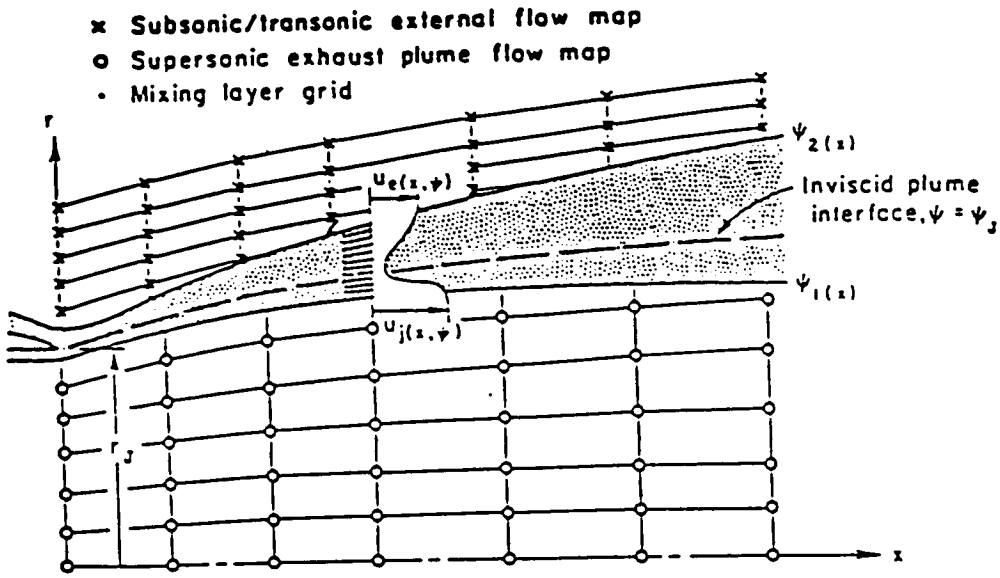

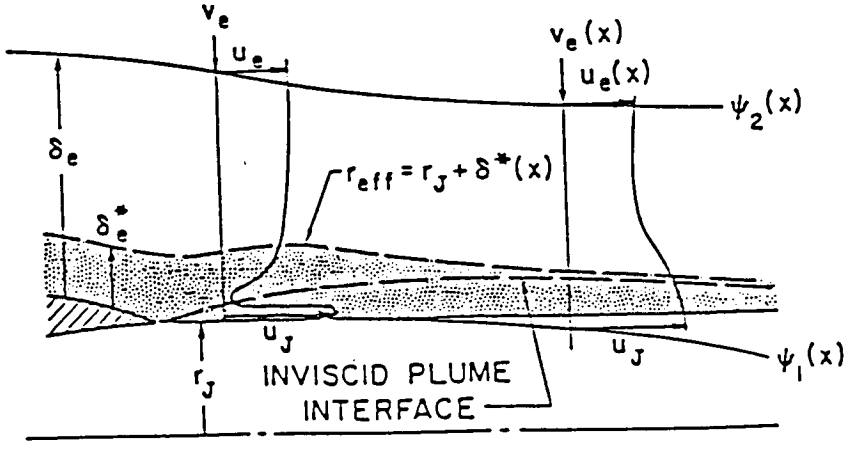

FIGURE 14. Overlaid Viscous/Inviscid Coupling Approach and Displacement-Thickness Representation of Plume Boundary.

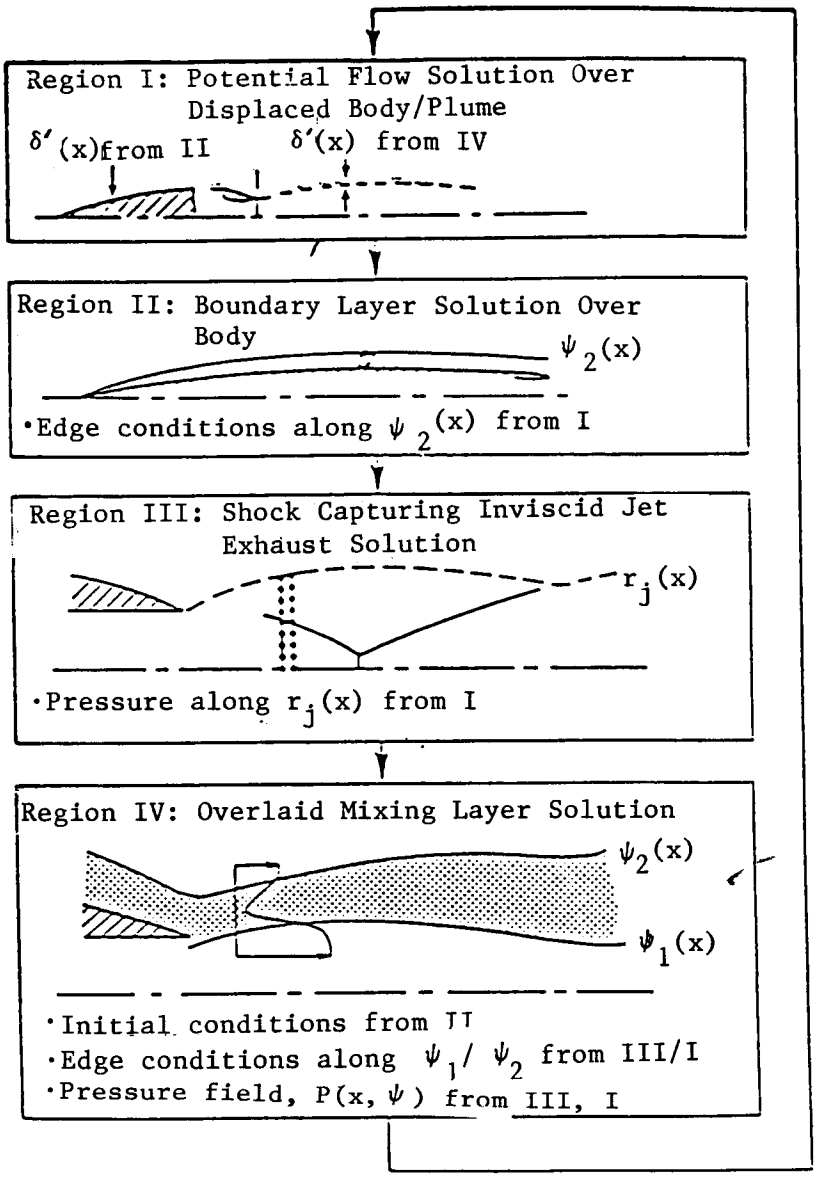

RAXJET COMPUTER MODEL (WILMOTH, NASA TM 83235, 1982)

- SOUTH/JAMESON POTENTIAL FLOW SOLVER
- INTEGRAL BL MODEL
- SCIPPY SHOCK-CAPTURING PLUME MODEL (DASH/THORPE)
- BOAT OVERLAID SHEAR LAYER SOLUTION (DASH/PERGAMENT)

FIGURE 15. **Components Utilized in RAXJET Code for Zonal Solutions of Nozzle Afterbody Drag.**

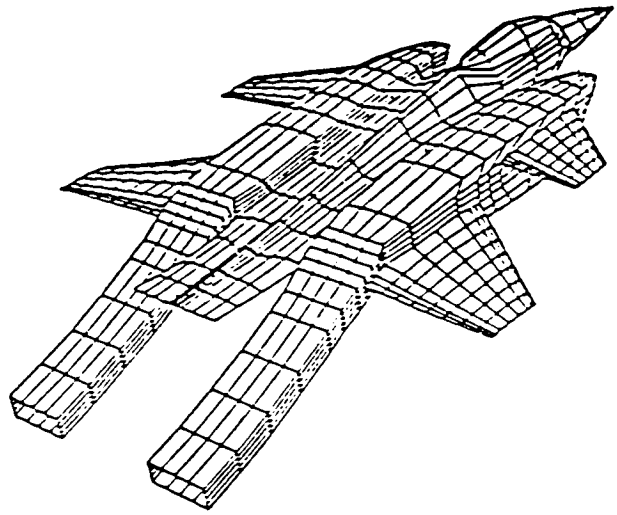

FIGURE 16. Panel Representation of STOL Fighter Model with Inclined, Rectangular Jet.

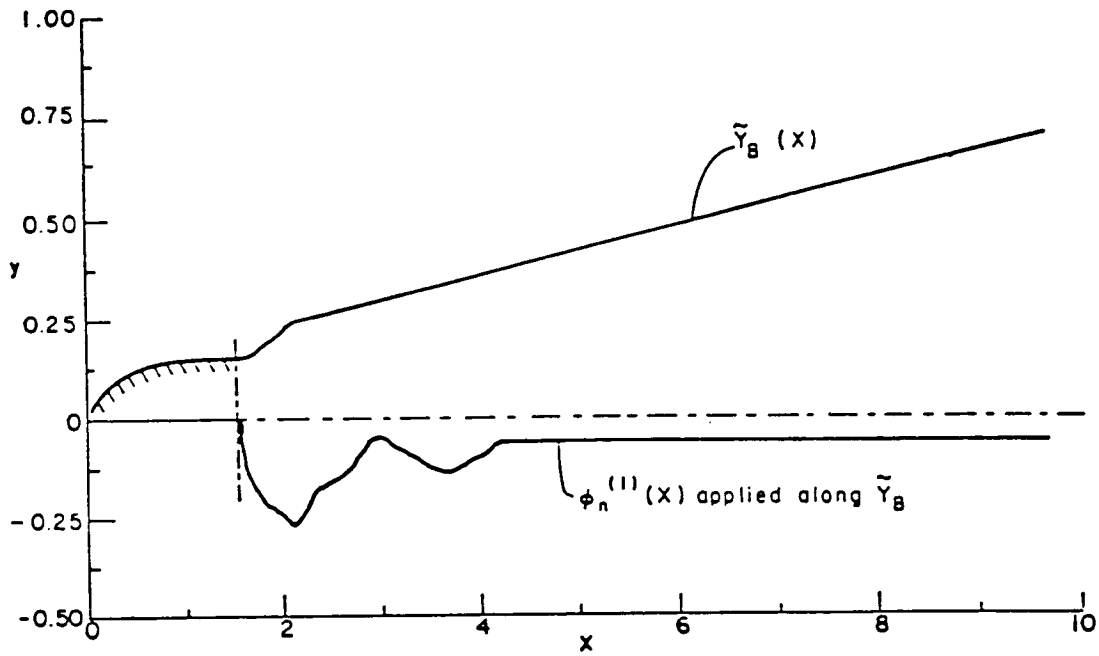

FIGURE 17. Direct-Coupling Boundary and Source Distribution.

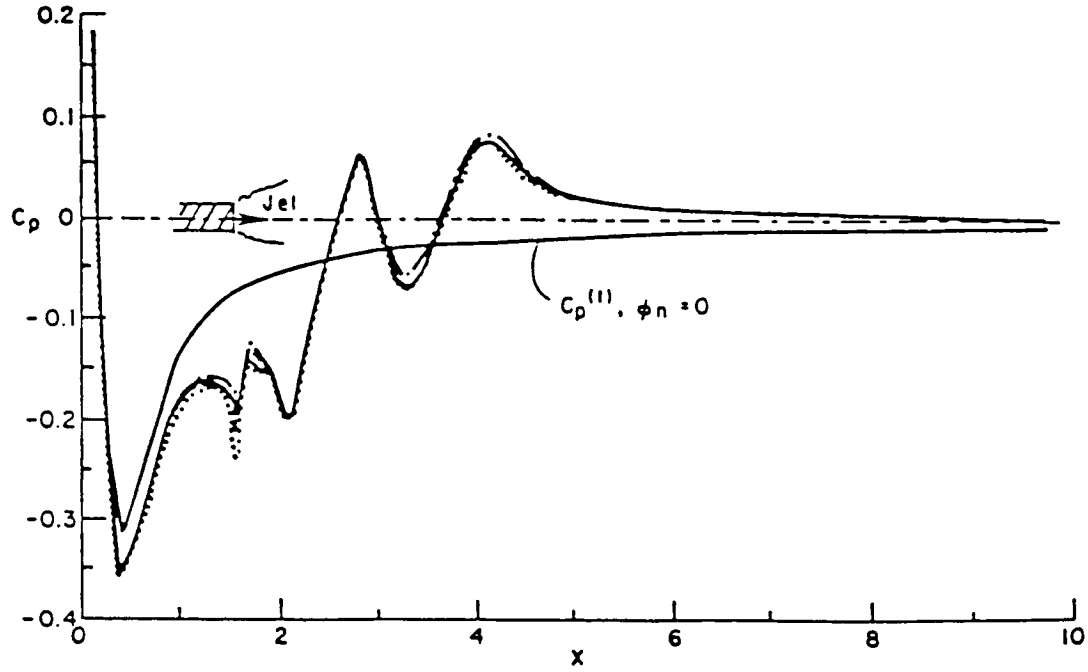

FIGURE 18. Coupling Boundary Pressure Variation for Several Shock Cells.

that of other investigators (e.g., see ref. 46) who used the $k\varepsilon$ model with a wall function near wall approximation. Also exhibited in Figure 19 is a comparison of predicted and measured maximum velocity decay with the data correlation of Rajaratnam[47]. Figure 20 compares predicted and measured[48] streamwise and normal velocity profiles at selected stations downstream of where similarity is achieved.

Planar Wall Jet with Moving Outer Stream

A number of calculations were performed[6,7] corresponding to experiments performed by Kacker and Whitelaw[49]. Figure 21 exhibits typical comparisons achieved for maximum velocity decay, half radius and maximum velocity locus variation, and wall skin friction variation. The comparisons are quite good.

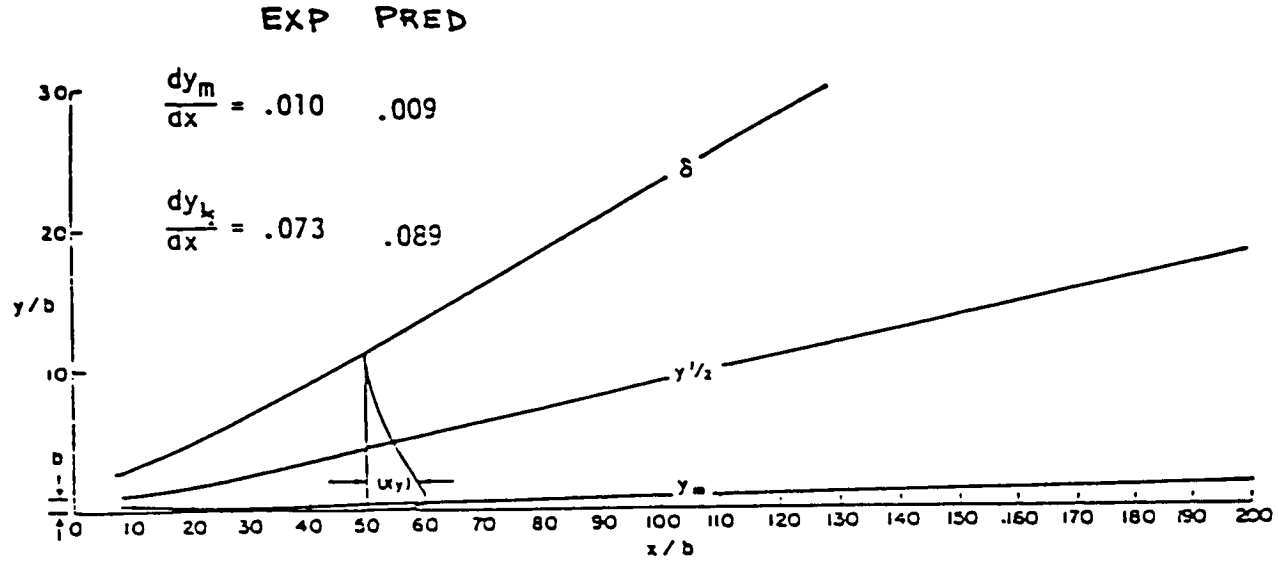

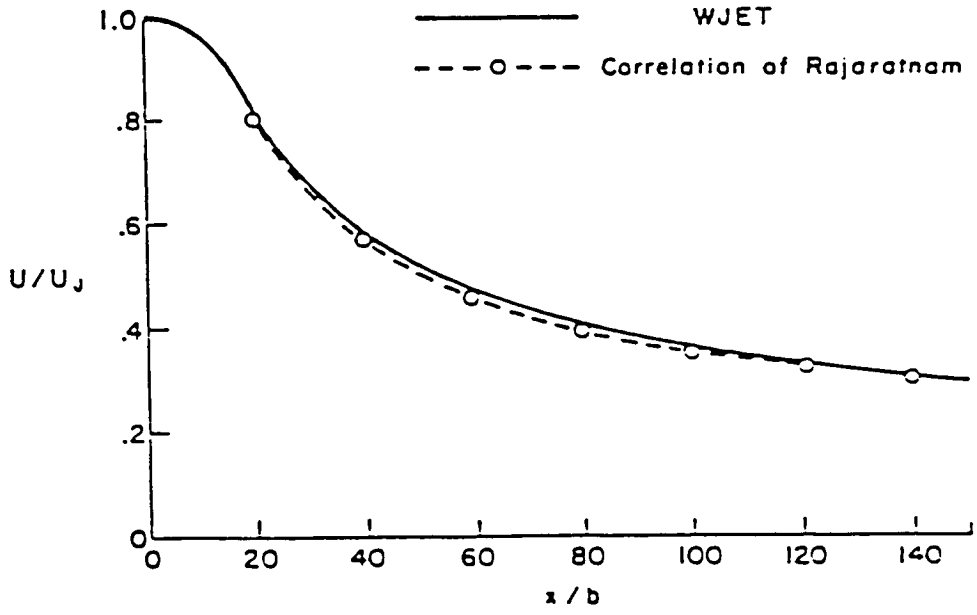

FIGURE 19. Jet Growth Parameters and Velocity Decay for Planar Wall Jet with Quiescent Outer Stream.

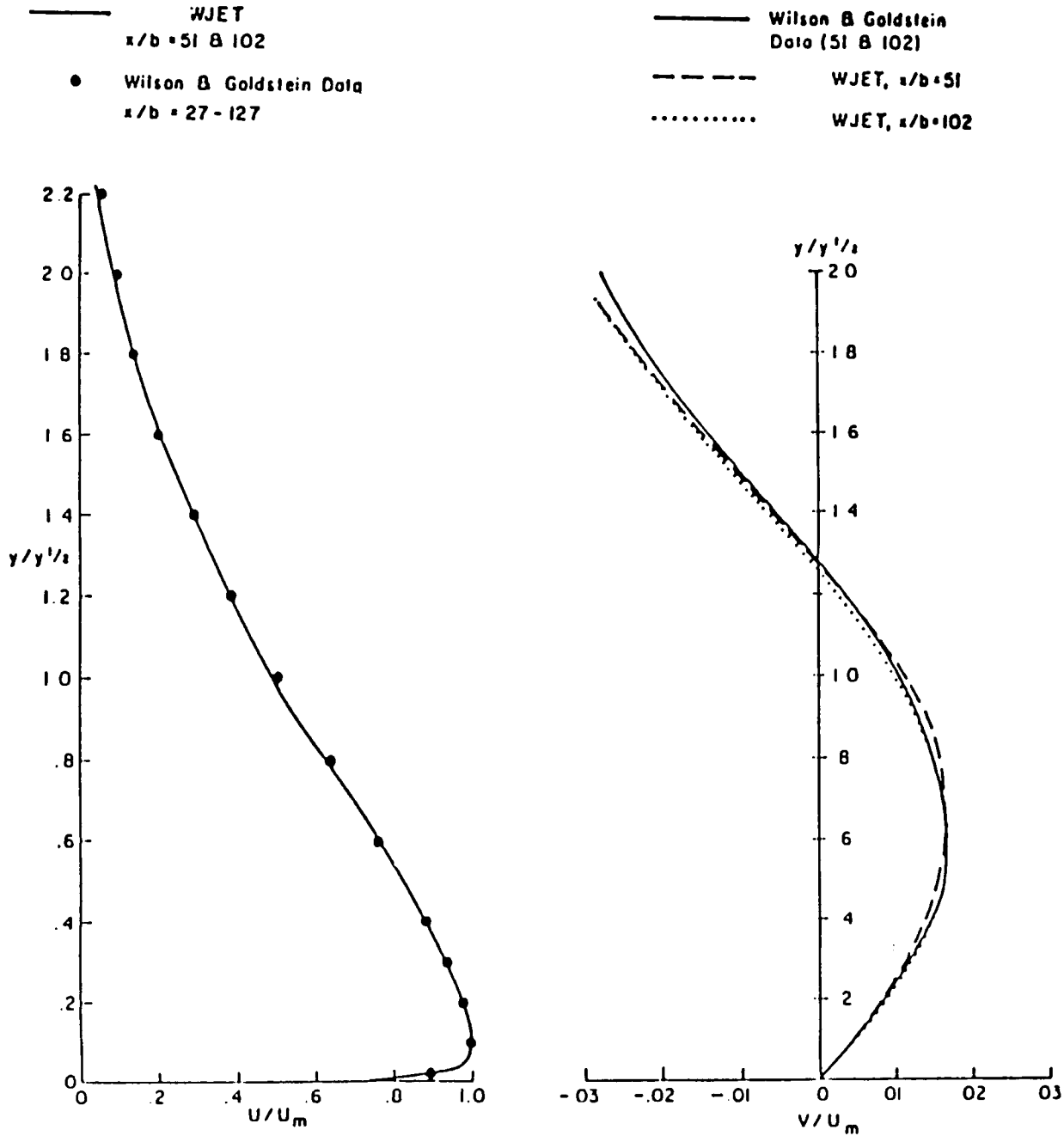

FIGURE 20. Comparison of Predicted and Measured Velocity Profiles for Planar Wall Jet with Quiescent Outer Stream.

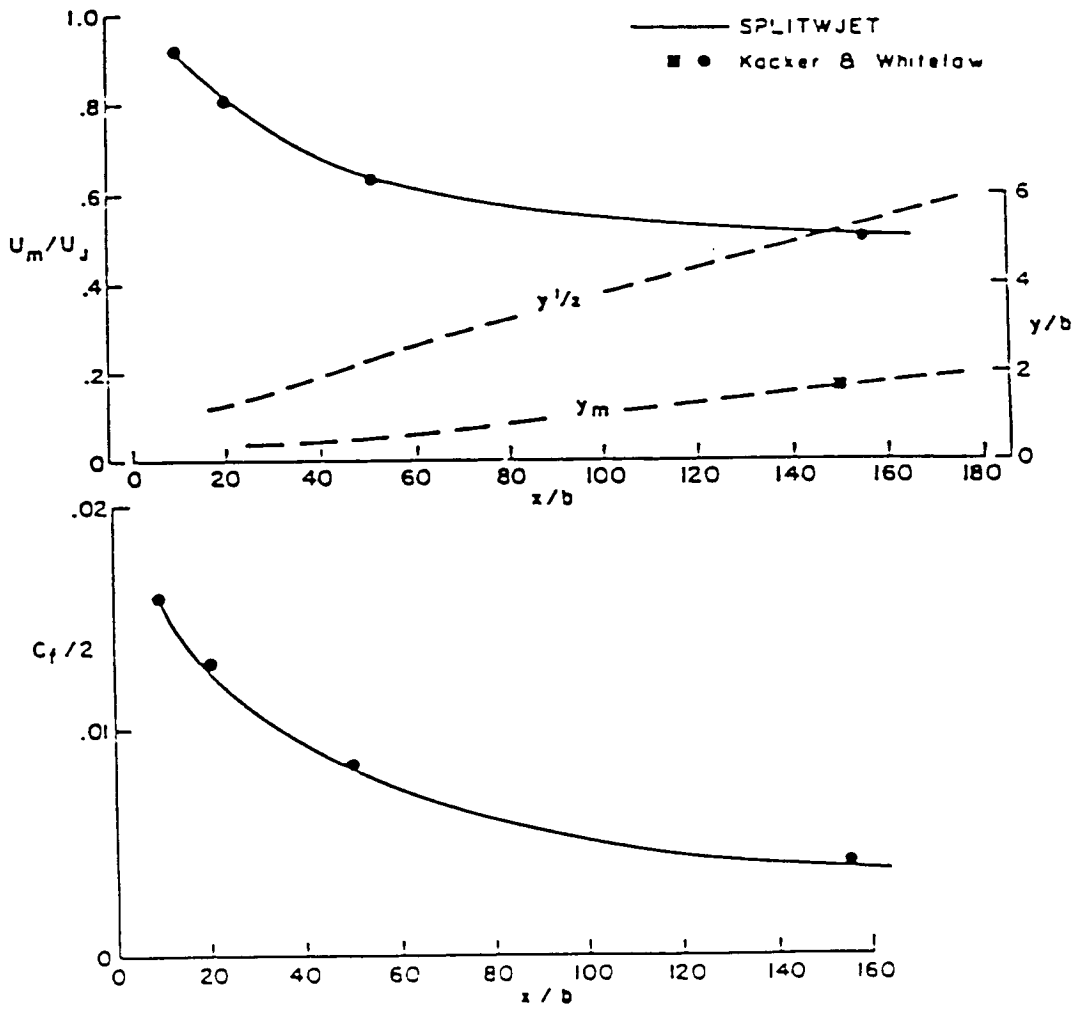

FIGURE 21. Streamwise Property Variations for Planar Wall Jet with Moving Outer Stream (U_J/U_E = 2.3).

Curved Wall Jet Issuing Into Still Air

Calculations were performed[6,7] corresponding to the experiments of Wilson and Goldstein[48]. Figure 22 depicts comparisons of half radius variation and maximum velocity decay utilizing the standard (curvilinear, s,n) $k\varepsilon$ model and versions with curvature correction terms[15,16]. The standard $k\varepsilon$-based prediction is seen to grossly underestimate the rate of mixing while curvature correction predictions (using the recommended curvature coefficient-based values of C_c = 0.2 [Launder[15]] and C_c = 0.16 [Penn State[16]]) agree quite well with the data. Profiles of turbulent shear stress performed with the two correction terms (Figure 23) agree reasonably well with each other and with the data at θ = 90°, but diverge at θ = 180°, as exhibited. Figure 24 exhibits the streamwise variation of peak turbulent shear stress and clearly exhibits the divergence in the predictions at θ = 90°. The data supports the Penn State correction, except for the abrupt jump at $\theta \sim 180°$.

Curved Wall Jet With Moving Outer Stream

The last calculation simulates one of the experiments of Kind[50], as schematized in Figure 25 - conditions correspond to the Flow II Case listed. The calculation was run using the pressure-split approach with conditions (pressure, streamwise velocity) prescribed at the jet outer edge. The predicted ΔC_p across the jet (Figure 26) is in very good agreement with the data except for $\theta > 60°$. The global pressure iteration approach was employed to eliminate the pressure-split approximation and after several iterative sweeps, significant improvement in the comparisons was obtained. The predicted variation in maximum velocity decay is exhibited in Figure 27 and the results with the curvature correction are significantly better that those with the standard $k\varepsilon$ model. The predicted variation in jet half radius is exhibited in Figure 28 and again, the improvements utilizing the curvature correction are quite significant.

CONCLUDING REMARKS

The ability to analyze fundamental wall jet data is clearly keyed to the capabilities of the turbulence model utilized. Our starting point had involved the use of a high Reynolds number two-equation $k\varepsilon$ model with heuristic corrections for streamwise curvature. This model was coupled to an inner (near wall) damped VanDriest mixing length model. Algebraic (eddy viscosity) models were not utilized since they cannot readily deal with complex jet/boundary layer length scales, with initial (slot/boundary layer) turbulence levels, and with lag effects. The curvature modifications to the ε equation[15,16], previously demonstrated to yield improvements for curved boundary layers, also appear to work quite well for curved wall jets. The use of these curvature

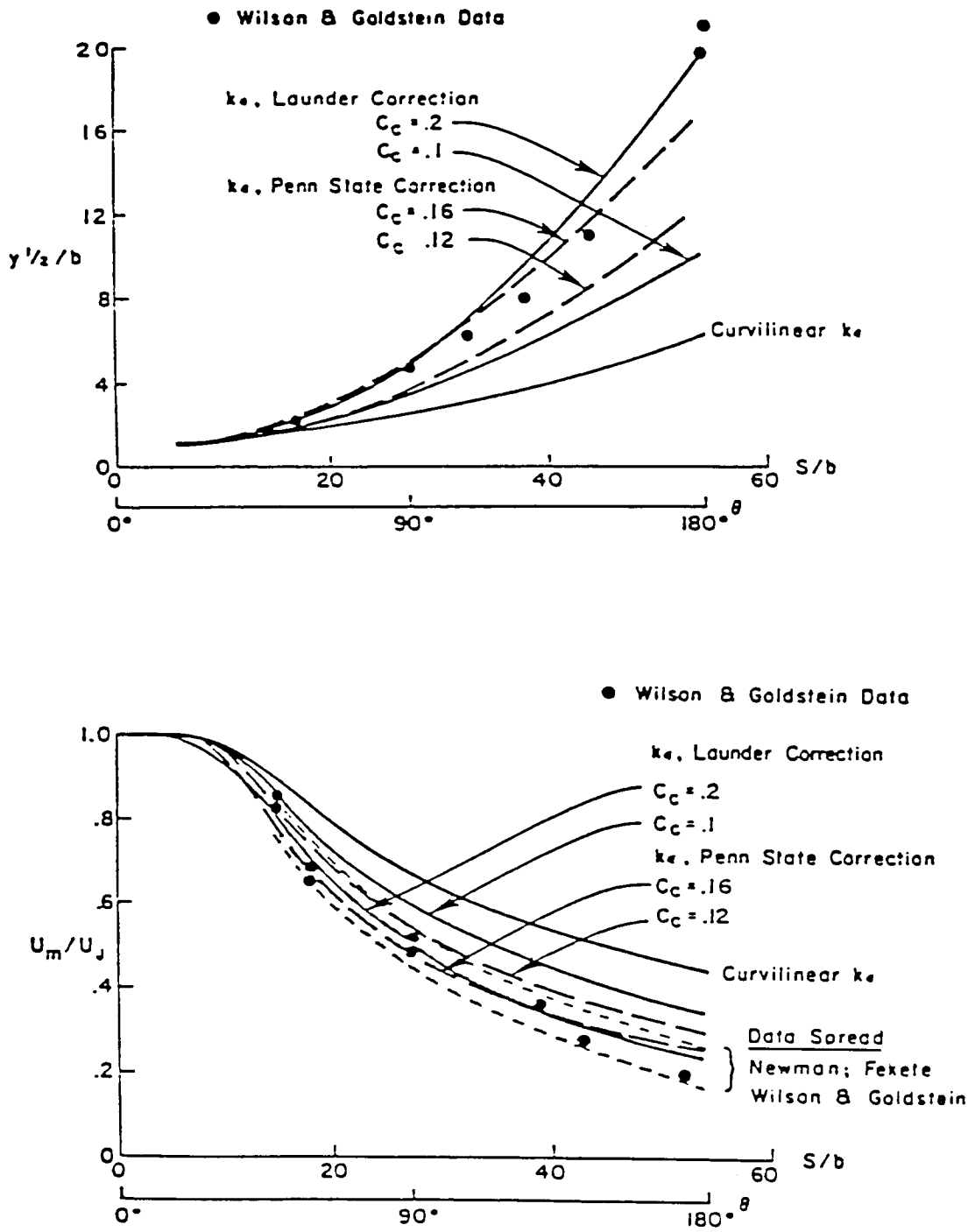

FIGURE 22. Half Radius Variation and Velocity Decay for Wall Jet Over Circular Cylinder.

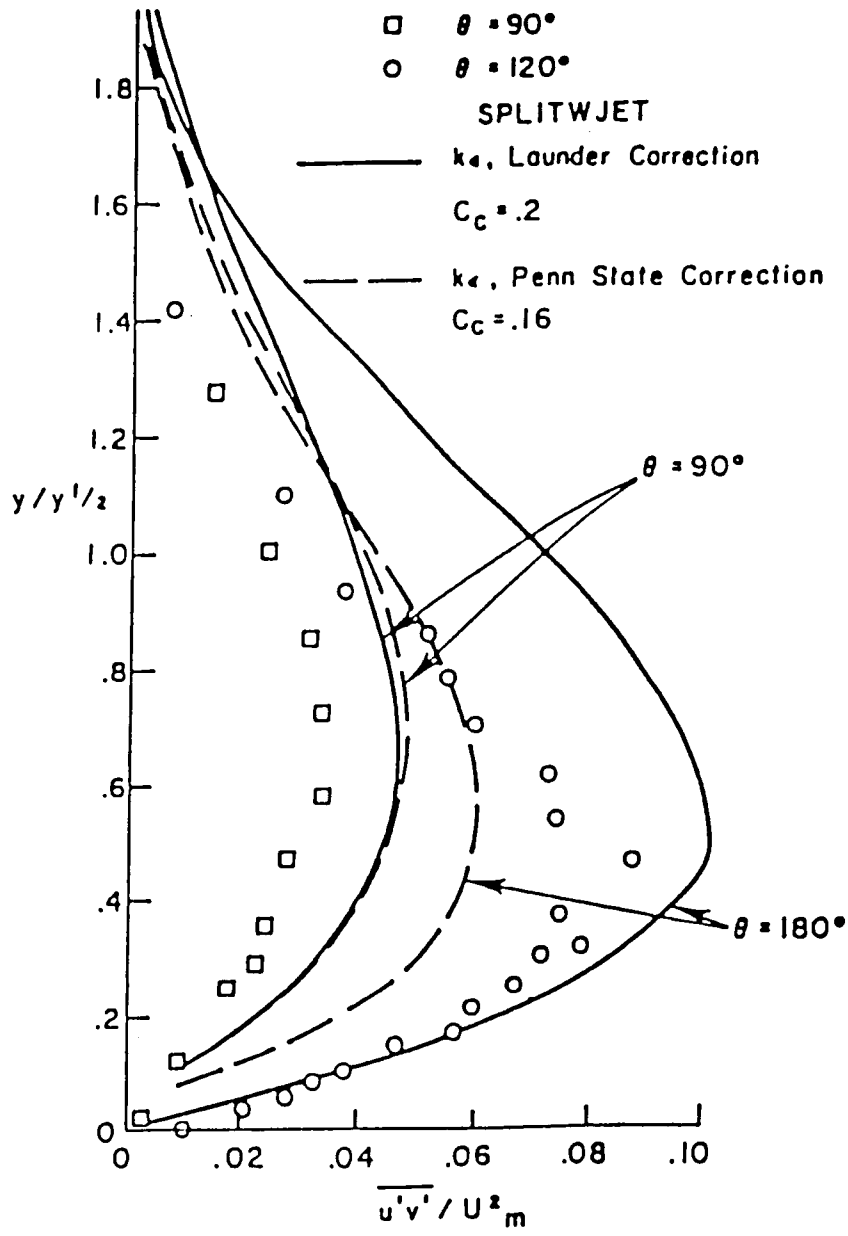

FIGURE 23. Profiles of Turbulent Shear Stress for Curved Wall Jet into Still Air.

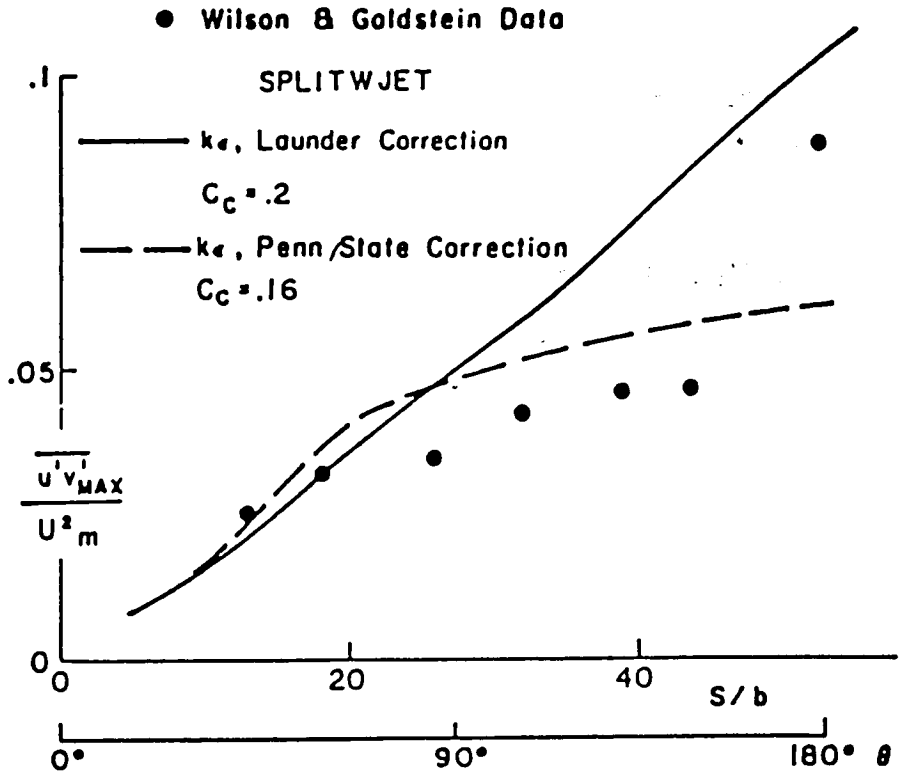

FIGURE 24. Streamwise Variation of Peak Turbulent Shear Stress for Curved Wall Jet into Still Air.

corrected models is recommended as a logical starting point for inclusion in CC NS solvers, since their ability to analyze fundamental wall jet data is reasonably well established. For supersonic wall jets, some type of compressibility correction may be required to deal with the near slot shear layer effects, but data is not presently available to support the heuristic modeling of such a correction.

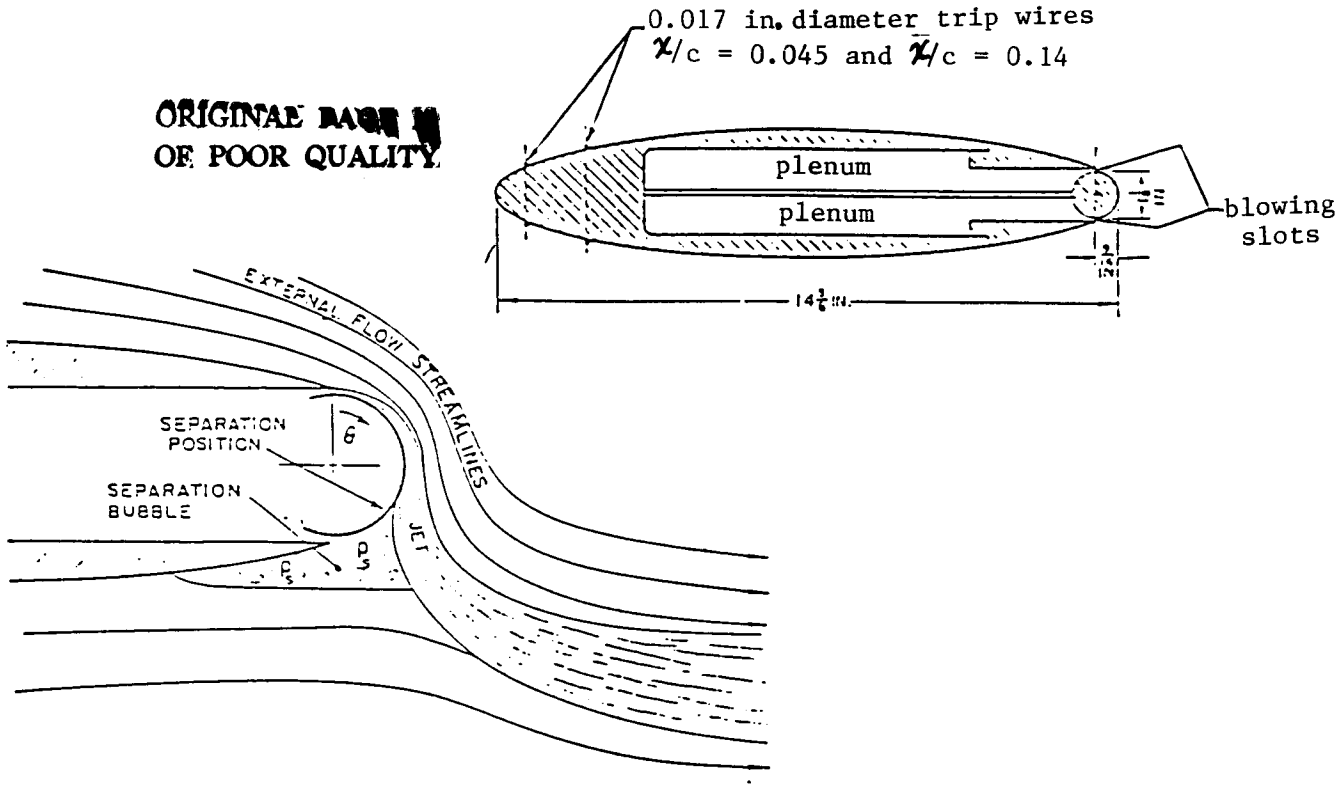

Parameters of the circulation-controlled flows for which wall-jet profile measurements were made.

	Flow I		Flow II		Flow III		Flow IV		Flow V	
C_ℓ	0.88		1.82		2.53		2.76		1.69	
α_{rel} (degrees)	-3.5		-0.7		+0.2		-0.8		-0.2	
C_μ	0.028		0.055		0.083		0.102		0.052	
t/c	0.0012		0.0012		0.0012		0.0012		0.0020	
U_∞ (ft/sec)	100		100		100		100		100	
R	7.5×10^5		7.5×10^5		7.5×10^5		7.5×10^5		7.5×10^5	
Surface Static Pressure Distribution	θ (deg)	$-C_{p_s}$	θ (deg)	$-C_{p_s}$	θ (deg)	$-C_{p_s}$	θ (deg)	$-C_{p_s}$	θ (deg)	$-C_{p_s}$
	0	1.54	0	2.5	0	3.54	0	4.2	0	2.25
	15	2.60	15	4.37	15	5.78	15	6.61	15	4.05
	30	3.23	30	4.88	30	6.66	30	7.81	30	4.85
	45	3.14	45	5.16	45	7.29	45	8.7	45	4.75
	60	2.39	60	4.54	60	6.63	60	8.29	60	3.95
	75	1.19	75	3.41	75	5.66	75	7.04	75	2.8
	90	-0.23	90	1.54	90	3.8	90	5.07	90	1.2
	105	-0.4	105	-0.29	105	1.4	105	2.66	105	-0.45
	120	-0.41	120	-0.58	120	-0.53	120	-0.26	120	-0.57
	135	-0.43	135	-0.63	135	-0.76	135	-0.77	135	-0.59
	150	-0.40	150	-0.64	150	-0.81	150	-0.86	150	-0.58

FIGURE 25. Kind CC Airfoil Experiment.

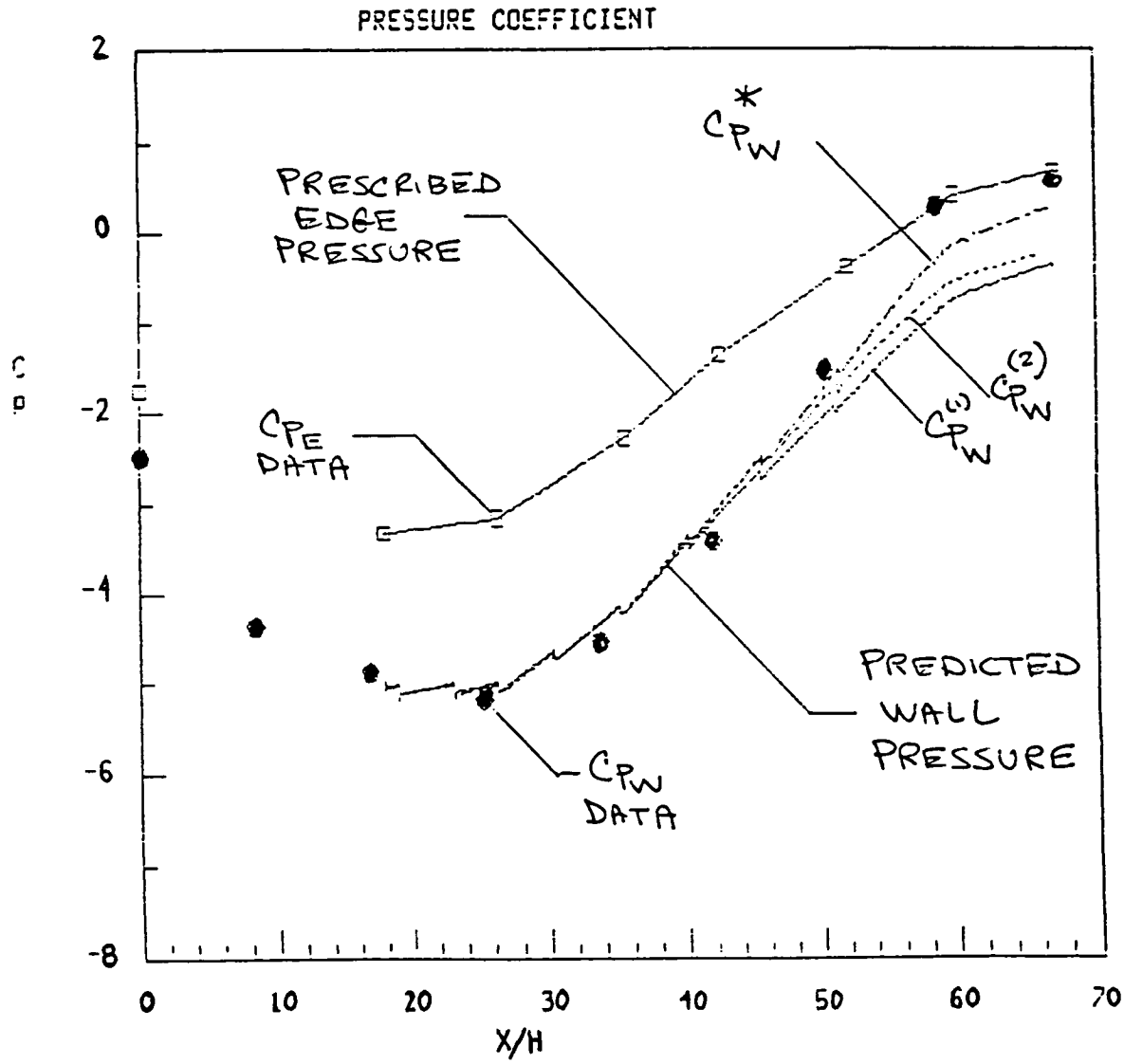

FIGURE 26. Prediction of ΔC_p Across Wall Jet for Kind CC Airfoil Problem.

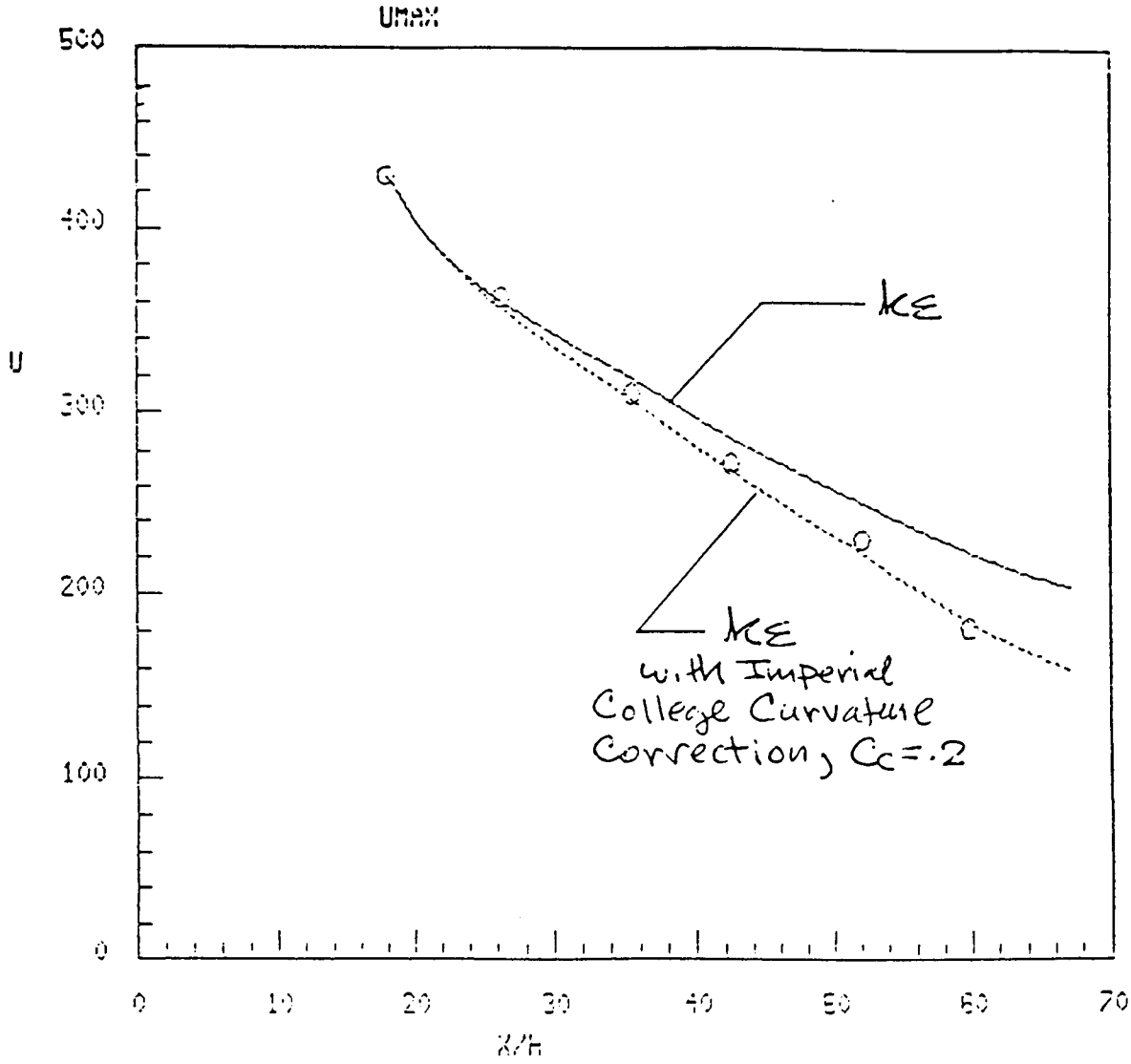

FIGURE 27. Prediction of Maximum Velocity Decay for Kind CC Airfoil Problem.

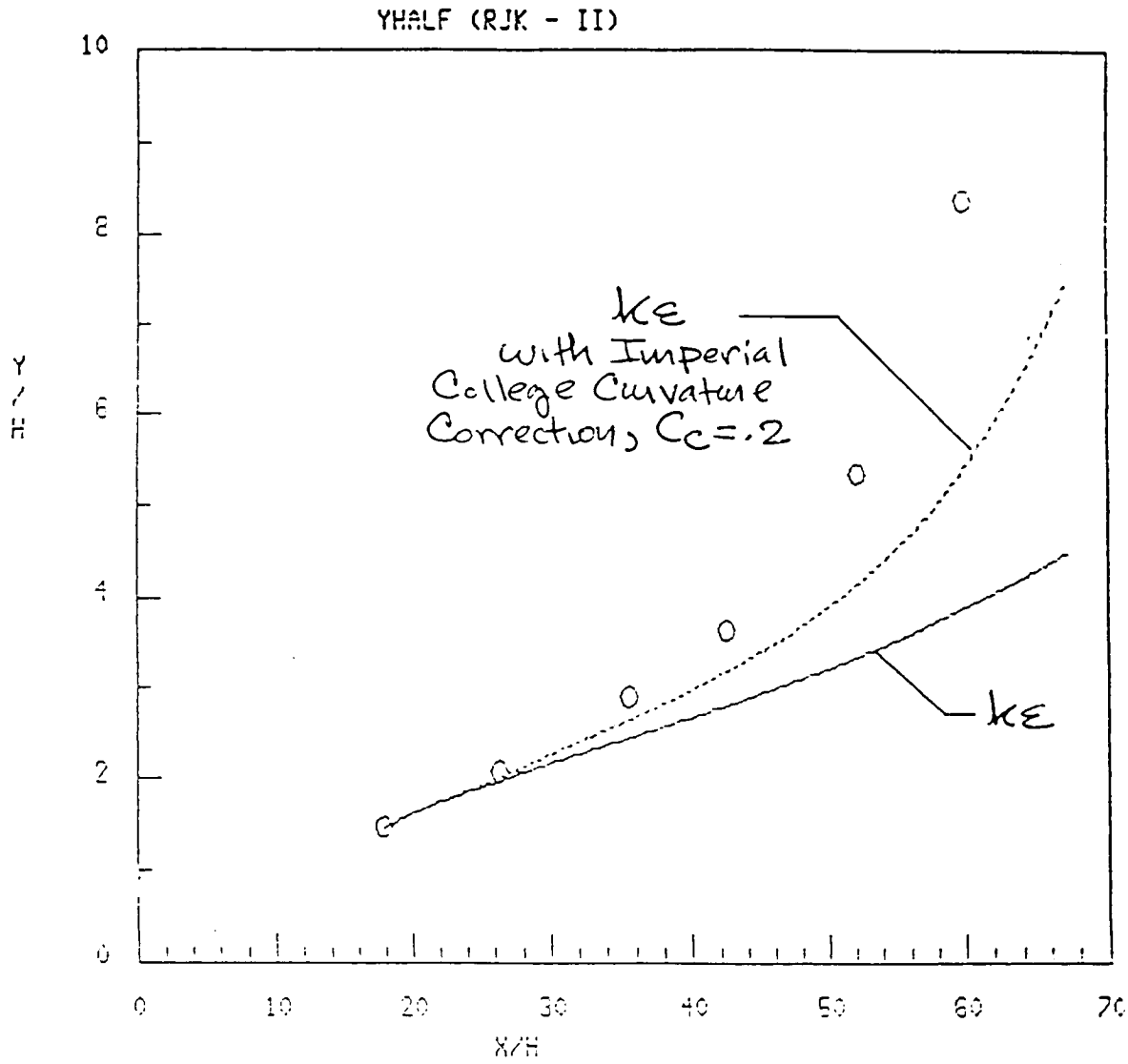

FIGURE 28. Prediction of Jet Half Radius Variation for Kind CC Airfoil Problem.

REFERENCES

1. Dvorak, F.A. and Choi, D.H., 'Analysis of Circulation-Controlled Airfoils in Transonic Flow', J. Aircraft, Vol. 20, April 1983.

2. Dvorak, F.A. and Choi, D.H., 'Development of an Analytical Method for Two-Dimensional Circulation-Control Airfoils in Transonic Flow', Analytical Methods, Inc., Redmond, WA, Report 8106, June 1981.

3. Dvorak, F.A., Calculation of Turbulent Boundary Layers and Wall Jets Over Curved Surfaces', AIAA J., Vol. 11, April 1973.

4. Dash, S.M., Beddini, R.A., Wolf, D.E. and Sinha, N., 'Viscous/ Inviscid Analysis of Curved Sub- or Supersonic Wall Jets', AIAA J., Vol. 23, January 1985, pp. 12-13.

5. Dash, S.M. and Beddini, R.A., 'Viscous/Inviscid Analysis of Curved Wall Jets: Part 2 - Viscous Pressure-Split Model (SPLITWJET)', Science Applications, Inc., Princeton, NJ, SAI/PR TR-7, November 1982.

6. Dash, S.M. and Sinha, N., 'Noniterative Cross-Flow Integration for the Pressure-Split Analysis of Subsonic Mixing Layer Problems', AIAA J., Vol. 23, January 1985, pp. 183-185.

7. Dash, S.M. and Sinha, N., 'Pressure-Split Extensions of SPLITWJET Model for Wall Jet/Potential Flow Coupling', Science Applications, Inc., Princeton, NJ, SAI/PR TR-17, February 1984.

8. Dash, S.M., Sinha, N. and York, B.J., 'Implicit/Explicit Analysis of Interactive Phenomena in Supersonic, Chemically-Reacting, Mixing and Boundary Layer Problems', AIAA Paper 85-1717, Cincinnati, OH, July 1985.

9. Dash, S.M. and York, B.J., 'Analysis of Curved, Underexpanded Wall Jets Using an Implicit/Explicit Parabolized Navier-Stokes Approach', Science Applications International Corporation, Princeton, NJ, SAIC/PR TR-29, June 1985.

10. Dvorak, F.A. and Dash, S.M., 'Improved Algorithms for Analysis of Circulation Control Rotors' Analytical Methods, Inc., Redmond, WA, Report No. 8407, May 1984.

11. Dvorak, F.A. and Dash, S.M., 'Wall Jet Analysis for Circulation Control Aerodynamics; Part II - Zonal Modeling Concepts for Wall Jet/Potential Flow Coupling', Circulation Control Workshop, NASA Ames Reserach Center, Moffett Field, CA, Feb. 18-20, 1985.

12. Arora, R., Kuo, K.K., and Razdan, M.K., 'Near Wall Treatment for Turbulent Boundary Layer Computations,' AIAA J., Nov. 1982. pp. 1481-2.

13. Bradshaw, P., 'The Analogy Between Streamline Curvature and Buoyancy in Turbulent Shear Flow', J. Fluid Mech., 36, 1969, pp. 177-191.

14. Foloyan, C.O. and Whitelaw, J.H., 'The Effectiveness of Two-Dimensional Film Cooling Over Curved Surfaces', ASME Paper 76-HT-31, 1976.

15. Launder, B.E., Priddin, C.H. and Sharma, B.I., 'The Calculation of Turbulent Boundary Layers on Spinning and Curved Surfaces,' ASME J. Fluids Eng., March 1977, pp. 231-239.

16. Hah, C. and Lakshminarayana, B., 'Prediction of Two- and Three-Dimensional Axisymmetric Turbulent Wakes, Including Curvature and Rotation Effects', AIAA J., Oct. 1980, pp. 1196-1204.

17. Dash, S.M., Weilerstein, G. and Vaglio-Laurin, R., 'Compressibility Effects in Free Turbulent Shear Flows', Air Force Office of Scientific Research, TR-75-1436, August 1975.

18. Mahgoub, H.E.H. and Bradshaw, P., 'Calculation of Turbulent-Inviscid Flow Interactions with Large Normal Pressure Gradients', AIAA Journal, October 1979, pp. 1025-1029.

19. Chen, Z.B. and Bradshaw, P., 'Calculation of Viscous Transonic Flow over Airfoils', AIAA J., February 1984, pp. 201-205 (also, AIAA Paper 82-0997, June 1982).

20. Moretti, G., 'Analysis of Two-Dimensional Problems of Supersonic Combustion Controlled by Mixing,' AIAA J., Vol. 3, 1965, pp. 223-229, (also AIAA Paper 64-96, Jan. 1964).

21. Ferri, A. and Dash, S.M., 'Viscous Flow at High Mach Numbers with Pressure Gradients', Viscous Interaction Phenomena in Supersonic and Hypersonic Flow, University of Dayton Press, Dayton, OH, 1970, pp. 271-318.

22. Sinha, N. and Dash, S.M., 'Parabolized Navier-Stokes Analysis of Ducted Turbulent Mixing Problems with Finite-Rate Chemistry,' AIAA Paper 86-0004, January 1976.

23. Dash, S.M. and Wolf, D.E., 'Fully-Coupled Analysis of Jet Mixing Problems, Part I: Shock-Capturing Model, SCIPVIS', NASA CR-3761, January 1984.

24. Dash, S.M. and Wolf, D.E., 'Interactive Phenomena in Supersonic Jet Mixing Problems, Part I: Phenomenology and Numerical Modeling Techniques', AIAA J., Vol. 22, July 1984, pp. 905-913.

25. Dash, S.M. and Wolf, D.E., 'Interactive Phenomena in Supersonic Jet Mixing Problems, Part II: Numerical Studies', AIAA J., Vol. 22, October 1984, pp. 1395-1404.

26. Dash, S.M., Wolf, D.E. and Seiner, J.M., 'Analysis of Turbulent Underexpanded Jets - Part I: Parabolized Navier-Stokes Model, SCIPVIS', AIAA J., Vol. 23, April 1985, pp. 505-514.

27. Dash, S.M. and Sinha, N., 'Fully-Coupled Analysis of Jet Mixing Problems, Part II: Pressure-Split Model, SPLITP', NASA CR in preparation.

28. Seiner, J.M., Dash, S.M. and Wolf, D.E., 'Analysis of Turbulent Underexpanded Jets - Part II: Shock Noise Features Using SCIPVIS', AIAA J., Vol. 23, May 1985.

29. Dash, S.M., 'Recent Developments in the Modeling of High Speed Jets, Plumes and Wakes - Invited Survey Paper', AIAA Paper 85-1616, Cincinnati, OH, July 1985.

30. Pergament, H.S., Dash, S.M. and Varma, A.K., 'Evaluation of Turbulence Model for Rocket and Aircraft Plume Flowfield Predictions', AIAA Paper 79-0359, New Orleans, LA, January 1979.

31. Pergament, H.S., 'Assessment and Recommendation of Two-Equation Turbulence Models for Rocket and Aircraft Plume Flowfield Predictions', Naval Weapons Center, China Lake, CA, TP 6364, July 1982.

32. Pergament, H.S., Sinha, N. and Dash, S.M., 'Hybrid Two-Equation Model for High Speed Propulsive Jets', to be presented at AIAA/ASME Joint Propulsion Conference, Huntsville, AL, June 1986.

33. Langanelli, A.L. and Leone, S.A., 'Inclined Slot Jet Evaluation Progress Report', Science Applications International Corporation, Valley Forge, PA, January 1986.

34. Dash, S.M., 'Compressibility Effects in High Mach Number Turbulent Mixing Problems', Science Applications International Corporation, Princeton, NJ, TL-234, August 1985.

35. Dodge, P.R., 'A Numerical Method for 2D and 3D Viscous Flows', AIAA J., July 1977, pp. 961-965 (also AIAA Paper 76-425, July 1976).

36. Khosla, P.K. and Rubin, S.G., 'A Composite Velocity Procedure for the Compressible Navier-Stokes Equations', AIAA Paper 82-0099, Jan. 1982.

37. Cosner, R.R., 'Fast Navier-Stokes Solution of Transonic Flowfield About Axisymmetric Afterbodies', AIAA Paper 80-0193, Jan. 1980.

38. Swanson, R.C., Rubin, S.G. and Khosla, P.K., 'Calculation of Afterbody Flows with a Composite Velocity Formulation', AIAA Paper 83-1736, July 1983.

39. Dash, S.M., Wilmoth, R.G. and Pergament, H.S., 'An Overlaid Viscous/Inviscid Model for the Prediction of Nearfield Jet Entrainment', AIAA J., Vol. 17, September 1979, pp. 950-958.

40. Wilmoth, R.G. and Dash, S.M., 'A Viscous-Inviscid Interaction Model of Jet Entrainment', Computation of Viscous-Inviscid Interactions, AGARD CP-291, September 1980, pp. 13.1 - 13.15.

41. Wilmoth, R.G., 'RAXJET: A Computer Program for Predicting Transonic Axisymmetric Flow Over Nozzle Afterbodies with Supersonic Jet Exhaust', NASA TM 83235, Feb. 1982.

42. Dash, S.M., 'An Overlaid Procedure for the Viscous/Inviscid Analysis of Wall Jets', Science Applications, Inc., Princeton, NJ, SAI/PR TM-2, December 1980.

43. Dash, S.M. and Lee, S.H., 'Exploratory Investigation of Jet/Potential Flow Coupling Using SPLITP Jet and VSAERO Panel Codes', Science Applications International Corporation, Princeton, NJ, SAIC/PR TM-39, April 1985.

44. Maskew, B., 'Program VSAERO: A Computer Program for Calculating the Non-Linear Aerodynamic Characteristics of Arbitrary Configurations', NASA CR-166476, December 1982.

45. Dash, S.M., Wolf, D.E., Sinha, N. and Lee, S.H., 'Progress in the Development of Parabolized Navier-Stokes Methodology for Analyzing 3D Propulsive Jet Flowfields', AIAA Paper 86-1115, AIAA/ASME 4th Fluid and Plasma Dynamics Meeting, Atlanta, GA, May 1986.

46. Ljuboja, M. and Rodi, W., 'Calculation of Turbulent Wall Jets with an Algebraic Reynolds Stress Model', ASME J. Fluids Eng., Sept. 1980, pp. 350-356.

47. Rajaratnam, N., Turbulent Jets, Elsavier, Amsterdam, The Netherlands, 1976, Chapter 10.

48. Wilson, D.J. and Goldstein, R.J., 'Turbulent Wall Jets with Cylindrical Streamwise Surface Curvature', ASME J. Fluids Eng., Sept. 1976, p. 550-557.

49. Kacker, S.C. and Whitelaw, J.H., 'The Turbulent Characteristics of Two-Dimensional Wall-Jet and Wall-Wake Flows', ASME J. App. Mech., March 1971, pp. 239-252.

50. Kind, R.J., 'A Calculation Method for Circulation Control by Tangential Blowing Around a Bluff Trailing Edge', Aeronautical Quarterly, August 1968, pp. 205-223.

Investigations of a Circulation Control Airfoil Flowfield using an Advanced Laser Velocimeter

Charles J. Novak and Kenneth C. Cornelius
Lockheed-Georgia Company, Marietta, Ga. 30063

ABSTRACT

The flowfield of a Circulation Control Airfoil has been examined in detail through the use of a specially designed wind tunnel model and test program. Surface pressures on the model were obtained and the velocity field was surveyed in the trailing edge region of the model airfoil using the non-intrusive Laser Velocimetry (LV) technique. In this region mean flow and turbulence measurements indicate that, while the flowfield is similar to other wall-bounded jet flows, the external freestream plays an important role in the overall mixing and structure of the wall bounded flow. Finally, the turbulence measurements have been used to compute eddy viscosities for the purpose of aiding Computational Fluid Dynamics (CFD) model development

NOMENCLATURE

b	airfoil model span (0.61 meters)
c	airfoil model chord length (0.38 meters)
C_L	lift coefficient
Cp	surface pressure coefficient
C_μ	jet momentum coefficient
C_1	curvature constant (= 25.0)
Dp	diameter of seeding particle
h	jet slot height
K	flowfield stability parameter
$\dot{m}j$	jet massflow
Q	wind tunnel dynamic pressure
r	radius of trailing edge
Re	Reynolds number based on airfoil chord length
S	airfoil model surface area
St	Stokes number = $\frac{1}{18}\ \frac{\rho_p}{\rho_a}\ \frac{U_j D_p}{\nu}\ \frac{Dp}{r}$
U,V	mean velocities in the tangential and normal directions respectively
U_e	velocity at the edge of the mixing region ($\overline{uv}$=0.0)
U_m	maximum tangential velocity
ΔU_m	defect velocity (=U_m-U_e)
U_j	mean jet velocity expanded isentropically to freestream static pressure
U_∞	wind tunnel freestream velocity
u_τ	friction velocity
$\bar{u}'$,$\bar{v}'$	time averaged turbulent velocities in tangential and normal directions respectively
$\overline{uv}$	time averaged turbulent shear stress
x	distance along the airfoil chordline
y	normal distance above airfoil surface

$y_{1/2}$	position above surface where $U=(U_m+U_e)/2$
y_m	position of Um above surface
y+	position above surface in Law of the Wall coordinates
α	airfoil angle of attack
ε	kinematic eddy viscosity
θ	angle defining coordinate on circular trailing edge on model
ρ_p	density of seeding particle
ρ_a	density of air
ν	kinematic viscosity of air

INTRODUCTION

Modern aircraft, either for military or civilian use, are resorting to powered lift as a viable means of meeting short field requirements. One method of increasing lift is the circulation control wing (CCW). In this configuration, as seen in figure 1, a small planar jet is issued from the cylindrical trailing edge of the wing in an effort to draw the aft stagnation point under and forward of the trailing edge. Hence, net circulation is dramatically increased without resorting to a complex mechanical flap system.

This behavior arises from the characteristics of wall jets on curved surfaces, an observation dating back to 1800 when Young (1800) first described the phenomena. However, much more attention was given to Coanda in 1910 who attempted to exploit the curved wall jet. More recent interest has arisen in applying the phenomenon to CCW systems and previous examples of investigations into CCW configurations are well described in papers by Englar (1973) and Wood (1985) in which performance considerations are emphasized. Additional work includes papers by Kind & Maull (1968) and Wilson & Goldstein (1976), where the jet turning characteristics are of greatest interest.

The purpose of the experimental investigation described in this paper is to provide a definitive set of mean velocity and turbulence measurements in the aft stagnation region of a CCW wind tunnel model. A non-intrusive, 2-D Laser Velocimeter (LV) was utilized in all velocity measurements and additionally, a complete set of airfoil surface pressure data was obtained on the CCW configuration.

These data provide a valuable description of the details of the flowfield and its turbulence characteristics and are suitable for validation and comparisons with computational analyses.

EXPERIMENTAL PROCEDURE

Model Description

In an effort to satisfy both circulation control airfoil performance criteria as well as to maintain good spatial resolution with the LV in high gradient regions, a model was specially designed for use in the Lockheed-Georgia Low Turbulence Wind Tunnel (0.61x 0.92 m. and 0.03% $\bar{u}'/U_\infty$). The model is shown in figure 2 and is constructed of aluminum. It has a 0.38 m. cord with leading edge coordinates of a modern supercritical section. The symmetric mid-section and 0.051 m. diameter circulation control aft section

are blended in such a manner so as to eliminate surface discontinuities. Note that the ratio of turning radius to chord length (r/c=0.067) is somewhat high and is not representative of practical flight systems. However, this enables larger slot heights to be employed which in turn improves the LV measurement resolution.

Compressed air enters the model plenum chamber from an inlet diffuser at 90 degrees to the jet exit plane. The model's internal geometry was designed so that the jet-slot exit profile and internal flow would be of high quality and free from the effects of surface discontinuities. Two internal screens are used to accommodate internal flow smoothing and an internal fillet provides a 10:1 contraction ratio between the plenum and the jet exit as shown in figure 2.

The slot geometry is arranged so that the flow exits from the plenum tangentially to the circular Coanda surface and parallel to the upper-surface boundary. Variation in slot height is accomplished with clamp bolts located at the 75% chord line yielding slot gaps of 0.064 mm. to 3.05 mm, with an upper surface slot lip trailing edge thickness of nominally 0.25 mm. This geometry, along with a hypothetical velocity profile and the nomenclature to be used in the following discussions, is shown in figure 3.

Instrumentation on the model consists of 45 static pressure ports, each 0.5 mm. in diameter, positioned along the model centerline. A total pressure probe was located within the plenum downstream of the last screen to monitor the internal flow conditions.

Laser Velocimeter Description

The 2-D LV system used to generate the data presented in this paper is shown schematically in figure 4. It utilizes an 18-watt Argon-Ion Laser operating at 3.0 watts on all color lines. The system was operated in backscatter mode at a focal length of 0.77 meters. Receiving optics consist of a 15.4 cm. diameter lens giving an optical speed of f/5 that can be positioned in a variety of off-axis locations greater than 5 degrees. Velocity components are measured at the orthogonal intersection of the dual-green (488.0 nm.) and dual-blue (514.5 nm.) beams which may be oriented arbitrarily with respect to the tunnel coordinate system. Frequency shifting of both a green and a blue beam by the use of a Bragg cell gives the system the capability of measuring reversed flows. The measurement volume at the beam intersection is nominally 0.075 mm. in diameter by 1.3 mm. in length and signals from the photomultiplier tubes are analyzed by a specially designed counter type processor.

Typical LV electronic signals consist of a carrier d.c. voltage and a Doppler burst with a period that corresponds to the time of transit of a particle through individual fringes. If the carrier d.c. voltage is removed the signal is seen to oscillate about zero voltage level. Treatment of the signal at this point is crucial to the quality of the velocity measurement and here is where major differences between the off-the-shelf and herein described system lies.

The single-cycle verification circuitry designed in-house by Whiffen (1979) assures that the period of each cycle of the incoming signal burst is equal, within a controlled error window, to the period of the cycle preceding

it and following it. The technique has several inherent advantages over the 5/8 and 4/8 schemes that are commercially used. First, it is the ultimate extension of those schemes since it effectively takes the period comparisons to their natural limit, and so provides seven tests during the signal burst instead of one. Also, the error window width is not critical. Since the most common error in a signal burst is a dropped cycle, it results in a 100% difference in a single cycle period; whereas, with a 5/8 validation, for instance, certain combinations of dropped cycles result in only a 4% difference in period and, therefore, require very narrow, highly critical, error windows which are difficult to achieve, particularly with standard circuity components over a wide bandwidth. The 4/8 validation scheme is even worse, since combinations of dropped cycles, symmetrical about the center of the burst, i.e., about the 4th count, are impossible to detect and are thus accepted as valid data. figure 5 shows the validation criteria determined by the circuity. In effect, the circuit invalidates any signal burst in which the period for two adjacent (in time) signal cycles differ by more than the window, W. For the circuits used, W is variable between 5% and 80% of the cycle period. The end result of this is a highly accurate digital representation of the particle/fringe crossing, and, superior to that of the commercially produced counterpart.

The second feature, inherent to the LV electronics system used, increases the quality of the turbulence quantities to levels comparable to other measurement techniques (i.e., hot-wire anemometry). Figure 6 shows the effect of noise on the processor detection process. It is seen that noise actually causes a jitter in the time of each zero crossing. This jitter in turn causes random changes in the period of the measurement gate which is timed by a 500 Mhz clock and sent to the computer as raw velocity data. It is readily seen that only the first and last detected zero crossing contributes to variations in the measured period. Since the zero crossing jitter is caused by a random process, the effect at each crossing is statistically independent and uncorrelated except as convoluted by the common transfer function of the mixer and bandpass filters prior to the detector. A cursory examination of these components suggested that only the bandpass filter had a time constant which could produce noise correlation within the time frame of the signal frequencies. This effect, however, was found to decay within 3 or 4 signal cycles. Therefore, a second measurement gate was generated from the same sequence of zero crossings and was displaced for different zero crossings by 4 cycles from the first gate. This gate was then in turn timed by a second 500 Mhz clock to eliminate possible correlation between digital counting processes and recorded as the second raw velocity data point.

After the electronic processing, each data word is transmitted to the host mini-computer along with a record of the acquisition time of the measurement. This information allows subsequent reconstruction of the temporal history of the flow from which spectral and correlation data may be obtained. Also, an internal trigger may be synthesized or a trigger may be provided externally to enable conditional sampling of a flowfield to reveal phase averaged structures in the flow.

Flowfield Seeding

Prior to testing, an investigation concerning the balance of centrifugal and viscous forces on a seeding particle (LV scattering media) was

undertaken. In testing of this nature, it is most important that the flowfield seeding follows the fluid streamlines. Dring and Suo (1978) studied this situation and showed theoretically that for spherical particles below a certain size range, the viscous forces (Stokes drag) balanced forces directly attributed to swirl in the flowfield. They report that a Stokes number of St= 0.016 is needed to ensure negligible centrifugal effects. For the present test this value corresponds to a one micron diameter particle of mineral oil subjected to the acceleration along the Coanda surface. Thus the use of a particle impactor was required since the seeding size distribution had to remain under 1 micron maximum. This need is clearly shown in figure 7, where an aerodynamic particle sizer was used to determine the particle distribution before impaction. Also shown is the predicted impaction range based on the design and operation curves for the particle impactor.

During the test program, model internal and external flowfield seeding was achieved with use of an engine lubrication atomizer. A bypass valve was used to divert a portion of the generated seed to the external flow in an effort to maintain a constant LV signal intensity across the shear layer. This factor becomes an important consideration when making jet measurements using the LV technique if the effects of velocity bias are to be minimized.

Test Conditions

For LV measurement purposes, the 2.54 mm. jet gap (h/r=0.1) was chosen to improve resolution in the large velocity gradient regions. However, surface pressure measurements were also conducted at h/r=0.035, or 0.89 mm. slot height. Angle of attack sweeps were conducted for each slot height and blowing coefficient and based on that information, LV test conditions were chosen as:

h/c	=	0.067
h/r	=	0.10
α	=	0.00 deg.
U_∞	=	30.50 m/sec.
U_j/U_∞	=	4.92
$Re(c)$	=	775000.
C_μ	=	$\dot{m}_j U_j / Q S = 0.255$

With these conditions established (such that tunnel floor and ceiling flows were fully attached as well as steady) LV surveys were conducted in the aft stagnation region of the CCW model. Additional LV surveys of limited scope were made under quiescent wind tunnel conditions with the same jet stagnation pressure (1192 Pa.) as the lifting case. Comparisons of the circular wall jet and the CCW result may be made directly if needed.

Individual profiles were acquired with the LV measurement volume traversed normal to the surface at the point of interest using a 1.23 x 1.23 meter traverse table with traverse range of .75 meters in all directions and positional accuracy of 0.025 mm. Several techniques were used to aid in LV data acquisition. For example, verification circuitry on the 2-D LV aided in raising the overall signal-to-noise ratio in the near-wall region where velocity information is of particular interest. In addition to the special electronics, a spatial filter was placed at the receiving optics pinhole or point of focus. With the lower transmitting laser beam parallel to the

surface and using 20 degrees off-axis backscatter, surface glare received by the photo-multiplier tubes was thus minimized. The wind tunnel, CCW model, and 2-D LV transmitting optics are shown in figure 8.

RESULTS

In the following, surface pressure measurements are used to describe the general lifting properties of the CCW configuration. Mean velocity measurements obtained using the LV are then discussed and related to the airfoil axial pressure gradient. Turbulence measurements and the derived quantities are discussed and similarities in the flowfield between this study and other wall bounded jet investigations are addressed.

Pressure Measurements

Measured surface pressures have been converted to non-dimensional coefficients of pressure and are presented as a function of their chordwise position in figure 9a for a slot gap of 2.5 mm.(h/r=0.10) and a fixed angle of attack of 0.0 degrees. The effect of varying the blowing momentum coefficient rate, $C\mu$, is also presented in the various curves. Large negative pressures are found in the aft circulation region and the forward and aft suction peaks are a strong function of the blowing coefficient $C\mu$. Similar results are seen in figure 9b, which apply to the smaller slot gap (0.86 mm. or h/r=0.034). A close comparison of figures 9a and 9b shows that, at a given momentum coefficient, higher suction values are obtained for the smaller slot gaps. This is indicative of the major role that jet velocity plays in flowfield development on the CCW model. Figure 10 contrasts the differences in surface pressure on the Coanda surface with and without wind tunnel freestream. Note the severe adverse pressure gradient imposed upon wall jet for the lifting case, whereas the static case exhibits a near zero gradient with respect to angular location on the circular trailing edge.

The effect of jet-to-freestream velocity ratio is seen more clearly when the surface pressures are integrated over the surface, yielding a section lift coefficient, C_L. Figure 11 shows the relationship of C_L with respect to momentum coefficient, $C\mu$. Note that at the smaller slot gap tested (0.86 mm. or h/r=0.034), the 7.6-degree angle of attack case shows evidence of separated flow at the higher values of the momentum coefficient. Again, as indicated in the previous pressure data, the higher lift values occur with the smaller slot gap for a given $C\mu$. This indicates that overall mixing of the jet with the external flow is driven by the ratio of their relative velocities.

Tunnel test conditions used for the LV surveys represent an attached flow case as indicated by the trend of C_L vs. $C\mu$ at 0.0 degrees angle of attack and h/r=0.10. The non-linearity in the lower jet velocities (low $C\mu$'s with the larger slot gap) with respect to lift appears to be typical of CCW performance (Englar (1973)).

Mean Flow Measurements

Figure 12 represents a composite vector plot of the LV mean flow measurements. The effect of the jet on the mean flowfield is apparent in the

large turning angles that are exhibited. The extent of jet mixing is also seen in the overall growth of the jet. Also, it can be observed that the upper surface boundary layer is fully attached for this case. If one looks closer at the region near jet detachment, as seen in figure 13, the rear stagnation point is seen to be between 130 and 140 degrees in angular location measured from the slot on the Coanda surface. This was also seen in the pressure measurements presented previously.

Similarly, the jet exit region, when magnified greatly as in figure 14, shows evidence of the finite slot lip trailing edge thickness. A small re-circulation region associated with the 0.25 mm. trailing edge thickness can be detected. Also exhibited in the data from this location are the mean jet characteristics and the significant entrainment of the external flow into the jet region.

The mean velocity data are shown in dimensional form, for different angular positions in figure 15. Here the velocities are defined as the component tangential to the surface. The spread of the wall jet is self-evident.

In comparing these data with similar data in the literature, it is necessary to define the appropriate dimensionless variables. Considering the curved wall jet region itself, there are two scales for velocity, U_∞ and U_j, and two scales for length, h and r. Because of these multiple scales, it is very difficult, in the absence of a very large volume of data, to determine the functional form of the dimensionless variables (based on these variables) that will collapse the data.

Despite this, some useful comparisons can be made if, instead, we consider the use of scales based upon the local wall jet characteristics. For example the outer mixing region of the curved jet flow will be driven by the velocity scale $\Delta U_m=U_m-U_e$ and will have a length scale $y_{1/2}-y_m$ (see figure 3). These are the length scales suggested by Launder and Rodi (1983).

In the present case, therefore, Ue must first be determined, and this is defined as that point where the Reynolds stresses become negligible. It is shown as a function of position in figure 16. The non-linear growth is evidence of the strong pressure gradients through which the wall jet must develop. Also shown are the corresponding values of $y_{1/2}$ and y_m.

When these variables are combined in the form suggested by Launder and Rodi (1983) then the data shown in figure 17 are obtained. Also shown are the data of Kind and Maull (1968) which exhibit similar behavior as the present data. Thus for the outer part of the jet flow at least, the flow is driven by the defect velocity $\Delta U_m=U_m-U_e$. In contrast, the circular wall jet uses scaling factors of U_m and $y_{1/2}$. This is seen in figure 18, where the data from quiescent conditions is seen to behave in the well known gaussian manner.

The inner region of the wall jet will not and should not be expected to display similarity in this form. For that region, in addition to the scales discussed above, there will be the viscous scales u_τ and y^+. However these could not be recorded in the present test program so that a suitable dimensionless form of the data can not be presented.

Turbulence Quantities

Emphasis was placed on the determination of accurate turbulence information in this test program, and for that reason, a total of 4096 data points were acquired at each measurement location. With the LV operated in a constant tunnel coordinate system, rotation of the velocity vectors to a model-fixed coordinate system was needed for comparison purposes from station to station. Thus at each angular position on the model, the turbulence intensity was resolved into a normal and tangential component. Similarly, the turbulent shear stress was transformed to a component tangential to the surface at the angular location on the where the measurements were obtained.

Figure 19 shows the tangential turbulence intensity component, $\bar{u}'$,in the similarity variables suggested by Wilson and Goldstein (1976) and indicates some similarity of profiles in the regions greater than $y_{1/2}$. Further, comparisons with the results for circular wall jet experiments collated in Launder and Rodi (1983) indicate that similarity exists between profiles in the outer mixing region. However, differences in the wall-bounded region exist, but this is to be expected in different configurations due to different viscous effects. As separation is approached, outer layer similarity is naturally lost, and large stresses are obtained. In all cases, peak values are obtained close to the wall and the existence of a minimum in the distribution is indicative of the two production regions: that near the wall (a boundary layer mechanism) region, and that in the outer region (a mixing layer mechanism).

The distributions in $\bar{v}'$ are shown in figure 20 and display similar trends, although collapse of the data in the outer region is decidedly poorer. The values are, however, comparable to those reported by Launder and Rodi (1983) except at separation where very large values arise.

Reynolds Stresses

An important turbulence quantity in 2-D flowfields is the turbulent shear stress $\overline{uv}$. During this experiment emphasis was placed on the determination of shear stresses, not only for understanding the physics of the flow, but also to provide information for turbulence modelling. The turbulent shear stress, $\overline{uv}$, is plotted with respect to the local surface normals in figure 21. Near the wall the stresses are negative due to the boundary layer production mechanism. In the outer region, where the gradient is of opposite sign, the stresses are positive and positive production is preserved. As the jet spreads, the extent of non-zero stress grows and the magnitudes become quite large at separation.

These trends are more clearly indicated in figure 22 which presents the same data, non-dimensionalized on the scales U_m and $y_{1/2}$. Similar trends in uv are seen in the high surface curvature results of Smits, Young, and Bradshaw (1979). The change in sign of the stress in the outer region after separation ($\theta = 135^{o}$) is to be expected in view of the change in sign of the velocity gradient of the incoming lower surface flow. Finally, figure 23 shows the effect of the bluff trailing edge of the upper surface. Here the large shear stress associated with the small recirculation region can be observed. The finite trailing edge thickness can thus play a role in the overall mixing and turbulence development.

Turbulent Eddy Viscosities

The ability of CFD methods to accurately predict performance can hinge upon an accurate turbulence model. For that reason some of the current work was motivated to explore the effect that curvature plays in the turbulent flowfield development. An early attempt was made by Prandtl (1961) in 1939 and later by Sawyer (1962) to account for the highly curved geometry. Their efforts have resulted in the following eddy viscosity formulation.

$$-\overline{uv} = \varepsilon \, dU/dy \, [\, 1-C_1 \, K]$$

where $K = U / (r+y) \, dU/dy$ and C_1 = curvature constant

Initial evaluation of this expression using the experimental data with curvature constant $C_1 = 5.0$ (after Wilson and Goldstein (1976)) yielded trends similar to those obtained for the planar wall jet geometry but with much elevated magnitudes. Varying the curvature constant upward, until reasonable agreement with the planar wall jet results was attained yielded a value of $C_1 = 25.0$. This value for C_1 being much larger than the "best fit" for Wilson and Goldstein (1976), may be accounted for by the much smaller curvature used by this experiment. Use of the large value for C_1 is further substantiated with the experimental results obtained by Wendt (1973) for an geometry consisting of the shear flow between concentric cylinders, where it was suggested that C_1 be of the of order of the value used at present.

The resulting data are shown in figure 24. It should be noted that the eddy viscosity values become undefined at $y=y_m$ due to the zero velocity gradient. However, this is confined to a small region and is not shown for clarity. At separation, large negative values are obtained as expected. Likewise, negative values are obtained near the wall before the separation.

The values that are obtained are comparable to those of the planar wall jet; however, no kind of universality is evident. The universal use of planar data in numerical simulation of these kinds of flow should therefore be undertaken with some caution.

Turbulence Modelling Considerations

Having conducted measurements in the aft stagnation region for both the lifting and static cases, direct comparisons of the turbulence quantities are possible.

As previously shown in figure 10, the wind tunnel freestream, and hence, the aft stagnation point acts as to impose a large adverse axial pressure gradient upon the developing circular wall jet. Comparably, the quiescent conditions gave rise to the near zero axial pressure gradient. The effect of this is seen in figure 25, where the turbulent shear stresses are plotted for both flow conditions tested. Note that the position of the jet centerline velocity does not coincide with the zero crossing of the turbulent shear stress for the 40 degree data sets. However, at 130 degrees, the region of countergradient flow diminishes for the lifting case and increases for the static case (as to be expected - after Wilson and Goldstein (1976) and Rodman et. al. (1986)).

Correspondingly, when comparing the eddy viscosities (as computed in a manner described previously using $C_1 = 25.$) a notable difference is seen. Shown in figure 26 are the computed values for both lifting and static cases at the 130 degree survey location. Eddy viscosities in the near wall region for the static case behave well when using the curvature correction scheme. For the lifting case, negative values are seen, indicating that additional and unaccounted effects are present.

Based on these differences, an order of magnitude analysis was performed to determine the significance of the external flow imposed pressure gradient. Experimental data at the jet centerline for the 90 degree locations (location of maximum pressure gradient) was inserted into the axial momentum equation and assessed. The results, compiled in figure 27, indicate that the pressure gradient in the axial direction is of the same order as the mean axial convection and the curvature terms. Conversly, the static flow assessment shows that the pressure gradient is secondary, and that the curvature effects play the dominant role in flow development. This directly supports the findings as previously shown in figures 24 and 25 and suggests the need for either a higher order turbulence model or a method to account for the large pressure gradient effects when using CFD methods to model such flows.

Closing Remarks

An experimental investigation has been made of the flowfield around a circulation control wing. The prime motivation for this study has been to generate a set of data against which CFD methods may be validated. The data that have been obtained consist of the following:

(1) Wing surface pressures and integrated lift coefficients,

(2) LV surveys of the mean flow in the wall jet region,

(3) Turbulence intensities and Reynolds stresses in the wall jet.

REFERENCES

Dring, R. P. and Suo, M.: Particle Trajectories in Swirling Flows. J. Energy, Vol. 2, No. 4, July-August 1978.

Englar, R. J.: Experimental Investigation of the High Velocity Coanda Wall Jet Applied to Bluff Trailing Edge Circulation Control Airfoils. NSRDC TN. AL-308.

Kind, R.J., and Maull, D.J.: An Experimental Investigation of a Low-Speed Circulation Controlled Aerofoil. Aeronautical Quarterly, Vol. XIX May 10, 1968, pp. 170-182.

Launder, B. A. and Rodi, W.: The Turbulent Wall Jet - Measurements and Modelling. Anu. Rev. Fluid Mech. 1983, 15:429-59

Prandtl, L.: Ludwig Prandtl Gesammelte Abhandlungen (W. Tollmein, H. Schlichting, and H. Georgtler, eds.) Springer 1961, p. 775.

Rodman L.C., Jarrah M.A., Wood N.J., and Roberts, L.: Turbulence Measurements in a Plane Wall Jet. AIAA Paper 86-209, 24th Aerospace Sciences Meeting, Reno NV, January 6-9, 1986

Sawyer, R. A.: Two-Dimensional Turbulent Jets with Adjacent Boundaries. PhD thesis, Cambridge Univ., 1962.

Smits, A. J., Young, S. T. B., and Bradshaw, P.: The effect of short regions of high surface curvature on turbulent boundary layers. J. Fluid Mech., 1979, vol. 94, part 2, pp 209-242.

Wendt, F.: Turbulente Stromungen Zwichen zwei rotierenden konaxialen Zylindern. Ing. Arch., Vol. 4, 1973, p. 577

Whiffen, M.C.: Periodicity Verification Circuit. Patent Application, Lockheed P-02-487, 1979

Wilson, D. J. and Goldstein, R. J.: Turbulent Wall Jets With Cylindrical Streamwise Surface Curvature. Journal of Fluids Engineering, Vol. 96, 1976, p. 550.

Wood, N., and Nielsen, J.: Circulation Control Airfoils Past, Present, Future. AIAA Paper 85-0204, January 14-17, 1985.

Young, T.: Outlines of Experiments and Inquiries Regarding Sound and Light. Lecture to the Royal Society Jan. 16, 1800 (see Jour. Roy. Aero. Soc. Vol. 61, 1957, p. 157.

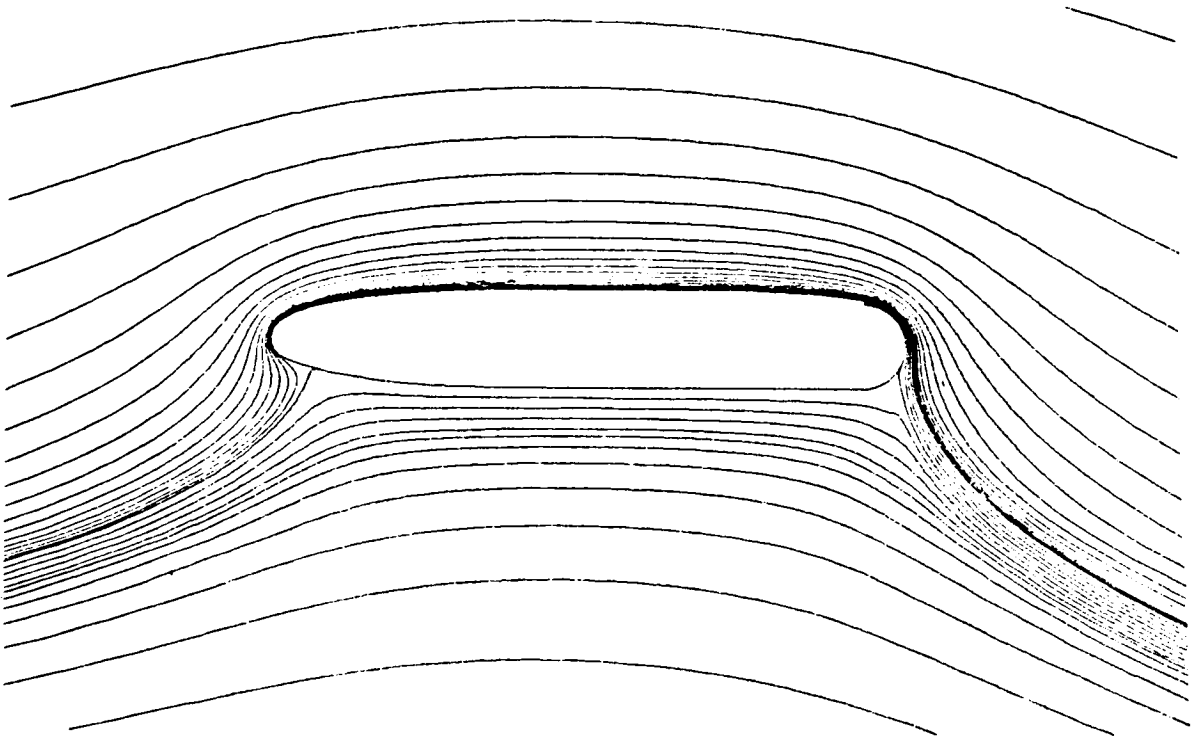

Figure 1. - Typical CCW Flowfield

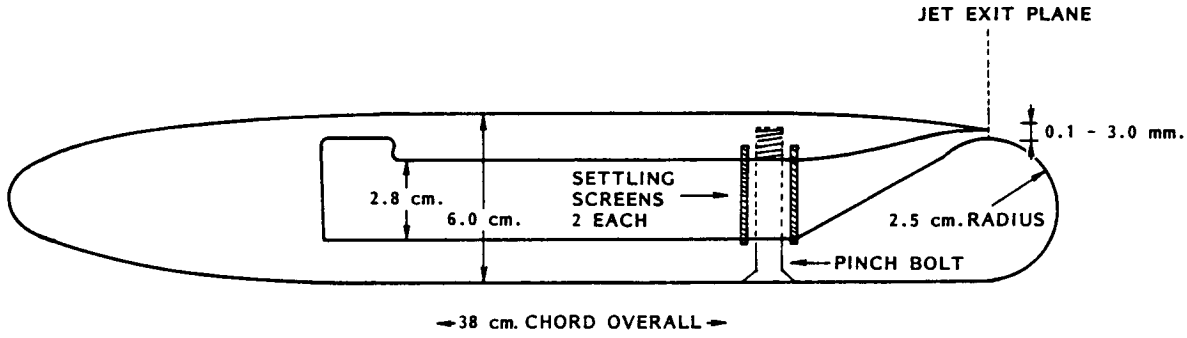

Figure 2. - CCW Model Construction

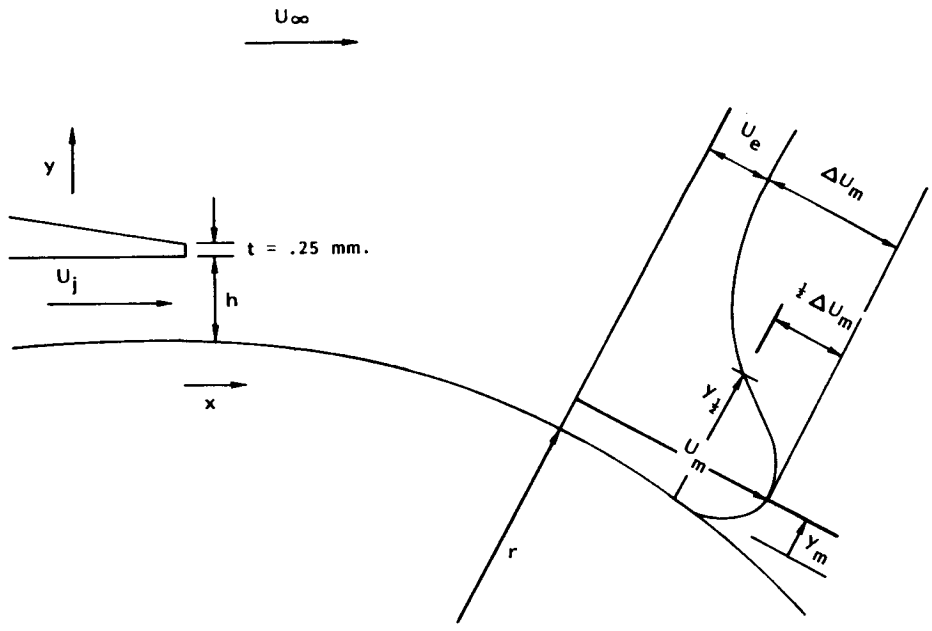

Figure 3. - CCW Slot Geometry and Nomenclature

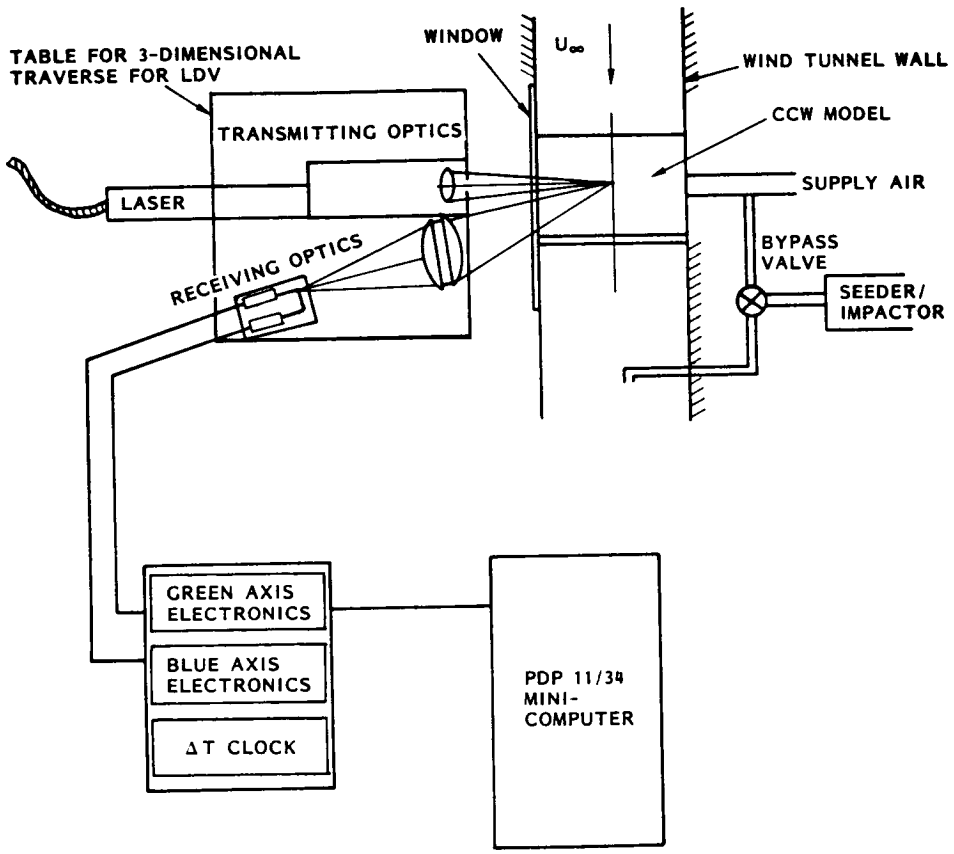

Figure 4. - 2-D LV Schematic

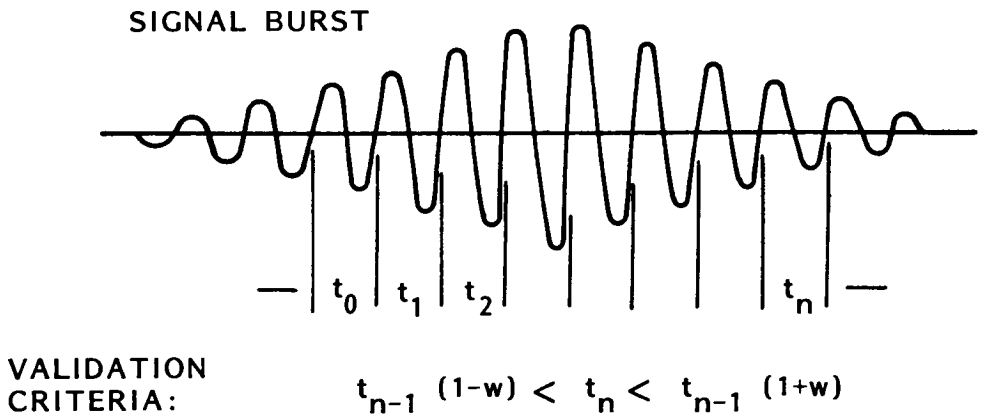

Figure 5. - Single Cycle Validation

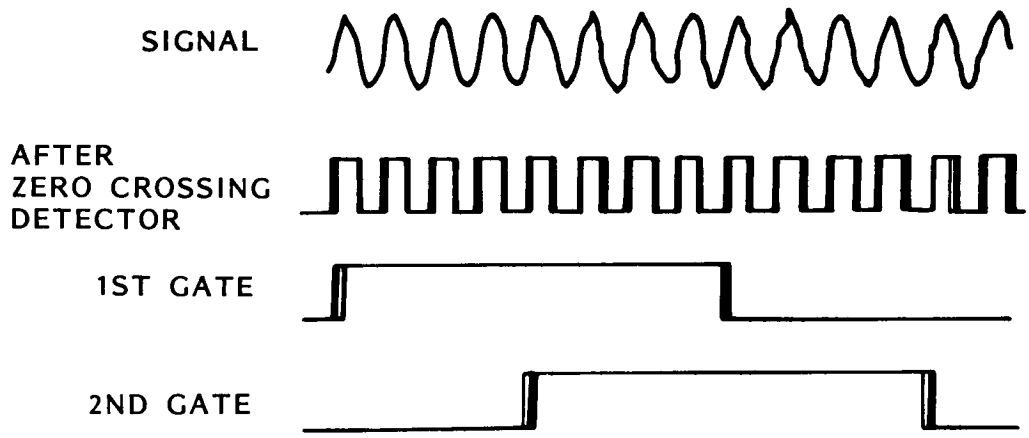

Figure 6. - Effect of Noise on Measurement Process

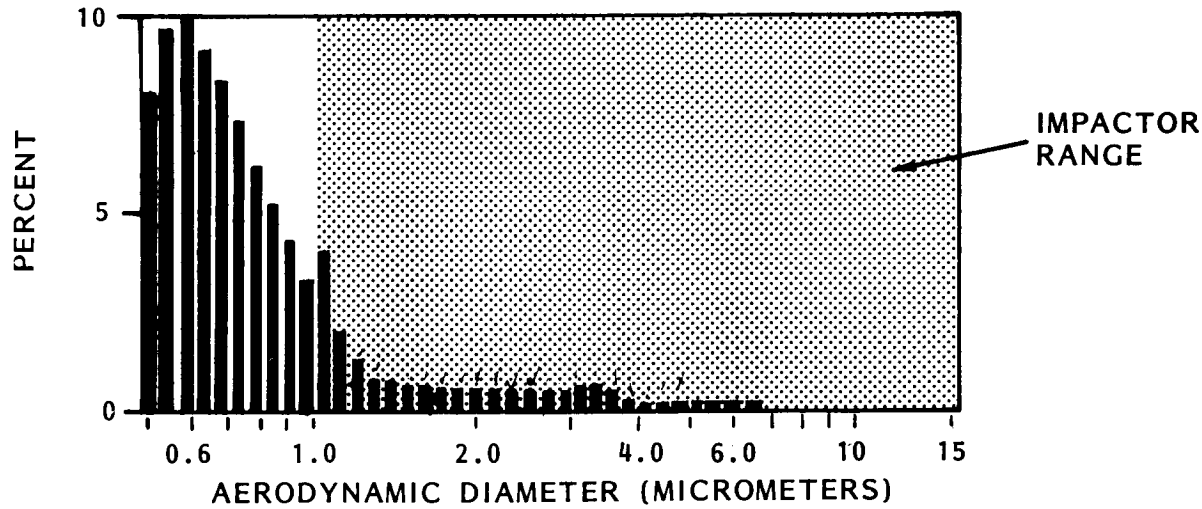

Figure 7. - Seed Size Distribution as Measured from Optical Particle Analyzer

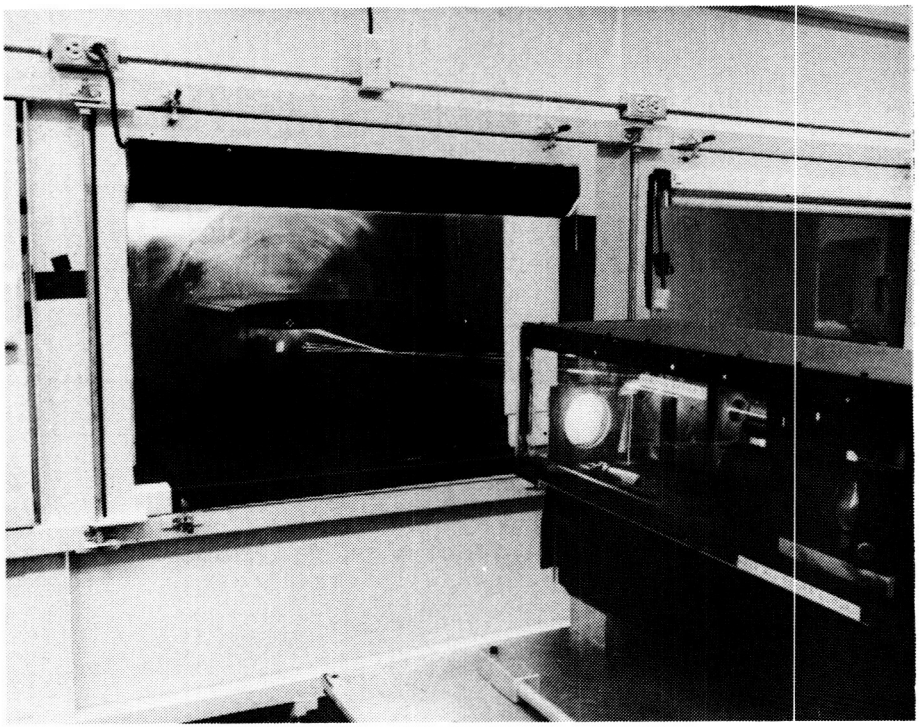

Figure 8. - CCW Model/Wing Tunnel Installation with LV Tranmitting Optics

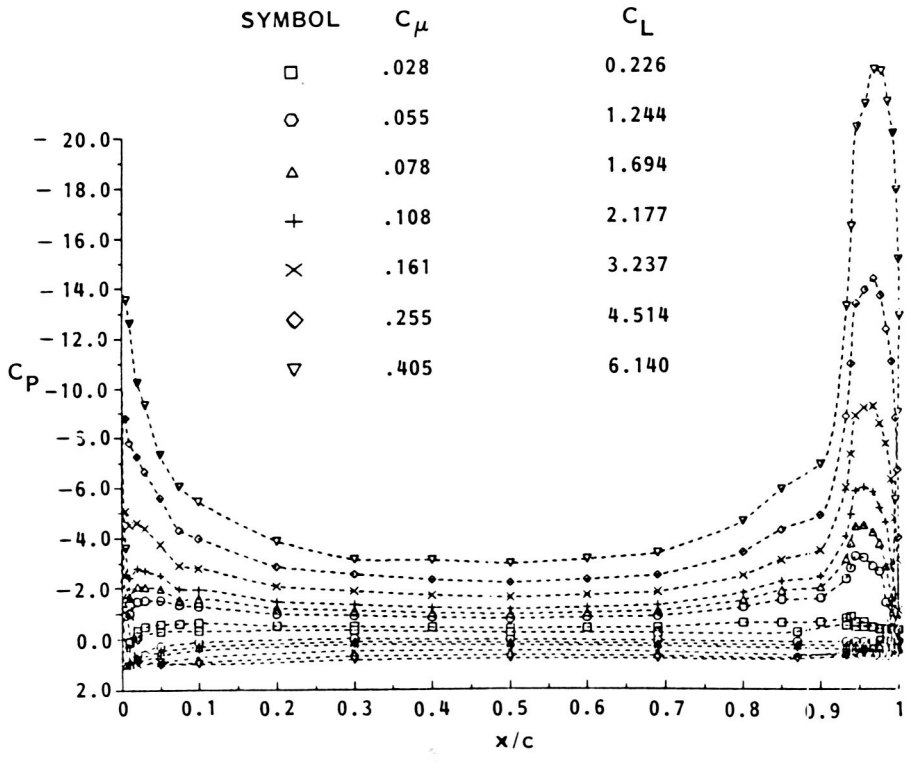

Figure 9a. - Surface Pressure Measurements at α =0.0 and h/r=0.10

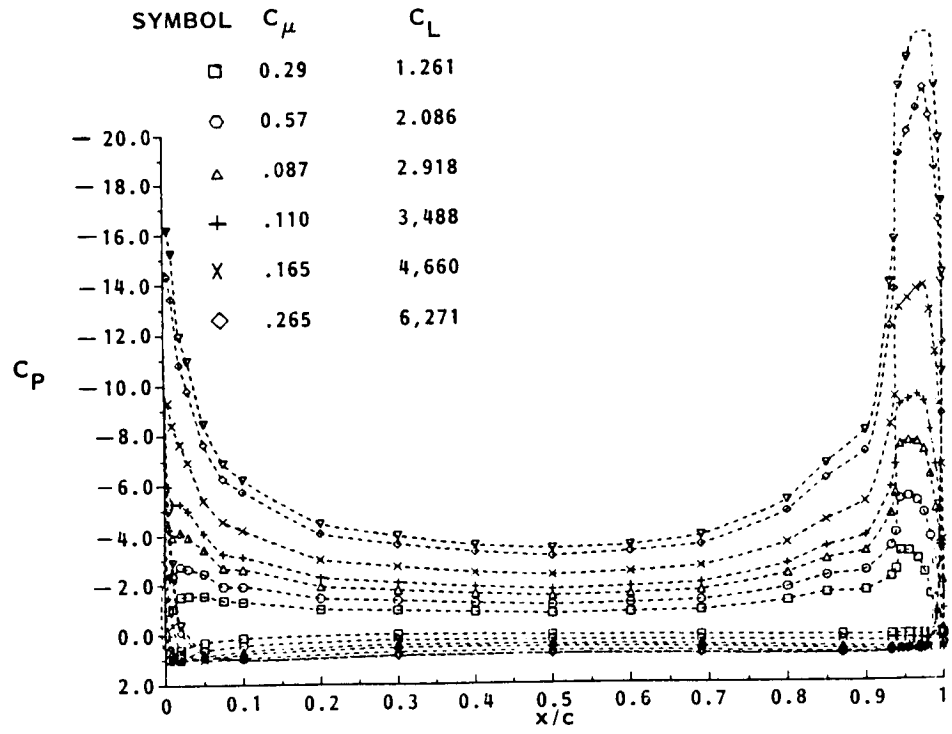

Figure 9b. - Surface Pressure Measurements at α =0.0 and h/r=0.034

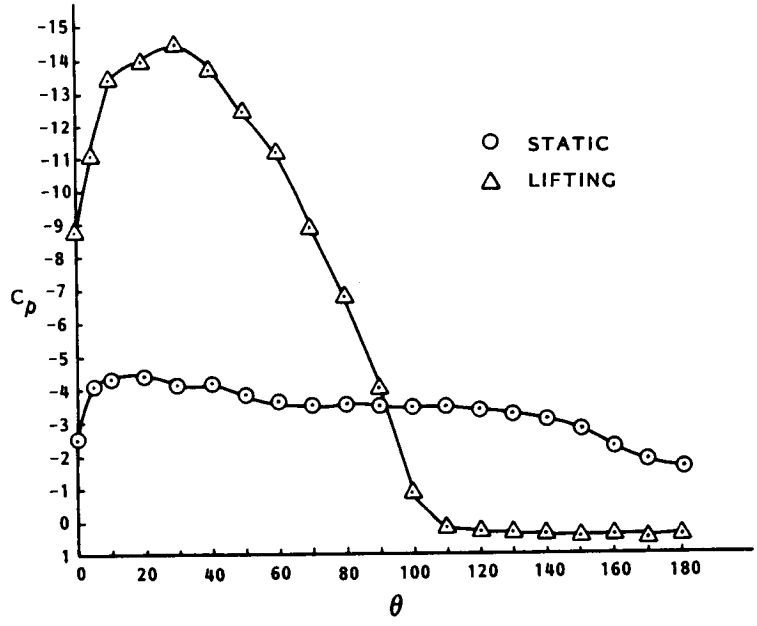

Figure 10. - Static Pressure Variation along the Coanda Surface

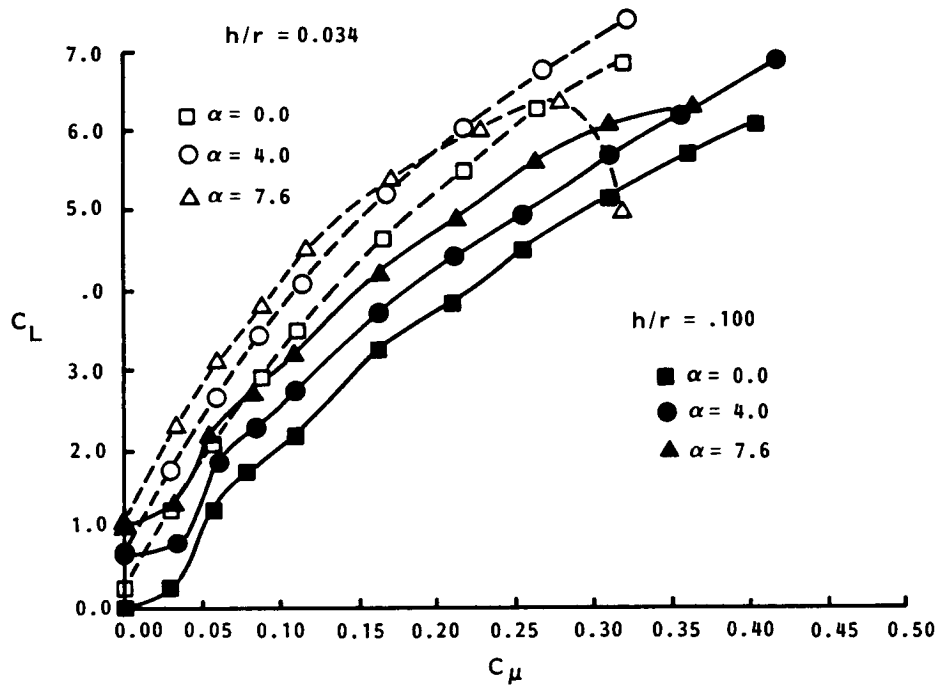

Figure 11. - Lift as a function of Jet Momentum and Angle of Attack

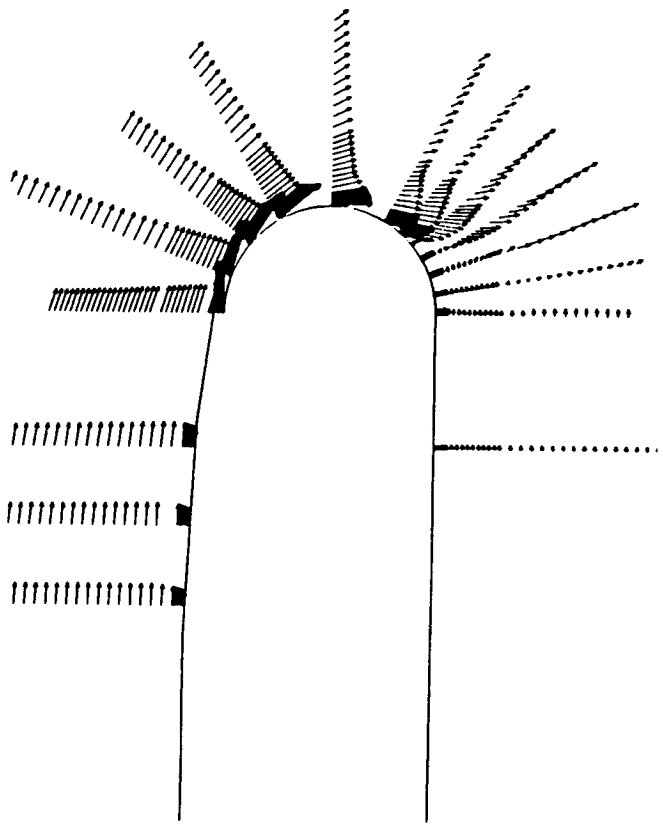

Figure 12. - CCW/LV Mean Velocity Vectors

C-2

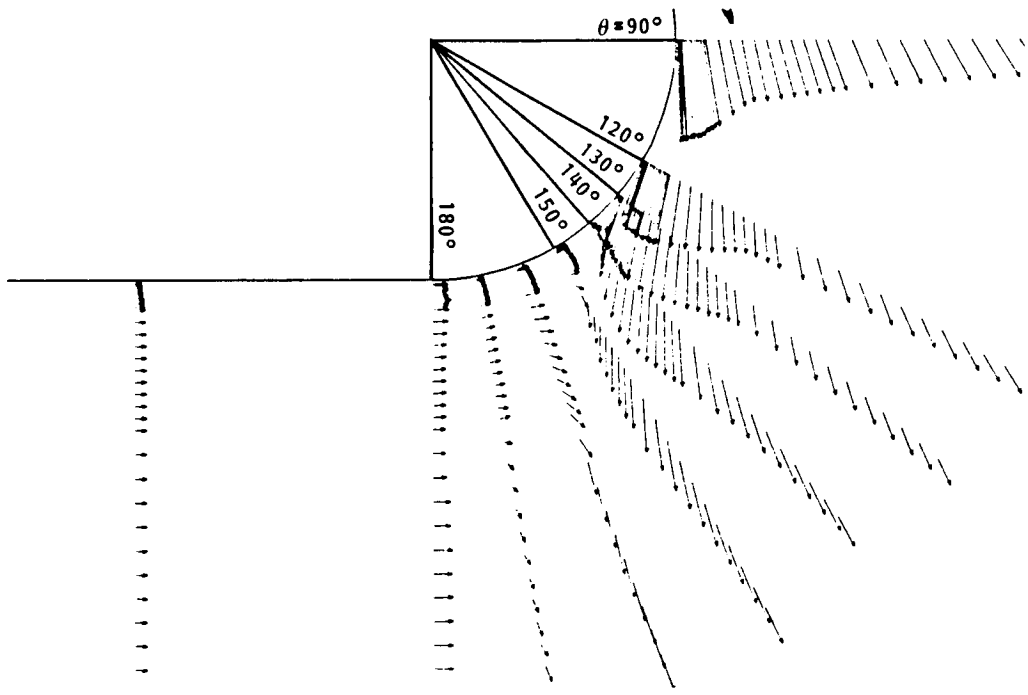

Figure 13. - CCW/LV Velocity Vectors in Aft-Stagnation Region

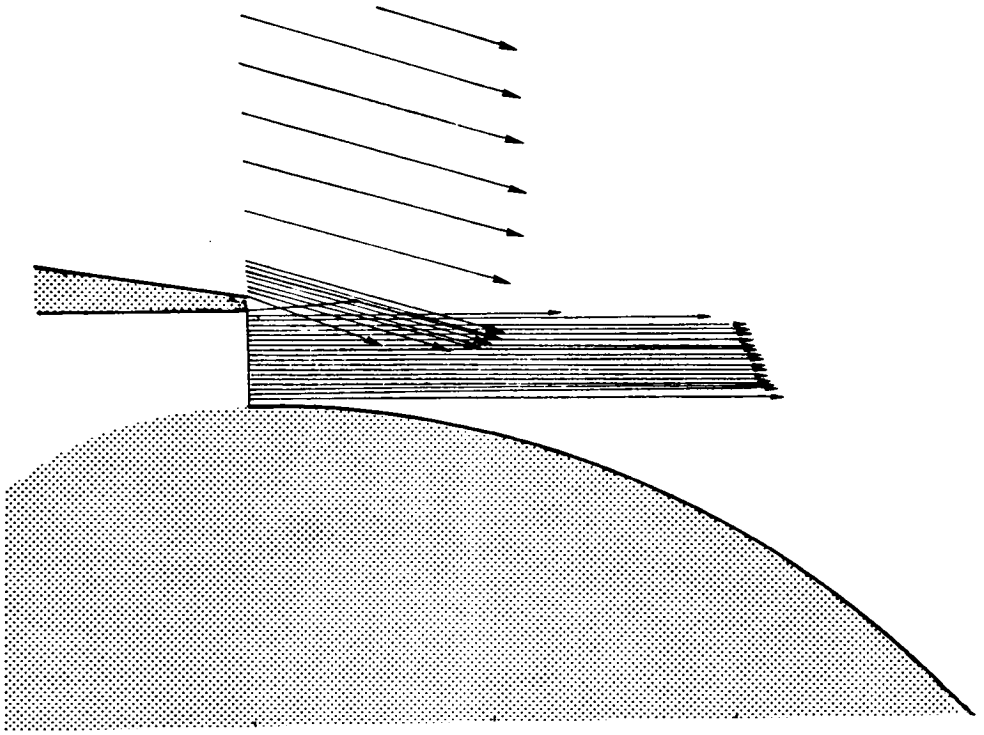

Figure 14. - CCW/LV Jet Exit Plane Velocity Vectors

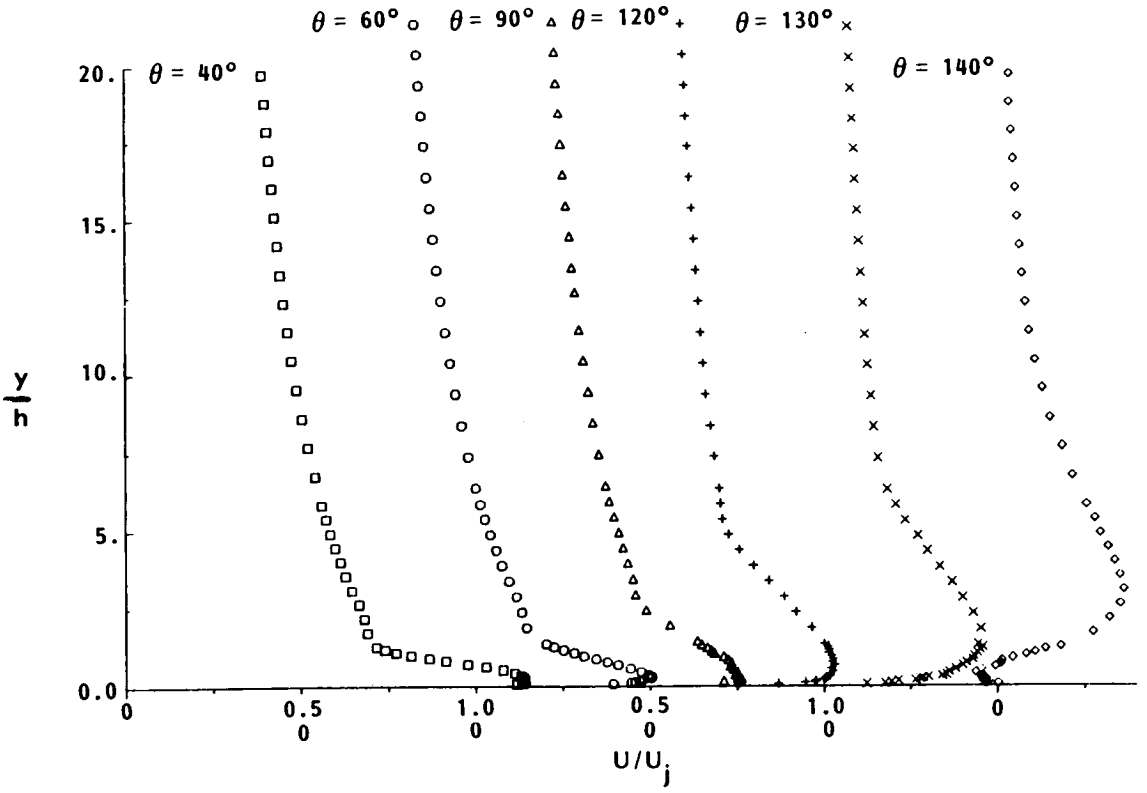

Figure 15. - Tangential Velocities in non-dimensional form

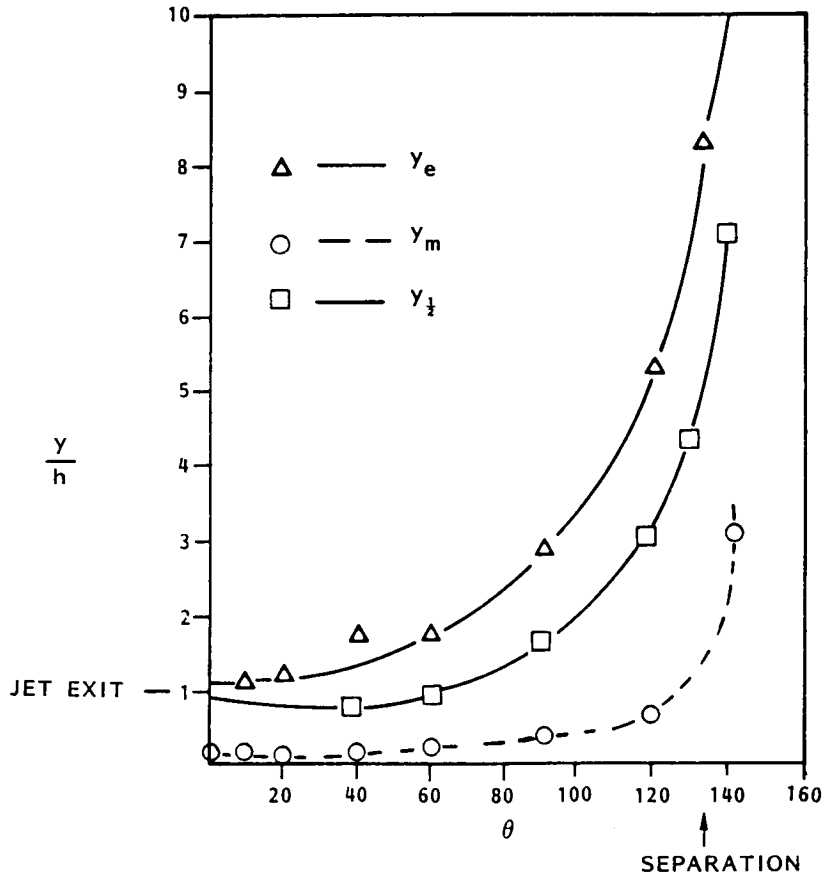

Figure 16. - Wall Jet Growth along Coanda Surface - Lifting case

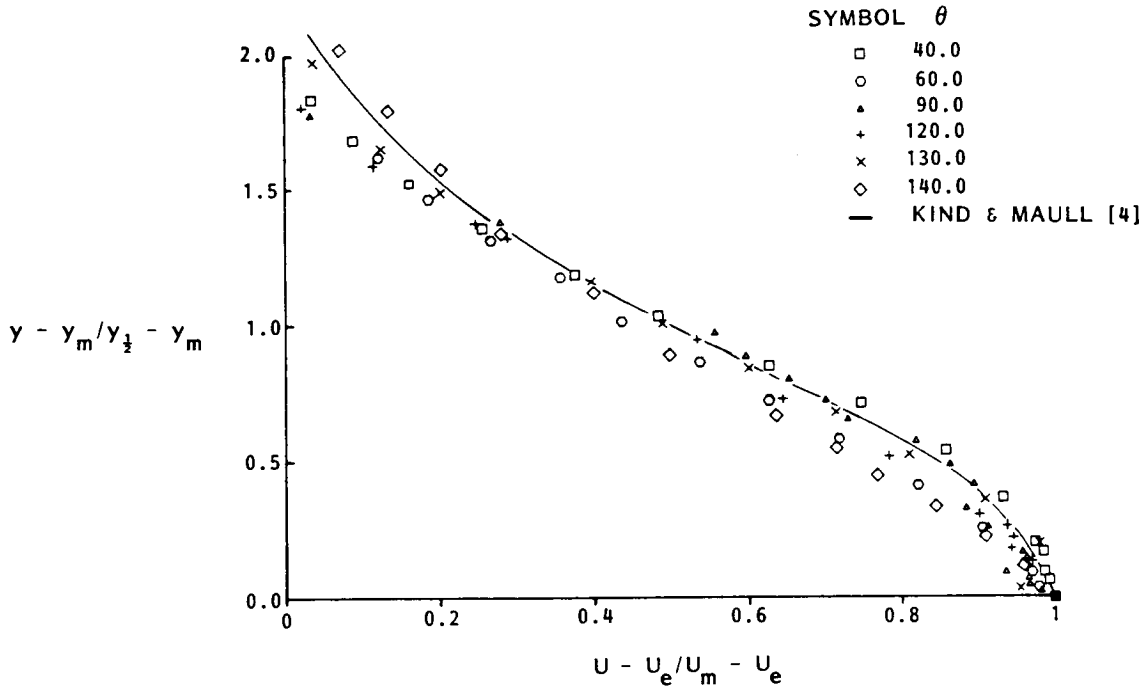

Figure 17. - Mean Tangential Velocity Profiles - Lifting case

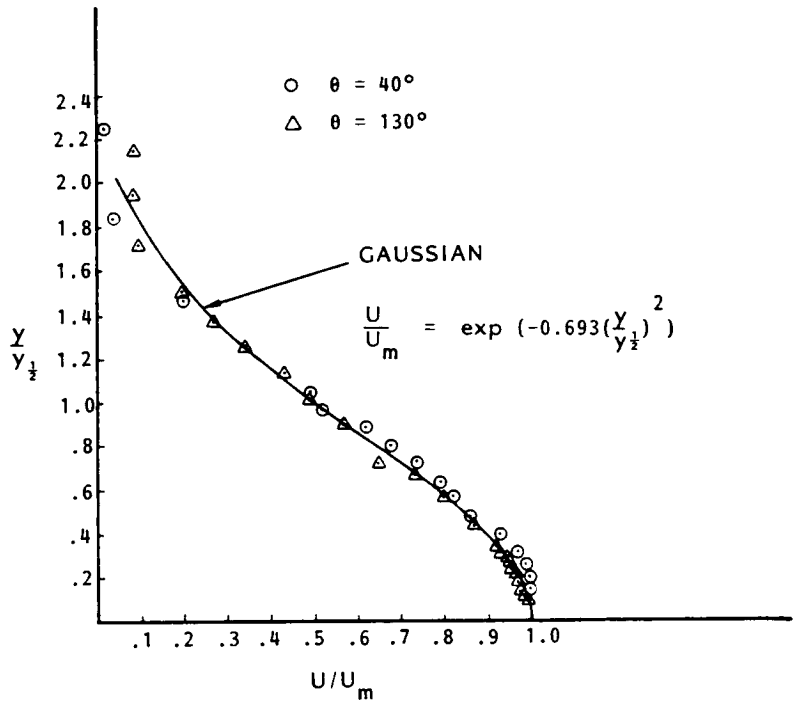

Figure 18. - Mean Tangential Velocity Profiles - Static conditions

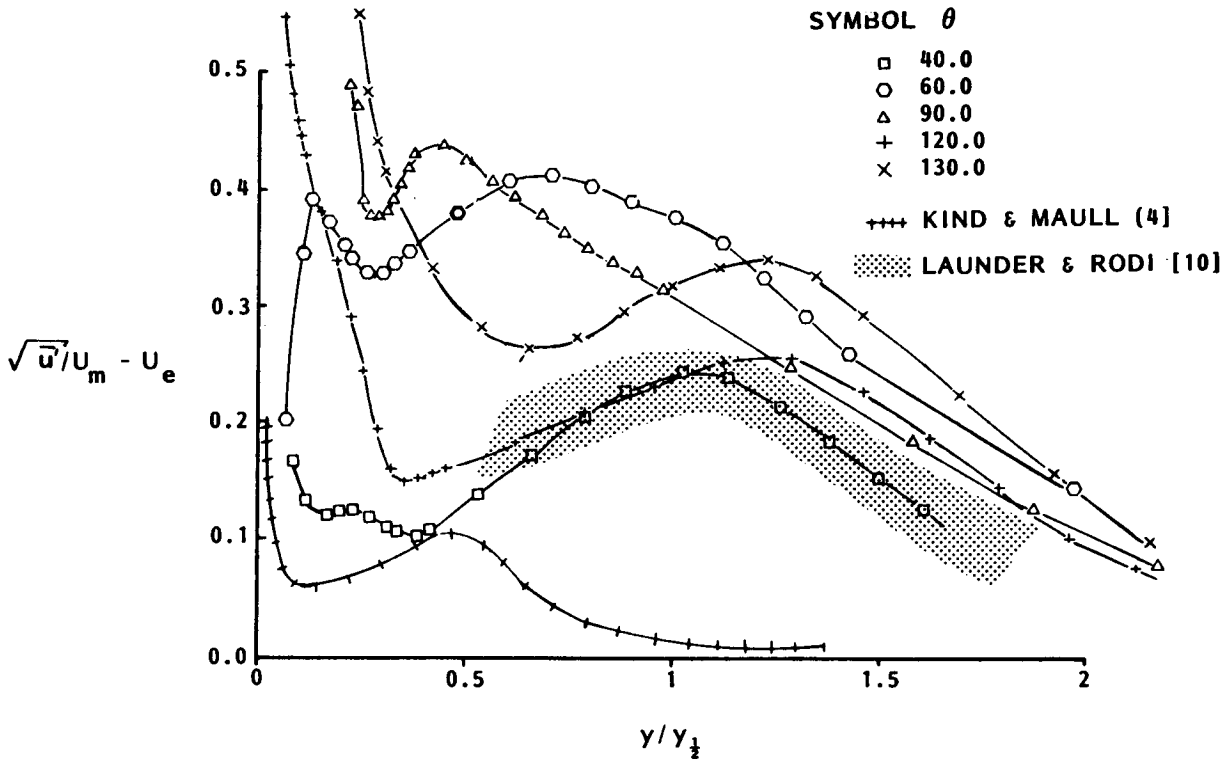

Figure 19. - Tangential Turbulence Intensity - Lifting case

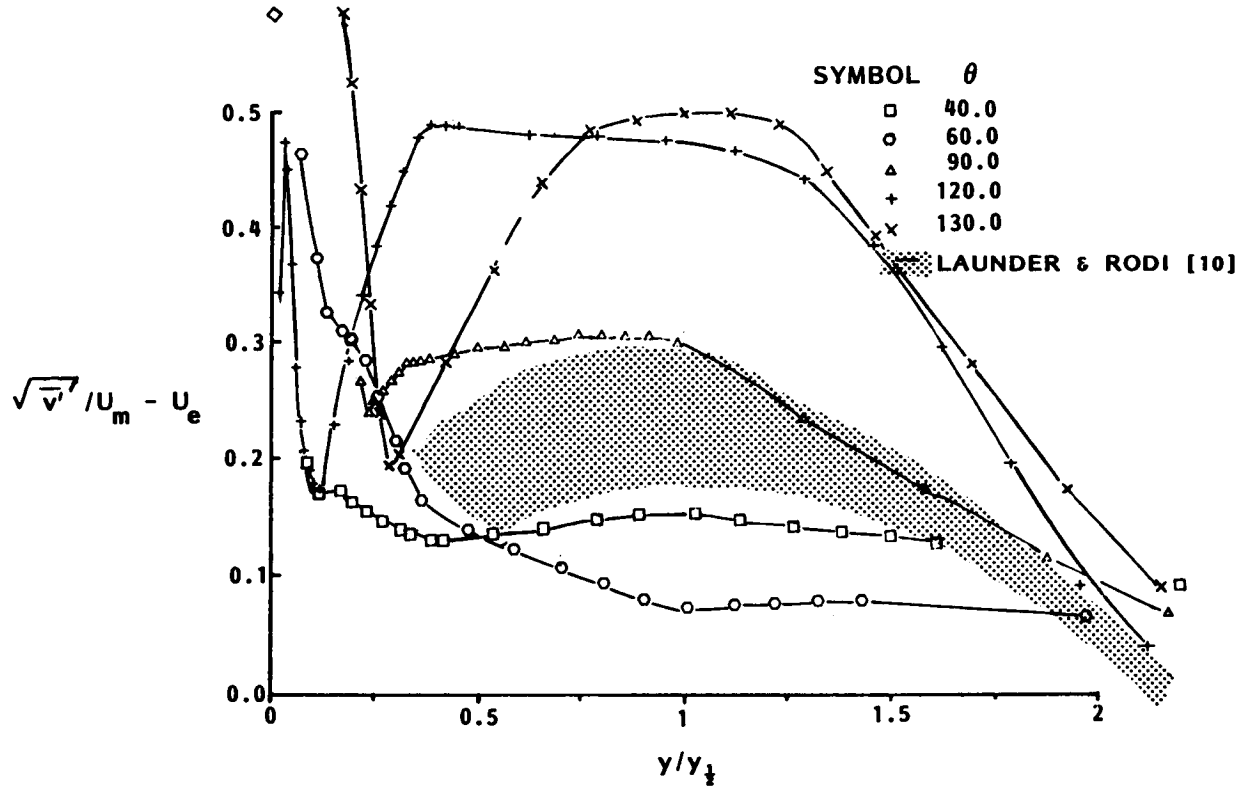

Figure 20. - Normal Turbulence Intensity - Lifting case

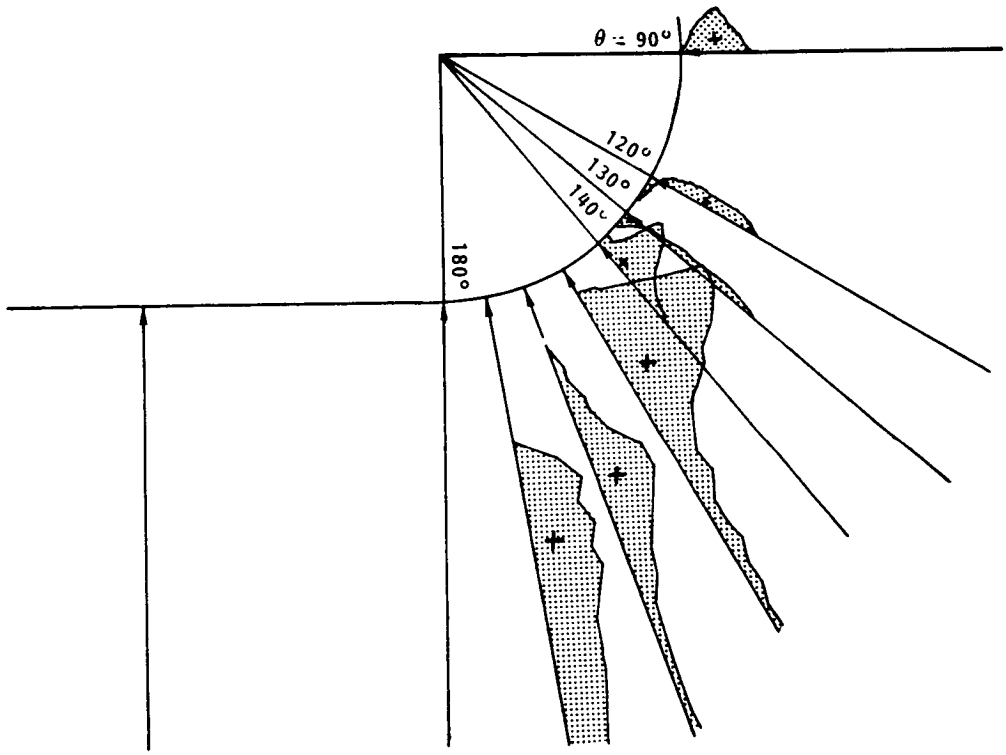

Figure 21. - Shear Stress Distributions in Aft-Stagnation Region - Lifting case

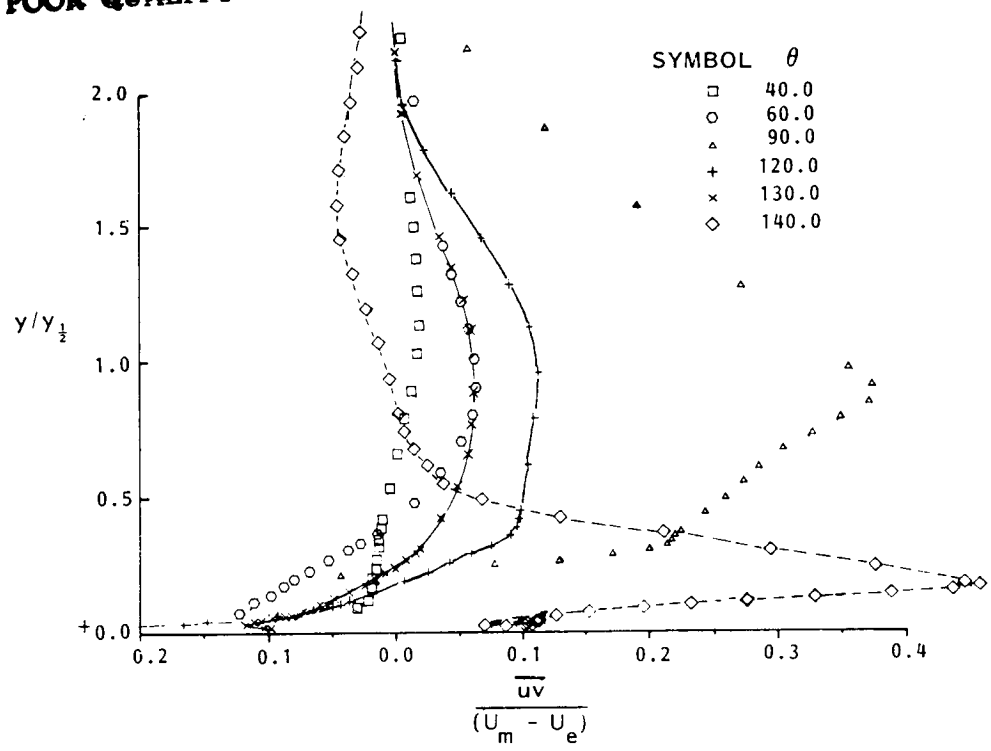

Figure 22. - Non-dimensional Shear Stresses - Lifting case

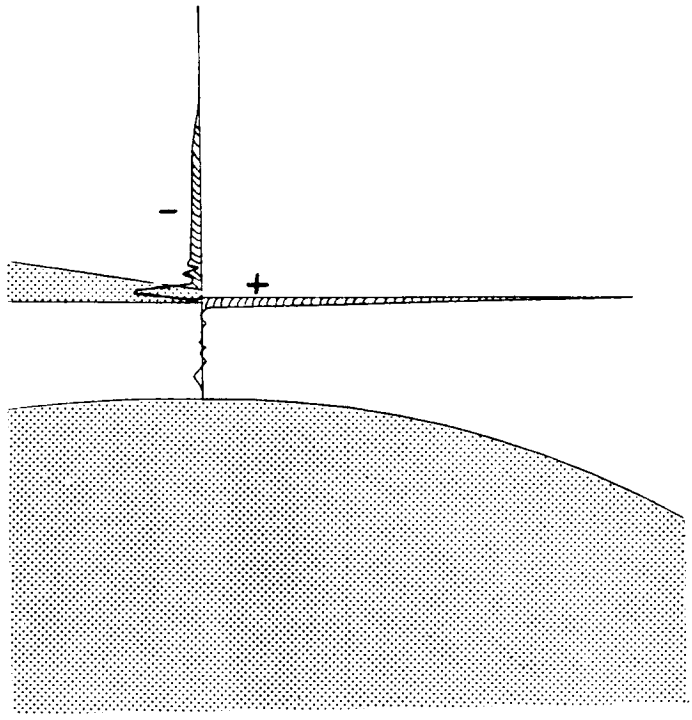

Figure 23. - Shear Stress Distribution in Jet Exit Plane - Lifting case

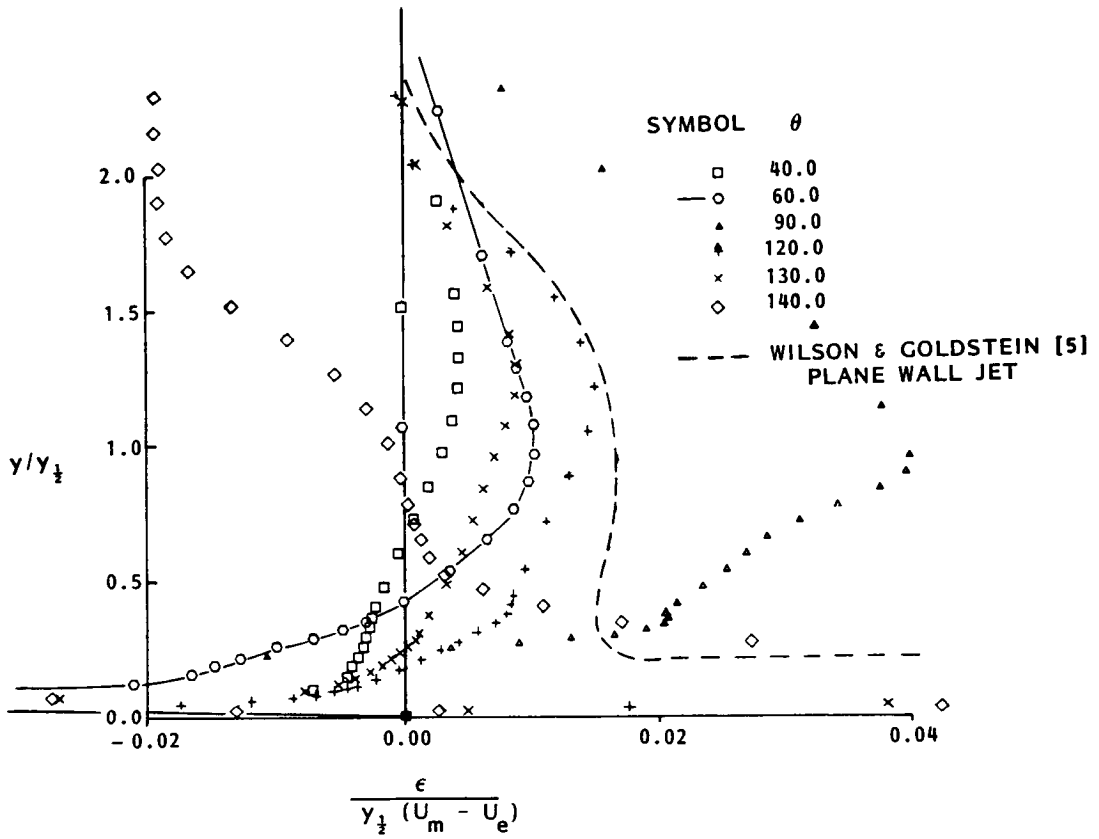

Figure 24. - Experimental Eddy Viscosities - Lifting case

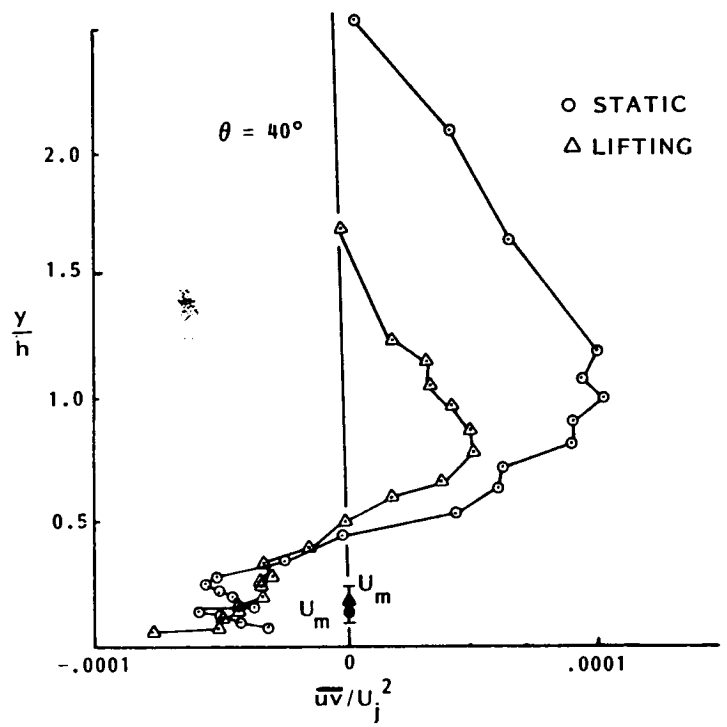

Figure 25a. - Near Wall Turbulent Shear Stresses, $\theta = 40^{o}$

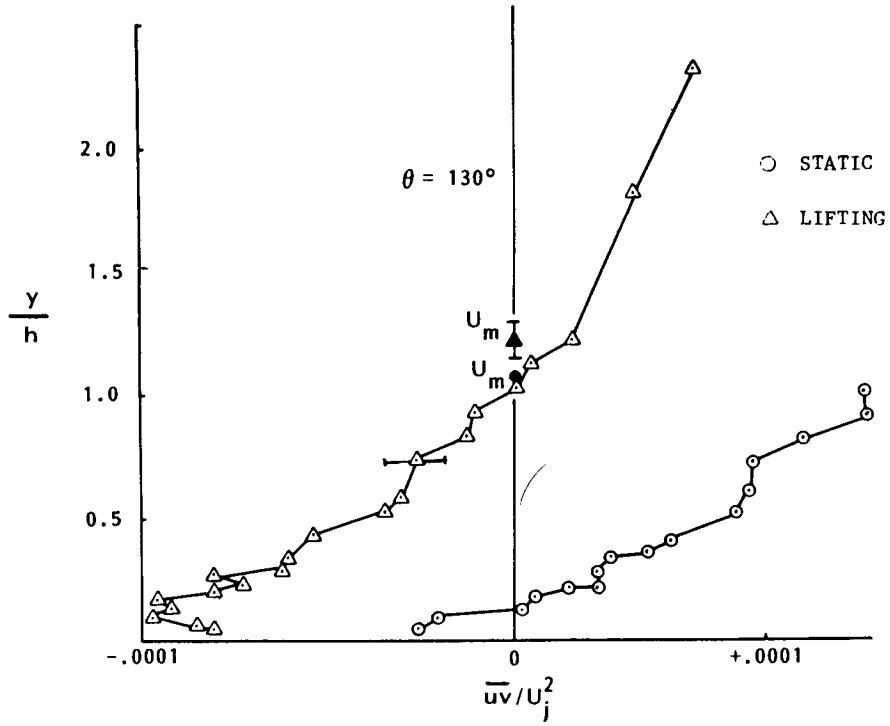

Figure 25b. - Near Wall Turbulent Shear Stresses, $\theta = 130^{o}$

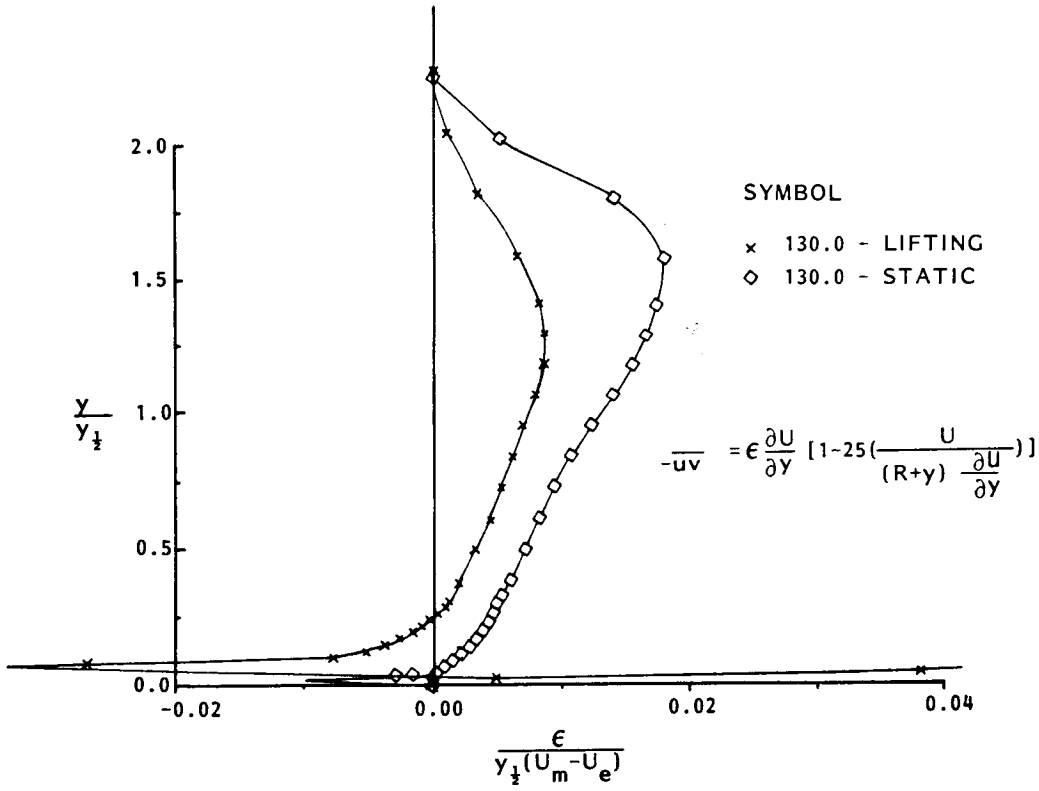

Figure 26. - Effect of Tunnel Freestream on Eddy Viscosities

	$U\frac{\partial U}{\partial x}$	$+\frac{UV}{R}$	$+(1+\frac{y}{R})V\frac{\partial U}{\partial y}$	$=$	$-\frac{1}{\rho}\frac{\partial(P+\rho\overline{v^2})}{\partial x}$	$-\frac{\partial}{\partial x}(\overline{u^2}-\overline{v^2})$	$-\frac{2\,\overline{uv}}{R}$	$-(1+\frac{y}{R})\frac{\partial\,\overline{uv}}{\partial y}$
LIFTING	$-O(10^0)+O(10^{-2})$		0	=	$-O(10^0)$	$+O(10^{-2})$	$-O(10^{-2})$	$-O(10^0)$
STATIC	$-O(10^0)+O(10^{-1})$		0	=	$-O(10^{-1})$	$-O(10^{-2})$	$-O(10^{-1})$	$-O(10^0)$

$\theta \doteq 90^0$

Figure 27. - Order of Magnitude Analysis at $\theta = 90^0$

A THEORY FOR TURBULENT CURVED WALL JETS

by

Leonard Roberts
Joint Institute for Aeronautics and Acoustics
Stanford University

Introduction

The behavior of a wall jet flowing around a curved surface has been the subject of study for almost two hundred years following the first observations of Young[1] in 1800. Practical application of this phenomena, popularly known as the Coanda effect, have been pursued in more recent times with a view to delaying separation of the boundary layer on lifting surfaces by using a wall jet over a rounded trailing edge: the wall jet causes the flow to remain attached to the surface, displaces the rear stagnation point and induces additional circulation, and therefore produces additional lift on the surface. The use of this phenomena in the design of circulation control wings (CCW) has received considerable attention in recent years and has been described by a number of investigators (see for example Wood[2] and Englar[3]).

Despite the fact that the phenomena is being used in practical applications to wing and rotor design the understanding of the properties of wall jets is still limited and depends primarily in experimental information regarding the turbulent mixing, its effect on the spreading rate of the wall jet and the corresponding deceleration of the flow as it proceeds along the wall. A thorough review was made by Launder and Rodi[4] in 1981 of available data for wall jets adjacent to surfaces of plane, cylinder and logarithmic spiral surfaces and substantial use may be made of this information to distinguish the influence of wall curvature, and rate of change of curvature in the stream direction, on the spreading rate of the jet. This information together with data from the same review on the mean velocity profile in the wall jet provides the basis for checking theoretical models of the flow.

In the present paper an attempt is made to formulate the simplest possible model for the flow of a wall jet emanating from a two dimensional source into quiescent surroundings in the presence of a wall of arbitrary shape. The method uses self similar profiles for the mean velocity together with a simple eddy viscosity model. The streamwise and radial momentum equations are integrated across the wall jet flow to give an expression for the momentum balance including the effect of the pressure gradient induced by the rate of change of surface curvature. The streamwise momentum equation is also evaluated at the point of maximum velocity to provide a second equation and thereby permit a solution for the two unknown quantities b, the jet half width and u_m, the maximum velocity. This approach provides approximate closed form solutions for the flow of the wall jet over surfaces of various shapes (for quiescent surroundings), and in particular permits a direct comparison with the available experimental results for plane, cylindrical or logarithmic spiral surfaces.

Analysis

The wall jet is considered to comprise two parts: an inner flow adjacent to the wall having a highly non-linear velocity profile characteristic of a turbulent wall flow, and an outer flow having a velocity profile more typical of a free turbulent plane jet.

The primary parameters that describe the flow are shown in figure 1. The jet emerges from a point source into a fluid at rest and spreads, increasing its width and decreasing its velocity due to turbulent diffusion in the jet and friction at the wall. At a distance s downstream of the jet exit the velocity to can be expressed as

$$u = u_m(s) f(y/b) \tag{1}$$

where u_m is the maximum velocity, occurring at $y = y_m(s)$, and $b = b(s)$ is the half width of the jet (at which point $u = \frac{1}{2}u_m$).

The velocity profile in the outer flow ($y > y_m$) is assumed to take the form:

$$u = u_m \operatorname{sech}^2 \left[\frac{k(\xi - \xi_m)}{1 - \xi_m} \right] , \xi > \xi_m \tag{2}$$

where $\xi = y/b$. This velocity profile is suggested by the classical free jet solution found by Tollmien, modified to give $u = u_m$ at $\xi = \xi_m$. The constant k is determined such that $u = \frac{1}{2}u_m$ at $\xi = 1 (y = b)$, thus

$$k = \tanh^{-1} \left(\frac{1}{\sqrt{2}} \right) = .8814 \tag{3}$$

The velocity profile for the inner flow is assumed to depend on the variable $(\xi/\xi_m)^{\frac{1}{n}}$ as suggested by turbulent wall flow, and is chosen to give a maximum value $u = u_m$ at $\xi = \xi_m$: the following profile satisfies these conditions

$$u = u_m \left[2 \left(\frac{\xi}{\xi_m} \right)^{\frac{1}{n}} - \left(\frac{\xi}{\xi_m} \right)^{\frac{2}{n}} \right] \tag{4}$$

The value ξ_m, giving the location of maximum velocity, is determined by matching the second derivative of the velocity profiles as given by equations (2) and (4), (the first derivative is zero since this is the maximum velocity point).

The result is written

$$\xi_m = (1 + kn)^{-1} \tag{5}$$

Before proceeding with the analysis, a comparison is made in figure 2 of the velocity profiles with the experimental data of Tailland[5][6]. The data are typical of those taken by a number of authors for wall jet flows over plane and curved surfaces and show that the assumed profile given by equations (2) and (4) is reasonable. Additionally in figure 3 a comparison is made of ξ_m, given by equation (5), with the experimentally determined values given by Forthmann[7], Sigalla[8] Bradshaw & Gill[9], Patel[10] and Giles[11]. All the data falls within a band $.14 < \xi_m < .16$ corresponding to $7 > n > 6$ for Reynolds number R_θ in the range 10^4 to 10^5; thus the values of n are consistent with those expected for turbulent wall flows.

In this paper the two primary flow variables to be determined are the jet half width, b, and the maximum velocity u_m. The continuity and momentum equations for an incompressible fluid are written

$$\frac{\partial u}{\partial s} + \frac{\partial}{\partial y}(hv) = 0 \tag{6}$$

$$hu\frac{\partial u}{\partial s} + hv\frac{\partial}{\partial y}(hu) = \frac{-h}{\rho}\frac{\partial p}{\partial s} + \frac{\partial}{\partial y}(h^2\tau) \tag{7}$$

and

$$\frac{u^2}{R} = \frac{1}{\rho}h\frac{\partial p}{\partial y} \tag{8}$$

where

$$h = 1 + y/R$$

Equations (6) to (8) can be combined to give

$$\frac{\partial}{\partial s}(u^2) + \frac{u^2 y}{R^2}\frac{dR}{ds} = \frac{\partial}{\partial y}\left(h^2\tau - h^2uv - \frac{\partial}{\partial s}\left(\frac{py}{\rho}\right)\right) \tag{9}$$

neglecting terms of $0\left(\frac{1}{R^2}\right)$. Integration across the flow gives the integral form of the momentum equation:

$$\frac{d}{ds}\left[\int_o^\infty u^2 dy\right] + \frac{1}{R^2}\frac{dR}{ds}\left[\int_o^\infty u^2 y dy\right] = -\tau_o/\rho \tag{10}$$

This equation retains the term which reflects the curvature-induced pressure gradient which may be large compared with τ_o/ρ, the wall shear stress.

Substitution of the velocity profiles (equations 3 and 4) into the integrals of equation (10) gives

$$A_n\left[\frac{1}{u_m^2}\frac{d}{ds}(bu_m^2)\right]+C_n\left[\frac{b^2}{R^2}\frac{dR}{ds}\right]=-\frac{1}{2}C_f \tag{11}$$

where

$$A_n=(1+\frac{2}{3}n)(1+kn)^{-1}$$
$$C_n=\frac{1}{2}\left[\left(\frac{4}{3}\log 2-\frac{1}{3}\right)n^2+\frac{4}{3}n+1\right](1+kn)^{-2}$$

From equation (11) it can be seen that in the absence of curvature effects the wall jet momentum (bu_m^2) decreases with distance due to skin friction at the wall. However for a wall of decreasing radius of curvature ($\frac{dR}{ds}<0$) it is possible for the wall jet momentum to increase with distance along the wall. This will occur if

$$C_n\frac{b^2}{R^2}\left(-\frac{dR}{ds}\right)>\frac{1}{2}C_f$$

An approximate form of equation (11) valid for large n and for $C_f\to 0$ may be written

$$\frac{1}{u_m^2}\frac{d}{ds}(bu_m^2)+\frac{(\log 2-\frac{1}{4})}{k}\frac{b^2}{R^2}\frac{dR}{dS}=0 \tag{11a}$$

a result which is applicable for large Reynolds number.

Since there are two unknown quantities in equation (11) it is necessary to use a second relationship in order to determine b and u_m. It is convenient to use the momentum equation (7) evaluated at the point of maximum velocity, (ie where $u=u_m, \frac{\partial u}{\partial y}=0$) which may be written

$$\left[u\frac{\partial u}{\partial s}+\frac{uv}{R}+\frac{1}{\rho}\frac{\partial p}{\partial s}\right]_m=\left[\frac{h}{\rho}\frac{\partial \tau}{\partial y}+\frac{2\tau}{\rho R}\right]_m \tag{12}$$

The terms on the left hand side may be written in dimensionless form, neglecting terms of $O(b/R)^2$ as follows:

$$\frac{b}{u_m^2}\left(u\frac{\partial u}{\partial s}\right)_m = \frac{1}{2}\left[\frac{1}{u_m^2}\frac{d}{ds}(bu_m^2) - \frac{db}{ds}\right]$$

and

$$\frac{b}{u_m^2}\left(\frac{uv}{R}\right) = \frac{1}{u_m}\left[-\int_o^{ym}\frac{\partial u}{\partial s}dy\right] b/R$$

$$= -\frac{1}{2(1+kn)}\left[\frac{1}{u_m^2}\frac{d}{ds}(bu_m^2) - \frac{db}{ds}\right] b/R$$

Finally,

$$\frac{b}{u_m^2}\cdot\frac{1}{\rho}\frac{\partial p}{\partial s} = -\frac{b}{u_m^2}\frac{d}{ds}\left[\int_{ym}^{\infty}\frac{u^2}{R}\,dy\right]$$

$$= -\frac{b}{u_m^2}\frac{d}{ds}\left(\frac{bu_m^2}{R}\int_{\xi_m}^{\infty}\left(\frac{u}{u_m}\right)^2 d\xi\right)$$

$$= -\frac{\frac{2}{3}n}{1+kn}\cdot\frac{b}{R}\cdot\left[\frac{1}{u_m^2}\frac{d}{ds}(bu_m^2) - \frac{b}{R}\frac{dR}{ds}\right]$$

Thus the left hand side of equation (12) becomes

$$\frac{1}{2}\left(1-\frac{1+\frac{4}{3}n}{1+kn}\,b/R\right)\left[\frac{1}{u_m^2}\frac{d}{ds}\,(bu_m^2)\right] - \frac{1}{2}\left(1-\frac{1}{1+kn}\,b/R\right)\frac{db}{ds}$$

$$+\frac{2}{3}\left(\frac{n}{1+kn}\right)\frac{b^2}{R^2}\frac{dR}{ds}$$

In the limiting case of large n this expression simplifies to

$$\frac{1}{2}\left\{\left(1-\frac{4}{3k}b/R\right)\frac{1}{u_m^2}\frac{d}{ds}(bu_m^2) - \frac{db}{ds} + \frac{4}{3k}b^2/R^2\frac{dR}{ds}\right\}$$

In order to evaluate the right hand side of equation (12) it is necessary to express τ in terms of u through an eddy viscosity ϵ based on a length scale $b(1-\xi_m)$ and a characteristic velocity u_m. It is convenient to write

$$\epsilon = \frac{K}{4k^2}\rho(1-\xi_m)b\,u_m\,g(\xi) \qquad (13)$$

where K is a constant to be determined experimentally. The function $g(\xi)$ is chosen such that $g(\xi_m) = 1$ and also satisfies the appropriate boundary condition at $\xi = O$.

The shear stress takes the form

$$\frac{\tau}{\rho} = \epsilon\left(\frac{\partial u}{\partial y} - \frac{u}{R}\right), \tag{14}$$

or, substituting for $u = u_m f(\xi)$ and ϵ

$$\frac{\tau}{\rho u_m^2} = \frac{K}{4k^2}(1 - \xi_m)\,[f'g - b/R\, fg] \tag{15}$$

Similarly,

$$\frac{b}{\rho u_m^2}\frac{\partial \tau}{\partial y} = \frac{K}{4k^2}(1 - \xi_m)\left[(f''g + f'g') - \frac{b}{R}(f'g + fg')\right] \tag{16}$$

where $'$ denotes a derivative with respect to ξ.

Since $f(\xi_m) = g(\xi_m) = 1$ and $f'(\xi_m) = O$ the foregoing expressions evaluated at $\xi = \xi_m$ combine to give:

$$\left(\frac{h}{\rho}\frac{\partial \tau}{\partial y} + \frac{2\tau}{\rho R}\right)_m = \frac{u_m^2}{b}\left\{\frac{K}{4k^2}(1 - \xi_m)(1 + \xi_m\, b/R) f_m''(1 - b/R\, g'/f'')_m + O(b/R)^2\right\} \tag{17}$$

The quantity f'' is evaluated from

$$f = \operatorname{sech}^2\left[\frac{k(\xi - \xi_m)}{1 - \xi}\right] \qquad \text{as}$$

$$f''(\xi_m) = -\frac{2k^2}{(1 - \xi_m)^2}$$

Turning now to the function $g(\xi)$ which describes the variation with ξ of the eddy viscosity, $g(\xi)$ is assumed to take the form:

$$g(\xi) = (\xi/\xi_m)^m(a + (1 - a)\xi/\xi_m) \tag{18}$$

where the exponent m and the constant a are determined by satisfying the condition that

$$\frac{\tau}{\rho u_m^2} = \epsilon\left(\frac{\partial u}{\partial y} - \frac{u}{R}\right) = \frac{1}{2} C_f \text{ at } \xi = o$$

Substitution for ϵ and u gives

$$\frac{K}{4k^2}\frac{1-\xi_m}{\xi_m} 2/n\, a \left(\frac{\xi}{\xi_m}\right)^{m+\frac{1}{n}-1} = \frac{1}{2} C_f$$

at $\xi = o$.

Thus

$$m = 1 - \frac{1}{n} \text{ and } a = \frac{C_f k}{K} \tag{19}$$

(since $\frac{1-\xi_m}{\xi_m} = kn$)

Thus

$$g(\xi) = \left(\frac{\xi}{\xi_m}\right)^{1-\frac{1}{n}} \left[\frac{C_f k}{K} + \left(1 - \frac{C_f k}{K}\right)\frac{\xi}{\xi_m}\right] \tag{20}$$

and $g'(\xi_m)$ is evaluated as

$$g'(\xi_m) = \left(2 - \frac{1}{n} - \frac{C_f k}{K}\right)(1 + kn) \tag{20a}$$

Thus equation 17 becomes

$$\frac{2b}{u_m^2}\left(\frac{h}{\rho}\frac{\partial \tau}{\partial y} + \frac{2\tau}{\rho R}\right)_m = -K \cdot \frac{kn}{1+kn}\left\{1 + \frac{\left[1 - n/2 + n^2\left(1 - \frac{C_f k}{2K}\right)\right]}{1+kn} b/R\right\}$$

which has the form, for n large and $C_f \to 0$:

$$\frac{2b}{u_m^2}\left(\frac{h}{\rho}\frac{\partial T}{\partial y} + \frac{2T}{\rho R}\right) = -K\left[1 + \frac{n}{k}\, b/R\right] \tag{21}$$

Substitution into equation (12), and elimination of the quantity $\frac{1}{u_m^2}\frac{d}{ds}(bu_m^2)$ using equation (11a) gives finally, an expression for the spreading rate $\frac{db}{ds}$:

$$\frac{db}{ds} = K\left[1 + \frac{n}{k}b/R\right] + \left(\frac{19}{12} - \frac{\log 2}{k}\right)\left(b/R\,\frac{dR}{ds}\right)b/R + O(b/R)^2 \qquad (22)$$

In this equation K is to be determined experimentally for the flat plate ($R \to \infty$) and the term involving $\left(b/R\frac{dR}{ds}\right)$ is retained since this may be the same order as $\frac{db}{dS}$ (for a log spiral shape, in fact $\left(b/R\frac{dR}{ds}\right) \equiv \frac{db}{ds}$

It is clear from equation 22 that the influence of small curvature (small b/R) may be quite significant since the quantity $\frac{n}{k} \cdot b/R$ appears in the expression for the spreading rate.

Comparison with Experimental Results

In order to validate the foregoing analysis a comparison is made of the spreading rate as given by equation (22) with available experimental results for two cases, namely, the circular cylinder (R = constant) and the logarithmic spiral $\left(\frac{dR}{dS} = \text{const}\right)$.

(a) Circular Cylinder

In this case equation 22 reduces to a linear differential equation for b/R namely

$$\frac{db}{ds} = K\left[1 + \frac{n}{k}\,b/R\right] \qquad (22a)$$

The solution to this equation may be written in the form

$$\frac{b}{s} = K\frac{\frac{n}{k}\cdot b/R}{\log(1 + \frac{n}{k}\,b/R)} \qquad (23)$$

or, neglecting terms of $O(b/R)^2$,

$$b/s = K\left(1 + \frac{n}{2k}\,b/R\right) \qquad (23a)$$

The constant K is determined from the flat plate wall jet ($b/R \equiv O$) as K = .07, and equation (23a) with k = .8814 gives

$$b/s = 07(1 + 4b/R) \qquad (n = 7) \tag{23b}$$

$$b/s = .07(1 + 3.4b/R) \qquad (n = 6) \tag{23c}$$

These expressions are shown in figure 4 together with the available experimental results of Fekete[12], and Wilson and Goldstein[13]. In this regard the review by Launder and Rodi[14] suggest that the data of Fekete is possibly more representative of two dimensional flow than that of Wilson and Goldstein. It is in fairly good agreement with the theoretical expression for $n = 6$ (the Reynolds number is in the range 4 to 13×10^5).

(b) Logarithmic Spiral

For a logarithmic spiral R/s = constant and equation (22) has a self similar solution

$$b/s = \frac{k\left[1 + \frac{n}{k}\, b/R\,\right]}{\left[1 - \frac{\frac{19}{12} - \log 2}{k} b/R\right]} \tag{24}$$

$$\approx .07\frac{[1 + 8b/R]}{[1 - b/R]} \qquad (n = 7) \tag{24a}$$

$$\approx \frac{.07[1 + 6.8b/R\,]}{[1 - b/R\,]} \qquad (n = 6) \tag{24b}$$

A comparison of these curves with the experimental results of Guitton and Newman[14] and Kamemoto[15] is made in fig. 5. Here Guitton and Newman's results are considered to be most representative of two dimensional flow. Equation (24) reflects the much greater increase of b/s with b/R for the logarithmic spiral, compared to the circular cylinder equation (23a), and this trend is also seen in the experimental data.

Conclusions

From the foregoing analysis and comparison with experimental results it is seen that the wall jet is influenced by three effects:

(a) The turbulent diffusion in the wall jet giving rise to a linear spreading rate $db/ds = K \approx .07$.

(b) A coupling between the eddy viscosity and the curvature of the wall arising from the term $\frac{\partial}{\partial y}(\epsilon u/R)$ in the stress gradient and yielding a contribution of $\frac{db}{ds} = K\frac{n}{k}b/R$.

(typically this contribution is $O(\frac{1}{2}b/R)$ for Reynolds numbers typical of laboratory experiments), and

(c) A curvature-induced streamwise pressure gradient giving rise to a contribution of $O(b/R)^2\frac{dR}{ds}$. When $\frac{dR}{dS} < O$ this effect causes the jet momentum (bu_m^2) to increase in the streamwise direction and help confine the jet to a thin layer as it proceeds along the surface. This is an inertial term, largely independent of Reynolds number, and is an essential feature of Coanda turning of the flow.

These influences are additive and give an approximate relationship between the spreading rate $\frac{db}{ds}$, the half width of the jet and the surface radius of curvature R, of the form

$$\frac{db}{ds} = K_o + K_1\frac{b}{R} + K_2\left(\frac{b}{R}\right)^2\frac{dR}{ds}$$

which can be integrated to give b(s) when the wall shape R(s) is known.

The use of this result for the circular cylinder (R = const) shows good agreement with the previous experimental results of several authors. This provides some confidence that a simple algebraic eddy viscosity model, used in conjunction with the appropriate expression for the shear stress (including curvature terms), is sufficient to describe the primary features of the wall jet.

REFERENCES

1. Young, T., "Outline of Experiments and Inquiries Regarding Sound and Light", Lecture to the Royal Society, January 16, 1800 (see Journal Royal Aeronautical Society Vol. 61 1957, p 10157).

2. Wood, N. and Nielsen, J., "Circulation Control Airfoils, Past, Present and Future", AIAA paper 85-0204, January 14-17, 1985.

3. Englar, R. J., "Experimental Investigation of the High Velocity Coanda Wall Jet Applied to Bluff Trailing Edge Circulation Control Airfoils", NSRDC TN AL-308.

4. Launder, B. A. and Rodi, W., "The Turbulent Wall Jet", Progress in Aerospace Sciences, Vol. 19, pp. 81-128, Pergaman Press Ltd 1981.

5. Tailland, A., and Mathieu, J., "Jet Paretial", Journal de Mecanique 6, 103, 1967.

6. Tailland, A., "Contribution à l' ẽtude d'un jet plan dirige tangentiellement à une paroi plane", Thèse de Docteur es Sciences, Univ. Claude Bernard, Lyon 1970.

7. Forthmann, E., "Uber Turbulent Strahlausbreitung", Ing Arch., 5, 42, 1934.

8. Sigalla, A., "Measurements of Skin Friction in a Plane Turbulent Wall Jet", J. Royal Aeronautical Society 62 873, 1958.

9. Bradshaw, P., and Gee, M. T., "Turbulent Wall Jets with and without an External Stream", Aero. Research Council, R & M 3252, 1960.

10. Patel, R. P., "Self-Perserving, Two-Dimensional Turbulent Jets and Wall Jets in a Moving Stream", M. Eng. Thesis, Dept. of Mechanical Engineering, McGill University, Montreal, 1962.

11. Giles, J. A., Hays, A. P., and Sawyer, R. A., "Turbulent Wall Jets on Logarithmic Spiral Surfaces", Aero Quart., 17 201, 1966.

12. Fekete, G. I., "Coanda Flow in a Two-Dimensional Wall Jet on the Outside of a Circular Cylinder" Mech. Engr. Dept. Rep. No. 63-11, McGill University 1963

13. Wilson D. J., and Goldstein, R. J., "Turbulent Wall Jets With Cylindrical Streamwise Surface Curvature", J. Fluids Eng., 98 550, 1976.

14. Guitton, D. E. and Newman, B. G., "Self Preserving Turbulent Wall Jets over Convex Surfaces", J. Fluid Mech. 81 155, 1977.

15. Kamemoto, K., "Investigation of Turbulent Wall Jets over Logarithmic Spiral Surfaces", Bulletin JSME 17 333 1974.

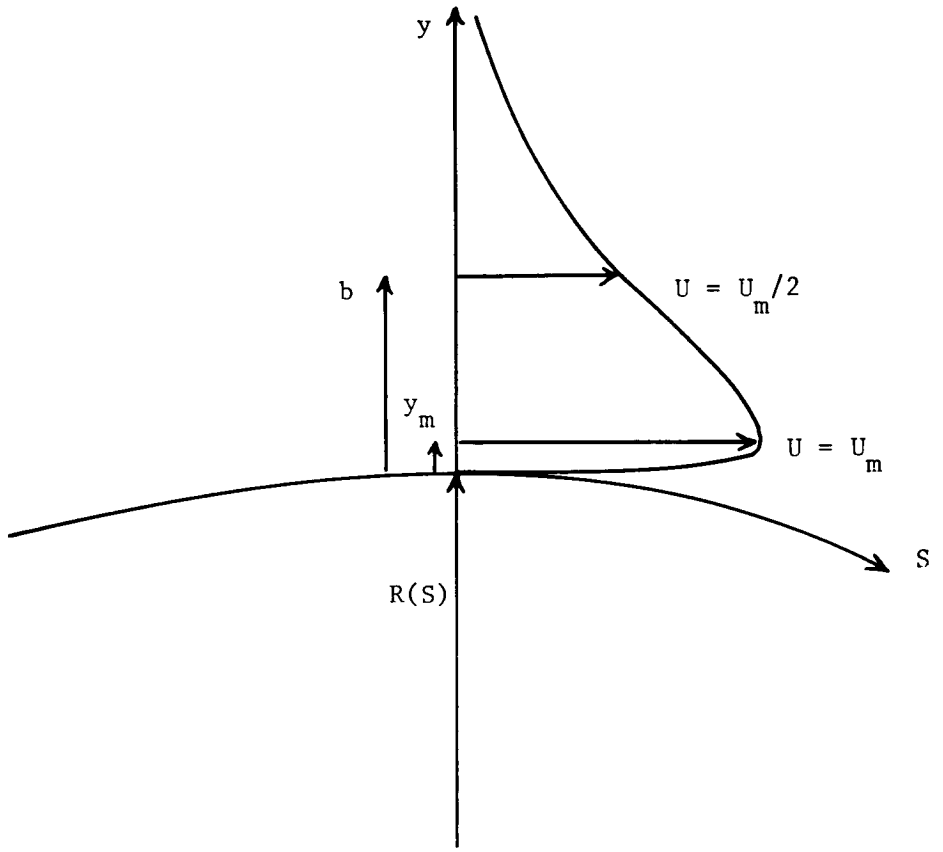

Figure 1. Geometry of two dimensional wall-jet.

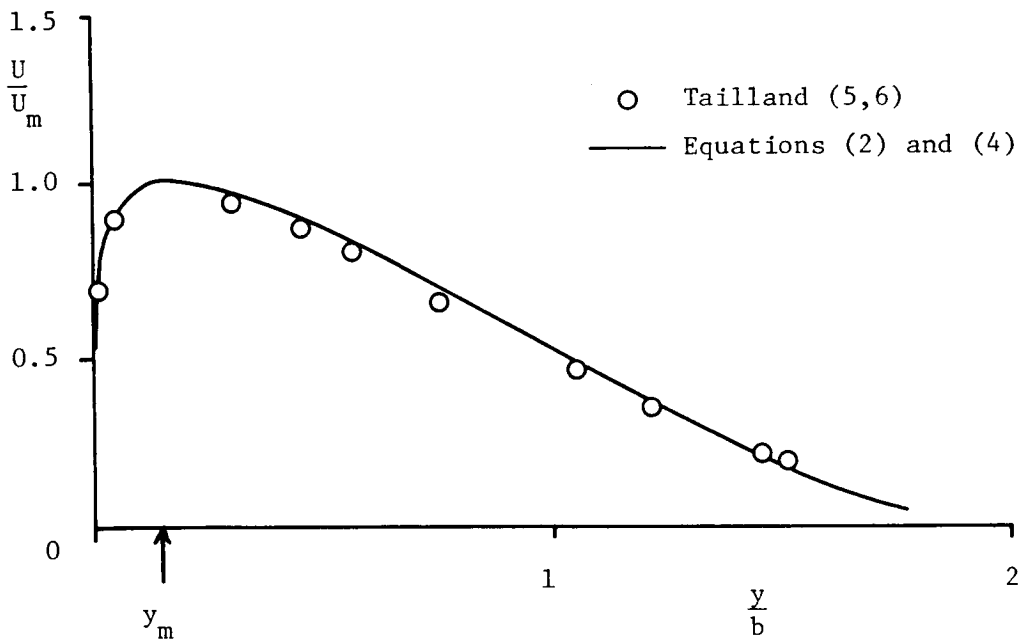

Figure 2. Comparison of assumed velocity profile with experimental data.

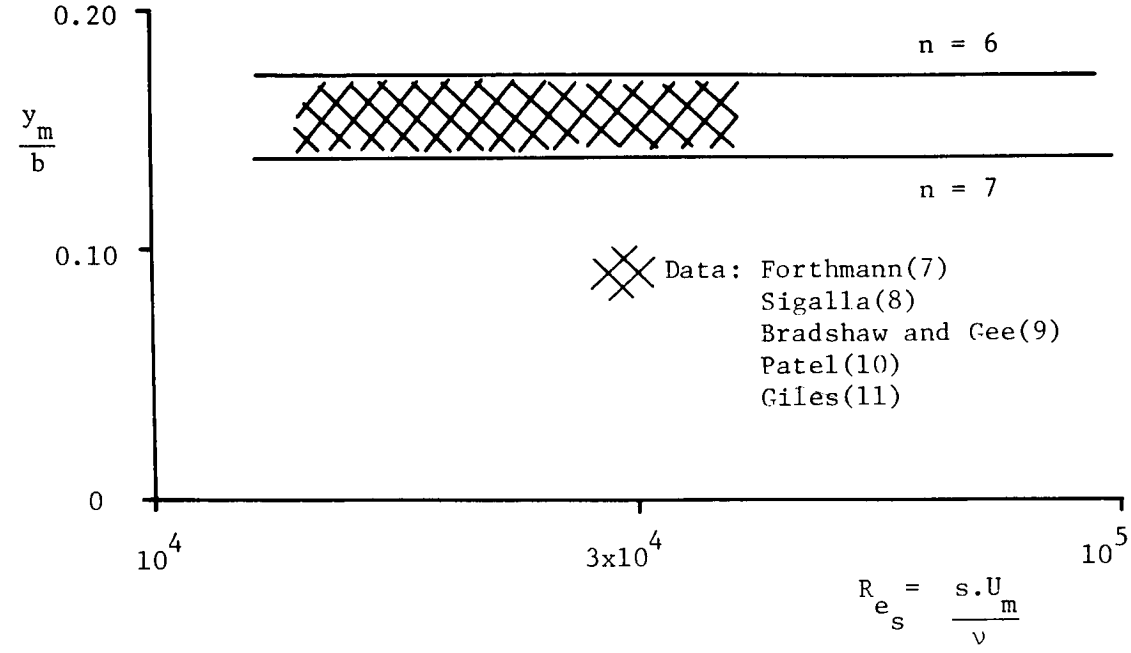

Figure 3. Comparison of calculated values of ξ_m for n = 6.7 with experimental values determined by several authors.

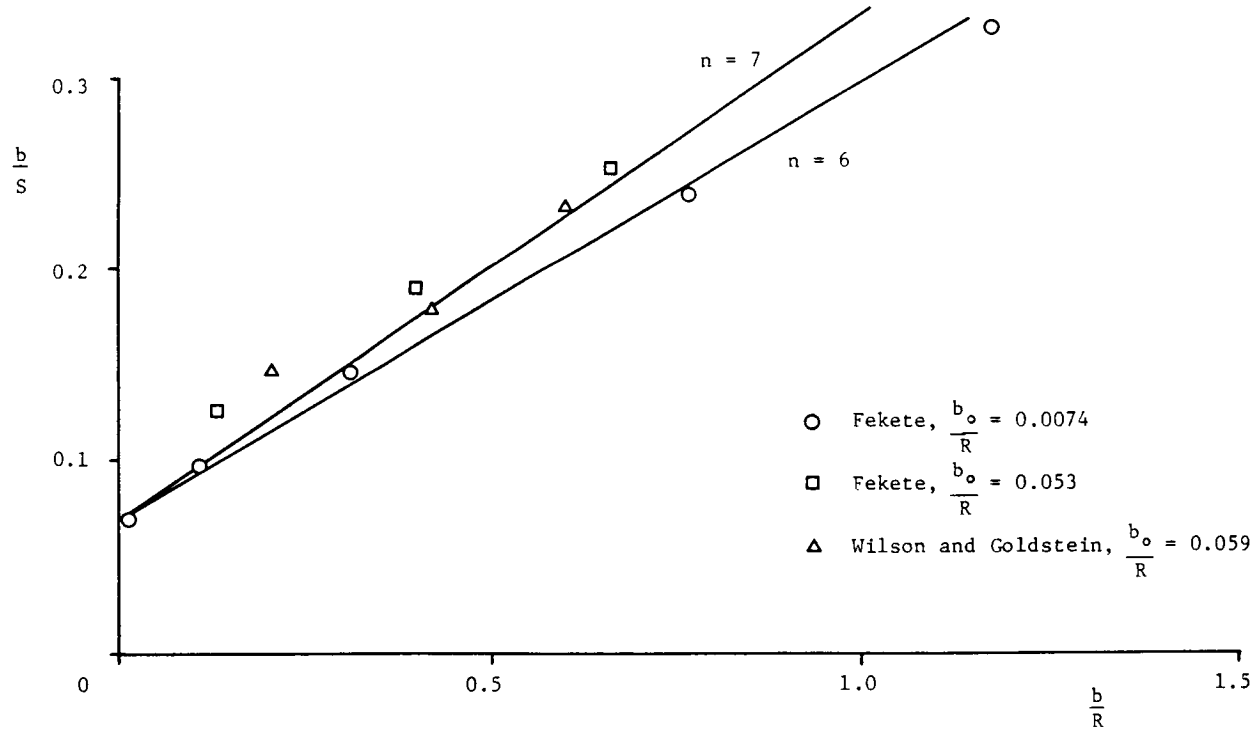

Figure 4. Comparison of theory and experiment for the wall jet spreading rate, b/S, as a function of b/R for circular cylinders.

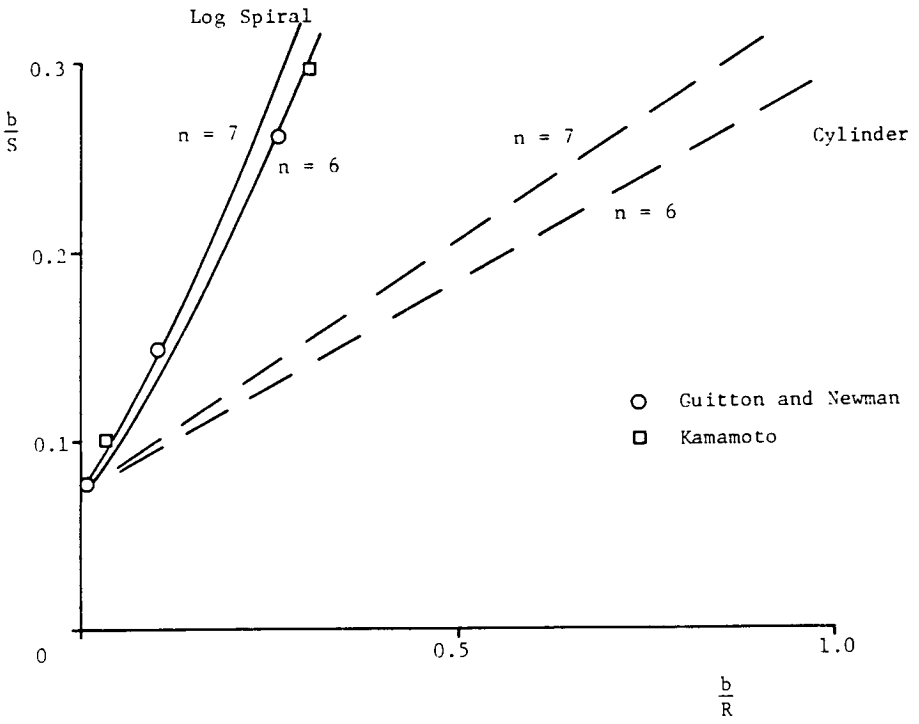

Figure 5. Comparison of function of b/R for logarithmic spiral surfaces.

Circulation-Control Airfoil Theory

EVALUATION OF A RESEARCH CIRCULATION CONTROL AIRFOIL USING NAVIER-STOKES METHODS

George D. Shrewsbury
Advanced Flight Sciences Department
Lockheed-Georgia Company, Marietta, Georgia

Abstract

The compressible Reynolds time averaged Navier-Stokes equations were used to obtain solutions for flows about a two-dimensional circulation control airfoil. The governing equations were written in conservation form for a body-fitted coordinate system and solved using an Alternating Direction Implicit (ADI) procedure. A modified algebraic eddy viscosity model was used to define the turbulent characteristics of the flow, including the wall jet flow over the Coanda surface at the trailing edge. Numerical results are compared to experimental data obtained for a research circulation control airfoil geometry. Excellent agreement with the experimental results was obtained.

Introduction

One of the most efficient of the various methods for generating increased lift is the circulation control (CC) airfoil. This concept was developed in England[1-2] and introduced into the United States by U.S. Navy researchers[3-5]. It has subsequently been the subject of extensive experimental test programs which have confirmed the high-lift capability of this innovative concept[6-9]. These airfoils obtain lift augmentation by tangentially exhausting a thin jet sheet over a rounded trailing edge with the jet sheet remaining attached well onto the airfoil lower surface due to the Coanda effect.

Formerly, analysis methods for CC airfoils[10-13] consisted of computational procedures which used weakly coupled viscous-inviscid procedures to define the complex flow fields resulting from the presence of the jet sheet exhausting into the trailing edge region. Particularly good results were obtained by using a potential flow CC airfoil solver developed by Dvorak, et al[11,13] coupled with a parabolized Navier-Stokes wall-jet analysis program written by Dash, and associates[12].

The complex flow fields of the CC airfoil are governed by highly interactive flow regimes, however, and a comprehensive analysis of the flow field and the associated phenomena, including the effects of jet entrainment and Coanda surface geometry, requires analysis procedures which account for the strongly coupled nature of the viscous and inviscid flow regimes.

Recently, Navier-Stokes methods have been used successfully to solve for the aerodynamics about CC airfoils[14-17]. The purpose of this paper is to present the results obtained by using the method developed in reference 15

to correlate numerical results with performance data from an extensive experimental study[18]. This method solves the fully elliptic Navier-Stokes equations in 2-D planar coordinates. The mathematical and numerical formulations are discussed, and appropriate boundary conditions and grid generation procedures are defined. Modifications to existing eddy viscosity turbulence models to account for curved wall jets are discussed.

Method

Mathematical Formulation

The development of the two-dimensional, unsteady, compressible Navier-Stokes equations used for this study are documented in Reference 19, and refinements to the method are reported in References 20-22.

The compressible Reynolds time averaged Navier-Stokes equations may be written in vector form as follows:

$$\frac{\partial}{\partial\tau}[\hat{q}] + \frac{\partial}{\partial\xi}[\hat{F}] + \frac{\partial}{\partial\eta}[\hat{G}] = \frac{1}{Re}\left\{\frac{\partial}{\partial\xi}[\hat{F}_1] + \frac{\partial}{\partial\eta}[\hat{G}_1]\right\} \quad (1)$$

Here ξ, η, and τ are the independent variables subject to the general transformation:

$$\begin{aligned} \xi &= \xi(x,y,t) \\ \eta &= \eta(x,y,t) \\ \tau &= t \end{aligned} \quad (2)$$

and:

$$\begin{aligned} [\hat{q}] &= \frac{1}{J}[\vec{q}] \\ [\hat{F}] &= \frac{1}{J}[\xi_t\vec{q} + \xi_x\vec{F} + \xi_y\vec{G}] \\ [\hat{G}] &= \frac{1}{J}[\eta_t\vec{q} + \eta_x\vec{F} + \eta_y\vec{G}] \\ [\hat{F}_1] &= \frac{1}{J}[\xi_x\vec{F}_1 + \xi_y\vec{G}_1] \\ [\hat{G}_1] &= \frac{1}{J}[\eta_x\vec{F}_1 + \eta_y\vec{G}_1] \end{aligned} \quad (3)$$

where:

$$\vec{q} = \begin{Bmatrix} \rho \\ \rho u \\ \rho v \\ \rho E \end{Bmatrix} \qquad \vec{F} = \begin{Bmatrix} \rho u \\ \rho u^2 + p \\ \rho uv \\ (\rho E + p)u \end{Bmatrix}$$

$$\vec{G} = \begin{Bmatrix} \rho \\ \rho uv \\ \rho v^2 + p \\ (\rho E + p)v \end{Bmatrix} \qquad \vec{F}_1 = \begin{Bmatrix} 0 \\ \tau_{xx} \\ \tau_{xy} \\ \frac{\gamma}{Pr} K \frac{\partial e}{\partial x} + u\tau_{xx} + v\tau_{xy} \end{Bmatrix} \qquad \vec{G}_1 = \begin{Bmatrix} 0 \\ \tau_{xy} \\ \tau_{yy} \\ \frac{\gamma}{Pr} K \frac{\partial e}{\partial y} + u\tau_{xy} + v\tau_{yy} \end{Bmatrix} \tag{4}$$

The components of the viscous stress tensor are given by

$$\tau_{xx} = (\lambda + 2\mu) \frac{\partial u}{\partial x} + \lambda \left(\frac{\partial v}{\partial y} \right)$$

$$\tau_{yy} = (\lambda + 2\mu) \frac{\partial v}{\partial y} + \lambda \left(\frac{\partial u}{\partial x} \right) \tag{5}$$

$$\tau_{xy} = \mu \left(\frac{\partial u}{\partial y} + \frac{\partial v}{\partial x} \right)$$

where p is the pressure, ρ is the density, μ is the bulk viscosity, e is the specific internal energy, and λ is taken as $-2/3\,\mu$, according to Stoke's hypothesis. The viscosity, μ, is defined by Sutherland's law. The equation of state:

$$p = \rho RT$$

is required for closure of the system of equations.

In the above equations, all distances are normalized with respect to the airfoil chord, the velocities are normalized with respect to the free stream velocity, V_∞, the density is normalized with respect to the free stream density, and the specific internal energy is normalized with respect to V_∞^2. Re and Pr are the Reynolds number and Prandtl number, respectively.

Numerical Formulation

The numerical procedure used to solve the system of governing equations is a modified form of the Briley-McDonald[23] Alternating Direction Implicit (ADI) procedure, which is based on the Douglas-Gunn[24] method. It is also closely related to the Warming-Beam[25] algorithm. Variable time steps and numerical dissipation have been incorporated to accelerate the convergence for steady state flow problems.

The method can be outlined as follows: The governing equations are parabolic with respect to time. Assuming the flow field is known at a time level t_n, the numerical procedure is used to advance the solution to a new time level t_{n+1} using a fairly large time step. If a steady state solution is desired, the procedure at each cell is advanced at a different time step based on the local cell Reynolds number. The metric terms ξ_x, ξ_y, etc., are evaluated numerically at an intermediate time level $t_{n+1/2}$. The mixed

derivatives that arise from terms such as $(\xi_x U \tau_{xx})$, etc., are lagged one time step. The flow quantities ρ, u, v, and e at the new time level are written in terms of their values at the known time level and the incremental quantities; i.e.,

$$\rho^{n+1} = \rho^n + \Delta\rho^n$$

The non-linear terms involved are linearized by using a Taylor expansion about the solution at the known time level t_n. Performing these operations and taking all the known quantities to the right hand side, one obtains a linear system of equations for the incremental quantities at each grid point in the computational plane, excluding the boundaries. The difference equations may be written in matrix form as:

$$[A]\{\Delta q\}^n + \frac{\partial}{\partial \zeta}[B]\{\Delta q\}^n + \frac{\partial}{\partial \eta}[C]\{\Delta q\}^n = [R]^n \tag{6}$$

The Douglas-Gunn procedure for generating an ADI scheme is used to solve the above system of equations by approximate factorization of equation (6) into two equations, where each involves only a one-dimensional operator:

$$[A]\{\Delta q\}^* + \frac{\partial}{\partial \xi}[B]\{\Delta q\}^* = \{R\}^n \tag{7}$$

$$[A]\{\Delta q\}^n + \frac{\partial}{\partial \eta}[C]\{\Delta q\}^n = [A]\{\Delta q\}^* \tag{8}$$

where

$$\{\Delta q\} = \{\Delta\rho, \Delta u, \Delta v, \Delta e\}^T \tag{9}$$

Equations (7) and (8) are discretized using second order accurate difference formulas for the spatial derivatives. This technique results in a matrix system with a block tridiagonal structure which may be solved efficiently by using standard block elimination procedures. The boundary conditions for the unknown vector $\{\Delta g\}$ are evaluated explicitly. Once $\{\Delta g\}^n$ is obtained, the flow field variables at the new time level are explicitly known.

Artificial Dissipation Terms

To suppress the high frequency components that appear in regions containing severe pressure gradients, i.e., the neighborhood of shock waves or stagnation points, artificial dissipation terms have been added in conservative form. In the present application, a blend of second and fourth order terms with coefficients which depend on the magnitude of the local pressure gradient have been added explicitly for each dependent variable in the manner suggested by Jameson[26], et al., and second order dissipation

terms have been added implicitly for each of the dependent variables. The coefficients of the implicit terms were added in the manner suggested by Steger[27]. Extensive numerical experiments have shown that the blending of the dissipation terms provided better shock wave prediction with controlled overshoot pressure distribution.

Turbulence Model

An algebraic eddy viscosity model developed by Baldwin and Lomax[28] was used to define the turbulence transport everywhere except in the wall jet free shear layer. This model permits the calculation of the turbulence characteristics of the boundary layer by defining a two layer system. The viscosity in the inner layer is given by simple mixing length theory, where the length scale is proportional to the distance from the wall multiplied by the van Driest damping term, and the velocity scale is proportional to the length multiplied by the absolute value of the vorticity

$$\nu_{t_{INNER}} = \rho \ell^2 |\omega| \tag{10}$$

where

$$\ell = ky\,[1-\exp(-y^+/A^+)] \tag{11}$$

In the outer layer, the velocity and length scales are constant and the turbulent viscosity is calculated from:

$$\nu_{t_{OUTER}} = KC_{cp}\rho F_{WAKE} F_{KLEB} \tag{12}$$

F_{WAKE} is defined as the minimum value of

$$y_{MAX}\, F_{MAX}$$

or

$$C_{WK} y_{MAX} U^2_{DIFF}/F_{MAX}$$

F_{MAX} is determined from the maximum value of

$$F(y) = y|\omega|[1 - \exp(-y^+/A^+)] \tag{13}$$

and y_{MAX} is defined as the y at which F_{MAX} occurs. F_{KLEB} and U_{DIFF} are defined by

$$F_{KLEB} = \left\{1 + 5.5\left(\frac{C_{KLEB}\, y}{y_{MAX}}\right)^6\right\}^{-1}$$

$$U_{DIFF} = \left(\sqrt{U^2 + v^2}\right)_{MAX} - \left(\sqrt{U^2 + v^2}\right)_{MIN}$$

The constants used in these equations are defined in Reference 28.

The division between the inner and outer layers is taken as that point at which

$$\nu_{tOUTER} = \nu_{tINNER}$$

The turbulence characteristics of the curved wall jet on the Coanda surface require special treatment, since the extra rates of strain produced by the curvature can exert an influence on the turbulence structure by augmenting or suppressing radial velocity fluctuations. In a curved wall jet, such as that shown in Figure 1, a balance of centrifugal and pressure forces on a fluid element reveals that increases in velocity with distance from the center of streamline curvature generate stable flows. while flows in which the velocity decreases from the center of curvature are destabilized[29]. In turbulent flow, these stabilities and instabilities lead to an increase or decrease in turbulent transport. This influence can result in viscosities which are an order of magnitude greater than those obtained in planar flows[30]. Accordingly, turbulence models using standard eddy viscosity relations will require significant empirical modifications to reproduce the characteristics of curved shear layer flows. For this study, the mixing length was multiplied by an empirical curvature correction

$$F = 1 - \alpha S$$

where α is an empirical constant whose value depends on the particular flow considered. A review of the literature suggests that most researchers place the constant in the range $6<\alpha<14$ for wall bounded flows. For this study, however, a value of 25 produced results more nearly in agreement with experimental data. S is a dimensionless parameter which is representative of the ratio of the extra rate of strain produced by the curvature to the inherent shear strain

$$S = \frac{U/r}{\partial U/\partial n}$$

where U is the velocity in the streamwise direction, n is the normal direction, and r is the local radius of curvature of the streamline considered. In areas where the curvature is small to moderate, the correction to the eddy viscosity is negligible.

The location of the wake was approximated by determining the point, nearest the trailing edge, at which the U component of the contravariant velocity at the second grid line changed direction. The wake was then arbitrarily defined to exist in the region contained in the four grid points on each side of that location. The calculation of the eddy viscosity began at the lower edge of the wake, and proceeded clockwise to the upper edge of the wake. Values of the turbulent viscosity for the wake were then interpolated linearly from the values at the wake edges.

Grid Generation and Boundary Conditions

A body-fitted coordinate system is desired for numerical analysis procedures since boundary surfaces in the physical plane are mapped onto rectangular surfaces in the transformed plane, and the boundary conditions in the transformed plane may be treated more accurately. Computer methods developed by Thomas[31] were employed to generate a suitable body-fitted, curvilinear grid system. This procedure uses a Poisson solver to define two-dimensional grids about airfoils and other shapes.

The unique trailing edge geometry and flow characteristics of CC airfoils makes the use of conventional C-grids difficult, since it is impossible to locate the cut line so that it corresponds to the physical location of the wake. Consequently, it was decided to use an O-grid topology for this analysis. This choice represents a compromise between suitable resolution on the Coanda surface and adequate definition in the near-wake region.

The grid spacing in the direction normal to the airfoil surface was sufficiently dense to permit satisfactory resolution of the boundary layer. Sixty-one grid lines were used in this direction, and approximately twenty of these were submerged in the boundary layer. The grid spacing in the normal direction varied from 0.00007 chords at the wall to 0.60 chords at the outer boundary. The outer boundary was defined as circular, and was fourteen chords in diameter. One-hundred and fifty-one points were used in the wrap-around direction. Grid points were clustered to permit satisfactory resolution at critical locations, such as the leading edge and blowing slot exit planes. One of the computational grids used for this study is shown in Figure 2.

Boundary conditions for the computational plane consisted of specifying the flow conditions along the airfoil surface, including the blowing slot exit plane, the O-grid cut line, and the outer boundary. On the airfoil surface, an adiabatic wall condition, $\partial e/\partial \eta = 0$, was imposed and extrapolated values of density were specified. A no-slip condition ($u = v = 0$) was used to define the velocities. At the slot blowing exit, specified values of total pressure and total temperature were used with an extrapolated value of pressure to define the boundary characteristics. Along the grid cut line, boundary conditions were applied explicitly as the average of the extrapolated values from each direction.

At the outer boundary, conditions were applied according to the rule that flow variables should be extrapolated along characteristics leaving the cell and specified along characteristics entering the cell. Accordingly, for subsonic conditions where the boundary is experiencing inflow, values of the velocity and pressure are specified, while the energy is extrapolated from the interior. For outflow conditions, the pressure is specified, while values of velocity and energy are extrapolated from the interior. Numerical disturbances generated by the body may be reflected back into the computational plane, creating an adverse influence on the convergence characteristics of the solution. To eliminate the reflection of unwanted propagations, the pressure is specified according to non-reflecting boundary criteria prescribed by Rudy and Strikwerda[32], which have been implemented at the outflow boundaries.

In all cases where extrapolated values were specified at the boundaries, a two-point extrapolation of the form

$$q_1 = \frac{4}{3} q_2 - \frac{1}{3} q_3$$

was used.

Results

Research CC Airfoil

Novak and Cornelius[18] conducted wind tunnel tests on a 15.6 per cent thick CC airfoil section which had been specifically designed to provide data for Navier-Stokes code validation. The blowing slot height-to-radius ratio was 0.1, and the overall chord length was 15 inches. This model was designed with a cylindrical Coanda surface with a radius-to-chord ratio of 0.067. While this ratio is relatively high and is certainly not representative of practical flight systems, it does provide a physically large slot height, which improves the quality of the measurements. Data were acquired in the Lockheed-Georgia Low Turbulence Wind Tunnel at a free-stream Mach number of 0.0853 and a Reynolds number of 780,000. The model angle of attack was zero degrees. The data consisted of airfoil surface pressure measurements and extensive flow field surveys using a laser velocimeter (LV). The general profile of the section can be visualized from the grid shown in Figure 2.

Once a suitable computaional grid had been constructed, numerical studies were conducted at a Mach number and Reynolds number corresponding to the experimental tests. The angle of attack was varied numerically until a lift coefficient based on integrated pressures was obtained which corresponded to the experimental zero incidence case. For the jet total pressure ratio investigated, the numerical angle of attack was -2 degrees, and the corresponding lift coefficient was 4.55. All computed and experimental data subsequently presented are for that lift coefficient. The jet total pressure ratio was 1.10, and the ratio of jet total temperature to free-stream total temperature was .964.

The numerical results were obtained by executing the code on the Lockheed/ASG Cray X-MP/24 computer. Approximately 1000 iterations were required to obtain a converged, steady-state solution. This formulation of the Navier-Stokes equations requires approximately 2.5×10^{-4} CPU seconds/grid-point/time-step of Cray execution time.

Computed streamlines for the research airfoil are shown in Figure 3. This figure clearly demonstrates the characteristic flows for CC airfoils, including the large, induced circulation which produces a strong downwash in the wake region and upwash at the leading edge. The jet entrainment effects on the upper surface and the Coanda turning of the jet can also be seen.

Computed velocity vectors and streamlines in the trailing edge region are shown for the same case in Figure 4. Details of wall jet development, as well as the interaction of the upper and lower surface flows can be clearly visualized. These results demonstrate the attached, well-behaved nature of the flow, which is characteristic of CC airfoils, even near stall[6].

Comparisons of computed and experimental velocity profiles at the jet exit plane are shown in Figure 5. The profiles are shown as ratios of the local velocity to the free-stream velocity versus the radial distance above the Coanda surface. The upper edge of the exhaust jet is located at a Y of .1 inches. The data in Figure 5(a) include the boundary layer which has been established on the airfoil upper surface as well as the jet slot exhaust flow. The comparison between the computed and experimental boundary layers

is very good, which suggests that the jet entrainment effects propagated upstream are being properly modeled.

A detailed comparison of the computed and experimental velocity profiles for the jet exhaust is shown in Figure 5(b). In order to produce corresponding values of jet exhaust velocities, the numerical data were run at a jet total pressure ratio of 1.10, compared to a value of 1.12 measured experimentally. The discrepancy may be due to total pressure losses experienced in the duct between the plenum measurement location and the jet exit plane. The numerical total pressure ratio used however, provides an excellent reproduction of the experimental velocity profile except at the upper edge of the jet, where an established jet boundary layer already existed. The consequences of failing to properly model this characteristic of the jet exhaust profile are not known.

The jet exit total pressure was assumed to be constant across the jet slot height except at the walls, where a no-slip ($u = v = 0$) condition was enforced. The small velocity deficit occurring near the bottom of the numerical profile is believed to be the result of errors introduced by poor grid characteristics in that region. The comparison between the computed and experimental velocity gradients produced by the strong radial pressure differentials is very good. The numerical velocities obtained from this total pressure ratio resulted in a jet momentum coefficient of approximaely 0.275.

It is interesting to note that the differences in experimental boundary layers observed at the upper and lower edges of the jet are consistent with the previously discussed postulate that positive radial velocity gradients in regions of curvature are stabilizing, while negative velocity gradients in that direction are destabilizing.

Experimental and computed velocity profiles for the wall jet flow at a circumferencial location of 90 degrees, measured clockwise from the jet exit location, are shown in Figure 6. The conditions at which these results were obtained are the same as for the previous figure. While the general magnitudes and wall jet thicknesses agree reasonably well, the differences in profile characteristics near the wall are significant. The extremely stable characteristics exhibited by the experimental flow adjacent to the wall are not reproduced adequately by the numerical data. Since the experimental conditions at the beginning of the Coanda region are closely approximated, it is concluded that an empirically corrected eddy viscosity turbulence formulation is not sufficient to properly model the turbulent characteristics of curved wall jets, particularly the strong stabilization that occurs near the boundary. As a consequence of this discrepancy, the numerical wall jet dissipates energy too rapidly and experiences premature detachment. The angle of attack correction of -2 degrees was underpredicted therefore, and the actual equivalent experimental angle of attack was somewhat more negative.

Experimental and computed CC airfoil pressure distributions are shown in Figure 7. The agreement between experimental and computed pressure distributions is very good. The strong suction peaks produced by the super-circulation at the leading edge and the jet sheet turning on the Coanda surface are very accurately predicted. The discrepancy between the computed and experimental data on the lower surface, near the trailing

edge, is probably the result of differences in the locations of the jet sheet detachment points, as observed experimentally and predicted numerically.

Conclusions

A computational procedure has been developed which permits the calculation of the performance characteristics of circulation control airfoils over a broad range of free-stream conditions. The fully elliptic, Reynolds time averaged Navier-Stokes equations were solved numerically, using an Alternating Direction Implicit (ADI) algorithm. The computed results compared well with experiments conducted on a research CC airfoil which had been specifically designed to provide data for Navier-Stokes code validation, including force data and detailed flow measurements taken in the trailing edge region. A specially modified algebraic eddy viscosity model was used to predict the behavior of the wall jet, and although the overall behavior of the curved wall jet was sufficiently approximated, important turbulent characteristics crucial to the prediction of the jet sheet detachment point were not adequately predicted. Extensions to the present work will include the incorporation of advanced turbulence models to provide improved analysis of the wall jet characteristics.

References

1. Cheeseman, I.C., and Seed, A.R., "The Application of Circulation Control by Blowing to Helicopter Rotors," lecture to the Royal Aeronautical Society (Feb. 1966), published in J.R.Ae.S., vol 71, no. 848, July 1966.

2. Kind, R.J., "A Calculation Method for Circulation Control by Tangential Blowing Around a Bluff Trailing Edge," Aeronautical Quarterly, Vol. XIX, August 1968, pp 205-233.

3. Williams, R.M., "Some Research on Rotor Circulation Control," Proc. of the Third Cal/AVLABS Symp., Vol. 11, June 1969.

4. Williams, R.M. and Howe, H.J., "Two-Dimensional Subsonic Wind Tunnel Tests On a 20% Thick, 5% Cambered Circulation Control Airfoil," NSRDC TN AL-176, August 1970.

5. Englar, Robert J., "Two-Dimensional Transonic Wind Tunnel Tests of Three 15-percent Thick-Circulation Control Airfoils," NSRDC Report ASED-182, December 1970.

6. Abramson, J. and Rogers, E.O., "High-Speed Characteristics of Circulation Control Airfoils," AIAA Paper 83-0265, Jan. 1983.

7. Loth, J.L. and Boasson, M., "Circulation Controlled STOL Wing Optimization," AIAA Paper 83-0082, Jan. 1983.

8. Wood, N.J., "The Performance of a Circulation Control Airfoil at Transonic Speeds," AIAA Paper 83-0083, Jan. 1983.

9. Englar, R.J. and Huson, G.G., "Development of Advanced Circulation Control Wing High Lift Airfoils," AIAA Paper 83-1847, July 1983.

10. Gibbs, E.H. and Ness, N., "Analysis of Circulation Controlled Airfoils," TR-43, Department of Aerospace Engineering, West Virginia University, June 1975.

11. Dvorak, F.A. and Kind, R.J., "Analysis Method for Viscous Flow Over Circulation-Controlled Airfoils," Journal of Aircraft, Vol. 16, No. 1, January 1979.

12. Dash, S.M. and Wolf, D.E., "Viscous/Inviscid Analysis of Curved Wall Jets: Part 1 - Inviscid Shock Capturing Model (SCIPWJET)," SAI/PR TR-5, September 1982.

13. Dvorak, F.A. and Choi, D.H., "Analysis of Circulation-Controlled Airfoils in Transonic Flow," Journal of Aircraft, Vol. 20, No.4, April 1983.

14. Shrewsbury, George, "Numerical Evaluation of Circulation Control Airfoil Performance Using Navier-Stokes Methods," AIAA Paper 86-0286, January 1986.

15. Shrewsbury, George D., "Analysis of Circulation Control Airfoils Using an Implicit Navier-Stokes Solver," AIAA Paper 85-0171, January 1985.

16. Berman, H.A., "A Navier-Stokes Investigation of a Circulation Control Airfoil," AIAA Paper 85-0300, January 1985.

17. Pulliam, Thomas H., Jesperson, Dennis C., and Barth, Timothy J., "Navier-Stokes Computations for Circulation Controlled Airfoils," AIAA Paper 85-1587, July, 1985.

18. Novak, Charles J. and Cornelius, Kenneth C., "An LDV Investigation of a Circulation Airfoil Flowfield," AIAA Paper 86-0503, January, 1986.

19. Tassa, Y., "An Implicit Method for Solving the Navier-Stokes Equations with Application to Shock Boundary Layer Interaction," Lockheed-Georgia Report LG79RR001, 1979.

20. Sankar, N.L. and Tassa, Y., "Reynolds Number and Compressibility Effects on Dynamic Stall of a NACA 0012 Airfoil," AIAA Paper 80-0010, Pasadena, CA., January 1980.

21. Shrewsbury, G.D. and Tassa, Y., "Numerical Simulation of Transonic Flow About Isolated Afterbodies," AIAA Paper 83-0498, January 1983.

22. Schuster, D.M. and Birckelbaw, L.D., "Numerical Computation of Viscous Flowfields about Multiple Component Airfoils," AIAA Paper 85-0167, Jan. 1985.

23. Briley, W.R., and McDonald, H., "An Implicit Numerical Method for Multidimensional Compressible Navier-Stokes Equations," Report M9113363-6, United Aircraft Research Laboratories, November 1973.

24. Douglas, J. and Gunn, J.E., "A General Formulation of Alternating Direction Methods," Numerishe Math., Vol. 6, 1967, pp 428.

25. Beam, R., and Warming, R.F., "An Implicit Factored Scheme for Compressible Navier-Stokes Equations," AIAA Paper 77-645, June 1977.

26. Jameson, A., Schmidt, W., and Turkel, E., "Numerical Solutions of the Euler Equations by Finite Volume Methods Using Runge-Kutta Time-Stepping Schemes," AIAA 81-1259, Palo Alto, CA, 1981.

27. Steger, J.L., "Implicit Finite Difference Simulation of Flow About Arbitrary Two-Dimensional Geometries," AIAA Journal, Vol. 16, No. 4, July 1978, pp. 679-686.

28. Baldwin, B.S., and Lomax, H., "Thin Layer Approximation and Algebraic Model for Separated Turbulent Flows," AIAA Paper 78-257, Jan. 1978.

29. Wilson, D.J., and Goldstein, R.J., "Turbulent Wall Jets with Cylindrical Streamwise Surface Curvature," Journal of Fluids Engineering, September 1976, pp 550-557.

30. Rodi, W., and Scheurer, G., "Calculation of Curved Shear Layers with Two-Equation Turbulence Models," Phys. Fluids 26(6), June 1983, pp1422-1436.

31. Thomas, P.D., "Construction of Composite Three-Dimensional Grids From Subregion Grids Generated by Elliptic Systems," AIAA Journal, Vol. 20, No. 9, Sept. 1982, pp.1195,1202.

32. Rudy, D., and Strikwerda, J., "A Non Reflecting Outflow Boundary Condition for Subsonic Navier-Stokes Calculations," Journal of Computational Physics, Volume 36, pp. 55-70, 1980.

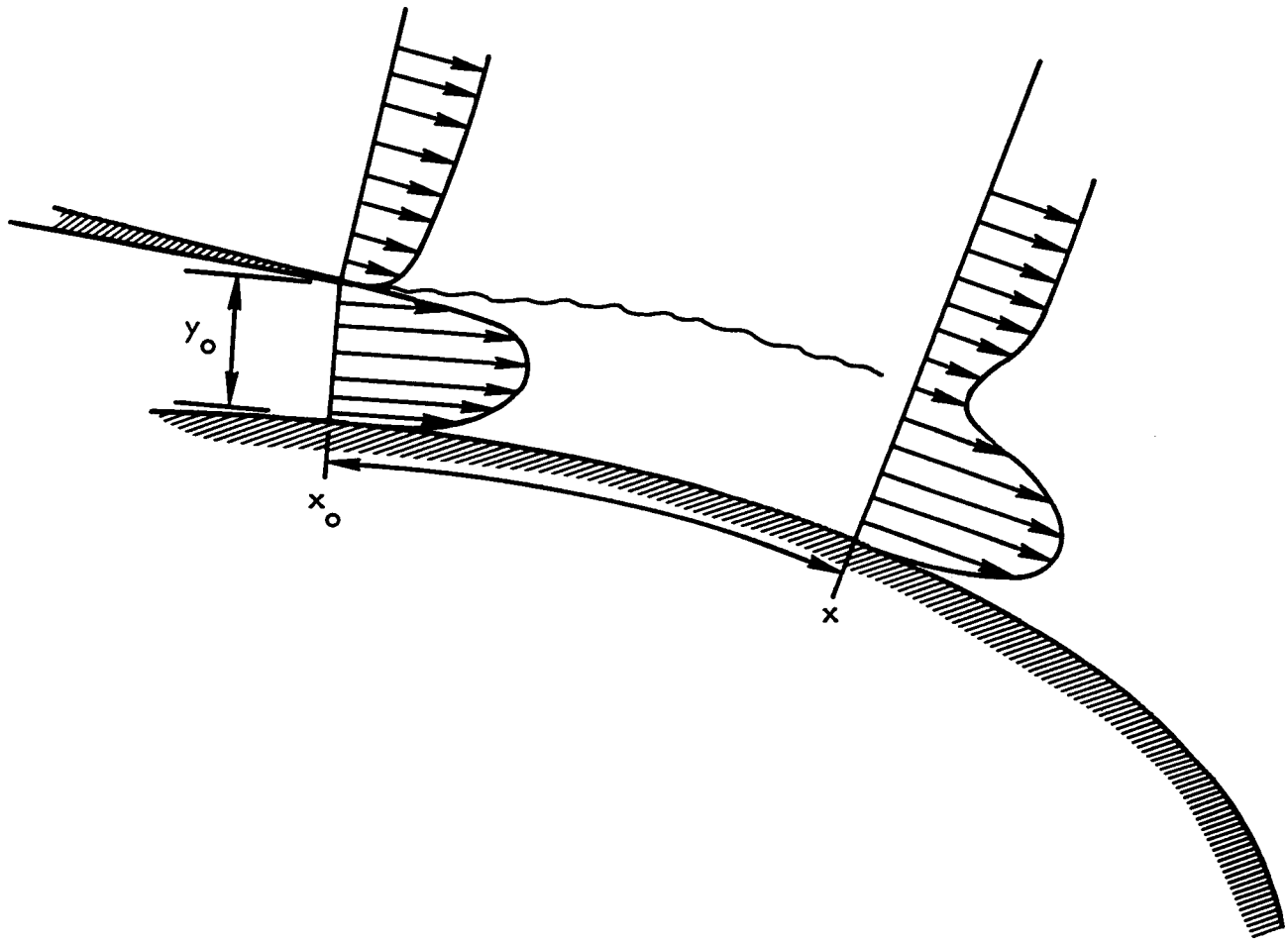

Figure 1. Wall-Jet/Coanda-Surface Nomenclature

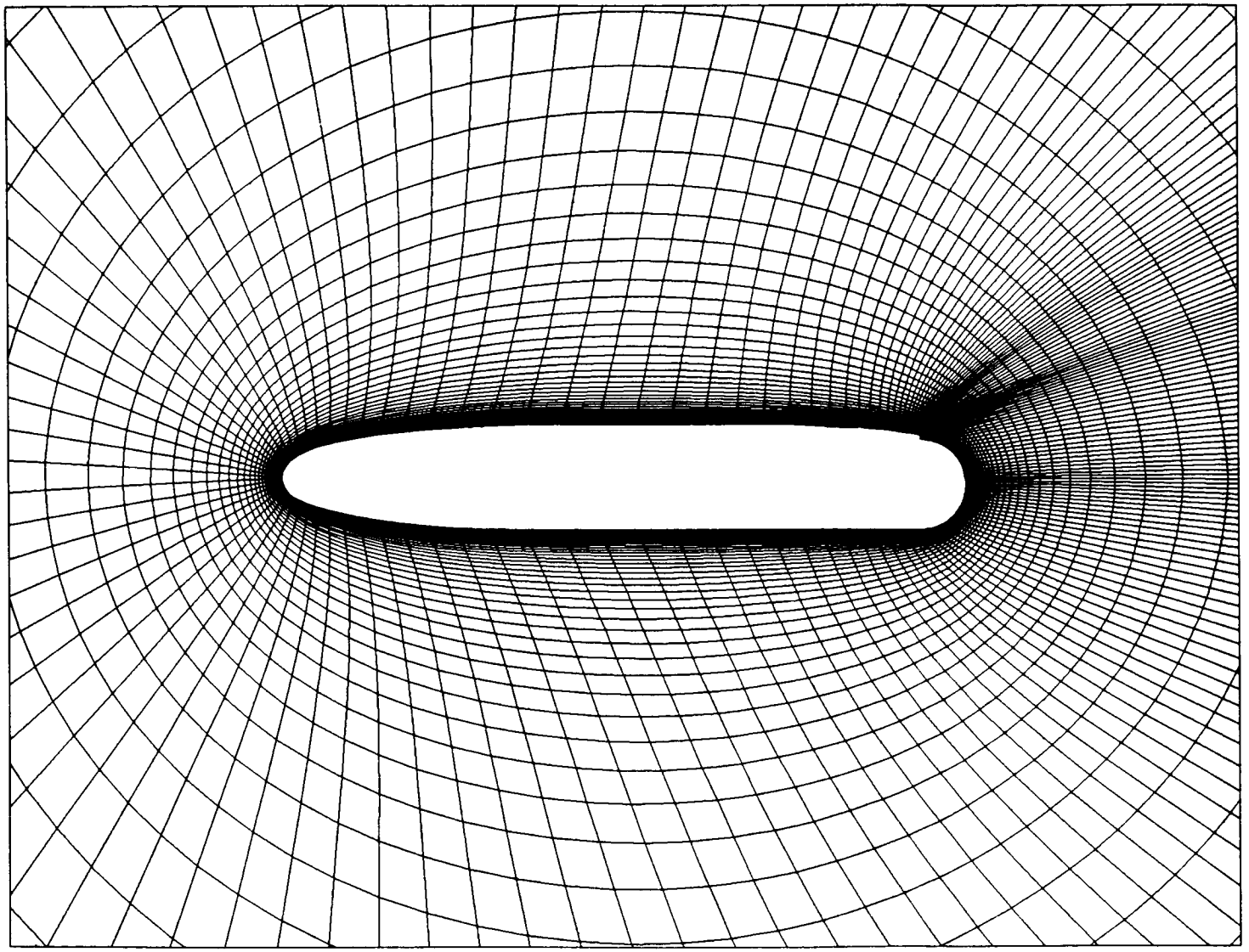

Figure 2. Computational Grid

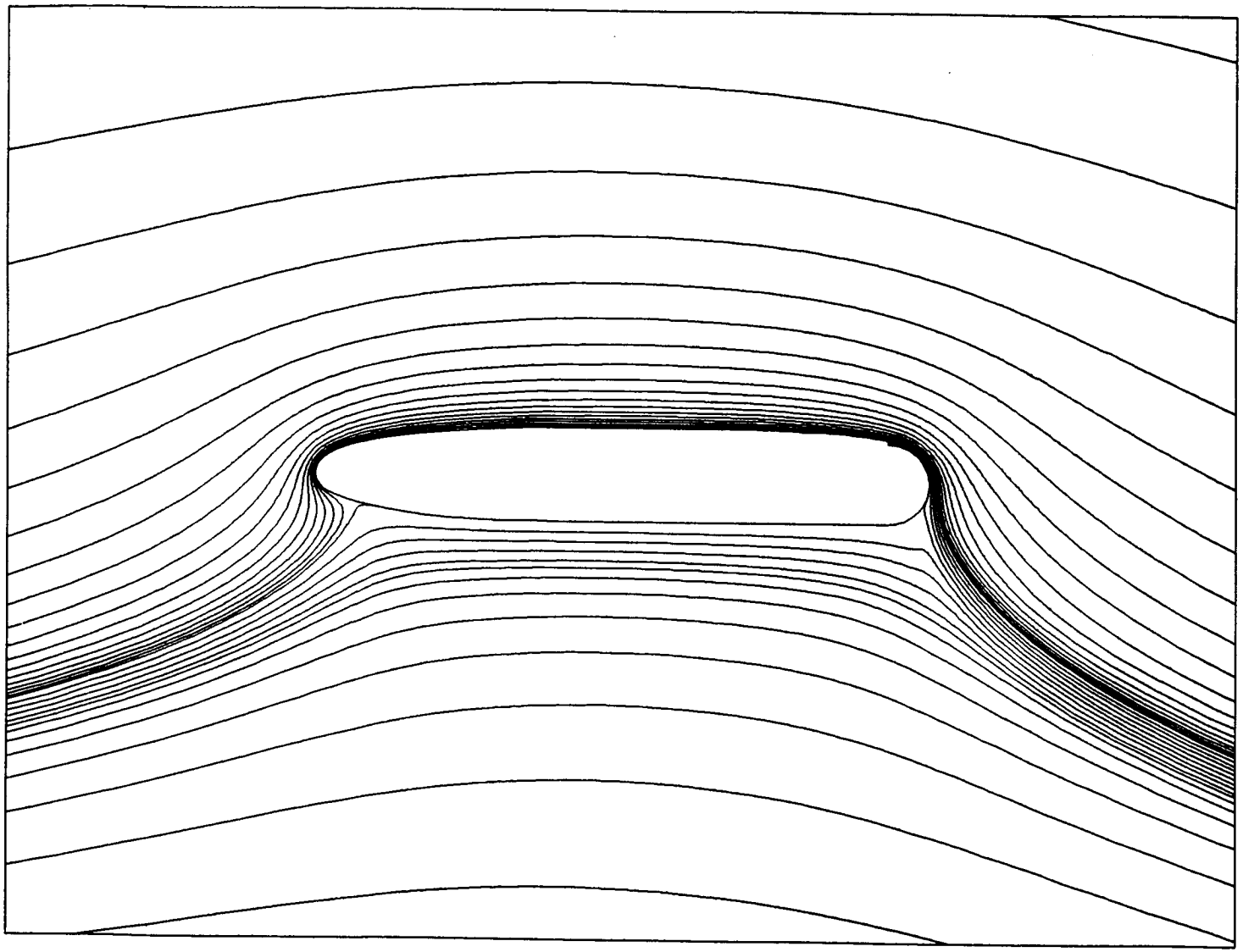

Figure 3. Computed Streamlines for Research CC Airfoil

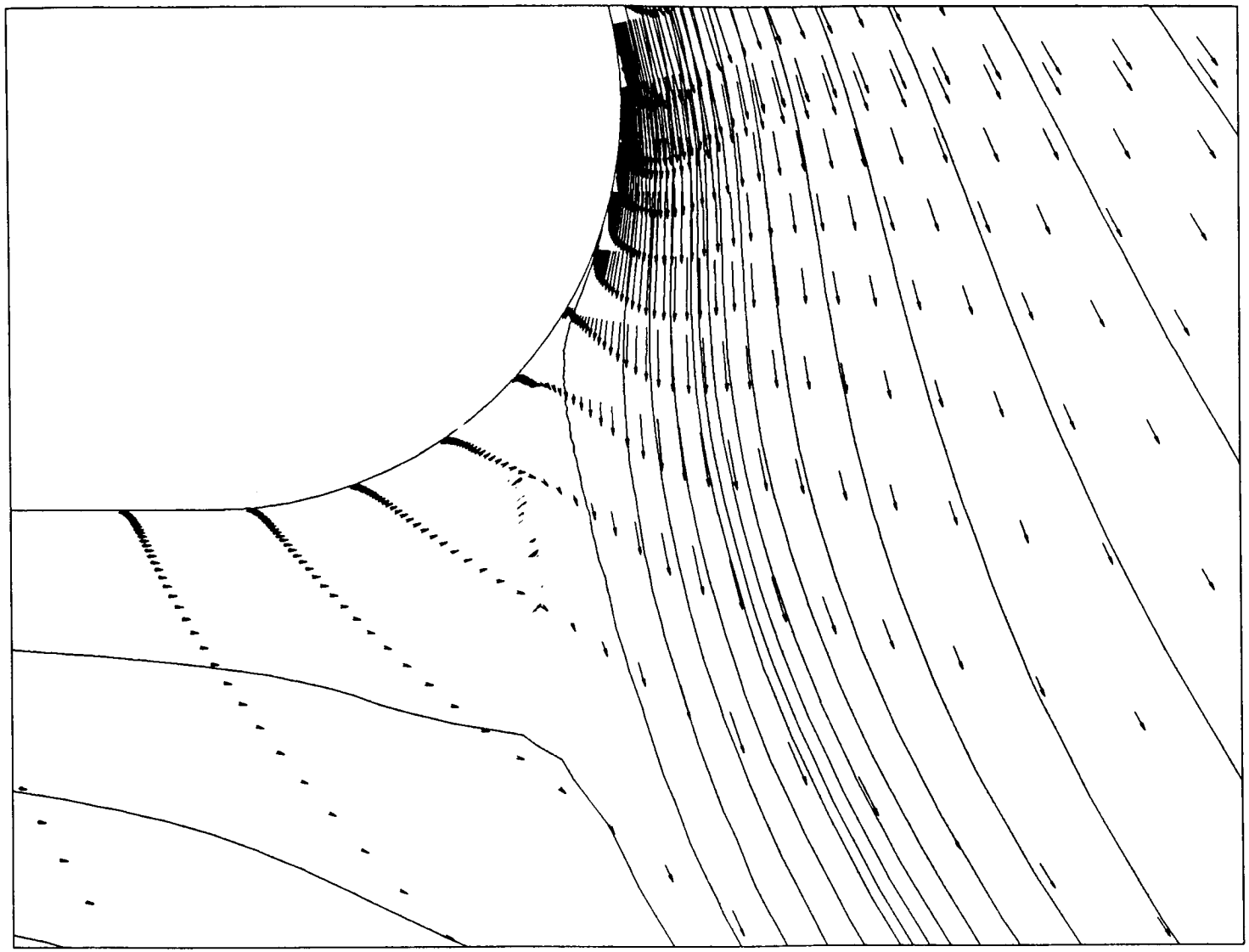

Figure 4. Computed Velocity Vectors and Streamlines

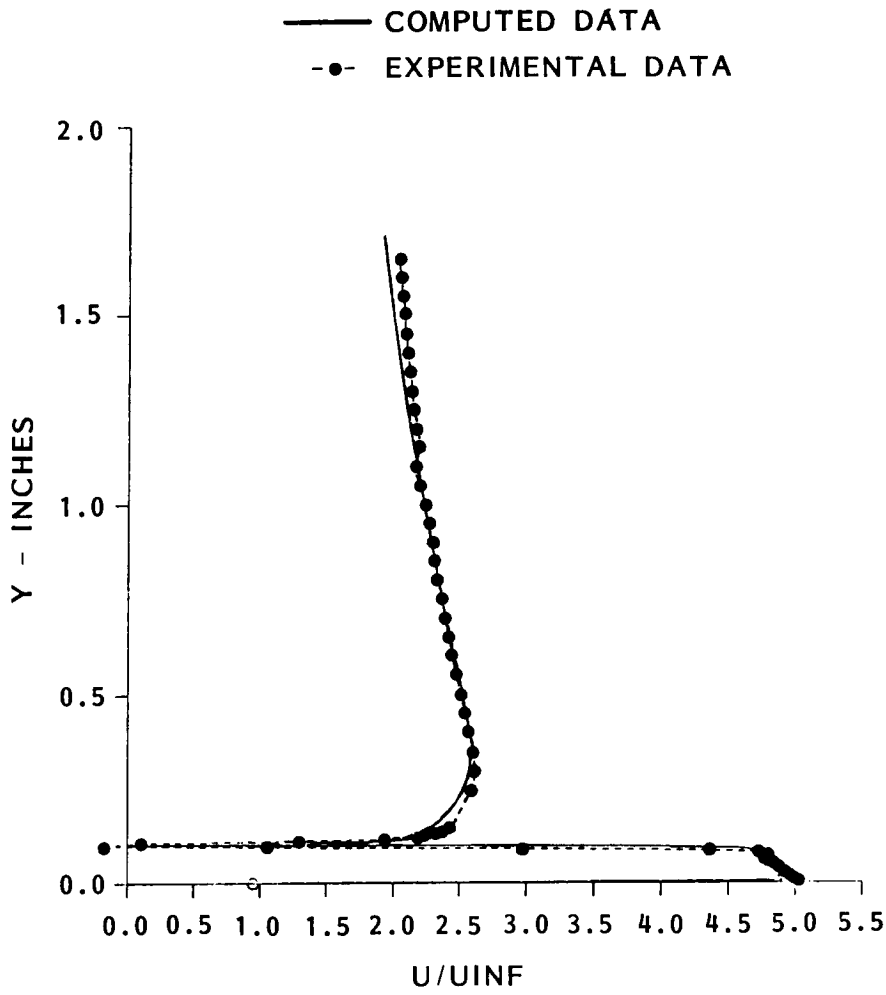

Figure 5(a). Computed and Experimental Velocity Profiles at Jet Exit Plane

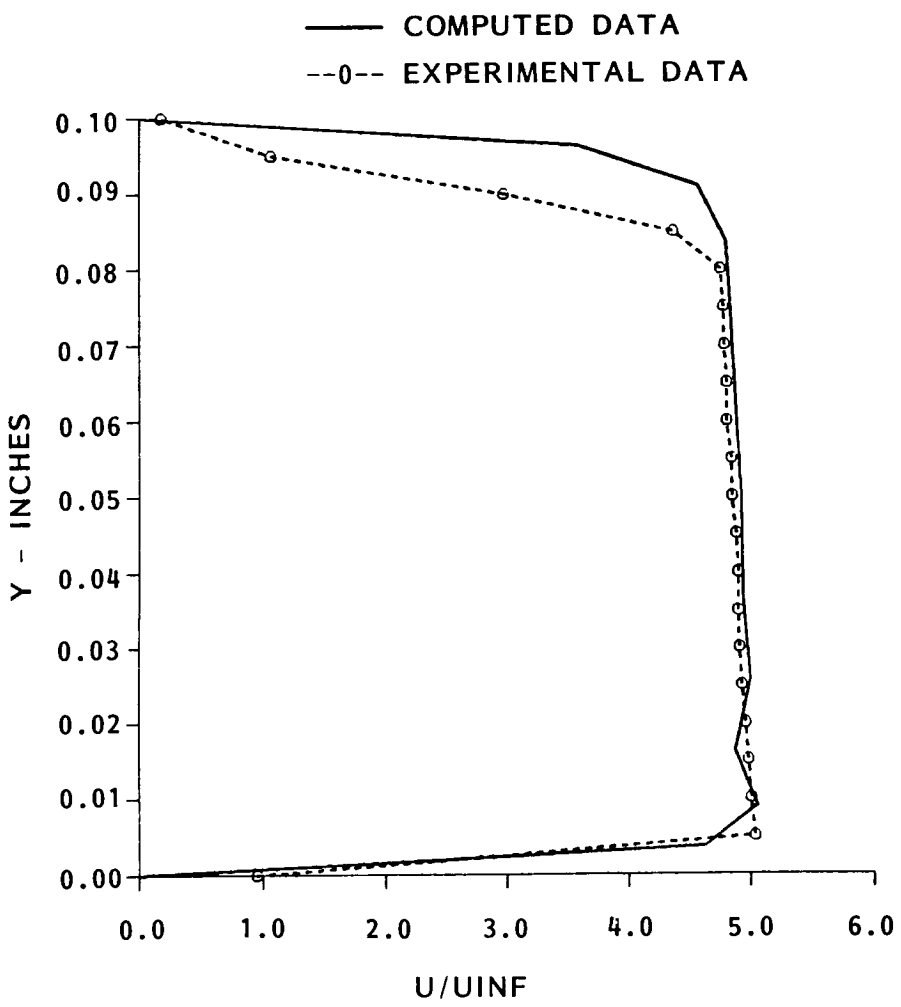

Figure 5(b). Computed and Experimental Velocity Profiles for Jet Slot Exit

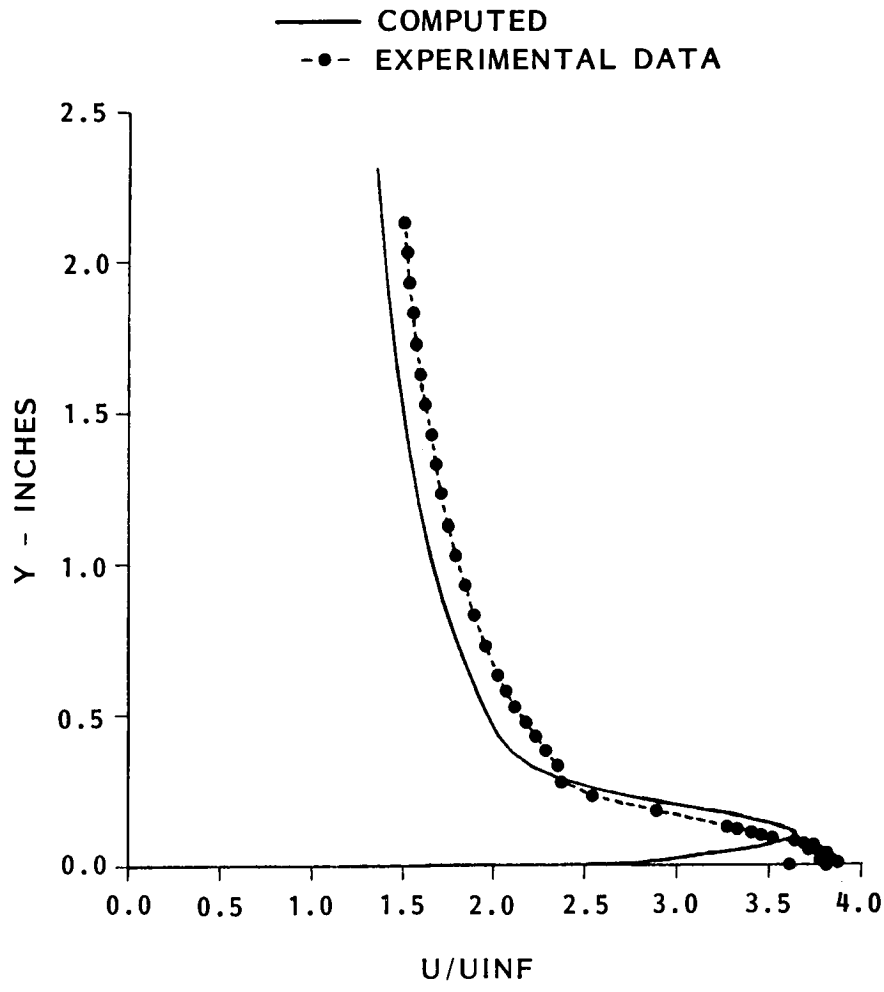

Figure 6. Computed and Experimental Velocity Profiles at Theta = 90 Degrees

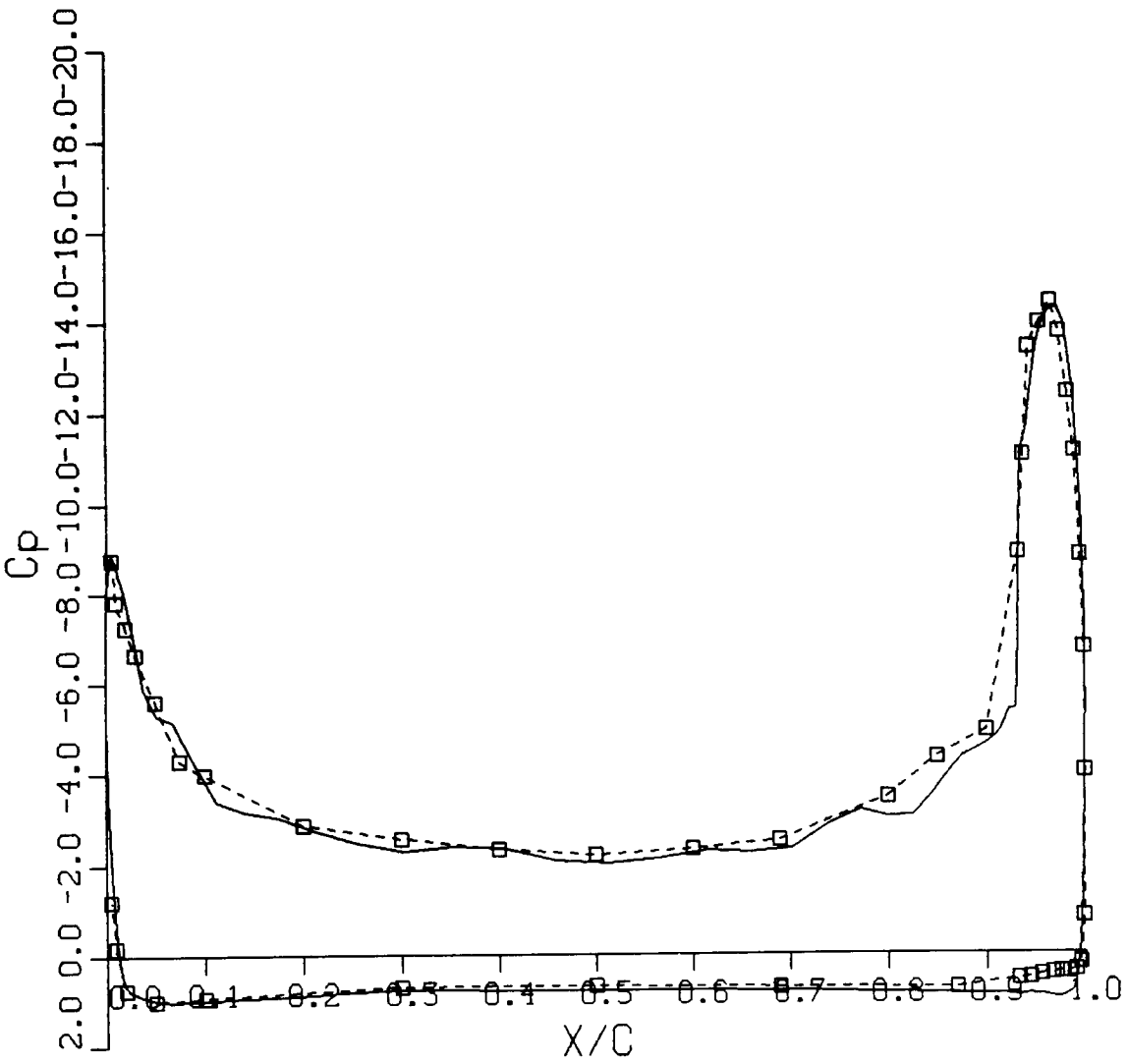

Figure 7. Computed and Experimental Pressure Coefficient Distributions

Navier-Stokes Computations for Circulation Control Airfoils

THOMAS H. PULLIAM,
DENNIS C. JESPERSEN,
AND
TIMOTHY J. BARTH

Research Scientists
Computational Fluid Dynamics Branch
NASA Ames Research Center

Abstract. Navier-Stokes computations of subsonic to transonic flow past airfoils with augmented lift due to rearward jet blowing over a curved trailing edge are presented. The approach uses an innovative spiral grid topology. Solutions are obtained using a Navier-Stokes code (ARC2D) which employs an implicit finite difference method, an algebraic turbulence model, and some recent developments which improve stability, convergence and accuracy. Results are compared against experiments for no jet blowing and moderate jet pressures and demonstrate the unique capability to compute these complicated flows.

I. INTRODUCTION

This paper presents details of an effort to compute the flow around an airfoil with augmented lift caused by an exhausting rearward jet over a curved trailing edge (Coanda effect). Abramson and Rogers[1] give a good discussion of the circulation control airfoil problem and Coanda effect. A recent review paper by Wood and Nielsen[2] also describes the physical problem and experimental methods. The computations performed here combine a well established flow solver for the thin-layer Navier-Stokes equations (ARC2D)[3] with a number of new concepts for grid generation and integration. A spiral grid topology is used to provide adequate resolution inside the jet plenum chamber, around the Coanda surface and then out to the far field boundary. By manipulating the data base an integration scheme for this topology is employed which does not create any nonphysical boundaries.

The computations are compared with experimental data for cases with and without jet blowing. Results show good agreement with experimental data with significant lift augmentation for the blowing cases. Lift augmentation (defined as the lift to blowing rate curve slope) is compared with experimental data for various Mach numbers, angles of attack, and two Coanda geometries. The data of Abramson and Rogers[1] provides a useful set of experimental results for comparison.

This computational effort provides a needed tool for examining these complicated flows, especially in the jet exit-Coanda surface region where experimental measurements are difficult to obtain. The purpose of this paper is to demonstrate the application of ARC2D to a very interesting physical problem. We are interested in demonstrating the capibility to compute relevant trends from the experimental data. Once a validation of the present method is accepted, we then hope to use these computational experiments to aid in our understanding of the physical mechanisms inherent in the circulation control problem.

II. SPIRAL GRID GENERATION

One goal of this effort was to compute rather than model the flow at the jet exit. To do this we require a grid extending into the plenum. In order to easily utilize the existing Navier-Stokes solver ARC2D, a mapping from physical space to a computational rectangle was desired. These considerations led us to design a spiral grid mapping. The grid "begins" in the chamber, continues out the plenum exit, and wraps around the airfoil several times, spiraling away from the airfoil as it wraps around. Figure 1 shows the correspondence between physical and computational space.

In implementing this procedure, we use an intermediate step employing the mapping $z = \cos(\zeta)$ from the complex ζ-plane to the complex z-plane. This function is 2π-periodic in ζ, takes horizontal lines in the ζ-plane to ellipses in the z-plane, takes vertical lines in the ζ-plane to hyperbolas in the z-plane, and takes lines with positive slope in the ζ-plane to outward-spiraling curves in the z-plane. We are given coordinates for the airfoil shape in physical space, defining a curve C_z running clockwise from a point on the Coanda surface beneath the jet exit around to the last point on the lip above the slot. Using the one-dimensional distribution function of Vinokur[4], we locate a given number of points around the airfoil with prescribed arclength spacings in the Coanda region and at the leading edge. (Sometimes the function from Vinokur[4] stretches too slowly, in which case we use a simple polynomial distribution function.) In a typical case we might have 281 points around the airfoil, with 120 of those points aft of 95% chord to give adequate circumferential resolution in the Coanda region. We then find the prei-mages ζ_j of these points z_j, i.e., $\cos(\zeta_j) = z_j = x_j + iy_j$. These points $\zeta_j = \alpha_j + i\beta_j$ are found by a simple Newton iteration and define a curve C_ζ in the ζ-plane. This curve is of the form $\beta = \beta(\alpha)$, $\alpha_{min} \leq \alpha \leq \alpha_{jet}$. We then extend this curve for $\alpha_{jet} \leq \alpha \leq \alpha_{max}$, where α_{max} is chosen so that the grid spirals around the airfoil a prescribed number of times (usually about 3.5) in physical space. Thus we have a curve $\beta = \beta_{bottom}(\alpha)$, $\alpha_{min} \leq \alpha \leq \alpha_{max}$, in the ζ-plane.

We then define the upper boundary of the region in the ζ-plane via $\beta = \beta_{top}(\alpha) = \beta_{bottom}(\alpha + 2\pi)$, and we also ensure that β_{top} is defined for $\alpha_{min} \leq \alpha \leq \alpha_{max}$. This results in a distorted rectangle in the ζ-plane, $\{(\alpha, \beta) : \alpha_{min} \leq \alpha \leq \alpha_{max}, \quad \beta_{bottom}(\alpha) \leq \beta \leq \beta_{top}(\alpha)\}$. We make a grid on this region as follows. The points α_j are defined by periodicity. A given number of points (typically 31) are distributed in the β-direction,

with the normal spacing in the ς-plane chosen to result in a prescribed normal spacing (typically 0.002% of chord) at the airfoil surface in the physical plane. The one-dimensional stretching function is used for the distribution in the β-direction. Care is also taken that the grid spacing in physical space is continuous as wrap boundaries are crossed moving away from the airfoil. Finally, a few (typically 10) Jacobi relaxation steps are taken, again working in ς-space, to enhance the smoothness of the grid.

The grid in the chamber is made in a separate step, working entirely in physical space. Continuity of grid spacing in the circumferential direction is enforced at the jet exit. Typically we use 71 grid points in the flow direction for the grid in the chamber. The last step is to transform the grid in the ς-plane to the z-plane via the cosine mapping and "weld" on the grid in the chamber. The total process is algebraic and explicit and results in a grid which extends into the plenum and gives good resolution in the Coanda region. The dimensions of the final grid are typically 1065×31. The mapping $z = \cos(\varsigma)$ is conformal but the grid in physical space is not orthogonal since the grid in ς-space is not orthogonal.

Abramson and Rogers[2] tested three different Coanda geometries for one basic elliptical slightly cambered airfoil. We have chosen two of the geometries, the rounded ellipse (RE) and the displaced ellipse (DE). The forebody for both cases is identical and a replaceable Coanda geometry was employed. Figure 2 shows the differences in shape and curvature between the RE and DE geometries. These may seem small, but experimental evidence shows a large effect of Coanda geometry on lift augmentation and response to various flow parameters such as Mach number and angle of attack. Plate 1 shows various views of the grid used for the RE computations. Note the continuity across wrap boundaries, the chamber–Coanda region and the clustering in the Coanda base region. The DE grid is similar. Both grids are 1065×31 with 281 points on the airfoil.

III. NAVIER-STOKES SOLVER

The Navier-Stokes solver (ARC2D)[3] used for the computations was written at NASA Ames Research Center. The thin-layer Navier-Stokes equations in generalized coordinates are solved using an implicit approximate factorization technique. This code is explained in detail in papers by Pulliam[3], Steger[5] and Pulliam and Steger[6] and will not be reviewed at length here. The main features of this code are presented below. The thin-layer Navier-Stokes equations written in generalized curvilinear coordinates are

$$\partial_\tau \hat{Q} + \partial_\xi \hat{E} + \partial_\eta \hat{F} = Re^{-1} \partial_\eta \hat{S} \tag{1}$$

where

$$\widehat{Q} = J^{-1}\begin{bmatrix}\rho\\ \rho u\\ \rho v\\ e\end{bmatrix}, \quad \widehat{E} = J^{-1}\begin{bmatrix}\rho U\\ \rho uU + \xi_x p\\ \rho vU + \xi_y p\\ U(e+p) - \xi_t p\end{bmatrix},$$

$$\widehat{F} = J^{-1}\begin{bmatrix}\rho V\\ \rho uV + \eta_x p\\ \rho vV + \eta_y p\\ V(e+p) - \eta_t p\end{bmatrix}$$

$$\widehat{S} = J^{-1}\begin{bmatrix}0\\ \eta_x m_1 + \eta_y m_2\\ \eta_x m_2 + \eta_y m_3\\ \eta_x(um_1 + vm_2 + m_4) + \eta_y(um_2 + vm_3 + m_5)\end{bmatrix}$$

with

$$U = \xi_t + \xi_x u + \xi_y v, \quad V = \eta_t + \eta_x u + \eta_y v$$

$$m_1 = \mu(4\eta_x u_\eta - 2\eta_y v_\eta)/3$$
$$m_2 = \mu(\eta_y u_\eta + \eta_x v_\eta)$$
$$m_3 = \mu(-2\eta_x u_\eta + 4\eta_y v_\eta)/3$$
$$m_4 = \mu Pr^{-1}(\gamma - 1)^{-1}\eta_x \partial_\eta(a^2)$$
$$m_5 = \mu Pr^{-1}(\gamma - 1)^{-1}\eta_y \partial_\eta(a^2)$$

These equations are central space differenced and implicitly advanced in time. For $h = \frac{1}{2}$ or 1. the time integration is trapezoidal rule (second order in time) or Euler implicit (first order in time)

$$\left[I + h\partial_\xi \widehat{A}^n\right]\left[I + h\partial_\eta \widehat{B}^n - Re^{-1}hJ^{-1}\partial_\eta \widehat{M}\right]\Delta\widehat{Q}^n = -h\left(\partial_\xi \widehat{E}^n + \partial_\eta \widehat{F}^n - Re^{-1}\partial_\eta \widehat{S}^n\right) = \widehat{R}^n \tag{2}$$

where $\widehat{A}, \widehat{B}$, and $\widehat{M}$ are Jacobians of $\widehat{E}, \widehat{F}$, and $\widehat{S}$ respectively.

An explicit nonlinear artificial dissipation term is added to enhance stability of the central difference scheme. The form, a mixture of constant coefficient fourth order and variable coefficient second order terms, has proven to be very successful in obtaining accurate results for subsonic and transonic calculations. Details can be found in References [3], [6] and [7].

For steady-state computations or first order time integrations, a diagonal form of Eq. (2) is used. In this case the left and right eigenvector matrices of $\widehat{A}$ and $\widehat{B}$ are

used to diagonalize the one-dimensional operators. Pulliam[3,8] gives a discussion and derivation of this algorithm. The diagonal algorithm can be written as

$$T_\xi \left[I + h\,\delta_\xi \Lambda_\xi\right] \hat{N} \left[I + h\,\delta_\eta \Lambda_\eta\right] T_\eta^{-1} \Delta \hat{Q}^n = \hat{R}^n \tag{3}$$

where

$$\Lambda_\xi = T_\xi^{-1} \hat{A} T_\xi \quad \text{and} \quad \Lambda_\eta = T_\eta^{-1} \hat{B} T_\eta$$

with T_ξ the matrix whose columns are the eigenvectors of $\hat{A}$ and T_η the corresponding eigenvector matrix for $\hat{B}$ and $\hat{N} = T_\xi^{-1} T_\eta$. The main advantage of this form is the simplification of the matrix inversions from block inversions to scalar inversions. This reduces the computational work and makes it easier to vectorize the implicit scheme. Also, the new scalar form for the inversion process allows for the use of scalar pentadiagonal solvers so that the added fourth order explicit artificial dissipation can be properly linearized and made fully implicit. This enhances stability and convergence rates (Refs. [3] and [6].) In viscous calculations the diagonal algorithm employs an approximation to the implicit viscous terms where the eigenvalues of the viscous Jacobian, are added to the inviscid eigenvalues for the η derivatives on the left-hand side of Eq. (3), Ref. [3]

IV. BOUNDARY CONDITIONS

The boundary conditions used at the airfoil surface and far field boundary are standard ones defined in Refs. [3] and [6]. Briefly, no slip is enforced at the surface along the plenum walls and airfoil surface. The normal pressure gradient is set to zero at the solid surfaces and an adiabatic temperature boundary condition is used. Characteristic conditions based on local one-dimensional Riemann invariants are used at the far field boundary. A correction based on a potential vortex at the airfoil center with a circulation consistent with the generated lift is also used to reduce the effect of the location of the outer boundary.

At the plenum inlet, conditions are specified so that a required mass flow rate is obtained at the slot exit. The geometry used in the plenum was supplied by Abramson and Rogers[1] along with an estimated slot height. For a pressure ratio P_r and temperature ratio T_r (plenum values to free stream values) mass flow rates were measured by Abramson and Rogers. A nondimensional mass flow parameter, C_μ is defined as

$$C_\mu = \frac{\dot{m} V_j}{\frac{1}{2} M_\infty} \tag{4}$$

where $\dot{m}$ is mass flow rate, M_∞ is free stream Mach number and

$$V_j = \sqrt{2 T_r \frac{\gamma}{\gamma - 1} \left[1 - P_r^{-(\gamma - 1/\gamma)}\right]} \tag{5}$$

is an isentropic jet velocity. Experimentally, some expansion of the slot can occur when the plenum is pressurized, which will then alter the mass flow rates. The slot heights given by Abramson and Rogers were estimated from an isentropic relation and were on the order of 0.0021 (based on a chord of 1.0) for the geometries considered. In order to match mass flow rates computationally, since the computational geometry is rigid, the slot heights for the RE and DE were modified slightly. We employed a value of 0.0025 for both cases which enabled us to match mass flow rates to within 3%. Figure 3 shows a correlation between the experimental mass flow rates and the computed values for the cases presented below. An exact correlation would be along the 45 degree line and we see quite acceptable results.

V. SPIRAL INTEGRATION

The grid generation procedure maps the flow region in physical space to a rectangular box in computational space (Fig. 1). The use of the spiral grid topology requires us to reexamine our usual integration procedures. The ξ integration of Eq. (3) is a straightforward integration from the plenum chamber boundary (a-b) to the farfield boundary (c-d). In the η direction, a first glance at the topology in computational space shows that spiral boundaries occur as interior boundaries in physical space. These are not physical boundaries but rather constructs of the grid generation. A continuous integration across these boundaries is obtained by reordering the computational domain. Plate 1 shows views of the spiral grid where the plenum is shown in red and sequential wraps of the grid are shown in different colors.

The implicit integration scheme, Eq. (3), can be rewritten symbolically as

$$L_\eta L_\xi \Delta \hat{Q}^n = (R_\xi + R_\eta)\, \hat{Q}^n \tag{6}$$

where L represents an implicit operator and R an explicit operator. The first step in the integration is to perform the explicit R_ξ differencing using the data in what will be called the ξ orientation, Fig. 1. The computational domain is then reordered by an in-place transpose to the η orientation. The reordered computational domain is shown in Fig. 4, and in Plate 2 the distinct η blocks are painted different colors. Here the blocks of data constituting a spiral wrap are stacked on top of each other. In this new computational space we integrate in η from wall to wall in the plenum region and from the body surface to the far field boundary in the outer region. Both the explicit R_η and implicit L_η operations are performed at this time. Note that if the last wrap is not a full wrap then we actually define three regions and integrate from boundary to boundary for each. After the η integration is complete the data is reordered to the ξ orientation and the implicit L_ξ integration is performed, completing the algorithm. Using this integration technique, we only encounter boundaries which are physically meaningfull (on the airfoil surface, at the plenum chamber inflow and at the far field boundary). The spiral wrap boundaries that physically lie in the interior of the domain of integration are treated at regular interior ponits and are solve using

the conservation equations. That is, they are treated no differently than any other interior point.

VI. TURBULENCE MODEL

There are a number of interesting physical mechanisms associated with the circulation control problem. In the absence of the exhausting rearward jet, the blunt body geometry produces base flow separation and the expected $C_l - \alpha$ responses. High positive and negative angles of attack produce viscous stall and at low angles of attack there is very little lift and substantial drag. As the pressure in the chamber increases a jet exhausts out the slot and remains attached to the Coanda surface. The flow off the upper airfoil surface is entrained at the jet–shear layer–upper boundary layer interface. This entrainment of the upper surface flow produces the augmented lift via increased circulation. As the blowing rate is increased the airfoil continues to gain lift until a stall boundary is reached. The nature and cause of this stall is not fully understood. It has been characterized as an "inviscid stall" as opposed to the classical viscous airfoil stall. Although the authors are quite interested in this stall mechanism, such cases are beyond the capabilities of the current turbulence model used here and also require more study into the basic physical mechanisms involved in the prestall conditions. Computations attempted at the post-stall conditions were unsteady and not quite acceptable.

One of the more important effects needed in this problem is the jet–upper boundary layer interaction. The boundary layer generated on the upper surface will be strongly dependent on the upper surface geometry, the flow conditions (such as freestream Mach number or angle of attack), and the increased accelerations due to the jet entrainment. The characteristics of the boundary layer (thickness, turbulence intensity) as it encounters the jet will have a significant influence on the entrainment. The Coanda jet attachment was surprisingly easy to obtain, but the effects of curvature on the attached jet and jet–boundary layer interface are only weakly modeled in this study. As the results below will suggest and numerous studies by others have shown, improved turbulence models are the key to this problem. Even so, the relatively simple algebraic turbulence model used here with its low order correction does an adequate job.

Turbulence modeling of the airfoil and Coanda surface was accomplished by modifying a zero equation model developed by Baldwin and Lomax[9] to account for the effect of streamwise streamline curvature on the eddy viscosity. Bradshaw[10] and others have reported on the large effect of streamline curvature in the plane of the mean shear on the turbulence quantities. These effects are often much larger (in some cases as much as an order of magnitude larger) than predicted by dimensional arguments. Bradshaw (1973) suggests modifying the apparent mixing length using a correction analogous to

the Monin-Obouhkov formula for buoyant flows

$$\frac{\ell}{\ell_0} = 1 + \beta \frac{2U/R}{\partial U/\partial y} \tag{7}$$

where R will be the streamline radius of curvature and β is an empirical constant on the order of 10. For this investigation a different correction formula, suggested by Baldwin (private communication), was used. This correction is derived from Prandtl's turbulent kinetic energy equation with a curvature suppression term, F_c, suggested by Baldwin, Chigier, and Sheaffer[11] in 1973 for a $k-\epsilon$ model. In the notation of Rodi[12], the steady kinetic energy equation with the curvature suppresion term suggestion by Baldwin, et.al[11] is written as

$$U_i \frac{\partial k}{\partial x_i} = \frac{\partial}{\partial x_i}\left(\frac{\nu_t}{\sigma_k}\frac{\partial k}{\partial x_i}\right) + \nu_t\left(\frac{\partial U_i}{\partial x_j} + \frac{\partial U_j}{\partial x_i}\right)\frac{\partial U_i}{\partial x_j} - \epsilon + F_c \tag{8}$$

$$F_c = \left[C_c (U_i U_i)^{\frac{1}{2}}\left(\frac{\partial U_i}{\partial x_j} + \frac{\partial U_j}{\partial x_i}\right)\ell\sqrt{2k}\right]/R \tag{9a}$$

and

$$\nu_t = c_\mu \frac{k^2}{\epsilon}, \quad \epsilon = \frac{c_\mu^{\frac{3}{4}} k^{\frac{3}{2}}}{\ell}, \quad c_\mu \approx .09 \tag{9b}$$

(Note that the c_μ as used here differs from the C_μ defined in Eq. (4).) For the high Reynolds number flow under consideration, only stress terms in the normal direction are retained. In addition, convection and diffusion processes are neglected. Under these assumptions the energy equation reduces to

$$\nu_t \omega^2 = \epsilon - \frac{C_c U \omega \ell \sqrt{2k}}{R} \tag{10}$$

This equation can then be solved for k and an expression for ν_t obtained.

$$\nu_t^2 = c_\mu^{\frac{1}{2}} k \ell^2 = \ell^4 \omega^2 - \frac{C_c U \omega \ell^4 \sqrt{2}}{c_\mu^{\frac{1}{4}} R} \approx \nu_{t_0}^2 - \frac{C_c U \omega \ell^4 \sqrt{2}}{c_\mu^{\frac{1}{4}} R} \tag{11}$$

In this equation ν_{t_0} is the eddy viscosity computed in the standard Baldwin-Lomax model and ℓ is a length scale such that

$$\ell = \begin{cases} \kappa \mathcal{D}(y) y, & \text{if } y \le y_{crossover}\ ; \\ \kappa \mathcal{D}(y_{crossover}) y_{crossover}, & \text{otherwise.} \end{cases} \tag{12}$$

where $y_{crossover}$ is the match point of the inner and outer layers, κ is the Karman constant and $\mathcal{D}$ is the usual VanDriest damping function for wall bounded flows.

The only constant to be determined at this point is C_c. The calibration of this constant based on other algebraic curvature models (e.g. Ref. 10 and 13) documented in the literature is not straightforward . The constant C_c in Ref. 11 was chosen to be unity, but this choice appears to have been somewhat arbitrary. A calibration of C_c from the β in Bradshaw's formula can not be done, as we see it, because of the different behavior of these models except for very small y^+ values where curvature is not important. Comparison with other Bradshaw like models proved equally unsatifactory and therfore a numerical calibration of C_c based on the experimental data was performed in the calculations presented below.

VII. RESULTS

The computational code (ARC2D) has been validated for a wide variety of cases, see Pulliam[1] and Barth, Pulliam, and Buning[14] for numerous examples. The code with the modification for the spiral integration was first validated against a nonspiral standard code for no jet blowing and showed excellent agreement. A conventional 'O' mesh with a closed slot was compared with a spiral mesh solution at $M_\infty = 0.3$ and $\alpha = -5.0°$. Pressure distributions for both computations are compared in Fig. 5. All other measures of accuracy show good to excellent agreement.

Computations for the two Coanda shapes were performed at two Mach numbers, $M_\infty = 0.3$ and $M_\infty = 0.6$. Abramson and Rogers[1] provided the experimental conditions and data. Significant angle of attack corrections for wind tunnel wall interference were suggested to us. An angle of attack correction of $-1.5 \times C_l$ was calibrated by the experimenters. A set of potential code results was used where lifts were matched to the experimental data and circulation was modified using angle of attack changes until the mid-chord pressure gap and leading edge pressure matched experimental values. A calibration across the experimental data produced the factor of -1.5. The computations presented here are for an experimental geometric angle of attack $\alpha_{geo} = 0°$ with angle of attack corrections $-1.5C_l$ where C_l is taken from the experimental data. Note that this can be a substantial correction factor since lift levels reach values of $C_l > 2.0$.

Tables 1-4 list the computed cases showing the Coanda type used, Mach number, pressure ratio P_r, angle of attack, experimental C_μ, C_l, and computed C_μ,C_l. The column labeled 'Point' refers to the experimental designation which will be used here to delineate cases.

Plots of C_l against C_μ for the above cases are shown in Fig. 6 and 7. The computations are able to predict the lift augmentation (lift-slope curves) quite well. In particular, the differences due to changes in Coanda geometry are predicted. For the RE geometry the $M_\infty = 0.3$ produces higher lift augmentation than the $M_\infty = 0.6$ case. For the DE geometry the $M_\infty = 0.6$ case produces more lift augmentation than the $M_\infty = 0.3$.

As can be seen the lift coefficients compare quite well over a broad range of blowing

rates. In order to obtain such good comparisons the turbulence model parameter C_c had to be adjusted. As mentioned above better turbulence modeling is crucial to this problem. Within the constraints of the simple curvature correction used here each case was calibrated by adjusting C_c. Specifically, we choose one point from each of the above Tables (Points 38, 304, 733, and 748) and adjusted C_c until the lifts matched the experimental data to within 3%. Once a value of C_c was obtained for one point, all other cases in the associated table were generated with that value. The values of C_c used are listed with the above tables.

The significance of these variations in C_c can only be speculated on. The effect of curvature on the jet–boundary layer interaction and jet–Coanda flowfield are not properly understood but are obviously important. Differences in upper surface boundary layer caused by differences in free stream Mach number and the differences in curvature due to the two Coanda geometries can account for the sensitivity to the curvature correction.

There seems to be a rather large discrepancy for the low Mach number ($M_\infty = 0.3$) nonblowing cases, Points 33 and 728, which occurs for both geometries. The computations simply do not produce the large level of lift obtained in the experiments. The basic airfoil section has about 1% camber which can account for the experimental lift. There may be laminar-turbulent transition effects which the computation cannot account for, or the angle of attack correction scheme may not be applicable for these cases. At the higher Mach number ($M_\infty = 0.6$) the experimental lift is essentially zero and the computations agree better with the experimental data.

Pressure distributions compared with the experimental data for selected cases are shown in Figs. 8-11. In Fig. 8, results are shown for the RE airfoil at $M_\infty = 0.3$, $\alpha_{geo} = 0^\circ$ and a Reynolds number $Re = 3.0 \times 10^6$ for various pressure ratios P_r. The key points to look for are comparison of leading edge pressure distribution and midchord pressure gap which indicate that the angle of attack correction is proper and the blowing rate (mass flow C_μ) is good. Note that since angle of attack corrections are needed and the mass flow out the jet has a strong influence on the solution, there is the possibility of predicting lifts that match experimental data for a wide variety of angles and mass flow rates. In the results shown here the leading edge pressure and midchord pressure match quite well at least up until the higher pressure ratio case. As shown in Table 1 lift coefficient is predicted accurately for these cases.

The pressure distributions in the regions before the jet–Coanda interaction on the upper and lower surface are important indicators of having a good prediction of the incoming boundary layers which stongly influence the entrainment mechanism. The results shown in Fig. 8 show fairly good pressure gradients in those regions.

Plates 3a and 3b show Mach contours in color for results from Point 33. The color contour range was taken between the minimum and maximum Mach number with blue being $M = 0.0$ and magenta $M = 0.36$. Note the continuity of Mach contours throughout the flow field even across wrap boundaries, as expected because

of the spiral integration discussed above. This a case with no jet blowing and we obtain the massive base flow separation. Plate 3b shows the extent of the separation region and gives an indication of the boundary layers on the upper and lower surfaces. Plates 4a and 4b show Mach contours for Point 38 and have the color scale blue for $M = 0.0$ to magenta for $M = 1.1$. The jet remains attached to the Coanda surface (the Coanda effect) which produces a region where the jet–upper surface boundary layer can interact. The shear layer between the jet and the upper surface flow produces an entrainment of fluid, i.e. a transfer of high momentum from the jet to the lower momentum upper surface boundary layer flow. It is easily seen from a comparison with Plate 3 that stagnation points have moved below the leading and trailing edges indicating increased circulation. The base flow separation has been moved to the lower part of the Coanda and reduced. The wake–shear layer region where the jet detaches from the Coanda surface is deflected.

Figure 9 shows pressure distributions for some of the $M_\infty = 0.6$, $\alpha_{geo} = 0°$, and $Re = 5.0 \times 10^6$ RE cases. The leading edge, midchord pressure gap and lifts are in good agreement with the experimental data. The trailing edge pressure gradients appear to be good but the absolute level of the pressure in those regions is a little low. Even so the results are quite good overall. In this case the jet detaches from the Coanda surface sooner than for the lower Mach number case because of the lower mass flow rate. There is less overall entrainment and therefore less lift augmentation. The separation region is more like a base flow separation.

Pressure distributions for the DE Coanda are shown in Fig. 10 ($M_\infty = 0.3$, $\alpha_{geo} = 0°$ and $Re = 2.88 \times 10^6$) and Fig. 11 ($M_\infty = 0.6$, $Re = 5.0 \times 10^6$). The quality of the results is similar to the RE solutions. The leading edge pressure, midchord pressure gaps and pressure gradients again compare quite well with the experimental data. For the DE, the jet detaches from the Coanda surface sooner than in the RE case even though the mass flow rates ($C_\mu = 0.0322$ for the RE and $C_\mu = 0.036$ for the DE) are similar. This is a direct response to the Coanda surface geometry (curvature) since both cases use the same forebody, incoming Mach number and geometric of attack. Note that since different lift levels were reached in the experiment different angle of attack corrections were needed in the computations.

In Plate 5 we show Mach color contours for four of the cases. Plate 5a is for RE Point 38, Plate 5b for RE Point 304, Plate 5c for DE Point 733 and Plate 5d for DE point 748. These are Mach contour maps where each region is colored based on the local Mach number. Contour lines are added to enhance levels. The Plates give a comparative picture of the structure of the flow fields. One can note the entrainment of the upper surface flow into the jet wake flow, the deflections of the wake centerlines and the relative lengths of the jets, detachment points, and separation regions.

VI SUMMARY

A computational capability for computing Navier-Stokes solutions for circulation controlled airfoils has been developed. The spiral grid topology allows us to integrate

the jet plenum chamber and exterior flow as a single unit. The cases presented here are representative of the computational capability. The results compare quite well with experiment, predicting pressure distributions, lift levels, lift augmentation, Coanda geometry effects, and flow field structure for a wide variety of blowing rates and two Mach numbers. The results are not completely predictive since the turbulence model had to be calibrated for a curvature correction. It is obvious that better turbulence modeling is needed for this problem. Future work will concentrate on the turbulence modeling and attempting to compute stall boundaries and understand the physics of the stall and general flow field.

VI ACKNOWLEDGEMENTS

The authors would like to thank Drs. J. Abramson and E. Rogers of David W. Taylor Naval Ship Research and Development Center for supplying the experimental data and for many helpful discussions on the experiments and in evaluating the computations. We also thank Dr. N Wood of Stanford for similar discussions and invaluable suggestions. Thanks to Dr. B. Baldwin for help with the turbulence modeling and Dr. P. Buning for help with the graphics and useful discussions on the physics of the computed flows.

Table 1. RE Coanda $M_\infty = 0.3$, $\alpha_{geo} = 0.0°$, $C_c = 1.6$						
Point	P_r	α	C_μ Exp.	C_l Exp.	C_μ Comp.	C_l Comp.
33	1.000	-0.11	0.0000	0.169	0.0000	0.055
35	1.137	-0.93	0.0094	0.616	0.0089	0.606
36	1.284	-1.66	0.0179	1.106	0.0176	1.127
37	1.432	-2.18	0.0253	1.454	0.0259	1.496
38	1.573	-2.65	0.0322	1.764	0.0322	1.743
39	1.705	-3.00	0.0376	2.000	0.0388	2.073

Table 2. RE Coanda $M_\infty = 0.6$, $\alpha_{geo} = 0.0°$, $C_c = 4.4$						
Point	P_r	α	C_μ Exp.	C_l Exp.	C_μ Comp.	C_l Comp.
301	1.000	00.00	0.0000	0.036	0.0000	0.033
302	1.202	-0.29	0.0032	0.191	0.0029	0.106
304	1.533	-0.58	0.0075	0.388	0.0074	0.375
305	1.701	-0.71	0.0094	0.472	0.0094	0.472
307	2.045	-0.95	0.0132	0.634	0.0134	0.695

Table 3. DE Coanda $M_\infty = 0.3$, $\alpha_{geo} = 0.0°$, $C_c = 2.0$						
Point	P_r	α	C_μ Exp.	C_l Exp.	C_μ Comp.	C_l Comp.
728	1.000	-0.25	0.0000	0.167	0.0000	0.033
729	1.068	-0.42	0.0041	0.281	0.0041	0.229
731	1.300	-1.06	0.0176	0.705	0.0182	0.745
732	1.488	-1.40	0.0252	0.932	0.0258	0.957
733	1.588	-1.79	0.0322	1.192	0.0326	1.202
734	1.716	-2.05	0.0377	1.367	0.0385	1.411
735	1.188	-2.31	0.0445	1.541	0.0461	1.550

Table 4. DE Coanda $M_\infty = 0.6$, $\alpha_{geo} = 0.0°$, $C_c = 2.2$						
Point	P_r	α	C_μ Exp.	C_l Exp.	C_μ Comp.	C_l Comp.
744	1.000	-0.11	0.0000	0.073	0.0000	0.048
745	1.168	-0.36	0.0026	0.237	0.0024	0.135
747	1.526	-0.78	0.0074	0.518	0.0074	0.513
748	1.709	-0.96	0.0095	0.614	0.0096	0.627
751	2.038	-1.21	0.0130	0.805	0.0133	0.806

REFERENCES

1. Abramson, J., and Rogers, E., *High Speed Characteristics of Circulation Control Airfoils*, AIAA Paper 83-0265 (1983).
2. Wood, N. and Nielsen, J., *Circulation Control Airfoils Past, Present, Future*, AIAA Paper 85-0204 (1985).
3. Pulliam, T. H., *Euler and Thin Layer Navier-Stokes Codes : ARC2D, ARC3D, Notes for Computational Fluid Dynamics User's Workshop*, UTSI E02-4005-023-84, March 1984.
4. Vinokur, M., *On One-Dimensional Stretching Functions for Finite-Difference Calculations*, J. Comp. Phys. (1983), p. 215–234.
5. Steger, J. L., *Implicit Finite Difference Simulation of Flow About Arbitrary Geometries with Application to Airfoils*, AIAA Paper 77-665 (1977).
6. Pulliam, T. H., and Steger, J. L., *Recent Improvements in Efficiency, Accuracy, and Convergence for Implicit Approximate Factorization Algorithms*, AIAA Paper 85-0360 (1985).
7. Pulliam, T. H., *Artificial Dissipation Models for the Euler Equations*, AIAA Paper 85-0438 (1985).
8. Pulliam, T. H., and Chaussee D.S., *A Diagonal Form of an Implicit Approximate Factorization Algorithm*, J. Comp. Phys. **39** (1981), p. 347.
9. Baldwin, B. S., and Lomax, H., *Thin Layer Approximation and Algebraic Model for Separated Turbulent Flows,*, AIAA Paper No. 78-257 (1978).
10. Bradshaw P., *The Effects of Streamline Curvature on Turbulent Flow.*, AGARDograph no. 169. (1973).
11. Baldwin B., Chigier N., and Sheaffer S., *Decay of Far-Flowfield Trailing Vortices.*, AIAA Journal, Vol 11 (1973), p. 1601.
12. Rodi W., *Proceedings of École d'Été d'Analyse Numérique - Modélisation numerique de la Turbulence, Clamart, France.*
13. Shrewsbury, G. D., *Analysis of Circulation Control Airfoils Using An Implicit Navier-Stokes Solver*, AIAA Paper 85-0171 (1985).
14. Barth, T. J., Pulliam, T. H., and Buning, P. G., *Navier Stokes Computations for Exotic Airfoils*, AIAA Paper 85-0109 (1985).

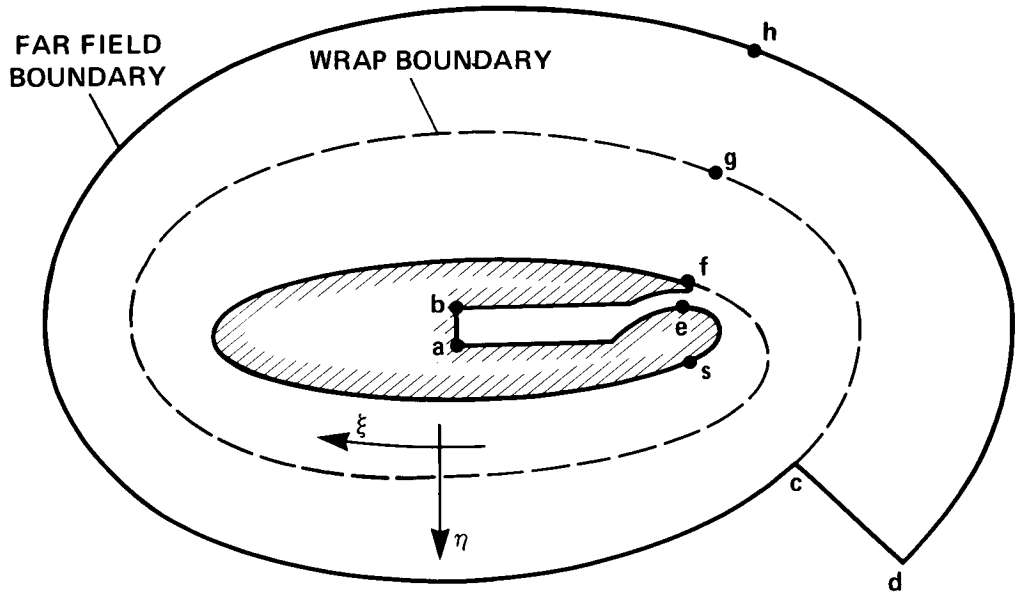

PHYSICAL SPACE

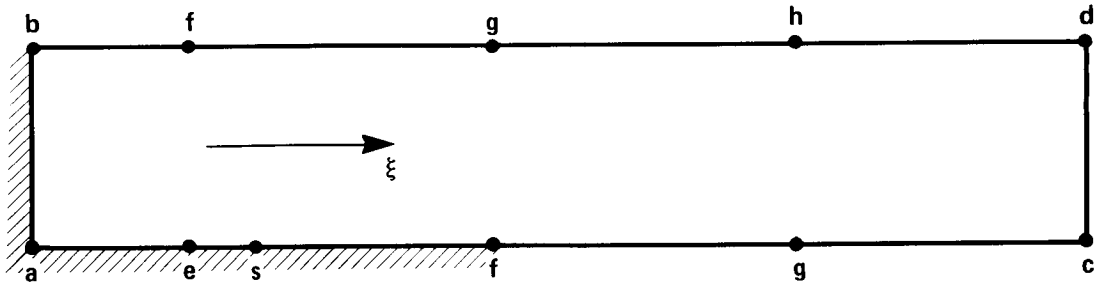

ξ-COMPUTATIONAL SPACE

Figure 1. Computational Mapping For ξ Orientation Topology.

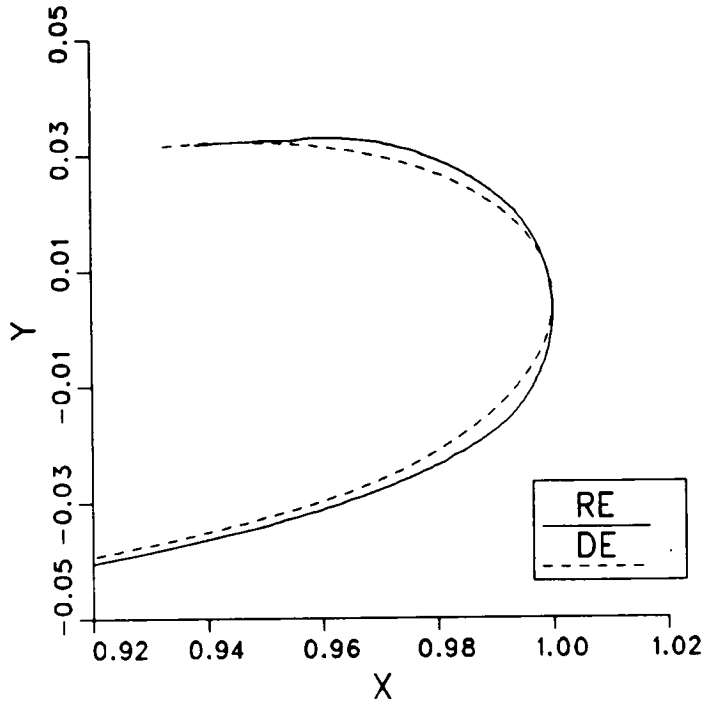

Figure 2. Coanda Geometry For RE and DE Airfoils.

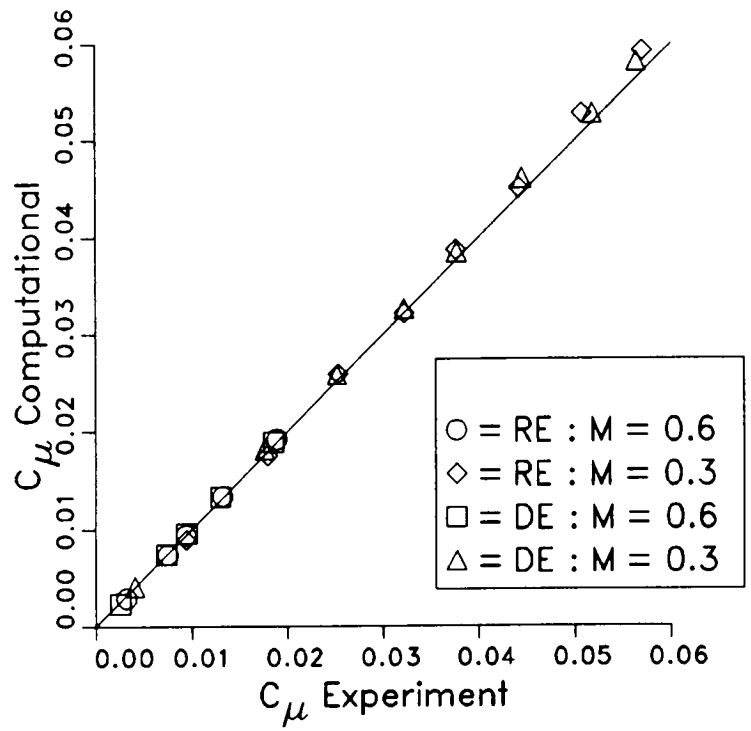

Figure 3. Correlation Between Experimental and Computational Mass Flows. Slot Height = 0.0025, α_{jet} = 0.0.

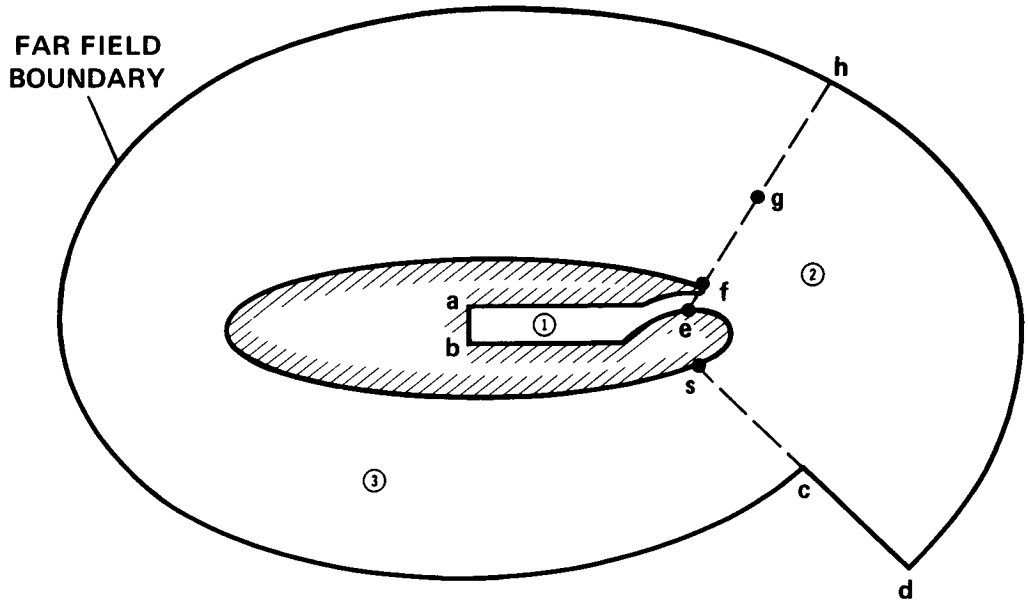

PHYSICAL SPACE

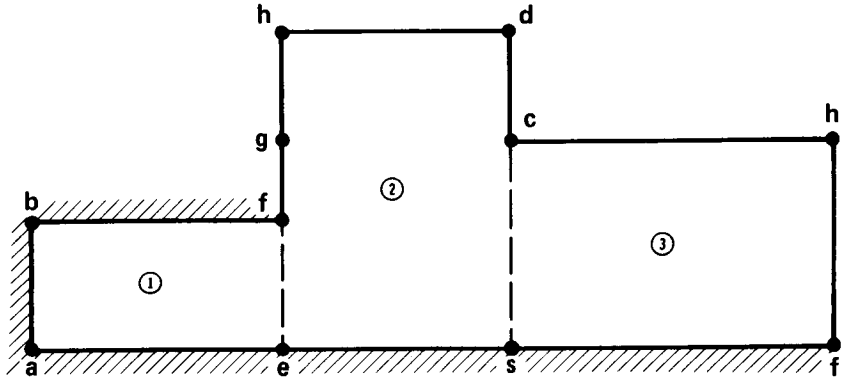

η-COMPUTATIONAL SPACE

Figure 4. Computational Mapping For η Orientation Topology.

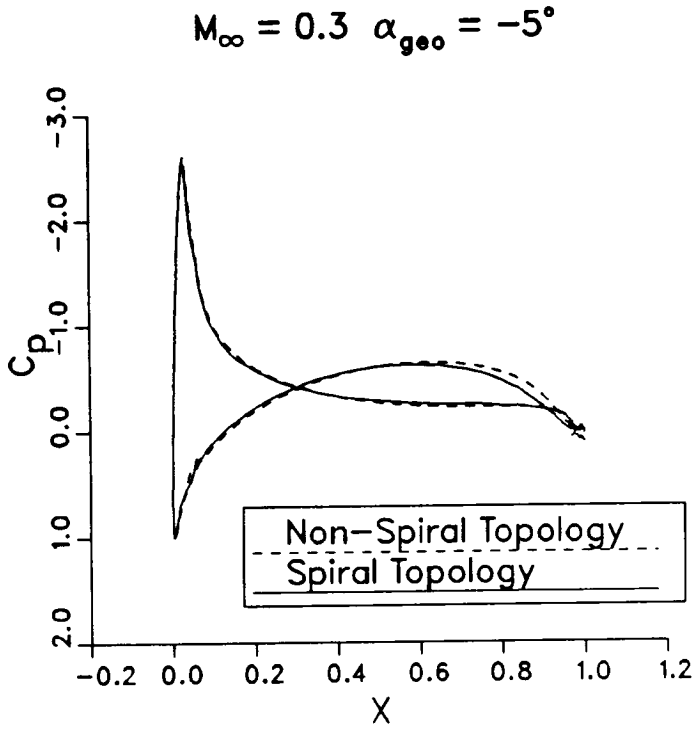

Figure 5. Comparison Between Non-Spiral and Spiral Integrations For A No Blowing Case.

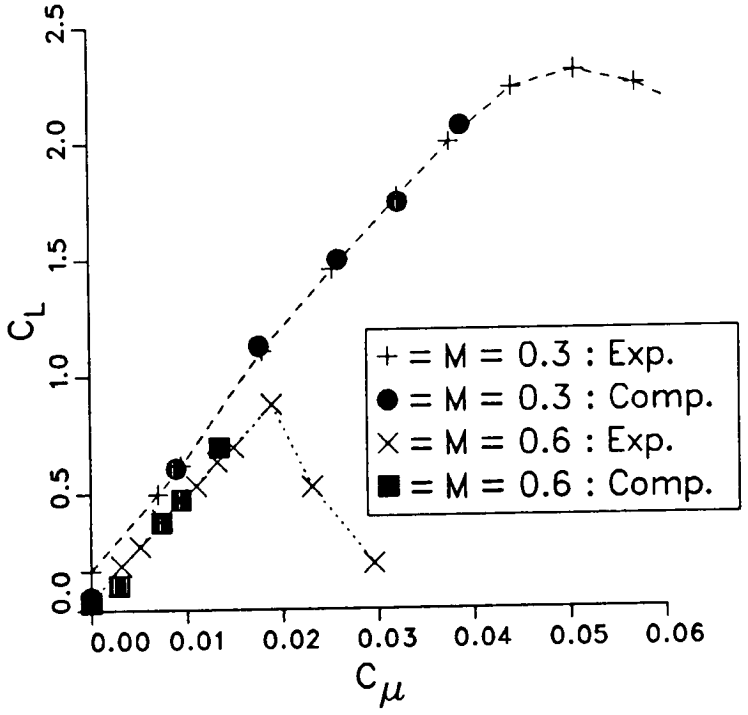

Figure 6. Lift Augmentation Curves For RE Geometry At $\alpha_{geo} = 0.0$.

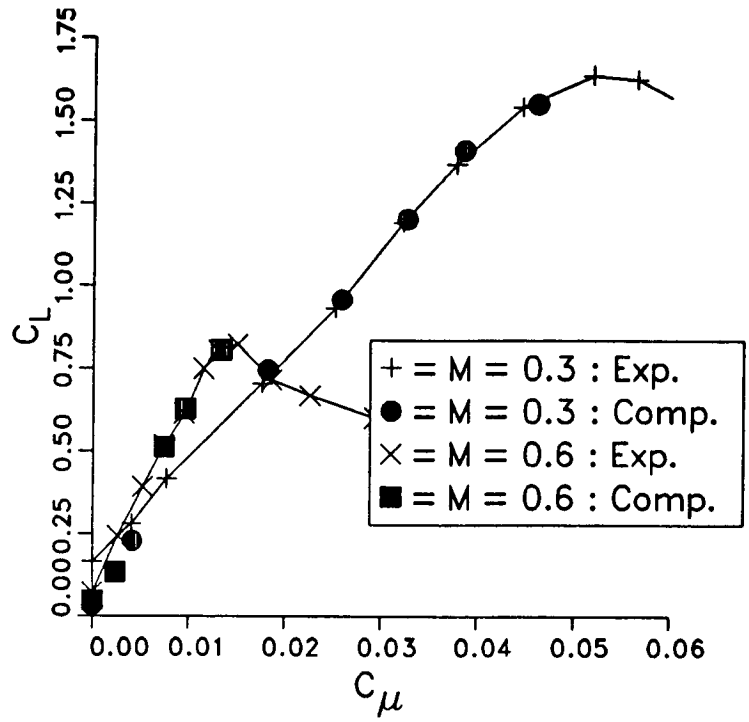

Figure 7. Lift Augmentation Curves For DE Geometry At $\alpha_{geo} = 0.0$.

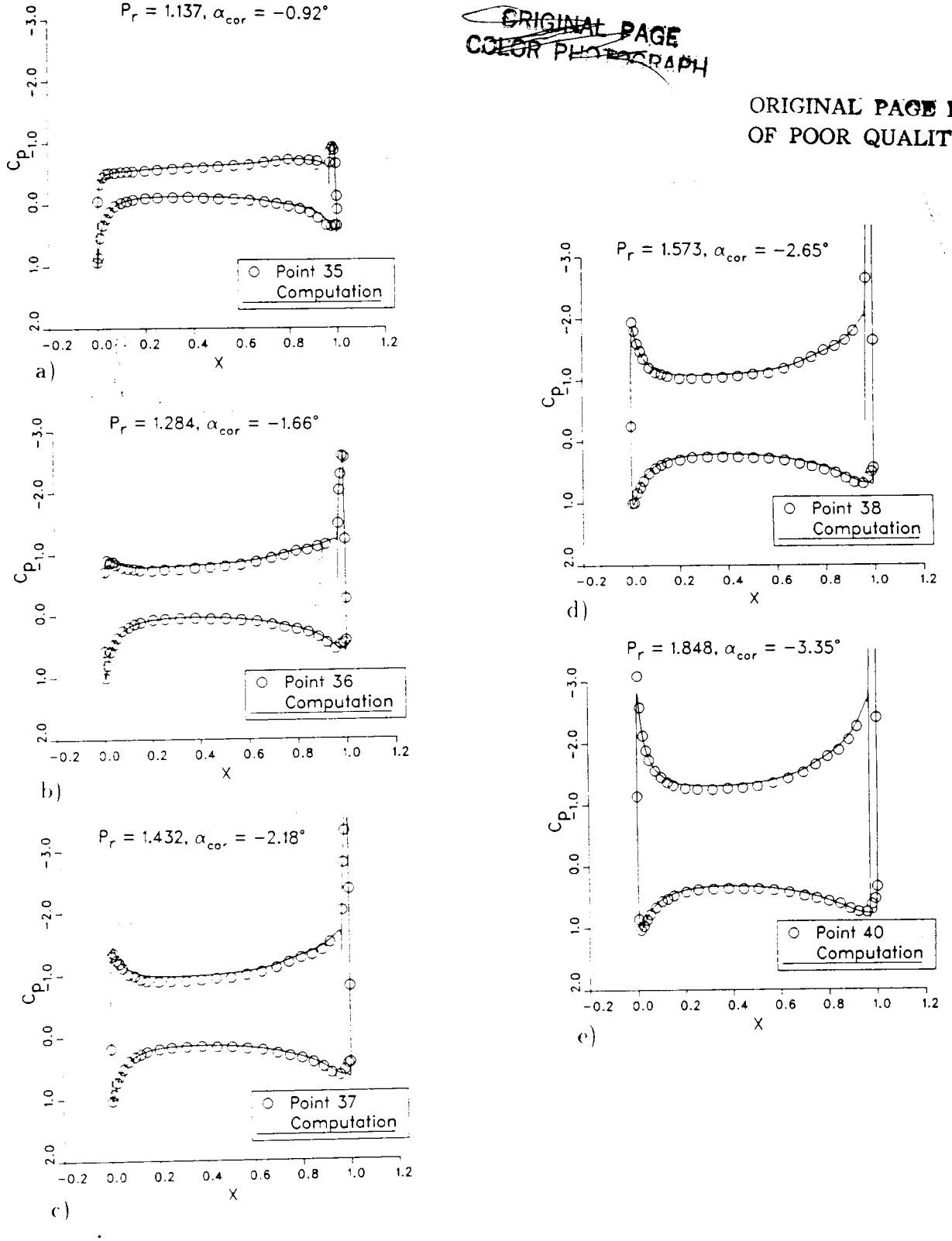

Figure 8. Pressure Distributions For RE Geometry, M_∞ = 0.3, $alpha_{geo}$ 0.0.

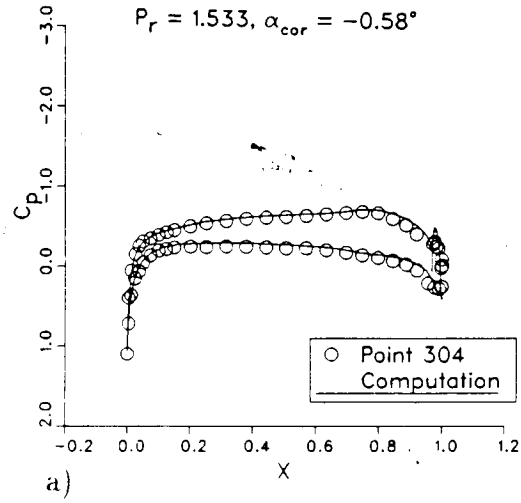

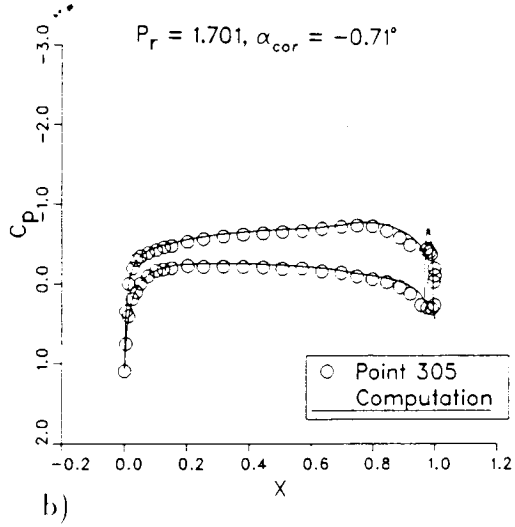

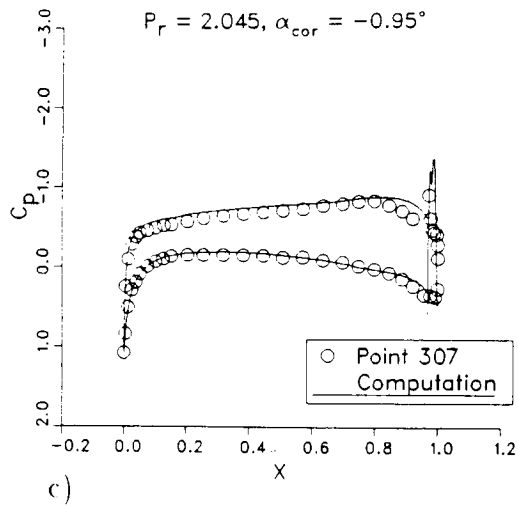

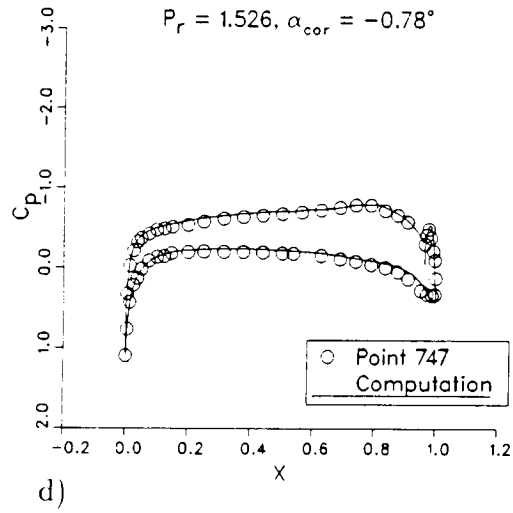

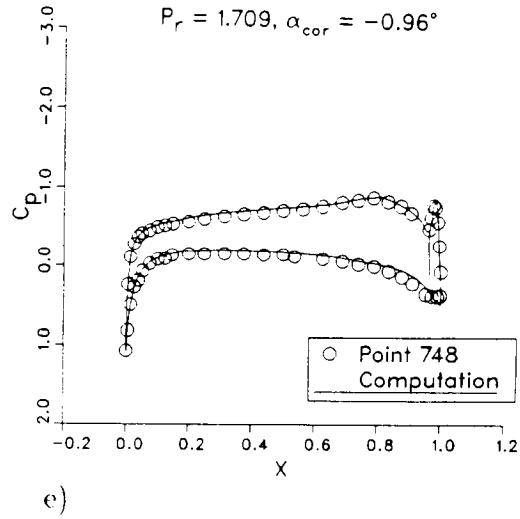

Figure 9. Pressure Distributions For RE Geometry.
M_∞ 0.6, $alpha_{geo}$ 0.0.

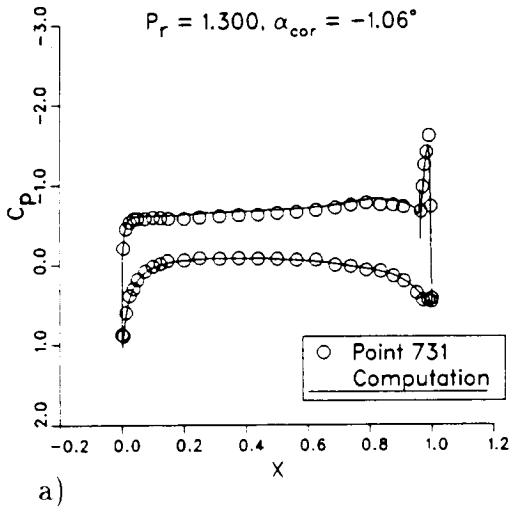

a)

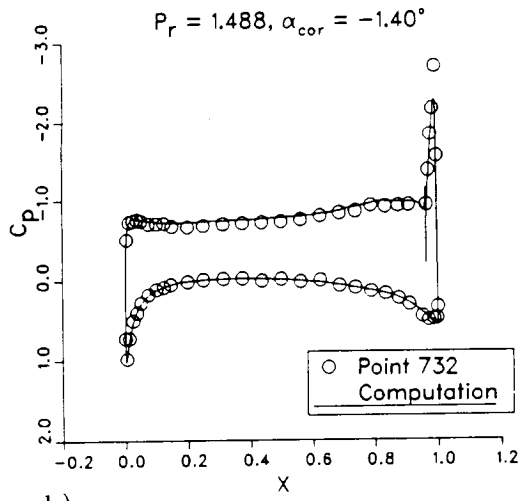

b)

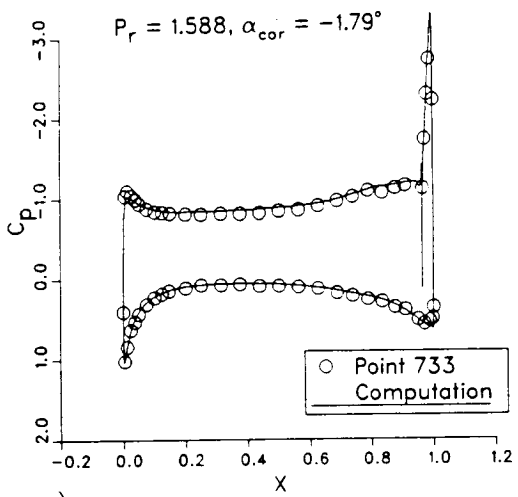

c)

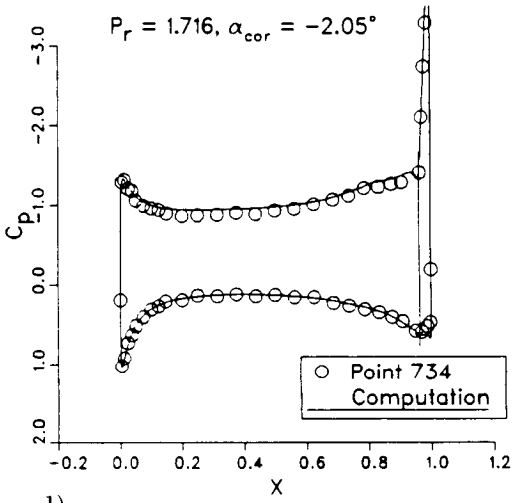

d)

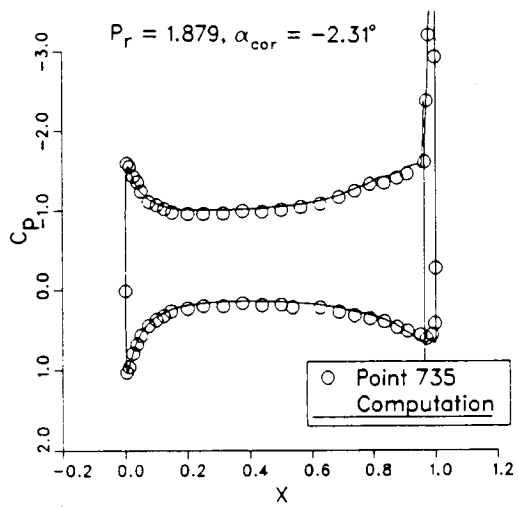

e)

Figure 10. Pressure Distributions For DE Geometry.
M_∞ = 0.3, $alpha_{geo}$ = 0.0.

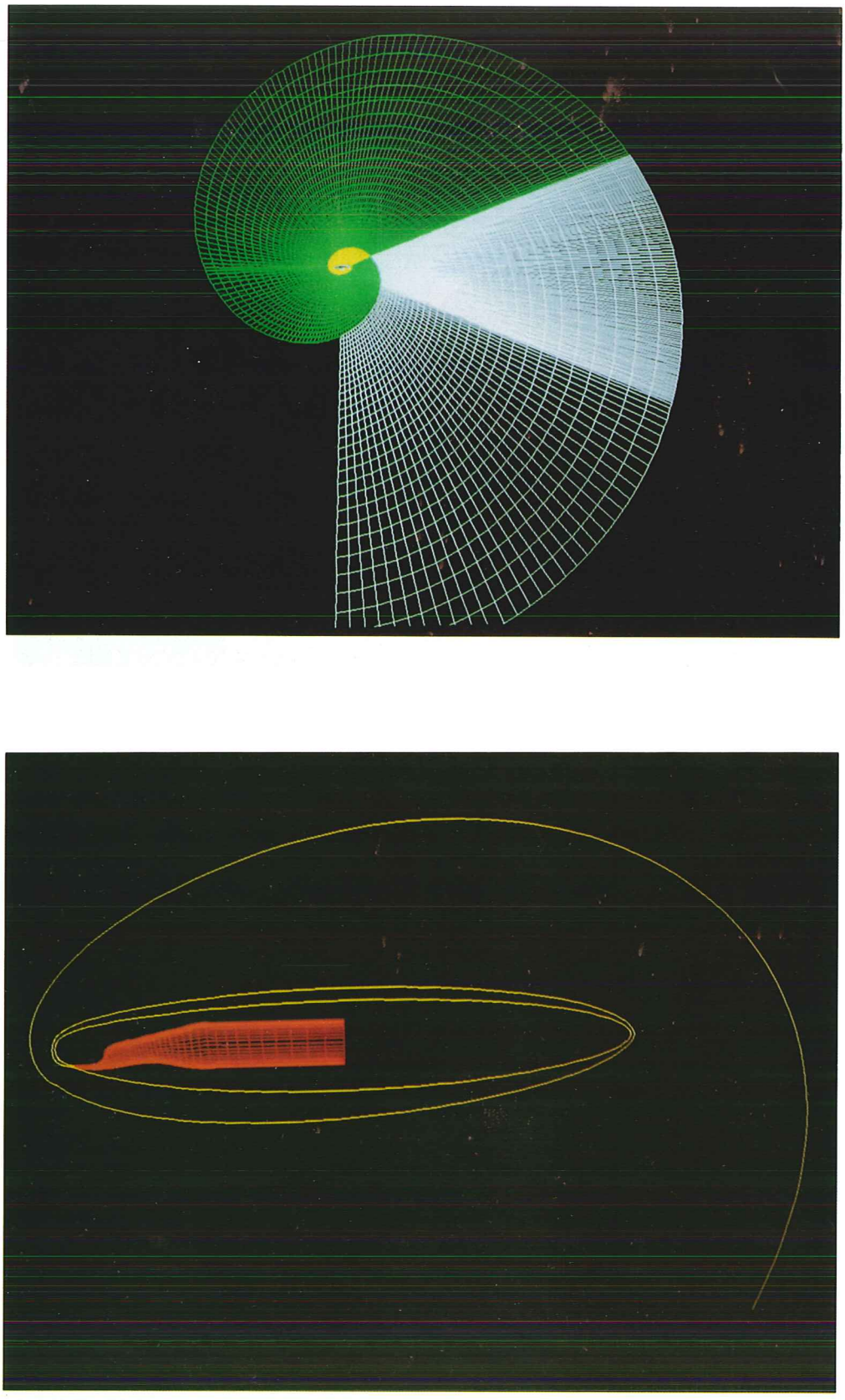

Plate 1. Spiral Grid Topology Used In Computations Showing grid Distributions and Spiral Wrap Boundaries For ξ Orientation.

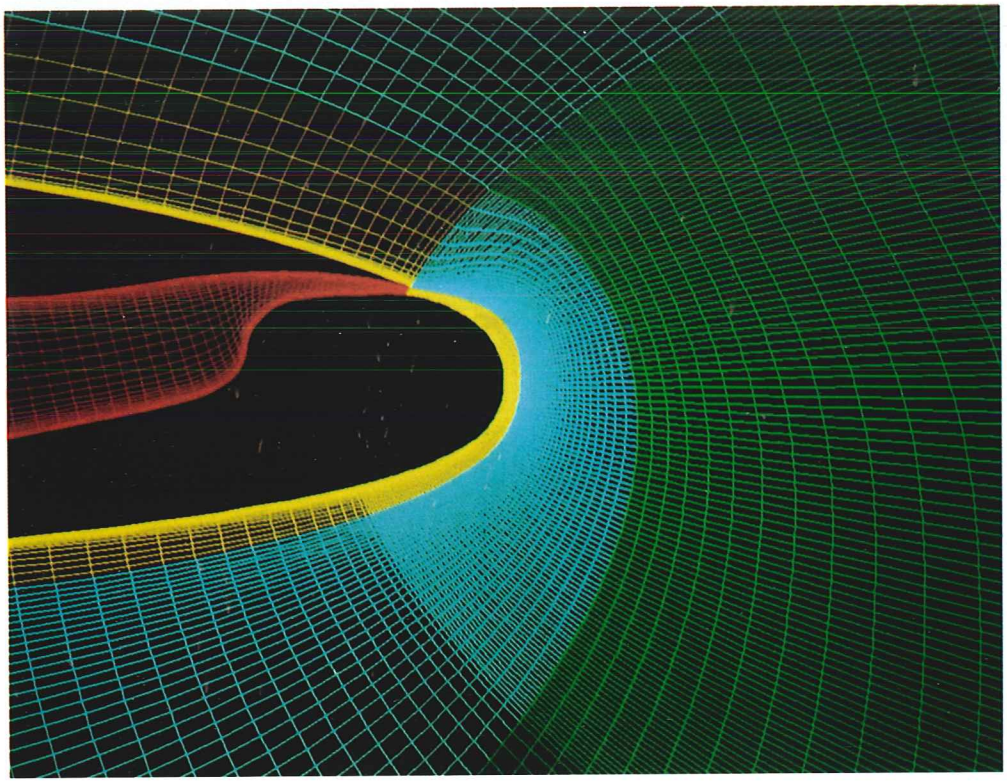

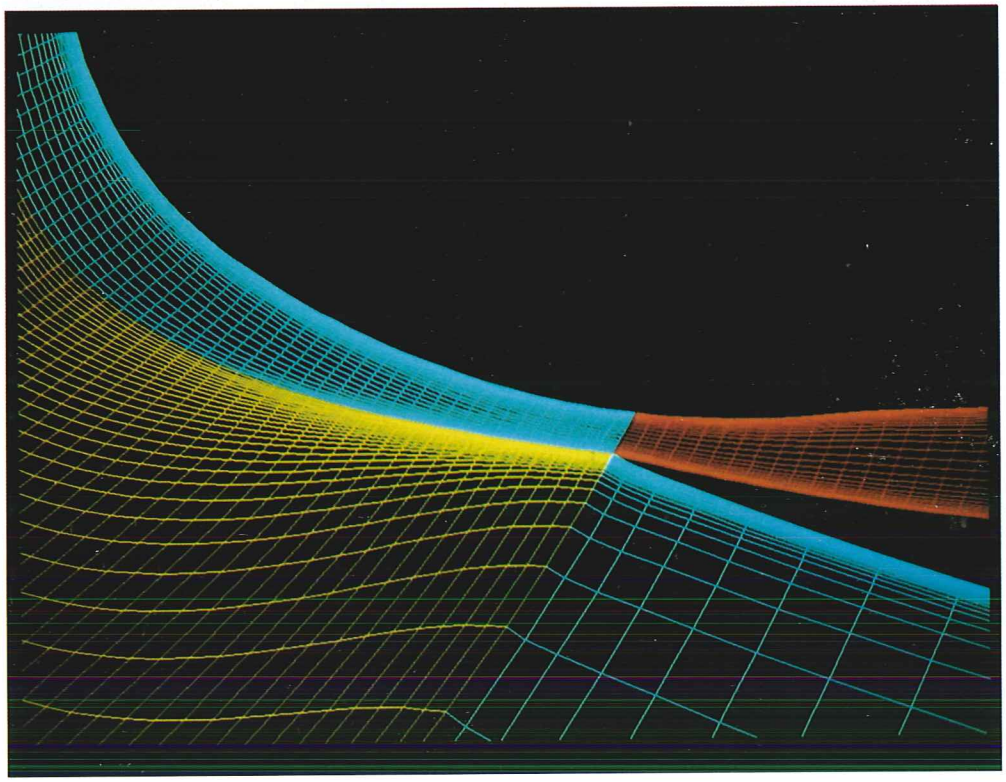

Plate 1. Concluded.

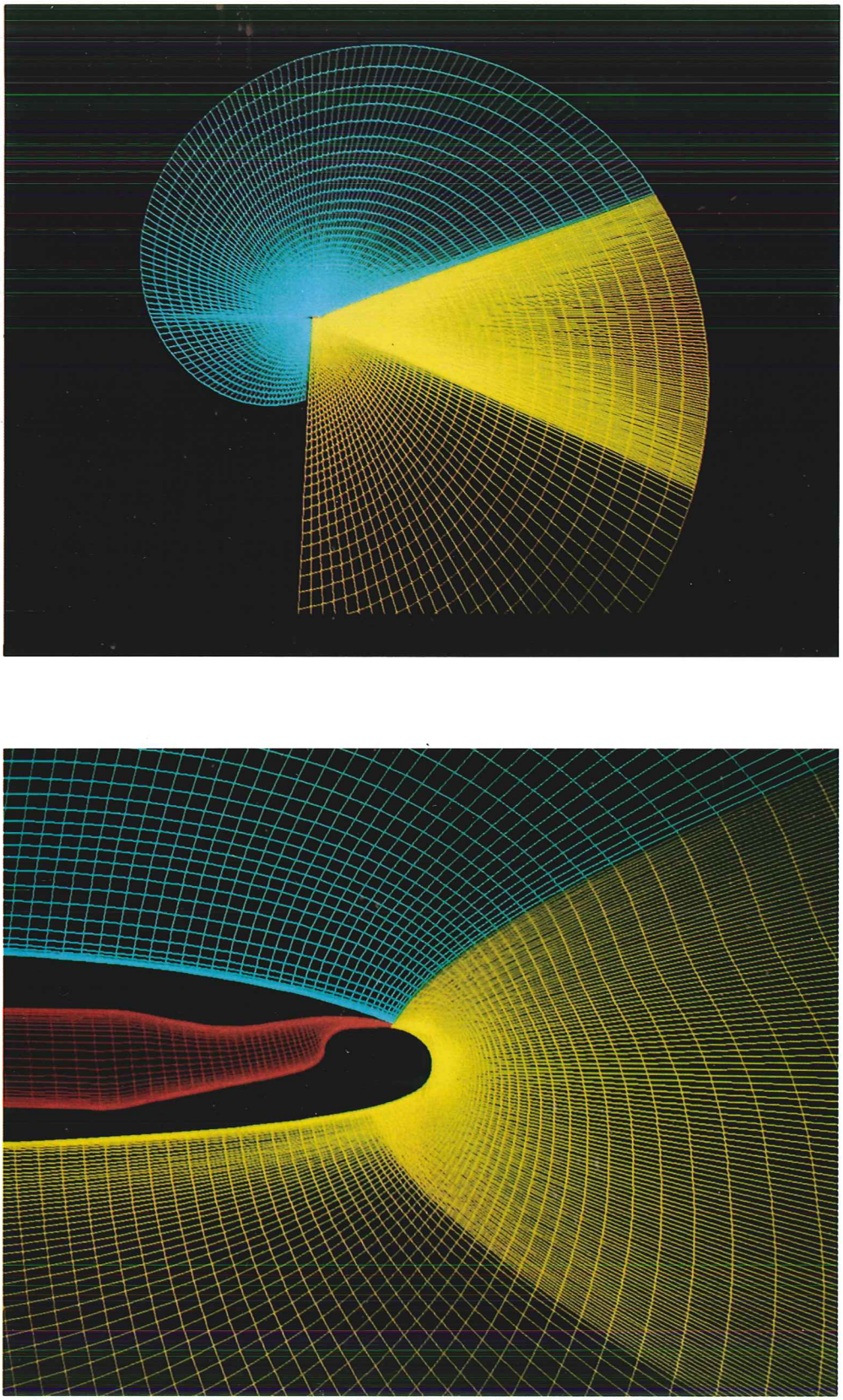

Plate 2. Spiral Grid Topology Used In Computations Showing grid Distributions and Spiral Wrap Boundaries For η Orientation.

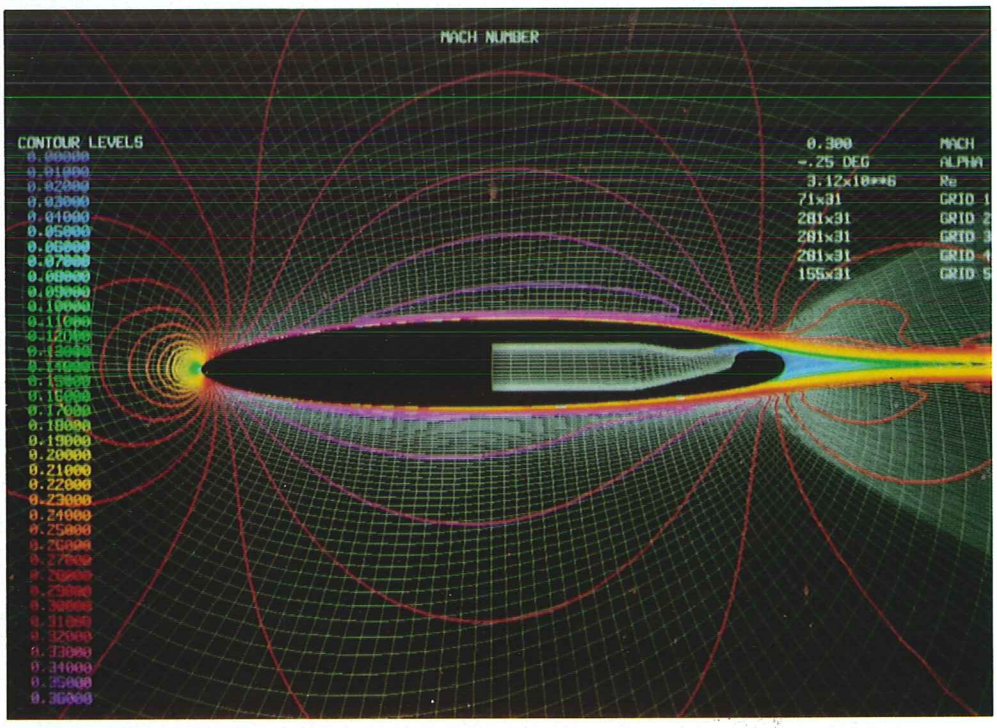

a) Far Field View.

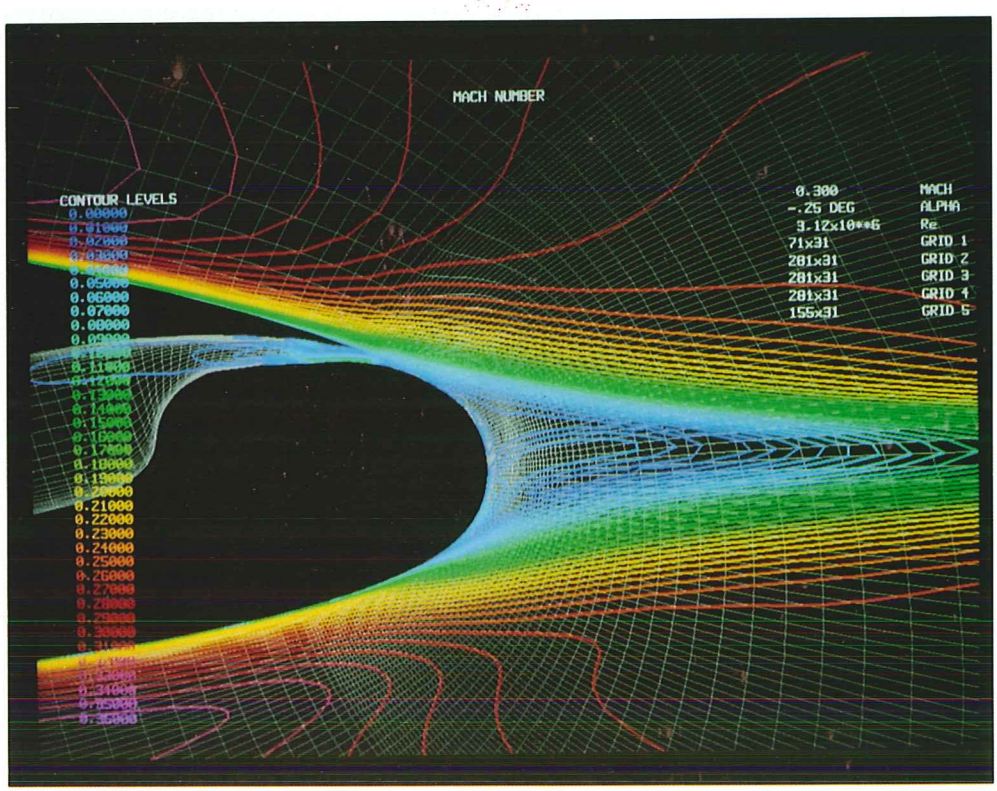

b) Trailing Edge Region.

Plate 3. Color Mach Contours For $M_\infty = 0.3$ RE No Blowing, Point 33.

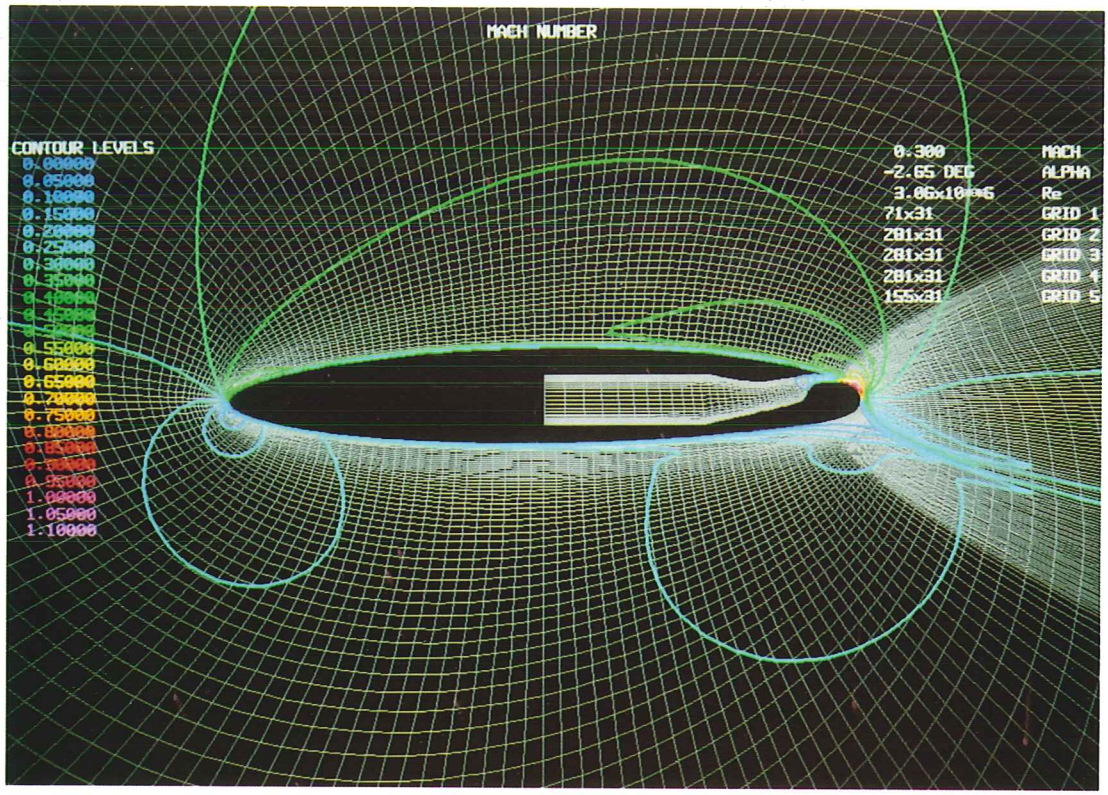

a) Far Field View.

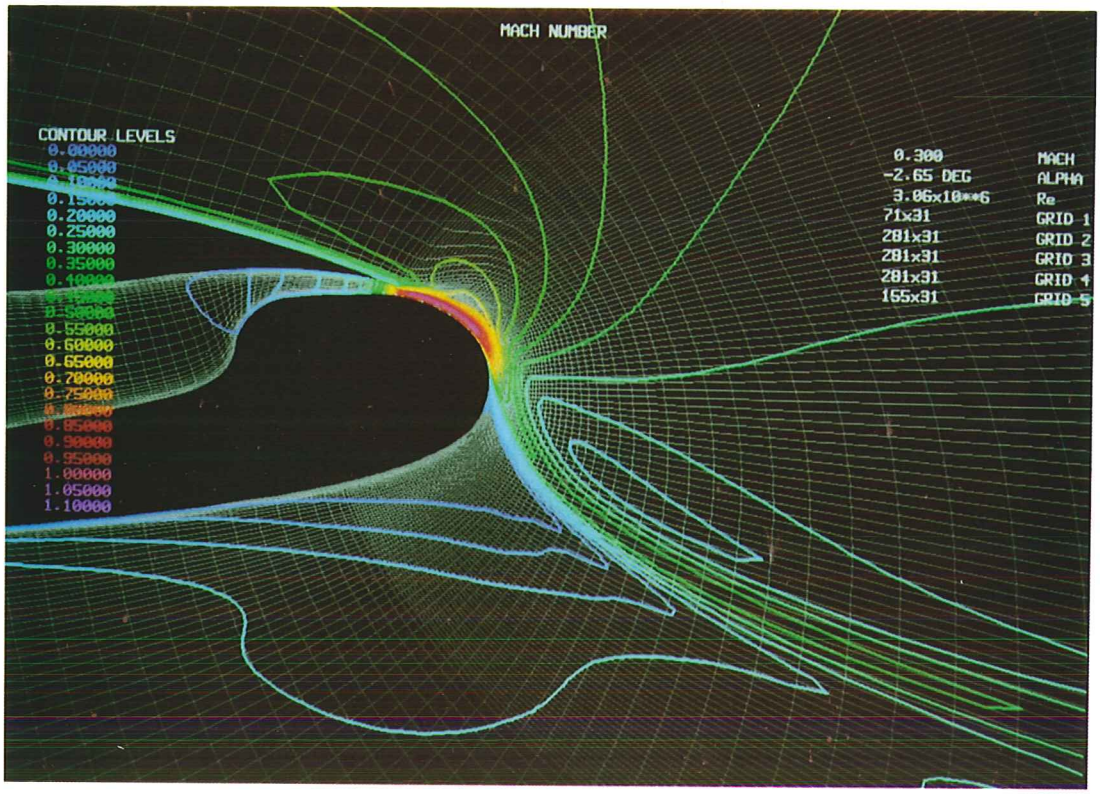

b) Trailing Edge Region.

Plate 4. Color Mach Contours For $M_\infty = 0.3$ RE With Blowing, Point 38.

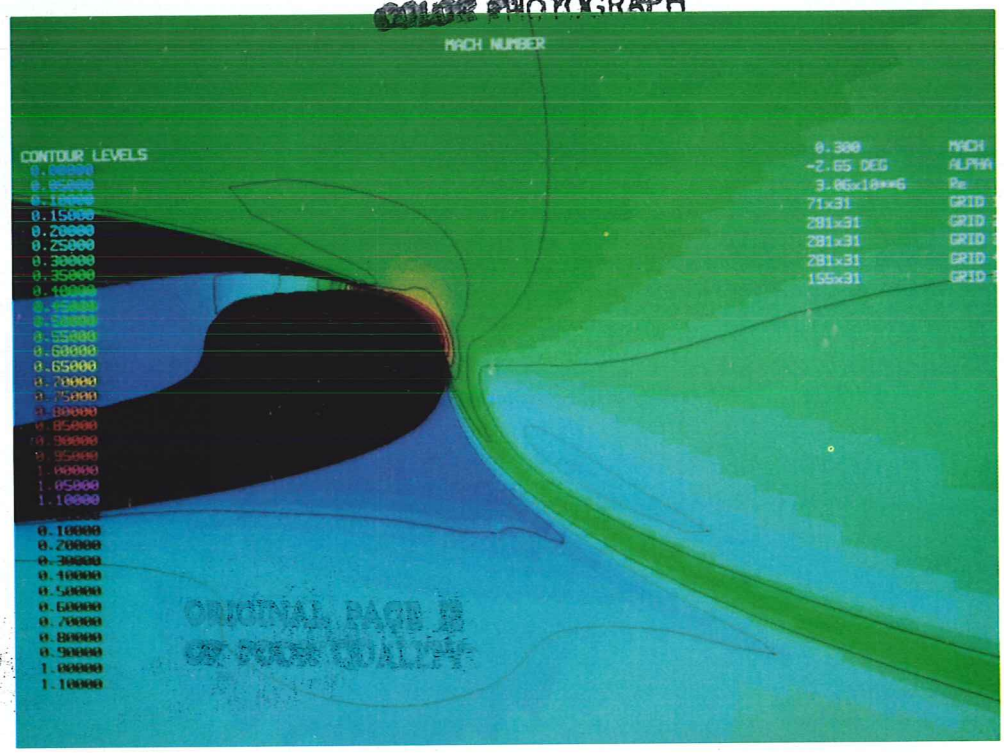

a) Point 38.

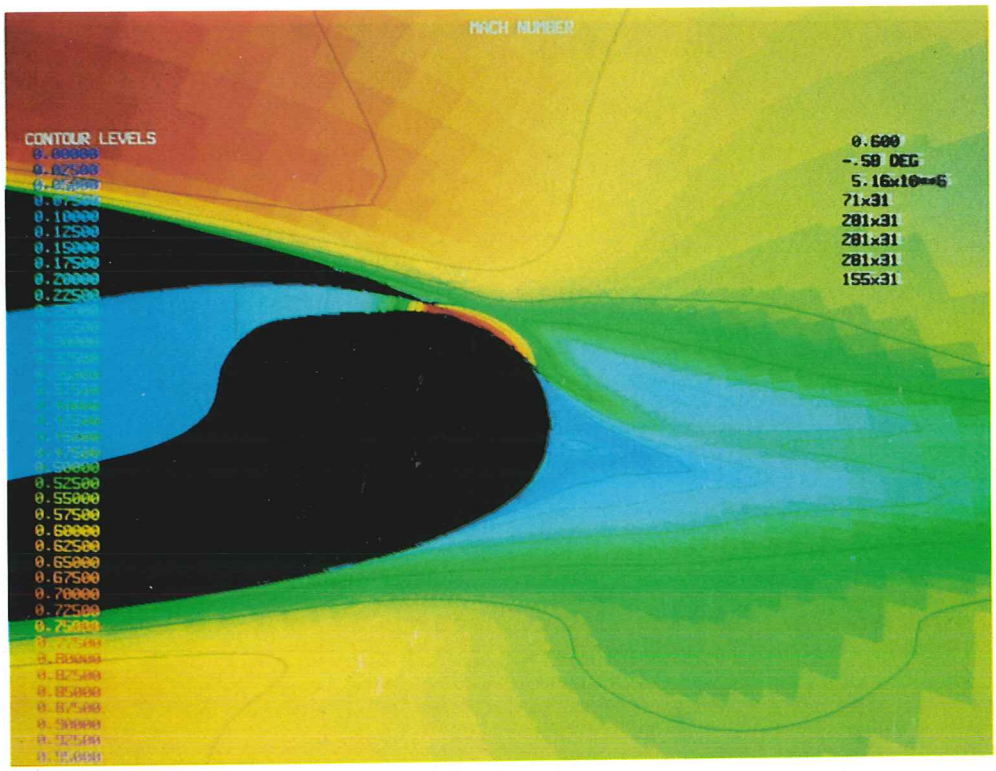

b) Point 304.

Plate 5. Color Mach Contours Showing The Relative Differences In The Flow Structures Due To Mach Number and Coanda Geometry.

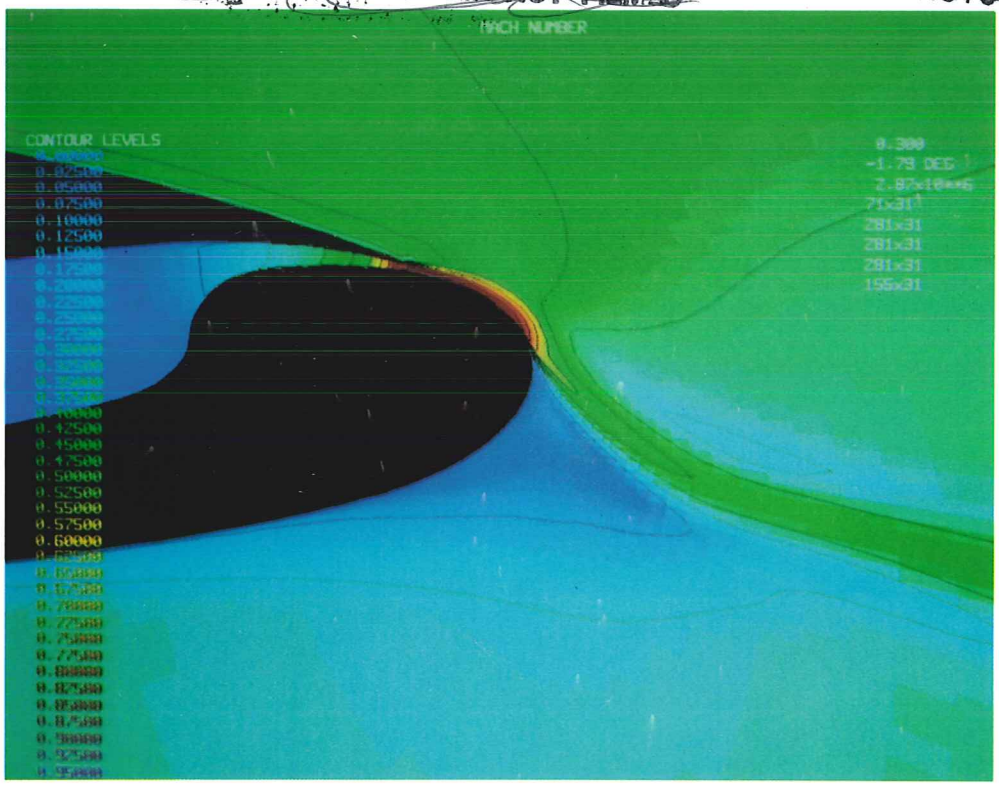

c) Point 733.

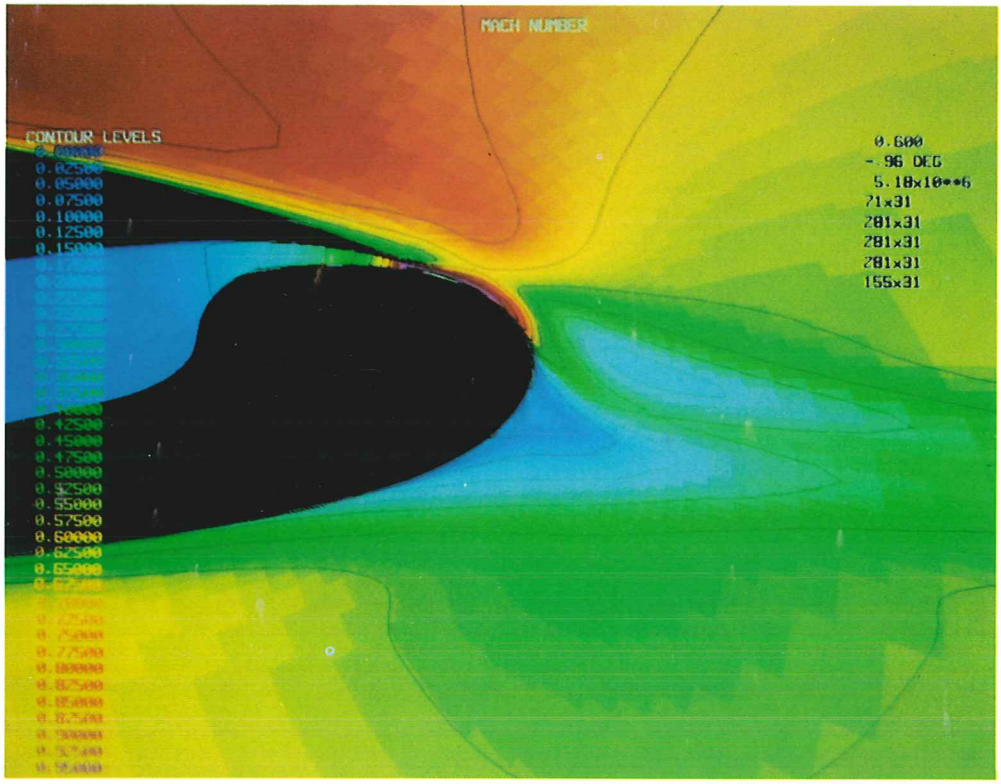

d) Point 748.

Plate 5. Concluded.

WALL JET ANALYSIS FOR CIRCULATION CONTROL AERODYNAMICS

PART II: ZONAL MODELING CONCEPTS FOR WALL JET/POTENTIAL FLOW COUPLING

Frank A. Dvorak
Analytical Methods, Inc.
Redmond, Washington

and

Sanford M. Dash
Science Applications International Corporation
Princeton, New Jersey

SUMMARY

This paper describes work currently in progress to update an existing transonic circulation control airfoil analysis method. Existing methods suffer from two deficiencies: the inability to predict the shock structure of the underexpanded supersonic jets; and the insensitivity of the calculation to small changes in the Coanda surface geometry. A method developed for the analysis of jet exhaust plumes in supersonic flow is being modified for the case of the underexpanded wall jet. In the subsonic case, the same wall jet model has been modified to include the calculation of the normal pressure gradient. This model is currently being coupled with the transonic circulation control airfoil analysis.

1.0 INTRODUCTION

In recent years two global aerodynamic analysis procedures have been developed at Analytical Methods, Inc. for application to circulation control airfoils. These methods, one subsonic and one transonic, perform well in comparison with experiment for low blowing coefficients. At high blowing coefficients, the nozzles operate in a choked condition resulting in an underexpanded supersonic jet. The resulting shock cell structure cannot be predicted by the present analyses. A second limitation of the present programs results from the way in which normal pressure gradient effects are modeled. The semi-empirical approach is not sufficiently sensitive to detect changes in pressure distributions arising from small changes in geometry. With the X-Wing stoppable rotor aircraft in an advanced stage of development, and with other applications of circulation control under consideration, there exists a need for an improved version of the analysis methods. The objective of this paper is to describe the component methods and coupling procedures developed recently, and the progress in incorporating them into the transonic viscous/inviscid circulation control airfoil code.

2.0 BACKGROUND

The flow field about a circulation control airfoil showing the various zones of importance is given in Figure 1. The transonic method, TRACON (1), solves for the flow about a circulation control airfoil using methods and procedures given in Figures 2 and 3.

The flow chart shown in Figure 3 illustrates the general structure of the code. The computation cycle, that is, the calculation of the potential flow, the boundary layer, the wall jet, and the viscid-inviscid interaction is repeated until the proper convergence criteria are met.

Jameson's transonic flow code (2), FLO6, was adopted with some modification for the potential flow calculation. Here, the exterior of an airfoil is mapped onto the interior of a unit circle so that the entire flow field can be solved in a finite domain. The equations are solved for the velocity potential, ϕ, with a guessed initial value of circulation, and the velocity field is obtained by simply differentiating ϕ.

The result is used for the boundary layer calculation after the array is rearranged starting from the forward stagnation point. The boundary layer calculation is initiated by the laminar boundary layer method of Cohen and Reshotko (3), and is continued for turbulent boundary layers using Green's "lag-entrainment" method (4). An improved version of the finite-difference method used previously is employed for the upper surface boundary layer development downstream of the blowing slot for the blowing case.

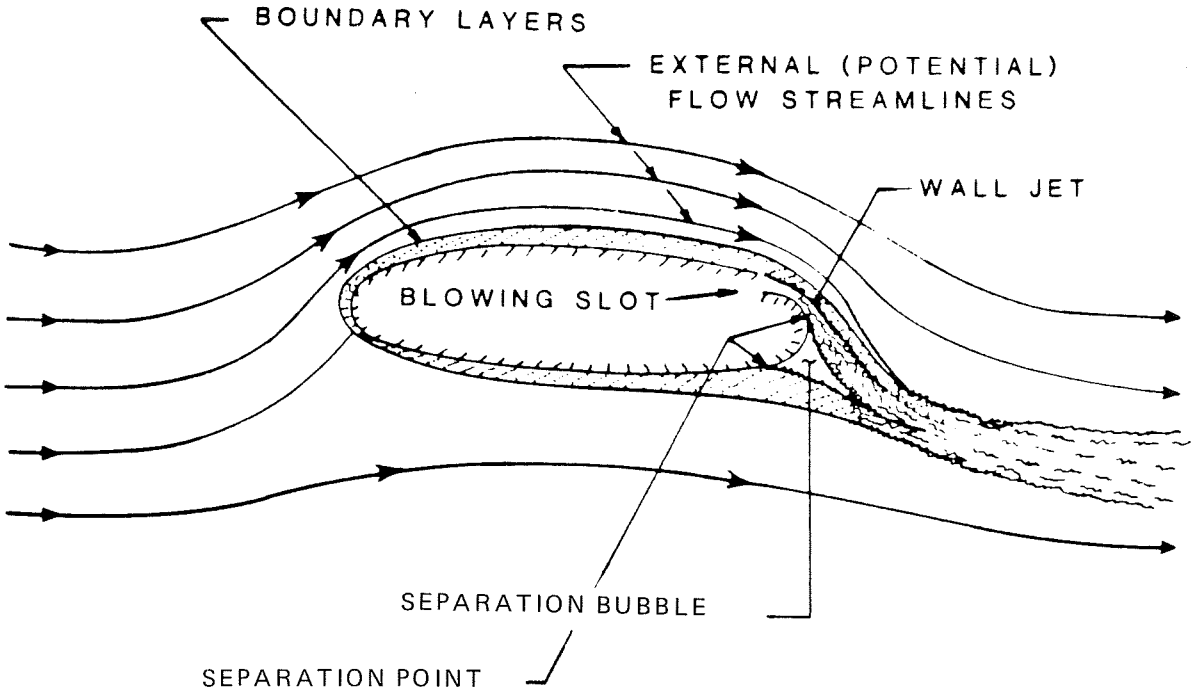

Figure 1. The Flow over a Circulation Controlled Airfoil.

T R A C O N

THEORETICAL APPROACH

- POTENTIAL FLOW
  - JAMESON'S FULL POTENTIAL METHOD
- VISCOUS FLOW
  - WALL JET REGION

    FINITE-DIFFERENCE METHOD USING AN EDDY VISCOSITY MODEL FOR CLOSURE
  - AIRFOIL UPPER SURFACE AHEAD OF SLOT AND ALL OF LOWER SURFACE

    INTEGRAL METHODS

    LAMINAR -- COHEN AND RESHOTKO

    TURBULENT -- GREEN ET AL.

Figure 2. TRACON--Component Analysis Procedures.

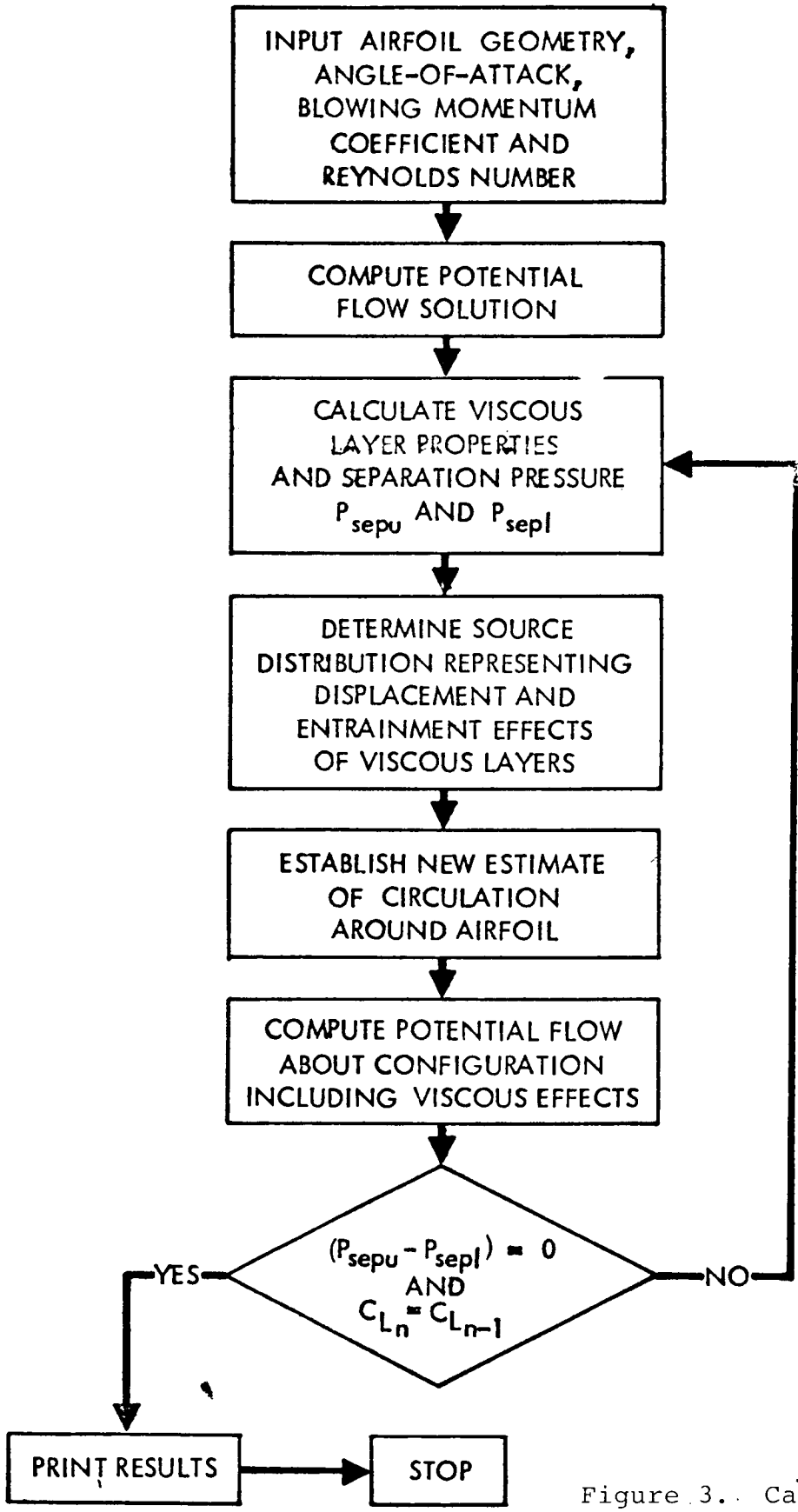

Figure 3. Calculation Procedure.

Having obtained the points of separation and corresponding static pressures for the upper and lower surfaces, a new value of circulation is estimated on the basis of separation pressures and current value of lift. A new potential flow solution can then be computed using this new estimate of circulation with the viscous effect, i.e., velocity component normal to the surface taken into account.

Convergence is checked at this stage. The calculation continues for another cycle unless P_{sepu} and P_{sepl} are in close agreement and the variation of the lift coefficient between successive iterations is in the range of convergence.

As shown in Figures 4 and 5, the basic analysis performed quite well. A relatively high Mach number case (0.6) at an angle of attack of -10° produces a strong shock wave as shown in Figure 4. The analysis accurately predicts the shock location and overall pressure distribution. Similarly in Figure 5 for a low Mach number but with blowing, the analysis again performs well in comparison with experiment. The strengths and weaknesses of TRACON are summarized in Figure 6.

3.0 CURRENT DEVELOPMENTS

The two basic objectives of the current work are as follows. (1) Formulation of the methodology to describe the inviscid flow of an underexpanded wall jet into a co-flowing stream. The method must be able to describe the supersonic flow that results from a nozzle operating choked into a stream having a free-stream Mach number in the range $0.3 \leq M \leq 0.8$. As part of this objective, procedures for coupling the wall jet calculation with the overall circulation control calculation method, TRACON, were considered. (2) Formulation of methodology to determine the effect of the Coanda jet on surface pressures. In this approach, the direct influence of the normal momentum equation is required. As with the first objective, procedures must be developed for coupling the normal pressure gradient calculation with solutions for the streamwise momentum and with the external potential flow (TRACON).

A literature survey indicated that although several researchers have investigated the flow field of supersonic jet plumes, including the underexpanded jet, only one group, from SAIC/Princeton led by Dash and co-workers (5), has considered the underexpanded wall jet. The shock structure of an underexpanded wall jet is physically very similar to that of a jet plume; because of this, Dash and Wolf (6) have recently modified one of their codes for application to curved wall jets. For the viscous model the finite difference, two-layer turbulence model of Dash and Beddini (7) has the required theoretical basis for application to circulation control wall jets. This analysis procedure, called SPLITWJET (hereinafter termed WJET), is completely described in (7) and (8). WJET solves a set of curvilinear, higher-

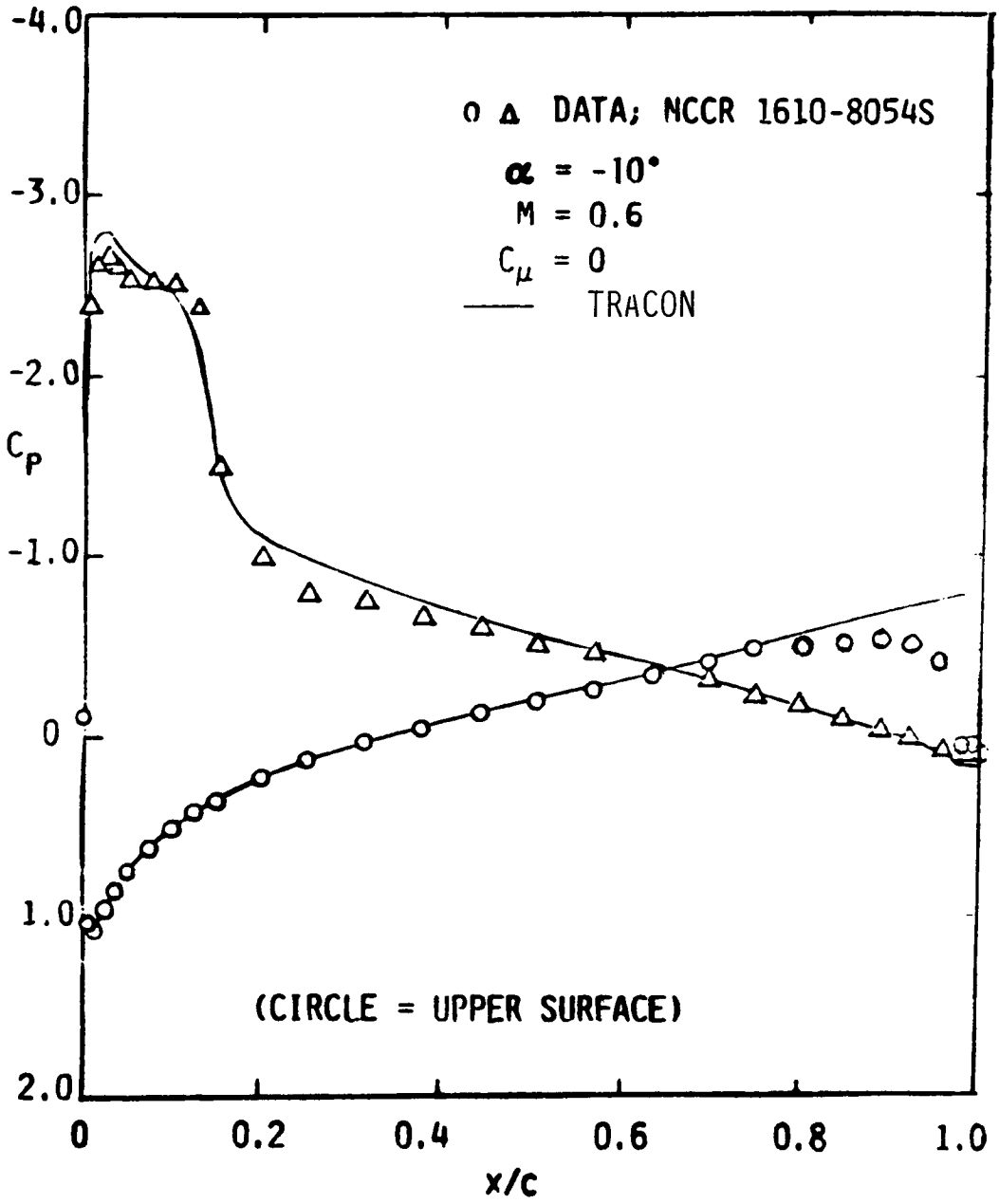

Figure 4. Comparison between Calculated and Measured Pressure Distributions; NCCR 1610-8045S.

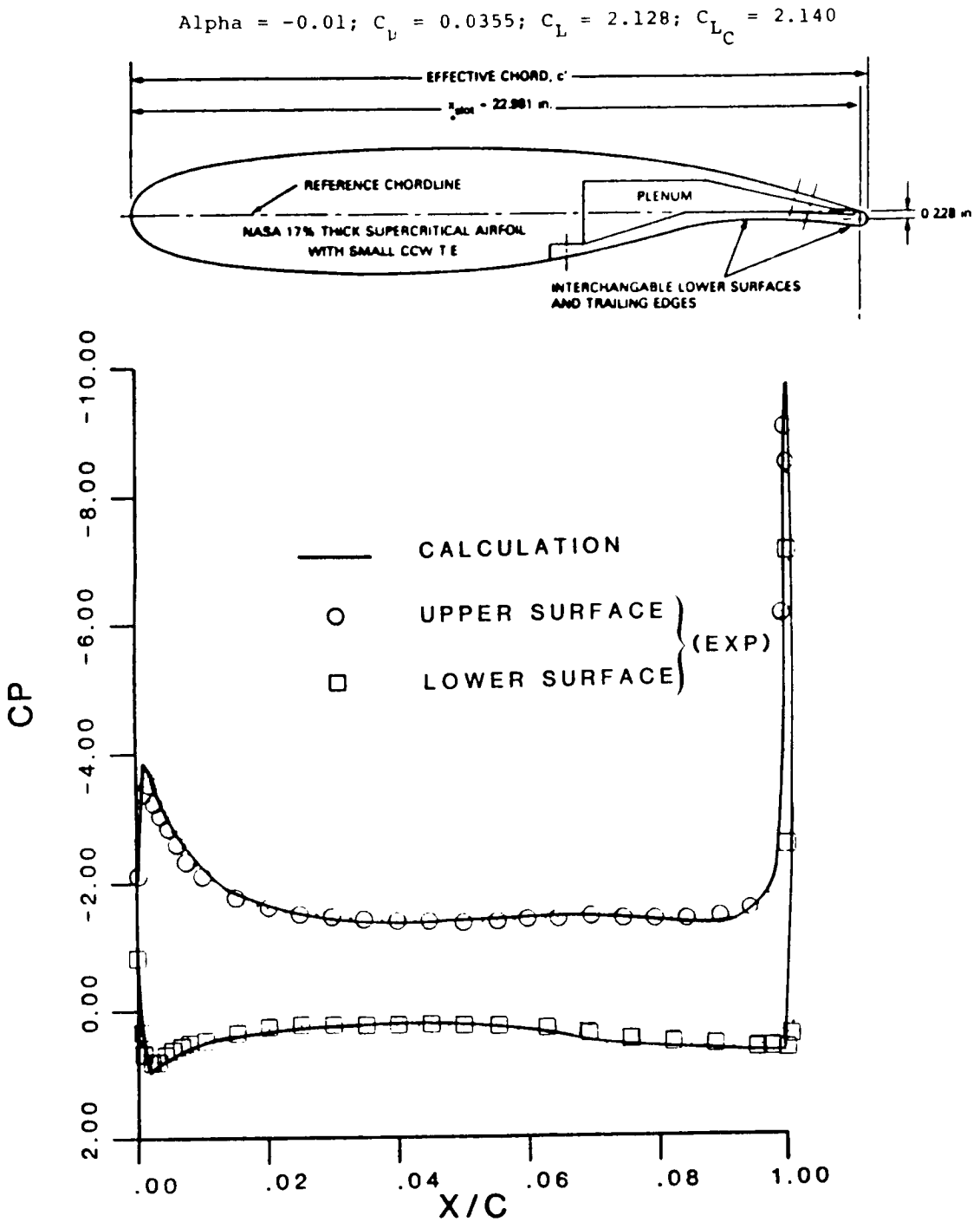

Figure 5. Comparison between Calculated and Measured Pressure Distributions; Supercritical Airfoil.

TRACON

SUMMARY

* ZERO BLOWING -- SHOCK LOCATIONS PREDICTED QUITE ACCURATELY FOR ROUNDED TRAILING-EDGE AIRFOILS

* LOW BLOWING -- PREDICTED PRESSURES AND $C_L - C_\mu$ IN GOOD AGREEMENT WITH EXPERIMENT

* HIGH BLOWING -- PREDICTED BEHAVIOR GOOD AT LOW MACH NUMBERS BUT AT HIGH MACH NUMBERS A MODEL OF THE JET SHOCK STRUCTURE IS NEEDED

* BECAUSE OF EMPIRICAL MODEL TO ACCOUNT FOR COANDA SUCTION, THE EFFECT OF SMALL CHANGES IN GEOMETRY CANNOT BE ACCOUNTED FOR IN A CONSISTENT MANNER

* DISPLACEMENT THICKNESS COUPLING BETWEEN VISCID AND INVISCID FLOWS MAY BE INADEQUATE AT HIGHER MACH NUMBERS

Figure 6. TRACON—Summary of Program Features.

order boundary layer equations employing a mapped surface--normal grid network. A key ingredient of WJET is the inclusion of a hybrid, two-layer turbulence model which couples a damped Van Driest inner mixing layer solution to a two-equation, $k\varepsilon$ outer solution, matching at the grid point corresponding to $y+ \sim 50 (y+ = n\tau_s \frac{1}{2}\rho^{\frac{1}{2}} / \mu_\ell)$, where n is the distance from the surface, τ_s is the wall shear stress, ρ is the density and μ_ℓ is the laminar viscosity. The turbulence model contains curvature corrections based on the work of Launder et al. (9) and Hah and Lakshminarayana (10) which are required to account for the significantly enhanced wall jet mixing rates associated with strong convex curvature. The combined system of mean flow and turbulence model equations are integrated using an efficient upwind fully implicit difference algorithm, and the jet growth is controlled by an ordinary differential equation keyed to the edge vorticity.

The inclusion of normal pressure gradient terms due to curvature in a boundary layer approach has been addressed by Mahgoub and Bradshaw (11). For the wall jet application the following approach has been developed.

1. Matching between the potential flow and the wall jet occurs at the wall jet edge.

2. The pressure variation across the wall jet is solved using the viscous normal momentum equation.

Since the inclusion of the normal momentum equation renders the wall jet equations elliptic, direct spatial marching of the complete set of wall jet equations is ill posed. The remedy involves splitting the pressure field such that:

1. the wall jet equations (<u>not</u> including the normal momentum equation) are solved in a parabolic fashion with the streamwise pressure gradient determined from a globally imposed pressure field, P(s,n); and

2. a revised pressure field, $\bar{P}(s,n)$, is determined in the course of the parabolic wall jet solution using the continuity and normal momentum equations; the revised pressure field is used in local thermodynamic relations and the normal velocity distribution arrived at from the coupled continuity/normal momentum equation solution at each step is used in the convective terms of the parabolic wall jet equations.

This procedure is summarized in Figure 7.

In the subsonic case the strategy for coupling WJET with TRACON (Figure 8) is as follows:

SUBSONIC WALL JET CALCULATION

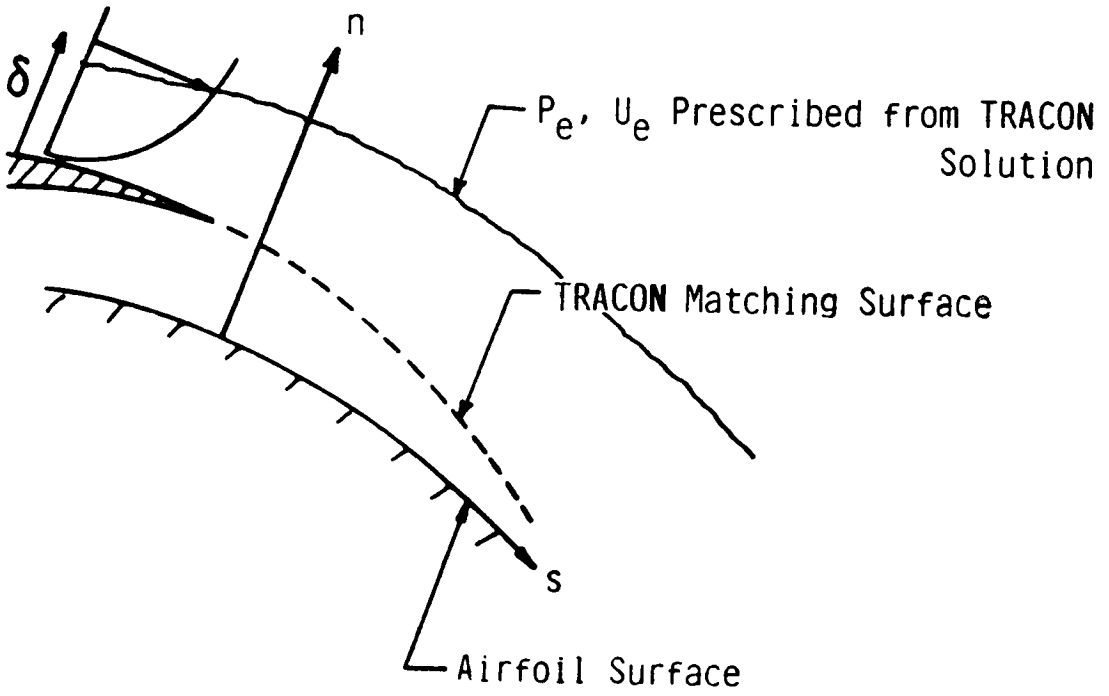

* PARABOLIC SOLUTION WITH $\partial/\partial s\,[P(\xi,\eta)]$ FROM POTENTIAL FLOW SOLUTION

* CROSS-FLOW SOLUTION BEGINNING AT OUTER EDGE OF WALL JET WITH BOUNDARY CONDITIONS FROM TRACON SOLUTION GIVES NEW $P(\xi,\eta)$

* SECOND ITERATION WITH $\partial/\partial s\,[P(\xi,\eta)]$ FROM UPDATED PRESSURE FIELD

Figure 7. Analysis Procedure for Subsonic Wall Jet.

OVERLAP COUPLING FOR A SUBSONIC WALL JET

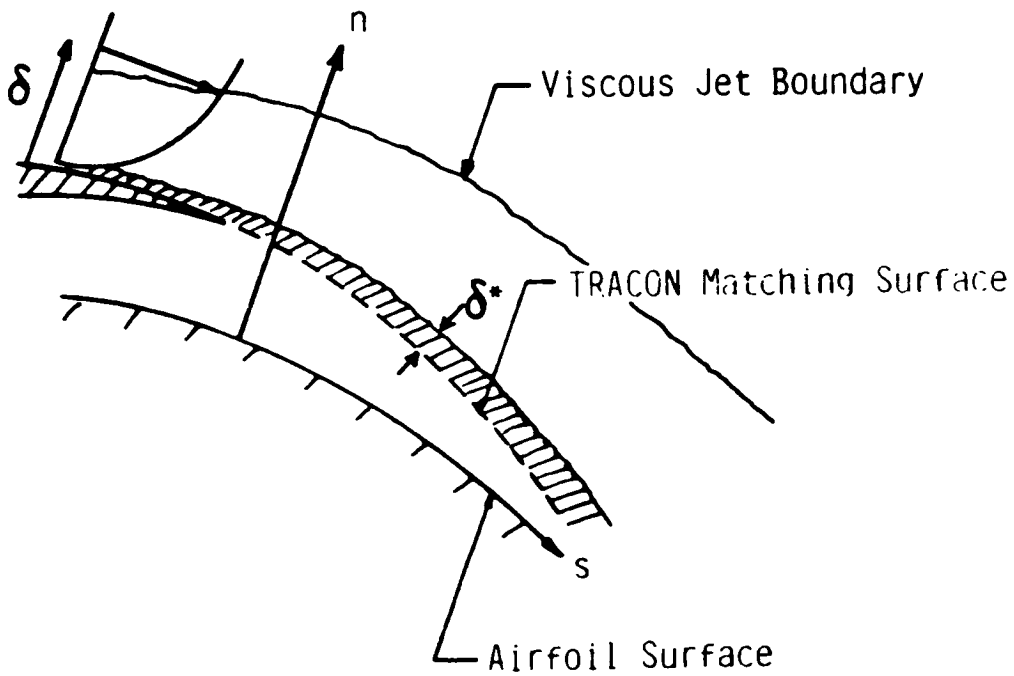

* SOLVE POTENTIAL FLOW OVER TRACON MATCHING SURFACE WITH $\varphi_n(s)$ PRESCRIBED

* SOLVE WALL JET USING PRESSURE SPLIT PNS APPROACH

* DETERMINE $\delta^*(s)$ FOR OVERLAP REGION AND GENERATE $\varphi_n(s)$ FOR NEXT POTENTIAL FLOW SOLUTION

Figure 8. Coupling Procedure for Subsonic Wall Jet.

1. the TRACON potential flow calculation is performed utilizing a trailing-edge geometry which smoothly blends the slot lip to the airfoil trailing edge (this surface is defined as the TRACON matching surface in Figure 8; and

2. the WJET wall jet calculation is performed over the actual airfoil surface (Figure 8).

To interactively couple the two solutions, the WJET calculation requires an inviscid flow map of the TRACON calculation to obtain outer edge conditions and streamwise pressure gradients, while the TRACON calculation requires the stipulation of the source strength distribution, $\phi_n(s)$, along the TRACON matching surface. The definition of the source strength distribution in a flow with large normal pressure variations requires careful derivation of displacement thickness relations. The usual simplifying approximations employed for standard boundary layer problems cannot be employed. To date, the wall jet analysis has been coupled with TRACON and preliminary calculations are being performed to check out the program logic.

In the supersonic (underexpanded wall jet) case a similar strategy has been developed. In recent years considerable research has been carried out on the analysis of supersonic plumes. Dash and co-workers at SAIC/Princeton (12) through (14), and Wilmoth (15) of NASA Langley Research Center have developed shock capturing technology which accurately models the multi-cell embedded shock structure of underexpanded jets. Steger (16) and Diewert (17) of NASA Ames research Center, Birch of Boeing (18), Perry and Forrester (19), Shang of AFWAL (20) and Cline of Los Alamos (21) have all in recent years considered the analysis of supersonic free jets. These analyses have ranged from two-dimensional parabolized Navier-Stokes solvers to full three-dimensional time-dependent codes. The shock wave structure of an underexpanded wall jet is very similar to that of a jet plume, with one exception: the wall jet does not have the extended inviscid core region that characterises underexpanded free jets, and hence, the waves in wall jets would be propagating in a fully turbulent environment several slot heights downstream of the slot exit, see Figure 9. To properly treat this viscous problem, a parabolized Navier-Stokes formulation is required which can be directly coupled with a potential flow solution.

The basic structure for a supersonic wall jet solver already exists in WJET. In order to avoid having two separate codes to analyze subsonic and supersonic wall jets, it is more practical to develop a supersonic pressure solver for WJET. Thus, WJET will be used in its present form to solve the entire wall jet with:

1. pressures in supersonic regions determined by a characteristic based pressure solver;

SUPERSONIC WALL JET CALCULATION

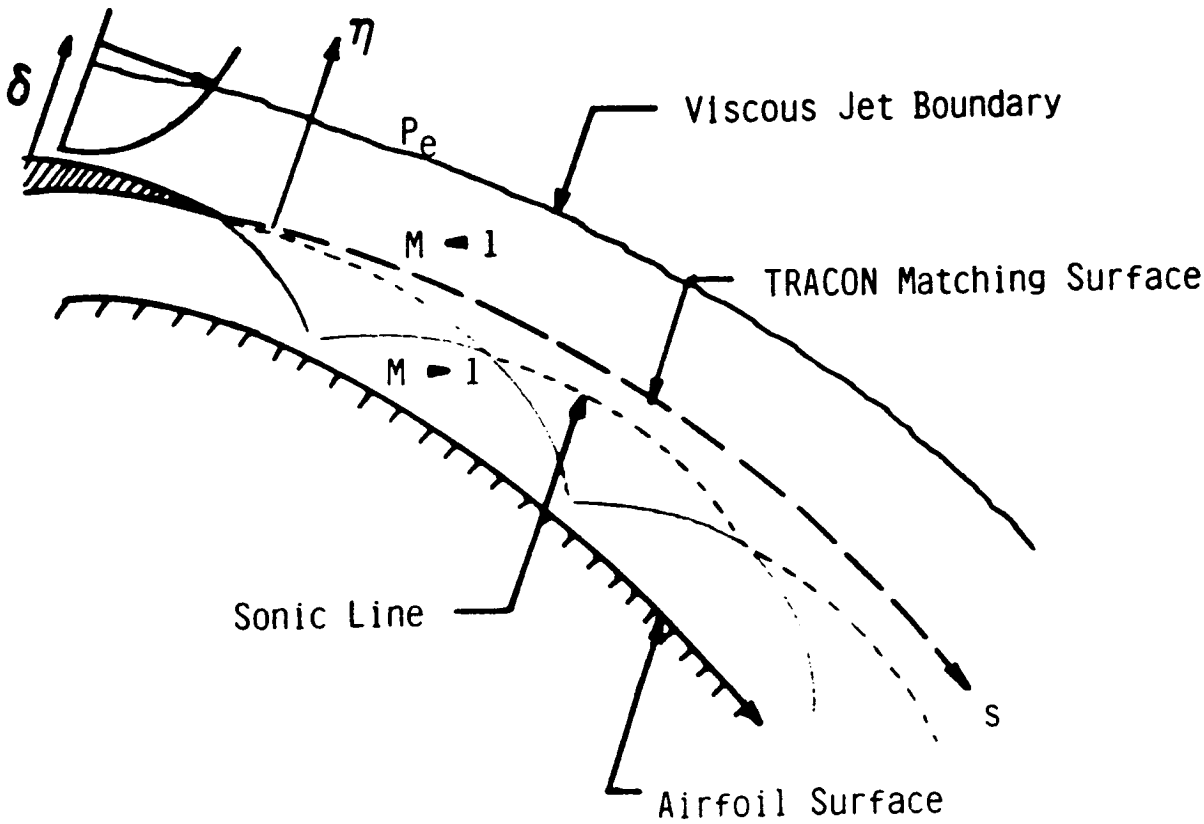

* SUPERSONIC REGION -- PARABOLIC SOLUTION WITH $\partial P/\partial s$ FROM VISCOUS CHARACTERISTIC METHOD (WAVE SOLVER)

* SUBSONIC REGION -- PARABOLIC SOLUTION WITH $\partial P/\partial s$ FROM POTENTIAL FLOW SOLUTION

* SONIC LINE MATCHING AS IN FREE JET APPROACH OF DASH

* CROSS-FLOW SOLUTION IN SUBSONIC REGION WITH BOUNDARY CONDITIONS:

$$V(\eta = 0) = U(\eta = 0) \text{ TAN } \theta_{CHARC.}$$

$$P(\eta = 1) = P_e$$

Figure 9. Analysis Procedure for Underexpanded Supersonic Wall Jet.

2. pressures in subsonic regions split with the streamwise gradient imposed from TRACON and the normal variation determined by solving the continuity and normal momentum equations; and

3. coupling procedures utilized to interface the pressures at the near wall jet and mixing layer sonic lines.

The same overlap procedure described previously will be utilized to couple the wall jet and TRACON potential flow solutions. However, the matching surface cannot be arbitrarily blended from the slot lip to the airfoil surface as if it is for the subsonic case, since it must remain above the jet mixing layer sonic line (Figure 10). The extension of the overlap approach to accommodate this modification is conceptually straightforward, but the details require significant consideration.

4.0 REFERENCES

1. Dvorak, F.A. and Choi, D.H., "Analysis of Circulation-Controlled Airfoils in Transonic Flow", J. Aircraft, Vol. 20, No. 4, April 1983.

2. Jameson, A., "Numerical Computation of Transonic Flows with Shock Waves", International Union of Theoretical and Applied Mechanics, Springer-Verlag, New York, Inc., September 1975, pp. 384-414.

3. Brune, G.W. and Manke, J.W., "An Improved Version of the NASA Lockheed Multi-Element Airfoil Analysis Computer Program", NASA CR-154323, March 1978, pp. 69-87.

4. Green, J.E., Weeks, D.J. and Brooman, J.W.F., "Prediction of Turbulent Boundary Layers and Wakes in Compresible Flow by a Lag-Entrainment Method", Royal Aircraft Establishment TR-72231, December 1972.

5. Dash, S.M. and Sinha, N., "Noniterative Cross-Flow Integration Procedure for the Pressure-Split Analysis of Two-Dimensional, Subsonic Mixing Layer Problems", To be Published in the AIAA Journal.

6. Dash, S.M., Beddini, R.A., Wolf, D.E. and Sinha, N., "Viscous/Inviscid Analysis of Curved Sub- or Supersonic Wall Jets", AIAA Paper No. 83-1679, Danvers, MA, July 1983.

7. Dash, S.M. and Beddini, R.A., "Viscous/Inviscid Analysis of Curved Wall Jets: Part 2, Viscous Pressure-Split Model (SPLITWJET)", Science Applications, Inc., Princeton, N.J., TR-7, November 1982.

8. Dash, S.M. and Sinha, N., "Pressure-Split Extensions of SPLITWJET Model for Wall Jet/Potential Flow Coupling",

OVERLAP COUPLING FOR A SUPERSONIC WALL JET

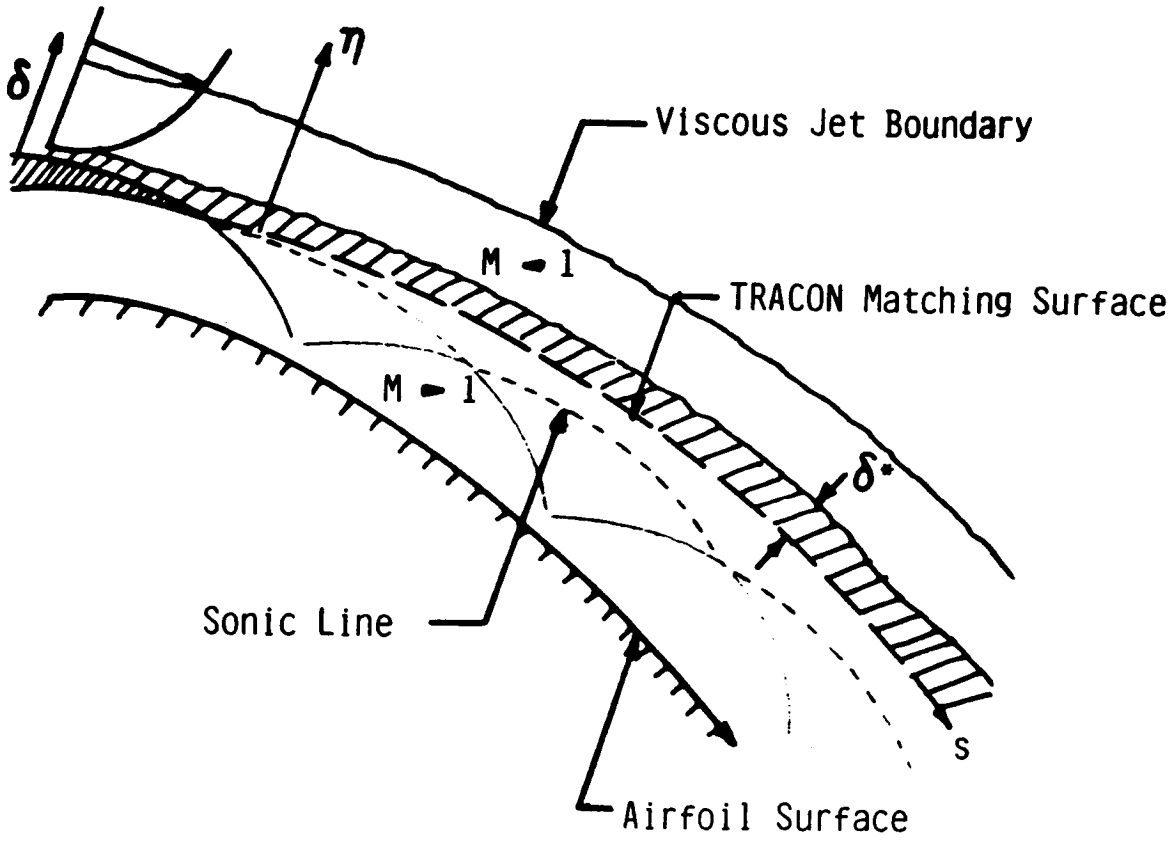

* MATCHING SURFACE CONFIGURED TO RESIDE ABOVE SONIC LINE

* POTENTIAL FLOW OVERLAP INCLUDES ONLY SUBSONIC REGION OF JET

* P(s) -- SUPERSONIC ($\eta \rightarrow 0$) -- WAKE SOLVER
  -- SUBSONIC ($\eta \rightarrow 0$) -- PRESSURE SPLIT

* $\delta^*(s)$ DETERMINED FOR SUBSONIC PORTION OF JET -- INCLUDES INFLUENCE OF JET UNDEREXPANSION

Figure 10. Coupling Procedure for Underexpanded Supersonic Wall Jet.

Science Applications, Inc., Princeton, N.J., TR-17, February 1984.

9. Launder, B.E., Priddin, C.H. and Sharma, B.I., "The Calculation of Turbulent Boundary Layers on Spinning and Curved Surfaces", ASME J. Fluids Engr., March 1977, pp. 231-239.

10. Hah, C. and Lakshminarayana, B., "Prediction of Two- and Three-Dimensional Asymmetrical Turbulent Wakes, Including Curvature and Rotation Effects", AIAA J., October 1980, pp. 1196-1204.

11. Mahgoub, H.E.H. and Bradshaw, P., "Calculation of Turbulent-Inviscid Flow Interactions with Large Normal Pressure Gradients", AIAA J., October 1979, pp. 1025-1029.

12. Dash, S.M. and Pergament, H.S., "A Computational Model for the Prediction of Jet Entrainment in the Vicinity of Nozzle Boattails (The BOAT Code)", NASA CR-3075, December 1978.

13. Dash, S.M., Pergament, H.S. and Thorpe, R.D., "Computational Models for the Viscous/Inviscid Analysis of Jet Aircraft Plumes", NASA CR-3289, May 1980.

14. Dash, S.M. and Thorpe, R.D., "Shock-Capturing Model for One- and Two-Phase Supersonic Exhaust Flow", AIAA J., Vol. 19, No. 7, July 1981.

15. Wilmoth, R.G., "RAXJET: A Computer Program for Predicting Transonic Axisymmetric Flow over Nozzle Afterbodies with Supersonic Jet Exhausts", NASA TM-83235, February 1982.

16. Steger, J.L., "Numerical Simulation of Steady Supersonic Viscous Flow", AIAA J., Vol. 18, No. 12, December 1980.

17. Diewert, G.S., "Numerical Simulation of Three-Dimensional Boattail Afterbody Flows", AIAA Paper No. 80-1347, July 1980.

18. Birch, S.F., Kern, P.R. and Cornette, W.J., "Numerical Modeling of Three-Dimensional Turbulent Exhaust Streams", Final Report, Navy Contract N700530-81-0159, 1982.

19. Perry, K.M. and Forrester, C.K., "Numerical Solution of Navier-Stokes Equations for a Three-Dimensional Cover", AIAA J., Vol. 1, No. 11, November 1977.

20. Shang, J.S. and Haney, W.L., "Numerical Solution of Navier-Stokes Equations for a Three-Dimensional Cover", AIAA J., Vol. 1, No. 11, November 1977.

21. Cline, M.C., "VNAP2: A Computer Program for Computation of Two-Dimensional, Time-Dependent Compressible Turbulent Flow", Report LA8872, Los Alamos National Laboratory, August 1981.

THE FURTHER DEVELOPMENT OF CIRCULATION CONTROL AIRFOILS

N. J. Wood
Stanford University

INTRODUCTION

During the last decade a significant amount of information has been obtained from wind tunnel tests, full scale experiments and numerical analysis regarding the factors which affect the performance of circulation control airfoils. The design of the present family of airfoils being applied to stopped rotor vehicles is predominantly a legacy of the early experiments where elliptic sections were used to facilitate the transformation for inviscid pressure distribution calculations. Whilst elliptic sections have many interesting mathematical properties it remains to be shown whether they are aerodynamically the optimum shape for circulation control. It is important to recognize that aerodynamic efficiency should take precedence over design simplicity in this instance.

The recent paper by Wood and Nielsen[1985] has summarised the global performance characteristics of two-dimensional circulation control airfoils including the effects of Reynolds number, Mach number, angle of attack, etc.. This improved understanding, coupled with the observations of some less successful experiments, should permit the isolation of design guidelines to satisfy the requirement for improved airfoil performance. Perhaps the most notable reason for the lack of second generation airfoils is the absence of a reliable analytical code which would allow the effects of variations in geometry to be examined. Apparently, the development of the analytical procedures is progressing to a point where the timing is appropriate to begin a more thorough examination of the design concepts of circulation control airfoils.

This paper will review the performance trends of circulation control airfoils and make observations as to where improvements in performance and expansion of the flight envelope may be feasible. A new analytically defined family of airfoils will be suggested, all of which maintain the fore and aft symmetry required for stopped rotor application. It is important to recognize that any improvements in section capabilities may not be totally applicable to the present vehicle operation. It remains for the designers of the rotor system to reappraise the three-dimensional operating environment in view of the different airfoil operating characteristics and for the airfoil definitions to be flexible while maintaining satisfactory levels of performance.

PERFORMANCE REVIEW

Figure 1 illustrates the performance trends of a typical circulation control airfoil for a fixed free stream Mach number. With regard to a discussion of future developments, it is of interest to observe the limitations to performance with respect to the lift coefficient. The most obvious of these limitations is of course the stall points, both alpha stall and jet stall. The alpha stall has been identified as a consequence of small separation bubbles at the leading edge of the airfoil which result from the ever increasing pressure gradients imposed by the increasing circulation. For thin airfoils, this phenomenon may occur at negative angles of attack. The jet stall remains an unidentified phenomenon although some correlation with the occurrence of C_p^* has been previously observed. The precursor to the alpha stall is a progressively reducing lift augmentation with increasing angle of attack, resulting from the increasing boundary layer thickness approaching the slot. Indeed, the thickness of the boundary layer approaching the slot has been identified as the prime factor in most performance effects, Mach number, Reynolds number and the effects of airfoil thickness and camber. The effect of increasing Mach number on lift generation is shown as figure 2 for a typical airfoil in the absence of leading edge separation. A further reduction in lift augmentation is observed if shocks exist on the upper surface of the airfoil. This again corresponds to the increased boundary layer thickness which results from the shock/boundary layer interaction. Experiments have also indicated two further performance limitations exhibited by thick, highly cambered airfoils and by airfoils with curvature discontinuities on the Coanda surface. For the first case, the boundary layer prematurely detaches from the upper surface just ahead of the slot causing a massive reduction in lift augmentation. The situation may in some cases be overcome by sufficiently high blowing momentum. For the second case, a feature labelled 'premature jet detachment' was observed. This phenomenon exhibits usual lift augmentation up to a point, whereupon the lift coefficient attains a constant value independent of increasing blowing momentum. The jet has separated from the Coanda surface at the point of discontinuity and is now acting like a jet flap. Figure 3 illustrates the characteristics of these two phenomena.

This raises two highly important, although seldom recognised, performance limitations. First the ability to simply modify a current airfoil to obtain a different slot location. Second, the discontinuities in surface curvature which result from the present techniques for Coanda surface definition and the blending of those surfaces into the elliptic profile.

AREAS FOR AIRFOIL MODIFICATION

It has become apparent that there are two mechanisms whereby the characteristics of circulation control airfoils may be improved. First, the geometrical definition of the airfoils could be modified such that arbitrary slot locations may be chosen and that all surfaces would have smooth and continuous second derivatives. This would certainly allow a more thorough appraisal of such important parameters as slot location, assuming of course that a reliable code becomes available or some controlled experiments are

performed. Second, the basic form of the airfoils' thickness distribution should be modified in order to delay the growth or separation of the upper surface boundary layer. In this way, airfoils could be designed to avoid or delay alpha stall, Mach number effects and even may be able to successfully include high degrees of camber at high speeds. The assumption is that modification of the thickness distribution may delay the occurrence of these performance limiting effects. Thus the primary objectives for this research are twofold:

1. To simplify and improve the geometrical definition of circulation control airfoils.

2. To delay the thickening of the upper surface boundary layer by modification of the thickness distribution of the airfoil.

This should yield airfoils which exhibit linear performance characteristics over a wider performance envelope.

The simplest mechanism to improve the overall performance of circulation control airfoils would, of course, be to improve the attainable lift augmentation level. Unfortunately, this parameter appears to be closely linked to the Coanda geometry, the slot height and the slot position in such a manner that precludes a simple redefinition. The present work will be confined to observing that the Coanda surface be smooth and free of discontinuities and that the radii of curvature be of similar magnitude to the present configurations.. It is expected that further improvements in performance be achieved by the optimization of the Coanda geometry alone, a task for the new analytical codes.

Two areas where benefits of a new design procedure may be accrued are the tip and root sections for stopped rotor application. Thick, non-elliptic sections may be designed specifically to fair over the large blade attachment points while maintaining satisfactory lift and drag characteristics. At the tip, drag rise might be relieved by the use of quasi-supercritical circulation control sections and the balancing of rolling moments to remove the need for collective pitch may be possible by the incorporation of different blade camber distributions. Those distributions made possible by the freedom of the new airfoil design scheme.

A NEW GEOMETRIC DEFINITION

It is desirable to define the airfoil coordinates numerically such that perturbations of the shape may be simply evaluated. A formulation was chosen that maintained the second derivative smooth and continuous at all points on the surface. The basic planform was defined as a function of the leading/trailing edge radius R, the airfoil mid-chord thickness T, and the degree of mid-chord camber S. To provide further flexibility on the definition of the camber line, two eccentricity parameters are defined, one for the upper surface, E_1, one for the lower surface, E_2. These provide the capability for accurate contouring of the local surface curvature such that fine control of

the pressure distribution and smoothing of the pressure peaks is available. The requirement for fore and aft symmetry is observed by establishing that the slope be zero at the mid-chord and that the curvature be continuous. The final form of the surface definition is:

$$y_{upper} = R.F(x) + (T/2 + S).G(X) + E_1.H(x) \quad [1]$$

$$y_{lower} = -R.F(x) - (T/2 - S).G(x) - E_2.H(x)$$

where F(x), G(x) and H(x) are functions of the chordwise coordinate.

It must be clearly stated that no attempt is being made to define optimized or improved Coanda profiles by the proposed functions. The fact that these profiles are smooth in the second derivative suggests that they should operate at least as efficiently as other previously tested shapes.

The eccentricities E_1 and E_2 are extremely powerful tools in the development of new airfoil contours. They can be used to control the shape of the camber line and as such can permit higher degrees of mid-chord camber before the onset of severe adverse pressure gradients in the region ahead of the slot. In essence, they may be used to spread the load over more of the airfoil chord and can be used to dissipate highly loaded areas. Some examples of the airfoils shapes that can be defined are shown in figure 4. Note that sections bearing a strong similarity to ellipses may be produced by the new geometric definition. Therefore any advantages of those sections may still be available to the new definitions.

The definition of the internal geometry and the placement of the slot exit is extremely simple with the new airfoil definition. Referring to figure 5, one must simply define the slot location x_s, the slot height h, and the slot lip thickness ℓ, At a second chordwise location x_1, the plenum height p, and the skin thickness δ are also defined to provide a solution for the geometric equations. If the lower surface geometry is maintained then a smooth blend of the internal surfaces occurs at the trailing edge point. The prescribed slot location gives $F(x_s)$,$G(x_s)$ and $H(x_s)$ which will be annotated as F_s, G_s and H_s. Similarly for F_1, G_1 and H_1. Assume that we need perturbations of the thickness, camber and upper surface eccentricities T', S' and E_1', and also note that to maintain the lower surface

$$(T/2 - S) = (T'/2 - S') \quad [2]$$

Let

$$\delta S = S - S' \quad [3]$$

$$\delta T = T - T'$$

$$\delta E_1 = E_1 - E_1'$$

The surface equations,[1] may now be solved for the three unknowns to give

$$\delta T = \frac{(A - B.H_1/H_s)}{(G_1 - G_s.H_1/H_s)}$$

$$\delta E_1 = \frac{B - \delta T.G_s}{H_s}$$

$$\delta S = \delta T/2$$

where for the slot lip

$$A = \delta \qquad B = \ell$$

and for the internal Coanda surface

$$A = \delta + p \qquad B = h + \ell$$

Some examples of the possible internal geometry for two different slot locations are shown in figure 6. This could of course be extended to include any number of slots, in any orientation while still preserving smoothness and continuity of the second derivative.

PERFORMANCE EVALUATION OF THE NEW AIRFOILS

At present a small number of airfoils defined by the new technique have been evaluated using an inviscid code (FLO6). A technique of rotating the airfoil about a predetermined point at the trailing edge, with a corresponding rotation of the free stream direction, 'fools' the code into injecting circulation at constant angle of attack. This requires no modification of the code to enable high lift cases to be examined without a wall jet code. This is justified since the match between experimental and inviscid analytical pressure distributions has been well documented. A further step has been to calculate the boundary layer growth on the upper surface of the test airfoils presently using a simple incompressible boundary layer code. Two airfoils have been compared, the first a thick, cambered ellipse., the second an airfoil similar to (b) in figure 4. Both airfoils produced similar lift coefficients at zero angle of attack without added circulation, but the second (new) airfoil has a distinctly different pressure distribution, figure 7. The comparable boundary layer growths are shown in figure 8. From the previous discussion of the performance characteristics, one would anticipate the new airfoil to exhibit a high augmentation over a wider range of operational parameters, α, M_∞, Re.

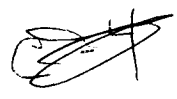

A simple optimization technique is proposed based on the evaluation of the partial derivatives of five airfoil properties with respect to the five airfoil definition parameters. The airfoil properties are

1. The boundary layer thickness ahead of the slot exit.

2. The maximum shape factor on the upper and lower surfaces.

3. The minimum pressure on the airfoil.

4 The lift increment.

Thus for any airfoil at any condition, the partials may be evaluated and a required ΔC_ℓ used to solve for the perturbations of the airfoil parameters. The choice of the five properties has some inherent characteristics. The maximum shape factors on the surfaces will avoid separation of the flow at any point ahead of the slot. The boundary layer thickness ahead of the slot will preserve a high level of lift augmentation. The maintenance of the minimum pressure on the airfoil should avoid jet stall conditions and the lift increment assures a net positive lift. This technique is yet to be fully implemented for a practical operational case.

Naturally the true test of the characteristics of the proposed airfoils will be evaluation by one or other of the full numerical codes which include wall jet modelling. At present no code is thought to be sufficiently robust or reliable to implement this phase in a more than exploratory manner.

CONCLUSIONS

A new analytical definition has been proposed for the design of circulation control airfoils. The scheme should greatly simplify the fairing in and contouring of the slot location, the Coanda surface and the internal geometry. The five parameter definition allows fine control of the thickness and camber distributions which in turn should be beneficial in maintaining satisfactory boundary layer growth over a wide range of operational conditions. The eccentricities applied to both the upper and lower surfaces should also allow dissipation of any peak loadings, thereby avoiding shocks and separations. The geometry also maintains a smooth and continuous second derivative which has been shown to be important.

The proposed analytical definition is very suitable for inclusion in two-dimensional optimization schemes once a suitable code has been made available. The freedom of the airfoil parameters to be varied and yet still produce acceptable circulation control contours should be a significant advantage. This freedom of design should also be of great importance in the further optimization of the blade geometry for vehicle performance improvement.

REFERENCES

Wood, Norman J.; and Nielsen, Jack N: Circulation Control Airfoils - Past, Present, Future. AIAA paper 85-0204, 1985.

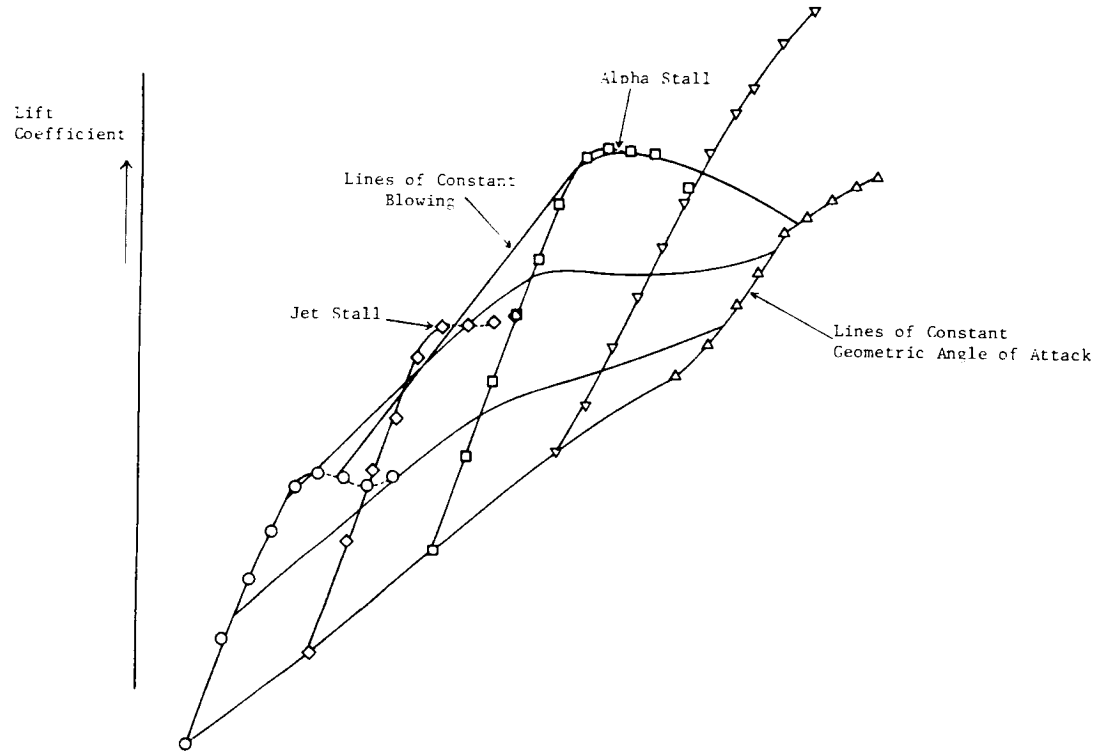

Figure 1.-Typical performance trends of a circulation control airfoil.

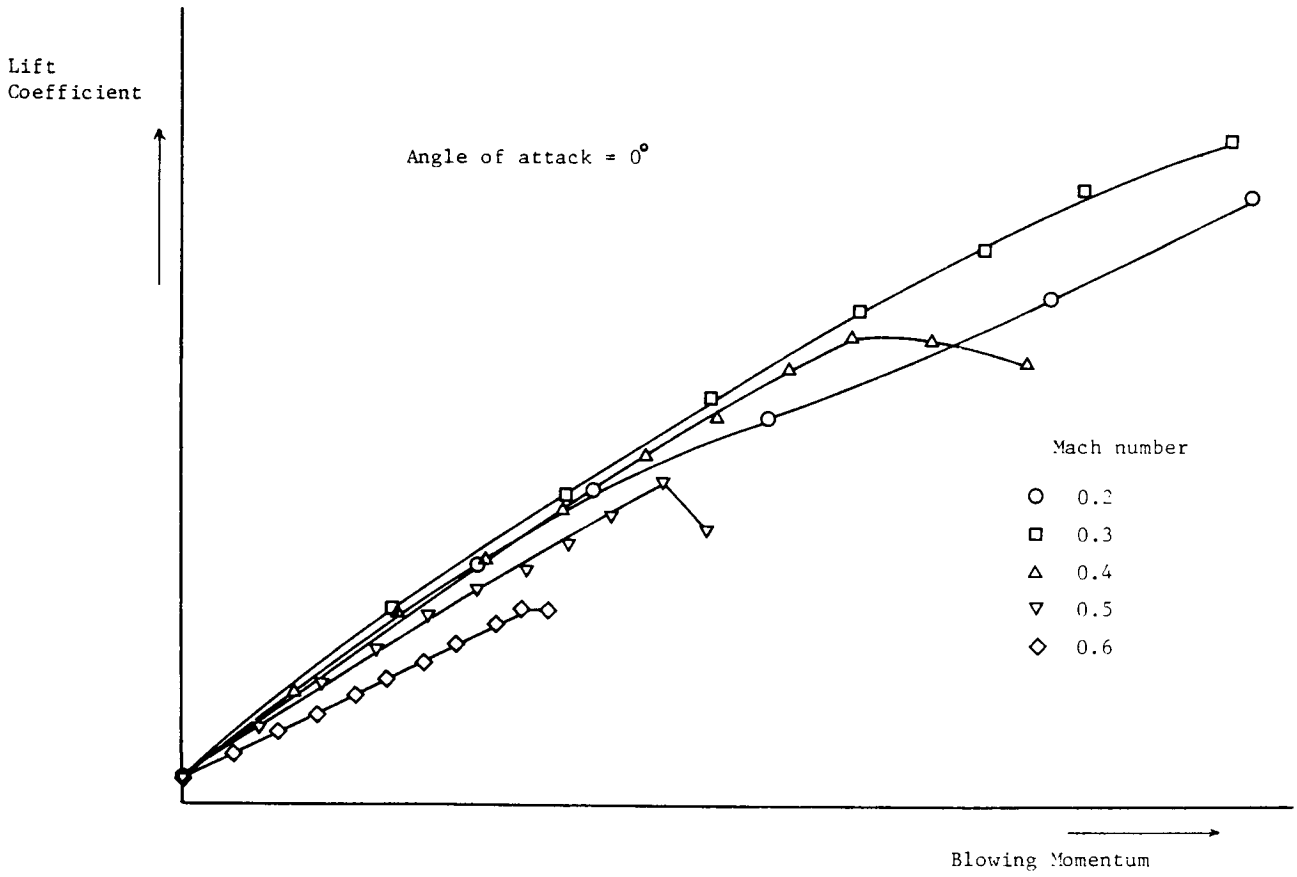

Figure 2.-Effects of Mach number on lifting performance.

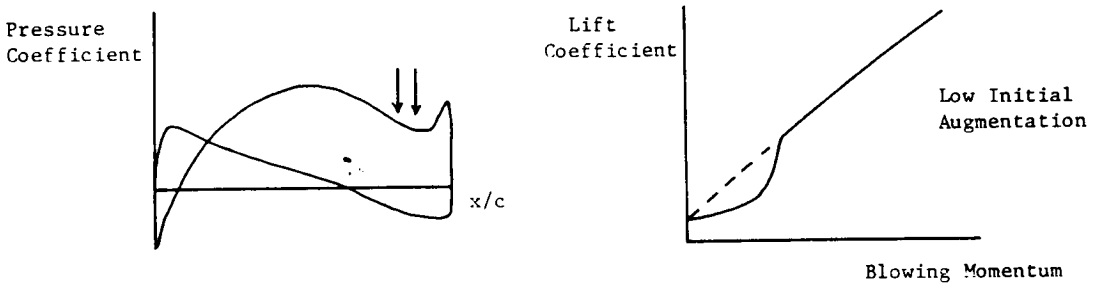

Effects of Aft Adverse Pressure Gradients

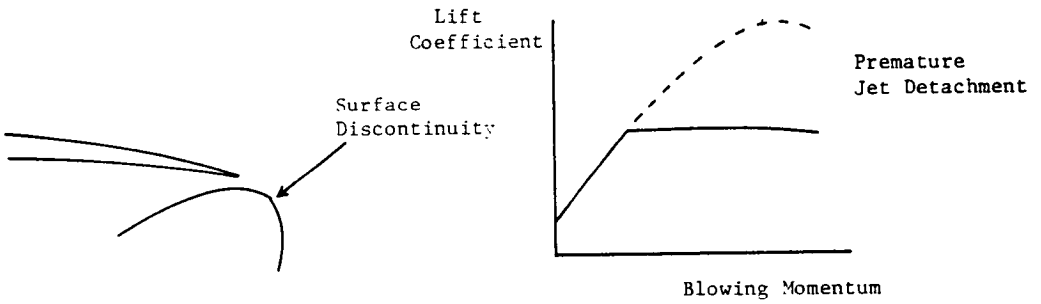

Effect of Coanda Surface Discontinuity

Figure 3.-Effects of surface discontinuities.

(a) T = 20%, R = 4%, zero camber, no surface eccentricities.

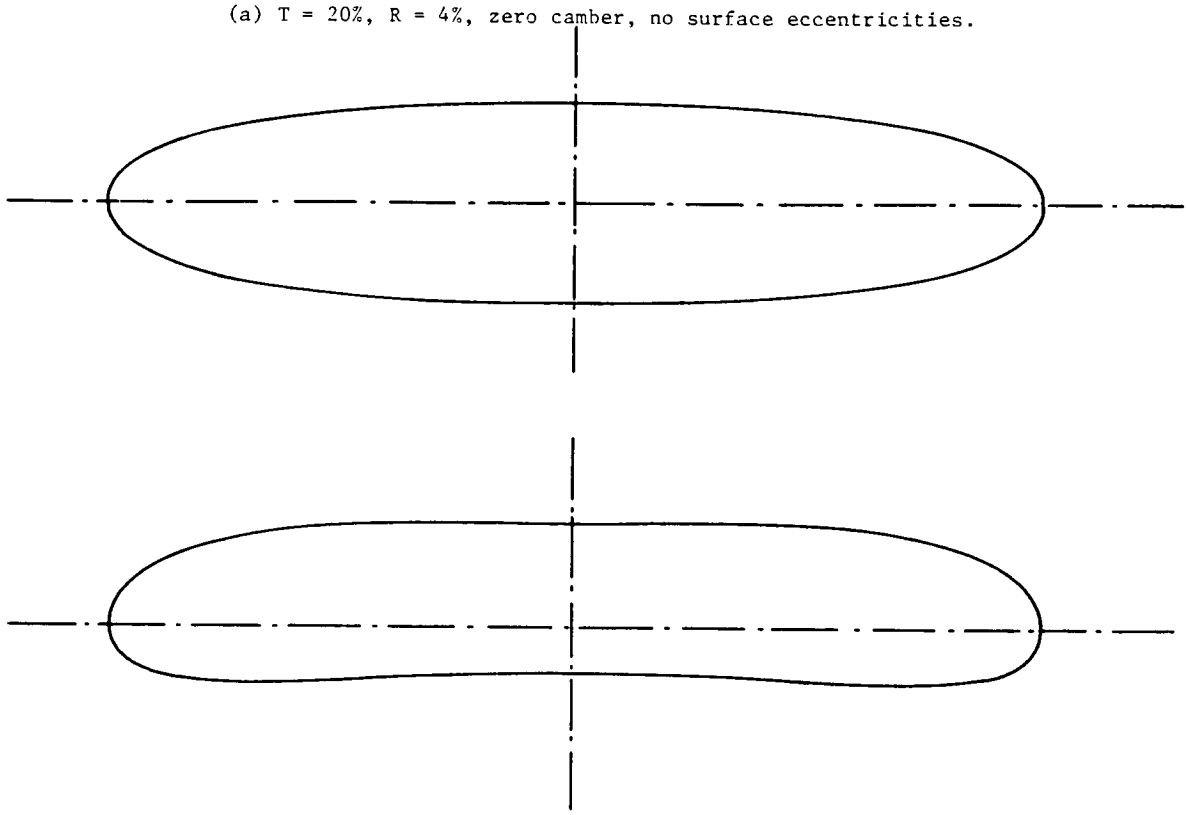

(b) T = 15%, R = 3%, 3% camber, 5% upper surface eccentricity

Figure 4.-Examples of new airfoil definitions.

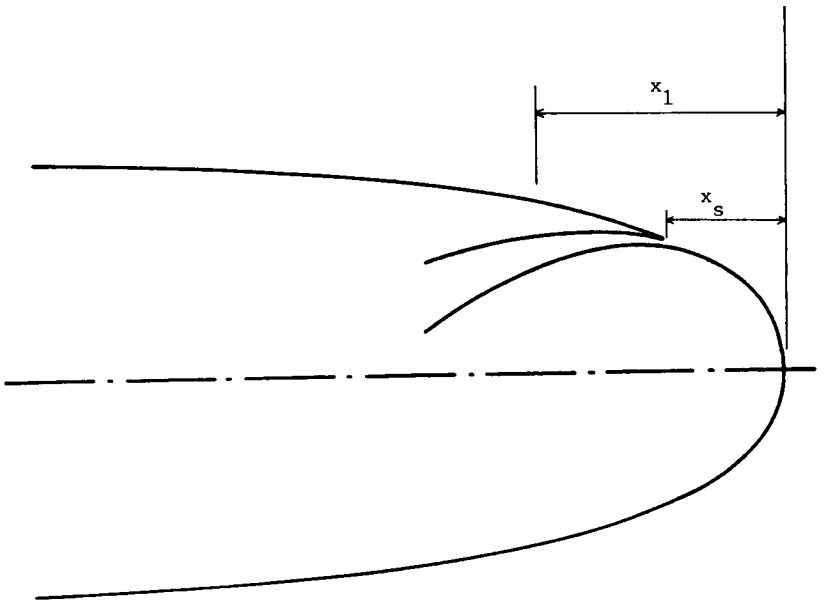

At x_s : h = slot height
ℓ = lip thickness
At x_1 : δ = plenum gap
p = lip thickness

Figure 5.-Notation for internal geometry definition.

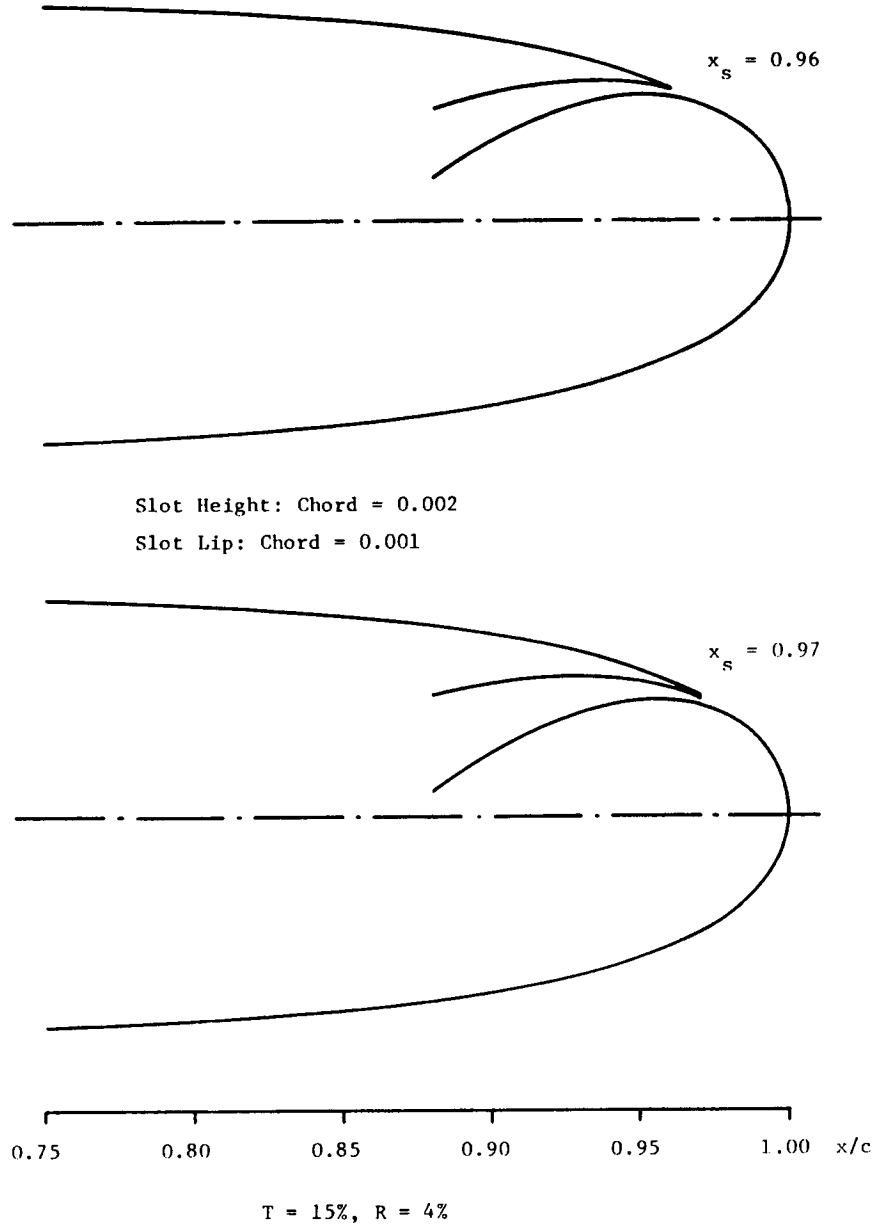

Figure 6.-Examples of internal geometry for different slot locations.

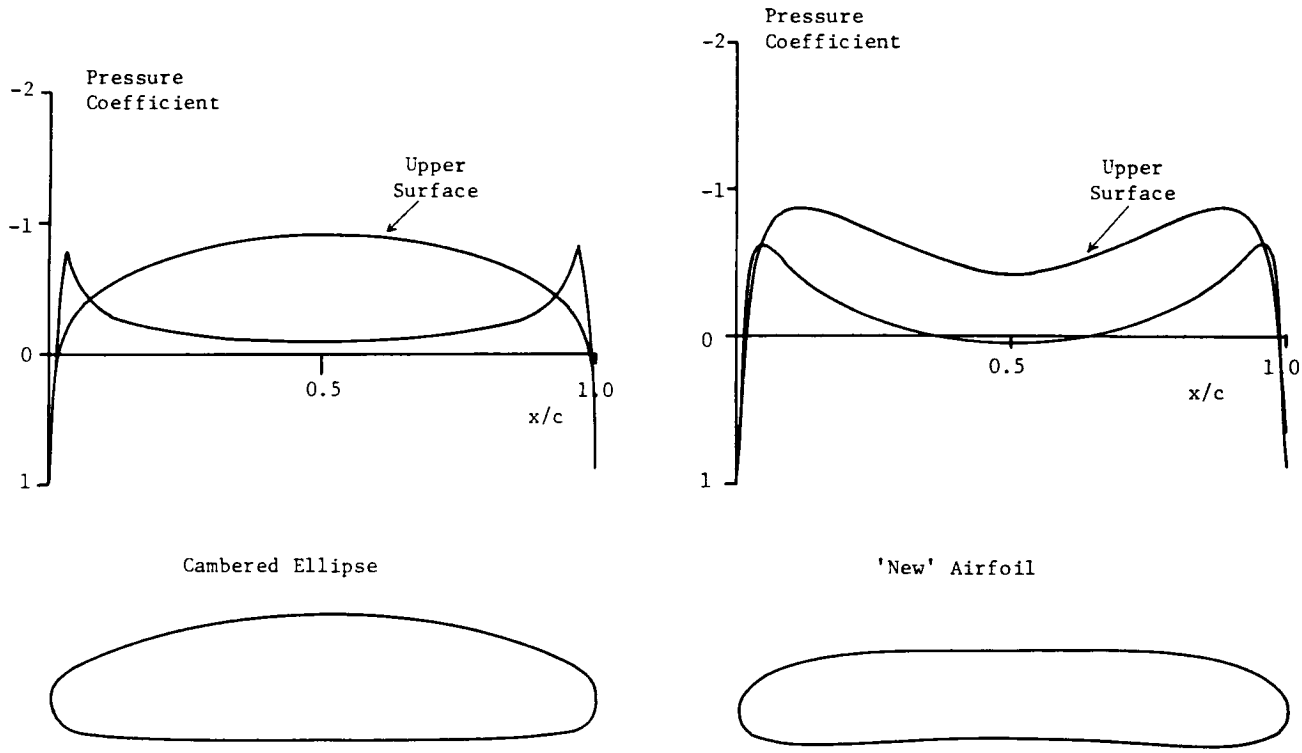

Figure 7.-Two different pressure distributions.

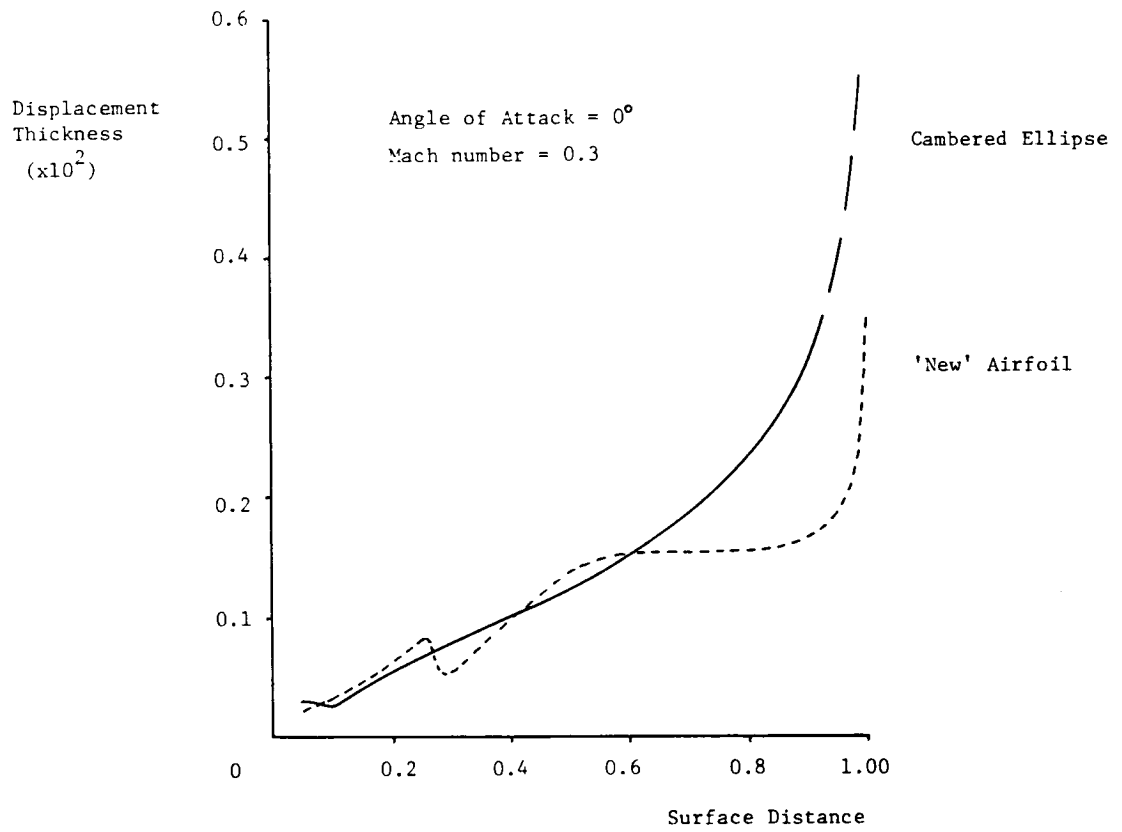

Figure 8.-Effects of pressure distributions upon boundary layer growth.

Circulation-Control Airfoil and Wing Experiments

ON THE EFFECT OF LEADING EDGE BLOWING ON CIRCULATION CONTROL AIRFOIL AERODYNAMICS

B.G. McLachlan
NASA-Ames Research Center
Fluid Dynamics Research Branch
M/S 227-8
Moffett Field, CA. 94035

Nomenclature

c	airfoil chord
C_ℓ	airfoil section lift coefficient, section lift/qc
C_μ	jet blowing momentum coefficient, $2(h/c)(U_j/U_\infty)^2$
h	jet slot height
q	free stream dynamic pressure, $(1/2)\rho U_\infty^2$
Re	Reynolds number, based on airfoil chord, $U_\infty c/\nu$
U_j	mean jet exit velocity
U_∞	mean free stream velocity
α	geometric angle of attack, deg.
ν	kinematic viscosity
ρ	free stream fluid density
Subscripts	
l.e.	leading edge jet
t.e.	trailing edge jet

Introduction

In the present context the term 'circulation control' is used to denote a method of lift generation that utilizes tangential jet blowing over the upper surface of a rounded trailing edge airfoil to determine the location of the boundary layer separation points, thus setting an effective Kutta condition. This form of circulation control applied to rotorcraft eliminates forward flight speed limitations due to conventional rotor retreating blade aerodynamic problems: lift loss due to reverse flow and dynamic stall. Using rotor blade sections symmetric about midchord, with upper surface leading and trailing edge jet blowing slots, permits simultaneous blowing on each edge of the retreating blade enabling the development of high lift coefficient values with the flow relative velocity coming from either direction (reverse or normal). At present little information exists on the flow structure generated by circulation control airfoils under leading edge blowing[1]. Consequently, no theoretical methods exist to predict airfoil performance under such conditions.

In view of this lack of information an experimental study of the flow field generated by a two-dimensional circulation control airfoil under steady leading and trailing edge blowing was undertaken. The objective of this study was to fundamentally understand the overall flow structure generated and its relation to airfoil performance. Flow visualization was

performed to define the overall flow field structure. Measurements of the airfoil forces were also made to provide a correlation of the observed flow field structure to airfoil performance.

This paper presents preliminary results from that study. It will specifically address the effect on the flow field structure of leading edge blowing, alone and in conjunction with trailing edge blowing. In addition, phenomena concerned with the effect of trailing edge blowing alone on the flow field structure will be addressed.

Description of Experiment

The experiments were performed in the 8.4 × 12.0 in. (21 × 31 cm) rectangular closed circuit water tunnel of the Army Aeromechanics Laboratory at the Ames Research Center. A steel two-dimensional 4 inch (10.2 cm) chord airfoil, horizontally spanning the test section, was tested (see figure 1). The airfoil had an uncambered elliptical section (20 percent thickness to chord ratio) with circular arc leading and trailing edges; upper surface leading and trailing edge jet slots; and, dual plenum chambers.

In the present study the angle of attack was held constant at 0 degree's and the jet slot height at .0015c. Measurements were made of the mean and fluctuating forces at Reynolds numbers, based on chord, ranging from 120,000 to 390,000. Flow visualization was also performed using the hydrogen bubble and air bubble methods for Reynolds numbers of 34,000 and 200,000, respectively. The visual data was recorded on a typical commercial grade video system. The force data presented was not corrected for blockage or jet momentum effects.

Of mention, is that all of the lift curves displayed, except figure 4, were obtained by running the lift load cell output directly to an analog plotter. No time averaging, i.e. filtering, of the load cell output was done. Thus the thickness of the lift curve trace is an indication of the unsteadiness of the lift.

Experimental Results

Trailing Edge Blowing Characteristics

Lift Characteristics

Typical lift characteristics are shown in figure 2. It is evident that as the jet blowing increases, the lift increases in a continuous fashion, and the lift curve slope decreases. A point is reached however where the lift abruptly decreases and with further increases in jet blowing the lift gradually decreases. In this reduced lift region the lift is highly unsteady.

Flow Visualization - Overall Flow Pattern

The major features of the flow pattern associated with trailing edge blowing are represented schematically in figure 3.

Increasing jet momentum moves the jet separation point around the trailing edge towards the lower surface inducing circulation around the airfoil. This increased circulation is reflected in the flow pattern through an increase in the curvature of the streamlines. The pressure field attendant to the increased streamline curvature results in boundary layer separation at the leading edge, with the resulting free shear layer reattaching itself to the airfoil surface at some distance from the leading edge forming a separation bubble. The extent of this separation bubble increases as the trailing edge blowing increases. As the jet momentum increases the wake of the separation bubble becomes highly unsteady and appears visually to affect the jet entrainment process. It is interesting to speculate that the wake of the leading edge separation bubble may be linked to the maximum lift value attainable in free air conditions: that is, the occurrence of jet blowing stall.

Another consequence of the pressure field accompanying the increased streamline curvature is boundary layer separation on the airfoil lower surface and the formation of a separation bubble ahead of the jet. On the other hand, as the jet momentum is increased a point is reached where entrainment of fluid by the jet reattaches the boundary layer and collapses the lower surface separation bubble.

Jet impingement on the lower test section floor occurs for large values of jet blowing. The result is a large blockage effect and the development of a highly unsteady flow condition in the test section. The occurrence of this condition correlates with the abrupt lift decrease and corresponding high lift unsteadiness displayed in figure 2. Thus the abrupt lift loss displayed in the present results is probably due to wall interference and cannot be termed jet blowing stall.

Effect of Boundary Layer State on Lift

The boundary layer state, laminar or turbulent, was found to have a pronounced effect on the lift characteristics displayed for small jet momentum values ($C_\mu < .03$). This effect of boundary layer state on the lift characteristics is shown in figure 4. Both boundary layer state cases display a lift increase as the jet blowing increases. However, for the laminar boundary layer case a discontinuity in the lift curve is apparent, which is in contrast to the turbulent boundary layer case where the lift increases in a continuous fashion as the jet blowing momentum increases.

Through visual observation of the flow it was possible to discover the cause of the above effect. The observed trailing edge flow patterns are illustrated in figure 5. In the absence of trailing edge blowing the boundary layer separates from the upper and lower surface of the airfoil resulting in a large wake characterized by vortex shedding. The boundary layer state determines where separation occurs in relation to the jet slot: ahead of the jet slot location when the boundary layer is laminar; and at the jet slot location when the boundary layer is turbulent. It is entrainment of fluid by the jet that reattaches the upper surface boundary layer. The different lift characteristics displayed by the laminar and turbulent boundary layer states are due to the different amounts of entrainment necessary to reattach the boundary layer in each state. Reattachment of the laminar boundary layer requires a finite amount of jet blowing. It is not a gradual process, visually it occurs

abruptly, and results in the discontinuity in the lift curve. Reattachment of the turbulent boundary layer occurs immediately upon the start of trailing edge blowing.

Leading Edge Blowing Characteristics

General Remarks

To a first approximation the trailing edge jet can be thought of as setting the flow field that the leading edge jet initially exits into. A feature that complicates this specific aspect of the overall flow is that the leading edge jet exits against the outer flow. A competition therefore occurs between the velocity and pressure field of the outer flow and the momentum and entrainment of the leading edge jet. The leading edge flow structure is determined by the balance reached between these elements. Flow visualization in the present study indicates that entrainment by the leading edge jet is a major determinant in setting the leading edge flow structure.

Lift Characteristics

The lift characteristics for simultaneous leading and trailing edge blowing were obtained by holding the momentum of one jet constant and varying the momentum of the other jet. A typical result of this procedure is shown in figure 6, where the lift coefficient is plotted[1] as a function of the trailing edge jet momentum coefficient for two constant values of the leading edge jet momentum coefficient, 0 and 0.046. For both leading edge values the lift increases with increasing trailing edge blowing. However, it is clear that the presence of leading edge blowing results in a lift decrease in comparison to the trailing edge blowing alone case. Also of note, is the increased unsteadiness of the lift in the leading edge blowing case.

A representative example of reversing the above procedure is shown in figure 7: displayed is the effect of leading edge jet momentum on the lift for constant trailing edge jet momentum coefficients of 0 and 0.052. In the presence of trailing edge blowing the lift is approximately constant for small to moderate jet momentum coefficients and is lower than the lift generated for jet momentum coefficient values outside that range. A feature to particularly note in the reduced lift zone, over a small jet momentum coefficient range, is a region where the lift is unsteady. In the absence of trailing edge blowing low lift is generated. Yet, the low lift generated does exhibit behavior of note: an abrupt decrease, though slight, in the lift and a change in the sign of the lift curve slope at $C_{\mu_{l.e.}} \approx .06$.

Flow Visualization - Leading Edge Flow Pattern

The flow visualization revealed that at low values of the leading edge jet momentum coefficient the leading edge jet goes completely over the upper surface, and that at high coefficient values the leading edge jet goes completely over the lower surface. For intermediate coefficient values the leading edge jet behavior is more complicated with the jet bifurcating or becoming bistable. Here the term bifurcation is used to describe the divi-

[1] In all the lift curves pertaining to leading edge blowing the vertical axis scale, though absent, is the same.

sion of the jet into two parts, one part proceeding over the upper surface, and the other part proceeding over the lower surface. The term bistable is used to denote an unsteady condition. This point will be further elaborated on shortly.

A prominent feature of the leading edge flow field for certain values of leading and trailing edge jet momentum is the formation of a circulatory flow pattern - namely, a 'vortex'. This feature occurs for conditions where the majority of the jet folds back, after extending itself out over the airfoil nose, and proceeds over the upper surface. Entrainment by the jet of part of itself induces the circulatory flow pattern.

The relation of these structural features of the leading edge flow field to the previously displayed lift characteristics is shown in figure 8.

It was possible to make a 'map' of the leading edge flow structure through correlation of the flow visualization observations with the leading and trailing edge jet momentum settings. The 'map' is displayed in figure 9 where the flow features described previously are indicated schematically. As noted already the term bistable is used to denote an unsteady leading edge jet flow state. Referring to figure 9, when bistable, the structure of the leading edge jet appears visually to move between the two steady flow states that border the bistable region along a line of constant $C_{\mu_{t.e.}}$.

Conclusions

The conclusions pertaining to leading edge blowing may be summarized as follows.

- Simultaneous leading and trailing edge blowing results in a lift decrease in comparison to trailing edge blowing alone. However, it must be noted that appreciable lift is still developed.
- Leading edge blowing can result in an unsteady flow condition.
- The leading edge flow structure is more complicated than previously hypothesized: e.g., under certain conditions jet entrainment induces a circulatory flow pattern at the leading edge of the airfoil.

References

1. Ottensoser, J., "Two-Dimensional Subsonic Evaluation of a 15-Percent Thick Circulation Control Airfoil with Slots at both Leading and Trailing Edges," DTNSRDC Report 4456, July 1974.

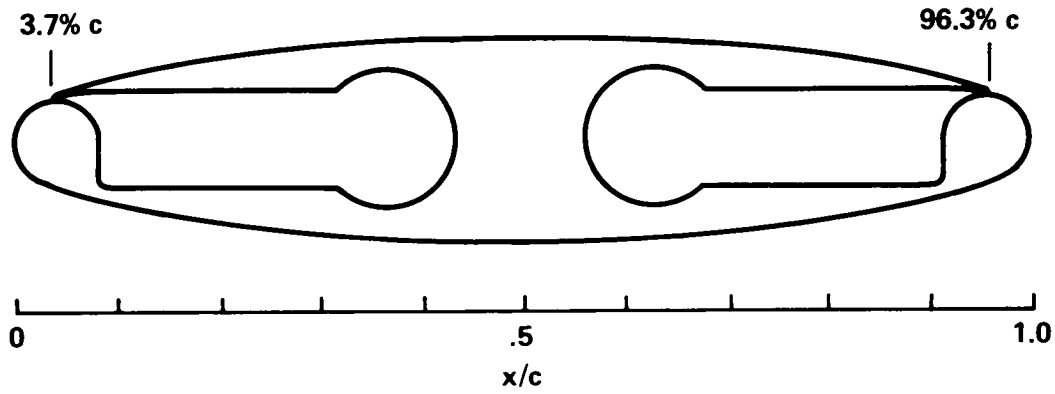

AIRFOIL PARAMETERS

CHORD – 4 in. (0.102 m)

THICKNESS – 0.2 c

JET SLOT HT. – 0.0015 c

L.E. & T.E. RADIUS – 0.04 c

Figure 1.-Airfoil geometry and parameters.

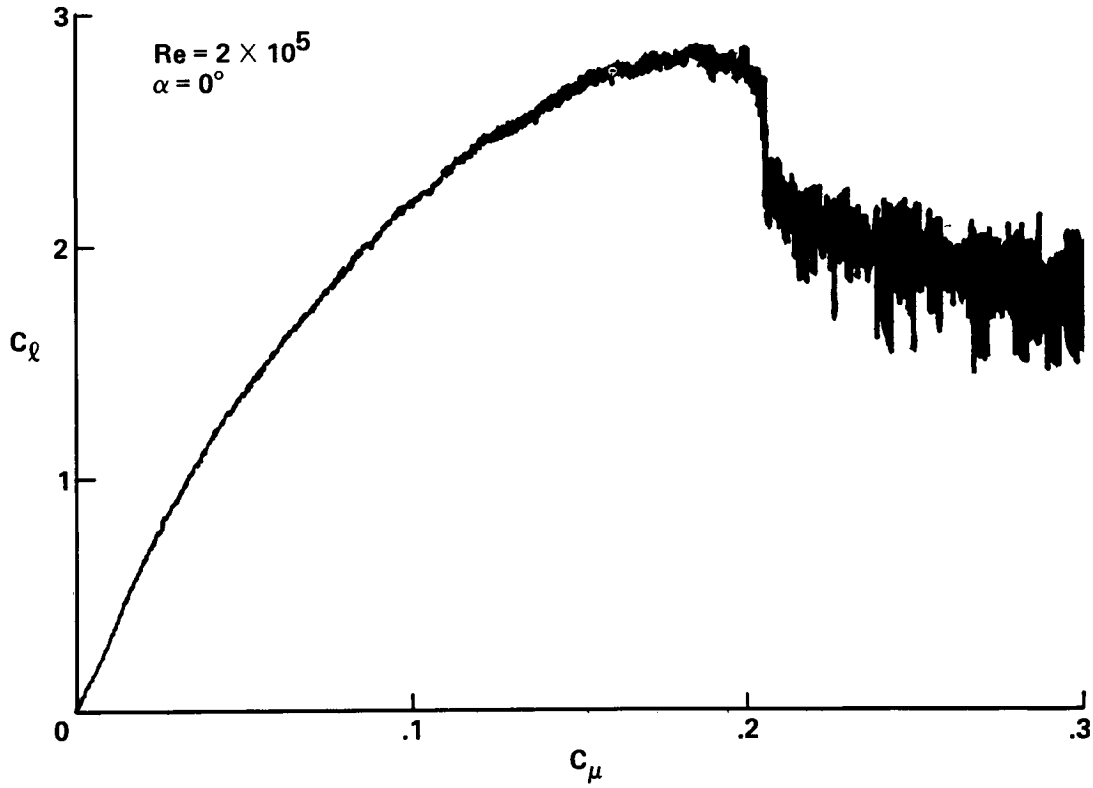

Figure 2.-Airfoil lift characteristics: trailing edge blowing alone; turbulent boundary layer case.

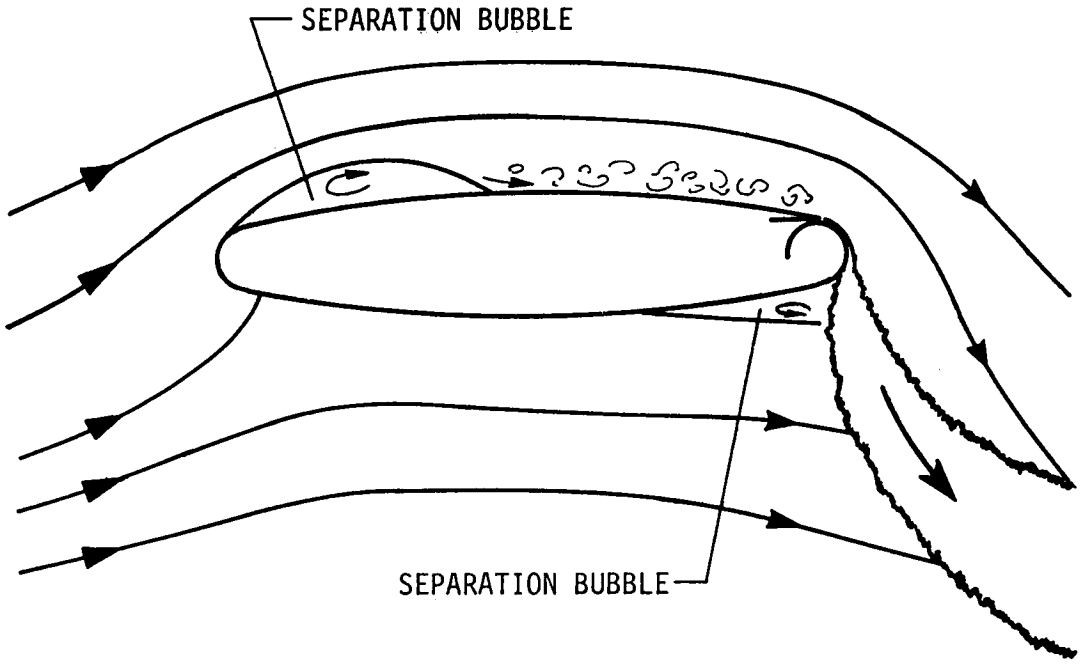

Figure 3.-Schematic of overall flow pattern associated with trailing edge blowing.

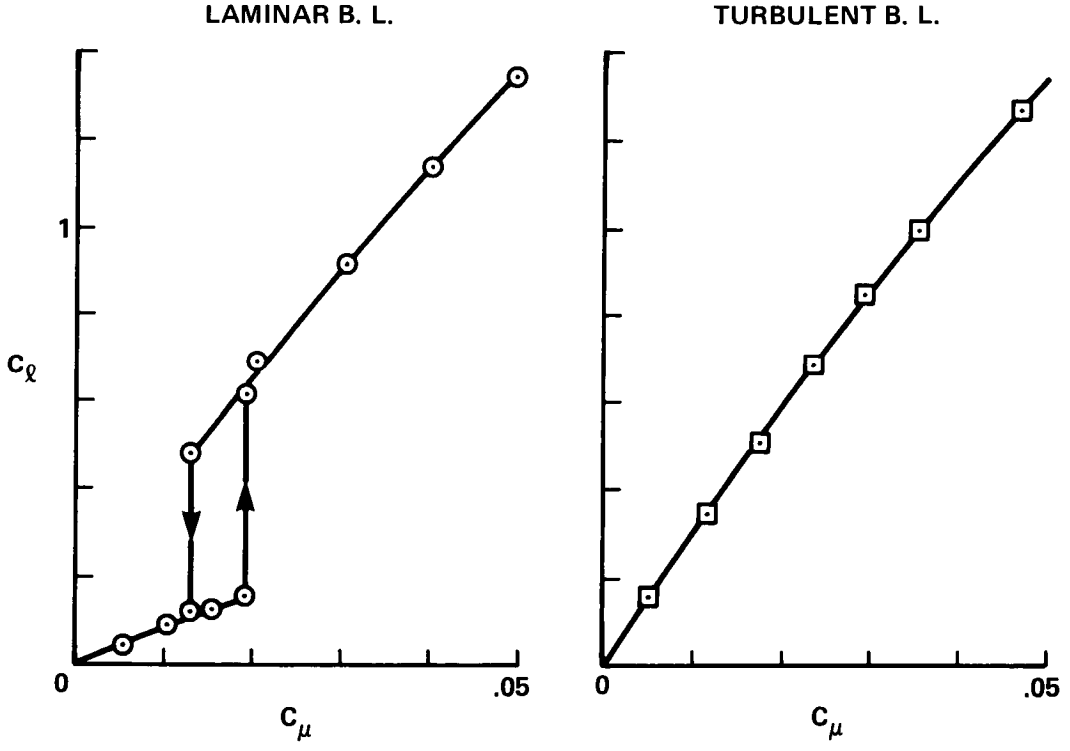

Figure 4.-Effect of boundary layer state on lift characteristics: Re $= 1.93 \times 10^5, \alpha = 0°$.

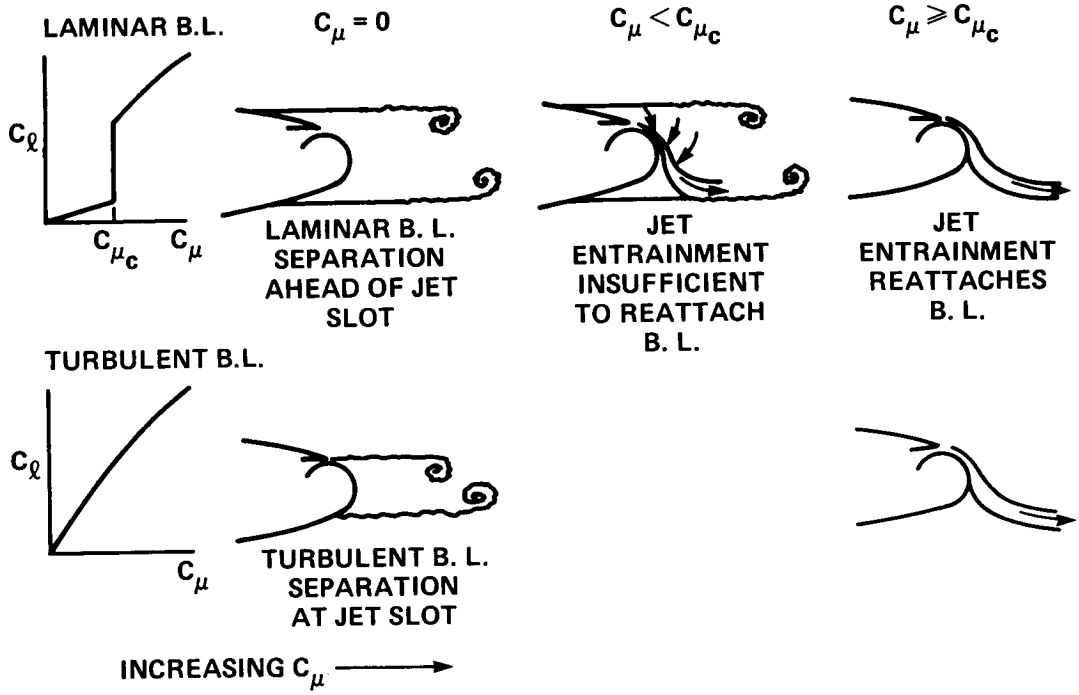

Figure 5.-Effect of boundary layer state on lift characteristics: schematic of trailing edge flow pattern.

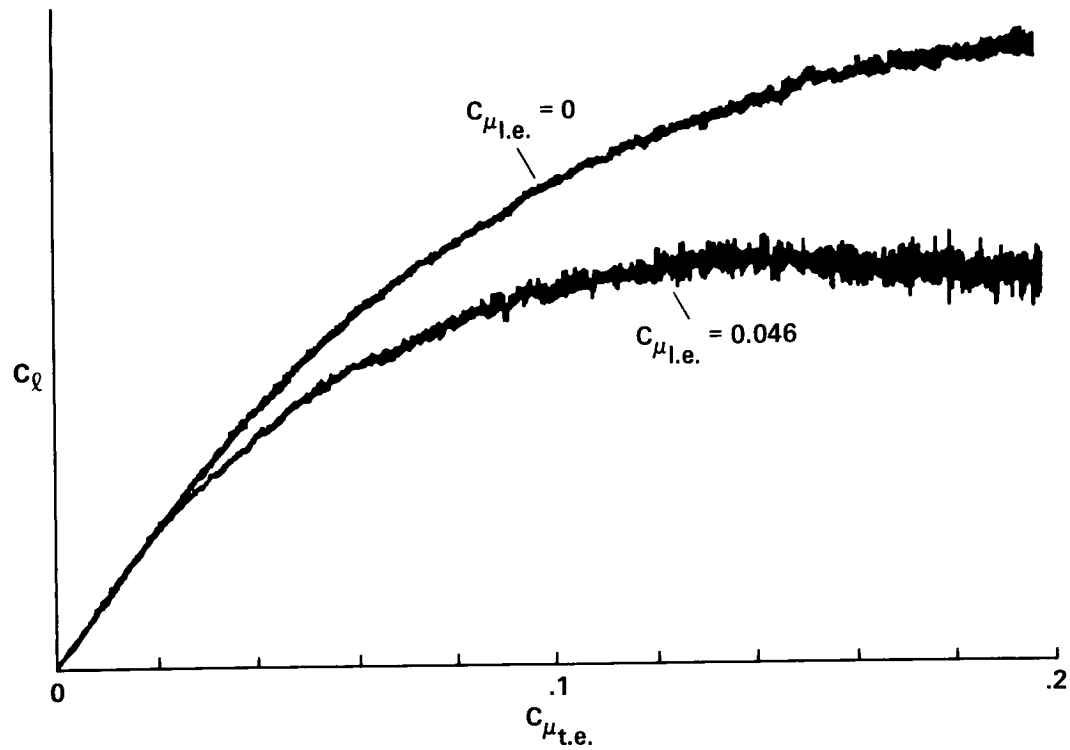

Figure 6.-Effect of trailing edge blowing on lift characteristics: constant leading edge blowing; Re = 2.1×10^5, $\alpha = 0°$. The vertical axis scale is the same for figures 6, 7, and 8.

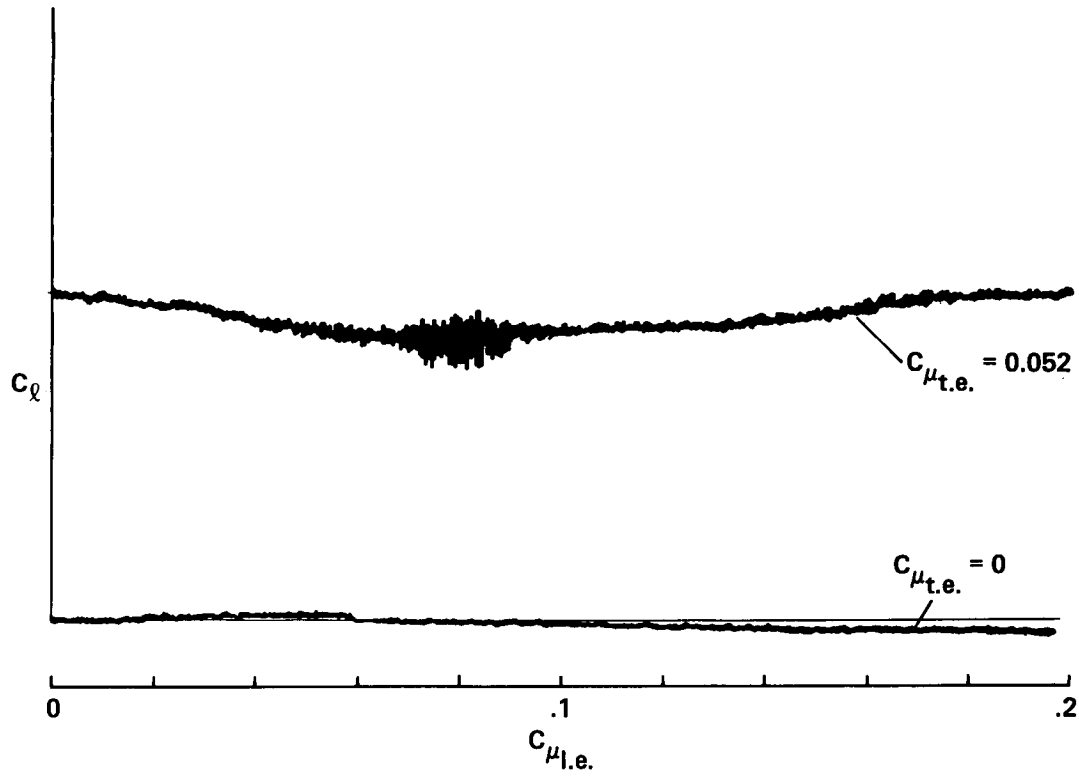

Figure 7.-Effect of leading edge blowing on lift characteristics: constant trailing edge blowing: Re = 2.1×10^5, $\alpha = 0°$.

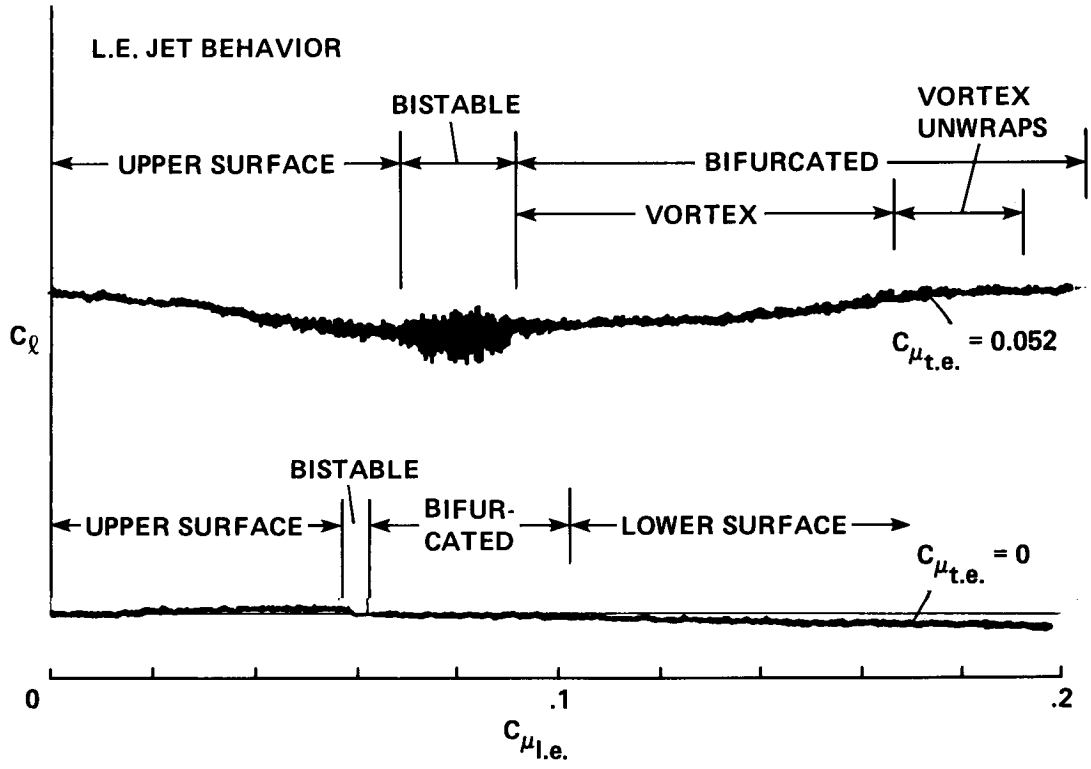

Figure 8.-Correlation of leading edge jet flow field structural features with lift characteristics: Re = 2.1×10^5, $\alpha = 0°$.

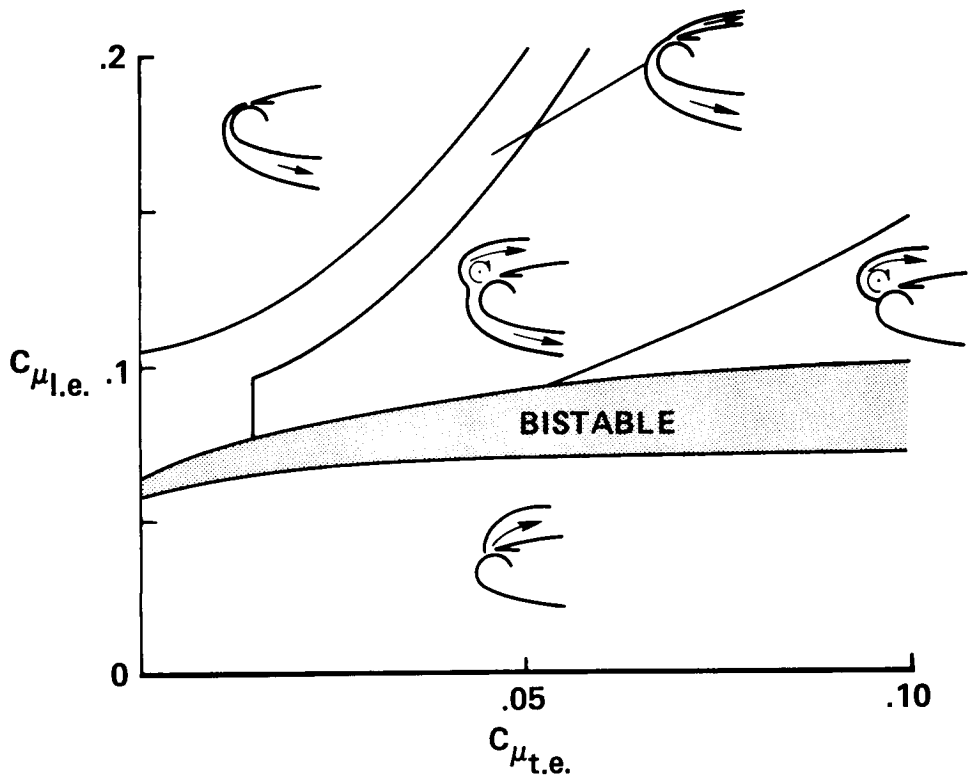

Figure 9.-Map of leading edge jet flow field structure: $\alpha = 0°$.

PRESSURE DISTRIBUTIONS AND OIL-FLOW PATTERNS FOR A SWEPT CIRCULATION-CONTROL WING

Earl R. Keener, Dwight T. Sanderfer, and Norman J. Wood*

Ames Research Center

SUMMARY

Pressure distributions and photographs of oil-flow patterns are presented for a circulation-control wing. The model was an aspect-ratio-four semispan wing mounted on the side wall of the NASA Ames 6- by 6-Foot Transonic Wind Tunnel. The airfoil was a 20%-thick ellipse, modified with circular leading and trailing edges of 4% radius, and had a 25.4-cm constant chord. This configuration does not represent a specific wing design, but is generic for research purposes. A full-span, tangential, rearward-blowing, circulation-control slot was incorporated ahead of the trailing edge on the upper surface. The wing was tested at Mach numbers from 0.3 to 0.75 at sweep angles of 0° and +45° with internal-to-external pressure ratios of 1.0 to 3.0. Lift and pitching-moment coefficients were obtained from measured pressure distributions at five span stations.

Oil-flow tests at 0° angle of attack show that the boundary layer separated just ahead of the slot. However, the flow attaches quickly with active jet blowing. The wing-surface flow at 45° sweep is nearly streamwise away from the leading edge. The wingtip flow is strongly entrained into the outer jet flow. The lower-surface boundary layer separates noticeably ahead of the Coanda-surface separation. The wingtip flow pattern is similar to that of the lee side of an ellipsoid at a 45° angle of attack. At 5° angle of attack, it is more difficult to attach the separated flow ahead of the slot with jet blowing at the lower speeds. At Mach 0.7 the separated flow cannot be attached ahead of the slot.

When the conventional corrections resulting from sweep angle are applied to the lift and moment of circulation-control sections, no additional corrections are necessary to account for changes in blowing efficiency. This is demonstrated herein for an aft sweep angle of 45°. An empirical technique for estimating the downwash distribution of a swept wing has been validated with the swept-wing data.

*Joint Institute for Aeronautics and Acoustics, Stanford University, Stanford, CA

NOMENCLATURE

AR	aspect ratio of semispan wing, b/2c
b/2	wing semispan, normal to plane of symmetry when swept
c	wing normal chord
c_ℓ	wing-section lift coefficient obtained from c_n and α
c_m	wing-section pitching-moment coefficient about c/2 obtained by numerical integration of pressures at each row of orifices
c_n	wing-section normal-force coefficient obtained by numerical integration of pressures at each row of orifices
C_p	pressure coefficient, $(p - p_\infty)/q_\infty$
C_μ	wing-section jet-momentum coefficient, $m_j V_j/q_\infty\ c\ l_j$
h/c	slot height/chord ratio
l_j	length of slot
M_∞	free-stream Mach number
m_j	jet mass flow computed from orifice-plate flow equations and measurements
PR	jet pressure ratio, plenum/tunnel static
q_∞	free-stream dynamic pressure
R_e	Reynolds number based on c
S/2	exposed wing area of semispan model
V_j	computed jet velocity assuming isentropic expansion from jet total pressure to free-stream static pressure
x	chordwise distance rearward of leading edge
y	spanwise distance outboard of wing root
α	angle of attack

Λ angle of sweep

η span station, 2y/b

Subscripts

j jet parameter

∞ free-stream conditions

N normal (free-stream) conditions

INTRODUCTION

There are several ways to control the aerodynamic circulation of wings and, thus, to control the amount of lift. One type of circulation control that is currently under investigation is tangential blowing out of a slot located ahead of a rounded trailing edge. For reasons not entirely understood, the flow adheres to the trailing-edge surface, which is known as the Coanda effect. The deflected flow increases the lift of a wing section to several times that obtained by the conventional method of increasing the angle of attack. A summary of circulation-control research is presented by Wood and Nielsen (1985).

A circulation-control wing test was recently completed in the Ames 6- by 6-Foot Transonic Wind Tunnel. The test was conducted to support the research needs of the NASA RSRA/X-Wing stopped-rotor research vehicle, which is a circulation-control rotor that can be stopped in the X-wing position for high-speed cruise (Wood and Nielson, 1985). The model was an aspect-ratio-four semispan wing mounted on the side wall of the wind tunnel. The airfoil was a 20%-thick ellipse, modified with circular leading and trailing edges of 4% radius, and had a 25.4-cm constant chord. This generic configuration does not represent a specific shape from current vehicle design concepts, which are in a state of development. A full-span, tangential, rearward-blowing, circulation-control slot was incorporated ahead of the trailing edge on the upper surface. The wing was tested at Mach numbers from 0.3 to 0.75 at sweep angles of 0° and +45° with internal-to-external pressure ratios of 1.0 to 3.0. Lift and pitching-moment coefficients were obtained from measured pressure distributions at five span stations. Surface-flow patterns were obtained using the oil-streak flow-visualization method. Boundary-layer and wake surveys with three- and five-hole flow-direction probes were obtained over the wing and in the wake near the midsemispan with the wing swept back 45°.

This paper presents selected pressure distributions and photographs of oil-flow patterns from this test. Boundary-layer and wake measurements are presented in a companion paper by Spaid and Keener (1986).

TEST FACILILTY

The Ames 6- by 6-Foot Transonic/Supersonic Wing Tunnel was chosen because the allowable model size is suitable for boundary-layer research. The tunnel is a variable-pressure, continuous-flow facility. The nozzle leading to the test section is of the asymmetric, sliding-block type that permits a continuous variation in Mach number from 0.25 to 2.3. The test section has a slotted floor and ceiling with 6% porosity and provisions for boundary-layer removal. The turbulence-velocity level is high, measured to be about 1.5% of the free-stream velocity.

MODEL

The model was a semispan wing incorporating circulation control by tangential blowing from a spanwise slot located ahead of a rounded trailing edge. The model was mounted on the side wall of the tunnel on a turntable that could be manually rotated through a -5° to +5° angle of attack range. The wing-root-mounting structure was covered with a fairing that had a 12.7-cm by 17.8-cm (5 × 7) elliptic transverse cross section. The cross section in the plane of symmetry had a length/major axis nose ratio of 1.0 and afterbody ratio of 1.5. Figure 1 is an artist's view of the model in the tunnel showing the effect of the jet flow from the slot on the airflow around the model. Figure 2 shows the model installation in the tunnel at both the 0° and 45° sweep positions. The resulting aspect ratios were 4.0 and 1.85, respectively, based on the normal component of the exposed span. Figure 3 shows three views of the model installation in the 0° and 45° sweep positions and a close-up view of the trailing-edge slot.

The wing section was designed with a simple 20%-thick elliptic airfoil, modified with circular leading and trailing edges of 4% radius, and had a 25.4-cm constant chord (fig. 4). This airfoil was similar to several previously tested circulation-control airfoils and was purposely selected to be generic and not to represent a specific shape from current vehicle design concepts. These concepts are in a state of development and it was felt that a generic shape would adequately serve the purpose of this test to explore the effect of sweep angle. A full-span, tangential, rearward-blowing, circulation-control slot was incorporated ahead of the trailing edge on the upper surface.

Design suggestions based on previous circulation-control tests were contributed by N. Wood of the Joint Institute for Aeronautics and Aeroacoustics of Stanford University and by E. Rogers and J. Abramson of the David W. Taylor Naval Ship Research and Development Center. Publications from their research are given in the summary paper of Wood and Nielsen (1985). The wing section follows closely the design concepts of Wood and Conlon (1983) and Wood and Sanderfer (1986). The model was designed in four parts (fig. 4), split along the plane of symmetry. The center of the model contained an internal plenum, which was connected to the external air supply at the wing root through the side wall of the tunnel. Ahead of the plenum

was a separate compartment to pass the pressure tubes from the forward parts to the wing root. The compartment was sealed from the plenum pressure with an O-ring seal. Such O-ring seals were also used between the forward parts and the slot and trailing-edge pieces, installed in a horizontal step so that a positive seal occurred when the top and bottom halves were bolted together. Several vertical posts, spaced every 7.11 cm spanwise, separated the split halves.

Figure 5 is a cross-sectional sketch showing the design of the slot and trailing edge. A leading and trailing radius of 4% was selected. From previous experience a nominal slot height of 0.0020 chord was recommended with a trailing-edge thickness of 0.0008 chord. For this particular model, the generating circle for the trailing edge was "rolled" forward along the lower surface of the generating ellipse until an acceptable gap occurred with the upper surface, forming the slot. The final design gap was $h = 0.483$ mm (REFERENCE $H/C = 0.0019$). The sharp slot trailing edge was removed to a trailing-edge thickness of $t = 0.0203$ mm (REFERENCE $t/c = 0.0008$), which is more controllable dimension than a sharp edge. The slot lip was designed with a 7° internal angle to the trailing-edge radius, forming a converging nozzle. This 7° internal angle was felt, from experience, to be the minumum angle required to avoid jet detachment from the Coanda surface. The remainder of the slot lower surface was faired forward with large radii, as shown. To allow adjustment of the slot height from the nominal design height, a flexure cutout was designed (as shown in fig. 4) with the objective that the radius be large enough that the outer surface would not experience a discontinuity in local slope and small enough that the cutout would not distort the shape from the internal pressure. The internal design of the trailing edge was finalized with a straight ramp to avoid a curvature that might induce Gortler vortices that would be fed into the jet. Such vortices have been observed in previous tests. Surface-pressure tubes in the slot piece were routed to the wing root through the flexure space, held in place with spot-welded metal strips and covered with a flexible epoxy. Surface-pressure tubes in the trailing-edge piece were routed through a slot cut into the inside surface and filled with epoxy.

Adjustment of slot height was provided by adjusting screws at several span stations. Fixing slot height was provided by setscrews placed ahead of each adjusting screw. This arrangement was determined from experience to be best for avoiding interaction of the two screws with the slot height, which would require several iterative adjustments. The two screws were placed in line (chordwise) with each other and with the support posts to reduce flow interference. A careful stress analysis was made of the flexure cutout and the effect of the adjusting screws.

From previous experience it was felt that several of the dimensions required close tolerances. The most critical tolerances were found to be the chordwise position of the slot lip with respect to the trailing edge and the trailing-edge contour. Thus, the trailing edge was chosen as a reference, with a tolerance of 0.050 mm for the slot-lip position and the trailing-edge radius along the length of the span. Machined vertical faces between the plenum and the rear pieces provided the necessary control of the tolerances between the rear and forward pieces.

For strength, corrosion resistance, and surface durability, the model was constructed from stainless steel and designed to withstand internal pressures of 60 psig.

The air supply was provided from the tunnel 80-psi dry-air sphere. The airflow was controlled by a regulator to set the total pressure in the wing plenum. An orifice plate in the system provided mass-flow measurements.

INSTRUMENTATION AND ACCURACY

The pressure instrumentation consisted of 252 orifices on the wing, installed at five spanwise stations (rows 1 to 5: $2y/b = 0.1$, 0.3, 0.5, 0.7, and 0.9, based on the exposed span at 0° sweep) and one row of orifices at the midspan of the wing-root fairing (fig. 6). More orifices were placed at row 4, $2y/b = 0.7$, especially over the trailing edge, to obtain more detail at one row. Additional orifices were placed at row 6 at a 45° angle between rows 3 and 4 ($2y/b = 0.5$ and 0.7) to assist in the analysis of the pressures at a sweep angle of 45° and to provide a row of orifices for boundary-layer measurements at this angle. Orifices were 0.50 mm in diameter, which is the standard wind-tunnel measurement, to avoid hole interference with the pressures. A 1.0-mm-diam tube was epoxied into a hole drilled into the back side of the orifice location. The tubes were routed to the wing root and through the side-wall turntable, as described in the MODEL section. Four pitot-static pressures and two thermocouples were installed internally. An accelerometer was installed in the wing tip to measure the frequency and amplitude of the vibrations of the steel wing, which was designed to be rigid.

The surface static pressures were measured using electronically actuated pressure-scanning valves containing pressure transducers that were connected to an automatic data-recording system. The self-calibrating feature of the scanning valves provided an accuracy of about 0.25% full scale of the ±8.62 N/sq cm (±12.5 psi) transducers, between ±0.006 and ±0.01 in pressure coefficient at the higher speeds. Tunnel test conditions were measured with precision pressure recorders giving a Mach number accuracy of about ±0.002. Tunnel-static pressure was measured on the tunnel wall 10 wing-chord lengths ahead of the wing-root leading edge. The angle of attack was set manually by rotating the wall turntable and setting the angle with an inclinometer with an accuracy of ±0.03°.

SIMPLE-SWEEP THEORY

In a selecting the test conditions for the two sweep angles, it was desired to test the application of simple-sweep theory to the pressure distributions. The theory applies to a wing section of an infinite or very-high-aspect wing. Therefore, it was realized that the present wing could have both wing-tip and wing-root

fairing effects. Nevertheless, it was of interest to analyze the midspan pressures in light of the simple-sweep theory.

The physical concept of the simple-sweep theory can be described as follows: suppose that a very long wing of constant chord and constant airfoil section is mounted at right angles in a wind tunnel through slots in the side wall. If the wing is drawn through the slots at constant speed, w, it is reasonable to believe that the pressures over the wing will not change (in the first order) from what they were when the wing was stationary. The resultant free-stream velocity, V, relative to a given point on the wing will then act at the angle, $\sin^{-1}(w/V)$, to a plane perpendicular to the wing leading edge, in which lies the normal wing chord and the normal velocity, VN, of the tunnel. Hence, the wing pressures are independent of w and dependent only on the projection of the relative free-stream velocity upon a plane perpendicular to the wing leading edge (the normal plane). Therefore, if a swept wing is tested at Mach number, M_∞, sweep angle, Λ, and angle of attack, α, the following expressions relate the aerodynamic pressure distributions, loading, and moments to the equivalent values at the normal Mach number, M_N:

Swept pressure distribution = Equivalent unswept pressure distribution
(at equivalent Mach number)
for this test, $\Lambda = 45°$

Mach number:
equivalent Mach number = $M_N = M_\infty \cos^2\Lambda = 0.7\ M_\infty$

Pressure Coefficient
Pressure, (swept section) = Pressure, (normal section)
$C_p = (p - p_\infty)/q_\infty$; $C_{p,n} = (p - p_\infty)/q_n$
$q_\infty = q_n/(\cos^2\Lambda)$

therefore,
$C_\ell = C_{\ell,n}\ (\cos^2\Lambda) = 0.50\ C_{\ell,n}$

Lift and Moment Coefficients:
load (swept) = load (normal)
$c_p = c_{p,N}\ (\cos^2\Lambda) = 0.50\ c_{p,N}$
c_m (sweep) = $c_{m,N}\ (\cos^2\Lambda)$ at $x = c/2$

Mass-Flow Coefficient:
jet velocity for swept wing, $V_j = V_{j,N}$ since jet velocity is normal to trailing edge

mass flow (swept) = mass flow (normal)

therefore,
$C_\mu = C_{\mu,N}\ (\cos^2\Lambda) = 0.50\ C_{\mu,N}$

Reynolds number:

$R_{e,N} = R_e, (\cos^2\Lambda)$ has no theoretical influence in the simple theory. The boundary-layer flow must be similar (no change in state that affects the pressure distribution). This occurs only for a laminar boundary layer. Allowing a turbulent boundary layer by keeping the location of transition common to both the swept wing and the equivalent unswept wing is not sufficient since the turbulent boundary layer does not scale the same in the spanwise direction as in the chordwise direction, as a laminar boundary layer does.

Angle of attack:

α (swept) = α (normal)/$(\cos^2\Lambda)$

Note: Finite span generates an induced angle of attack, in addition to the geometric angle generated by sweep. Also, if the aspect ratio is small, there can be root effects, like the effect of the fairing for this wing.

TEST CONDITIONS AND PROCEDURES

Jet-blowing effectiveness was first evaluated with tunnel air off. Wing pressures were then measured without boundary-layer trips at M = 0.70 at 0° sweep angle. Sublimation flow-visualization tests showed that boundary-layer transition occurred near the midsection. Boundary-layer trips were then installed on the wing at 0.09 chord using sifted glass spherules having a nominal size of 0.23 cm, selected from standard curves. Sublimation flow-visualization tests made at a Mach number of 0.70 verified that this size was adequate at both the 0° and 45° sweep angle to cause transition at the trips.

Pressures were measured over the wing and wing-root fairing at Mach numbers of 0.3, 0.4, and 0.5 at 0° sweep angle and at Mach numbers of 0.425, 0.566 and 0.7 (determined from simple-sweep theory, M/cos 45°) at 45° sweep angle. Angles of attack were 0°, ±2.5°, and ±5° at 0° and 45° sweep angles and ±1.8°, and ±3.5° additional angles at 45° sweep (determined from simple-sweep theory, α cos 45°). Reynolds number was limited to a maximum of 3 million (based on wing chord) to keep the wing loads within the design conditions. Most of the tests were conducted at a total pressure of 1 atm.

Oil-flow-visualization tests were made at both sweep angles at several Mach numbers. It was found that for most cases a single spanwise strip of oil on each surface behind the boundary-layer trips and a sheet of oil on the wingtip produced adequate results.

DISCUSSION

Tunnel Wind-Off Tests

An initial evaluation of the performance of the Coanda surface can be determined with jet-blowing tests alone. This test would follow the model inspections of the Coanda surface as described by Wood and Conlon (1983). Accordingly, a tunnel wind-off test was made with a blowing-pressure ratio of 1.8. The jet flow formed a long "tuft" which followed the trailing edge and blew forward along the lower surface. The flow even tried to turn around the leading edge but finally separated. This test showed that the Coanda surface was working effectively. The tuft was traversed along the span and showed a discontinuity in the flow along the lower surface at about one-third span. Inboard, the tuft was inclined toward the root at a noticeable angle. According to previous experience the change in flow angle over the lower surface results from internal flow disturbances that are amplified in the flow over the Coanda surface. For the present model it was concluded that the the flow disturbance resulted from the design of the air supply at 0° sweep angle through the forward air port, which directed airflow toward the trailing edge at about one-third span (fig. 6). At 45° sweep, this disturbance did not occur since the air was supplied through the rearward air port, which was directed spanwise.

Next, a pitot-pressure survey was made along the span of the jet. The pitot pressure was uniform along the span at both sweep angles, indicating that the internal flow disturbances at 0° sweep were not severe. No recognizable problems were caused by this internal flow disturbance during the tests with the tunnel wind on.

Oil-Flow Visualization

Selected oil-flow-visualization photographs are shown for a sweep angle of 45°. Figure 7 is a photograph of an oil-flow test on the upper surface at a sweep angle of 45°, $M_\infty = 0.425$, $\alpha = 0°$, and no jet blowing. The boundary-layer trip strip can be seen at 0.095 chord, as can the chordwise and spanwise strips of transparent tape protecting the orifices. Oil was applied behind the trips at about 0.20 chord. The boundary layer separates ahead of the jet slot (located at 0.96 chord) as determined by the oil streaks turning outboard to run spanwise, forming an oil-flow separation line.

The next series of oil-flow photographs (fig. 8) are for the same test conditions ($M_\infty = 0.425$, $\alpha = 0°$) but with jet blowing at a pressure ratio of 1.8. The top-surface flow (fig. 8(a)) is almost streamwise over the swept wing. (The separated flow near the slot with no blowing attaches quickly with small blowing.) Near the slot the flow turns slightly inboard toward the jet flow, which is nearly normal to the trailing edge. There is no prominent disturbance of the surface flow at either end of the slot. It is impressive that at the wing root the jet is detached on the fairing but strongly attaches to the Coanda surface within about 1.5 cm of the fairing. The inboard edge of the jet sheet must roll up into a vortex as evidenced by the print of the trailing vortex on the fairing after tunnel

shutdown. The wingtip flow is strongly entrained into the jet flow. Close post-run inspections of the oil flow at the outboard end of the slot revealed a trace of the onset of the trailing vortex that forms at the outboard edge of the jet sheet, as depicted in figure 1. The lower-surface view (fig. 8(b)) shows the location of the lower-surface flow separation caused by the Coanda separation. The oil streaks turn outboard forming an oil-flow separation line. At this blowing-pressure ratio of 1.8, which is before jet stall, the separated lower-surface and upper-surface flows come together in the downwash very close to the trailing edge, enclosing the separated region into a bubble-like flow (see interferograms and shadowgraphs in Wood and Nielsen, 1985).

The wingtip flow is seen in the top and bottom views from the left-side tunnel window (figs. 8(b) and (c)). The top- and bottom-surface flow is directed toward the tip. Therefore, the flow around the tip is similar to the flow on the lee side of an ellipsoid. Around the leading edge, the flow separates in a laminar separation line that extends back to the boundary-layer trips. Behind the trips the boundary-layer flow is turbulent so that the flow separates at a turbulent separation line that is located farther around the lee of the tip (most clear in fig. 8(c)). (For a circular body the laminar and turbulent separation lines are located about 90° and 140°, respectively, from the the windward crossflow stagnation line.) To the lee of the primary separation lines are the secondary separation lines. The tip-flow pattern is obviously asymmetric, so that this flow must contribute two asymmetric vortices to the tip flow field, in addition to the vortex at the outboard edge of the jet sheet starting at the end of the slot. The asymmetry of the tip vortices is probably affected by a change in angle of attack.

Figures 9 and 10 show oil-flow photographs for the case of $\alpha = 5°$ and $M_\infty = 0.425$ and 0.70. At this angle of attack it is more difficult for the jet to maintain attached flow on the upper surface. Fluorescent oil was injected through selected orifices. Instead of forming a narrow streak the oil spreads slightly. Figure 9 shows three views of the flow without blowing and with blowing pressure ratios of 1.2 and 1.3. At blowing pressure ratios up to 1.2, the flow separates ahead of the jet slot as indicated by the oil streaks turning outboard, but at a blowing pressure ratio of 1.3 the flow attaches because of the influence of the jet. The photographs also show that a leading-edge separation bubble exists at about 0.04 chord. The oil streak from the leading-edge orifice feeds oil into the bubble so that the oil flows spanwise in the bubble to the wing tip. If a similar oil streak is injected near the wing root, the full spanwise extent of the bubble would be revealed. This bubble is not revealed by smearing a film of oil at several places along the leading edge, although in other tests similar bubbles have been revealed by this method. The bubble exists at all pressure ratios tested. It is interesting that the bubble is located close to the point of tangency between the circular leading edge and the ellipse. Figure 10 shows that at $M_\infty = 0.70$ even a high blowing pressure ratio of 2.0 is not sufficient to induce the flow to attach.

Pressure Distributions

The measured pressure distributions were analyzed using the simple-sweep theory. Figure 11 illustrates the collapse of the section lift data for the swept and unswept configurations at the 70% spanwise location. Data for the swept configuration have been corrected using the standard equations to account for sweep on the angle of attack and dynamic pressure as previously stated. The correction to the dynamic pressure has also been introduced into the blowing momentum coefficient. It is clear that overall performance trends are repeated quite accurately, including jet-stall and α stall locations. The slight variations in the unblown lift curve slope were isolated to an effect of changing the location of the model in the wind tunnel working section for the two configurations. A large, static-pressure gradient was found to exist in the working section and was observed by a vertical shift of the presesure-coefficient distributions in the swept configuration. This is indicative of a change in the local static pressure at the measurement station.

The agreement between the swept and the unswept configurations was observed at each of the Mach number combinations that were tested. However, analysis of all the data shows that increases in the maximum lift coefficient were obtained at the highest Mach number (0.5 normal to the leading edge), the cause of which has not yet been isolated but is the subject of ongoing investigations.

Figure 12 illustrates the difference between the two configurations in terms of spanwise load distribution. For the unswept case, the wing is fairly uniformly loaded with a tip lift loss initiated at approximately 0.70 span (1 chord). For the swept configuration, an asymmetric loading is observed as is typical for a conventional swept wing. This asymmetry is a result of the changes in the downwash distribution caused by curvature of the bound vortices at the tip and root of the wing. Further analysis has recently shown that the downwash at the 0.70 spanwise station was identical for both the swept and unswept configurations, enabling the direct comparison of the section characteristics, as in figure 13. Also shown in figure 12 are the points at which jet stall was first observed (indicated by the dotted lines). While it is seen that the tip stalls first in the swept configuration for this set of conditions, this was not verified as a typical performance trend. it was observed, however, that jet stall appeared at the points of maximum downwash, which could be at any point on the span.

Figure 13 shows that the data are not significantly affected by the free-stream Mach number. The initial lift augmentation is defined as the slope of the lift coefficient vs. blowing momentum curve. The agreement is quite satisfactory for both the 0.70 (row 4) and 0.90 (row 5) spanwise stations. These data were taken at a fixed geometric angle of attack and the levels of lift augmentation are in good agreement with previous two-dimensional data.

A principal difference between swept and unswept wings is the induced downwash distribution. Recently, it has been shown that the induced angle of attack of a circulation-control airfoil may be deduced from examination of the variation of the mid-chord pitching moment with lift coefficient (Wood and Rogers, 1986). For a two-dimensional airfoil, the mid-chord pitching moment is decoupled from the lift as a

result of blowing and becomes a function of only the angle of attack. Thus, in figure 14, the slopes of the lines represent a combination of a change in angle of attack caused by tunnel interference and a change resulting from the imposed downwash distribution. For the unswept configuration, a trend of increasing downwash toward the tip is evident, while the trend is clearly reversed for the swept configuration. Since the variation of the mid-chord pitching moment with angle of attack is known, the actual downwash angles may be deduced. Results are given in figure 15. The unswept results are compared with a simple analysis based on a series expansion representation of the spanwise load distribution. The agreement is satisfactory and provides some confidence in the extension of the empirical technique to the swept configuration. Results for the swept case show a rotation of the distributions in a clockwise sense which indicates increased downwash at the root and decreased downwash at the tip. This trend was observed for all test conditions. It is also interesting to note the similarity in the downwash levels at the 0.70 spanwise location; this qualifies the agreement between the section lift data shown in figure 11.

CONCLUSIONS

A preliminary wind-tunnel investigation of the aerodynamics of a circulation-control, semispan wing model at two sweep angles was conducted at Mach numbers ranging from 0.3 to 0.75, angles of attack from -5° to +5°, and internal-to-external pressure ratios of 1.0 to 3.0. Conclusions from the pressure distributions at 0° and 45° sweep and photographs of oil-flow patterns at 45° sweep show:

1. The oil-flow tests at 0° angle of attack with no blowing show that the boundary layer separates just ahead of the slot.

2. With jet blowing, the wing-surface flow is attached and nearly streamwise away from the leading edge at a 45° sweep. There is no prominent flow disturbance at each end of the slot. The wingtip flow is strongly entrained into the outer jet flow. The lower-surface boudnary layer separates ahead of the Coanda-surface separation.

3. The wingtip flow pattern is similar to that of the lee side of an ellipsoid at a 45° angle of attack. An asymmetric vortex-separation pattern occurs with primary and secondary separation lines.

4. At a 5° angle of attack it is more difficult to attach the separated flow ahead of the slot with jet blowing at the lower speeds. At Mach 0.7, the flow cannot be attached at any blowing-pressure ratio.

5. When conventional corrections are applied at the 45° sweep position, no additional corrections are necessary to account for changes in blowing efficiency.

6. An empirical technique for estimating the downwash distribution of a swept wing has been validated with the swept-wing data and could be used to investigate three-dimensional effects on a circulation-control wing.

RECOMMENDATIONS

Further experiments are necessary on generic configurations to fully validate the use of simple-sweep theory. Configurations with both increased aft sweep angles and forward sweep angles need to be investigated over a range of slot blowing.

REFERENCES

1. Spaid, Frank W.; and Keener, Earl R.: Boundary-Layer and Wake Measurements on a Swept, Circulation-Control Wing. Circulation Control Workshop, NASA Ames Research Center, Feb. 18-20, 1986. NASA CP-2432, 1986. (Paper 11 of this compilation.)

2. Wood, Norman J.; and Conlon, John A.: The Performance of a Circulation Control Airfoil at Transonic Speeds. AIAA Paper 84-0083, Jan. 1983.

3. Wood, N. J.; and Nielsen, Jack N.: Circulation Control Airfoils Past, Present, Future. AIAA Paper 85-0204, Jan. 1985.

4. Wood, N. J.; and Rogers, E. O.: An Estimation of the Wall Interference on a Two-Dimensional Circulation Control Airfoil. AIAA Paper 86-0738CP, March 1986.

5. Wood, Norman J.; and Sanderfer, Dwight T.: Transonic Performance of Two Circulation Control Airfoils. NASA TM X-86767, 1986.

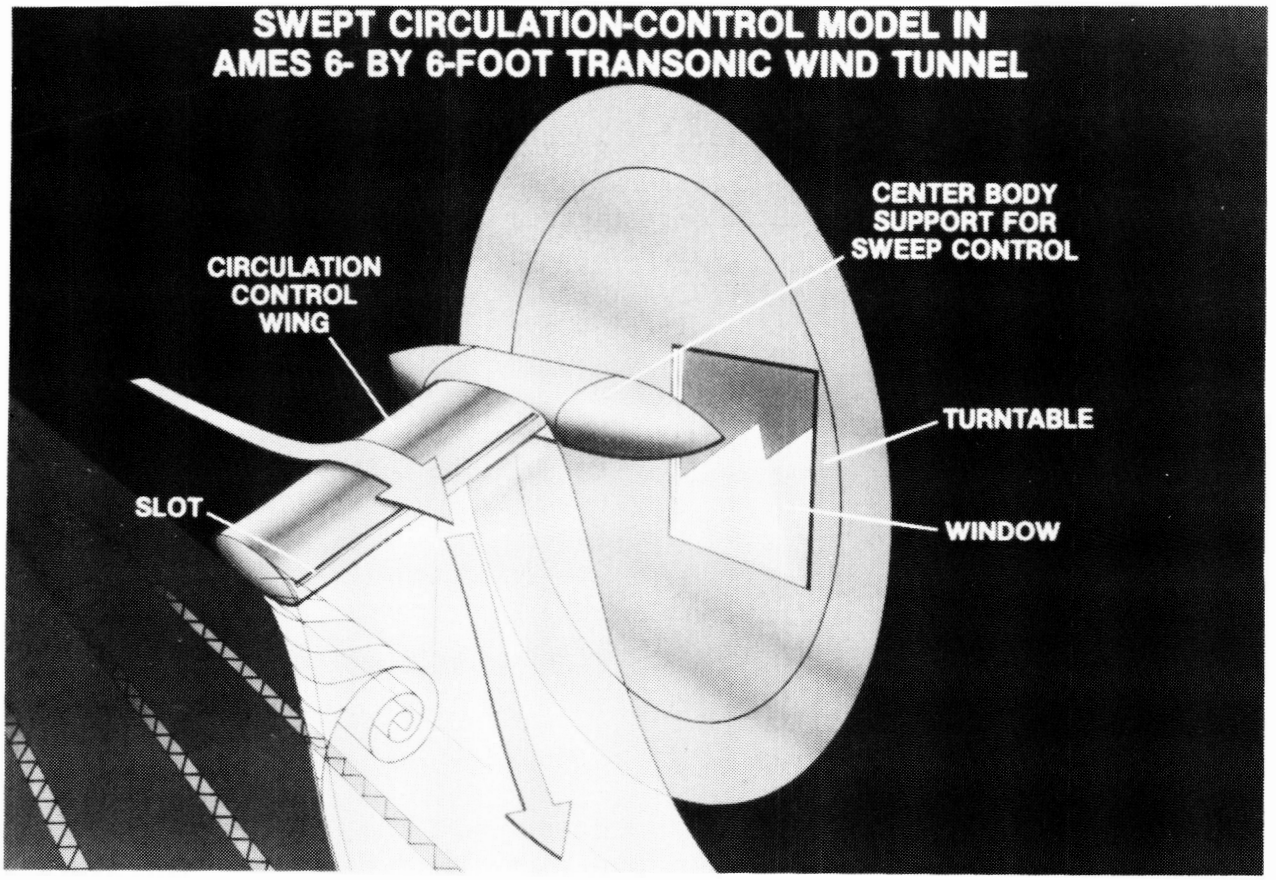

Figure 1.- Artist's view of model and flow field in Ames 6- by 6-Foot Transonic/Supersonic Wind Tunnel.

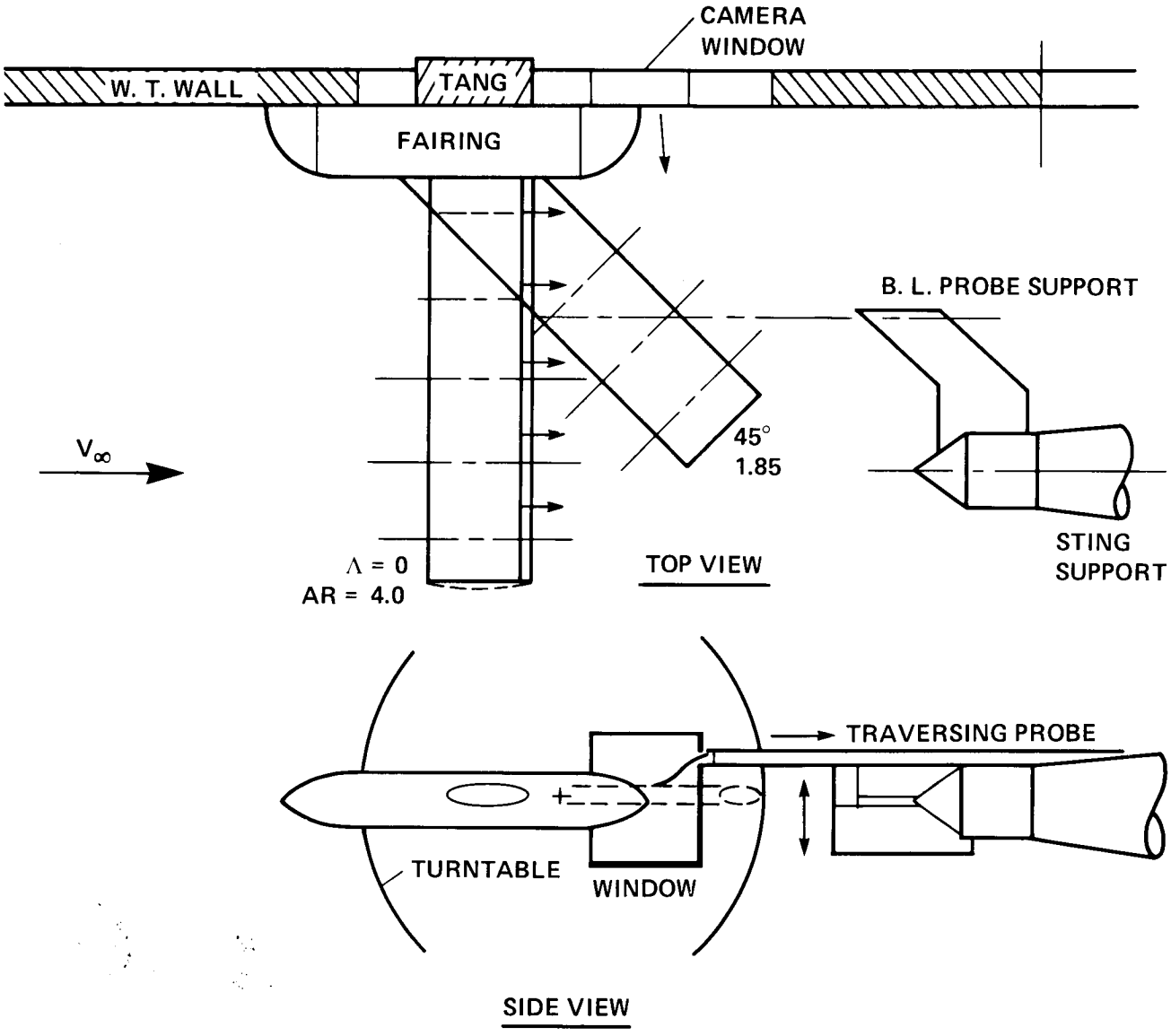

Figure 2.- Sketch of wing installation.

(a) 3/4 front view, sweep angle = 0°.

Figure 3.- Wing installation; sweep angle = 0°.

(b) 3/4 front view, sweep angle = 45°.

Figure 3.- Continued.

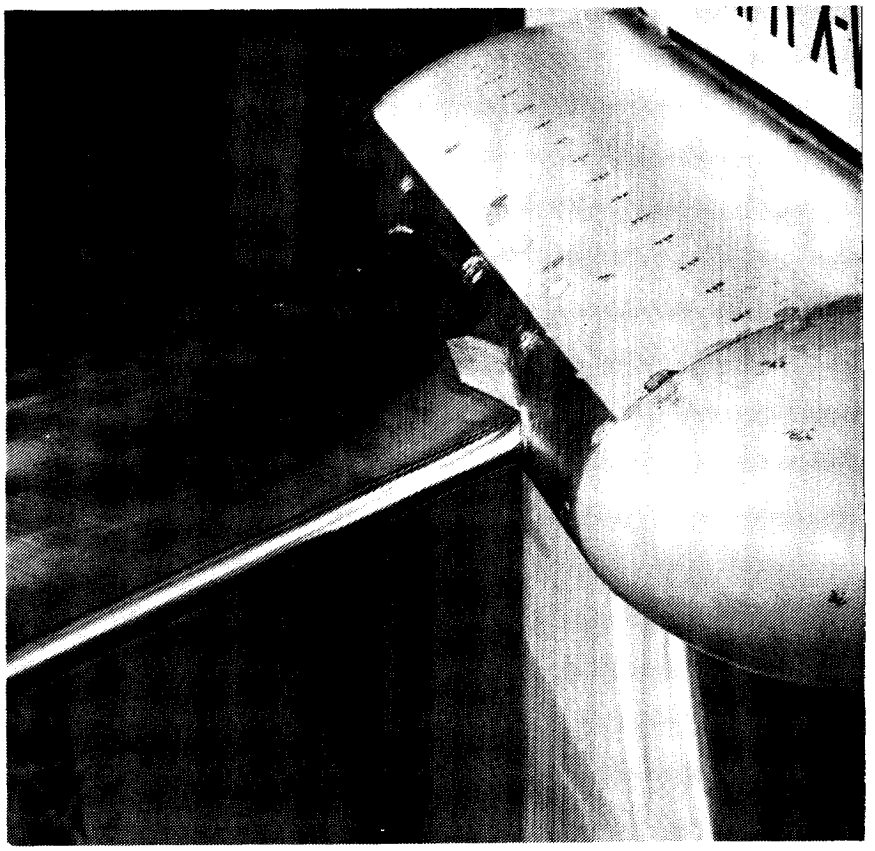

(c) Closeup-view of trailing-edge slot sweep angle = 45°.

Figure 3.- Concluded.

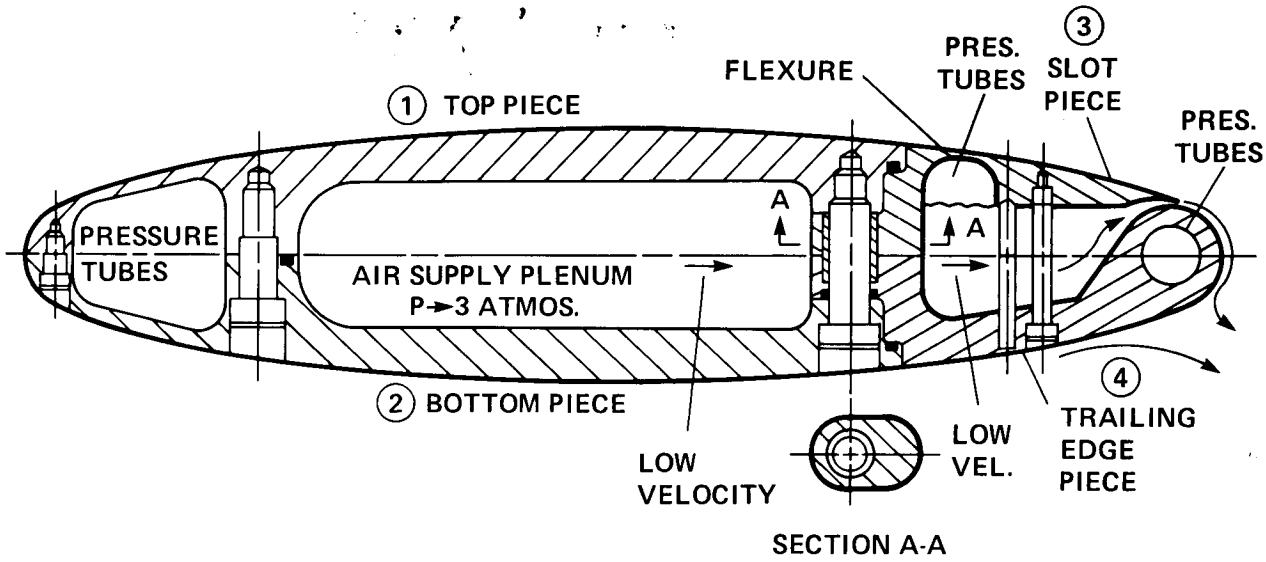

Figure 4.- Wing section showing four-piece construction, bolts setscrew, and adjusting screw for slot height.

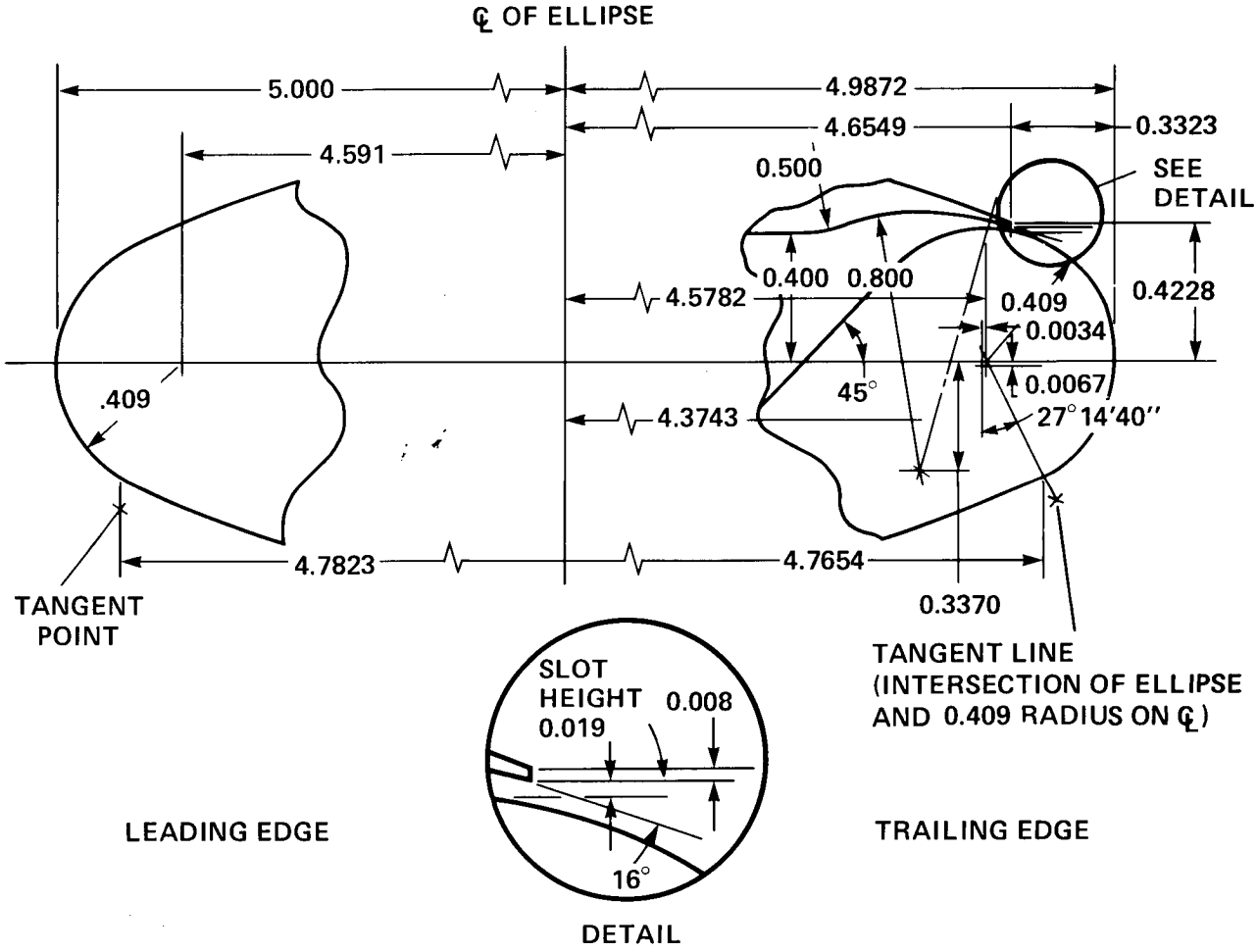

Figure 5.- Details of slot and trailing-edge design of the present model.

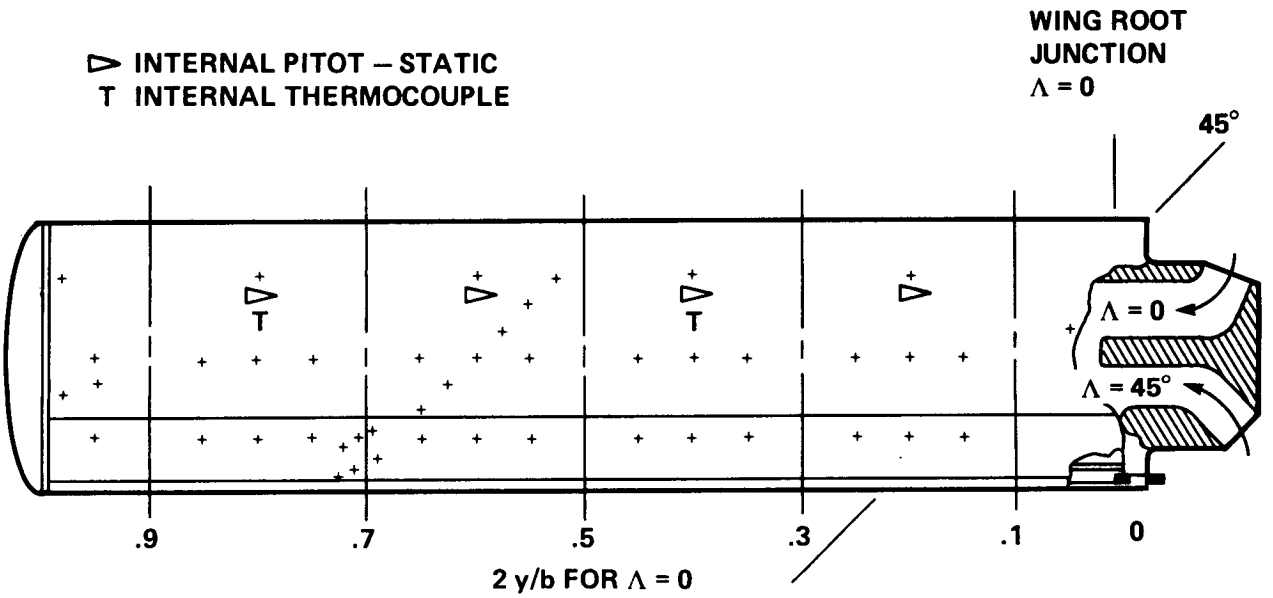

Figure 6.- Layout of static-pressure orifices on upper surface and air supply passage.

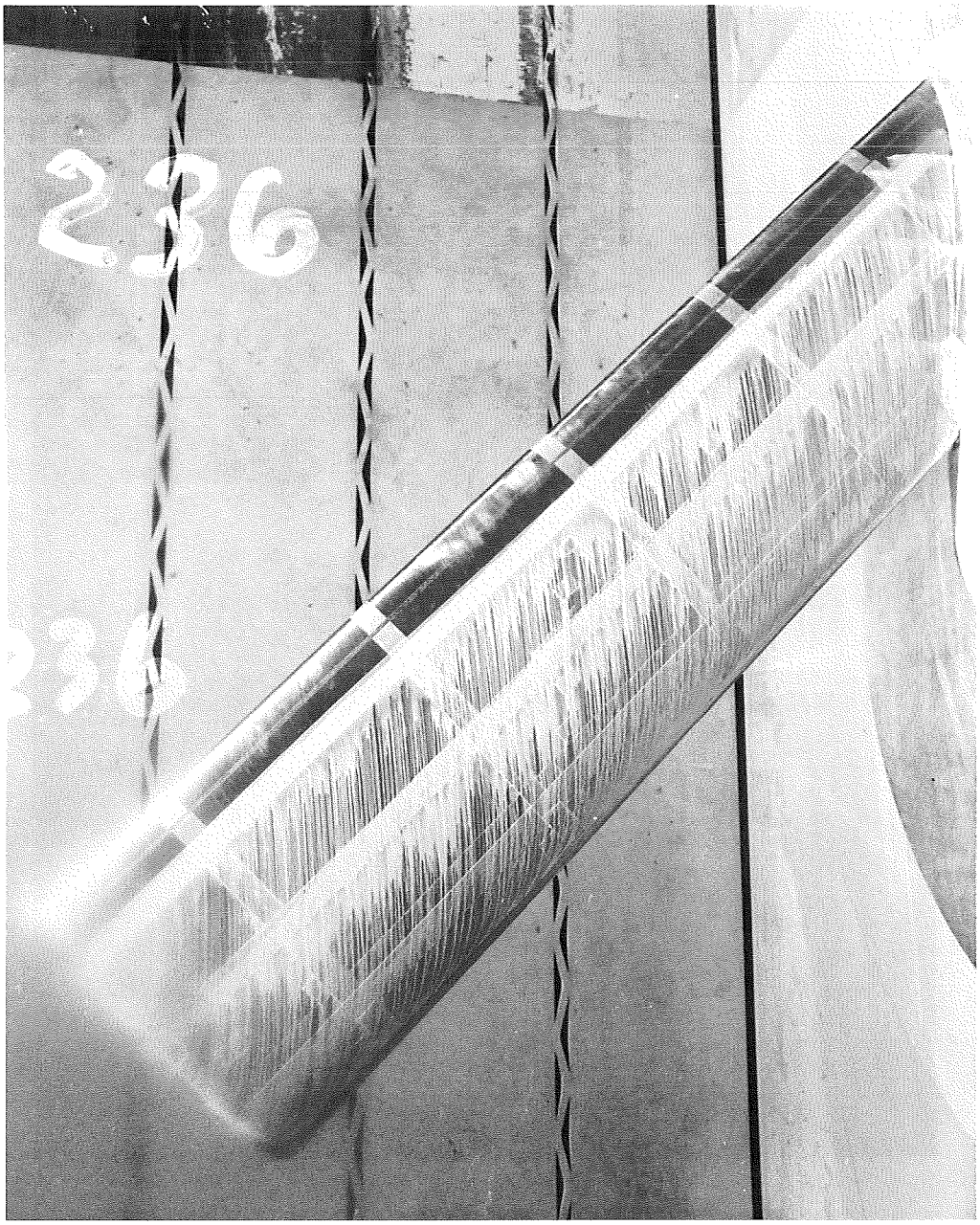

Figure 7.- Oil-flow photograph of upper-surface flow pattern with no jet blowing; $M = 0.425$, $\alpha = 0°$.

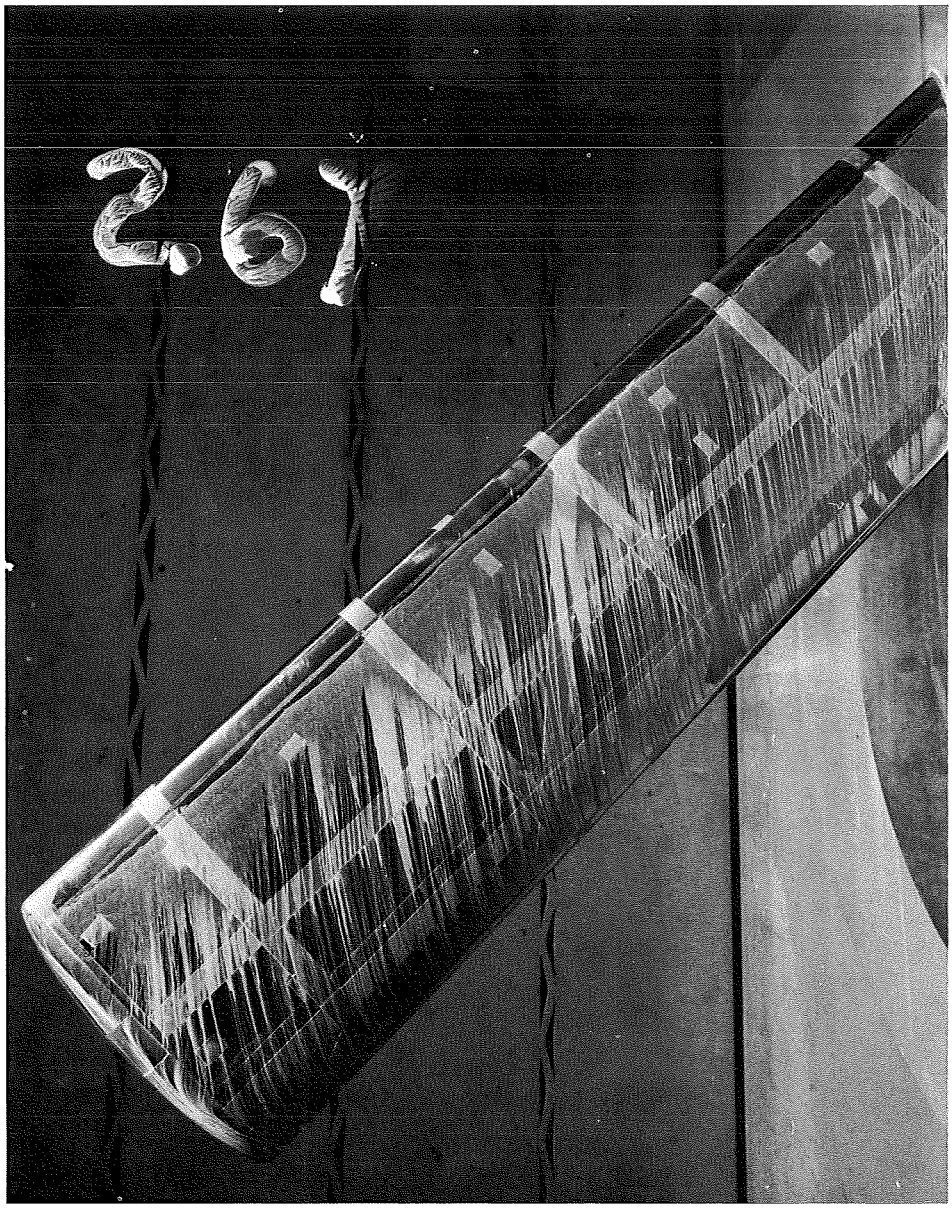

(a) Upper surface view.

Figure 8.- Oil-flow photographs of upper- and lower-surface flow patterns with jet blowing; M = 0.425, α = 0°, pressure ratio of 1.8.

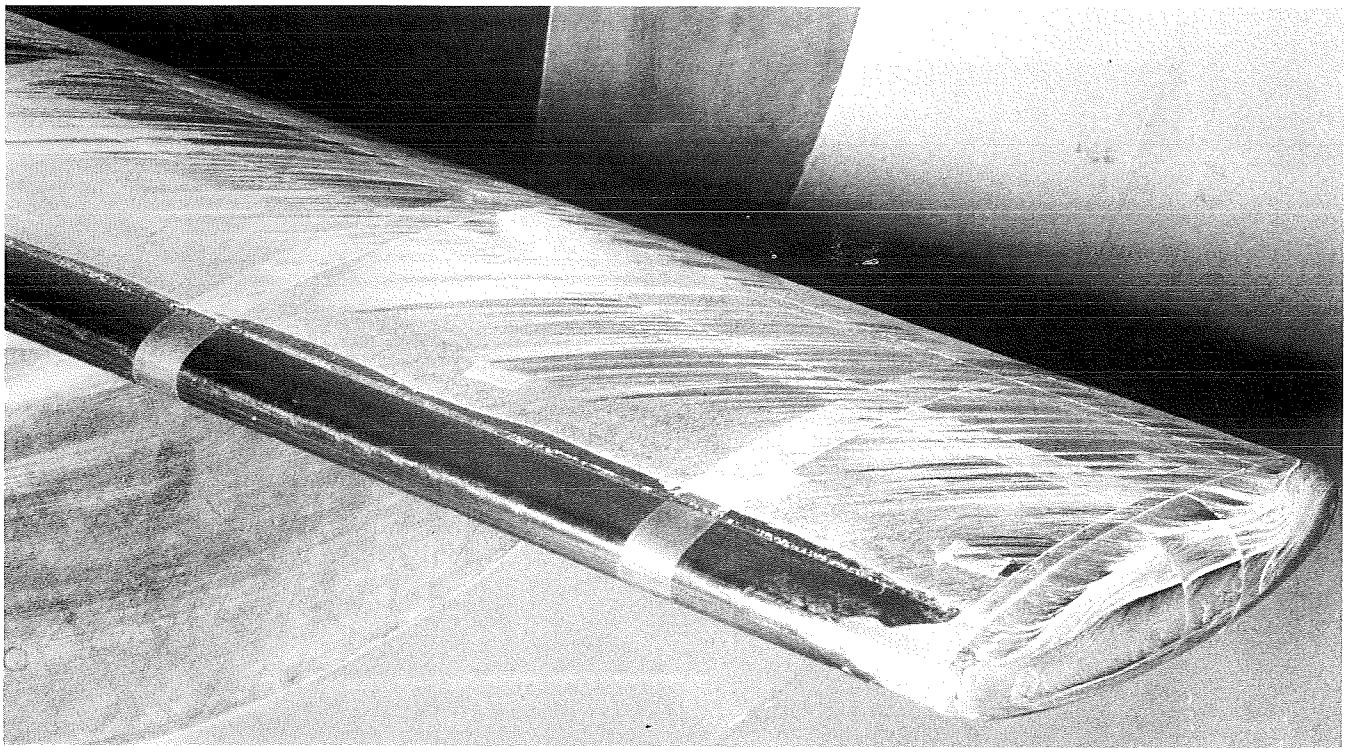

(b) Upper surface and end view.

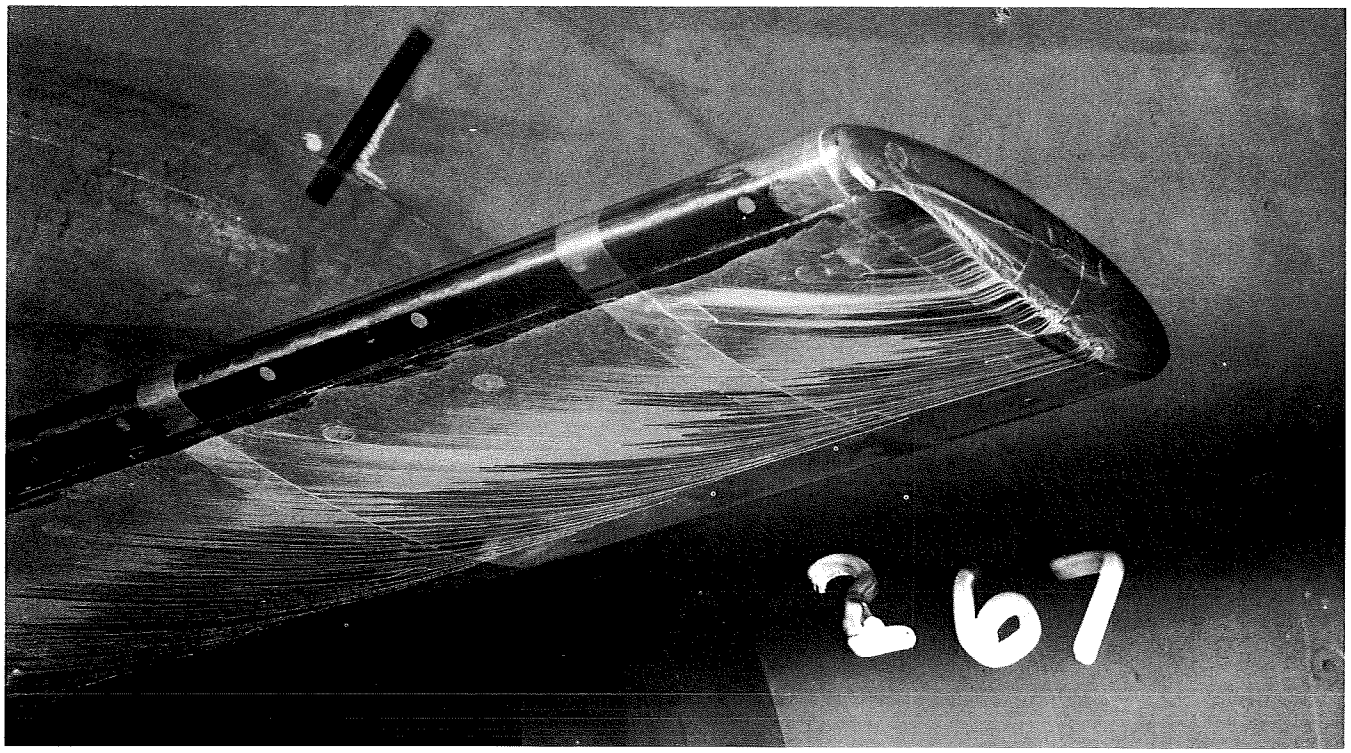

(c) Lower surface and end view.

Figure 8.- Concluded.

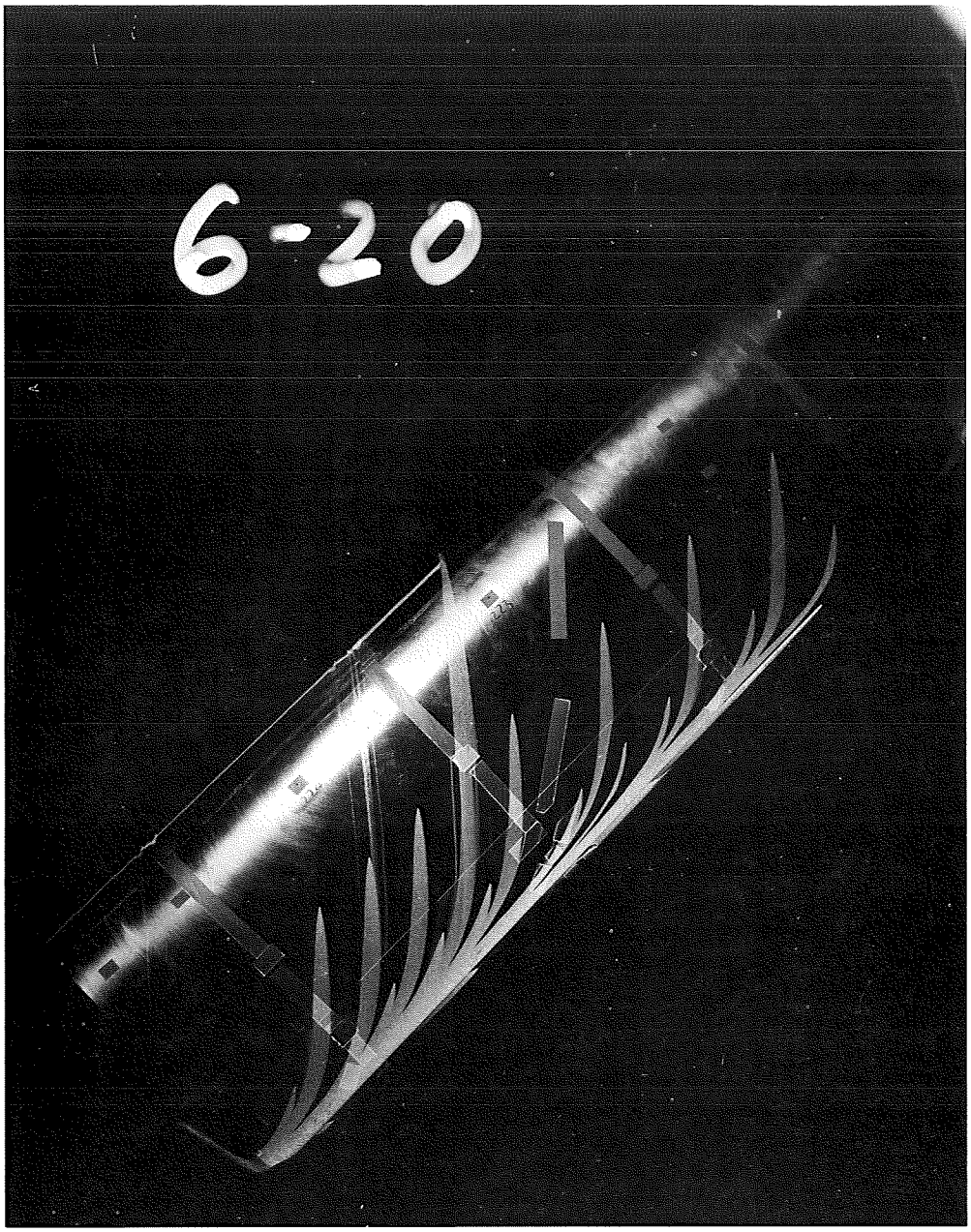

(a) pressure ratio of 1.0

Figure 9.- Oil-flow photographs of upper surface flow patterns at $\alpha = 5°$, $M = 0.425$.

(b) pressure ratio of 1.2

Figure 9.- Continued.

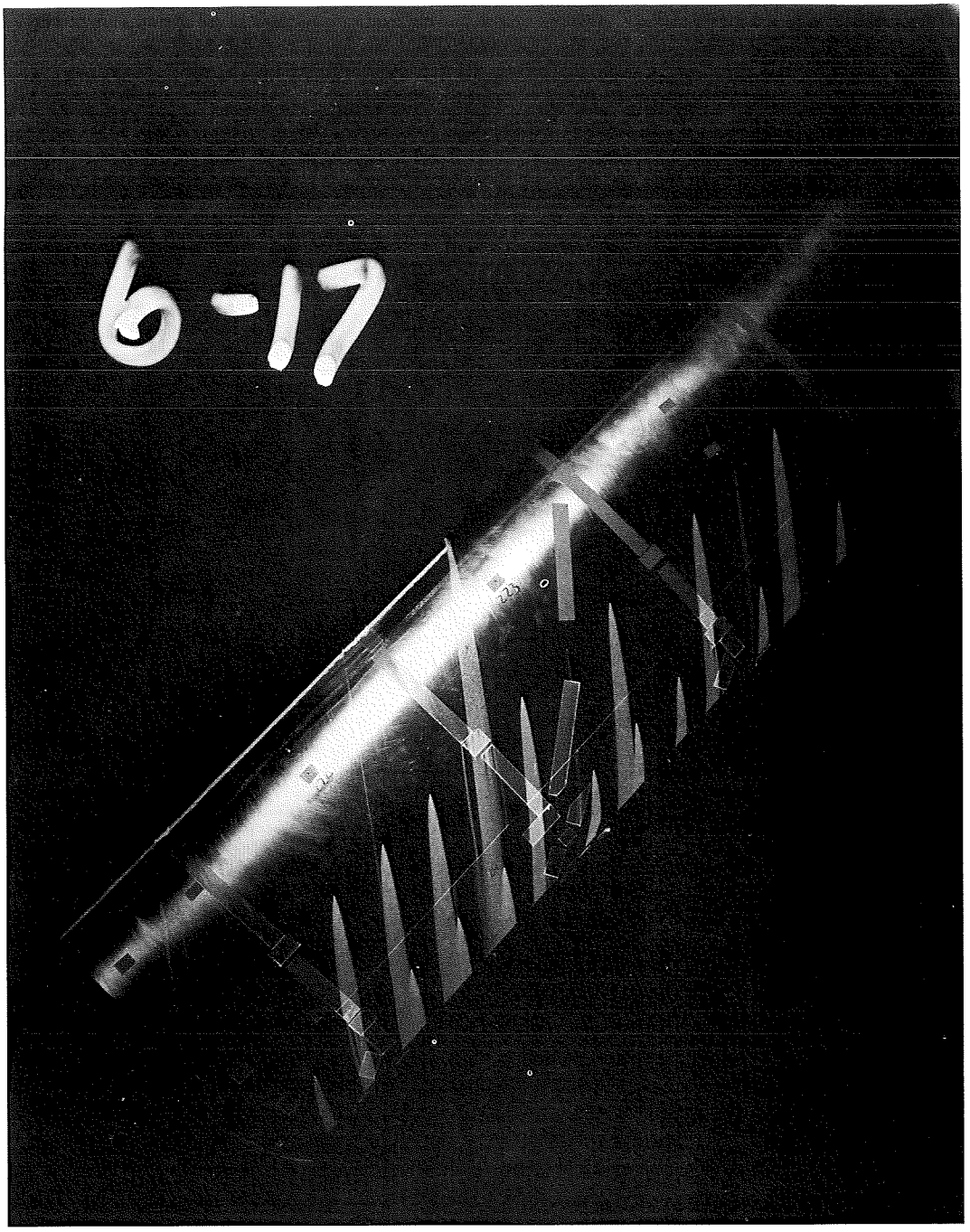

(c) pressure ratio of 1.3

Figure 9.- Concluded.

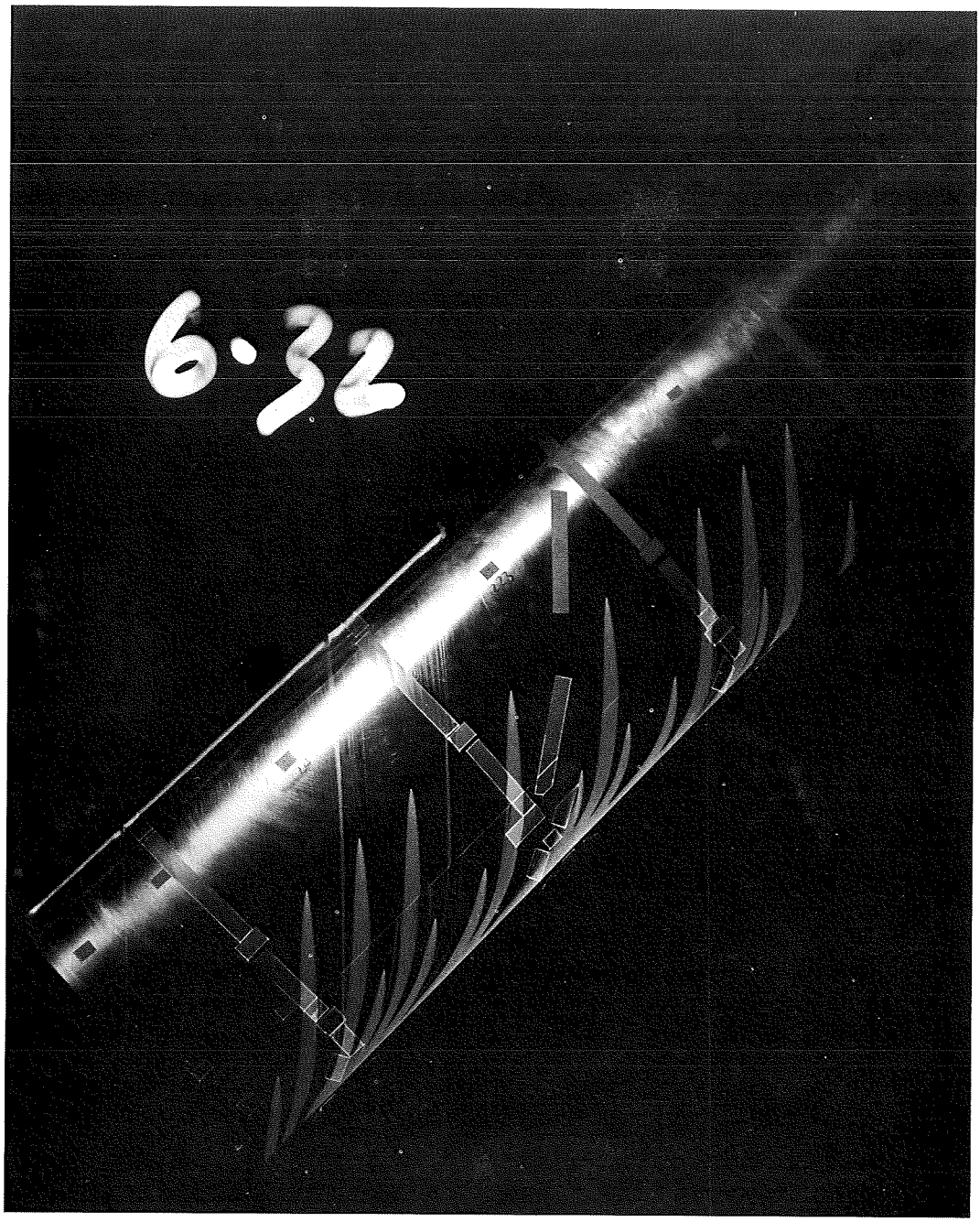

Figure 10.- Oil-flow photograph of upper-surface flow pattern at $\alpha = 5°$, $M = 0.70$, pressure ratio of 2.0.

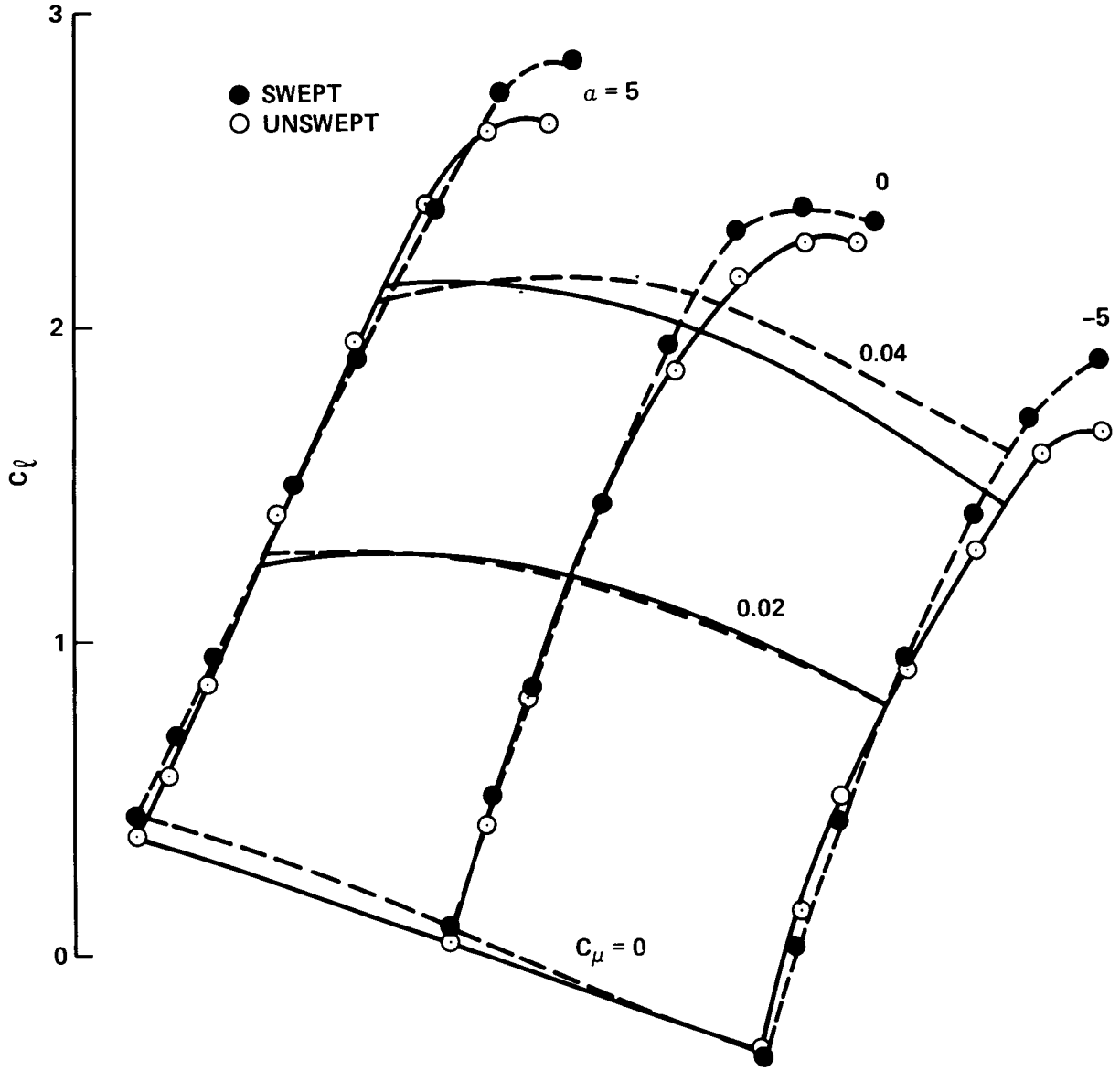

Figure 11.- Collapse of swept/unswept section-lift coefficient at M_∞ = 0.425 (swept)/M_∞ = 0.3 (unswept).

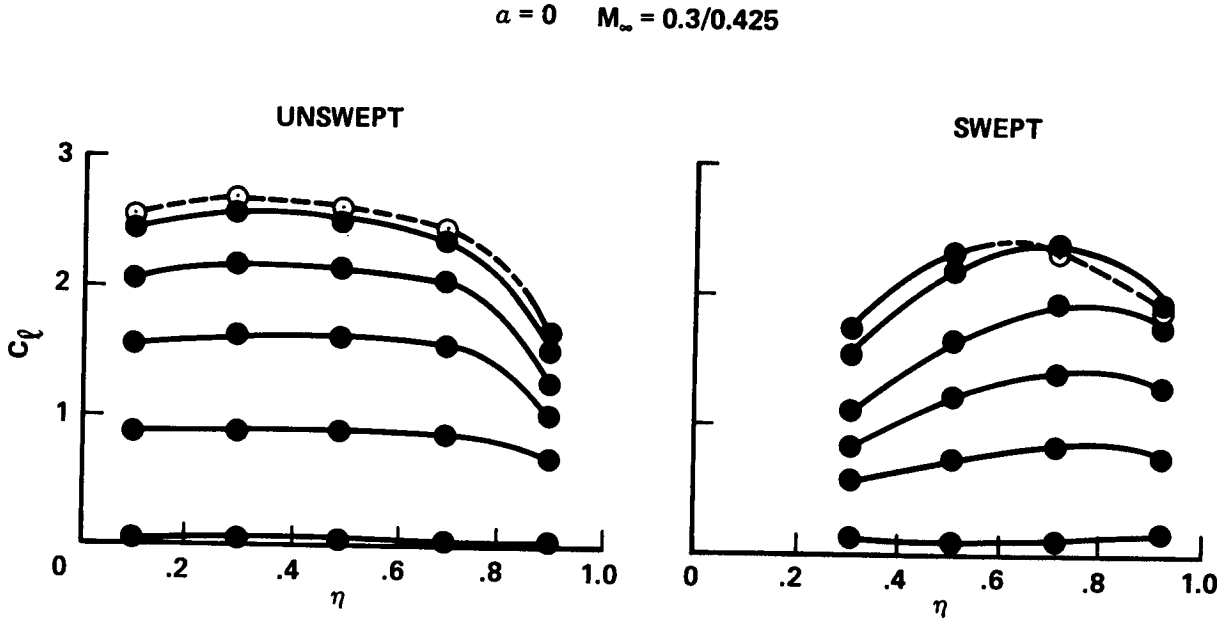

Figure 12.- A comparison of spanwise loading for swept/unswept configurations; $M_\infty = 0.425$ (swept)/$M_\infty = 0.3$ (unswept), $\alpha = 0°$.

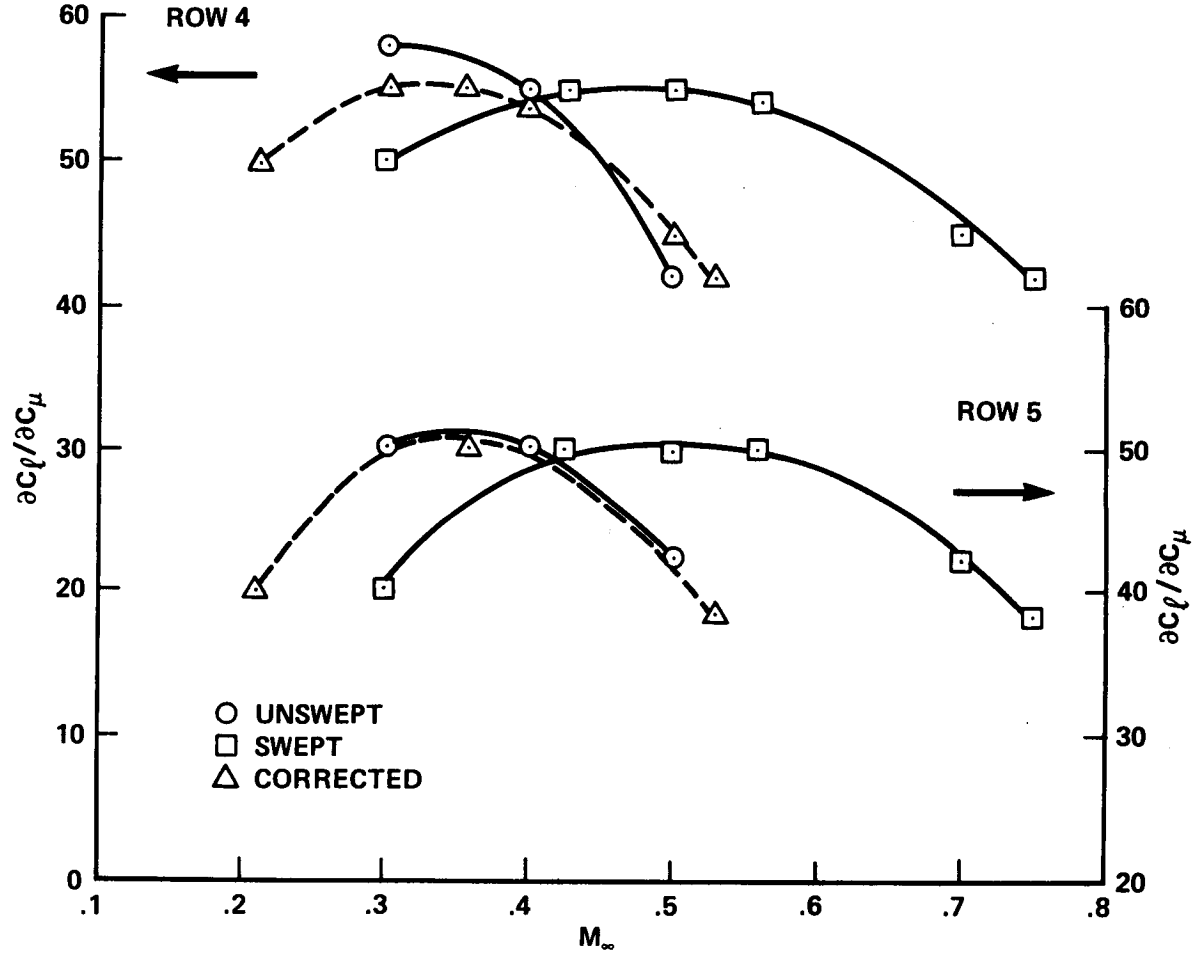

Figure 13.- A comparison of initial lift augmentations for swept/unswept configurations, $\alpha = 0°$.

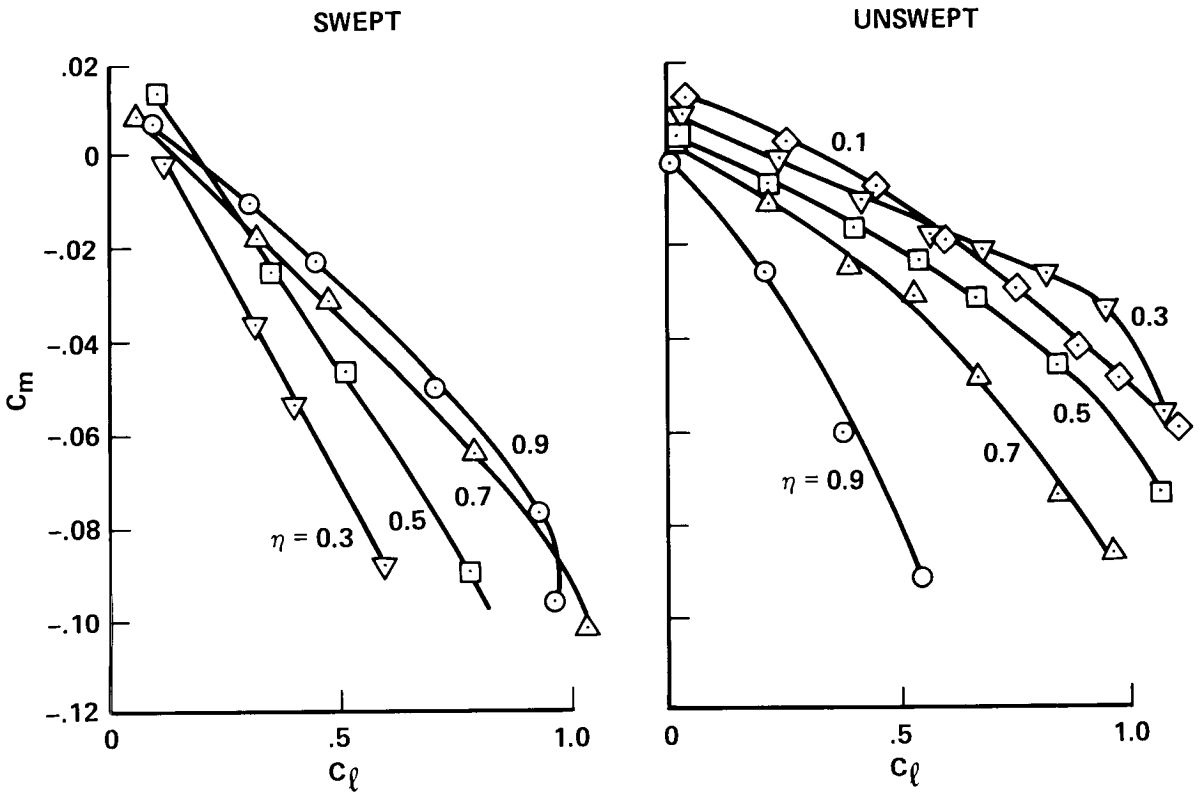

Figure 14.- Experimental results for the variation in mid-chord pitching moment with M_∞ = 0.425 (swept)/M_∞ = 0.3 (unswept), α = 0°.

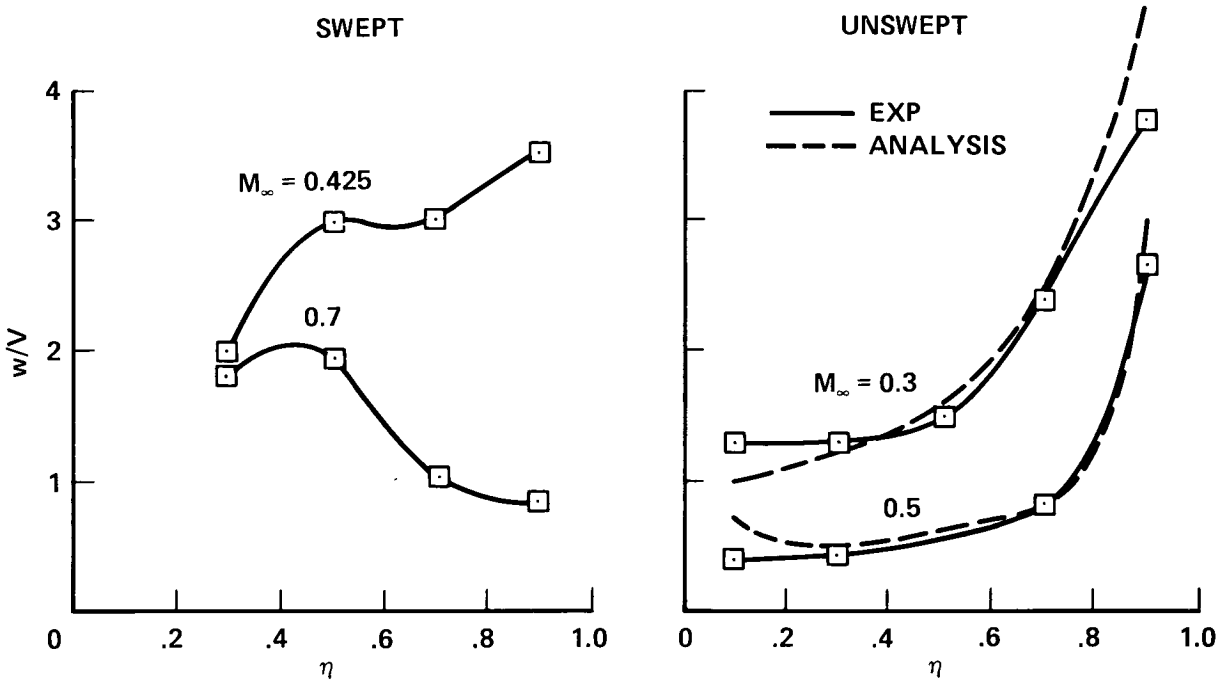

Figure 15.- Different downwash distributions for swept/unswept configurations, α = 0°.

BOUNDARY-LAYER AND WAKE MEASUREMENTS ON A SWEPT, CIRCULATION-CONTROL WING

Frank W. Spaid
McDonnell Douglas Research Laboratories

Earl R. Keener
NASA Ames Research Center

SUMMARY

Wind-tunnel measurements of boundary-layer and wake velocity profiles and surface static-pressure distributions are presented for a swept, circulation-control wing. The model is an aspect-ratio-four semispan wing mounted on the tunnel side wall at a sweep angle of 45°. The 25.4-cm constant-chord airfoil is a 20% ellipse, modified with circular leading and trailing edges of 4% radius. This configuration does not represent a specific shape from current vehicle design concepts which are being developed. A full-span, tangential, rearward-blowing, circulation-control slot is located ahead of the trailing edge on the upper surface. Flow surveys were obtained at mid-semispan at freestream Mach numbers of 0.425 and 0.70, Reynolds numbers based on streamwise chord of 2.3×10^6 and 3.2×10^6, angles of attack of 0° and 5°, and jet stagnation to freestream static-pressure ratios of 1.0 to 2.2. Boundary-layer profiles measured on the forward portions of the wing's upper and lower surfaces are approximately streamwise and two-dimensional. The flow in the vicinity of the jet exit and in the near wake is highly three-dimensional. The jet flow near the slot on the Coanda surface is directed normal to the slot, or 45° inboard. All near-wake surveys show large outboard flows at the center of the wake. At Mach 0.425 and a 5° angle of attack, a range of jet blowing rates was found for which an abrupt transition from incipient separation to attached flow occurs in the boundary layer upstream of the slot. The variation in the lower-surface separation location with blowing rate was determined from boundary-layer measurements at Mach 0.425.

*This research was conducted under the McDonnell Douglas Independent Research and Development Program in cooperation with the NASA Ames Research Center.

NOMENCLATURE

$b/2$ semispan

c streamwise wing chord

c_ℓ section lift coefficient

C_f local skin-friction coefficient, τ_w/q_e

C_p pressure coefficient, $(p-p_\infty)/q_\infty$

C_μ jet momentum coefficient, $m_j V_j/q_\infty S$

m_j jet mass-flow rate

M Mach number

p pressure

q dynamic pressure, $(1/2)\rho u^2$

Re_c Reynolds number based on chord

S wing area, defined as the product of the slot length and the wing chord measured normal to the section generators

u velocity magnitude

u_s component of velocity parallel to flow direction at edge of boundary layer

u_τ shear velocity, $\sqrt{\tau_w/\rho_w}$

V_j computed jet velocity assuming isentropic expansion from jet stagnation pressure to p_∞

x coordinate measured parallel to freestream direction

y spanwise coordinate

z coordinate normal to wing plane

z^+ law-of-the-wall coordinate, $(zu_\tau)/\nu_w$

α wing angle of attack

β yaw-plane flow direction angle, positive outboard

δ_1^* streamwise displacement thickness, $\int_0^\delta \left(1 - \frac{\rho u_s}{\rho_e u_e}\right) dz$

ν kinematic viscosity

ρ density

σ pitch-plane flow direction angle, positive upward

τ_w wall shear stress

Subscripts

e conditions at edge of boundary layer

j jet parameter

w conditions at surface

∞ freestream conditions

INTRODUCTION

There are several ways to control the aerodynamic circulation of wings and thus, the amount of lift. One type of circulation control that is currently under investigation is tangential blowing from a slot located ahead of a rounded trailing edge. The tendency of the flow to adhere to the trailing-edge surface is known as the Coanda effect. The deflected flow can increase the lift of a wing section to several times that obtained by the conventional method of increasing the angle of attack. Wood and Nielsen (1985) present a summary of circulation-control research.

A cooperative investigation of the boundary layer and wake of a swept, circulation-control wing was recently conducted by NASA Ames Research Center and McDonnell Douglas Research Laboratories in the Ames Six- by Six-Foot Transonic Wind Tunnel. The test was conducted in support of the NASA X-Wing stopped-rotor research vehicle, which is designed to cruise at high speed with the rotor stopped in the X-wing configuration (Wood and Nielsen, 1985). The model is an aspect-ratio-four semispan wing mounted on the side wall. The 25.4-cm constant-chord airfoil is a 20% ellipse, modified with circular leading and trailing edges. This generic configuration does not represent a specific shape from current vehicle design concepts which are being developed. A full-span, tangential, rearward-blowing circulation-control slot is located ahead of the trailing edge on the upper surface. The wing was tested at Mach numbers from 0.3 to 0.75 at sweep angles of 0° and 45° with internal-to-external pressure ratios of 1.0 to 3.0. Lift and pitching-moment coefficients were obtained from measured pressure distributions. Surface-flow patterns were photographed using the oil-streak flow-visualization method.

This paper presents the results of the boundary-layer and wake measurements at Mach numbers of 0.425 and 0.70 at 45° sweep angle. The pressure measurements and oil-flow photographs are presented by Keener et al. (1986).

TEST FACILITY

The Ames Six- by Six-Foot Transonic/Supersonic Wind Tunnel was chosen because the allowable model size and the tunnel operational characteristics are suitable for boundary-layer research. The tunnel is a variable-pressure, continuous-flow facility. The nozzle leading to the test section is of the asymmetric sliding-block type that permits a continuous variation of Mach number from 0.25 to 2.3. The test section has a slotted floor and ceiling with 6% porosity and provisions for boundary-layer removal. The turbulence level is measured to be about 1.5% rms of the freestream velocity.

MODEL

Details of the model design are given by Keener et al. (1986). The model is a semispan wing incorporating circulation control by tangential blowing from a spanwise slot located ahead of a rounded trailing edge. The model was mounted on the sidewall of the tunnel on a turntable that could be manually rotated through a ±5° range in angle of attack. The wing-root mounting structure is covered by a fairing. Figure 1 is a sketch of the model installation in the tunnel showing the zero- and 45° sweep positions. The resulting aspect ratios are 4.0 and 1.85, respectively, based on the normal component of the exposed span. The sketch also shows the position of the boundary-layer traversing unit, which was mounted on a bracket attached to the tunnel center-body support. Figure 2 shows views of the model in the 45° sweep position and the boundary-layer traversing unit.

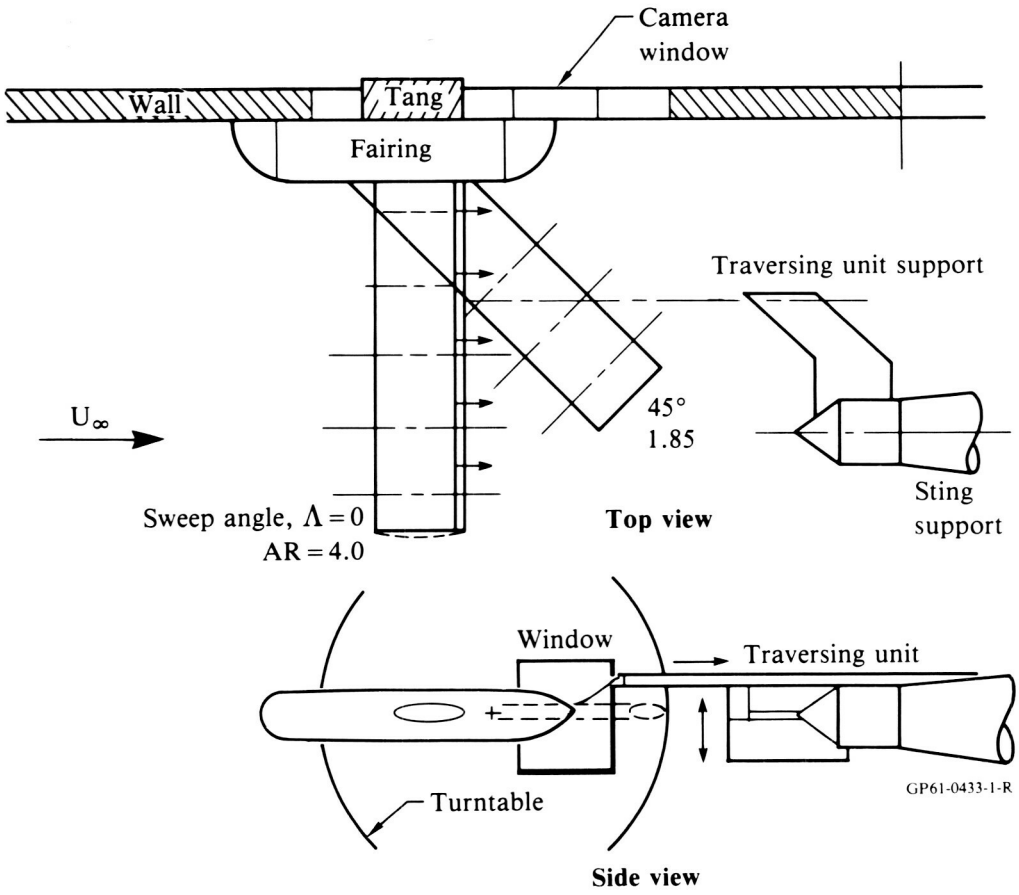

Figure 1. Sketch of model and traversing unit installation.

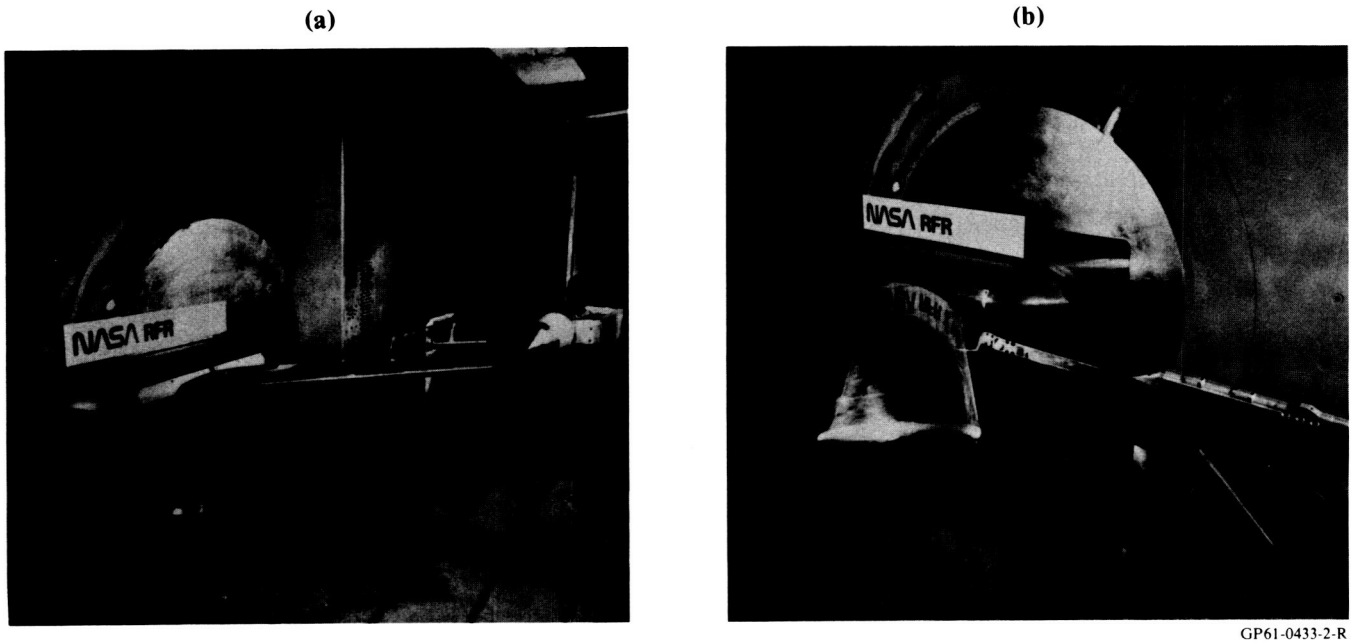

Figure 2. Wing model at a sweep angle of 45° and probe traversing unit.

The wing has a 20% elliptical section and a 25.4-cm constant chord, modified with circular leading and trailing edges of 4% radius (figure 3). A full-span, tangential, rearward-blowing, circulation-control slot, with a nominal slot height of 0.0020 chord and a trailing-edge thickness of 0.0008 chord, was incorporated ahead of the trailing edge on the upper surface.

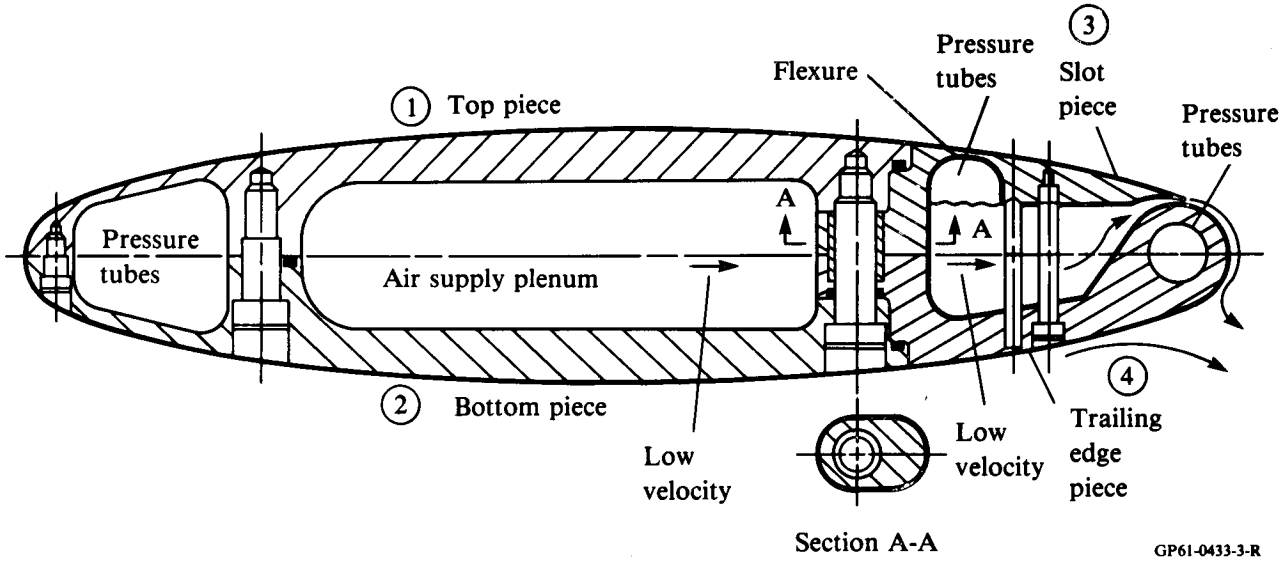

Figure 3. Sketch of wing section showing four-piece construction, bolts, set screw, and adjusting screw for slot height.

Design suggestions based on experience with previous circulation-control tests were contributed by N. Wood, Stanford Institute for Aeronautics and Aeroacoustics, and by E. Rogers and J. Abramson, David W. Taylor Naval Ship Research and Development Center. Publications from their research are discussed in the review paper by Wood and Nielsen (1985). The model design follows closely the design concepts of Wood and Conlon (1983), and Wood and Sanderfer (1987).

The model was designed in four parts (figure 3), split along the plane of symmetry. The center of the model contains an internal plenum, which was connected to the external air supply at the wing root through the sidewall of the tunnel. The air supply was provided from the tunnel 550-kPa dry-air sphere. The air flow was controlled by a regulator to set the total pressure in the wing plenum. The design of the trailing-edge Coanda surface and slot is described by Keener et al. (1986).

INSTRUMENTATION AND DATA REDUCTION

Details of the pressure instrumentation are given by Keener et al. (1986). The pressure instrumentation consisted of 252 orifices on the wing, installed at five spanwise stations (rows 1 to 5: $2y/b = 0.1$, 0.3, 0.5, 0.7, and 0.9, based on the exposed span at zero sweep) and one row of orifices at the midspan of the wing-root fairing (figure 4). More orifices were placed at row 4, $2y/b = 0.7$, especially over

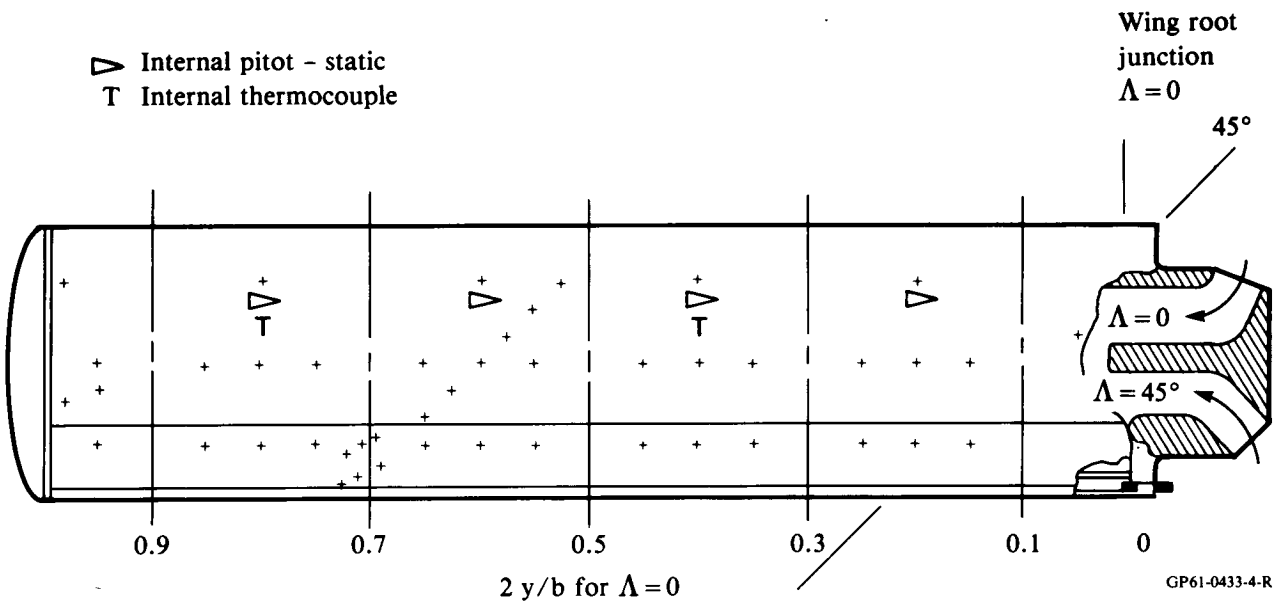

Figure 4. Layout of wing static-pressure orifices.

the trailing edge, in order to obtain more detail at one row. Additional orifices were placed at row 6 at a 45° angle between rows 3 and 4 (2y/b = 0.5 and 0.7) to assist in the analysis of the pressures at a sweep angle of 45° and to provide a row of orifices near the location of the upper-surface boundary-layer measurements.

The surface static pressures were measured with electronically actuated pressure-scanning valves containing pressure transducers that were connected to an automatic data-recording system. The self-calibrating feature of the scanning valves provided an accuracy of about 0.25% of full scale of the ±86.2-kPa transducers, providing an accuracy in pressure coefficient of approximately ±0.01. Tunnel test conditions were measured with precision pressure transducers, resulting in a Mach number accuracy of about ±0.002. Tunnel static pressure was measured on the tunnel wall 10 wing-chord lengths ahead of the wing-root leading edge. Angle of attack was set manually by rotating the wall turntable and setting the angle with an inclinometer with an accuracy of ±0.03°.

Static-pressure measurements were reduced to standard pressure coefficients by use of the tunnel conditions which were measured at the beginning of each data set. The data were recorded, processed, and plotted by the tunnel data-acquisition system. Pressure coefficients for each spanwise station were numerically integrated by the trapezoidal rule to determine wing-section normal-force and pitching-moment coefficients. Wing-panel normal-force, pitching-moment, and bending-moment coefficients were determined by Simpson's-rule numerical integration of the span-load distributions. Jet total mass flow was determined from a calibrated orifice plate mounted in the air supply line. The jet velocity was calculated using the freestream static pressure as the jet-exhaust pressure.

The traversing unit shown in figures 1 and 2 contains stepper motors that allow remote movement of the probe tip in the streamwise and vertical directions; the probe location is determined with the aid of encoders. Streamwise position resolution is 0.087 mm per encoder pulse, and vertical resolution is 0.0052 mm per encoder pulse. A

microcomputer-based probe control system allows manual operation of the unit and also provides an automatic mode in which data are obtained in a preprogrammed sequence of probe movements and data-acquisition cycles. The wing surface was located by electrical contact between the wing and the probe tip at the beginning of a boundary-layer survey. The probe tips used for most boundary-layer surveys are small, flattened, three-hole probes; the wake surveys and some wall-jet surveys (flowfield surveys above the Coanda surface) were made with a small five-hole probe. Sketches of the probes are shown in figure 5. The tip of the five-hole probe was inclined upward 15°, to reduce its flow interference in the wake downwash. To reduce flow interference and minimize flow angle and stagnation-pressure measurement errors, the three-hole probes were adjusted in pitch angle so that the tips were nearly parallel to the wing surface. The probes are similar to those described by Dudzinski and Krause (1969).

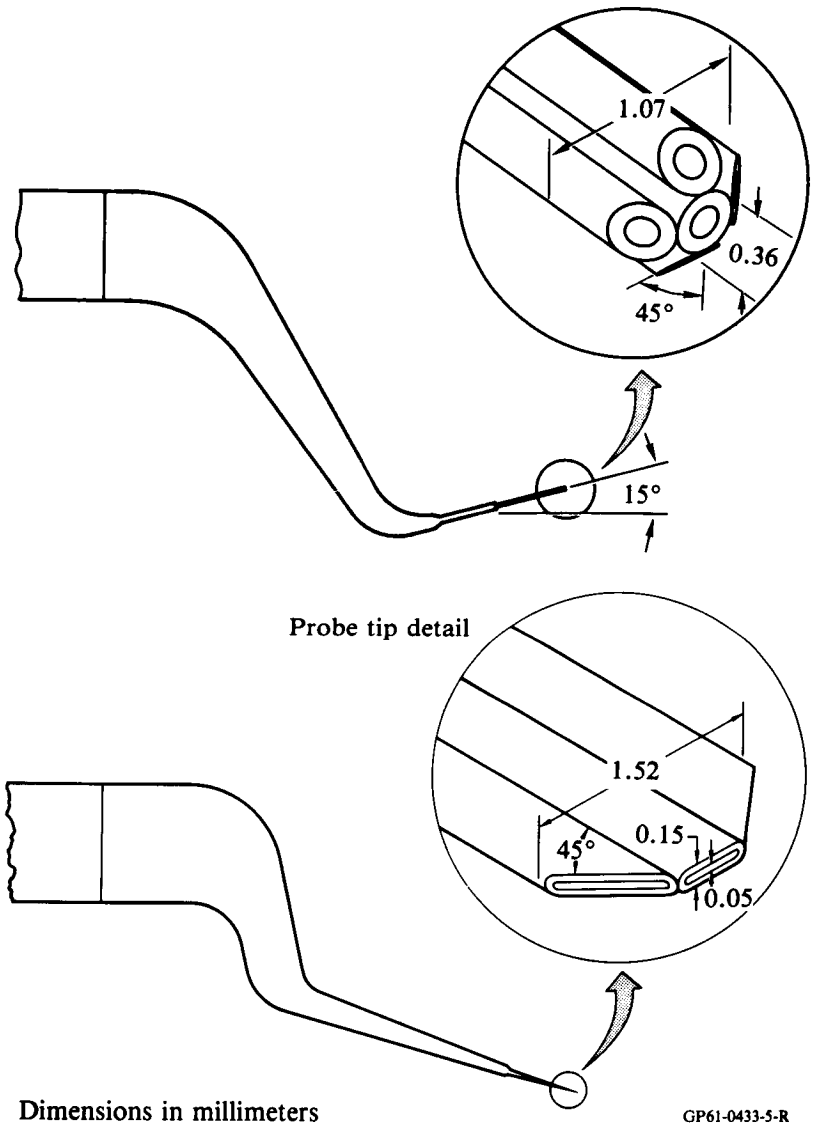

Figure 5. Three- and five-hole probes.

A pressure transducer was connected to each probe orifice through a fluid switch. Data for a two-point calibration of each transducer were obtained by cycling the switch at the beginning and end of each boundary-layer survey. The accuracy of individual probe pressure measurements was estimated to be ±0.15 kPa, corresponding to approximately ±1.3% and ±0.6% of freestream dynamic pressure at Mach 0.425 and 0.70, respectively. Probe pressure errors were estimated by root-mean-square combination of estimated errors resulting from uncertainties in reference and calibration pressures, nonlinearity and hysteresis of the transducers, and the recording resolution of the microcomputer.

Probe calibrations were performed in a free-jet calibration facility, following the procedures outlined by Dudzinski and Krause (1969). Probe-angle-measurement accuracy was ±0.1°, and accuracy of pressure measurement was estimated to be ±0.15 kPa, as before. Calibrations were performed at six Mach numbers, ranging from 0.25 to 1.0. Three-hole-probe calibrations were performed over an angle range of ±40° in the yaw plane, and five-hole-probe calibrations were performed over a range of ±40° in the pitch plane and +60° to -40° in the yaw plane, relative to the probe tip. Probe readings corresponding to the freestream flow direction were determined in the wind tunnel by taking probe data at a position approximately 0.7 m above the wing, with the wing at 0° angle of attack, and a low jet-blowing rate, to stabilize the wing wake. In reducing the three-hole-probe data, stagnation-pressure corrections and angles were determined from the probe data alone, since this can be done accurately without knowledge of the local static pressure. Mach number and velocity profiles were computed from the three-hole-probe data with the aid of the local static pressure interpolated from the surface-orifice data. Pitot pressure, flow angles, and static pressure were determined from the five-hole-probe measurements. A search and interpolation procedure, in which the local Mach number was explicitly included as an independent variable, was performed on the entire probe-calibration data base.

TEST CONDITIONS AND PROCEDURES

The wing pressures were first measured without boundary-layer trips at $M_\infty = 0.70$ at zero sweep. Next, boundary-layer trips were installed on the wing by use of sifted glass spherules at 9% chord. Sublimation flow-visualization tests were made at a Mach number of 0.70 to verify that the estimated trip size of 0.23-mm diameter was adequate to cause transition. When the wing was swept to 45°, a sublimation test verified that the trips were also effective at this angle.

Flow surveys were obtained at freestream Mach numbers, M_∞, of 0.425 and 0.70, Reynolds numbers based on streamwise chord, Re_c, of 2.3×10^6 and 3.2×10^6, angles of attack, α, of 0° and 5°, and ratios of jet stagnation to freestream static pressure, p_j/p_∞, of 1.0 to 2.2. The Mach numbers 0.425 and 0.70 correspond to the Mach numbers 0.30 and 0.50 at zero sweep, determined from simple sweep theory, $M_\infty/\cos 45°$. Performance data corresponding to both the swept and unswept conditions are presented by Keener et al. (1986). Boundary-layer surveys were made at one span station starting at about 20% chord at static-pressure orifice row 3, back to near the trailing edge outboard of row 4, on both upper and lower surfaces (figure 4). Wake surveys were obtained in a region 1% to 30% chord downstream of the trailing edge.

Oil-flow-visualization tests were made at both sweep angles at several Mach numbers to assist the analysis of the pressure and boundary-layer measurements (Keener et al, 1986).

RESULTS AND DISCUSSION

Three static-pressure distributions corresponding to test conditions for which probe data were obtained are shown in figure 6. The upper-surface data were obtained from the diagonal row of orifices located at the spanwise survey station, and the lower-surface data were interpolated to that station from the adjacent chordwise orifices. Blowing rates are indicated both by p_j/p_∞, and by the momentum coefficient, C_μ, the jet momentum flux normalized by the freestream dynamic pressure and the wing area. The corresponding section lift coefficient, c_ℓ, is also shown. Pressure distributions corresponding to the two values of blowing are characterized by weak suction peaks at the leading edge, near-zero pressure gradients at mid-chord, and large suction peaks on the upper surface downstream of the jet. The flow is locally supersonic in this region at the higher blowing rate; the minimum value of C_p is -4.75 (not shown).

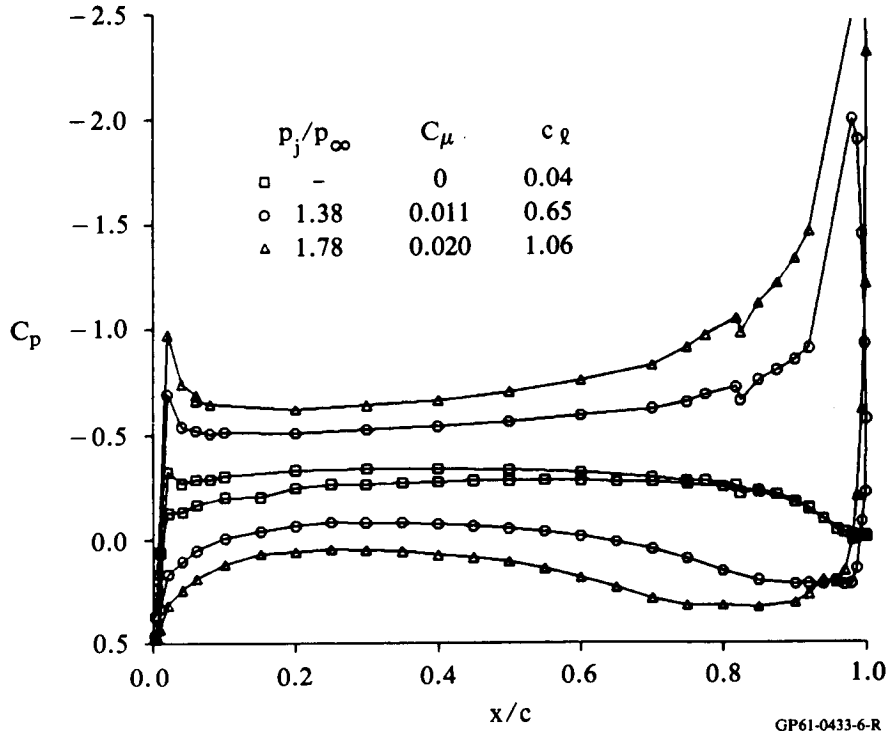

Figure 6. Wing static-pressure distributions at mid-semispan; $M_\infty = 0.425$, $Re_c = 2.27 \times 10^6$, $\alpha = 0°$.

Figures 7 and 8 are composite views in the streamwise section plane of the aft portion of the model, including the slot inlet, and the surrounding flowfields. This style of presentation is used in several of the subsequent figures to help clarify the qualitative features of these complex three-dimensional flows. The velocity vectors are projections in the streamwise plane, and the vector labeled u_∞ in the upper left corner of both figures corresponds to the freestream velocity. The boundary-layer profiles were obtained with a three-hole probe, and the vectors are drawn parallel to the local surface. The wake profiles and the wall-jet profile (the flow survey above the Coanda surface downstream of the jet exit station in figure 8) were obtained with a five-hole probe, and are drawn at the measured inclination angle.

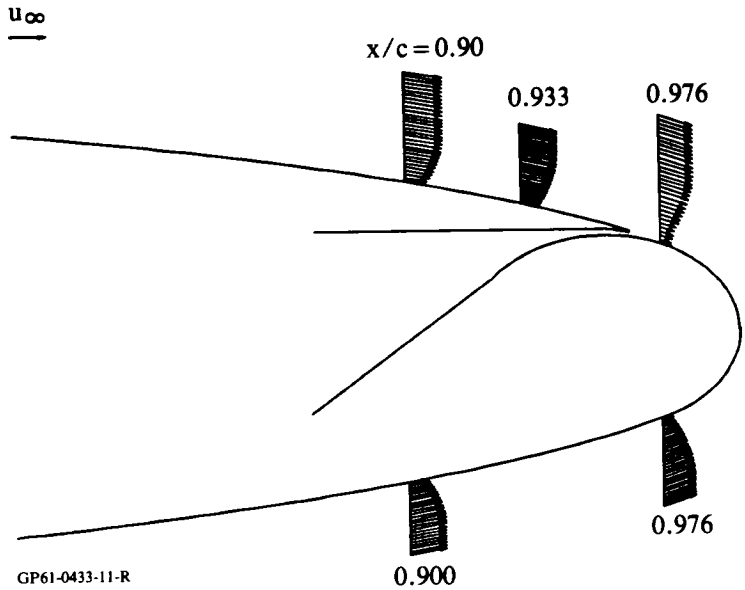

Figure 7. Velocity components in streamwise section plane; $M_\infty = 0.425$, $\alpha = 0°$, no blowing.

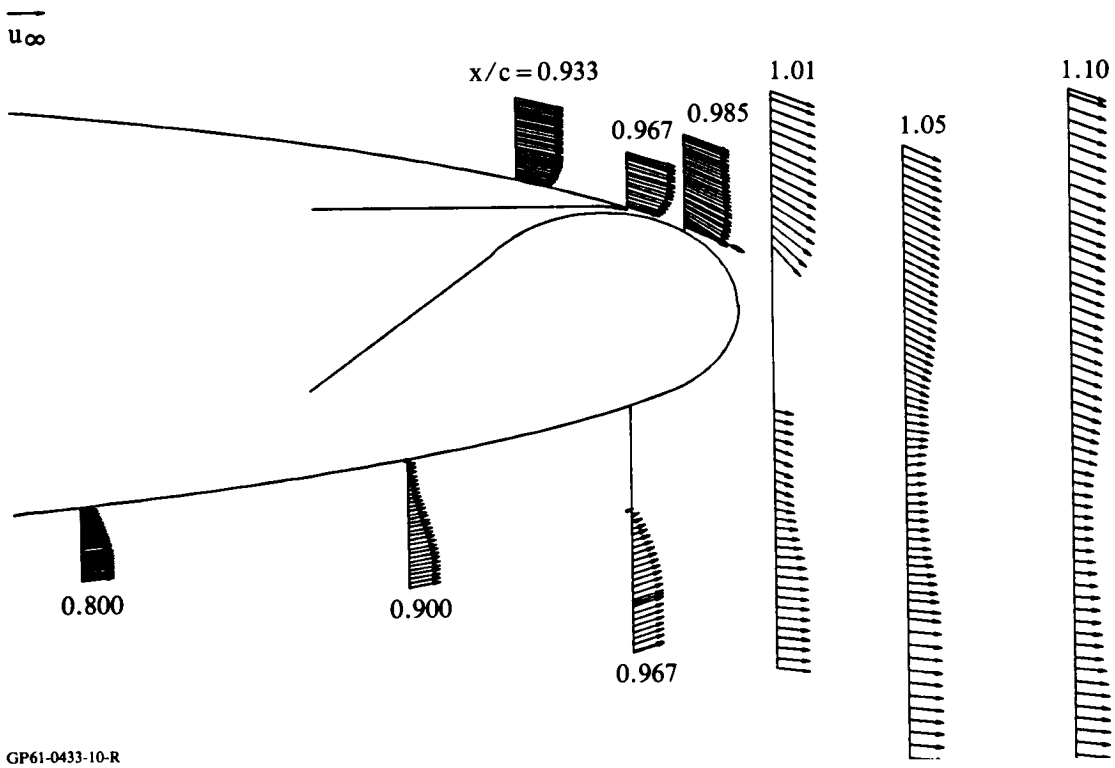

Figure 8. Velocity components in streamwise section plane; $M_\infty = 0.425$, $\alpha = 0°$, $p_j/p_\infty = 1.4$.

The data of figure 7 correspond to $M_\infty = 0.425$, $\alpha = 0°$, and no blowing. No wake data were obtained at this test condition. The boundary-layer profiles show approximately symmetrical flow, as expected, with separation apparently occurring slightly downstream of the last measuring station (x/c = 0.976) on both the upper and lower surfaces.

Figure 8 is a composite view corresponding to $M_\infty = 0.425$, $\alpha = 0°$, and $p_j/p_\infty = 1.4$, the baseline test condition selected for flowfield surveys in this investigation. The characteristics of this flowfield are in sharp contrast to data corresponding to no blowing presented in the preceding figure. The boundary-layer profiles on the upper surface upstream of the slot and at the slot lip (x/c = 0.967) are full, showing the effect of entrainment by the jet. The jet is evident in the profile obtained at x/c = 0.985. A separated region is indicated by the lower-surface boundary-layer profiles. Significant variations in pitch-plane inclination angles are present in the wake profiles; the gradients decrease with increasing x/c. The gap in the wake profile at x/c = 1.01 is a region where the flow direction exceeded the probe calibration range. The upper portion of the wake nearest the trailing edge is characterized by large negative values of the pitch-plane angle. Below the trailing edge, the pitch-plane angles are still negative, but are smaller in magnitude. Large cross-stream velocity components are present in this flowfield; the cross-stream flow is shown in subsequent figures.

Figures 9-11 present conventional velocity-magnitude and flow-angularity profiles for each of the locations surveyed at the baseline test condition of figure 8; the boundary-layer and wall-jet data of figures 9 and 10 were obtained with a three-hole probe, and the wake data of figure 11 were obtained with a five-hole probe. Figure 9a

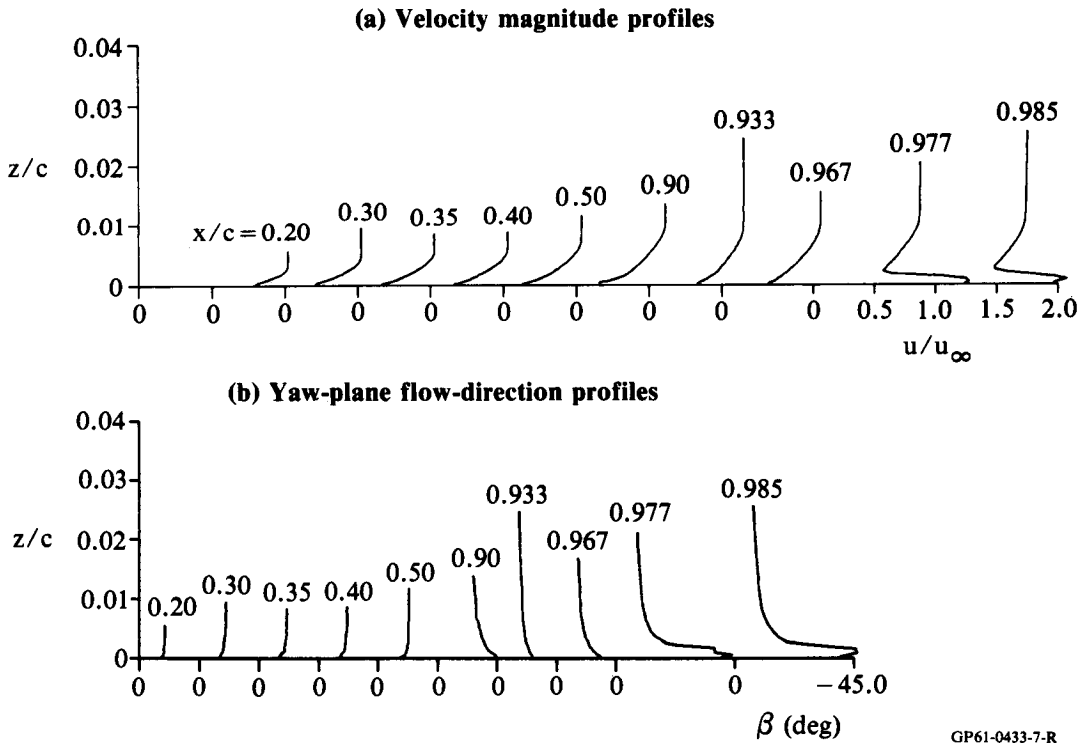

Figure 9. Upper-surface boundary-layer profiles; $M_\infty = 0.425$, $\alpha = 0°$, $p_j/p_\infty = 1.4$.

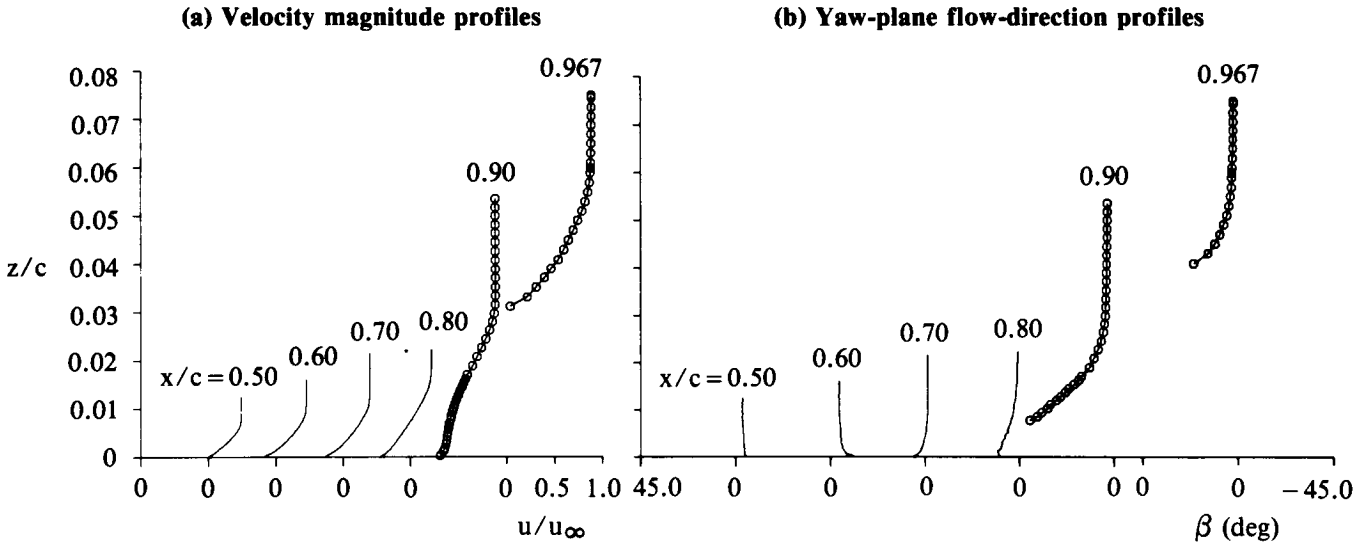

Figure 10. Lower-surface boundary-layer profiles; $M_\infty = 0.425$, $\alpha = 0°$, $p_j/p_\infty = 1.4$

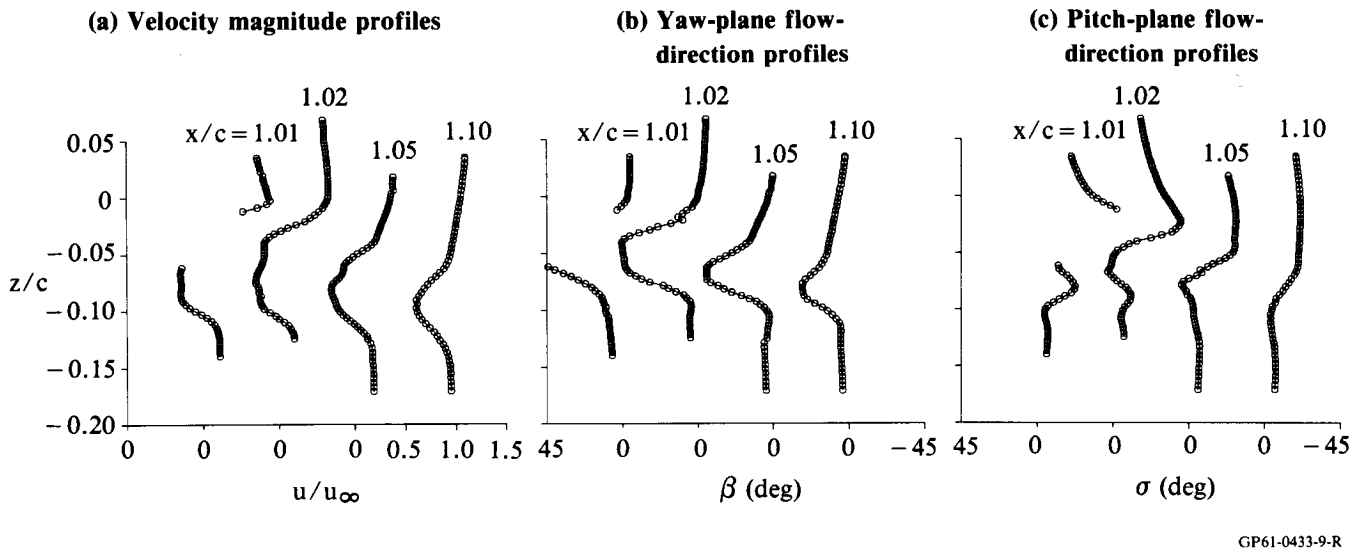

Figure 11. Wake profiles; $M_\infty = 0.425$, $\alpha = 0°$, $p_j/p_\infty = 1.4$.

gives u/u_∞, the velocity magnitude normalized by the freestream velocity, plotted against z/c, the distance from the surface normalized by the streamwise chord, for each of the upper-surface survey stations, $0.2 \leq x/c \leq 0.985$. The distance from the surface, z, is measured normal to the tunnel axis, which is also normal to the mean plane of the wing at $\alpha = 0°$. Corresponding profiles of yaw-plane flow angle, β, are shown in figure 9b (outboard flow is defined as positive β). Because of the small scale of the plots in figure 9 and in some of the subsequent figures, individual plotting symbols are not used. Approximately 40 points were obtained for each of the profiles of figure 9. The boundary-layer thickness does not increase appreciably from mid-chord to the slot station. The profiles of β upstream of the slot indicate that the flow was approximately colinear, with a mean inboard inclination which increases with increasing downstream distance. Both the thin, full character of the velocity

magnitude profiles near the slot station and the inboard values of β imply strong entrainment by the jet. The two wall-jet profiles show that the jet is directed normal to the slot (β ≈ -45°). The corresponding lower-surface profiles are shown in figure 10, beginning at x/c = 0.5. The profiles for 0.5 ≤ x/c ≤ 0.7 are full, and the flow is approximately streamwise. Downstream of x/c = 0.7, the boundary-layer growth is rapid; at x/c = 0.9 the flow is near separation. In the inner region of the profile at x/c = 0.967, the probe pressures are approximately equal to the local static pressure, indicating reverse flow, and no data are plotted. Measured values of β become increasingly outboard with decreasing distance from the surface in the two downstream profiles. Near the surface at x/c = 0.9, the probe pressure-differences are too small to allow accurate determination of β; thus, the last few points on the flow-angle profile are omitted.

Velocity magnitude, β, and pitch-plane flow-angle (σ) profiles are presented in figure 11 for four wake survey stations (upward flow is defined as positive σ). The origin of the z-coordinate for the wake profiles is the upper lip of the slot. The upper and lower portions of each profile include regions of constant stagnation pressure, indicating that the flow nonuniformities result from both inviscid and viscous effects. The upper edge of the wake near the trailing edge is characterized by high velocity magnitudes, large downwash, and nearly streamwise flow in the yaw plane; the lower edge has lower velocity magnitudes and is more nearly streamwise in both planes. The flow in the central portion of the wake is predominantly outboard, despite the fact that jet, which is strong enough to control the wing circulation, is directed 45° inboard. At x/c = 1.02, the flow at the center of the wake is approximately parallel to the trailing edge. The qualitative behavior of the flow in the gap at x/c = 1.01 is consistent with these trends; the signs of the flow angles can be determined from the signs of the appropriate probe-pressure differences even when the probe calibration range is exceeded. Apparently, the flow in the viscous central wake is dominated by the outboard flow in the separated region on the lower surface.

An illustration of the influence of the jet on the flow immediately downstream of the slot is shown in figure 12, where three-dimensional velocity-vector profiles on the Coanda surface, 1% chord downstream of the slot, are compared with and without jet flow. These are three-dimensional vector plots viewed from a point above and outboard

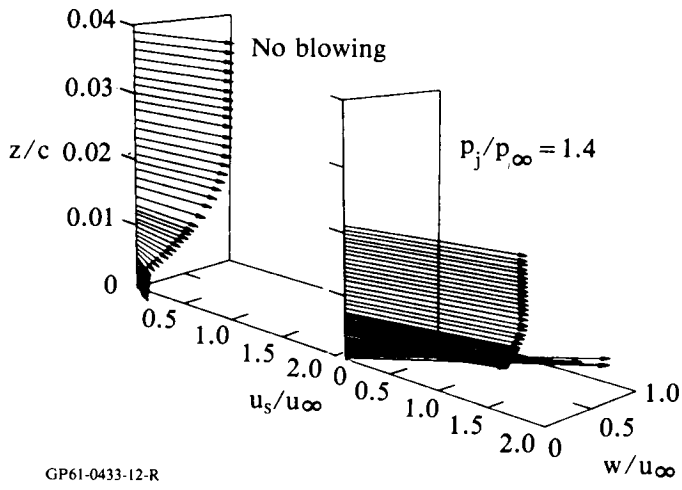

Figure 12. Velocity vector profiles; $M_\infty = 0.425$, $\alpha = 0°$, $x/c = 0.976$.

of the measuring station. The profiles were obtained with the three-hole probe and the vectors are drawn parallel to the horizontal plane of the figure. The sharp distinction between the jet flow and the remnant of the approaching boundary layer is apparent in the wall-jet profile. The outboard rotation of the velocity vectors with decreasing distance from the surface is less obvious for the no-blowing case, but the qualitative differences between the two profiles are clear. The flow near the wall for the no-blowing case corresponds to the previously mentioned situation in which the probe-pressure differences were too small to allow accurate determination of β. In this instance, values of β were extrapolated from above.

Close-ups of wall-jet and wake profiles corresponding to the baseline test condition are presented in figures 13-15. These data were obtained with the five-hole probe and are presented in the form of streamwise velocity components, cross-stream velocity components (velocity components lying in a plane normal to the freestream velocity vector) and static-pressure distributions. The profiles of figures 13-15 correspond to x/c = 0.984, 1.02, and 1.10. The streamwise profiles at x/c = 0.984 and 1.10 are also shown in figure 8. The velocity vectors are plotted to the same scale in figures 13-15, but differences in the mean value and range of variation in static pressure among the profiles required significant changes in the C_p scale.

The five-hole probe is too large to resolve the flowfield features accurately near the Coanda surface. In reducing the data shown in figure 13 corresponding to $0 \leq z/c \leq 0.0035$, the static pressure was assumed to be the value measured at the surface, the stagnation pressure was assumed to be the maximum of the values measured by the probe orifices, and the pitch-plane flow direction was assumed to be parallel to the local surface.

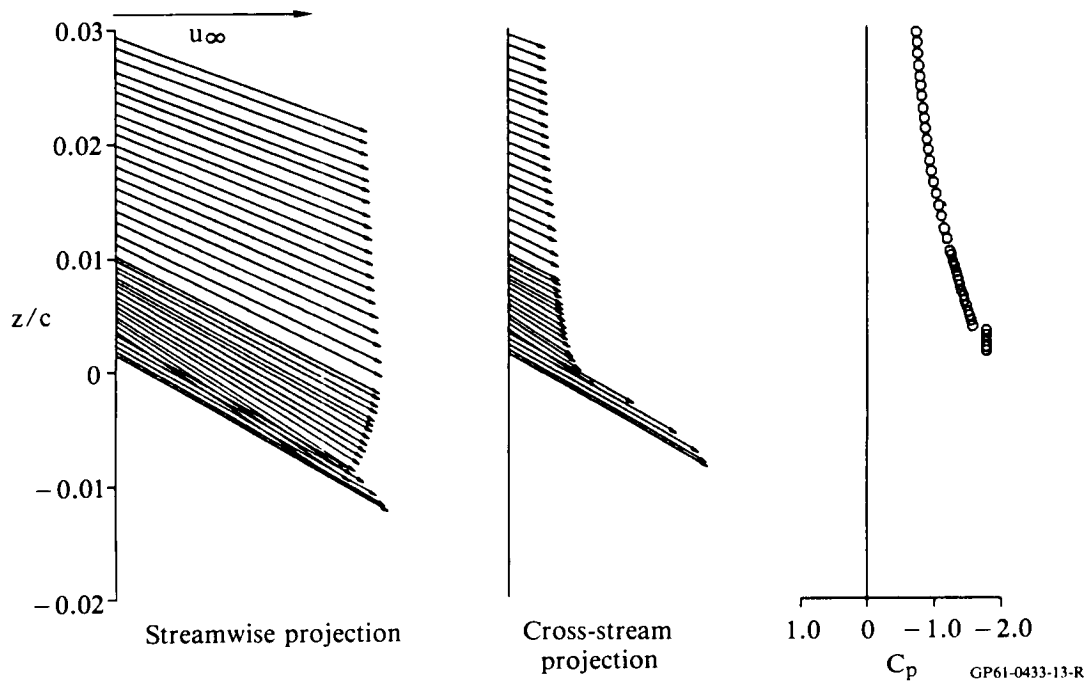

Figure 13. Wall-jet velocity and static-pressure profiles; $M_\infty = 0.425$, $\alpha = 0°$, $p_j/p_\infty = 1.4$, $x/c = 0.984$.

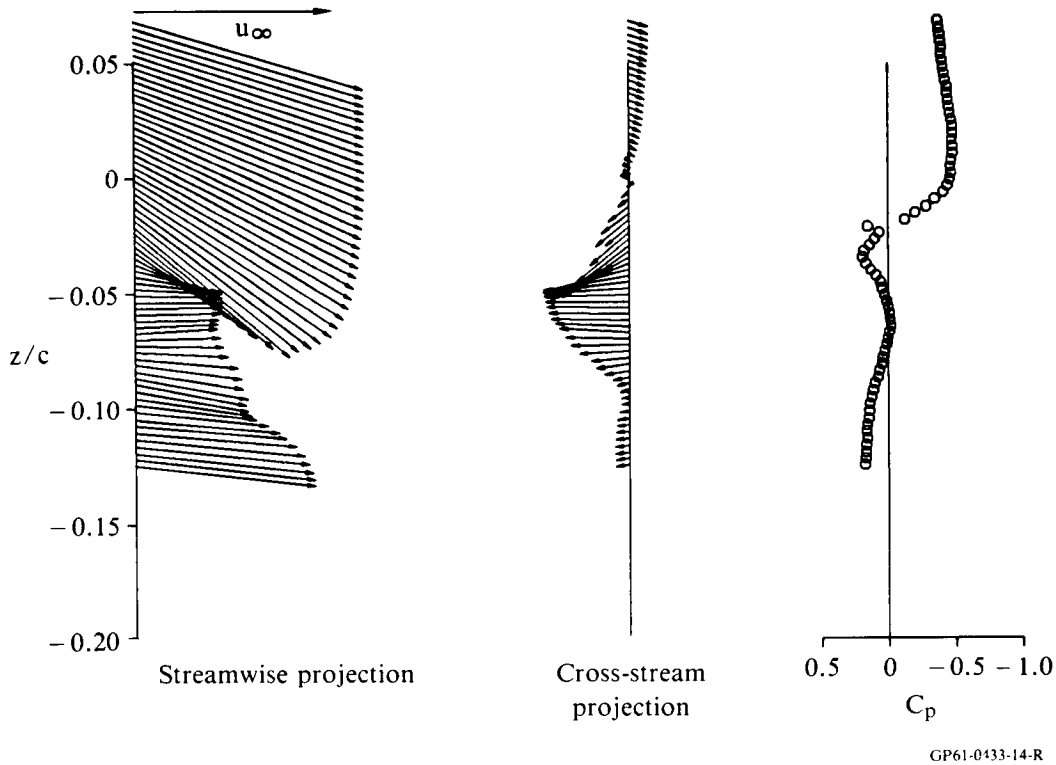

Figure 14. Wake velocity and static-pressure profiles; $M_\infty = 0.425$, $\alpha = 0°$, $p_j/p_\infty = 1.4$, $x/c = 1.02$.

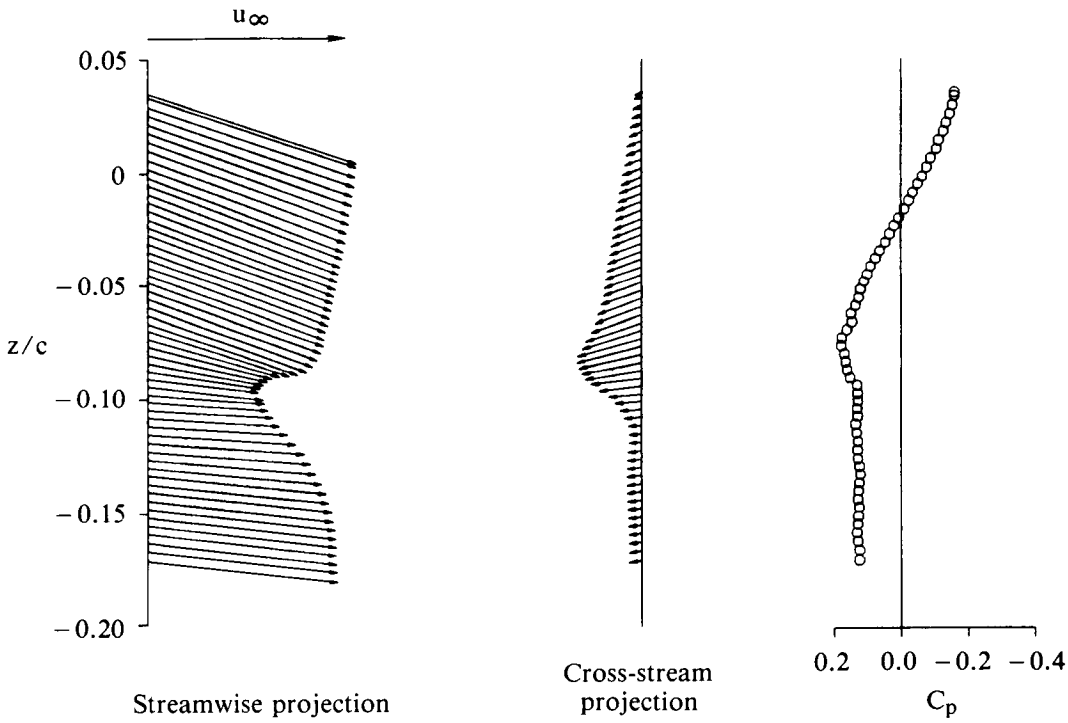

Figure 15. Wake velocity and static-pressure profiles; $M_\infty = 0.425$, $\alpha = 0°$, $p_j/p_\infty = 1.4$, $x/c = 1.10$.

The contrast between the inboard inclination of the entire profile at x/c = 0.984 and the outboard flow in the centers of the wake profiles is evident in these figures, as are the substantial variations in static pressure. As expected, the gradients decrease with increasing distance downstream.

The influence of an increase in blowing rate may be seen by comparing figures 8 and 16. The upper-surface boundary layer and wake velocities are significantly greater at the higher blowing rate, and the values of σ in the wake are more negative, resulting in a substantial region of flow outside the probe-calibration range for the innermost wake profile. These data also show large positive values of β downstream of the trailing edge. The two lower-surface boundary-layer profiles shown in figure 16 indicate that the increased blowing rate has also resulted in a forward movement of the lower-surface separation point.

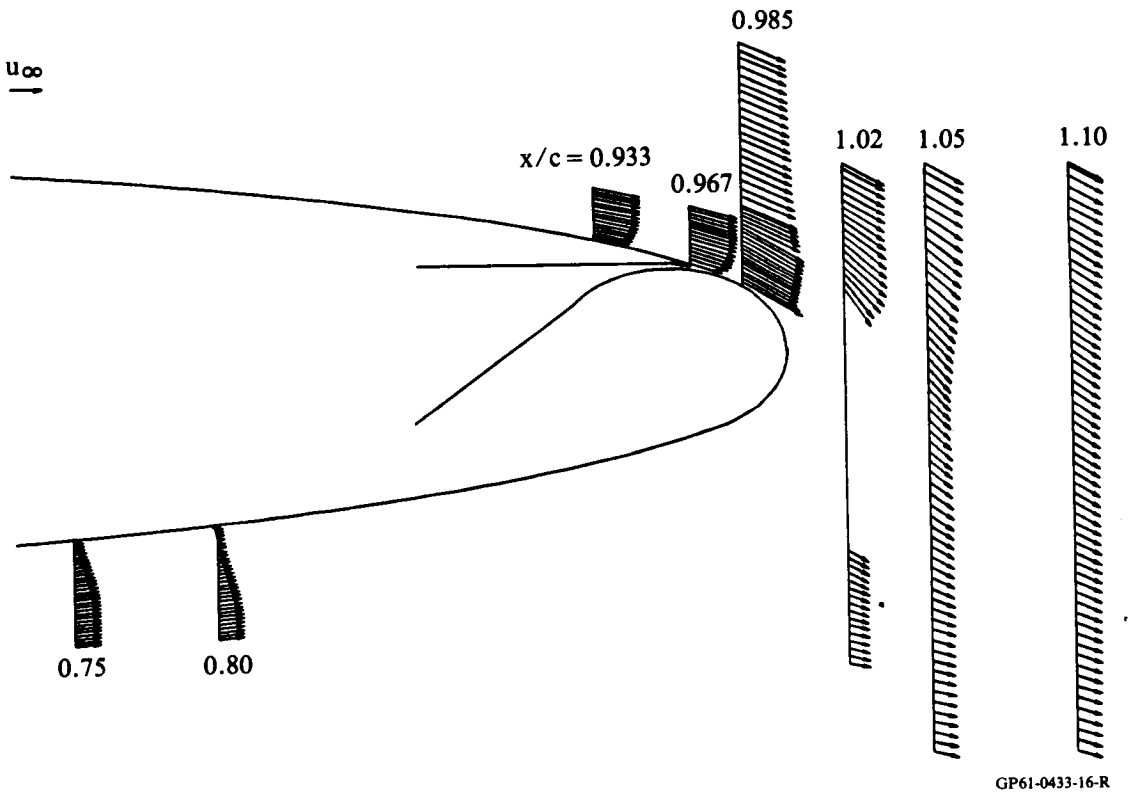

Figure 16. Velocity components in streamwise section plane; $M_\infty = 0.425$, $\alpha = 0°$, $p_j/p_\infty = 1.8$.

Figures 17-19 present close-ups of wall-jet and wake profiles for the test conditions of figure 16 in the manner of figures 13-15.

Static-pressure distributions corresponding to no blowing and three blowing rates at M_∞ = 0.70 and α = 0°, test conditions for which boundary-layer and wake data were obtained, are presented in figure 20. The data correspond to approximately the same pressure-ratio range as those of figure 6, but the values of C_μ and c_ℓ are smaller.

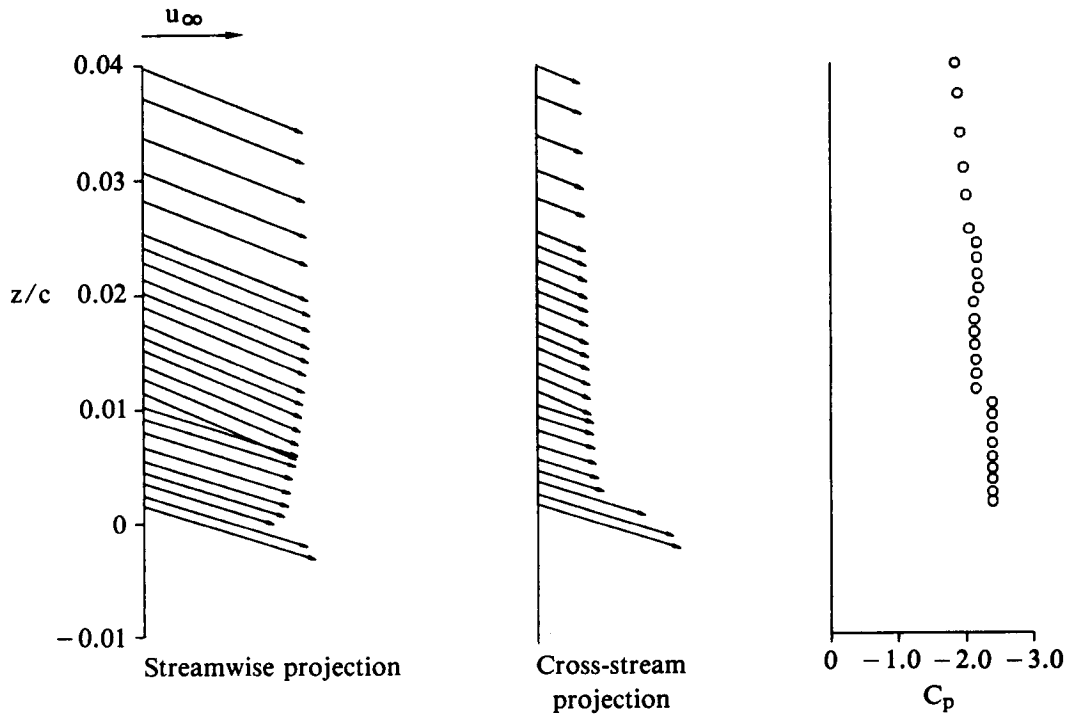

Figure 17. Wall-jet velocity and static-pressure profiles; $M_\infty = 0.425$, $\alpha = 0°$, $p_j/p_\infty = 1.8$, $x/c = 0.976$.

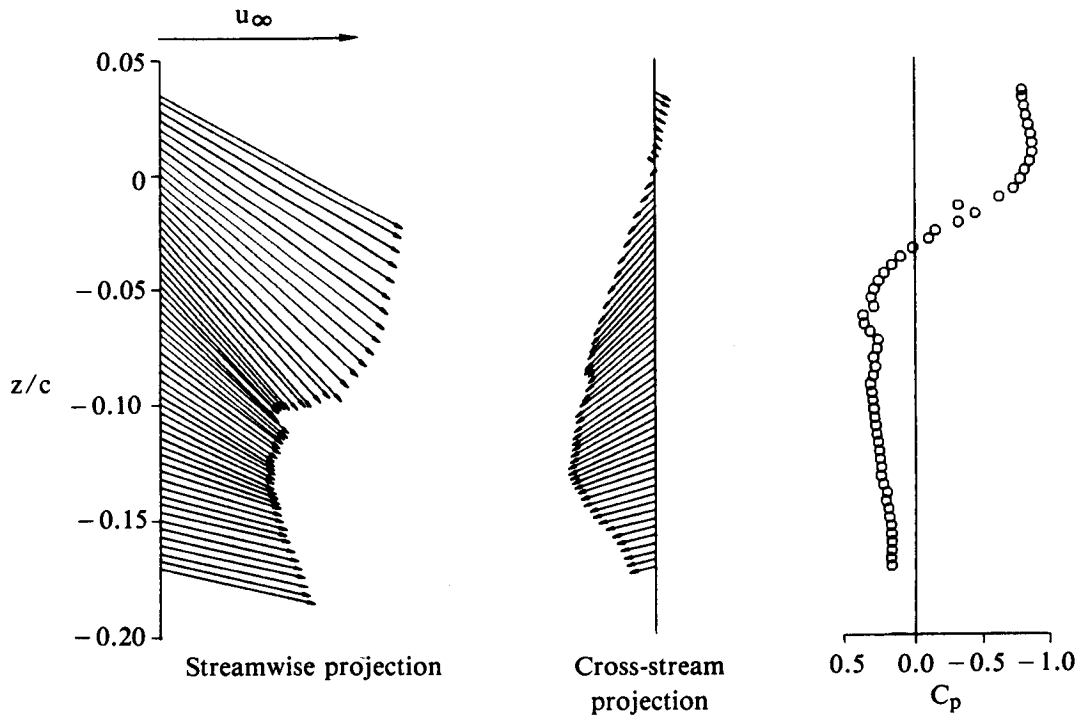

Figure 18. Wake velocity and static-pressure profiles; $M_\infty = 0.425$, $\alpha = 0°$, $p_j/p_\infty = 1.8$, $x/c = 1.05$.

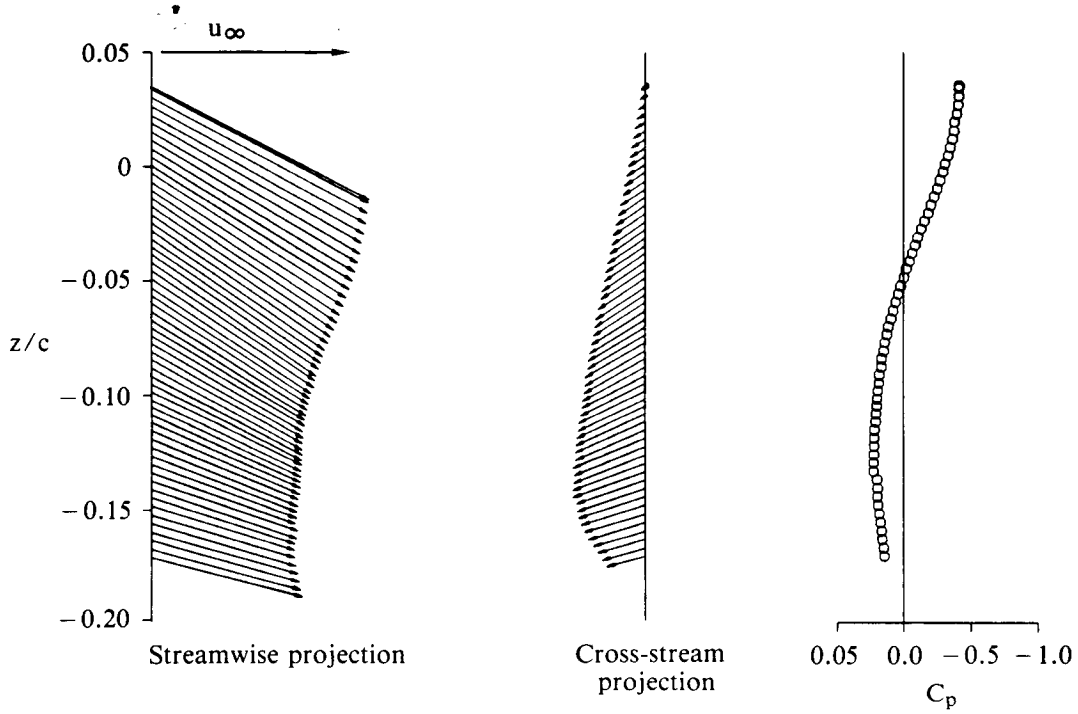

Figure 19. Wake velocity and static-pressure profiles; $M_\infty = 0.425$, $\alpha = 0°$, $p_j/p_\infty = 1.8$, $x/c = 1.10$.

GP61-0433-19-R

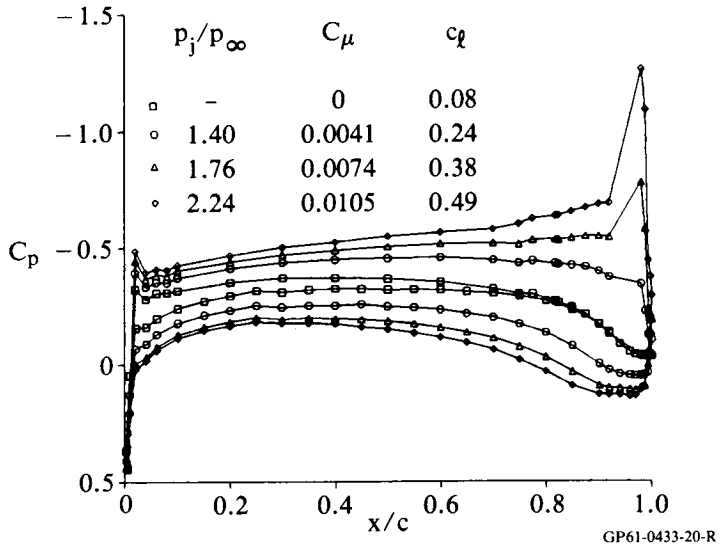

GP61-0433-20-R

Figure 20. Wing static-pressure distributions at mid-semispan; $M_\infty = 0.70$, $Re_c = 3.15 \times 10^6$, $\alpha = 0°$.

The composite view presented in figure 21, and the detailed profile data of figures 22-24, correspond to $M_\infty = 0.70$, the same jet pressure ratio as in figure 8, $p_j/p_\infty = 1.4$, but a lower jet-momentum coefficient, $C_\mu = 0.0041$. The influence of the jet on the surrounding flow is clearly much less pronounced at this test condition. The upper-surface boundary-layer profiles in the vicinity of the jet are less full and

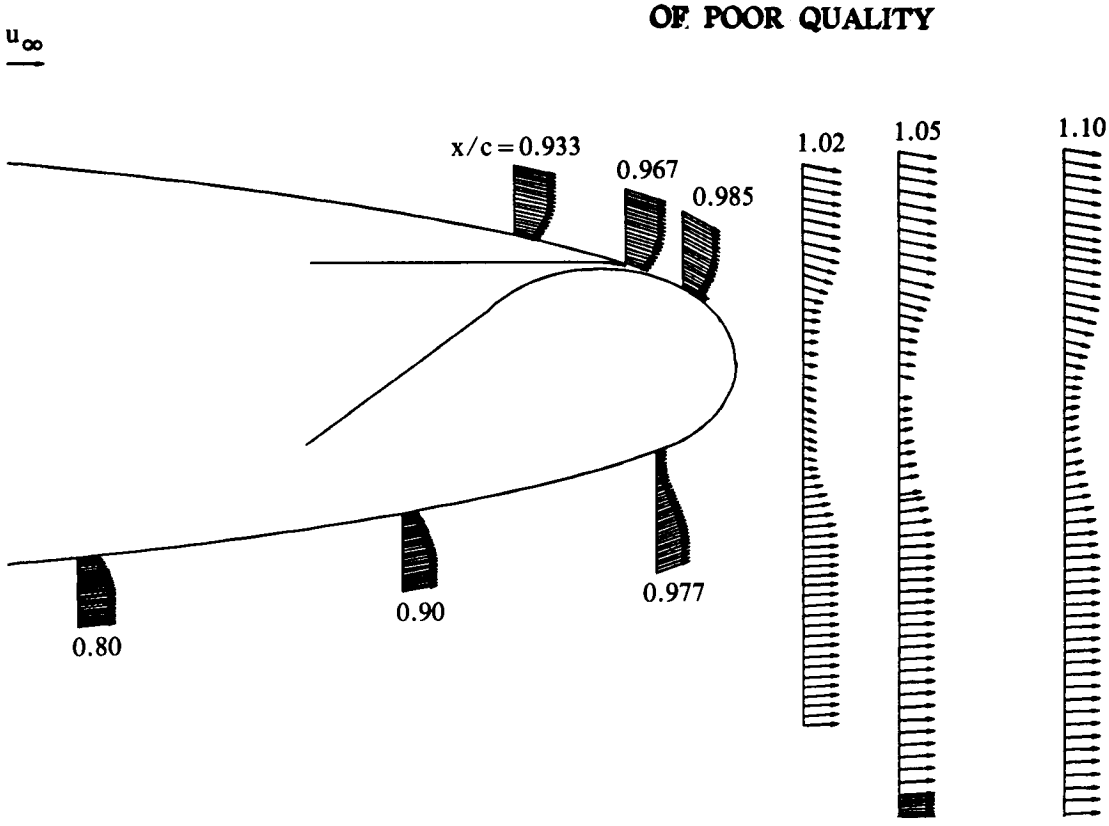

Figure 21. Velocity components in streamwise section plane; $M_\infty = 0.70$, $\alpha = 0°$, $p_j/p_\infty = 1.4$.

GP61-0433-21-R

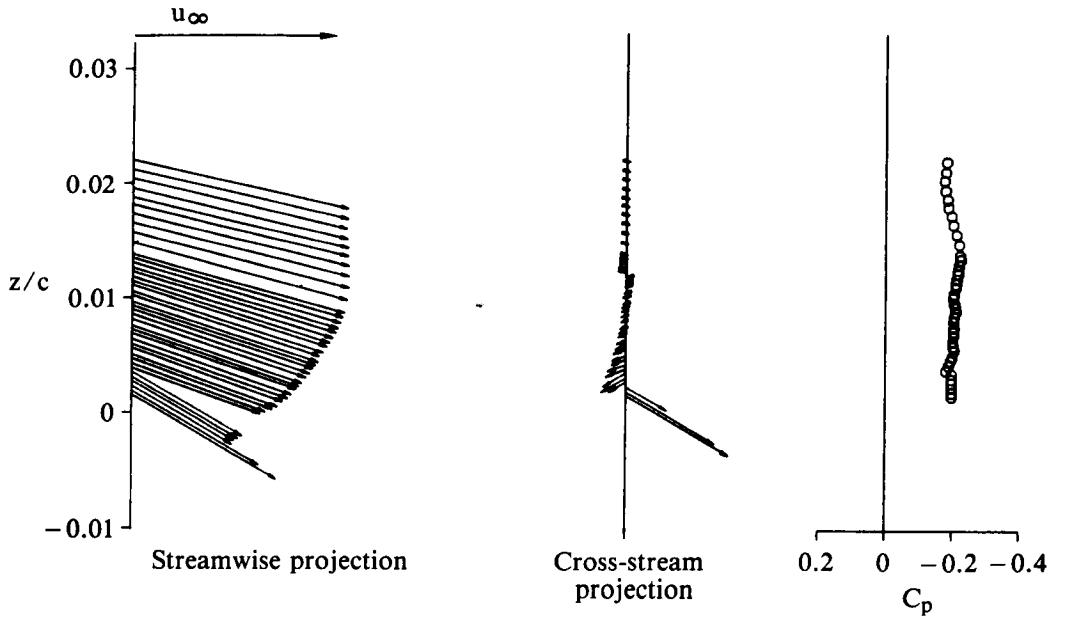

GP61-0433-22-R

Figure 22. Wall jet velocity and static-pressure profiles; $M_\infty = 0.700$, $\alpha = 0°$, $p_j/p_\infty = 1.4$, $x/c = 0.985$.

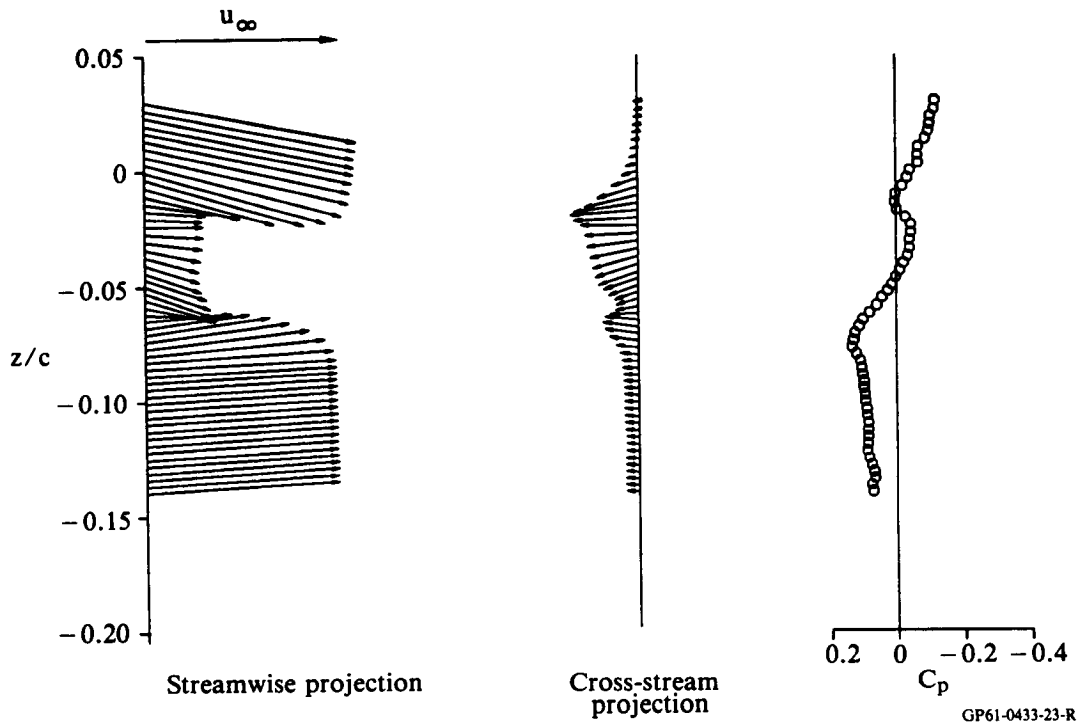

Figure 23. Wake velocity and static-pressure profiles; $M_\infty = 0.700$, $\alpha = 0°$, $p_j/p_\infty = 1.4$, $x/c = 1.02$.

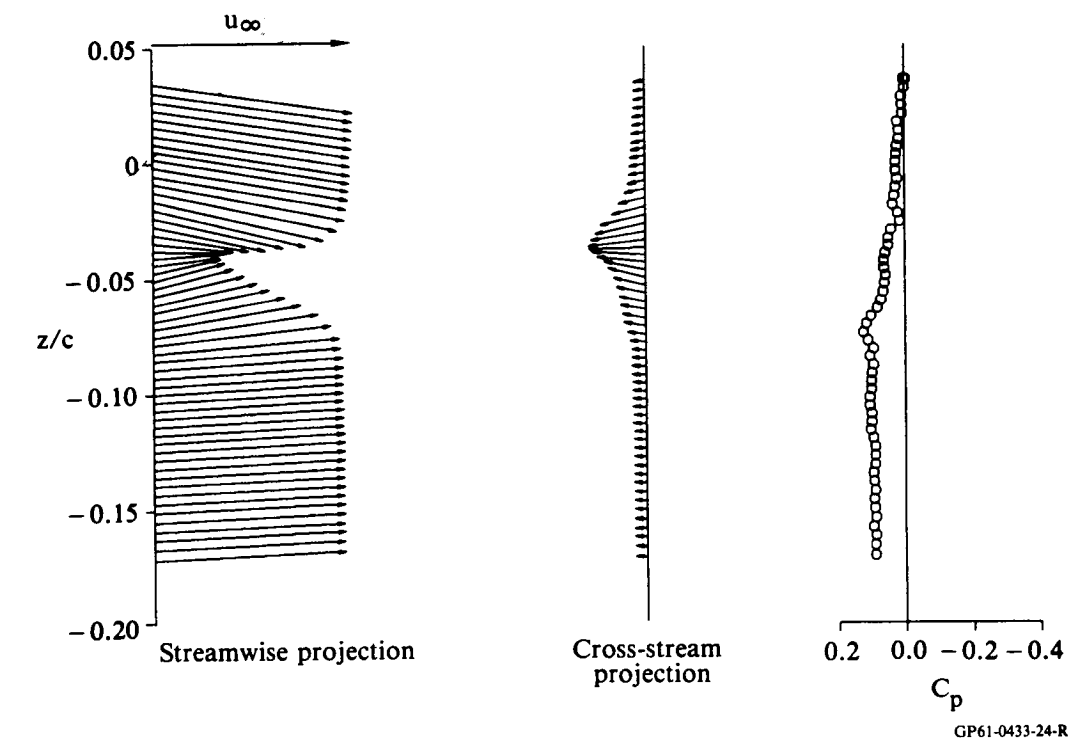

Figure 24. Wake velocity and static-pressure profiles; $M_\infty = 0.700$, $\alpha = 0°$, $p_j/p_\infty = 1.4$, $x/c = 1.1$.

show positive values of β near the surface upstream of the jet and at the location of minimum velocity in the profile downstream of the jet. The lower-surface separation line is apparently near the last measuring station on the lower surface. The reduced circulation is indicated by the reduced downward displacement of the wake centerline, relative to the data of figure 8.

Upper-surface, streamwise displacement-thickness distributions, normalized by the streamwise chord, δ_1^*/c, are presented in figure 25 for $M_\infty = 0.425$, $\alpha = 0°$, and jet conditions of no blowing, $p_j/p_\infty = 1.4$, and 1.8. The boundary-layer thickness distribution is apparently unaffected by blowing for $x/c \leq 0.5$. The displacement thickness at $x/c = 0.5$ is approximately the same as that corresponding to flow over a flat plate at the freestream conditions. In the vicinity of the slot, the displacement-thickness distribution for no blowing grows rapidly as the flow approaches separation. Data for the two blowing rates show values of displacement thickness immediately upstream of the slot which are essentially the same as those measured at mid-chord.

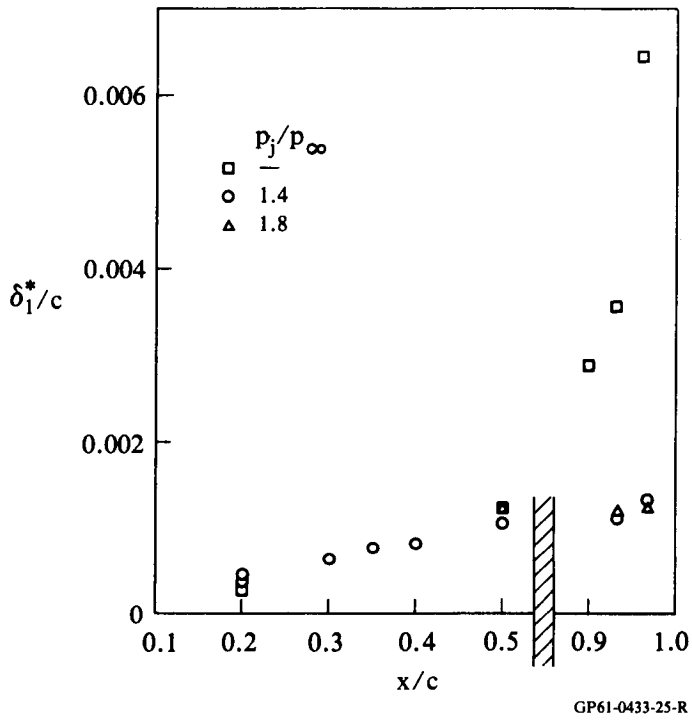

Figure 25. Upper-surface streamwise displacement-thickness distributions; $M_\infty = 0.425$, $\alpha = 0°$.

The next group of figures illustrates an abrupt transition from incipient separation at the slot location to attached flow at $M_\infty = 0.425$ and $\alpha = 5°$. Upper-surface static-pressure distributions for the relevant test conditions are shown in figure 26. Velocity-magnitude profiles at two chordwise stations downstream of the jet exit location, $x/c = 0.977$ and 0.985, are shown in figure 27 for three blowing rates. The shapes of the velocity profiles above the jet corresponding to $p_j/p_\infty = 1.2$ are characteristic of boundary layers near separation, and the minimum values of velocity measured at the interface between the wall jet and the outer flow are low, indicating min-

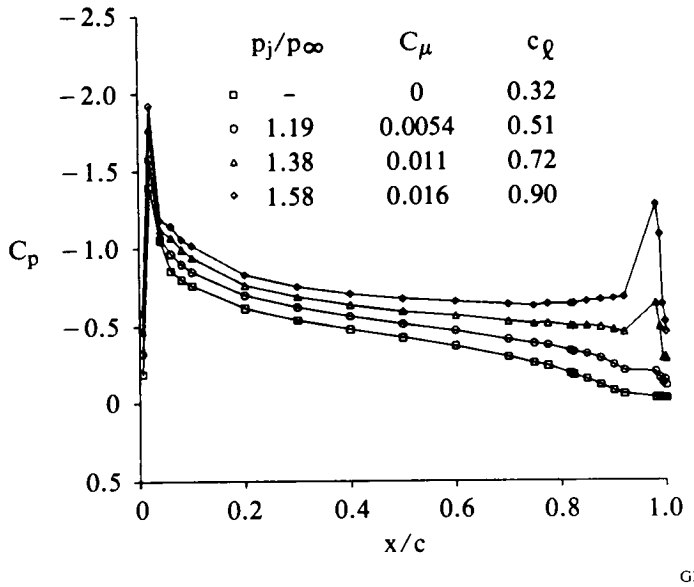

Figure 26. Upper-surface wing static-pressure distributions at mid-semispan; $M_\infty = 0.425$, $Re_c = 2.24 \times 10^6$, $\alpha = 5.0°$.

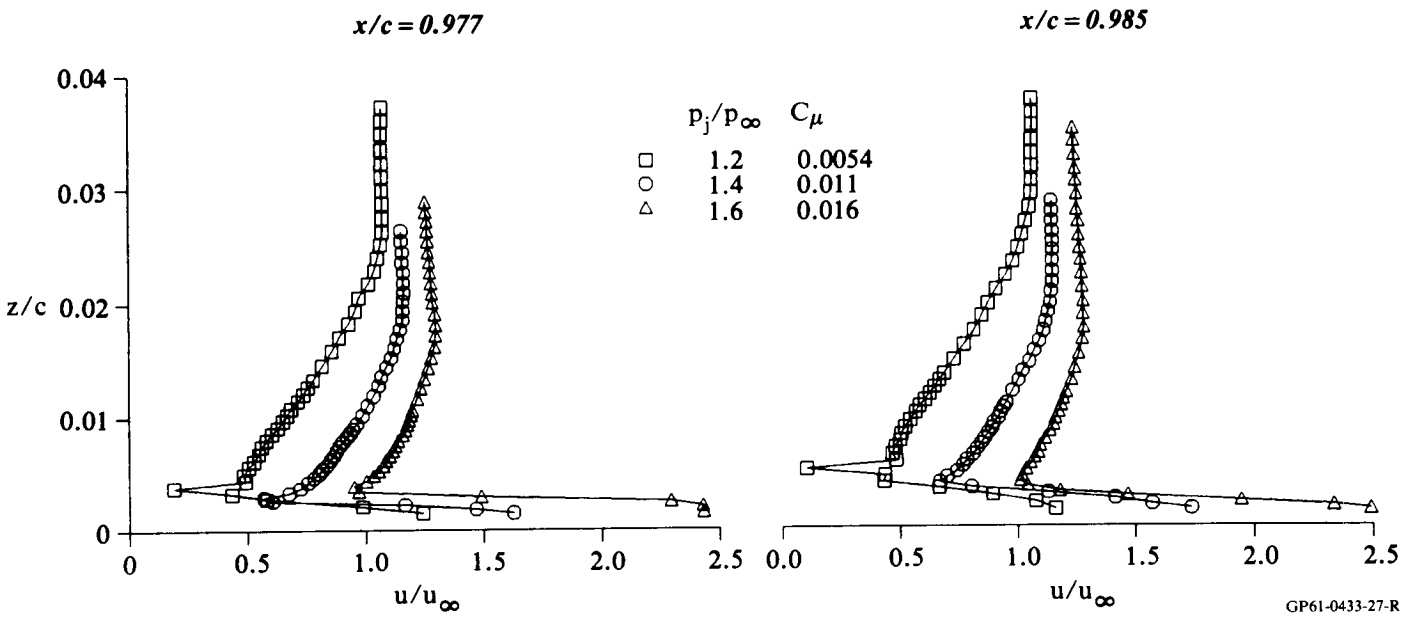

Figure 27. Velocity magnitude profiles; $M_\infty = 0.425$, $\alpha = 5°$.

imal entrainment of the outer flow by the jet. The situation for p_j/p_∞ = 1.4 is different, in that the boundary-layer portions of the profiles are relatively thin and full, and the minimum values of velocity are significantly greater. The velocity magnitudes are higher at the next higher blowing rate, p_j/p_∞ = 1.6, but the qualitative features are similar to those exhibited by the profiles corresponding to p_j/p_∞ = 1.4.

Figure 28 shows two upper-surface fluorescent oil-flow photographs corresponding to $M_\infty = 0.425$, $\alpha = 5°$, and $p_j/p_\infty = 1.2$ and 1.3, obtained from Keener et al., (1986). The oil was injected from surface orifices and photographed during a run. At the lower blowing rate, the oil streaks turn toward the spanwise direction near the slot, indicating separation at the slot, except in the immediate vicinity of the tip. The pattern obtained for $p_j/p_\infty = 1.3$ is significantly different, showing streamwise flow along the span up to the slot, indicating attached flow at the slot.

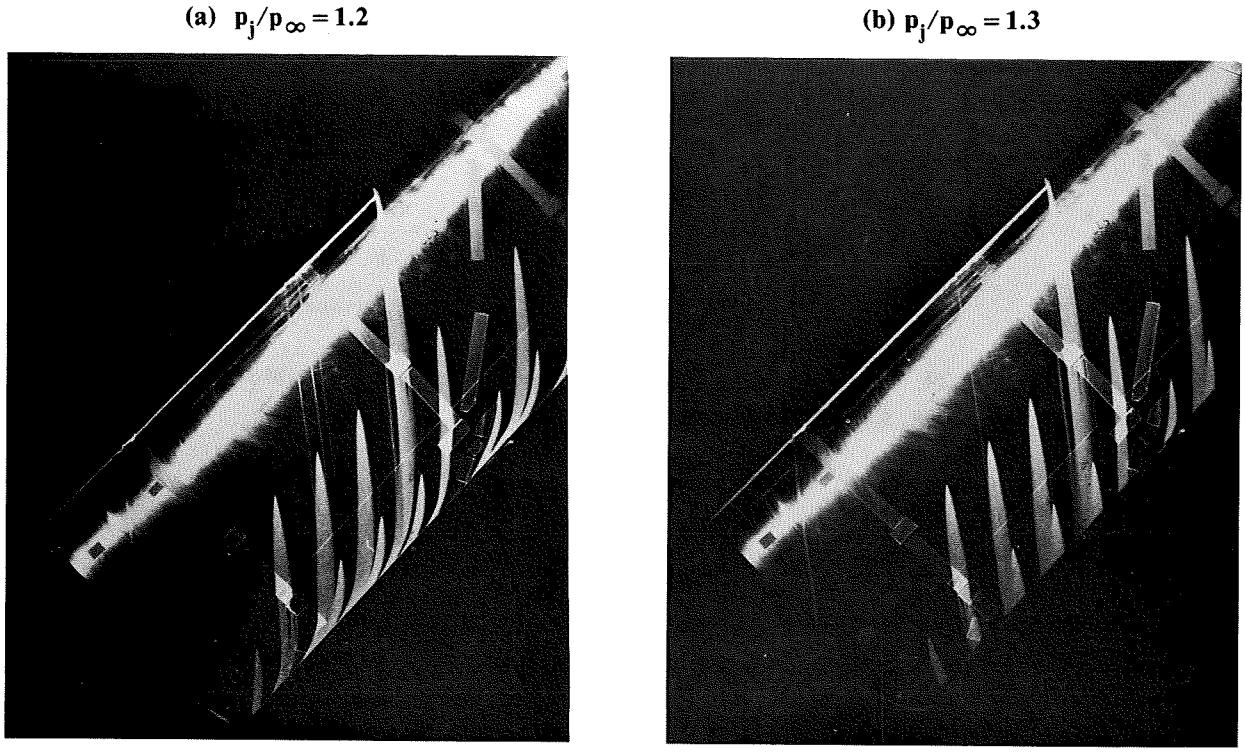

Figure 28. Fluorescent oil-flow photographs of wing upper surface; $M_\infty = 0.425$, $\alpha = 5°$.

Data at $M_\infty = 0.70$ and $\alpha = 5°$ were examined for evidence of similar behavior. Upper-surface static-pressure distributions corresponding to this Mach number and angle of attack for which flowfield survey data were obtained are shown in figure 29. Wall-jet profiles at $x/c = 0.977$, having the most nearly similar characteristics to those of figure 27, are shown in figure 30, corresponding to $p_j/p_\infty = 1.6$ and 2.0. However, the oil-flow photograph of figure 31, obtained at conditions corresponding to the higher-blowing-rate data of figure 30, indicates flow separation at the slot.

Values of skin-friction coefficient, C_f, were determined from the attached boundary-layer profiles by fitting the inner region of the velocity magnitude profiles to the following generally accepted similarity law,

$$\frac{u}{u_\tau} = \frac{1}{0.41} \ln\left(\frac{zu_\tau}{\nu}\right) + 5.0 \qquad (1)$$

where u_τ is the shear velocity, $\sqrt{\tau_w/\rho}$; τ_w is the wall shear stress, ρ is the density, and ν is the kinematic viscosity. A range of values has been proposed for the con-

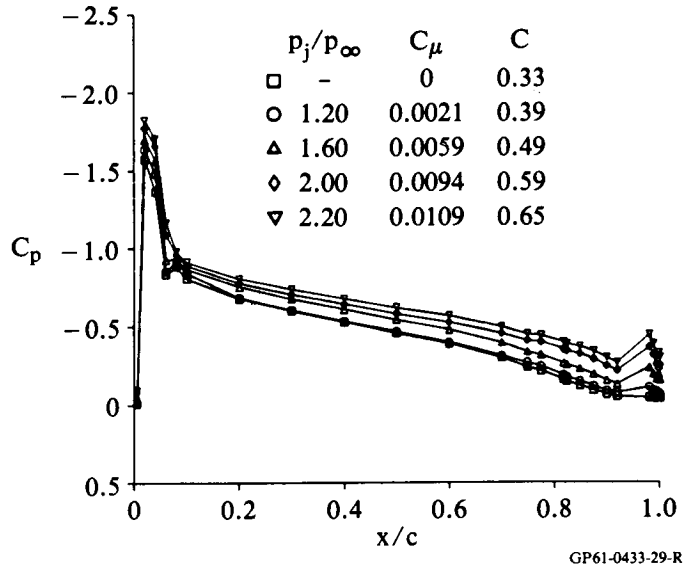

Figure 29. Upper-surface wing-static-pressure distributions at mid-semispan; $M_\infty = 0.70$, $Re_c = 3.15 \times 10^6$, $\alpha = 5°$.

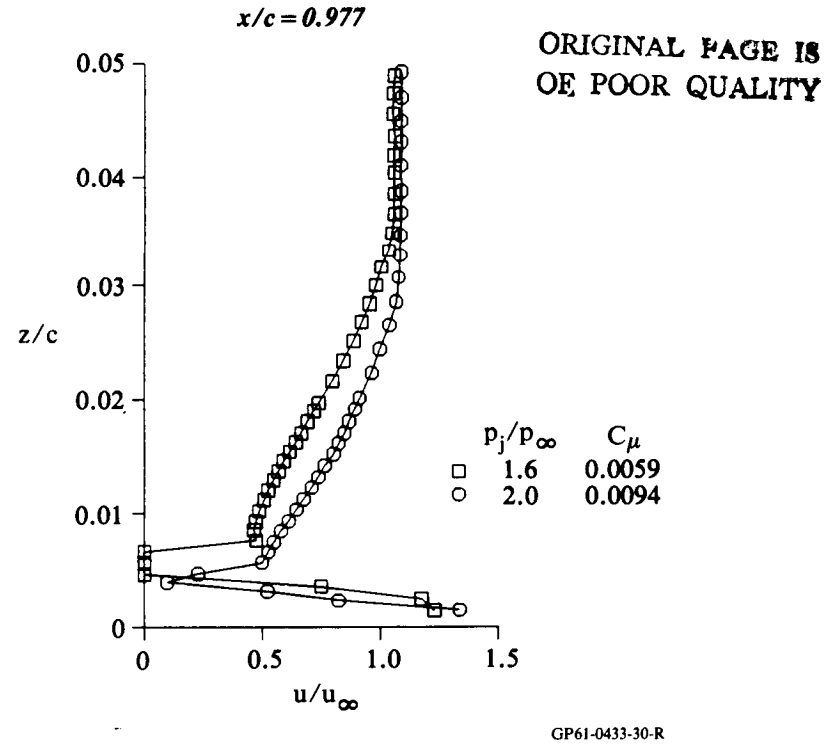

Figure 30. Velocity magnitude profiles; $M_\infty = 0.700$, $\alpha = 5°$.

ORIGINAL PAGE IS
OF POOR QUALITY

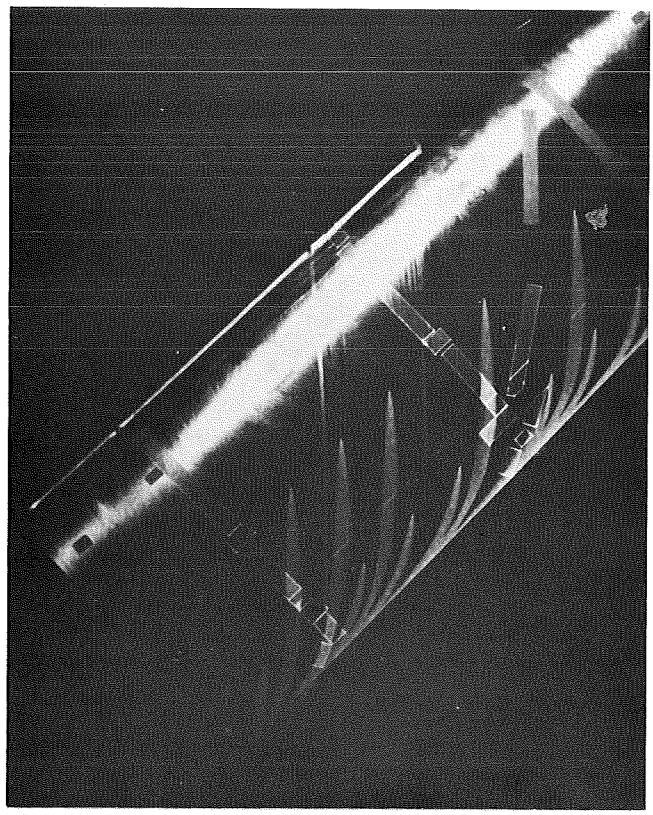

GP61-0433-31-R

Figure 31. Fluorescent oil-flow photograph; $M_\infty = 0.7$, $\alpha = 5°$, $p_j/p_\infty = 2.0$.

stants in this equation; this situation is reviewed by Pierce et al. (1982,1). Extension of the incompressible law-of-the-wall to flows with moderate compressibility effects is usually accomplished by evaluating the density and viscosity at the wall temperature. Prahlad (1968) proposed that this similarity law be extended to three-dimensional flows by replacing the two-dimensional velocity in equation (1) with the velocity magnitude. Pierce et al. (1982,2) concluded that the magnitude of the wall shear stress could be determined by the Clauser-chart technique (Clauser, 1954) to within 5-10% if data in the range $10 \leq z^+ \leq 100$ ($z^+ = zu_\tau/\nu_w$) were used. This conclusion was limited to monotonically-skewed boundary layers with an approximate maximum of 15-20° of skew. The attached boundary-layer profiles of figures 7 and 8 are nearly colinear, and are representative of the attached profiles measured in this investigation. It is concluded that the Clauser-chart technique should be adequate for estimating skin-friction magnitudes from the present data.

Figure 32 illustrates the method by which this technique was applied to the present data. Lower-surface velocity-magnitude profiles corresponding to the baseline test conditions are plotted in semi-logarithmic coordinates. In these coordinates, equation (1) represents a family of straight lines with C_f as a parameter. Since the straight lines in figure 32 represent the range $10 \leq zu_\tau/\nu \leq 1000$, it is apparent that the sublayer and the inner portion of the logarithmic region are not resolved in these data. The data show a monotonically decreasing trend of C_f with x/c.

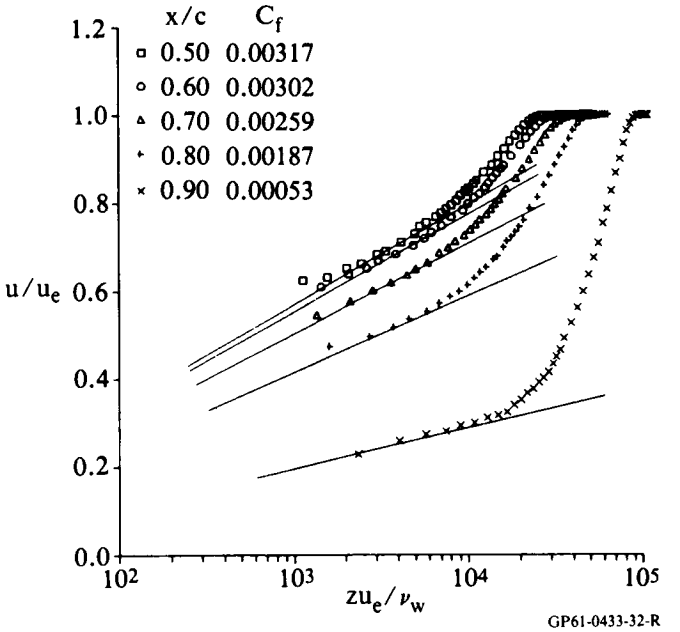

Figure 32. Lower-surface velocity magnitude profiles in semi-log coordinates; $M_\infty = 0.425$, $\alpha = 0°$, $p_j/p_\infty = 1.4$

The influence of blowing rate on the position of the lower-surface separation line is shown in figure 33, in which C_f is plotted as a function of x/c for a range of blowing rates. It is assumed that extrapolation of values of C_f to zero provides a reasonable estimate of the separation-line location. (Actually, the velocity magnitudes become small and the local flow direction becomes parallel to the wing generators near separation.) It is shown that the separation line moves upstream with increasing blowing rate, up to p_j/p_∞ = 1.8, but an additional increase of p_j/p_∞ to 2.2 does not produce an additional forward movement of the separation line. It is in this range of blowing rates that the performance data (c_ℓ versus C_μ) show no additional increase of lift with increasing blowing rate.

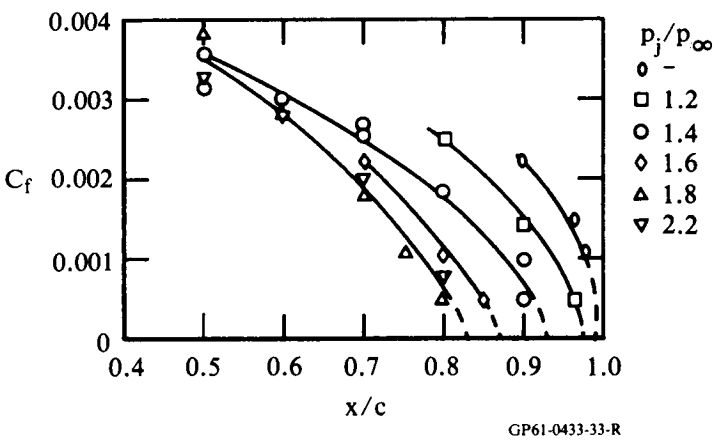

Figure 33. Lower-surface skin-friction distributions; $M_\infty = 0.425$, $\alpha = 0°$.

Streamwise displacement-thickness data corresponding to the skin-friction data of figure 33 are presented in figure 34, where the approach to separation is indicated by a rapid growth in displacement thickness with increasing downstream distance. Vertical dashed lines in figure 34 indicate the separation locations inferred from the skin-friction data.

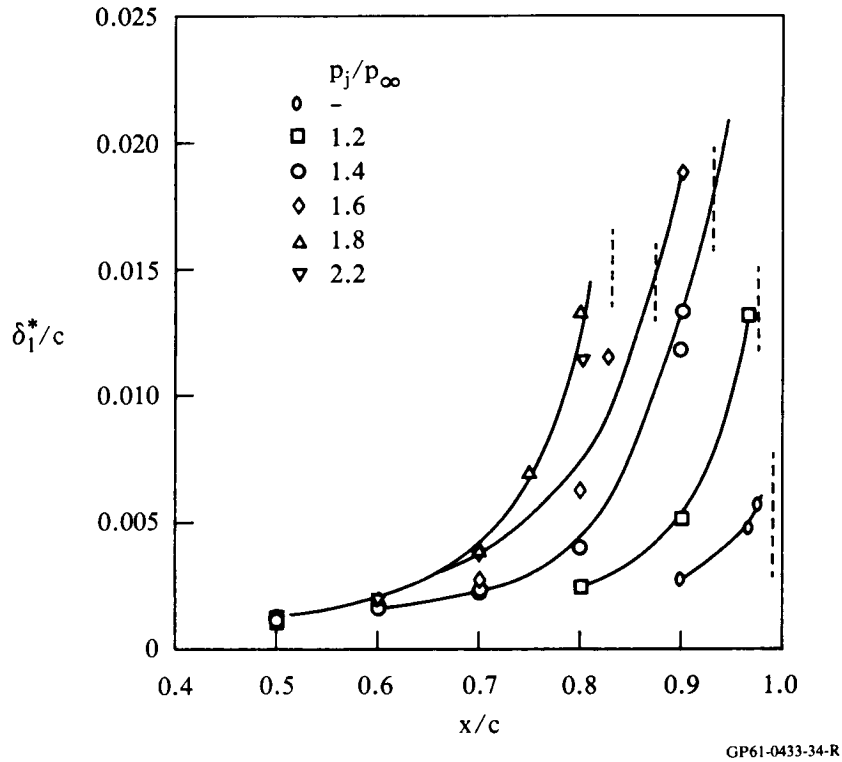

Figure 34. Lower-surface streamwise displacement-thickness distributions; $M_\infty = 0.425$, $\alpha = 0°$.

CONCLUDING REMARKS

Boundary-layer and wake-survey data were obtained at mid-semispan in the flow about a 45° swept, circulation-control wing at freestream Mach numbers of 0.425 and 0.70. Boundary-layer profiles forward on the wing on both upper and lower surfaces are approximately streamwise and two-dimensional. The flow in the vicinity of the jet exit and in the near wake is highly three-dimensional. Qualitative variations in flowfield features with freestream Mach number and jet blowing rate are illustrated by velocity vector plots. The jet flow near the slot on the Coanda surface is directed normal to the slot, or 45° inboard. All near-wake surveys, including surveys obtained 1% chord downstream of the trailing edge, show large outboard flows at the center of the wake. At Mach 0.425 and 5° angle of attack, a range of jet blowing rates was found for which an abrupt transition from incipient separation to attached flow occurs in the boundary layer upstream of the slot. The variation in the lower-surface separation location with blowing rate was determined from boundary-layer measurements at Mach 0.425.

REFERENCES

Clauser, F. H.: Turbulent Boundary Layers in Adverse Pressure Gradients, J. Aero. Sci., vol. 21, no. 2, Feb. 1954, pp. 91-108.

Dudzinski, Thomas J.; and Krause, Lloyd N.: Flow-Direction Measurement with Fixed-Position Probes. NASA TM X-1904, 1969.

Keener, Earl R.; Sanderfer, Dwight T.; and Wood, Norman J.: Pressure Distributions and Oil-Flow Patterns for a Swept Circulation-Control Wing. NASA CP-2432, 1986. (Paper 10 of this compilation.)

Pierce, F. J.; McAllister, J. E.; and Tennant, M. H.: Near-Wall Similarity in Three-Dimensional Turbulent Boundary Layers, Part I: Model Review. **Three-Dimensional Turbulent Shear Flows**, American Society of Mechanical Engineers, New York, 1982, pp. 85-95.

Pierce, F. J; McAllister, J.E.; and Tennant, M. H.: Near-Wall Similarity in Three-Dimensional Turbulent Boundary Layers, Part II: Pressure-Driven Flow Results. **Three-Dimensional Turbulent Shear Flows**, The American Society of Mechanical Engineers, New York, 1982, pp. 96-103.

Prahlad, T. S.: Wall Similarity in Three-Dimensional Turbulent Boundary Layers. AIAA J., vol. 6. no. 9, Sept. 1968, pp. 1772-1774.

Wood, Norman, J.; and Conlon, John A.: The Performance of a Circulation Control Airfoil at Transonic Speeds. AIAA Paper No. 83-0083, Jan. 1983.

Wood, Norman J.; and Nielsen, Jack N.: Circulation Control Airfoils Past, Present, Future. AIAA Paper No. 85-0204, Jan. 1985.

Wood, Norman J.; and Sanderfer, Dwight T.: Transonic Performance of Two Circulation Control Airfoils. NASA TM X-86767, 1987.

WIND TUNNEL STUDIES OF

CIRCULATION CONTROL ELLIPTICAL AIRFOILS

M. E. Franke and J. K. Harvell
Air Force Institute of Technology

SUMMARY

Effects of blown jets on the lift and drag of cambered elliptical airfoils are described. Performance changes due to a splitter plate attached to the lower surface of an elliptical airfoil near the trailing edge with and without blowing are indicated. Lift and drag characteristics of airfoils with two blown jets are compared with airfoils with single blowing jets. Airfoil designs that vary the location of a second jet relative to a fixed jet are described.

INTRODUCTION

Numerous studies have demonstrated the basic concepts of circulation control airfoils (refs. 1 to 13). These studies have been supplemented by flight tests which have demonstrated further the application of circulation control lifting surfaces (refs. 14 to 16). A review paper has summarized circulation control technology (ref. 17).

Several areas that have not been studied extensively include the use of splitter plates and multiple-jet blowing in the airfoil trailing-edge region. The objective of this paper is to describe experimental studies that have been conducted to determine the low-speed lift and drag characteristics of circulation control elliptical airfoils using splitter plates and multiple jet blowing in the trailing-edge region. The paper will describe the effects of a number of parameters on the lift coefficient and the drag coefficient. These parameters include number of blown jets, locations of the blowing slots, splitter plate, splitter plate configuration, trailing-edge contour, airfoil angle of attack, and combinations of the above.

SYMBOLS

b	splitter plate chord
c	airfoil chord
C_d	section drag coefficient
C_{d_e}	equivalent drag coefficient

C_{d_f} equivalent force drag coefficient

C_{d_o} corrected profile drag coefficient

C_{d_r} profile (rake) drag coefficient

C_ℓ section lift coefficient

C_μ section momentum coefficient, $\dot{m}V_j/q_\infty c$

C_{μ_c} cylindrical plenum momentum coefficient

C_{μ_m} main plenum momentum coefficient

C_{μ_s} second plenum momentum coefficient; also C_{μ_c}

C_{μ_T} total momentum coefficient, $C_{\mu_m} + C_{\mu_s}$ or $C_{\mu_m} + C_{\mu_c}$

h slot height

$\dot{m}$ jet mass flow rate per unit span

q dynamic pressure, $\rho V_\infty^2/2$

R_e Reynolds number, $\rho V_\infty c/\mu$

V velocity

x coordinate along chord

α geometric angle of attack

β splitter plate deflection angle from airfoil chord

δ slot 2 deflection angle from airfoil chord

θ slot jet angle relative to chord

μ viscosity

ρ density

ϕ cylinder slot 2 rotation angle

Subscripts

c cylindrical plenum

j jet

m main plenum

s second plenum

∞ freestream

AIRFOIL DESCRIPTIONS

Several different airfoil configurations were tested in this study. Schematics of the airfoil models are shown in figures 1 to 4. The experimental models were 20-percent-thick elliptical airfoils with cambers ranging from 5 to 8 1/2 per cent. The models had a span of 0.66 m, a chord of 0.51 m, and blowing slot heights of 0.5 mm.

The airfoil model shown in figure 1 contained a single plenum. Blowing air entered the plenum through a 3.8-cm-diam pipe and discharged through the blowing slot located at $x/c = 0.96$. An enlarged view of the trailing-edge region is shown in figure 2. The jet at the blowing slot was directed approximately parallel to the chord as shown in figure 2. Forty-eight pressure taps were used to measure the static pressure along the upper and lower surfaces of the airfoil. Forty-four of these taps were located at centerspan and four taps were located off centerspan to check the uniformity of the flow.

The model shown in figure 3 contained two separate plena and two blowing slots. Otherwise, the model was similar to that shown in figure 1. Two different trailing edge inserts were used to provide different jet exit directions ($\delta = 45$ deg or $\delta = 58$ deg) for the second slot. The third model (fig. 4) also contained two separate plena. The circular trailing-edge surface of the airfoil was formed by the surface of the circular cylinder. The cylinder was also used as the plenum for the second blowing jet. The second slot was formed in the cylinder as shown in the enlarged view in figure 4. The second slot location was varied by rotating the cylinder. The main plenum contained two screens and a foam block placed along the span that helped to provide a more uniform spanwise pressure distribution and, consequently, a more uniform jet velocity along the span. Three dead stop and three tensioning screws, spaced evenly along the span, were used to fix the slot height h at 0.5 mm. The location of the main plenum blowing slot was fixed at 94.5% chord. The second slot height was set and maintained at 0.5 mm by caps at the ends of the cylinder and by cross members held in place with screws. No screens or foam were used in the cylindrical plenum.

Sixty-seven static pressure taps were distributed along the centerspan of the model; 27 on the suction surface, 23 on the pressure surface, and 17 on the circular trailing edge. Three static pressure taps were located 0.15 m on each side of centerspan to monitor the two-dimensionality of the flow. Further details of the models are available (refs. 18 to 21).

TEST APPARATUS

Tests were conducted in the Air Force Institute of Technology 1.5-m-diam wind tunnel, which is an open-circuit tunnel with a maximum test speed of approximately 134 m/s. The tests were run at speeds ranging from approximately 25 to 30 m/s which is equivalent to a tunnel dynamic pressure of approximately 0.05 m of water. Four pitot-static tubes were used to measure the dynamic pressure. The Reynolds number varied between 7.3×10^5 and 10^6. The turbulence factor of the tunnel is 1.5, which accounts for the effect of the propeller, guide vanes, and tunnel wall vibrations.

Each model was installed in the wind tunnel with its span vertical and was supported at each end of the span. Two large wooden side panels were installed in the 1.5-m-diam circular test section to provide a more two- dimensional section that was 0.8 x 1.5 m. Adjustments to the side walls were made to provide uniform flow in the section. The two-dimensionality was further increased by using endplates -- 1.2-m-diam, 5-mm thick and beveled at the edges -- on both ends of the airfoil to reduce boundary layer and finite span effects. The combination of the plates and the wind tunnel walls formed the 0.66 x 1.5 m test section.

The air supplied to both plena was routed through the supports. A 12.7-mm-throat-diameter venturi meter, located in each air supply line, was used to measure the mass flow rate to each plenum. Static pressure readings were obtained at taps located at and immediately upstream of each venturi throat. The temperature was measured with a copper-constantan thermocouple located upstream of each venturi meter.

A wake survey rake placed horizontally across the tunnel and 1.5c to 1.9c behind the airfoil was used to measure the momentum deficit in the wake. Ninety-four total head tubes and six static tubes, distributed along the span of the rake, were used to measure the pressure in the airfoil wake.

Alcohol manometers were used to measure the static pressure on the airfoil suface. Mercury manometers were used to measure the pressure at the venturi meters, and water manometers were used to measure the total pressure in the main and cylindrical plena.

DATA REDUCTION AND PROCEDURE

The manometer data were recorded on film, digitized, and then used to calculate the section coefficients. The standard wind tunnel corrections suggested by Pope (ref. 22) for solid blockage, wake blockage, and streamline curvature were applied to C_ℓ. Solid and wake blockage corrections were used also to adjust drag, freestream velocity, dynamic pressure, and Reynolds number.

The blowing jet momentum coefficient was defined in the usual manner as indicated in the list of symbols. When two blowing slots were used, a

total momentum coefficient was defined as the sum of the main plenum and second plenum momentum coefficients:

$$C_{\mu_T} = C_{\mu_m} + C_{\mu_s} \tag{1}$$

where $C_{\mu_s} = C_{\mu_c}$ for the cylindrical plenum.

The section lift coefficient C_ℓ was calculated from the pressure distribution on the airfoil surface. The section corrected profile drag coefficient was obtained from the profile (rake) coefficient based on the momentum deficit methods of Betz and Jones (ref. 23) and then corrected for the blowing slot jet flow that did not originate upstream of the airfoil, i.e.,

$$C_{d_o} = C_{d_r} - C_\mu \frac{V_\infty}{V_j} \tag{2}$$

where V_j was the calculated jet velocity in the jet exit plane based on isentropic expansion from plenum total pressure to freestream static pressure. The jet exit velocity actually depends, however, on the local static pressure at the slot exit. For two blowing slots

$$C_{d_o} = C_{d_r} - C_{\mu_m} \frac{V_\infty}{V_{j_m}} - C_{\mu_s} \frac{V_\infty}{V_{j_s}} \tag{3}$$

where $V_{j_s} = V_{j_c}$ for the cylindrical plenum. To facilitate comparison of circulation control airfoil performance with that of conventional airfoils, C_{d_o} was modified following Englar et al. (refs. 3 to 6) by the addition of dimensionless terms to account for energy expenditure to produce the blowing air flow and a ram drag effect. This results in an equivalent drag coefficient, which was defined in this study for two blowing slots as

$$C_{d_e} = C_{d_o} + C_{\mu_m} \left(\frac{V_{j_m}}{2V_\infty} + \frac{V_\infty}{V_{j_m}}\right) + C_{\mu_s} \left(\frac{V_{j_s}}{2V_\infty} + \frac{V_\infty}{V_{j_s}}\right) \tag{4}$$

Englar et al. (ref. 10) also defined an equivalent force drag coefficient. For this study the equivalent force drag coefficient was defined as

$$C_{d_f} = C_{d_o} + C_{\mu_m} + C_{\mu_s} \tag{5}$$

It is important to note before proceeding that sometimes corrections to C_{d_r} can be an order of magnitude larger than the actual measured drag. Thus, the effect of calculating C_μ based on expansion to freestream or to local static pressure can introduce variations in C_{d_e} or C_{d_f} of 25% or more. To be consistent with the lift results of others, C_μ was based on expansion to freestream pressure.

A second problem is that pointed out by Pope (ref. 22) that the wake rake, when used with the momentum deficit method, is only accurate when measuring drag on an airfoil that is not stalled. There are other considerations as well. One is that a wake rake, used in conjunction with a manometer bank, is a time-averaging device and readings of a cyclic behavior may be affected by the response time of the system. Another is that drag results have been reported in numerous ways in the literature and care must be taken when comparing results from different sources. Also, the penalties applied to the profile drag for energy expenditure and ram drag may not be approproate in all cases.

RESULTS AND DISCUSSION

Typical results showing the effects of a splitter plate, blowing slots, training-edge contour, angle of attack and various combinations are shown in figures 5 to 16. The effect of splitter plate chord for the x/c = 0.99 and β = 45 deg splitter plate configuration is shown in figure 5. The results indicate that the lift coefficient increased as the splitter plate chord was increased. The effect of angle of attack was as expected. Some separation occurred at positive angles of attack.

The effects of blowing (in terms of C_μ), splitter plate angle, and splitter plate location on C_ℓ and C_{d_f} are shown in figures 6 and 7, respectively. The lift coefficient generally increased with increases in C_μ for the range of C_μ considered and was higher for splitter plate angles of 45 and 60 deg then for a 30 deg angle. Compared with a clean airfoil, the splitter plate caused an increase in C_{d_f} of the airfoil at the lower values of C_μ considered. At the higher values of C_μ, C_{d_f} either increased or decreased relative to that of a clean airfoil depending on the splitter plate location and angle. Further results and details on the effects of a splitter plate on airfoil lift and drag are given by Stevenson et al. (ref. 18).

The results in figure 8, obtained by Oxford (ref. 19), show the effect of trailing-edge contour, slot position x/c, and slot angle θ on C_ℓ of an airfoil with a splitter plate. The variations were found to have little effect on C_ℓ over the range of C_μ shown in figure 8. The slot angle θ was the angle between the jet exit direction and the airfoil chord.

The use of two blowing jets was studied by Pajayakrit (ref. 20) using the airfoil model shown in figure 3. The lift coefficient and drag coefficient of the model (fig. 3) as a function of C_μ are shown in figures 9 and 10 for two different trailing-edge inserts. The results are for main plenum blowing only and are compared with the lift coefficient and drag

coefficient of airfoil (fig. 1) without a splitter plate. As shown in figures 9 and 10, the curves for the two models differ somewhat but have the same general trends. The curves for the same model (fig. 3) with the different inserts indicate that slight differences in the installation in the tunnel or in trailing-edge contour can cause differences in the measurements. It was also found that nonuniformity in slot height led to a nonuniform jet and reduced performance.

The effects of two-slot blowing on C_ℓ are shown in figure 11 for the airfoil (fig. 3) with the 58-deg-jet-blowing insert. Main plenum blowing alone was shown to be as effective as two-slot blowing over the range and combinations of C_{μ_T} studied. Results (not shown) with the 45-deg-jet-blowing insert showed that this configuration was less effective in increasing C_ℓ than with δ = 58 deg. Plots of C_ℓ vs C_{d_f} are shown in figures 12 and 13 for second-slot blowing angles δ of 58 deg and 45 deg, respectively. The results with δ = 58 deg, figure 12, indicate that C_{d_f} was somewhat less with two-slot blowing compared with C_{d_f} for main plenum blowing alone at a given C_ℓ. For δ = 45 deg, C_{d_f} was higher at a given C_ℓ for two-slot blowing compared with that for main plenum blowing alone, figure 13.

The model shown in figure 4 was designed so that the location of a second slot could be varied relative to a fixed, main-blowing slot. Tests showed that the spanwise pressure and velocity distributions were uniform within a few precent and that there was good flow attachment around the trailing edge. Separation normally occurred at angles ranging from ϕ = 70 to 90 deg with blowing only from the main slot. Tests were run with the second slot located at ϕ = 73 and 83 deg.

The lift coefficient as a function of total momentum coefficient C_{μ_T} is shown in figure 14 for ϕ = 73 deg. The baseline curve with blowing only from the main plenum (C_{μ_c} = 0) is also shown as a reference. In the tests with two-slot blowing, C_{μ_m} was held constant (within $\pm$ 0.002), while the blowing rate from the cylindrical plenum was varied. The value of C_{μ_m} for each curve is identified in figure 14. The curves illustrate the advantage of two-slot blowing over single-slot blowing. For example, at C_{μ_T} = 0.05 there was up to a 50% increase in C_ℓ for two-slot blowing depending on the value of C_{μ_m}. The results indicate that once the main plenum blowing was sufficient to keep the boundary layer attached up to the second blowing slot, any additional main plenum blowing in terms of C_μ did not increase lift as much as that for an equivalent incremental amount of blowing (in terms of C_μ) from the second slot. When the value of C_{μ_m} was below that required for boundary-layer attachment up to the second slot, blowing from the second slot was slightly less effective than an equivalent amount of C_μ based on single-slot main plenum blowing. This is illustrated in figure 14 by comparing the C_{μ_m} = 0 and 0.007 curves with the baseline C_{μ_c} = 0 curve. The tests with C_{μ_m} = 0 and 0.007 were terminated at C_{μ_T} = 0.015 and 0.05, respectively, due to an unexplained audible resonance experienced at the next test condition for each case. The results for ϕ = 83 deg (ref. 21) were similar to those for ϕ = 73 deg, except that the minimum value of C_{μ_m} had to be increased to keep the flow attached up to the second

blowing slot.

The blown jet velocities at the slot exits were always less than sonic. Typical jet exit velocities for single-slot blowing alone at $C_{\mu_m} \approx 0.9$ were $V_{j_m} \approx 190$ m/s, whereas for two-slot blowing at $C_{\mu_T} \approx 0.9$, V_{j_m} and V_{j_c} were on the order of 140 m/s. Loth and Boasson (ref. 24) replotted data from Englar (ref. 25) and showed that, at constant slot height, ΔC_ℓ increases rather linearly with V_j/V_∞. The results with single-slot (main plenum) blowing in this study showed a somewhat similar relationship. Loth and Boasson (ref. 24) also determined that for single-slot blowing at constant C_μ, the maximum value of ΔC_ℓ will be obtained at a V_j/V_∞ value of approximately 4.6. However, at a given C_μ, there is only about a 10% variation in ΔC_ℓ over a range of V_j/V_∞ values between 2.5 and 12. Herein, V_j/V_∞ was varied over a range of approximately 2 to 7, and, consequently, for single-slot blowing at constant C_μ, less than a 10% variation in ΔC_ℓ would be expected. With two-slot blowing, however, larger increases in ΔC_ℓ at constant C_{μ_T} are shown in figure 14. Apparently, by reducing jet velocity and introducing a second blown jet, the momentum and energy of the two jets are used more effectively in increasing C_ℓ.

Typical equivalent drag results are shown in figure 15. With single-slot blowing, C_{d_e} was found to be slightly greater than that of the two-slot configurations at equivalent C_{μ_T}. Since lift as a function of C_{μ_T} was significantly enhanced with two-slot blowing, lift-to-drag ratios C_ℓ/C_{d_e} shown in figure 16 were higher for two-slot blowing than for single-slot blowing.

CONCLUDING REMARKS

A single blown jet was effective in increasing the lift coefficient of an elliptical airfoil as the momentum coefficient was increased. At the same total momentum coefficient C_{μ_T}, two blown jets were more effective than a single jet in some cases. The relative location of the two jets was found to be important. When using two slots, maximum C_ℓ/C_{d_e} was obtained by limiting the blowing from the primary slot to just the amount needed to ensure good flow attachment up to the secondary slot. However, too little blowing from the primary slot reduced the effectiveness of blowing from the second slot to being equivalent to or less than that for a single slot. A fixed splitter plate improved performance under most conditions. Splitter plate effectiveness depended on splitter plate chord, angle, and location. Trailing-edge contour did not influence lift as much in combination with a splitter plate as otherwise might be expected. Better performance was obtained with uniform slot height.

REFERENCES

1. Englar, R.J.: Experimental Investigation of the High Velocity Coanda Wall Jet Applied to Bluff Trailing Edge Circulation Control Airfoils. Naval Ship Research and Development Center, Bethesda, MD, NSRDC Rept. 4708, 1975.

2. Davidson, I.M.: Aerofoil Boundary-Layer Control System. British Patent 913754, 1960.

3. Kind, R.J. and Maull, D.J.: An Experimental Investigation of a Low-Speed Circulation-Controlled Aerofoil. The Aeronautical Quarterly, Vol. 19, May 1968, pp. 170-182.

4. Williams, R.M. and Howe, H.J.: Two-Dimensional Subsonic Wind Tunnel Tests on a 20-Percent Thick, 5-Percent Cambered Circulation Control Airfoil. Naval Ship Research and Development Center, Bethesda, MD, NSRDC Tech. Note AL-176, 1970.

5. Englar, R.J.: Two-Dimensional Subsonic Wind Tunnel Tests of Two 15-Percent Thick Circulation Control Airfoils. David Taylor Naval Ship Research and Development Center, Bethsda, MD, DTNSRDC Tech. Note AL-211, 1971.

6. Englar, R.J.: Two-Dimensional Subsonic Wind Tunnel Investigations of a Cambered 30-Percent Thick Circulation Control Airfoil. Naval Ship Research and Development Center, Bethesda, MD, NSRDC Tech. Note AL-201, 1972.

7. Englar, R.J.: Subsonic Two-Dimensional Wind Tunnel Investigations of the High Lift Capability of Circulation Control Wing Sections. David Taylor Naval Ship Research and Development Center, Bethesda, MD, DTNSRDC Tech. Rept. ASED-274, 1975.

8. Walters, R.E., Myer D.P., and Holt D.J.: Circulation Control by Steady and Pulsed Blowing for a Cambered Elliptical Airfoil. West Virginia University, Morgantown, WV, AD751045, Aerospace Engineering TR-32, 1972.

9. Englar, R.J.: Circulation Control for High Lift and Drag Generation on STOL Aircraft. Journal of Aircraft, Vol. 12, May 1975, pp. 457-463.

10. Englar, R.J. Williams, R.M.: Test Techniques for High-Lift, Two-Dimensional Airfoils with Boundary Layer and Circulation Control for Application to Rotary Wing Aircraft. Naval Ship Research and Development Center, Bethesda, MD, NSRDC Report 4645, 1975.

11. Abramson, J.: Two-Dimensional Subsonic Wind Tunnel Evaluation of a 20-Percent Thick Circulation Control Airfoil. David Taylor Naval Ship Research and Development Center, Bethesda, MD, DTNSRDC Rept. ASED-311, Code 1619, 1975.

12. Abramson, J.: Two-Dimensional Subsonic Wind Tunnel Evaluation of Two Related Cambered 15-Percent Thick Circulation Control Airfoils. David Taylor Naval Ship Research and Development Center, Bethesda, MD, DTNSRDC Rept. ASED-373, 1977.

13. Smith, R.V.: A Theoretical and Experimental Study of Circulation Control with Reference to Fixed Wing Applications. University of Southampton, United Kingdom, Research Paper 582, 1978.

14. Loth, J.L., Fanucci, J.B., and Roberts, S.C.: Flight Performance of a Circulation Controlled STOL Aircraft. Journal of Aircraft, Vol. 13, March 1976, pp. 169-173.

15. Englar, R.J.: Development of the A-6/Circulation Control Wing Flight Demonstrator Configuration. David Taylor Naval Ship Research and Development Center, Bethesda, MD, DTNSRDC Rept. ASED 79/01, 1979.

16. Nichols, J.H., Jr., Englar, R.J., Harris M.J., and Huson, G.G.: Experimental Development of an Advanced Circulation Control Wing System for Navy STOL Aircraft. AIAA Paper 81-0151, January 1981.

17. Wood, N. and Nielsen, J.: Circulation Control Airfoils Past, Present, Future. AIAA Paper 85-0204, AIAA 23rd Aerospace Sciences Meeting, Reno, NV, January 1985.

18. Stevenson, T.A., Franke, M.E., Rhynard, W.E., Jr., and Snyder, J.R.: Wind-Tunnel Study of a Circulation-Controlled Elliptical Airfoil. Journal of Aircraft, Vol. 14, September 1977, pp. 881-885.

19. Oxford, Vayl S.: A Wind Tunnel Study of the Effects of Trailing Edge Modifications on the Lift-Drag Ratio of a Circulation Controlled Airfoil. MS Thesis, GAE/AA/75D-16, Air Force Institute of Technology, Wright-Patterson AFB, OH, 1975.

20. Pajayakrit, Palanunt: A Wind Tunnel Study of the Effects of Lower Surface Blowing on the Lift, Drag, and Lift-to-Drag Ratio of a Circulation Control Elliptical Airfoil. MS Thesis, GAE/AA/79D-13, Air Force Institute of Technology, Wright-Patterson AFB, OH, 1980.

21. Harvell, J.K. and Franke, M.E.: Aerodynamic Characteristics of a Circulation Control Elliptical Airfoil with Two Blown Jets. Journal of Aircraft, Vol. 22, No. 9, September 1985, pp. 737-742.

22. Pope, A.: Wind Tunnel Testing. John Wiley and Sons, Inc., New York, 1954.

23. Schlichting, H.: Boundary Layer Theory. 7th Ed., McGraw-Hill Book Co., New York, 1979.

24. Loth, J.L. and Boasson, M.: Circulation Controlled STOL Wing Optimization. Journal of Aircraft, Vol. 21, February 1984, pp. 128-134.

25. Englar, R.J.: Low-Speed Aerodynamic Characteristics of a Small Fixed Trailing-Edge Circulation Control Wing Configuration Fitted to a Supercritical Airfoil. David Taylor Naval Ship Research and Development Center, Bethesda, MD, DTNSRDC Rept. ASED-81/08, 1981.

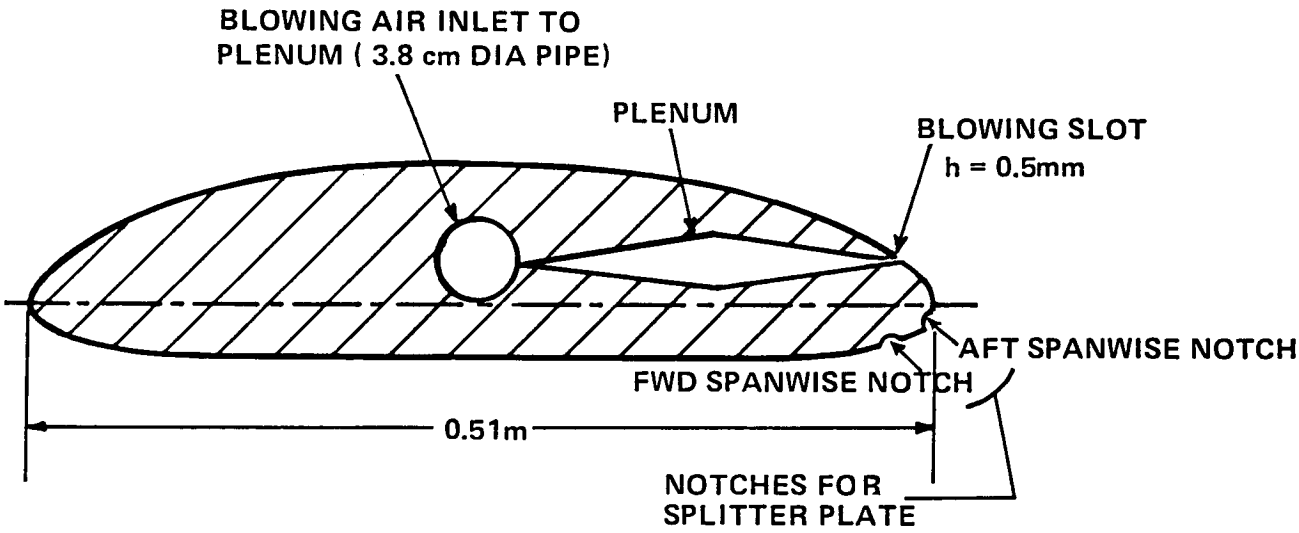

Figure 1. - Schematic of airfoil with single plenum.

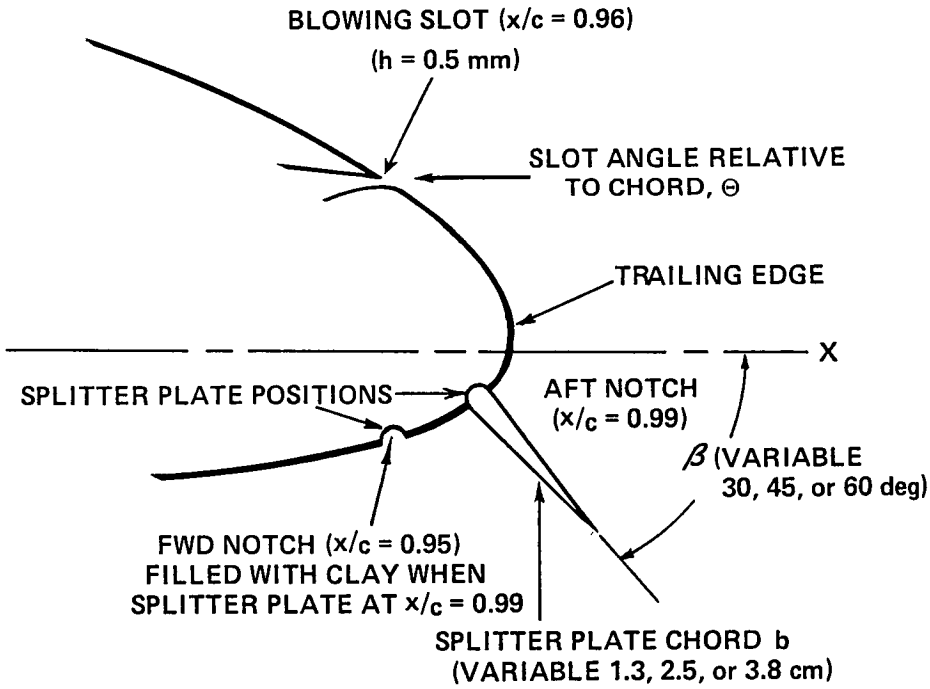

Figure 2. - Sketch of trailing edge with attached splitter plate.

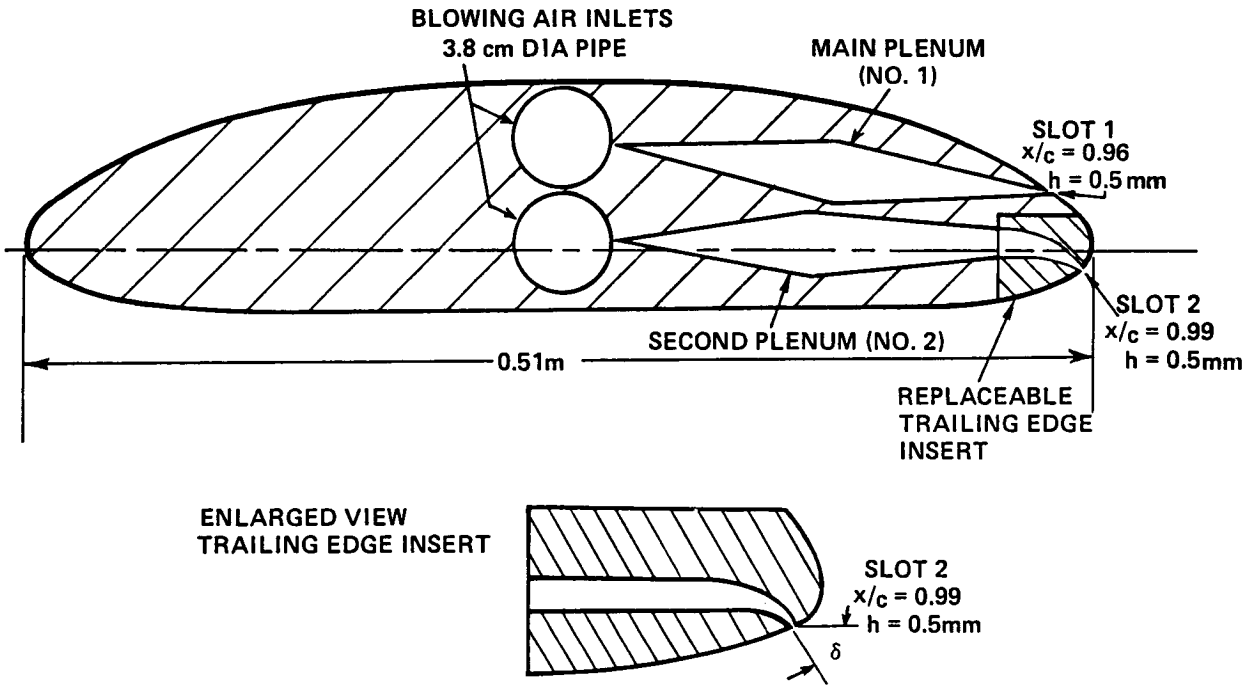

Figure 3. - Schematic of airfoil with two plena.

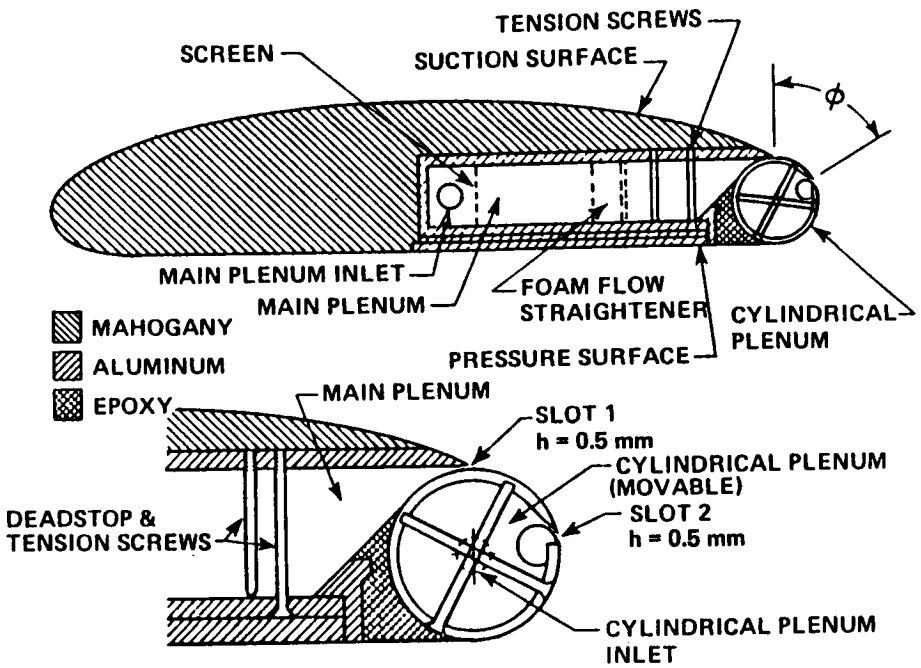

Figure 4. - Schematic of airfoil with two plena and rotatable circular trailing edge.

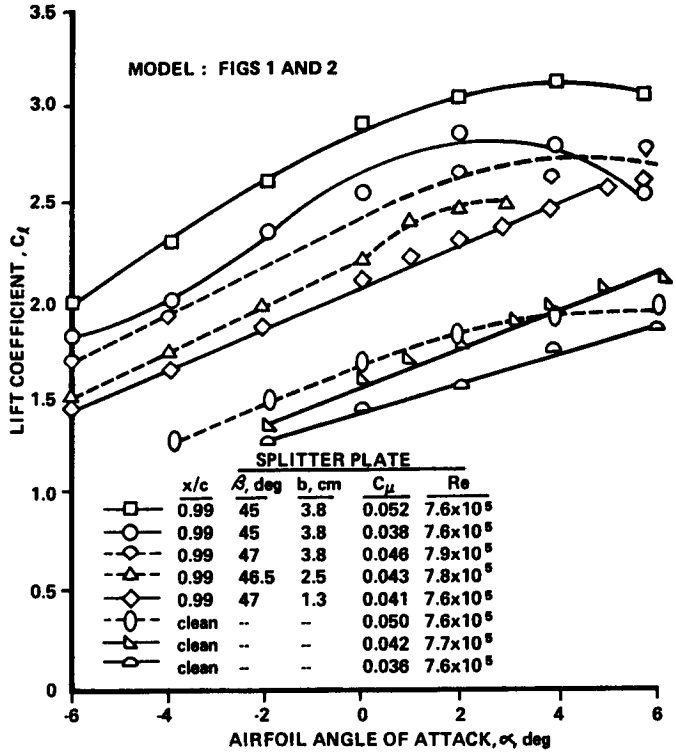

Figure 5. - Effect of blowing and splitter plate chord on lift coefficient.

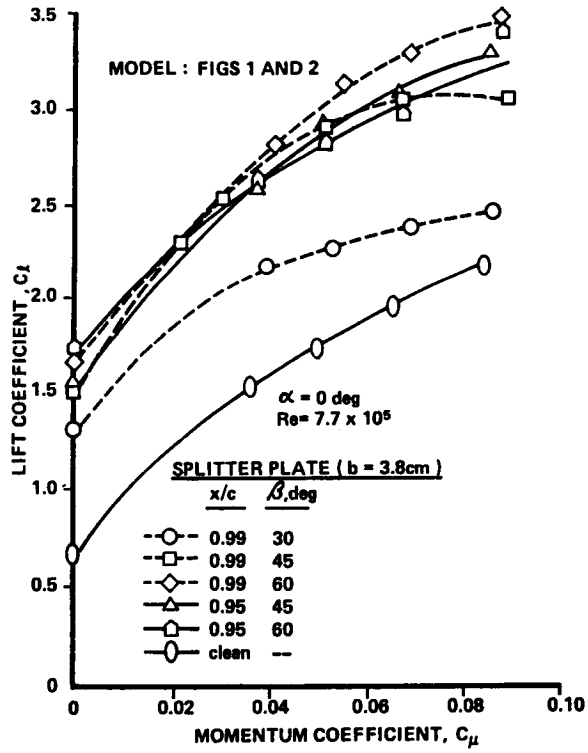

Figure 6. - Effect of blowing and splitter plate configuration on lift coefficient.

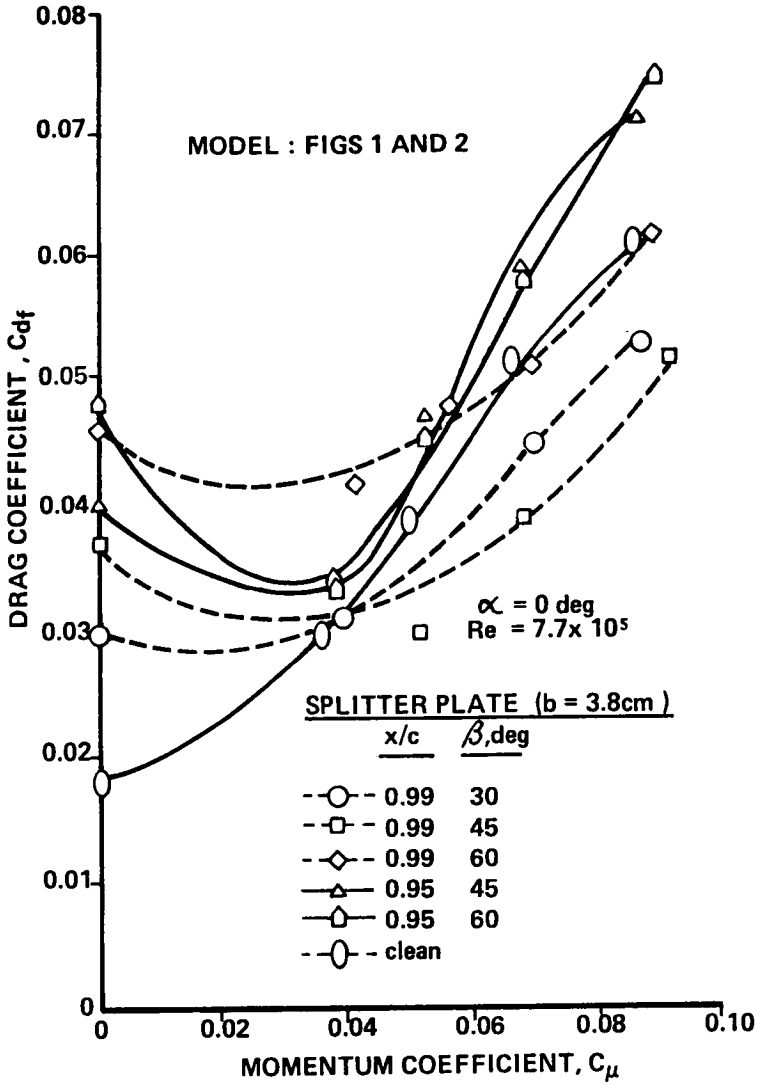

Figure 7. - Effect of blowing and splitter plate configuration on drag coefficient.

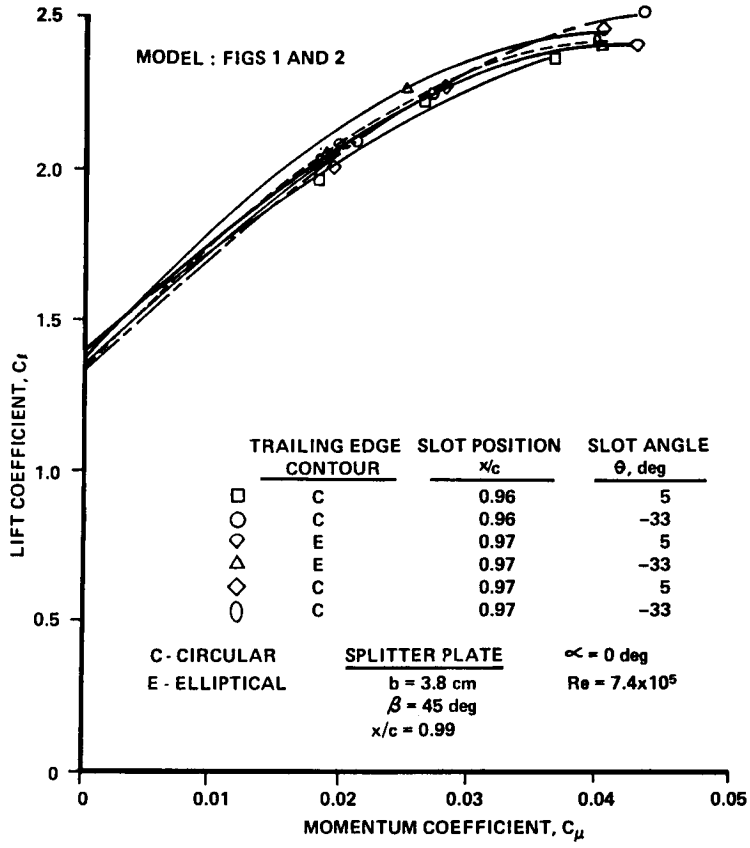

Figure 8. - Effect of trailing-edge configuration on lift coefficient with a splitter plate.

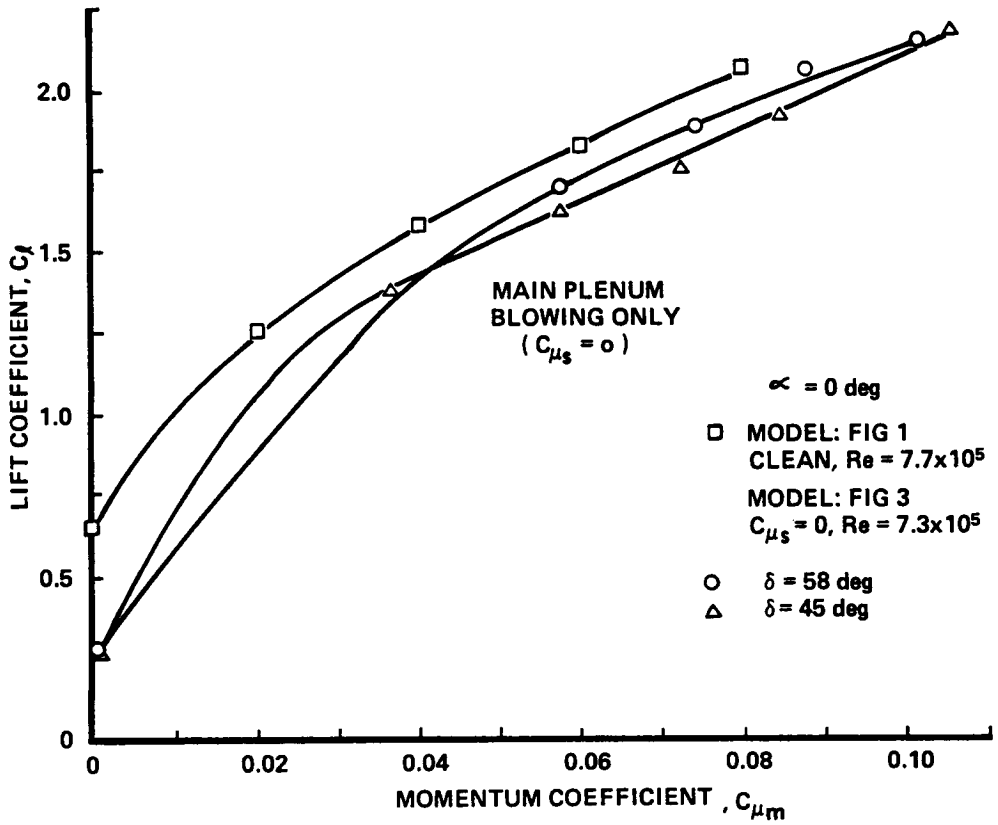

Figure 9. - Comparison of lift coefficient of airfoil (fig. 3) with that of airfoil (fig. 1).

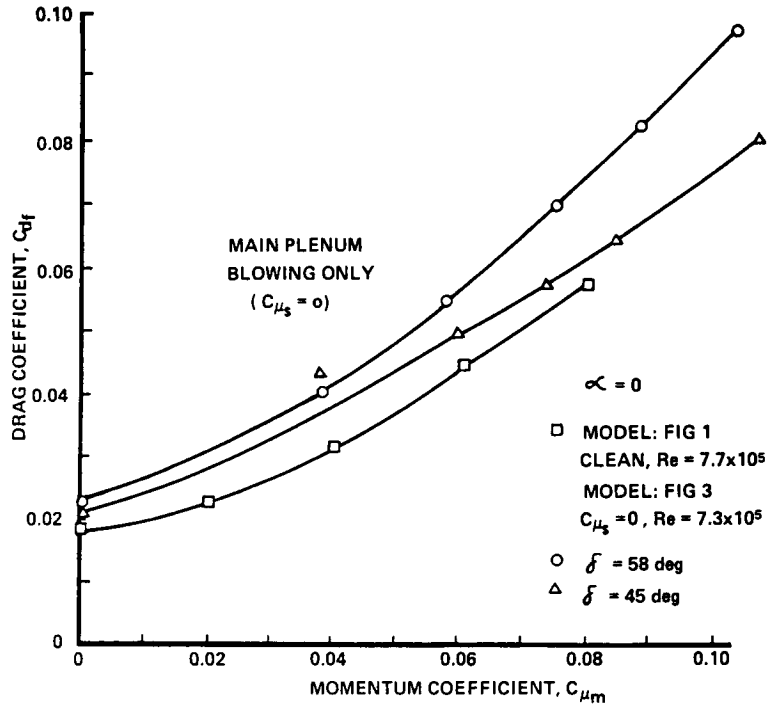

Figure 10. - Comparison of drag coefficient of airfoil (fig. 3) with that of airfoil (fig. 1).

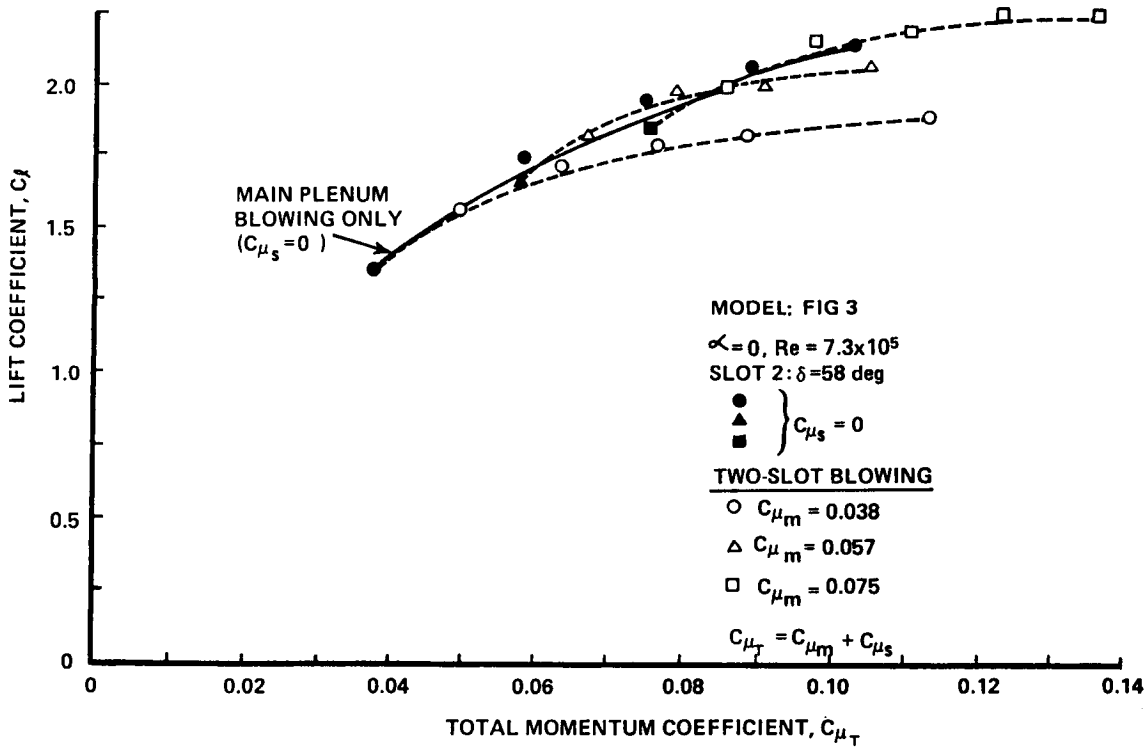

Figure 11. - Effect of two-slot blowing on lift coefficient.

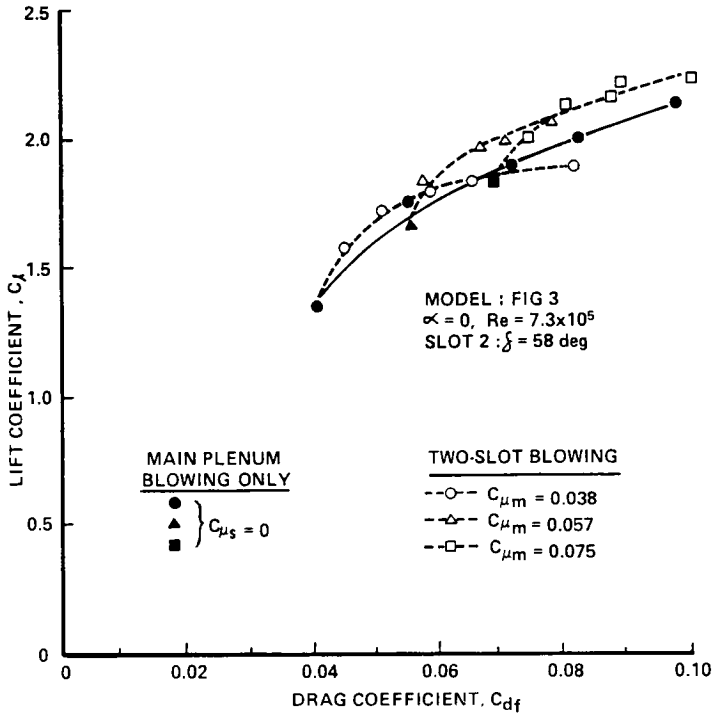

Figure 12. - Lift coefficient as a function of drag coefficient with blowing, δ = 58 deg.

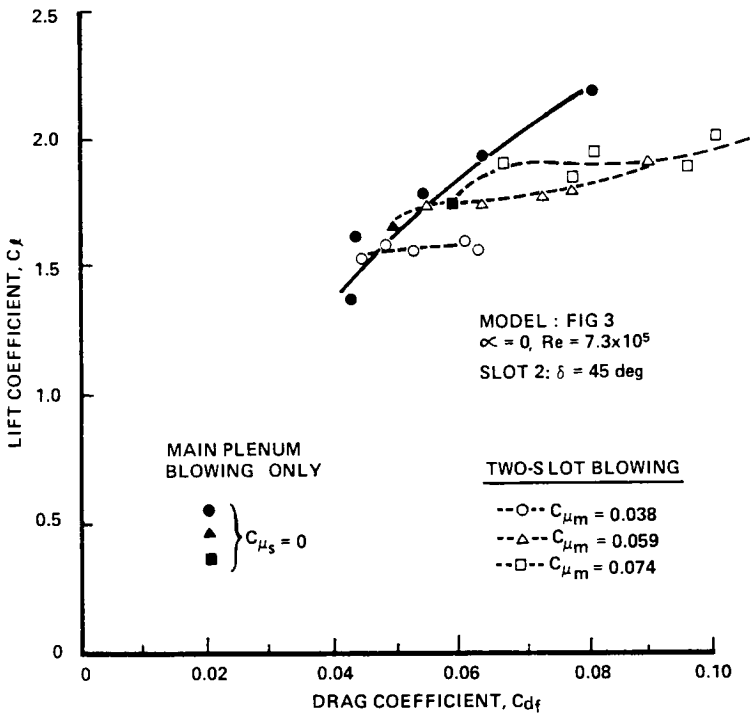

Figure 13. - Lift coefficient as a function of drag coefficient with blowing, δ = 45 deg.

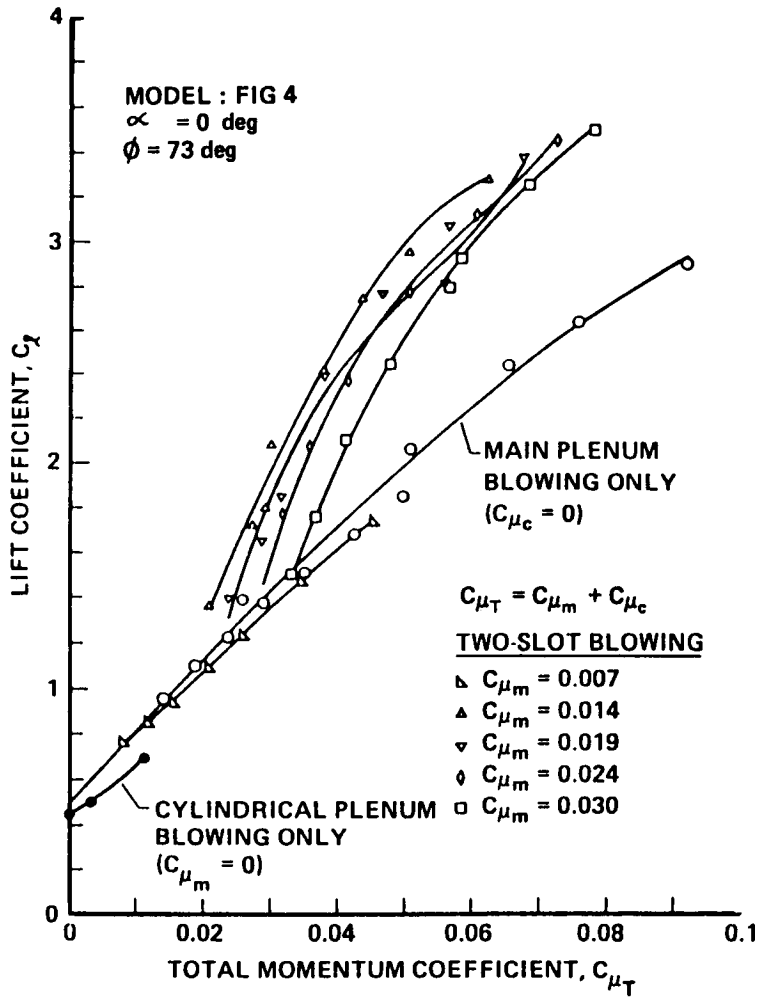

Figure 14. - Effect of two-slot blowing on lift coefficient, ϕ = 73 deg.

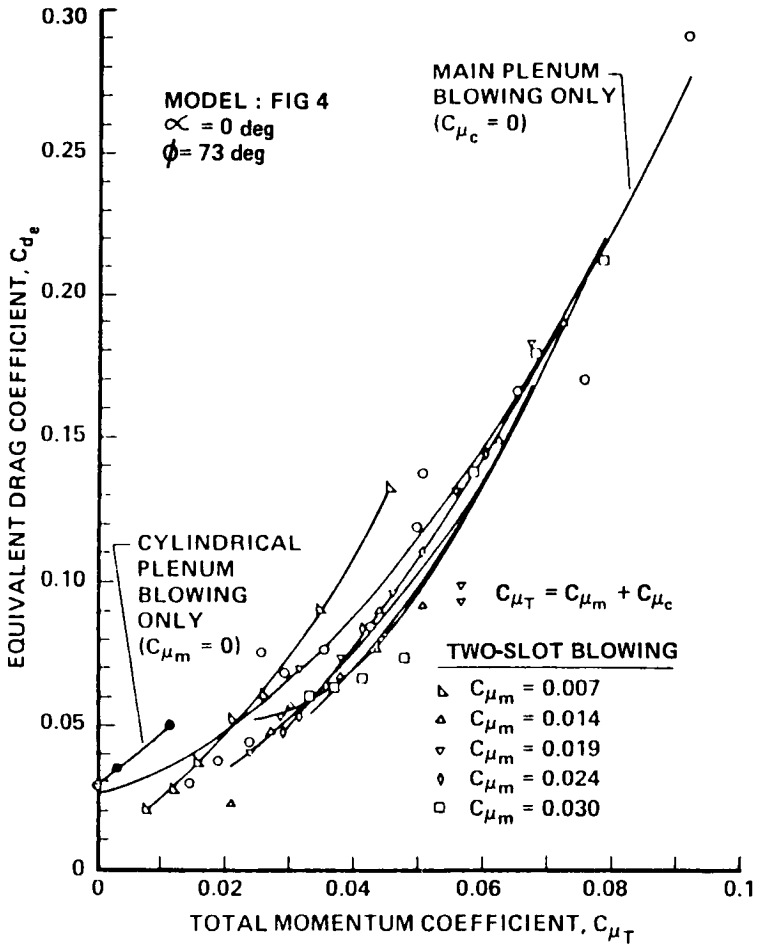

Figure 15. - Effect of two-slot blowing on drag coefficient, ϕ = 73 deg.

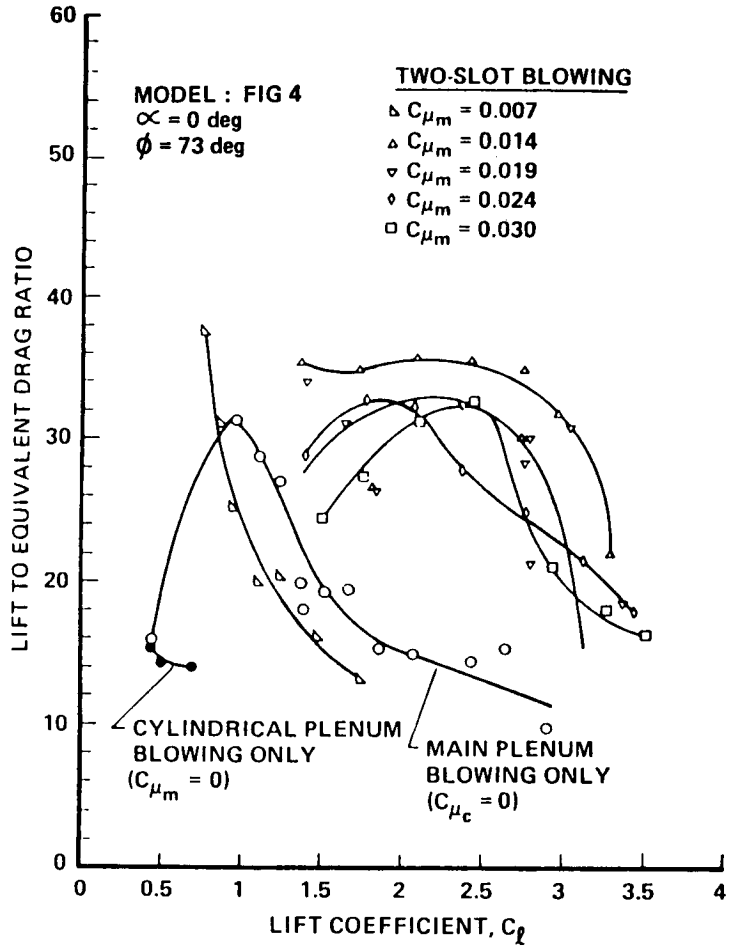

Figure 16. - Lift-to-equivalent-drag ratio as a function of lift coefficient, ϕ = 73 deg.

DESIGN OF SUPERSONIC COANDA JET NOZZLES*

Paul M. Bevilaqua
Lockheed Advanced Aeronautics Company
John D. Lee
Ohio State University, Columbus, Ohio

ABSTRACT

The thrust vectoring of supersonic Coanda jets was experimentally studied to determine the effect of skewing the initial velocity profile to eliminate expansion and turning shocks. A new nozzle design procedure, based on the method of characteristics, was developed to design an asymmetric convergent-divergent nozzle for skewing the velocity profile. The performances of a simple convergent nozzle, a symmetric C-D nozzle, and an asymmetric C-D nozzle were experimentally compared over a range of pressure ratios from 1.5 to 3.5. Eliminating the expansion shocks with the symmetric C-D nozzle was found to improve the thrust vectoring; skewing the velocity profile to eliminate the turning shocks further improved the vectoring.

NOMENCLATURE

k	Vorticity Factor
$\dot{m}$	Mass Flow Rate
M	Mach Number
P	Pressure
PR	Pressure Ratio
R	Radius of Curvature
R	Gas Constant
Re	Reynolds Number
T	Jet Momentum
t	Nozzle Gap
r,ϕ	Polar Coordinates
x,y	Cartesian Coordinates
V	Jet Velocity
∂	Differential Operator
Δ	Difference Operator
δ	Local Jet Thickness
r	Ratio of Specific Heats
ρ	Jet Density
τ	Temperature
θ	Flow Angle
ν	Prandtl-Myer Function
γ	Ratio of Specific Heats

Subscripts

∞	Infinity
sep	Separation
o	Stagnation

INTRODUCTION

A particularly simple and, therefore, attractive means of developing the additional lift required by V/STOL aircraft is to utilize the Coanda effect to deflect the engine exhaust jet, as shown in Figure 1. The Coanda effect is the tendency for a fluid jet to attach itself to an adjacent surface and follow its contour. The jet is pulled onto the surface by the low pressure region which develops as entrainment pumps fluid from the region between the jet and the surface. The jet is then held to the wall by the resulting radial pressure gradient, which balances the jet's inertial resistance to turning.

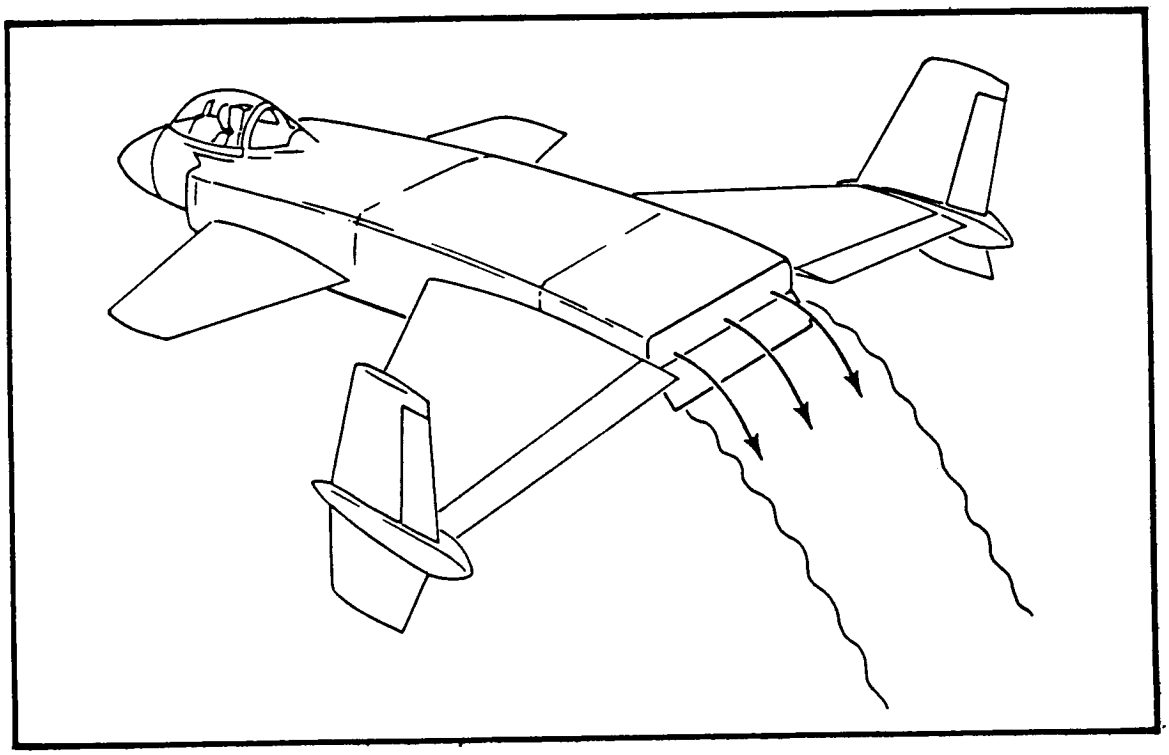

Figure 1. Use of the Coanda Effect for Thrust Vectoring

If the radius of the Coanda surface is large compared to the initial jet thickness, the jet readily attaches to the surface and may be deflected through more than 180°. However, if the radius of curvature is small, the jet turns through a smaller angle, or may not attach to the surface at all. Because size and weight limitations limit the radius of aircraft deflection surfaces, jet deflection angles greater than 60° have been difficult to achieve. Consequently, various techniques have been devised to improve the jet deflection. Von Glahn and Groesbuck (Von Glahn, U. and Groesbuck, D., 1976) used external deflector vanes to turn the jet toward the surface, while Davenport and Hunt (Davenport, F.J. and Hunt, D.N., 1975) used surface mounted director vanes to spread the jet out and reduce its thickness, thus increasing the effective turning radius. They also studied the effect of surface contour, by comparing the deflection of a series of two-piece flaps, which consisted of a circular arc and a straight section. The jet was found to be deflected further by a surface with a small initial radius, followed by a long straight section, than by one with a large initial radius followed by a short straight section.

Several methods of boundary layer control have also been considered. Both Coanda (Metral, Z. and Zerner, F., 1953) and Von Glahn (Von Glahn, U., 1958) studied the effectiveness of multiple flat plate turning surfaces, whose corners were intended to trip the boundary layer and re-energize it. However, not enough data was obtained to show an advantage. Bradbury and Wood (Bradbury, L.J.S., and Wood, M.N., 1965) examined the effect of auxiliary jets along the Coanda surface. These were found to be effective in delaying the separation of subsonic jets, but had no effect on supersonic jets.

Supersonic Coanda jets, which would be used in an aircraft system, present a special problem. The adjustment of the jet to the pressure outside the nozzle involves a system of shock waves which can detach the jet from the Coanda surface. The purpose of this paper is to present the results of a study into the effect of the expansion and turning shocks on the deflection of supersonic Coanda jets, and to describe a nozzle devised to improve thrust vectoring by eliminating this shock system. A combination of analysis and testing has been utilized. In the next section, the phenomena which determine the deflection of Coanda jets are considered in more detail. The design of a new nozzle, devised to test the hypothesis that eliminating the turning shocks will improve the thrust vectoring, is presented in the following section. The test apparatus and the procedures used to measure the jet thrust and turning angle are described in the section after that. In the last section, the test results are presented and analyzed. It is concluded that eliminating the expansion shocks with a convergent-divergent nozzle significantly improves the thrust vectoring compared to the simple convergent nozzles in current use, and that shaping the velocity profile to eliminate turning shocks further improves the thrust vectoring.

COANDA JET DEFLECTION

There are actually two problems in deflecting a jet over small radius curves (generally, those with a radius less than 10 jet thicknesses): that of initially attaching the jet, and that of delaying the eventual separation of the attached jet. The inertia of the jet itself resists its initial attachment. As the radius of the turn decreases, the inertial force, $\rho V^2/R$, becomes larger than the radial pressure gradient, $\partial P/\partial r$, which draws the jet to the surface. At some point, the jet will not attach. Attachment limits have not been established, but the minimum radius of attachment decreased with increasing Mach number. (Bradbury, L. J. S., Wood, M. N., 1965). We believe this is because it becomes more difficult for the jet to adjust to the influence of the Coanda surface: the flow on the lower wall inside the nozzle must accelerate faster than the flow on the upper wall in order to skew the velocity profile and adjust to the radial pressure gradient at the nozzle exit. The radial pressure gradient enables the jet to turn smoothly onto the Coanda surface. In a subsonic jet, this adjustment is made easily, because the effect of the surface curvature can be transmitted upstream into the nozzle. A supersonic jet cannot make this adjustment, so that it has greater resistance to turning.

A jet which has attached to a flat plate will remain attached, in the absence of external disturbances. However, due to the action of viscosity, a jet which has attached to a curved plate will eventually separate. Viscosity causes the development of a boundary layer at the inner edge of the jet and a mixing layer at the outer edge, where the surrounding fluid is entrained. This eventually causes the boundary layer to separate in the following way: as the jet flows around the curved surface, the inertia force is balanced by the radial pressure gradient; that is,

$$\frac{\partial P}{\partial r} = \frac{\rho V^2}{R} \qquad (1)$$

as shown schematically in Figure 2. Dimensionally, this equation may be interpreted as

$$\frac{\Delta P}{\delta} = \frac{\rho V^2}{R} \qquad (2)$$

in which δ is the thickness of the jet. Thus, to first order, the pressure on the Coanda surface is given by

$$P(\phi) = P_\infty - T(\phi)/R(\phi) \qquad (3)$$

in which $T = \rho V^2 \delta$ is the local momentum of the jet and ϕ is the angular position along the surface. As the jet flows around the surface, its thrust is reduced by wall friction and the average radius of curvature, R, is increased by mixing with the surroundings. Both these effects cause the surface pressure to rise. The jet boundary layer eventually separates in the resulting adverse pressure gradient. Of course, the boundary layer may separate sooner, if a more severe gradient is imposed on it, as by an impinging shock wave or an increase in surface curvature.

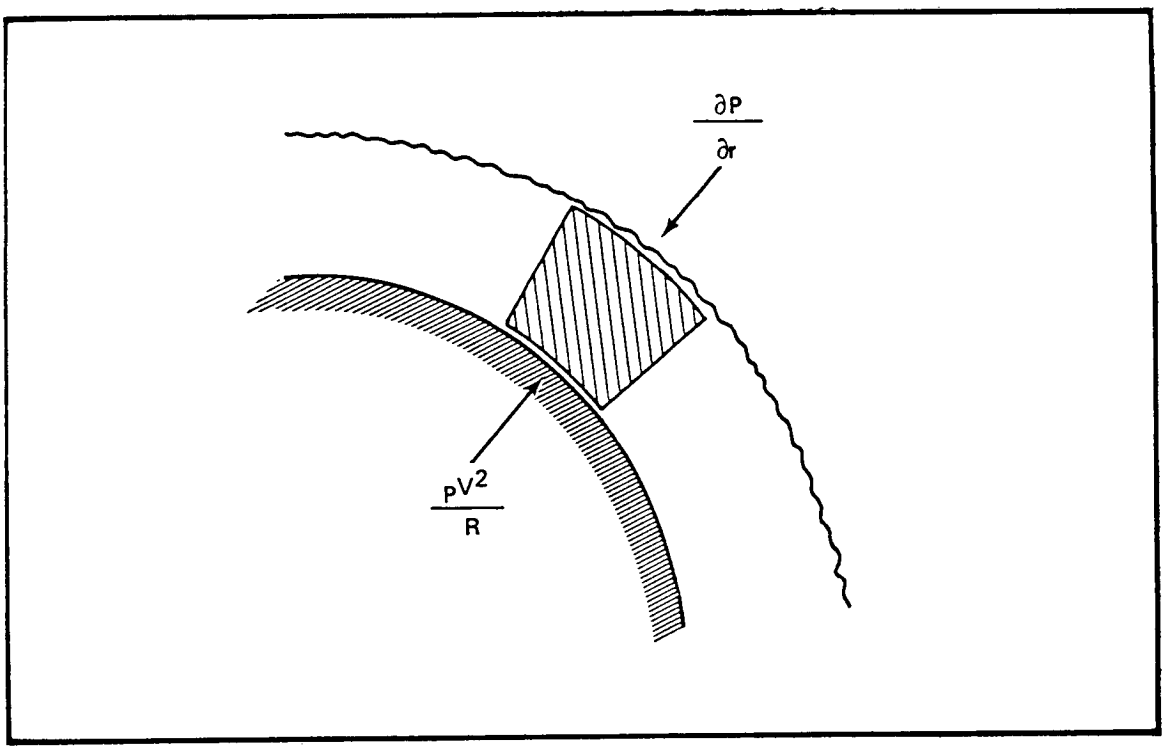

Figure 2. Radial force balance in a Coanda jet segment

There are no theories for predicting the point of separation. But, if it is assumed that the separation angle depends on the initial thrust of the jet, the radius of the Coanda surface, and the properties of the fluid, dimensional analysis gives

$$\phi sep = \phi(R/t, Re, M) \qquad (4)$$

Re and M are the jet Reynolds number and Mach number, respectively. The form of this function can be determined from experimental data. Although not enough data has been obtained to do so, the value of this function has been determined in some

limiting cases: for incompressible flow (M = 0), Newman (Newman, B.G., 1961) found that the separation angle increases with R/t and Re to a maximum value of about 245°. At R/t = 5, the turning angle is about 170°. In the transonic regime, Davenport and Hunt (Davenport, F.J., and Hunt, D.N., 1975) did not obtain more than 100° of turning, and achieved only about 60° at R/t = 5. There is very little data for supersonic Coanda jets, but Bradbury and Wood (Bradbury, L.J.S., and Wood, M.N., 1965) found that the separation angle decreases as the Mach number is increased. All these data were obtained with convergent nozzles.

The system of expansion shocks which adjusts the jet from a convergent nozzle to the exit pressure may be eliminated by using a convergent-divergent nozzle. It seems reasonable to expect that this would improve the jet turning by eliminating shock-induced boundary layer separation. However, such a jet would still resist the initial attachment, because the radial pressure gradient is zero at the nozzle exit. Even if the entrainment is strong enough to attach the jet, the system of expansion waves which then develops may cause it to separate again within a short distance. The wave system is sketched in Figure 3. The expansion waves which are formed when the jet deflects onto the surface are reflected from the outer jet boundary as a system of compression (shock) waves. These compression waves then impinge on the jet boundary layer. If the impinging shock is strong enough, the jet will separate from the surface at this point.

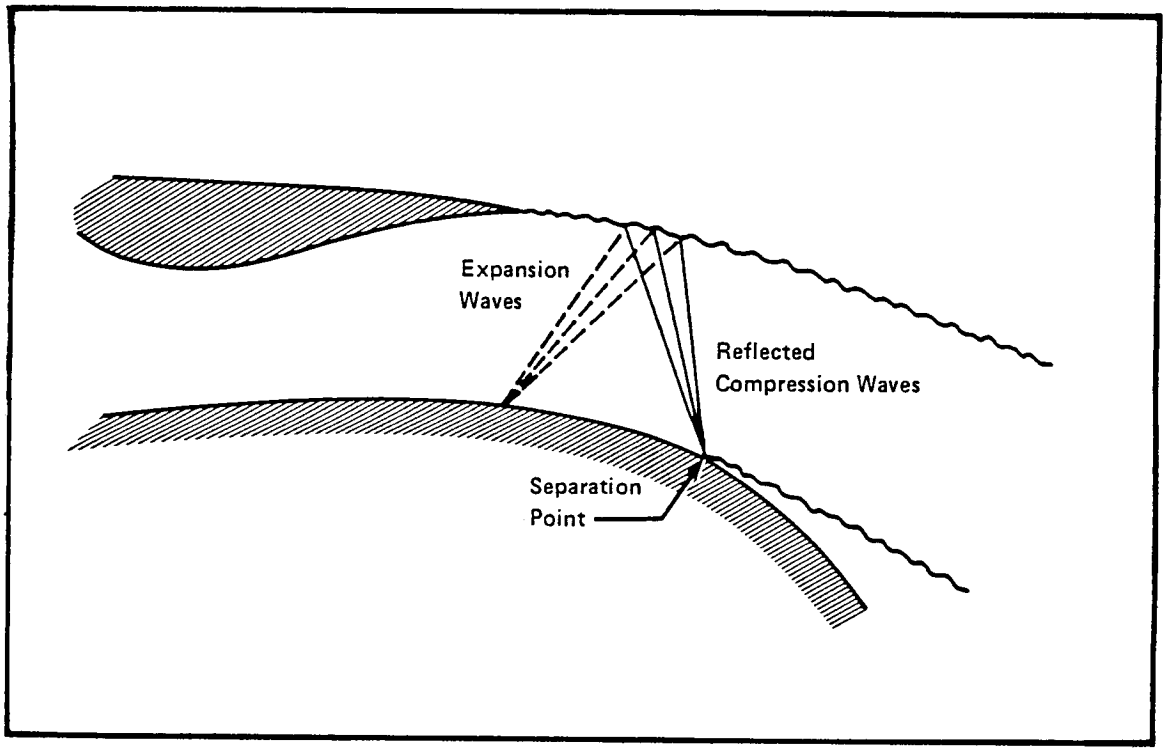

Figure 3. Jet Detachment due to Wave Interaction

A convergent-divergent nozzle can be designed to produce a skewed velocity distribution. If the high velocity, low pressure side is on the surface, the radial pressure gradient will act to deflect the jet in that direction. In fact, by suitable shaping of the velocity profile, the jet deflection can theoretically be matched to the curvature of the Coanda surface. For example, the streamlines of an irrotational vortex flow are circular, and the velocity varies inversely with distance from the center of rotation, $V = K/R$. A jet having such a velocity distribution can be matched to the radius of a circular Coanda surface, and should flow around that surface without turning losses due to expansion waves, Figure 4. One objective of our study was to evaluate the hypothesis that shaping the jet velocity profile improves the thrust vectoring of supersonic Coanda jets. This was accomplished by designing a convergent-divergent nozzle which produces a skewed velocity profile, and then comparing its turning angle and thrust to those of a simple converging nozzle and a conventional convergent-divergent nozzle.

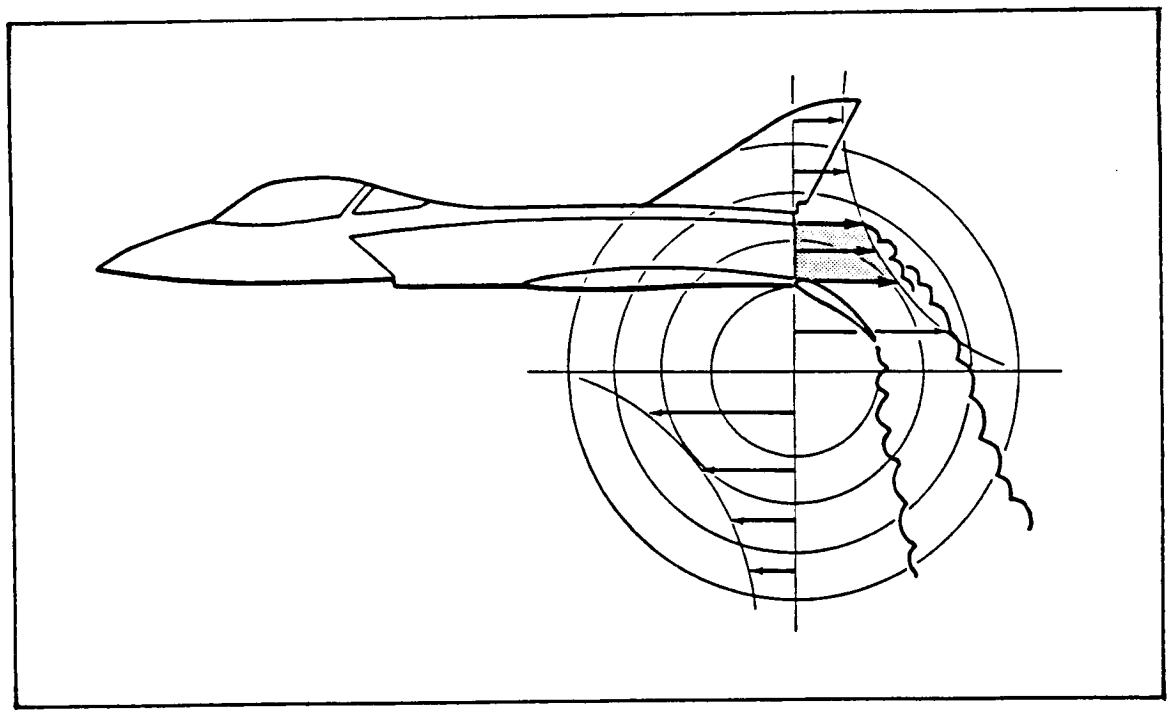

Figure 4. Jet Velocity Distribution Matched to a Circular Coanda Surface

NOZZLE DESIGN PROCEDURE

Method of Analysis

Although a method of designing nozzles which deliver a vortex velocity profile ($V = K/R$) was developed by Guile (Guile, B.G., 1961) for his work on aerodynamic windows, it was felt a more flexible procedure was needed for our Coanda jet application. Guile's method involves first expanding the flow to some uniform Mach number, and then expanding the flow further in order to skew the velocity profile. Such a two-stage design procedure results in a nozzle which is too long for most aircraft systems. Further, this approach constrains the shape of the

exit velocity profile, which then constrains the shape of the Coanda surface. Therefore, a method of designing a single-stage nozzle which delivers an arbitrary exit velocity profile was developed for this study.

Consider a nozzle discharging a supersonic jet onto a curved surface, as sketched in Figure 5. If the jet turns isentropically, the governing equations are hyperbolic, so that the nozzle velocity profile must satisfy the compatibility relations on the network of characteristics which connect the nozzle exit to the jet boundaries. In this sense, the curvature and Mach number at the jet boundaries determine the velocity profile at the nozzle exit. The relevant sections of the boundary appear to be ZA and YB; however, conditions along YB are influenced by the free boundary segment XZ, as well as by the shape of YB. Thus, the velocity profile is determined by the shape of the wall along YB and the shape and Mach number along XA.

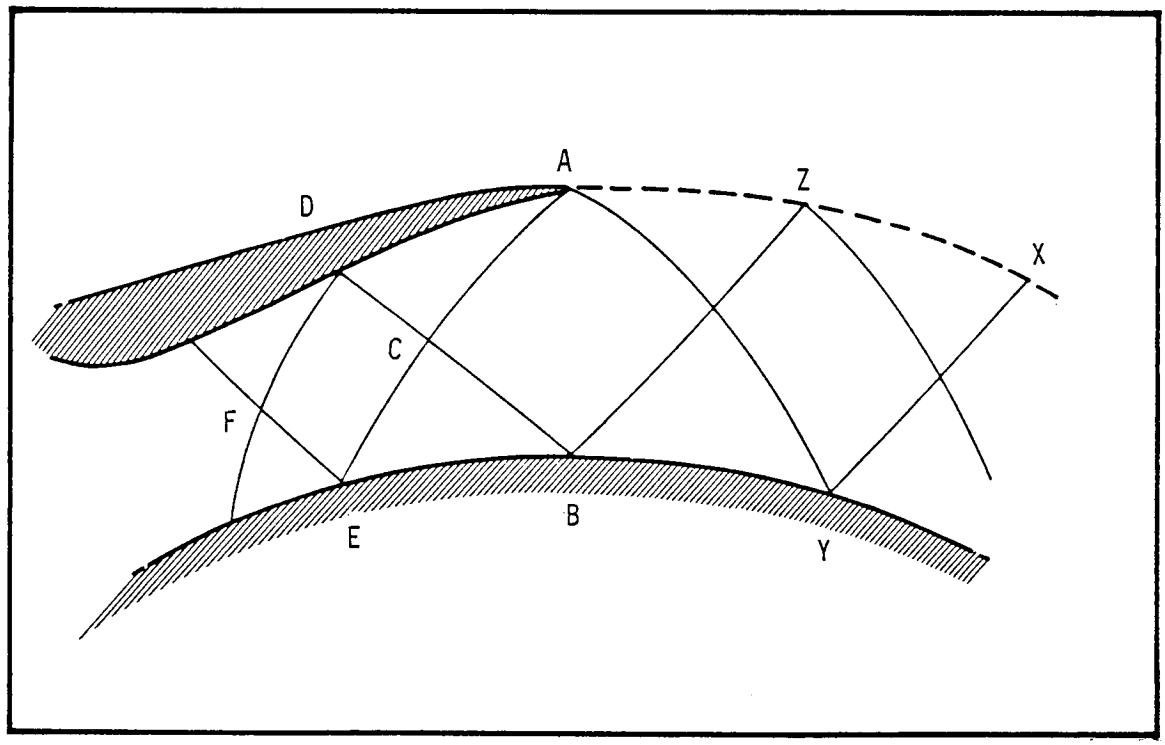

Figure 5. Characteristics Net of a Supersonic Coanda Jet

The method of characteristics (Liepman, H. W. and Roshko, A.) may be used to calculate the initial velocity profile which matches the Coanda jet to a particular surface. The method is based on satisfying the compatibility relations, $\theta \pm \nu(M)$ = constant, between the Prandtl-Myer function, ν, and the flow angle, θ. To determine the initial velocity profile, a characteristics net is run upstream from the jet boundaries. For example, if the Mach number at point Z is M = 1.5 (corresponding to $\nu = 12^{o}$) and the flow angle is $\theta = -10^{o}$, then the compatibility constant on the left running characteristic through point B is $12^{o}-(-10^{o}) = 22^{o}$. Since the angle at point B is defined to be $\theta = 0^{o}$, the compatibility relation gives $\nu = 22^{o}$, which corresponds to a Mach number of 1.8. The Mach number distribution of the inviscid flow along YB may be determined in this way. The Mach number profile at the nozzle exit is similarly determined by the intersecting characteristics from ZA and YB.

The internal contours of the nozzle which will produce the desired velocity profile may be computed by continuing this solution procedure upstream into the nozzle. The shape of the zone ABC and the flow within it are determined by the characteristics from the exit profile; outside this zone the flow is influenced by the wall contours. A wide range of contours can be defined which yield the goal upstream of uniform flow at M = 1 (a nozzle throat). Guile's method (Guile, R.N., 1975) yields one such contour; our one-step method yields other shapes.

Because the range of possible contours is so large, our basic procedure is to define an approximate shape using the coarse net of characteristics from the points AB and MN, as shown in Figure 6. This shape is then developed using a fine-net operator. The region ABKLJ is an expansion zone for the jet, but it is designed as a compression zone for a fictitious flow which goes backwards through the nozzle. This region contains both left- and right-running characteristics which are curved. The regions JLM and KLN are cancellation zones designed to eliminate the compression waves generated in the region ABKLJ. Thus, these are simple regions containing waves of only one family. In the region LMN the flow is uniform and parallel, at the throat Mach number (e.g., M = 1.001).

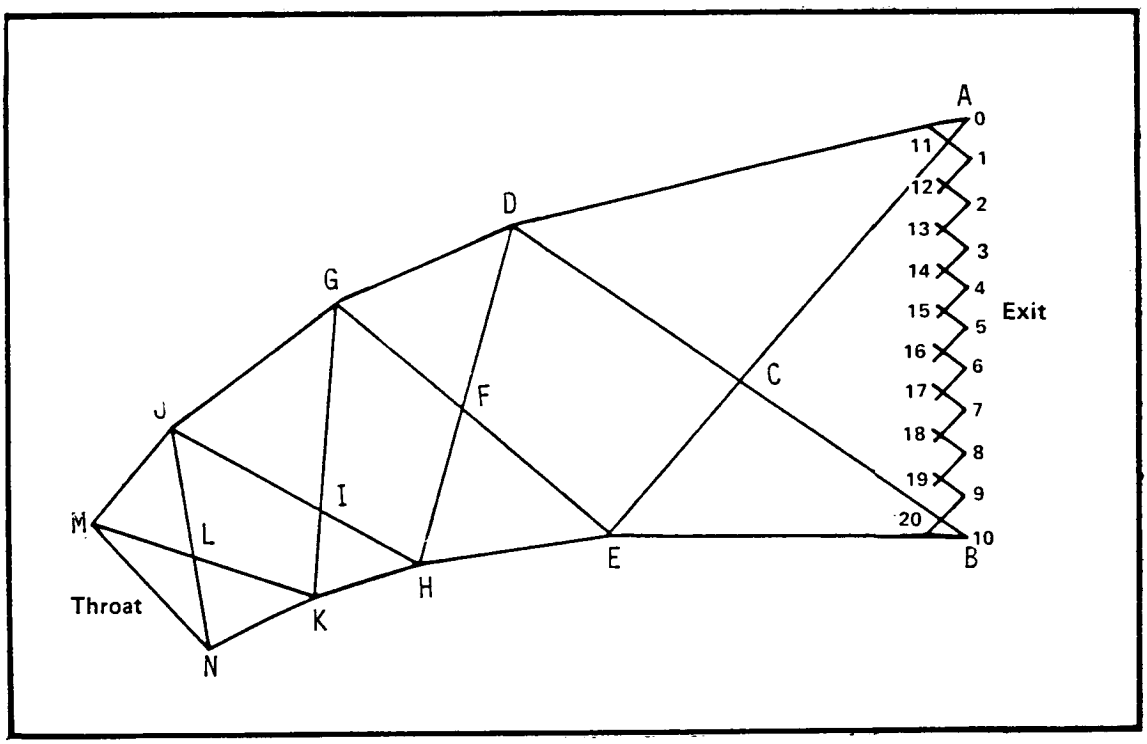

Figure 6. Coarse and Fine Net Operators for Nozzle Design

To define the coarse net, the Mach number and flow direction at Point I are specified, and the coarse net is then analyzed for compatibility. For example, the conditions at Point G are related to those at A through the Point E and to those at M through the Point K. The Mach numbers on the walls of a "suitable" coarse net increase monotonically from the throat to the exit. The conditions at Point I are varied until a suitable coarse net is defined. The nozzle flow is then calculated in detail by marching upstream from the nozzle exit using a fine characteristics net. The wall conditions are then examined to insure that the Mach number distribution is satisfactory. If necessary, the coarse net is modified and the fine net analysis is repeated. The integral method of boundary layer analysis devised by Dayman (Dayman, B., 1963) was used to correct the inviscid nozzle contours for the boundary layer displacement thickness. Details of the nozzle design procedure and computer code are given by Bevilaqua and Lee (Bevilaqua, P. M. and Lee, J. D., 1980).

The initializing mesh points and the starting profiles at the nozzle exit for the vortex nozzle and the baseline uniform flow nozzle tested in this study are shown in Figure 7. The nozzles were designed to deliver these profiles. The same subsonic section was added to the upstream end of both nozzles. The subsonic section is a simple cubic surface having both first and second derivatives going to zero at the throat. Both nozzles are shown in Figure 8.

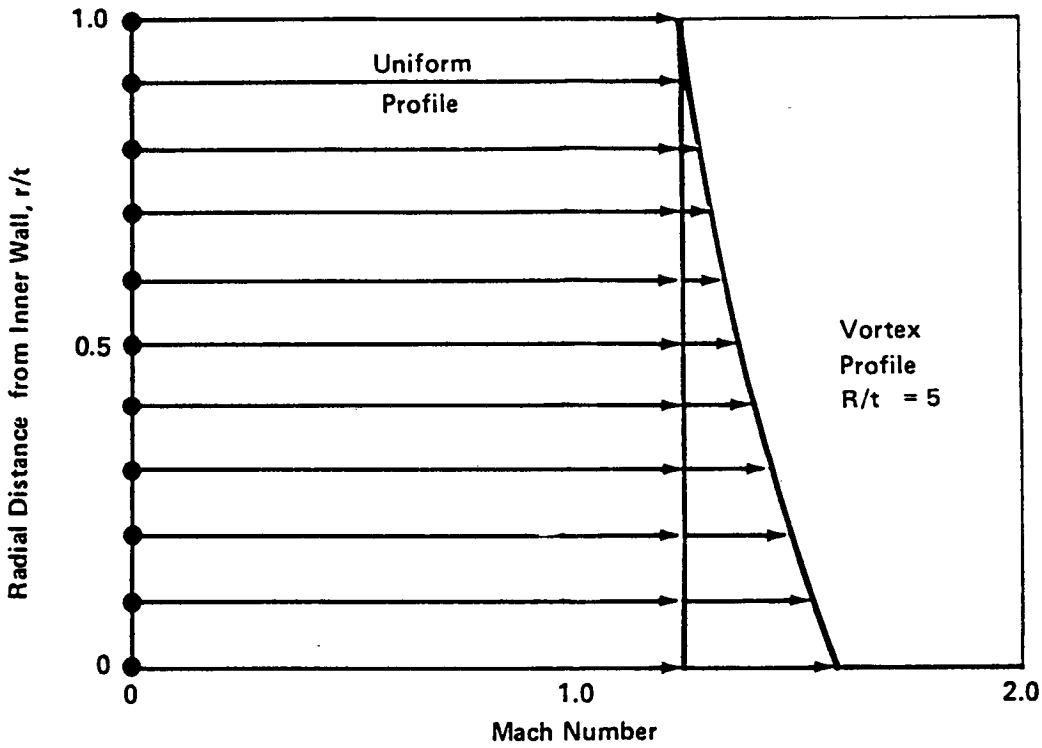

Figure 7. Uniform and Skewed Nozzle Exit Velocity Distributions

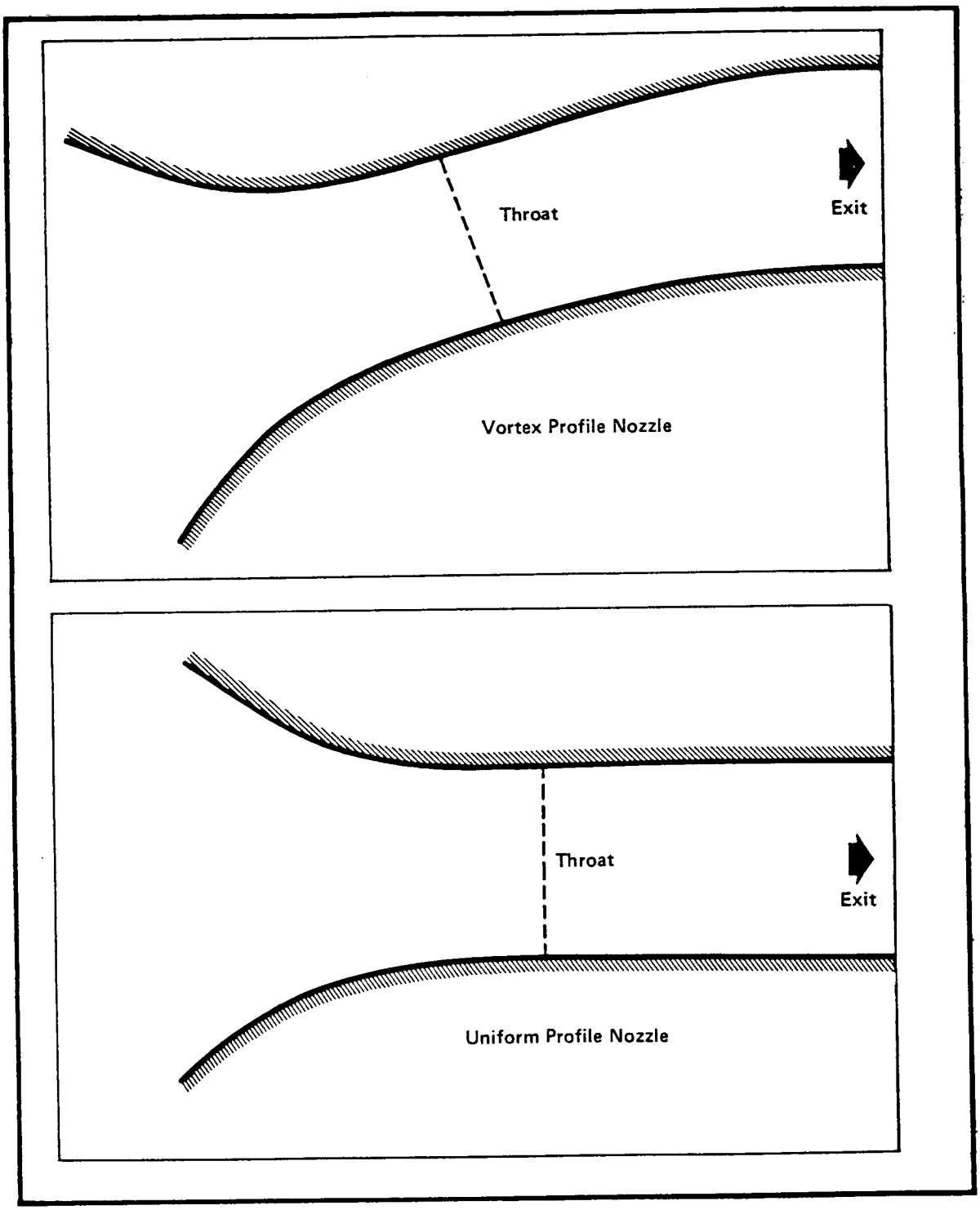

Figure 8. Contours of the Convergent-Divergent Nozzles

EXPERIMENTAL APPARATUS

Description of the Model

The model consisted of a steel plenum box on which interchangeable nozzle and Coanda surface assemblies could be mounted, as shown in Figure 9. This plenum was attached to the balance post and connected to the air supply hoses with two four-inch pipes. A pressure tap in the plenum sidewall was used to measure the plenum pressure. Provisions were made to mount air distribution baffles in the plenum, but it was found that none were needed.

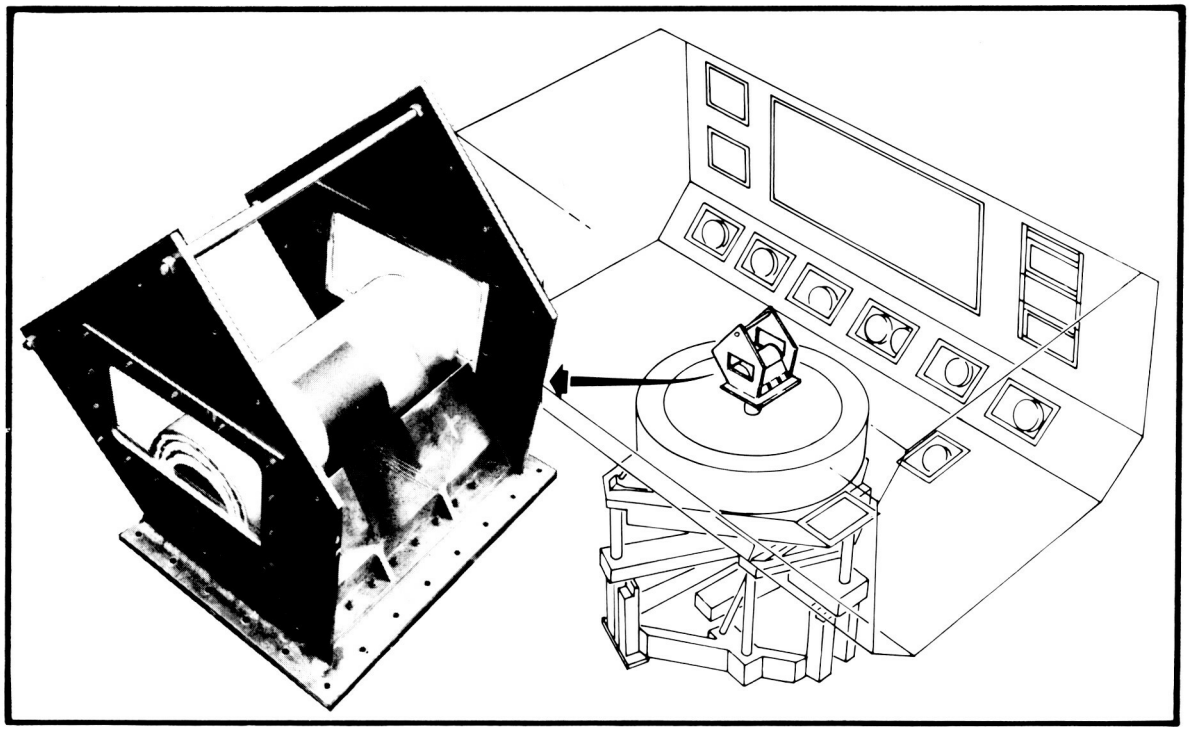

Figure 9. Coanda Jet Nozzle Test Assembly

Both nozzle assemblies were nominally identical except for the nozzle contours. Each assembly consisted of aluminum nozzle and Coanda surfaces mounted between steel endwalls. The nozzles had a span of 30.5 cm and nominal exit dimensions of 1.27 cm. The circular Coandas had a radius of 6.35 cm, giving R/t = 5. Both endwalls had openings which could be fitted with optical glass windows for flow visualization or with steel inserts for the force data runs. When the windows were not installed, the nozzle assembly was fitted with endwall boundary layer splitter plates. These splitter plates were 1.5 mm thick. These were mounted 1.27 cm and 2.54 cm from each endwall and were intended to insure the two-dimensionality of the flow by removing the corner vortices. This technique was developed by Guitton and Newmann (Guitton, D. E., Newman, B. G., (1977).

The entire nozzle assembly was bolted to the plenum such that the nozzle exit plane was 45° from the horizontal with the jet exhausting upward. Each nozzle assembly was instrumented with fifteen pressure taps located on the inside nozzle contours and every 30° along the Coanda surface at midspan.

The model was tested in the 7' x 10' test section of the North American Aircraft low speed wind tunnel in Columbus, Ohio. The plenum was attached to a post connected to the six component external pyramidal balance. The model air supply was brought through two venturis and cono-flow control valves. Two four-inch flexible hoses were used to bridge the balance with a minimum of interference.

Instrumentation

Model forces were measured by the external six-component balance. The air supply mass flow was measured by two venturis in which the supply pressure, differential pressure, and temperature were measured. The nozzle exit total pressure was calibrated versus the model plenum pressure which was obtained from the plenum wall static tap. Model surface pressures were recorded using a scanivalve. The air supply hose pressure was measured to be used for computing hose tares. All instrumentation was calibrated and read through the wind tunnel data system. The data was recorded and reduced by an IBM 1800 data acquisition computer. Nozzle exit and jet profile survey data were acquired on an x-y recorder using a pressure transducer and a calibrated traverse position potentiometer.

RESULTS AND DISCUSSION

Convergent Nozzle

In order to provide a baseline for evaluating the performance of the convergent-divergent nozzles, the jet from a simple converging nozzle was tested first. The measured variation of the jet thrust coefficient and deflection angle are shown in Figures 10 and 11. These were determined from the measured vertical and horizontal components of the force according to the relations $T = (F_V^2 + F_H^2)^{1/2}$ and $\phi = \tan^{-1}(F_V/F_H)$. The thrust deflection angle is not the same as the jet separation angle, because the mixing of the jet with the surrounding fluid causes the outer jet boundary to turn more slowly than the inner boundary. As a result, the thrust vector is not tangent to the surface at the separation point.

In Figure 10, it can be seen that the attachment and detachment of the jet shows some hysteresis in the range of pressure ratios between 2.0 and 2.6; that is, the jet remains attached as the pressure ratio is increased through this range, and remains detached as it is decreased through this range. Perhaps more surprising is the magnitude of the angle through which the jet was deflected. The maximum deflection of almost 145° is nearly two and a half times that achieved by Davenport and Hunt (Davenport, F.J. and Hunt, D.N., 1975). Thus, it seems possible that the straight section which they added to the Coanda surface actually caused premature separation of the jet by inducing a sudden increase in the surface pressure gradient.

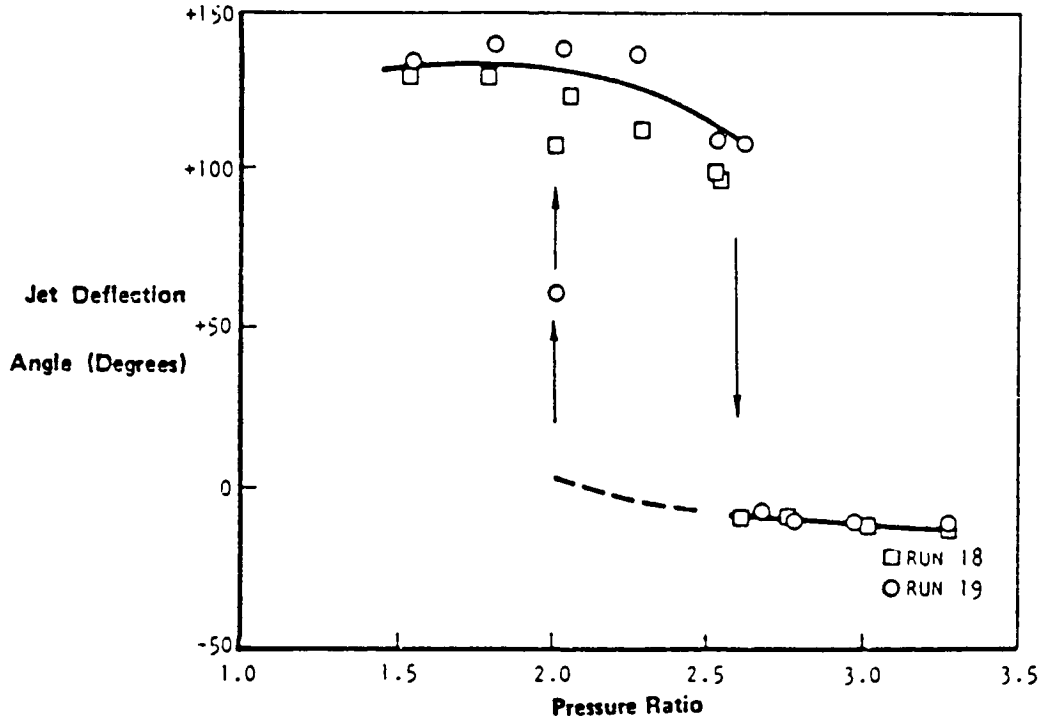

Figure 10. Converging Nozzle Thrust Coefficient

The variation of the jet thrust coefficient is shown in Figure 11. This coefficient is defined as the ratio of the measured jet thrust to the thrust calculated for an isentropic expansion of the measured nozzle mass flow to atmospheric pressure. When the jet is attached to the Coanda surface, its thrust is reduced by wall friction. As seen in the figure, this loss can be significant for large jet turning angles.

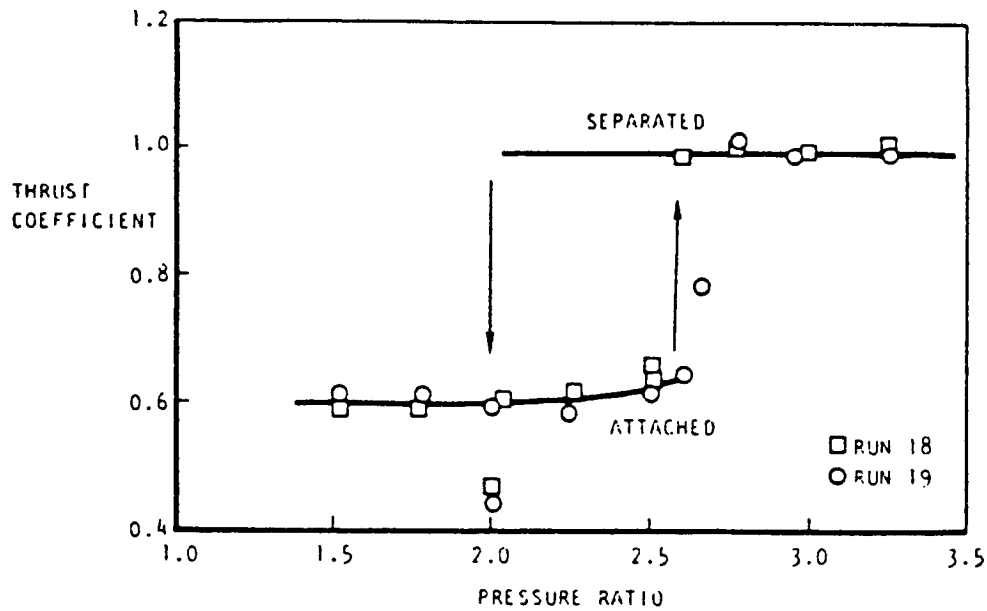

Figure 11. Converging Nozzle Jet Deflection

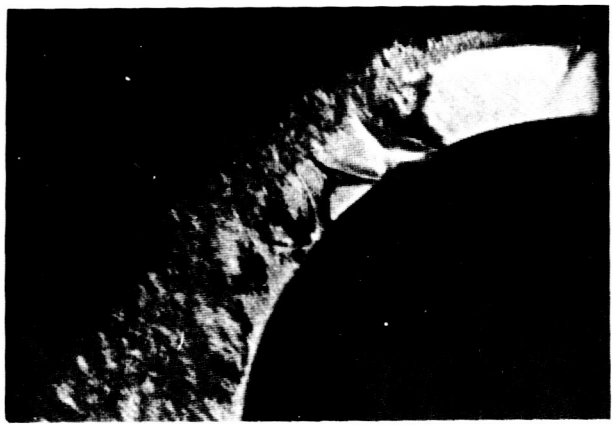

PR~2.25

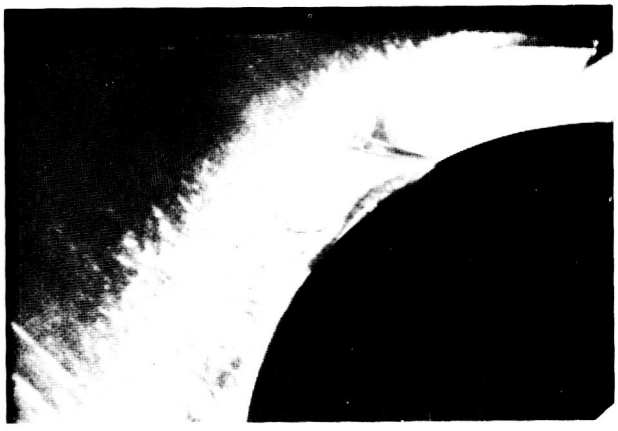

PR~2.5 ATTACHED

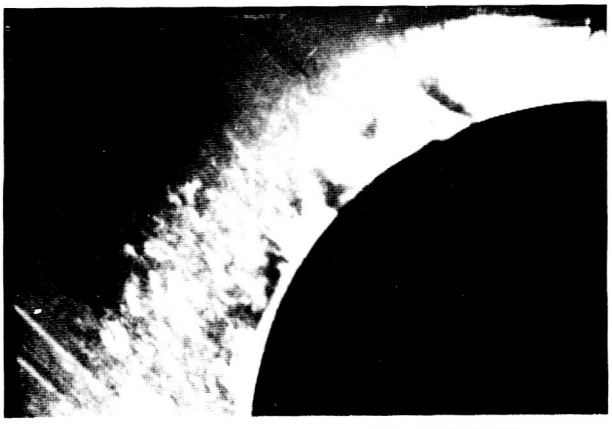

PR~2.0 AFTER REATTACHMENT

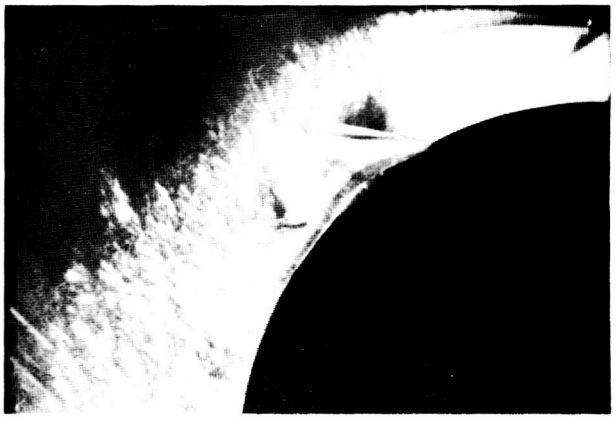

PR~2.65 BEFORE DETACHMENT

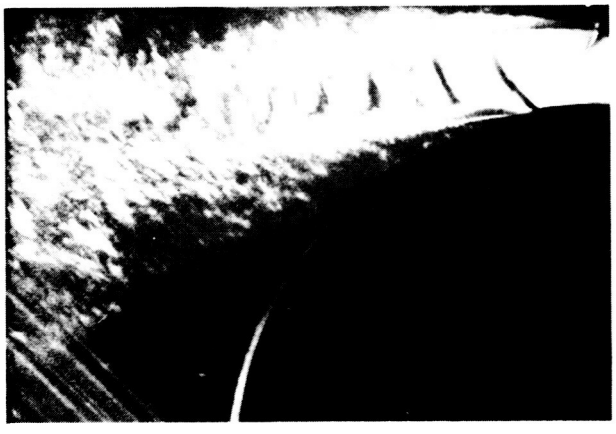

PR~2.0 BEFORE REATTACHMENT

PR~2.65 AFTER DETACHMENT

Figure 12. Schlieren Photographs of the Jets from the Convergent Nozzle

As an aid in understanding the behavior of the jet, Schlieren photographs were made of the region downstream of the nozzle exit. In Figure 12, it can be seen that detachment of the jet is caused by shock induced boundary layer separation. As the pressure ratio is increased, the first compression wave reflected from the wall can be seen to strengthen, so that the separation bubble behind it becomes larger. Eventually, the wave system becomes strong enough to completely separate the boundary layer and thus detach the jet. The separation point of the detached jet is closer to the nozzle than the initial separation point. If the pressure ratio is subsequently reduced, the jet can be seen to deflect slightly towards the wall, although it does not immediately reattach to the surface.

Convergent-Divergent Nozzles

For both convergent-divergent nozzles, surface pressure distributions and total pressure distributions were measured, in addition to the force data and Schlieren photographs, in order to verify the nozzle performance. In Figure 13, the pitot pressure profile at the exit of the vortex nozzle is compared to the predicted distribution. Since the local Mach number is higher near the inner wall, the loss of total pressure due to the probe shock is larger there. Thus, the slope of the total pressure profile is opposite to the slope of the velocity profile. The agreement between measurement and prediction is very good, which indicates that the desired skewing of the exit velocity profile was achieved. The spike in the profile at the inner boundary was also seen in the uniform profile from the conventional convergent-divergent nozzle, which suggests that probe interference may be the cause.

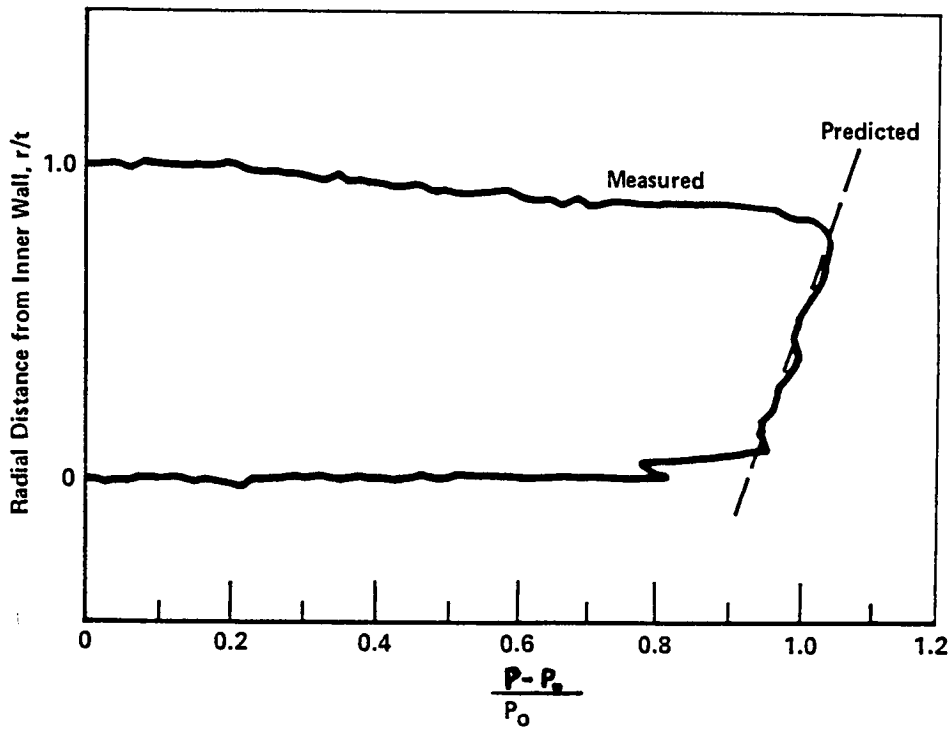

Figure 13. Vortex Nozzle Total Pressure Profiles

In Figures 14 and 15, the measured nozzle wall static pressure distributions are compared to the design pressure distributions. The agreement is very good for the uniform profile nozzle. However, a pressure tap on both the upper and lower surfaces of the vortex profile nozzle falls off the design distribution. Since these taps show similar pressure variations at subsonic pressure ratios, it is likely that they are defective, but it is also possible that a compression wave originates on the upper surface of the nozzle where the pressure gradient is relatively flat. If such a wave exists, it is weak, since the desired total pressure distribution was observed at the nozzle exit.

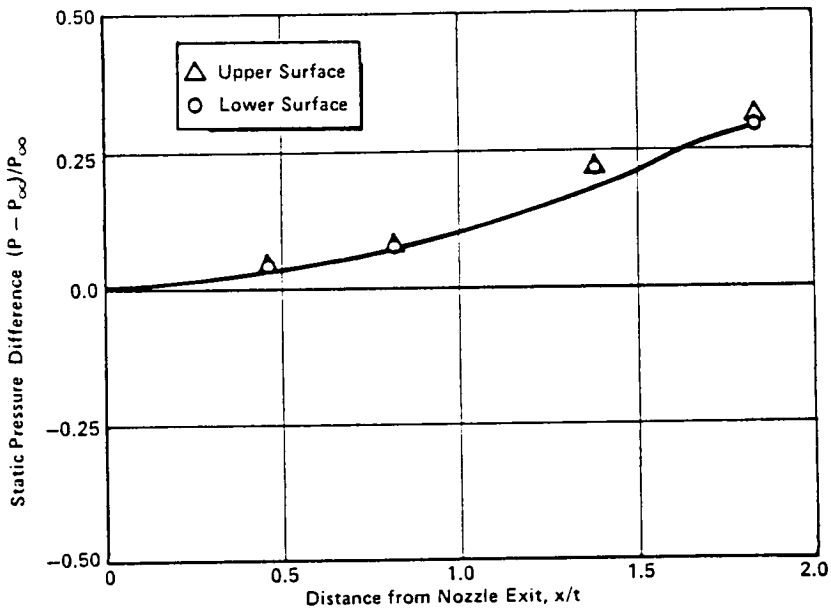

Figure 14. Surface Pressures in the Symmetric Nozzle

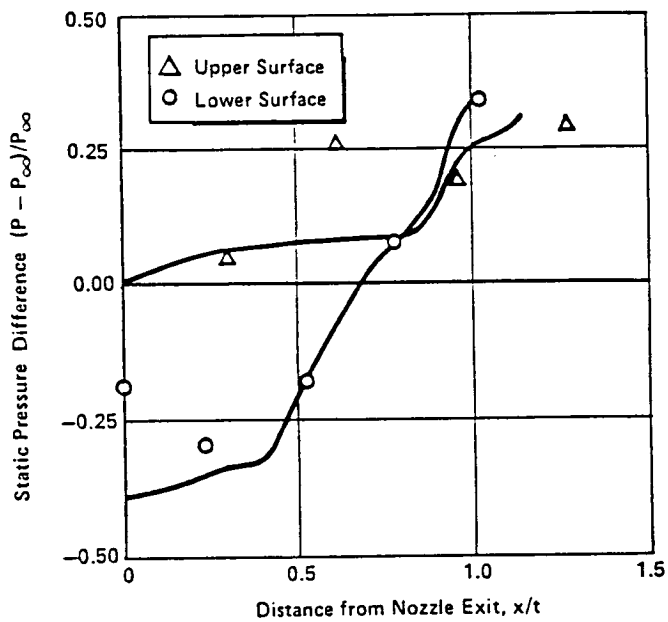

Figure 15. Surface Pressures in the Vortex Nozzle

The static pressure distributions on the Coanda surface at the design pressure ratio of 2.5 are shown in Figures 16 and 17. In both figures, the nozzle exit is at the top. There are 5 equally spaced taps between the throat and the exit of each nozzle, and a tap every 30° along the Coanda surface. The general shape of the measured pressure distributions are similar for both nozzles. As the flow expands through the nozzle, the pressure decreases to atmospheric pressure. Then, as the jet is turned onto the Coanda surface, the pressure drops well below atmospheric pressure. Viscous effects then cause it to increase again.

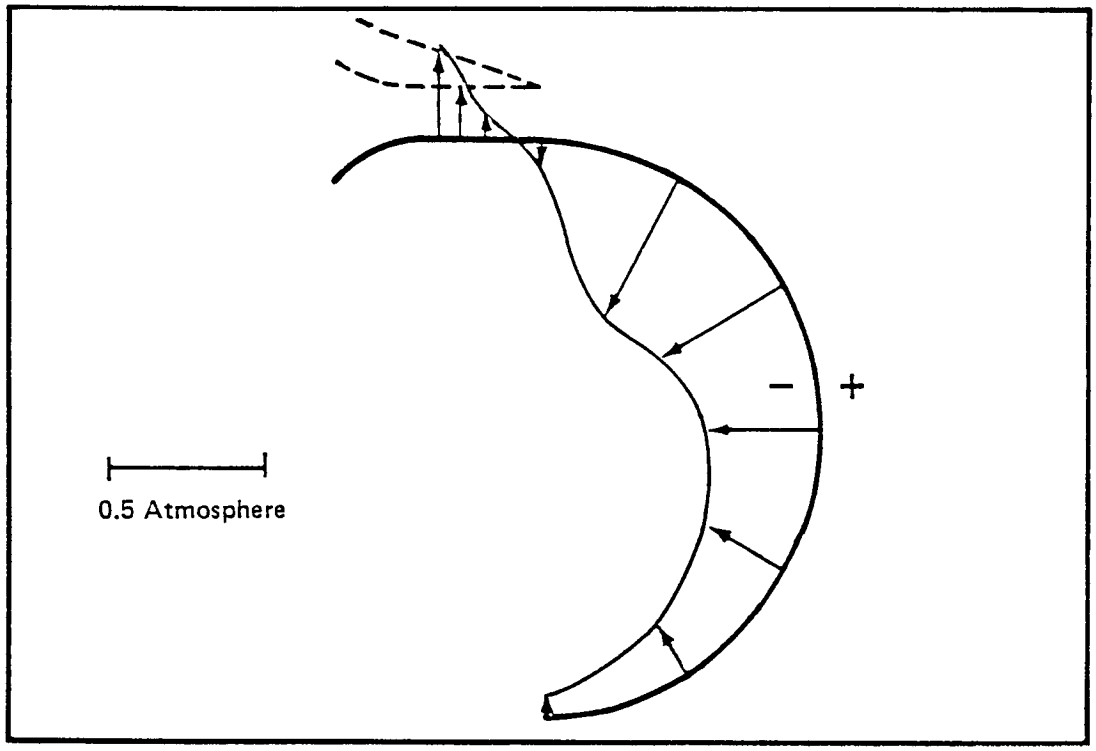

Figure 16. Surface Pressures Outside the Symmetric Nozzle

The pressure on the upper wall of the convergent-divergent nozzle decreases smoothly to atmospheric pressure, as expected. On the lower wall, however, the pressure at the exit is slightly below atmospheric pressure, as seen in Figure 16. This may be due to the formation of a separation bubble, which develops because the jet resists turning, and attaches downstream of the nozzle exit.

The surface pressure under the Coanda jet can be estimated using Equation 3. The jet thrust was calculated from the measured mass flow, $\dot{m}$, and the nozzle pressure ratio, according to the relation

$$T = \left[\dot{m} \frac{2\gamma}{\gamma-1} R\tau_o \quad (1 - (P_\infty/P_o)^{1/\gamma})\right]^{1/2}$$

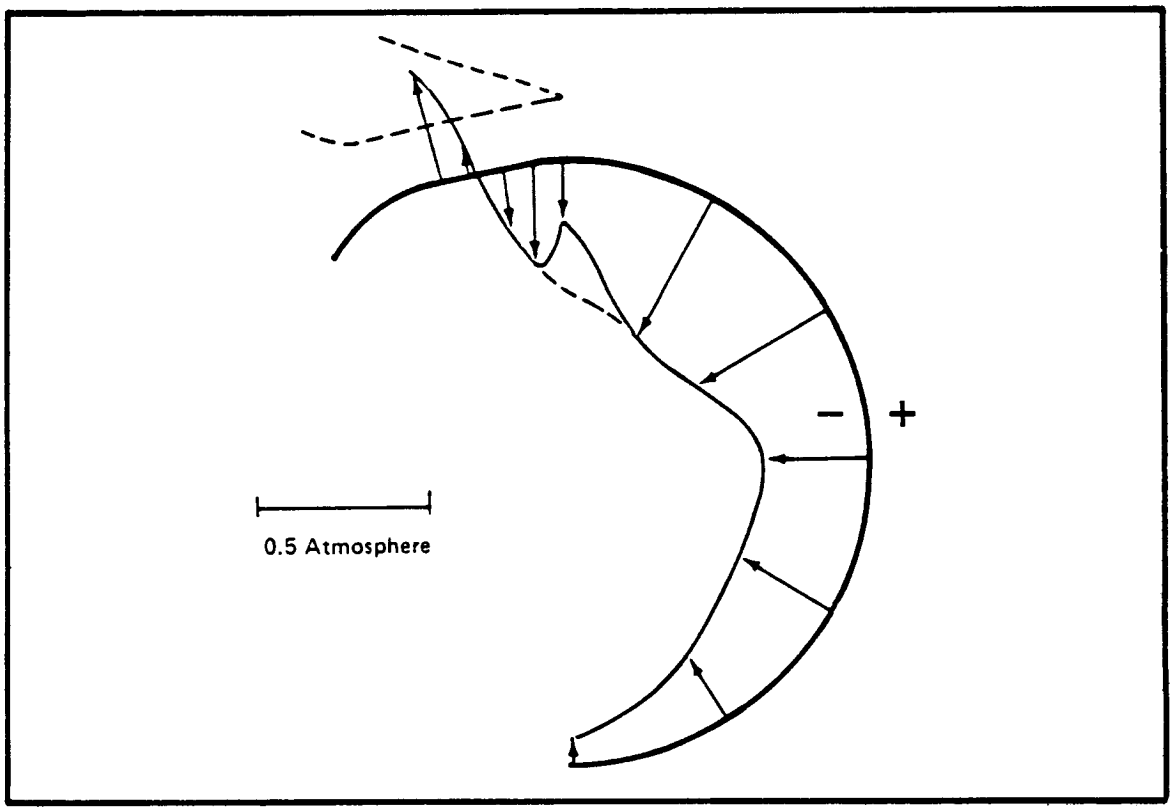

Figure 17. Surface Pressures Outside the Vortex Nozzle

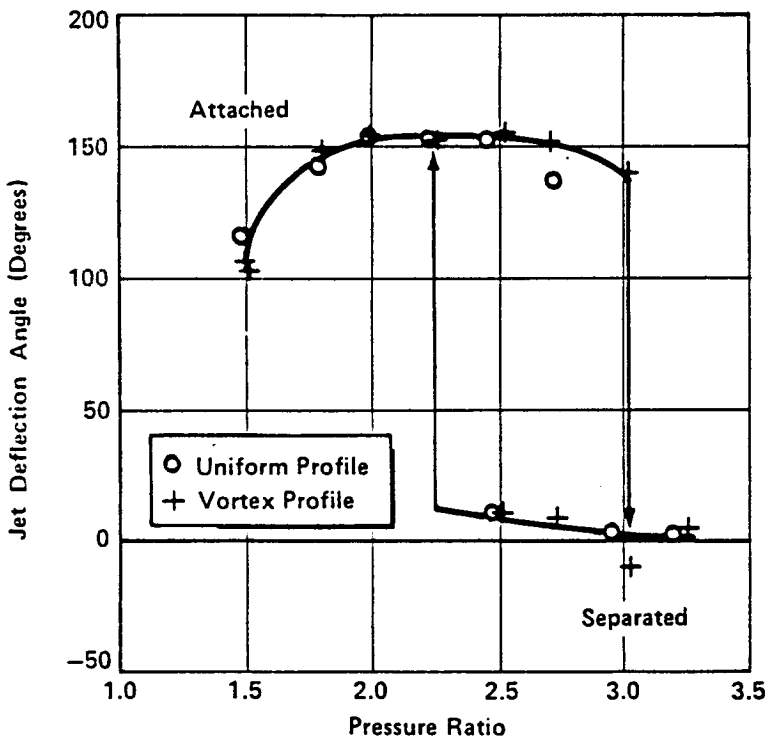

Figure 18. Convergent-Divergent Nozzle Jet Deflection

in which R is the gas constant, while P_o and T_o are the stagnation pressure and temperature. At the design pressure ratio, the thrust of the jet is about 27 newtons/cm of span, and the computed pressure drop is 0.39 atmospheres. The lowest pressure measured on the Coanda surface (at $\phi = 30^o$) is essentially the same. In Figure 17, the pressure on the inner wall of the vortex nozzle is seen to decrease more rapidly than in the uniform profile nozzle. It approaches the value required to turn the jet at the nozzle exit, as intended.

The measured variation of the jet thrust coefficient and deflection angle are compared in Figures 18 and 19. The attachment and detachment of the jets show some hysteresis for these nozzles also. However, the pressure ratio range for hysteresis, from 2.2 to 3.0, is higher than for the convergent nozzle, and the jet deflection angle, almost 155^o, is higher than for the convergent nozzle. In fact, the turning of both jets was probably limited by interference with the nozzle plenum on the back side of the Coanda surface, and not by separation from the Coanda surface.

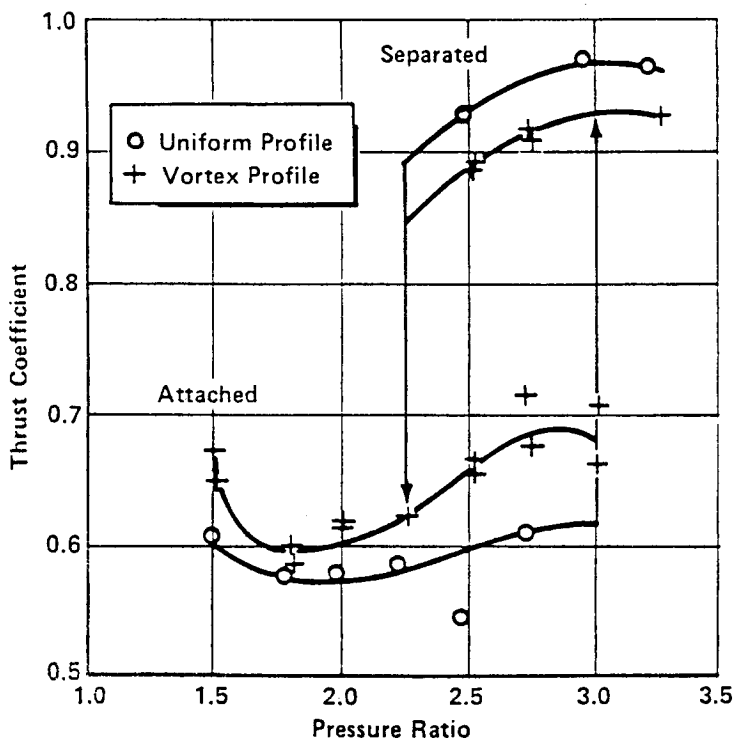

Figure 19. Convergent-Divergent Nozzle Thrust

The variation of the thrust coefficient seen in Figure 19 is consistent with the observed deflection of the jet. Initially, as the pressure ratio increases, the jet deflection increases and its thrust is reduced. Then as the pressure ratio increases past the design value of 2.5, the deflection decreases and the thrust correspondingly increases. After detachment, decreasing the pressure ratio causes the jet to deflect toward the surface and the thrust to decrease slightly.

The reason for the difference in the pressure ratio for detachment of these two jets, as compared to the jet from the converging nozzle, may be deduced from the Schlieren photographs in Figures 20 and 21. At the design pressure ratio of 2.5, the first expansion wave is not present in the jets from either convergent-divergent nozzle. Similarly, the turning waves in the jet from the conventional convergent-divergent nozzle are not strong enough to produce a separation bubble. However, by a pressure ratio of 3.0, both jets are sufficiently underexpanded that the expansion wave system does appear. A separation bubble is apparent in this case, and the jets do detach at a slightly higher pressure ratio.

The spreading of the jets is shown by the development of the total pressure profiles in Figures 22 and 23. Both jets develop in the same way. The inner boundary layer and the outer mixing layer have merged by the 30^{o} station to form the total pressure profile typical of wall jets. However, the spreading of these jets is considerably more rapid than that of a wall jet on a flat plate. Also, the jet from vortex nozzle spreads noticeably slower than the jet from the conventional nozzle.

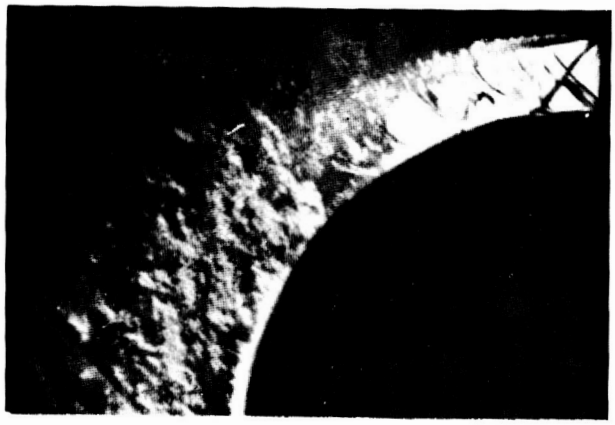

PR~2.0

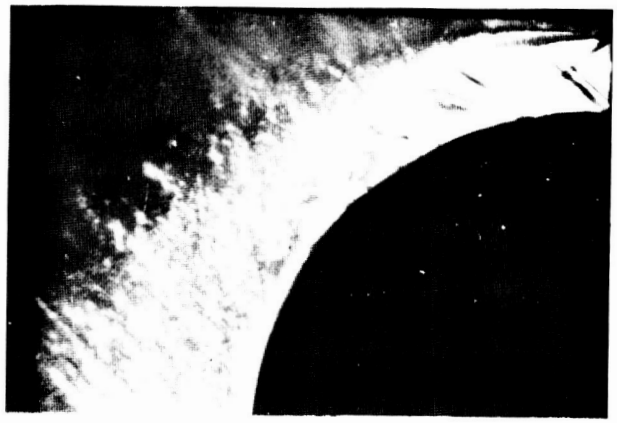

PR~2.5 DESIGN POINT

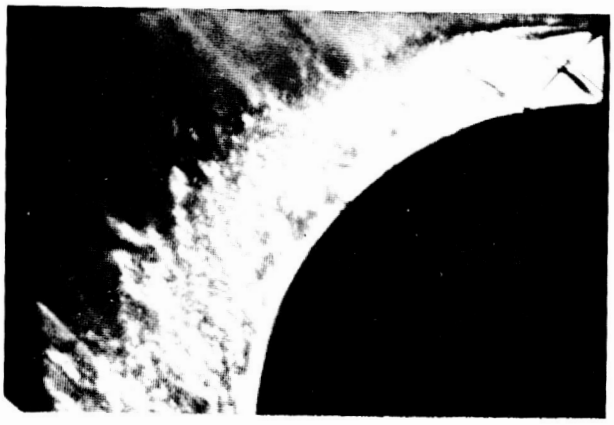

PR~2.25 AFTER REATTACHMENT

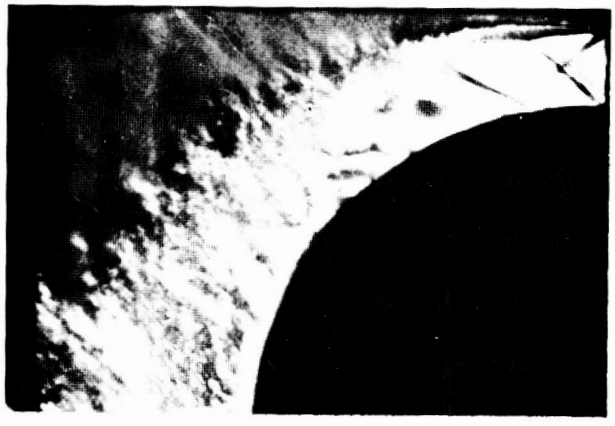

PR~2.8 BEFORE DETACHMENT

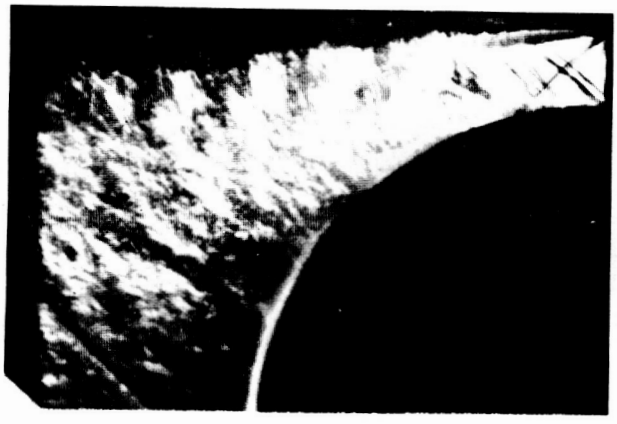

PR~2.25 BEFORE REATTACHMENT

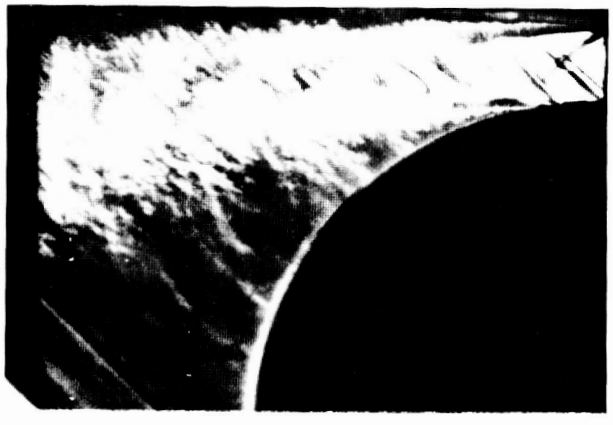

PR~3.0 AFTER DETACHMENT

Figure 21. Schlieren Photographs of the Jets from the Vortex Profile Nozzle

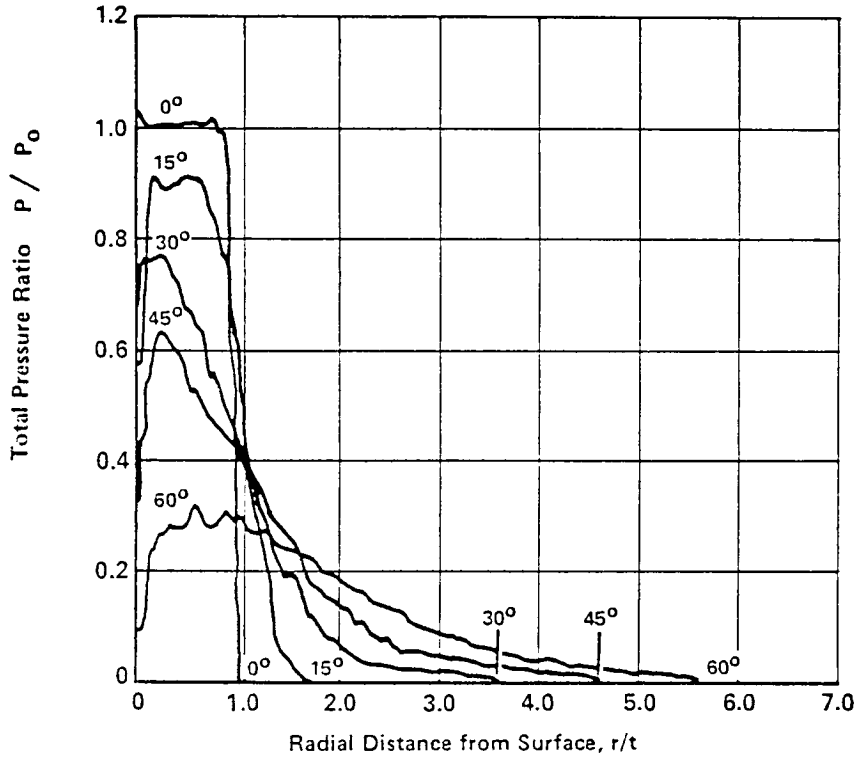

Figure 22. Symmetric Jet Total Pressure Profiles

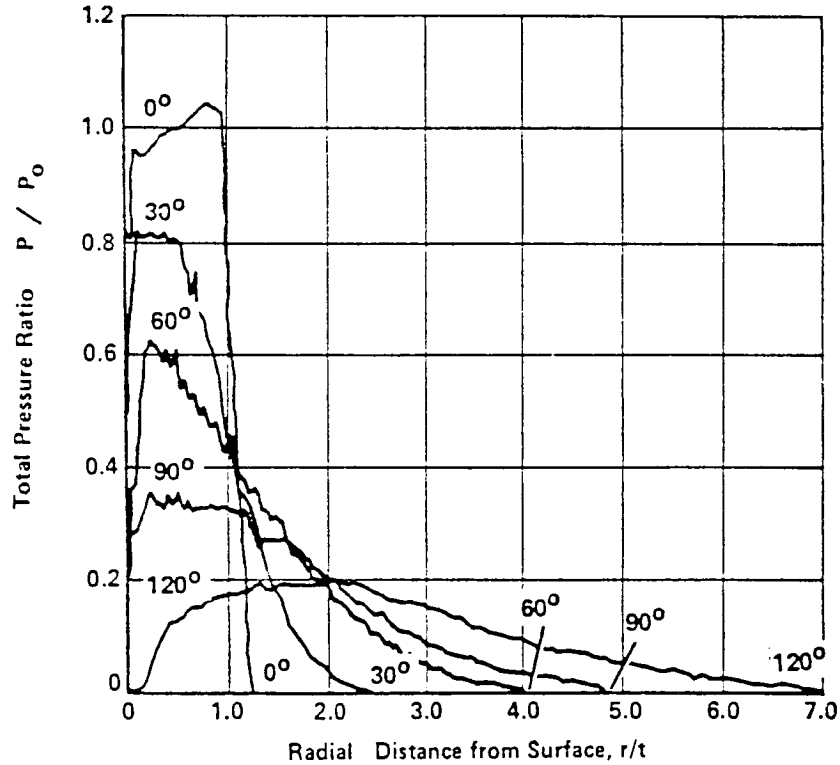

Figure 23. Vortex Jet Total Pressure Profiles

CONCLUSION

Several conclusions regarding the thrust vectoring of supersonic Coanda jets can be drawn from this study. First, the principal cause of supersonic jet detachment is boundary layer separation induced by the shocks in the wave system of the underexpanded jet. By comparing Figures 10 and 18, it can be seen that the jets from the CD nozzles detach and reattach at higher pressure ratios (3.0 and 2.2) than the jet from the convergent nozzle (2.6 and 2.0). As seen in the Schlieren photographs, the jets from the CD nozzles do detach at pressure ratios above their design point, when the shocks in the expansion wave system become strong enough to separate the boundary layer. Presumably, designing the nozzle for a higher pressure ratio would also raise the pressure ratios due to overexpansion waves. This is a subject for further investigation.

As seen in Figure 19, the thrust of the deflected jet from the vortex nozzle is approximately 5% greater than the thrust of the jet from the symmetrical CD nozzle; when the jets are detached, the thrust of the jet from the symmetrical nozzle is approximately 5% greater. Thus, there seems to be a thrust loss of this magnitude associated with adjusting the uniform profile to curvature, or the skewed profile to uniform pressure. In a deflected jet system, such as the X wing or circulation control wing, the vortex nozzle does provide more thrust. On the other hand, as seen in Figure 19, the vortex nozzle does not increase the pressure ratios for detachment or reattachment of the Coanda jet. This must be because the turning shocks in the jet with the uniform profile are not strong enough to cause detachment. At a higher pressure ratio, or for a smaller radius turn, the turning shocks in the uniform jet would be stronger and might then cause detachment. In this case, the vortex nozzle may delay detachment. However, further testing is required to determine if this is so.

To summarize, the thrust vectoring of supersonic Coanda jets may be significantly improved by the use of a convergent-divergent nozzle rather than a simple converging nozzle, because this eliminates the expansion shocks which cause boundary layer separation. On the other hand, for the pressure ratio and turning radius tested, the turning waves were not strong enough to cause detachment, so that skewing the velocity profile to match the radial pressure gradient does improve the thrust, but not the detachment pressure ratio of the deflected jet.

An improved vortex nozzle design procedure, which results in a shorter and lighter nozzle was also developed as part of this study. This procedure may also be useful for reducing the length of the vortex nozzles used to generate aerodynamic windows for gas dynamic lasers.

*ACKNOWLEDGEMENT - This study was supported in part by the Air Force Wright Aeronautical Laboratories under Contract Number F33615-79-C-3026.

REFERENCES

1. Von Glahn, U., and Groesbuck, D.: Effect of External Jet-Flow Deflector Geometry on Over-the-Wing Aero-Acoustic Characteristics. NASA TM X-73460, 1976.

2. Davenport, F. J., Hunt, D. N.: Deflection of a Thick Jet by a Convex Surface: A Practical Problem for Powered Lift. AIAA Paper 75-167, AIAA 13th Aerospace Sciences Meeting, Pasadena, California, Jan. 20-22, 1975.

3. Metral, A., Zerner, F.: The Coanda Effect. Publication Scientifiques et Techniques du Ministere de l'Air, No. 218 (1948); M.O.S., TIB/T4027 (1953).

4. Von Glahn, U.: Use of the Coanda Effect for Jet Deflection and Vertical Lift with a Multiple-Flat-Plate and Curved-Plate and Curved-Plate Deflection Surfaces. NACA TN 4377, September 1958.

5. Bradbury, L. J. S., Wood, M. N.: An Exploratory Investigation into the Deflection of Thick Jets by the Coanda Effect. Royal Aircraft Establishment, Technical Report No. 65235, October 1965.

6. Newman, B. G.: Deflection of Plane Jets by Adjacent Boundaries - Coanda Effect. Article in Boundary Layer and Flow Control, Its Principles and Application, Pergamon Press, 1961.

7. Guile, R. N., Hilding, W. E.: Investigation of a Free-Vortex Aerodynamic Window. AIAA Paper 75-122, AIAA 13th Aerospace Sciences Meeting, Pasadena, California, Jan. 20-22, 1975.

8. Liepman, H. W. and Roshko, A.: Elements of Gas Dynamics. J. Willet and Sons.

9. Dayman, B.: Comparison of Calculated with Measured Boundary Layer Thicknesses on the Curved Walls of the JPL-20-inch Supersonic Wind Tunnel Two-Dimensional Nozzle. JPL-TR No. 32-349, 1963.

10. Bevilaqua, P. M. and Lee, J. D.: Development of a Nozzle to Improve the Turning of Supersonic Coanda Jets. AFWAL TR 80-3027, April 1980.

11. Guitton, D. E., Newman, B. G.: Self-Preserving Turbulent Wall Jets over Convex Surfaces. J. Fluid Mech (1977), Vol. 81, Part I, pp. 155-185.

Circulation-Control Rotor Theory

FLAP-LAG-TORSION AEROELASTIC STABILITY OF A CIRCULATION CONTROL ROTOR IN FORWARD FLIGHT

INDERJIT CHOPRA and
CHANG-HO HONG
University of Maryland

ABSTRACT

The aeroelastic stability of a circulation control rotor blade undergoing three degrees of motion (flap, lag, and torsion) is investigated in forward flight. Quasi-steady strip theory is used to evaluate the aerodynamic forces; and the airfoil characteristics are from data tables. The propulsive and the auxiliary power trims are calculated from vehicle and rotor equilibrium equations through the numerical integration of element forces in azimuth as well as in radial directions. The nonlinear time dependent periodic blade response is calculated using an iterative procedure based on Floquet theory. The periodic perturbation equations are solved for stability using Floquet transition matrix theory. The effects of several parameters on blade stability are examined, including advance ratio, collective pitch, thrust level, shaft tilt, structural stiffnesses variation, and propulsive and auxiliary power trims.

INTRODUCTION

The airfoil on a circulation control (CC) rotor typically has quasi-elliptic profile and uses a tangential wall jet ejected over the rounded trailing edge to produce circulatory lift; (fig. 1). Due to the Coanda effect, the air remains attached at the rounded trailing edge and the stagnation point shifts to the lower surface. The lift of a CC airfoil can be controlled by jet momentum as well as by geometric incidence. It is possible to achieve high lift coefficients (four to five) with CC airfoils. Also, the aerodynamic center due to blowing circulation is near half-chord. For a general bibliography of circulation control see Englar and Applegate (1984). The application of CC technology to full-scale rotor design is currently being investigated (Linden and Biggers, 1985). The cyclic lift control of a CC rotor is obtained by a cyclic modulation of blowing. This eliminates the need for cyclic pitch and results in a simplified hub design. Collective lift control is obtained either by collective blowing or by collective pitch; see figure 2. Important features of a CC rotor are high thrust capability at reduced tip speeds and easy implementation of a higher harmonic control system. One area of concern, however, is the effect of CC aerodynamics on blade dynamics.

Johnson (1985) documented recent developments in the dynamics of advanced rotor systems. Few attempts have sbeen made to examine the aeroelastic stability of a CCR rotor blade (Chopra and Johnson, 1979; Chopra, 1984-85). An aeroelastic stability analysis of a CC rotor blade in hover was conducted by Chopra and Johnson in 1979. Three degrees of motion were considered: rigid flap, lag, and feather rotations about hinges at the blade root. The CC airfoil characteristics were represented in terms of analytical expressions. It was shown that the trailing edge blowing can have an important influence on blade dynamics and must, therefore, be addressed in rotor design. Chopra

---

*Work partially supported by David Taylor Naval Ship R & D Center under Contract No. N0016785-M-4464.
Presented at Circulation Control Workshop NASA Ames Research Center, February 1986.

(1984) also examined the aeroelastic stability of flap bending, lead-lag bending, and torsion of a CC rotor hingeless blade in hover using a finite element formulation. The CC airfoil characteristics were taken from data tables. Again, the stability results of hingeless rotors showed that the blowing has an important influence on blade dynamics. The finite element formulation was extended to analyze the aeroelastic stability of a bearingless rotor blade in hover (Chopra, 1985).

The objective of the present work is to examine the aeroelastic stability of a CC rotor blade in forward flight. For this, a simple flap-lag-torsion blade model consisting of three degrees of motion is considered. Quasi-steady strip theory is used to obtain aerodynamic forces. The effect of unsteady aerodynamics is introduced approximately through dynamic inflow modeling. The effects of pneumodynamics (Watkins et al., 1985) and centrifugal pumping in the pressure duct are included to calculate the jet momentum at a radial station.

The propulsive trim is calculated iteratively from the vehicle nonlinear equilibrium equations. Three force equations (vertical, longitudinal, and lateral) and two moment equations (pitch and roll) are obtained by numerically integrating the element forces both along the azimuth as well as the radial directions. The trim solution gives the rotor control setting and the vehicle orientation for a prescribed flight condition. The blade steady response is then calculated from nonlinear periodic blade equations using an iterative procedure based on Floquet theory. For stability, the blade motion is assumed to be a small perturbation about the steady response, and the linearized periodic blade equations are solved using Floquet transition matrix theory (Panda and Chopra, 1985). Stability results are calculated for typical CC rotor blades for several flight conditions.

FORMULATION

The blade is assumed to undergo three degrees of motion: rigid flap, lag, and feather rotations about hinges at the blade root, with hinge springs to obtain the desired natural frequencies. The hinge sequence is flap inboard, followed by lag, and then feather outboard. The flap angle β is positive up, the lag angle ζ is positive aft (opposite to rotation), and the feather angle θ is positive leading-edge up. The structural equations of motion include the inertial forces about three hinges and are documented by Panda and Chopra (1985). In general, terms up to second-order are retained in the flap and lag equations and terms up to third order are retained in the feather equation.

The aerodynamic forces are obtained using quasisteady strip theory. The section lift, drag, and moment about the mid-chord (per unit span) are

$$L = \frac{1}{2}\rho V^2 c C_{\ell}(\alpha, C_{\mu})$$

$$D = \frac{1}{2}\rho V^2 c C_{d}(\alpha, C_{\mu}) \qquad (1)$$

$$M_{.5} = \frac{1}{2}\rho V^2 c^2 C_{m.5}(\alpha, C_{\mu})$$

The aerodynamic coefficients C_ℓ, C_d, and $C_{m.5}$ are from data tables; the numerical values for these coefficients are available at small steps, $\Delta\alpha$ of 3 degrees and ΔC_μ of 1/200. These coefficients depend on the airfoil geometry, including slot height, and are also a function of angle of attack α, blowing momentum coefficient C_μ, and local Mach number. However, in the present work, the effect of compressibility (Mach number) is neglected. The C_μ is defined as

$$C_\mu = \frac{\dot{m}V_j^2}{qc} \tag{2}$$

where $\dot{m}V_j$ is the jet momentum, q (= 1/2 ρV^2) is the dynamic pressure, and c is the blade chord.

For an incompressible flow, using an isentropic expansion relationship, the momentum coefficient C_μ can be related to the local duct pressure P_d.

$$C_\mu = 2\frac{\bar{h}}{c}\frac{1}{q}(P_d - P_\infty) \tag{3}$$

where $\bar{h}/c$ is slot height-to-chord ratio (typically 0.002) and $P_d - P_\infty$ is duct gage pressure. The dynamic pressure at a radial station is

$$q = \frac{1}{2}\rho\,(\Omega R)^2\,(\frac{r}{R} + \mu\sin\psi)^2$$

For a compressible flow with a subsonic jet condition, the blowing momentum coefficient (Rogers et al., 1985) is

$$C_\mu = 2\frac{\bar{h}}{c}(M_j/M_\infty)^2 \quad \text{for} \quad (M_j < 1) \tag{4}$$

where M_j is the jet Mach number and M_∞ is free-stream Mach number. These relations, eqs. (3) and (4), for incompressible and compressible flows are valid only for the unchoked flow condition (when P_d/P_∞ is less than 1.892. For a P_d/P_∞ larger than 1.892, the flow becomes choked in the nozzle (slot). Then, the jet momentum coefficient is obtained as

$$C_\mu = \frac{2\frac{\bar{h}}{c}\frac{P_d}{P_\infty}M_j\,(\frac{2}{\gamma+1})^{\frac{\gamma+1}{2(\gamma-1)}}}{M_\infty^2\sqrt{1 + \frac{\gamma-1}{2}M_j^2}} \tag{5}$$

For both cases of unchoked and choked flows, the jet Mach number can be calculated in terms of duct pressure

$$M_j = \sqrt{5\left[\left(\frac{P_d}{P_\infty}\right)^{\frac{\gamma-1}{\gamma}} - 1\right]} \tag{6}$$

For an accurate representation of the blade internal duct pressure characteristics at an arbitrary local rotor disc location, pneumodynamic considerations are included in the analysis (Watkins et al., 1985). Between the duct pressure at a radial station and the cyclic pressure at the pneumatic valving system (blade root), there is a phase lag due to length, a pressure attenuation due to duct friction loss, and a pressure rise due to the centrifugal pumping effect. The duct pressure is obtained as

$$P_d = (P_{d_r} - P_\infty)\left\{1 - \eta_{duct}\left[\frac{r}{R} - \left(\frac{r}{R}\right)_{root}\right]\right\} + (P_{d_r}/P_\infty)\,\frac{\rho}{2}\left(\frac{r}{R}V_{tip}\right)^2 \eta_{pump} \tag{7}$$

and

$$P_{dr} = P_o + P_{1c}\cos(\psi - \phi) + P_{1s}\sin(\psi - \phi) \tag{8}$$

where ϕ is the phase lag for the pressure pulse at a radial station defined as

$$\phi = \frac{6\ rpm}{a_{duct}}(r - r_{root}) \quad deg \tag{9}$$

The term P_o is collective pressure, P_{1c} and P_{1s} are cyclic pressures at the blade root. The η_{duct} and η_{pump} are respectively the duct friction loss coefficient and the centrifugal pumping efficiency, respectively. The V_{tip} is tip speed (ΩR), r_{root} is root radius (where the pressure duct starts), P_∞ is atmospheric pressure (1827 lb/ft^2) and a_{duct} is speed of sound in the duct (1274 ft/sec).

Equations (7) through (9) show that the blowing momentum coefficient is a function of radial position r as well as azimuth angle ψ.

VEHICLE TRIM SOLUTION

Two types of trim solutions are considered corresponding to separate CC rotor aircraft concepts. The propulsive trim solution represents a CC rotor implemented in a conventional helicopter flight mode. There, the rotor produces all lift and propulsive forces. Alternatively, the constrained trim solution represents a CC rotor employed on a compound hleicopter configuration that also features auxiliary propulsive devices.

Propulsive Trim

The propulsive trim simulates the free flight condition. For specified weight

coefficient C_w, collective pitch θ_o, and forward speed μ, the trim solution calculates blowing settings (P_o, P_{1c} and P_{1s}), steady flap response (β_o, β_{1c}, and β_{1s}), vehicle orientation (α_s and ϕ_s) and steady inflow ratio λ.

The present propulsive trim is calculated from the satisfaction of three forces (vertical, horizontal and lateral) and two moments (pitch and roll) equilibrium equations. Figure 3 shows the forces and moments acting on the vehicle. The equilibrium equations have been defined by Panda and Chopra (1985).

For the vehicle trim solution, only the flap motion up to first harmonic is considered. Therefore, the following rotor equations are used.

$$\beta_o: \quad \frac{1}{2\pi}\int_o^{2\pi} (\text{flap equation})\, d\psi = 0 \tag{10}$$

$$\beta_{1c}: \quad \frac{1}{2\pi}\int_o^{2\pi} (\text{flap equation})\, \cos\psi\, d\psi = 0 \tag{11}$$

$$\beta_{1s}: \quad \frac{1}{2\pi}\int_o^{2\pi} (\text{flap equation})\, \sin\psi\, d\psi = 0 \tag{12}$$

For steady inflow, a linear distribution model developed by Drees is used,

$$\lambda = \mu \tan\alpha_s + \frac{1}{2}\,\frac{C_T}{\sqrt{\mu^2+\lambda^2}}\left(1 + K_x \frac{r}{R}\cos\psi + K_y \frac{r}{R}\sin\psi\right) \tag{13}$$

where

$$K_x = \frac{4}{3}\left[(1-1.8\mu^2)\sqrt{1+\left(\frac{\lambda}{\mu}\right)^2} - \frac{\lambda}{\mu}\right]$$

$$K_y = -2\mu$$

For hover, K_x and K_y become zero.

As stated earlier, the blowing momentum coefficient varies in both the radial as well as azimuth directions. Therefore, the aerodynamic coefficients (C_ℓ, C_d, and C_m) cannot be expressed in simple analytical expressions. To obtain the rotor coefficients (C_T, C_Y and C_H) for trim solution, the element forces must be integrated numerically in both the radial and the azimuth directions. Thus,

$$C_T = \frac{1}{4\pi(\Omega R)^2}\int_o^{2\pi}\int_o^{1} \sigma(x)\left(C_\ell \frac{U_T}{\Omega R}\frac{V}{\Omega R} - C_d \frac{U_P}{\Omega R}\frac{V}{\Omega R}\right) dx\, d\psi \tag{14}$$

$$C_H = \frac{1}{4\pi(\Omega R)^2} \int_0^{2\pi} \int_0^1 \sigma(x) \left[\left(C_\ell \frac{U_P}{\Omega R} \frac{V}{\Omega R} + C_d \frac{U_T}{\Omega R} \frac{V}{\Omega R} \right) \sin\psi \right.$$

$$\left. + \left(C_d \frac{U_R}{\Omega R} \frac{V}{\Omega R} - \beta\, C_\ell \frac{V}{\Omega R} \frac{V}{\Omega R} \right) \cos\psi \right] dx\, d\psi \qquad (15)$$

$$C_Y = \frac{1}{4\pi(\Omega R)^2} \int_0^{2\pi} \int_0^1 \sigma(x) \left[-\left(C_\ell \frac{U_P}{\Omega R} \frac{V}{\Omega R} + C_d \frac{U_T}{\Omega R} \frac{V}{\Omega R} \right) \cos\psi \right.$$

$$\left. + \left(C_d \frac{U_R}{\Omega R} \frac{V}{\Omega R} - \beta\, C_\ell \frac{V}{\Omega R} \frac{V}{\Omega R} \right) \sin\psi \right] dx\, d\psi$$

where U_P, U_T, U_R and V are section flow velocity components; see figure 4. The x is the nondimensional coordinate r/R, and $\sigma(x)$ is the local solidity ratio.

The vehicle and rotor equilibrium equations are obtained for large angles. These equations which are expressed in nondimensional form, are presented in the appendix. The nonlinear equations are solved iteratively for the trim solution using the Newton-Raphson procedure.

CONSTRAINED TRIM

The constrained trim solution, where propulsive force is partially obtained from auxiliary power, is calculated by satisfying the vertical force, pitch moment, and roll moment equilibrium equations. The vehicle orientation is specified in terms of shaft tilt α_s; lateral tilt ϕ_s is zero. Since the trim solution is for an isolated rotor, the characteristics of the vehicle are not needed. For the specified weight coefficient C_W, collective pitch θ_o, and advance ratio μ, the trim solution calculates blowing settings (P_o, P_{1c} and P_{1s}) and rotor response (β_o, β_{1c} and β_{1s}). This solution procedure is similar to that used in the propulsive trim solution.

Alternative constrained trim procedure is to fix the collective blowing pressure (e.g. $P_o = 1.5\ P_\infty$) and adjust the collective geometric pitch to obtain the desired thrust level. This trim procedure though not implemented in the present work, would yield equivalent blade stability results.

BLADE RESPONSE SOLUTION

The blade response solution involves the determination of the time dependent blade deflected position. For steady flight conditions, the blade response is periodic, and hence the solution is calculated for only one complete cycle. For this, the nonlinear coupled blade equations containing periodic terms are solved in the rotating frame using an iterative procedure based on Floquet theory (Dugundji and Wendell, 1983). For the blade response solution, the pilot controls and the vehicle orientation obtained from

the trim solution are used. The numerical procedure to calculate the initial conditions and the blade response along the azimuth are detailed by Panda and Chopra (1985). The calculated response solution consists of all harmonics for flap, lag, and torsion motions.

It should be noted that there is another cycle of iterations (typically two) between the trim solution and the blade response solution to include the effect of blade elastic twist in the trim calculations.

STABILITY SOLUTIONS

The stability of blade perturbation motion about its steady deflected position is examined using the vehicle trim and the blade response solutions. For perturbation motion, unsteady aerodynamic effects are introduced approximately through a dynamic inflow modeling. The dynamic inflow is assumed to be a perturbation about the steady value, and its components are related to rotor perturbation forces and moments (Panda and Chopra, 1985).

The blade perturbation equations are transformed to the fixed reference frame using Fourier coordinate transformation. These equations, which contain selected harmonic terms, are solved for stability using Floquet transition matrix theory.

RESULTS AND DISCUSSION

Numerical results are calculated for a four-bladed CC rotor with Lock number $\gamma = 5$, solidity ratio $\sigma = 0.13$, and zero precone. The blade flap, lag and torsion rotating frequencies are 2.3/rev, 2.6/rev and 18/rev, respectively. The chordwise offsets of the center of mass and the reference aerodynamic center from the elastic axis are considered to be zero, and the elastic axis is assumed to be at the midchord position. For stability calculations, the structural damping is assumed to be zero for all modes. For airfoil characteristics, tabular data of a typical CC airfoil with trailing edge blowing (single slot) is used. Other rotor and vehicle characteristics are given in table I.

PROPULSIVE TRIM

Numerical results are calculated for $C_w/\sigma = 0.1$. Figure 5 shows the vehicle propulsive trim solution for a collective pitch of zero. The propulsive trim parameters P_o, P_{1C}, P_{1S}, α_S, ϕ_S, and λ are plotted for different forward speeds (in terms of advance ratio μ). An advance ratio of 0.6 represents a forward speed of about 300 ft/sec and a maximum tip speed of 850 ft/sec. The root blowing pressures, collective (P_o) and cyclic (P_{1C} and P_{1S}), are presented in terms of atmospheric pressure (P_∞). The flap angles (β_o, β_{1C} and β_{1S}) are negligible for this highly stiff rotor and hence are not presented. The trim solution is calculated iteratively from nonlinear equilibruim equations. As conventional rotor, the shaft has to tilt more forward at larger μ in order to compensate for the increasing parasite drag. The inflow λ first decreases and then increases with forward speed due to the combined effect of decreasing induced velocity and increasing disk tilt (α_S) at larger μ. There is only a slight influence of μ on side shaft tilt ϕ_S. The collective and cyclic blowing pressure requirements with advance ratio μ appear quite similar to the respective geometric pitch requirements of a

conventional rotor (Panda and Chopra, 1985). The cyclic blowing pressures (P_{1C} and P_{1S}) are much smaller than the collective blowing pressure (P_0). The periodic variation of dynamic pressure is compensated for by the cyclic blowing components. At low forward speeds both P_{1C} and P_{1S} are of equal importance because of the nonuniform induced velocity; however at higher speeds, P_{1S} becomes larger than P_{1C}.

TABLE I - CCR Rotor Characteristics in Analysis

Rotor radius R	28.5 ft
Tip speed ΩR	500 ft/sec
Chord-to-radius ratio, c/R	0.1
Airfoil thickness ratio, t/c	0.15
Slot height-to-chord ratio, $\bar{h}$	0.002
Feather inertia-to-flap inertia ratio, I_f/I_b	0.0024
Reference lift curve slope, a	5.7
Vertical cg offset from hub, h	0.2R
Duct speed of sound a_{duct}	1274 ft/sec
Duct friction loss coefficient, η_{duct}	0.15
Centrifugal pumping efficiency, η_{pump}	0.57
Root radius-to-rotor radius ratio, $(r/R)_{root}$	0.1

A word of caution: these and subsequent results are calculated using the linear inflow model of Drees, which perhaps underestimates the longitudinal inflow variation at low forward speeds ($\mu < 0.15$). In addition, blowing in the reversed flow regions is assumed to produce no circulatory lift.

Figure 6 presents the propulsive trim solution for a collective pitch of -10 degrees. For this pitch setting, a larger collective blowing pressure is needed to achieve the prescribed thrust level. With this negative collective pitch, there are changes on other trim parameters (λ, α_s, and ϕ_s); in fact, their values become almost double those of zero pitch. Trim results without pneumodynamic effects (pressure loss, phase lag, and centrifugal pumping) are shown in figure 6(b). There is a small step decrease in collective blowing pressure for all forward speeds because of reduced losses. Neglecting pneumodynamics in the calculations also influences cyclic pressures; P_{1S} decreases and P_{1C} increases.

In figure 7, the time-dependent position of the blade is presented for one complete cycle. The blade is set at zero collective pitch, and the propulsive trim solution is employed. These results are obtained by solving the nonlinear periodic equations using an iterative procedure based on Floquet theory. For numerical integration, a fourth-order Runge-Kutta method and 240 time steps per cycle ($\Delta\psi$ = 1.5 degrees) are used. The blade is extremely stiff in flap mode (flap frequency = 2.3/rev) and, therefore, a small flap response is expected. At a low forward speed (μ = 0.2), there is a very little flap response. However, at high forward speeds, the flap response becomes greater induced by a larger variation in aerodynamic environment along the azimuth. At μ = 0.4, the flap response consists primarily of the second harmonic with a maximum peak-to-peak amplitude of about 0.75 degrees. At high μ of 0.6, the flap response is again dominated by a 2/rev component with a maximum peak-to-peak amplitude of about 2.5 degrees, which is perhaps a large flap response for this highly stiff rotor.

Figure 8 shows the damping of the low frequency cyclic lag mode for different advance ratios and collective pitch. Results are obtained from the eigen solution of Floquet transition matrix. Again, for the stability solution, 240 time steps per cycle are used for time integration. The eigenvalues represent rotor frequencies in the fixed reference frame. For this case, the low frequency lag mode is a regressive mode. The damping is presented in terms of the real part of the complex eigenvalue, α_ζ. Note that $\alpha_\zeta = \zeta_L \omega_\zeta$, where ζ_L is the viscous damping ratio of the lag mode, and ω_ζ is the frequency of lag mode nondimensionalized with respect to rotational speed. For the case of zero collective pitch, the blade is stable but the damping level in lag damping is quite low. However, the inclusion of structural damping will increase blade stability. In addition, negative collective pitch also has a stabilizing influence on lag mode. It is interesting to note that the variation of forward speed has only a slight influence on lag damping.

Figures 9 through 11 show the effect of thrust level on blade lag mode stability. For a fixed-collective pitch, the rotor thrust level is a near linear function of blowing pressure. Using the previous thrust coefficient of C_T/σ of 0.1. as a reference, three additional thrust levels are considered: C_T/σ = 0.05, 0.15, and 0.2. Figure 9 presents the lag mode damping for zero collective pitch. In general, the reduced thrust level stabilzes lag mode at low forward speeds and destabililizes lag mode at high forward speeds. For C_T/σ = 0.15, lag mode is unstable for $\mu < 0.15$, whereas, for C_T/σ = 0.05, lag mode is unstable for $\mu > 0.41$. This observed instability is quite weak in nature and can be easily stabilized with the inclusion of a small amount of structural damping in lag mode. In Figure 10, somewhat similar results are seen for a collective pitch of -5 degrees. For a low thrust level condition of C_T/σ = 0.05, the lag mode becomes unstable for $\mu > 0.42$. At this thrust level, the solution is not obtained for $\mu >$ 0.51. The lateral cyclic blowing component becomes larger than the collectiv blowing level; therefore, P_{root} becomes less than P_∞ locally on the advancing side of the rotor. Again the damping requirements to stabilize the lag mode are not high, and the expected levels of internal structural damping would ensure this stability. Figure 11 shows lag mode damping for a collective pitch of -10 degrees. With this high negative pitch, the lag mode damping generally becomes more stable. The exception is C_T/σ = 0.2, for which the blade lag mode becomes less stable at high forward speeds.

Figure 12 shows the effect of torsional stiffness on lag mode stability. The earlier results are for a rotating torsional frequency of 18/rev. Figure 12(a) presents results for zero collective pitch. If the torsion frequency is reduced to 10/rev, there is only a slight effect on lag mode damping. A further reduction in torsional stiffness

has an appreciable effect on lag mode stability. For a torsional frequency of 5/rev, the lag mode becomes unstable and the instability increases at high advance ratios. In figure 12(b), results are presented for a collective pitch of -10 degrees. Again, reducing torsional stiffness decreases lag mode damping.

The effect of lag stiffness on lag mode damping is presented in figure 13. The earlier results are for a rotating lag frequency of 2.6/rev. As compared with conventional rotors, this is a case of extremely high lag stiffness. For zero collective pitch, figure 13(a), if the lag frequency is reduced to the level of a typical stiff-inplane hingeless rotor ($\nu_\zeta = 1.4$), the lag damping is only slightly reduced. If the lag damping is further reduced to the level of a typical soft-inplane rotor ($\nu_\zeta = 0.7$), again the effect on lag damping again is quite negligible. For a negative collective pitch of 10 degrees figure 13(b), the effect of reducing lag stiffness to the conventional rotor value is quite destabilizing.

Figure 14 presents the effect of flap stiffness on lag mode damping. The earlier results are obtained for a rotating flap frequency of 2.3/rev. In comparing with the existing rotors, this is an extremely high flap stiffness. For zero collective pitch figure 14(a), if the flap frequency is reduced to 1.5/rev (level of ABC Rotor), the lag mode becomes slightly more stable, and even more so at high advance ratios. If the flap frequency is further reduced to 1.1/rev, to the level of a typical hingeless rotor(e.g. BO-105), the lag mode becomes unstable at high advance ratios ($\mu > 0.48$). For a collective pitch of -10 degrees Figure 14(b), the trends of lag mode damping with decreasing flap stiffness are somewhat different. The blade, however, remains stable.

Figure 15 shows the effect of pneumodynamics on lag mode damping. The blade is set at a collective pitch of -10 degrees. Neglecting pneumodynamics effects reduces lag mode damping slightly.

CONSTRAINED TRIM

Constrained trim calculates rotor controls to achieve a desired thrust and shaft orientation. This type of trim condition is possible through an auxiliary propulsive device. The solution is obtained by satisfying three rotor equilibrium equations (vertical force, pitch moment, and roll moment). This is an isolated rotor trim solution, and the airframe characteristics are not needed. With an auxiliary propulsive device, it is possible to achieve high forward speeds without causing excessive shaft tilts. Thus, the subsequent results using constrained trim include a larger range of advance ratios (up to 1.0). An advance ratio of 1.0 represents a forward speed of about 500 ft/sec and a maximum tip speed of 1000 ft/sec. The compressibility effects, however, have not been considered in the present work.

The constrained trim solution for zero collective pitch and zero shaft angle is shown in figure 16. The collective and cyclic components of blowing pressure at blade root are quite similar to those obtained with propulsive trim for zero collective pitch; Figure 5. The collective pressure P_o is somewhat smaller at higher advance ratios because of reduced inflow through the disk. For $\mu > 0.41$, the solution is not practical because of the pressure constraint ($P_{root} < P_\infty$). In figure 17, the constraint trim solution is presented for zero shaft angle and a collective pitch of -5 degrees. Once again, the collective pressure requirements at high μ are comparatively smaller than those of the propulsive rotor.

Figure 18 presents the blade flap response for one complete cycle. For this cycle, the rotor is set at zero shaft angle and zero collective pitch. For a low advance ratio ($\mu = 0.2$), the flap response amplitude is small. At high advance ratios, there is considerable flap response, consisting primarily of a 2/rev component. For $\mu = 0.5$, the peak-to-peak amplitude is about 1 degrees, whereas, for $\mu = 1.0$, the peak-to-peak amplitude is about 3.5 degrees.

Figure 19 shows the lag mode stability results for zero shaft angle. The lag mode is less damped for zero collective pitch. The negative collective pitch stabilizes lag mode damping. For collective pitch of 0 degrees the results are discontinued for μ larger than 0.42 because of the blowing pressure constraint ($P_{root} < P_{\infty}$).

In figure 20, the lag mode damping results are presented for a shaft angle of 5 degrees. This is a forward tilt of rotor shaft and the inflow through the rotor disk increases, resulting in an increased collective pressure requirement. Compared with results obtained for zero shaft angle (Fig. 19), the lag mode is slightly less stable for both cases of collective pitch. Note that the zero collective case can now be extended up to an advance of 1.0.

Figure 21 shows lag mode stability results for a shaft angle of -5 degrees. This is a rearward tilt of rotor shaft, and the inflow through the rotor disk decreases, resulting in a decreased collective pressure requirement. Compared with results obtained for zero shaft angle (Fig. 19) the lag mode is more stable for both cases of collective pitch. With the reduced collective pressure the range of μ for zero collective pitch is now reduced to 0.31.

CONCLUSIONS

Aeroelastic stability of a simple, three-degree-of-freedom (flap-lag-torsion) CCR blade model in forward flight is examined. Results are obtained using propulsive trim as well as auxiliary power trim. Based on the results of this study, the following conclusions are drawn.

Flap response consists primarily of 2/rev, and its amplitude increases with μ (peak-to-peak amplitude of 2.5 degrees at $\mu = 0.6$ for propulsive rotor)

Lag mode damping becomes more stable as collective pitch is decreased.

At high forward speeds ($\mu > 0.4$), lag mode becomes unstable at low thrust levels ($C_T/\sigma = .05$).

Reducing the stiffness of a highly stiff CC rotor blade to the level of a typical hingeless blade can cause lag mode instability.

The results obtained with auxiliary power trim are quite similar to those obtained with propulsive trim.

REFERENCES

Chopra, I.: Aeroelastic Stability of an Elastic Circulation Control Rotor Blade in Hover. Vertica, Vol. 8, No. 4, Oct 1984.

Chopra, I.: Dynamic Stability of a Bearingless Circulation Control Rotor Blade in Hover. Journal of the American Helicopter Society, Vol. 30, No. 4, Oct 1985.

Chopra, I. and Johnson, W.: Flap-lag-torsion Aeroelastic Stability of Circulation-Controlled Rotors in Hover. Journal of the American Helicopter Society, Vol. 24, No. 2, Apr 1979.

Dugundji, J. and Wendell, H.: Some Analysis Methods for Rotating Systems with Periodic Coefficients. AIAA Journal, Vol. 21, No. 6, Jun 1983.

Englar, R.J. and Applegate, C.A.: Circulation Control - A Bibliography of DTNSRDC Research and Selected Outside References. David W. Taylor Research and Development Center Report DTNSRDC-84/052, Sep 1984.

Johnson, W.: Recent Developments in the Dynamics of Advanced Rotor Systems. NASA TM 86669, Mar 1985.

Linden, A.W. and Biggers, J.C.: X-Wing Potential for Navy Applications. Paper presented at 41st Annual Forum of American Helicopter Society, Fort Worth, Texas, 15-17 May 1985.

Panda B. and Chopra I.: Flap-lag-torsion Stability in Forward Flight. Journal of the American Helicopter Society, Vol. 30, No. 4, Oct 1985.

Rogers, E.O., Schwartz, A.W. and Abramson, J.S.: Applied Aerodynamics of Circulation Control Airfoils and Rotors. Paper presented at 41st Annual Forum of the American Helicopter Society, Fort Worth, Texas, May 1985.

Watkins, C.B., Reader, K.R. and Dutta, S.K.: Pneumodynamic Characteristics of a Circulation Control Rotor Model. Journal of the American Helicopter Society, Vol. 30, No. 3, Jul 1985.

Appendix

Nonlinear Equations for Trim Solution

$$F(1) = \frac{-(\nu_\beta^2-1)/\gamma}{2\,\frac{h}{R}\,C_T/\sigma a}\,\beta_{1C} - X_{cg}/h\,\cos\alpha_s + \sin\alpha_s - \frac{1}{2}\,\mu^2\,\frac{f}{A}\,\frac{1}{C_w}$$

$$(\cos\alpha_s - \frac{X_{cg}}{h}\,\sin\alpha_s) + \frac{M_{yF}}{hW} \qquad \text{(Pitch moment)}$$

$$F(2) = 1 - \frac{C_T}{C_w}\cos\phi_s\,\cos\alpha_s - \frac{C_H}{C_w}\sin\alpha_s + \frac{C_Y}{C_w}\sin\phi_s$$

$$+ \frac{C_{YF}}{C_w}\sin\phi_s + \frac{1}{2}\,\mu^2\,\frac{f}{A}\,\frac{1}{C_w}\sin\phi_s \qquad \text{(Vertical force)}$$

$$F(3) = \frac{1}{2}\,\mu^2\,\frac{f}{A}\,\frac{1}{C_w} + \frac{C_H}{C_w}\cos\alpha_s - \frac{C_T}{C_w}\sin\alpha_s\,\cos\phi_s \qquad \text{(Longitudinal force)}$$

$$F(4) = (\frac{C_{YF}}{C_w} + \frac{C_Y)}{C_w}\cos\phi_s + \frac{C_T}{C_w}\sin\phi_s\,\cos\alpha_s \qquad \text{(Lateral force)}$$

$$F(5) = \frac{-(\nu_\beta^2-1)/\gamma}{2\,\frac{h}{R}\,C_T/\sigma a}\,\beta_{1s} + (\cos\phi_s + \frac{Y_{cg}}{h}\sin\phi_s)\,\frac{C_{YF}}{C_w}$$

$$+ \sin\phi_s - \frac{Y_{cg}}{h}\cos\phi_s + \frac{M_{xF}}{hW} \qquad \text{(Roll moment)}$$

$$F(6) = \lambda - \mu\,\tan\alpha_s - \frac{C_w}{2}\,\frac{1}{\sqrt{\mu^2+\lambda^2}}\,(1 + K_x\,\frac{r}{R}\cos\psi + K_y\,\frac{r}{R}\sin\psi) \qquad \text{(Inflow)}$$

$$F(7) = \beta_o - \frac{1}{4\pi}\,\frac{\gamma}{\nu_\beta^2}\int_0^{2\pi}\int_0^1 x\,V^2 C_\ell\,dx\,d\psi \qquad \text{(Flap } \beta_o\text{)}$$

$$F(8) = \beta_{1C} - \frac{1}{4\pi} \frac{\gamma}{(\nu_\beta^2 - 1)} \int_0^{2\pi} \int_0^1 x V^2 C_\ell \cos\psi \, dx \, d\psi \qquad \text{(Flap } \beta_{1C}\text{)}$$

$$F(9) = \beta_{1S} - \frac{1}{4\pi} \frac{\gamma}{(\nu_\beta^2 - 1)} \int_0^{2\pi} \int_0^1 x V^2 C_\ell \sin\psi \, dx \, d\psi \qquad \text{(Flap } \beta_{1S}\text{)}$$

$$F(10) = \frac{C_T}{C_w} - \frac{a}{4\pi} \frac{1}{C_w} \int_0^{2\pi} \int_0^1 \sigma U_T V C_\ell \, dx \, d\psi \qquad \text{(Rotor thrust)}$$

$$F(11) = \frac{C_H}{C_w} - \frac{a}{4\pi} \frac{1}{C_w} \int_0^{2\pi} \int_0^1 \sigma \left[U_P V C_\ell + U_T V C_d \right) \sin\psi$$

$$+ \left(U_R V C_d - V^2 \beta C_\ell \right) \cos\psi \Big] \, dx \, d\psi \qquad \text{(Rotor drag)}$$

$$F(12) = \frac{C_Y}{C_w} - \frac{a}{4\pi} \frac{1}{C_w} \int_0^{2\pi} \int_0^1 \sigma \left[-(U_P V C_\ell + U_T V C_d) \cos\psi \right.$$

$$\left. + (U_R V C_d - V^2 \beta C_\ell) \sin\psi \right] dx \, d\psi \qquad \text{(Rotor side force)}$$

In the expressions, the flow components U_P, U_T, and V are nondimensionalized with respect to ΩR.

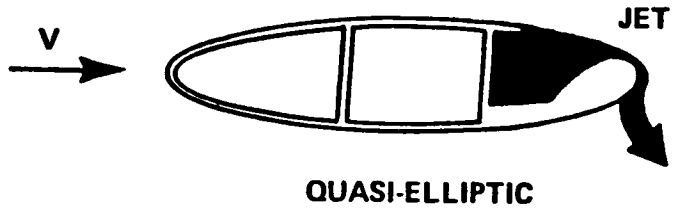

Figure 1. - Circulation control airfoil.

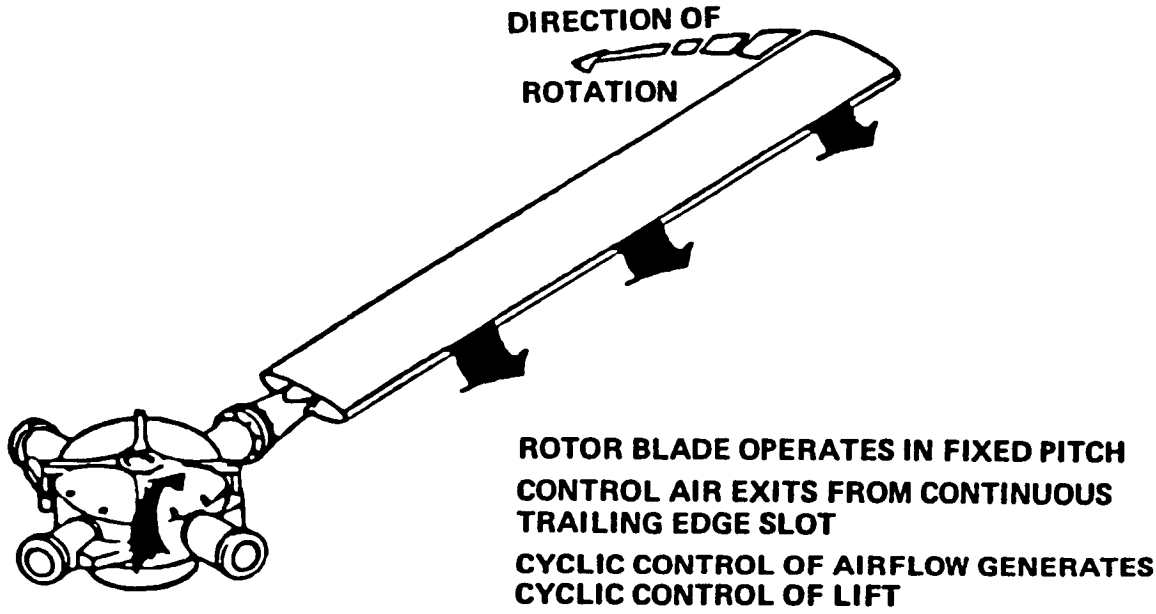

Figure 2. - Circulation control rotor concept.

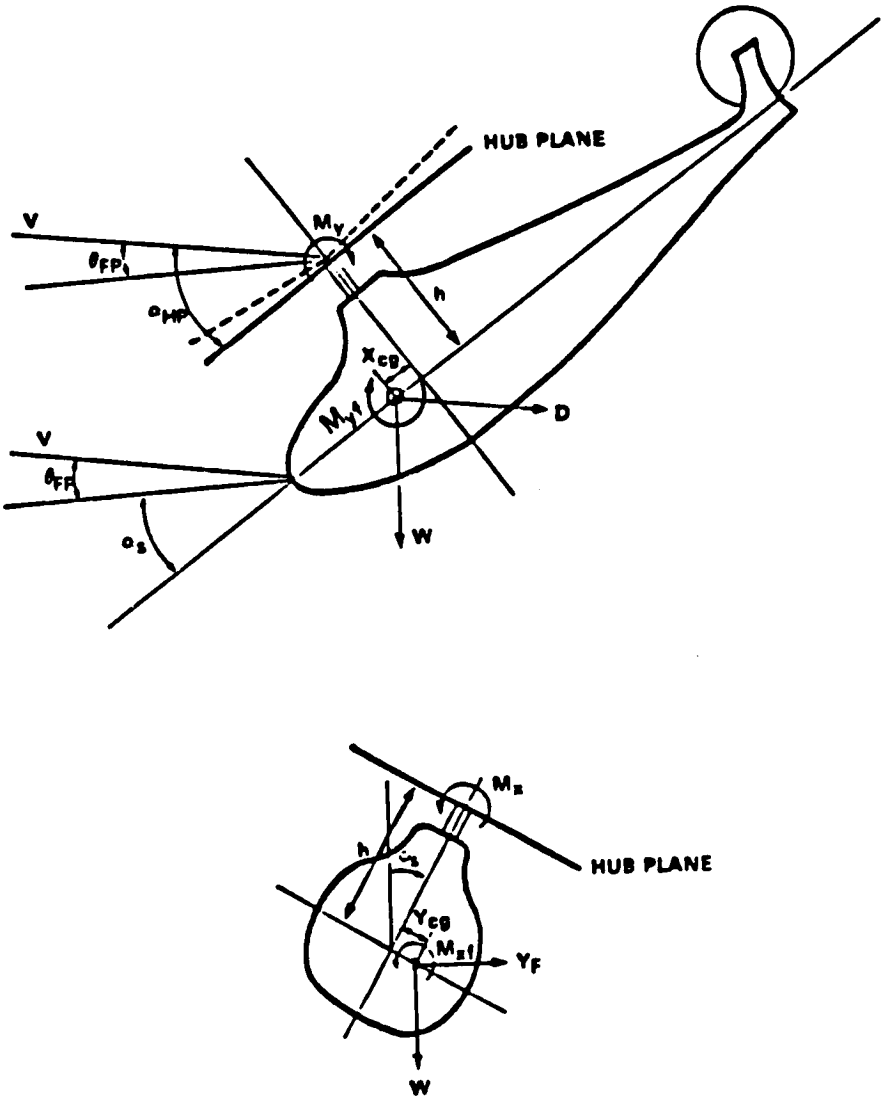

Figure 3. - Vehicle trim configurations.

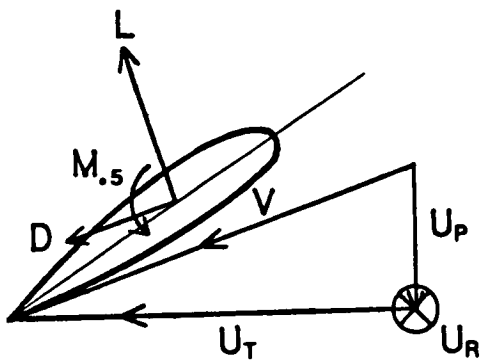

Figure 4. - Blade-section aerodynamics.

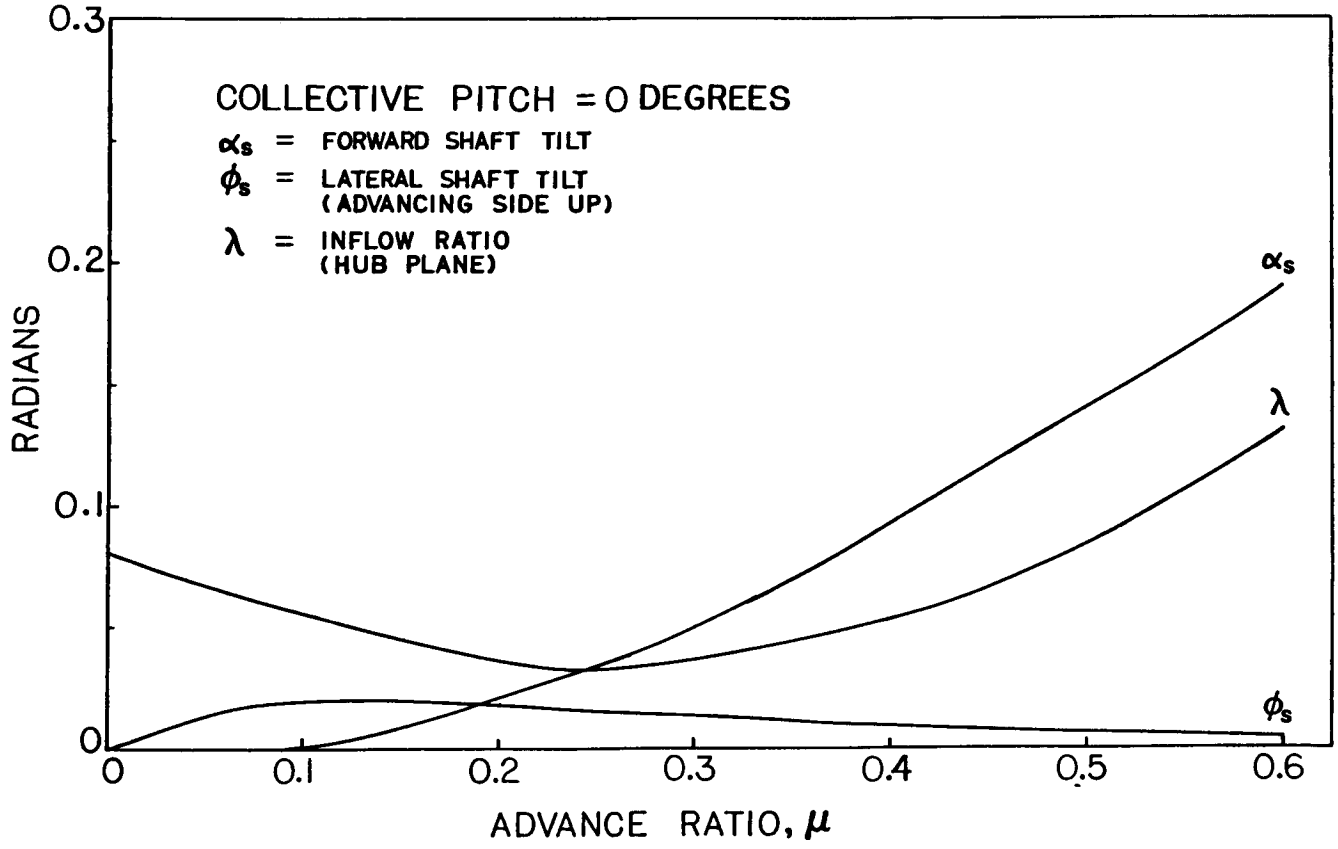

(a) Rotor altitude and mean inflow.

Figure 5. - Vehicle propulsive trim solutions for a collective pitch of zero degree ($C_T/\sigma = 0.1$, $\nu_\beta = 2.3$, $\nu_\zeta = 2.6$, $\nu_\theta = 18$)

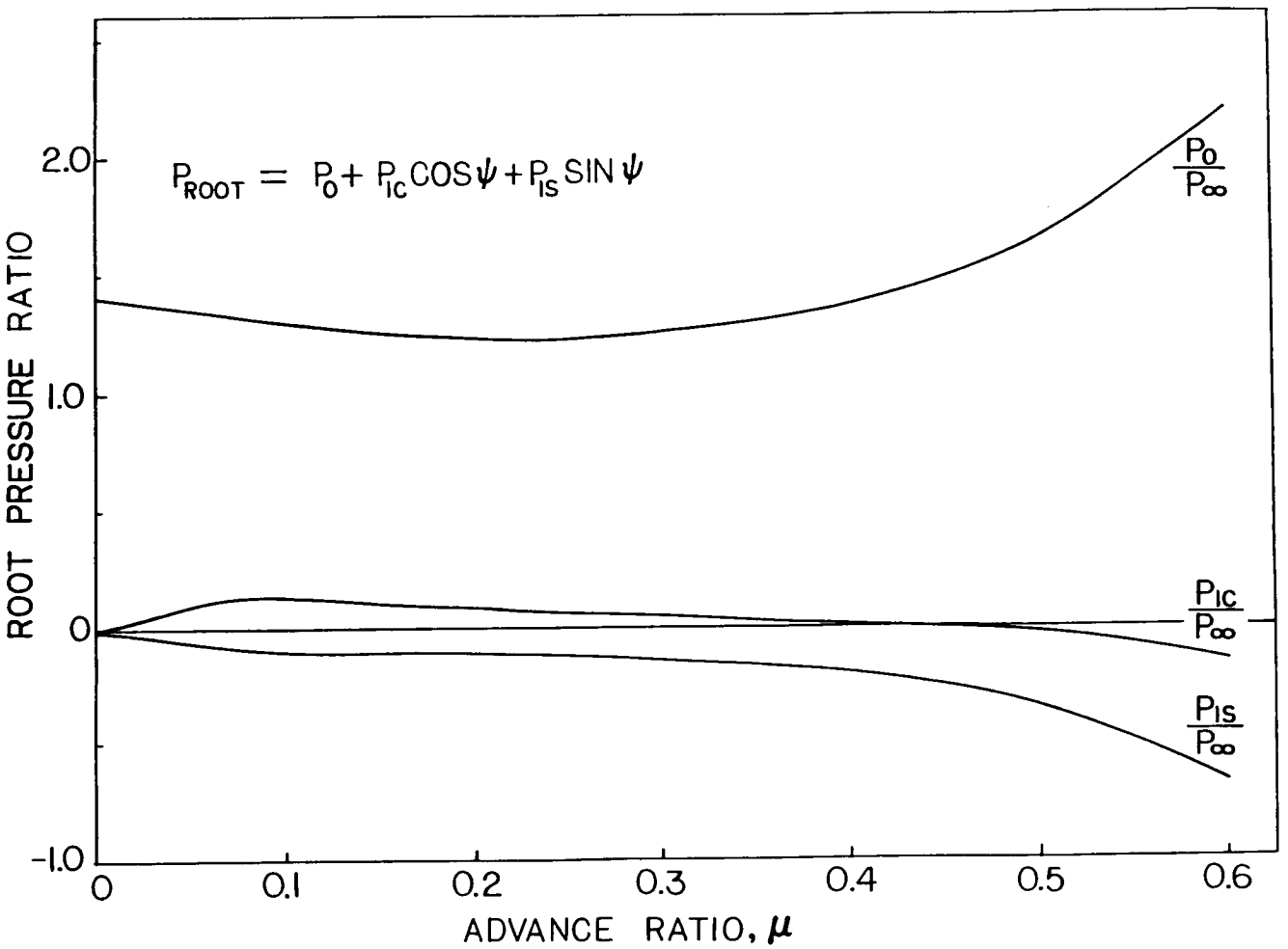

(b) Blowing pressure requirements for trim.

Figure 5.- Continued.

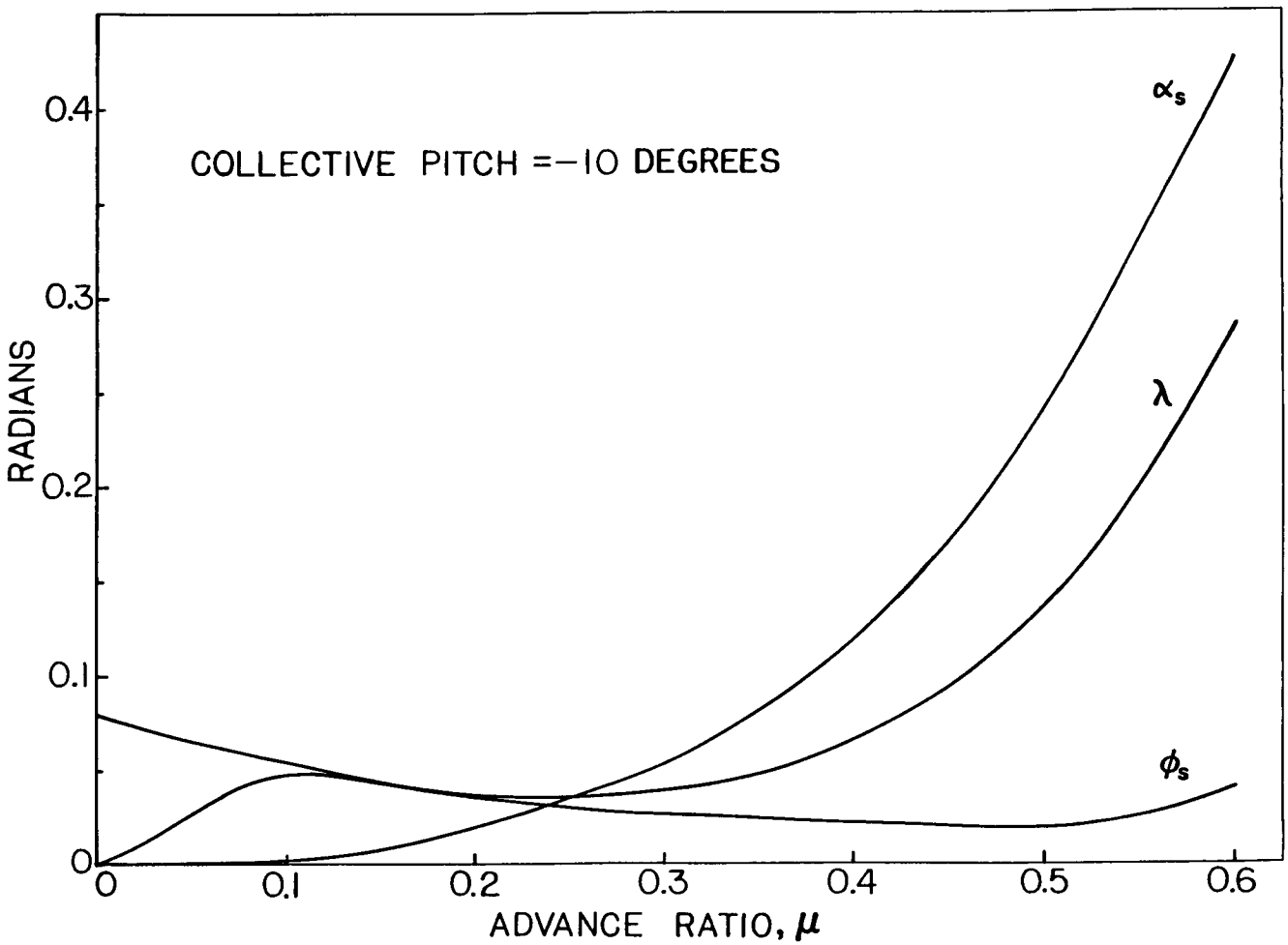

(a) Rotor altitude and mean inflow.

Figure 6. - Vehicle propulsive trim solutions for a collective pitch of -10 degrees. ($C_T/\sigma = 0.1$, $\nu_\beta = 2.3$, $\nu_\zeta = 2.6$, $\nu_\theta = 18$)

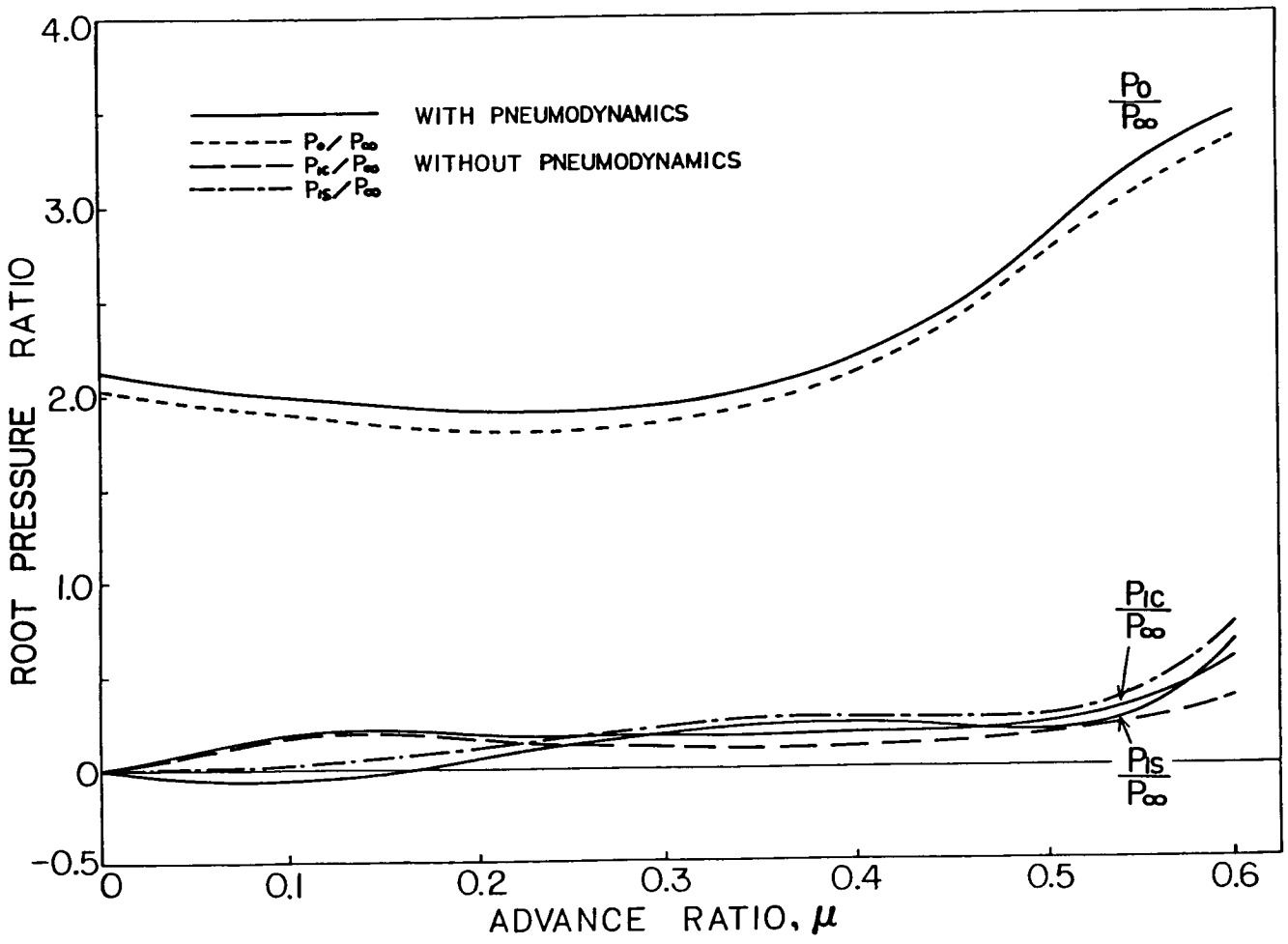

(b) Blowing pressure requirements for trim.

Figure 6.- Concluded.

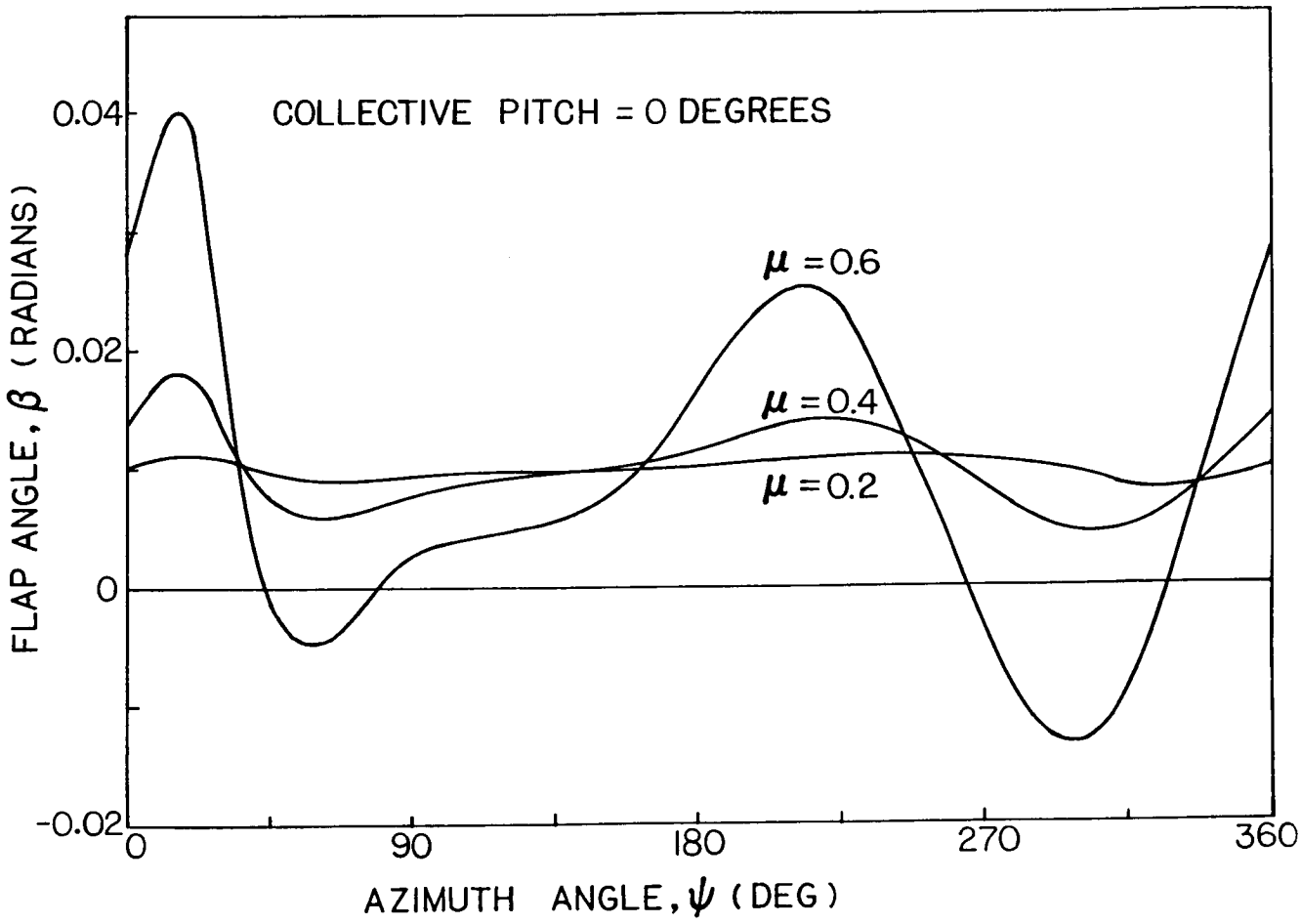

Figure 7. - Blade flap responses for various advance ratios. (C_T/σ = 0.1, ν_β = 2.3, ν_ζ = 2.6, ν_θ = 18)

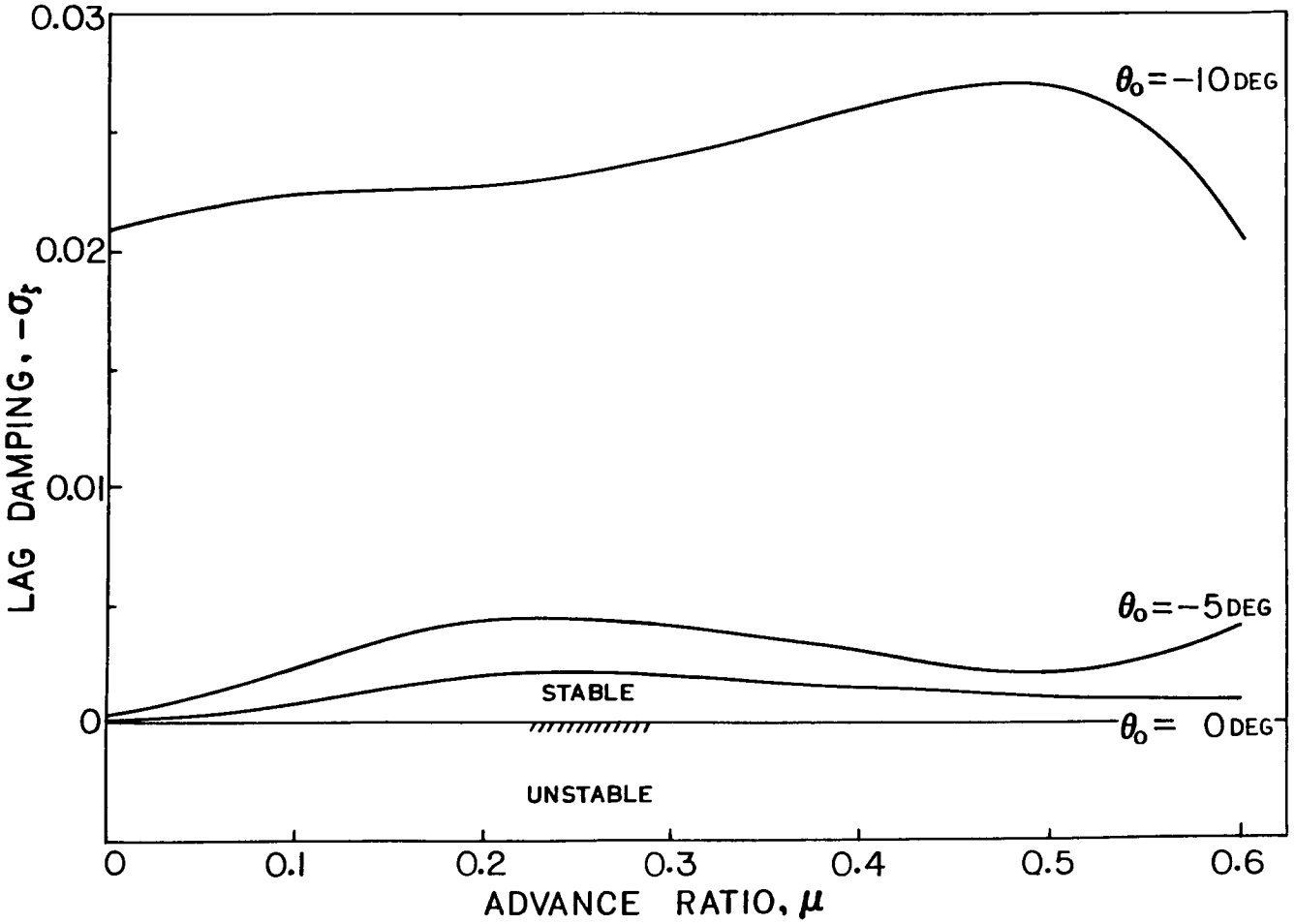

Figure 8. - Effect of collective pitch on low frequency cyclic lag mode. ($C_T/\sigma = 0.1$, $\nu_\beta = 2.3$, $\nu_\zeta = 2.6$, $\nu_\theta = 18$)

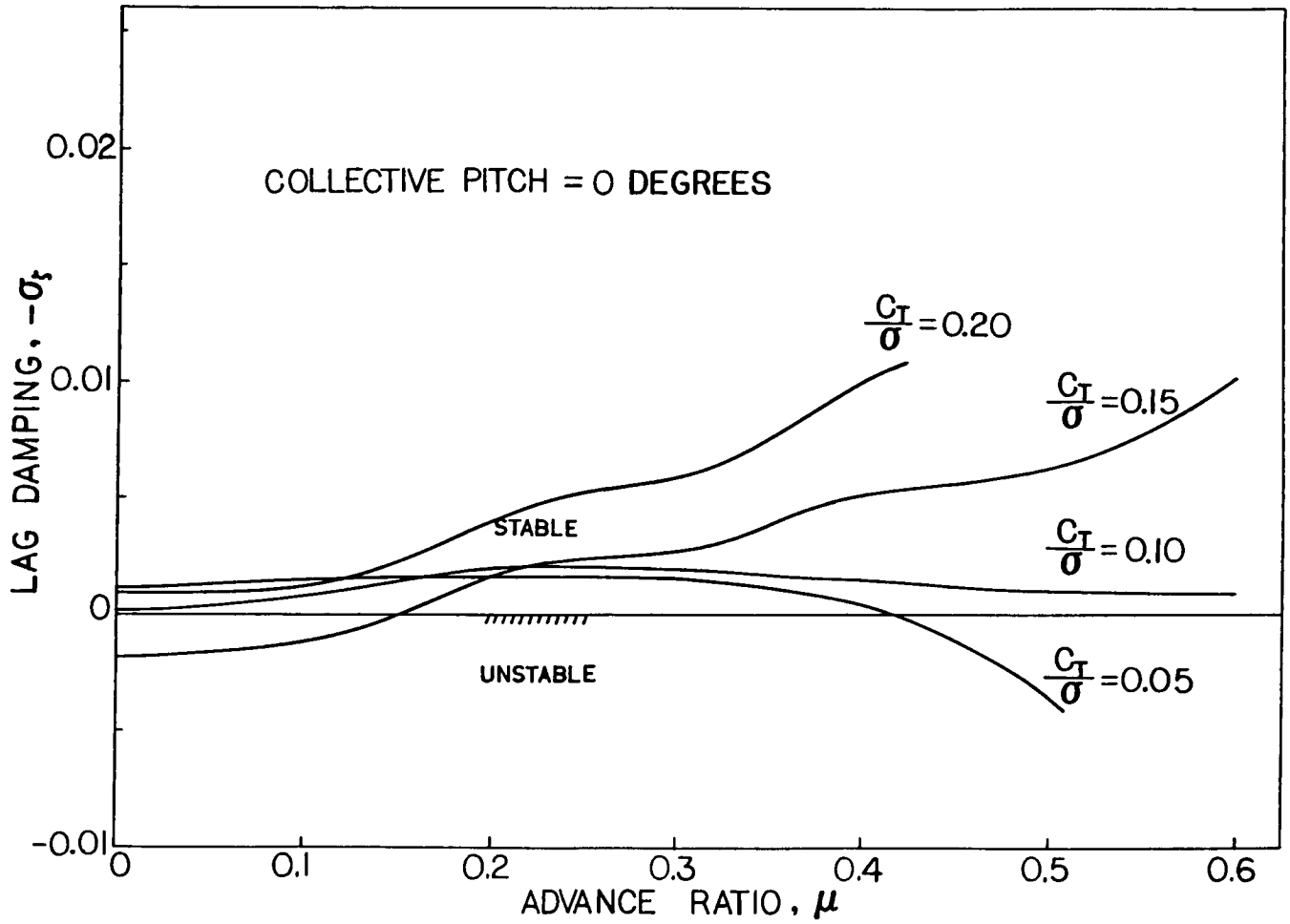

Figure 9. - Effect of thrust level on low frequency cyclic lag mode. (ν_β = 2.3, υ_ζ = 2.6, υ_θ)

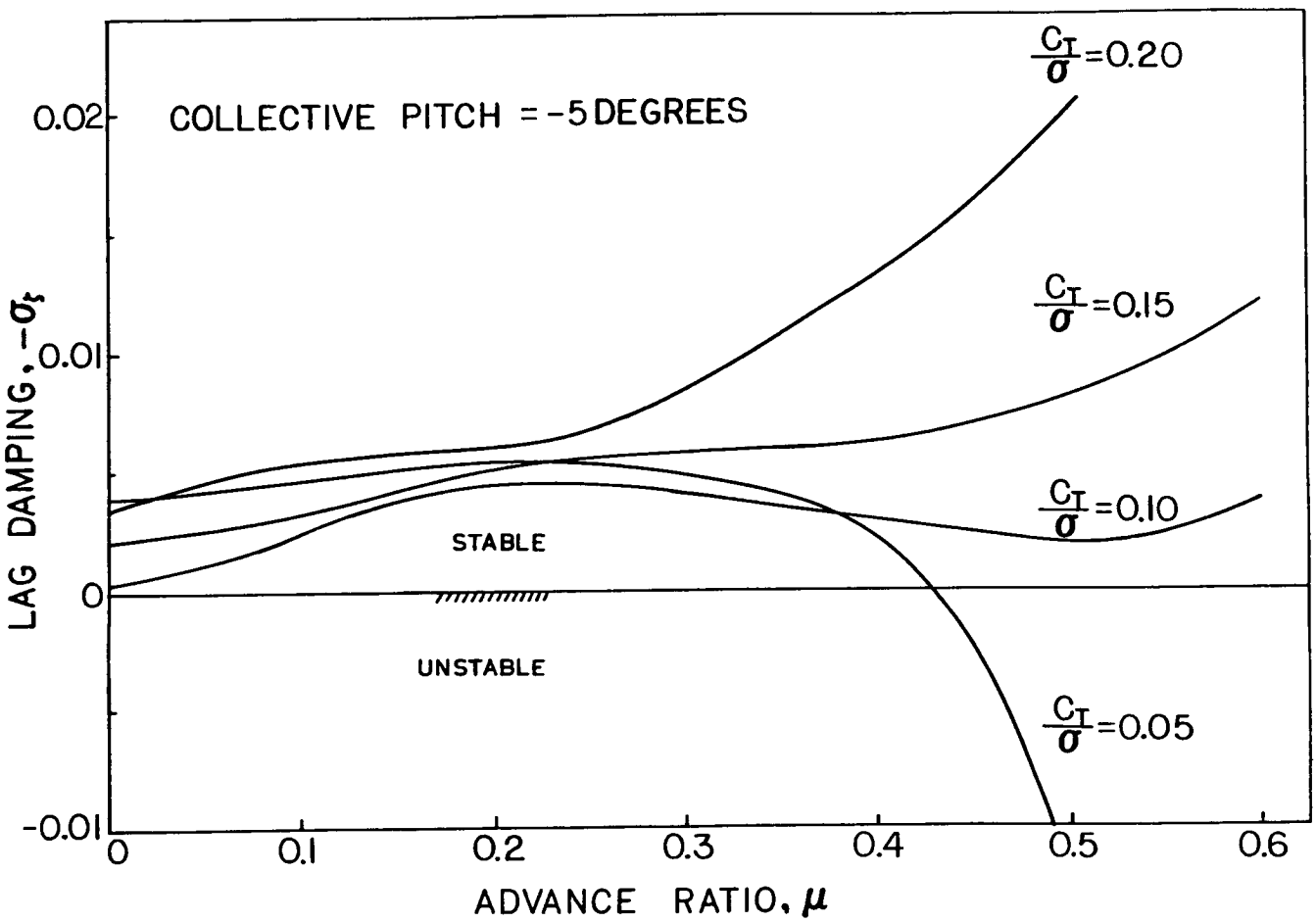

Figure 10. - Effect of thrust level on low frequency cyclic lag mode. ($\nu_\beta = 2.3$, $\nu_\zeta = \nu_\theta = 18$)

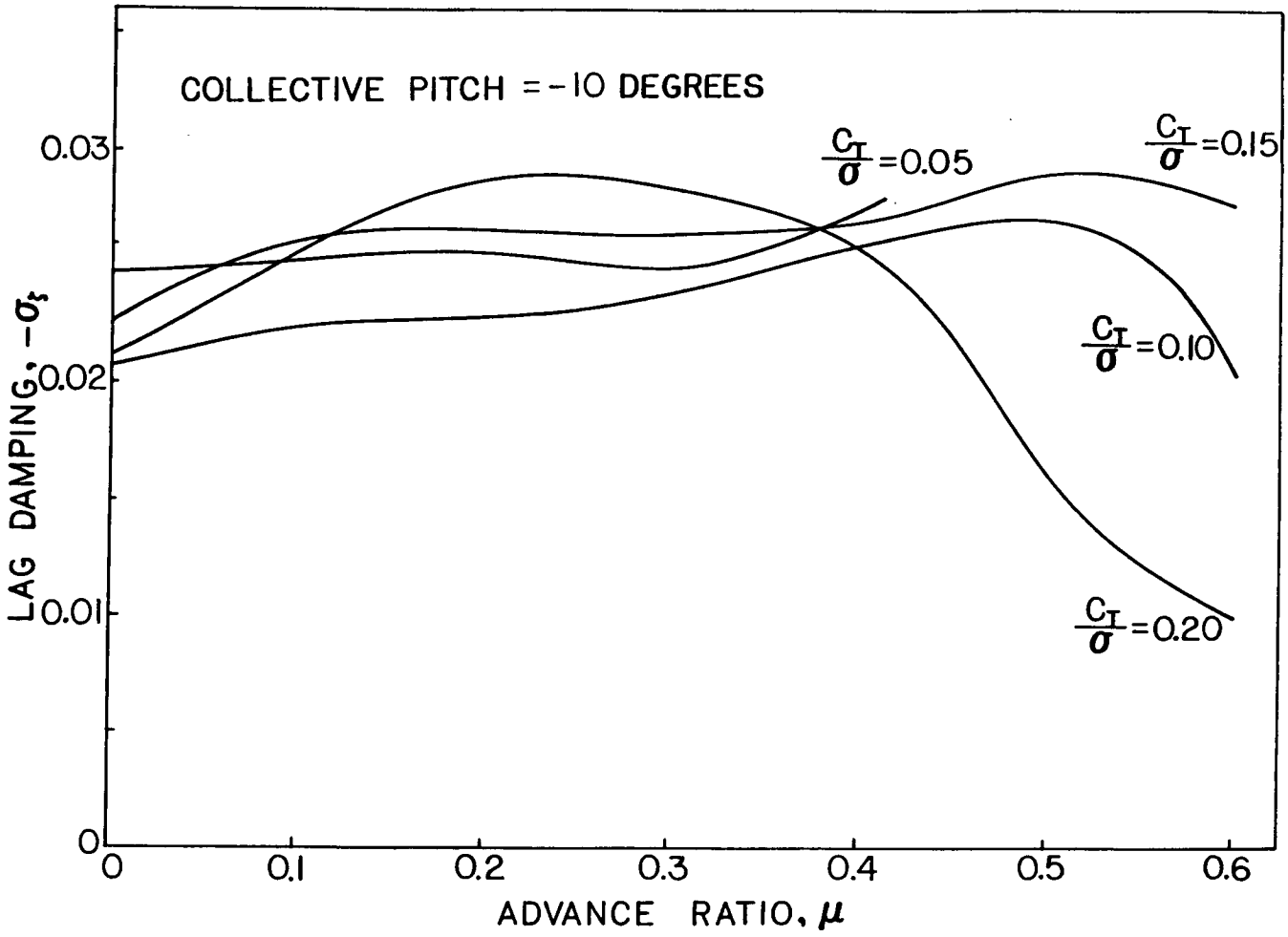

Figure 11. - Effect of thrust level on low frequency cyclic lag mode. (ν_β = 2.3, $\nu_\zeta = \nu_\theta$ = 18)

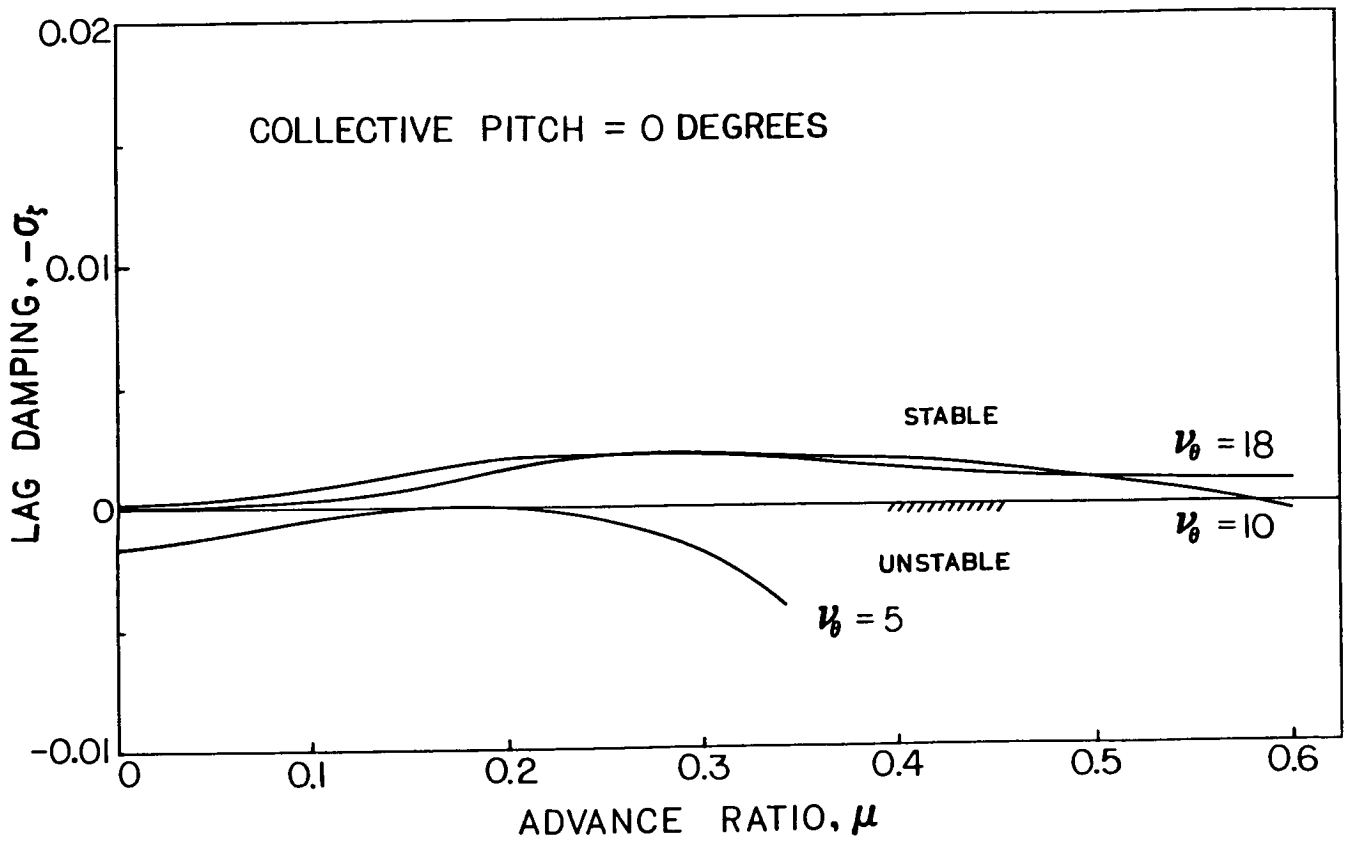

(a) Collective pitch = 0 degrees.

Figure 12. - Effect of torsional stiffness on low frequency cyclic lag mode. ($C_T/\sigma = 0.1$, $\nu_\beta = 2.3$, $\nu_\zeta = 2.6$)

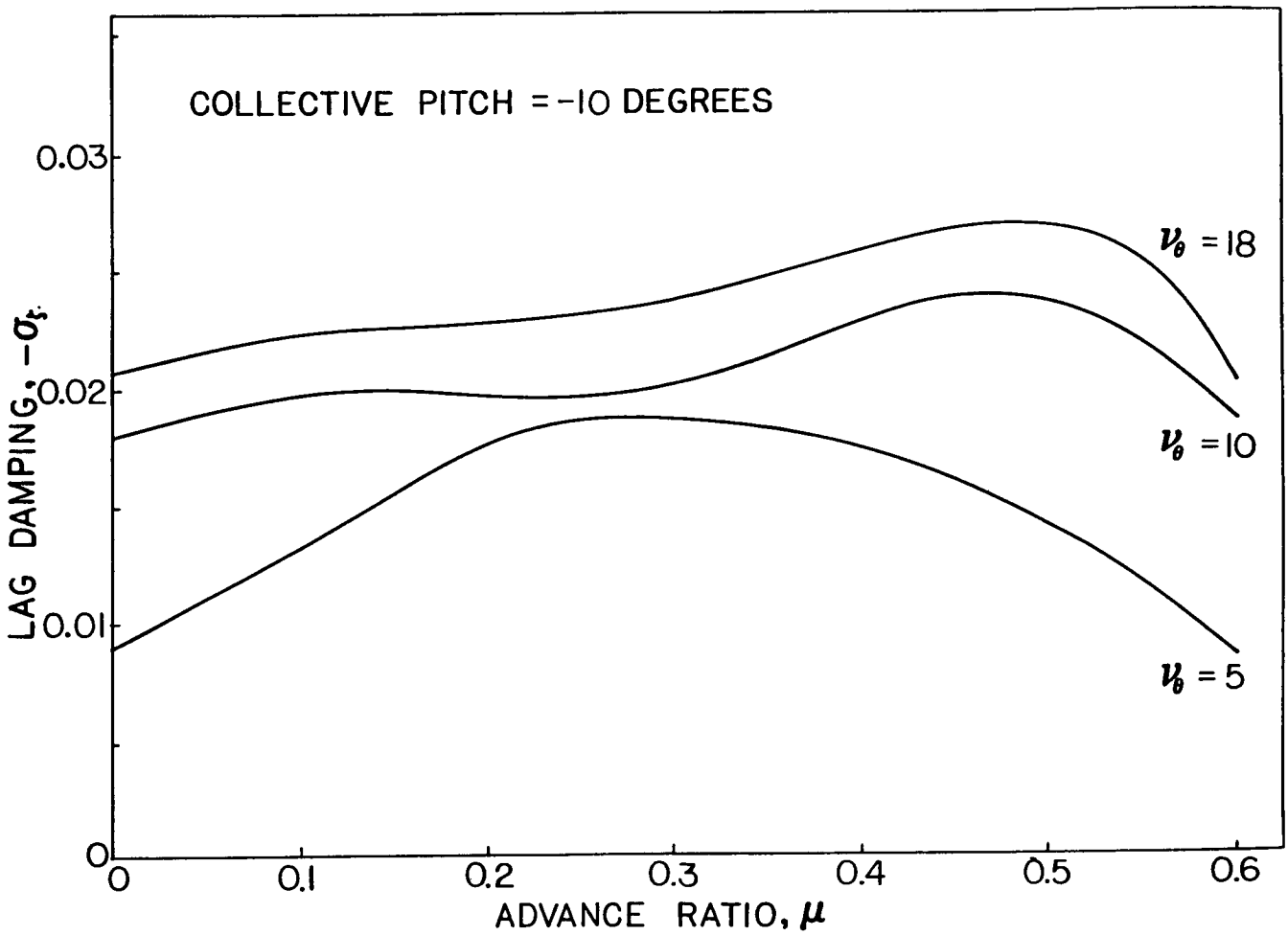

(b) Collective pitch -10 degrees.

Figure 12.- Concluded.

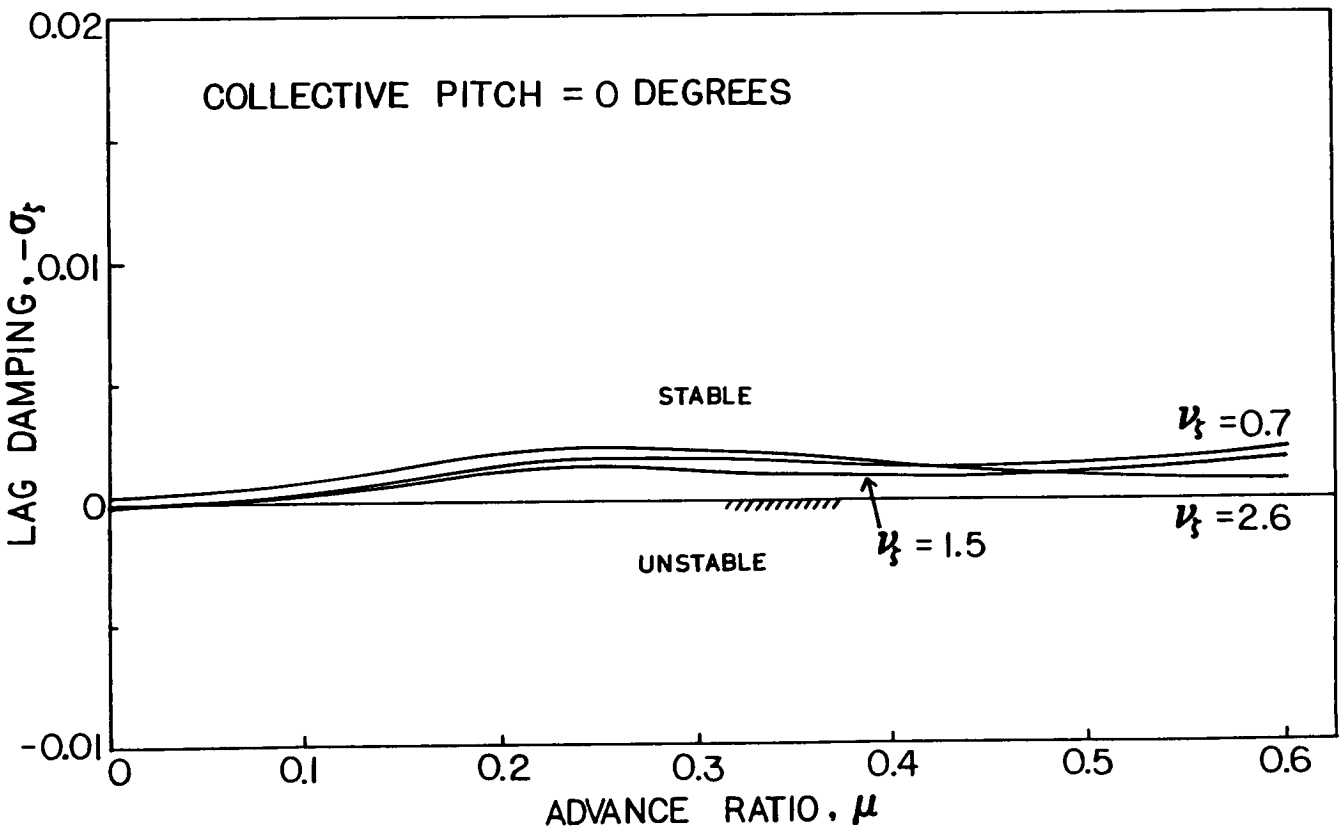

(a) Collective pitch = 0 degrees.

Figure 13. - Effect of lag stiffness on low frequency cyclic lag mode. (C_T/σ = 0.1, ν_β = 2.3, ν_θ = 18)

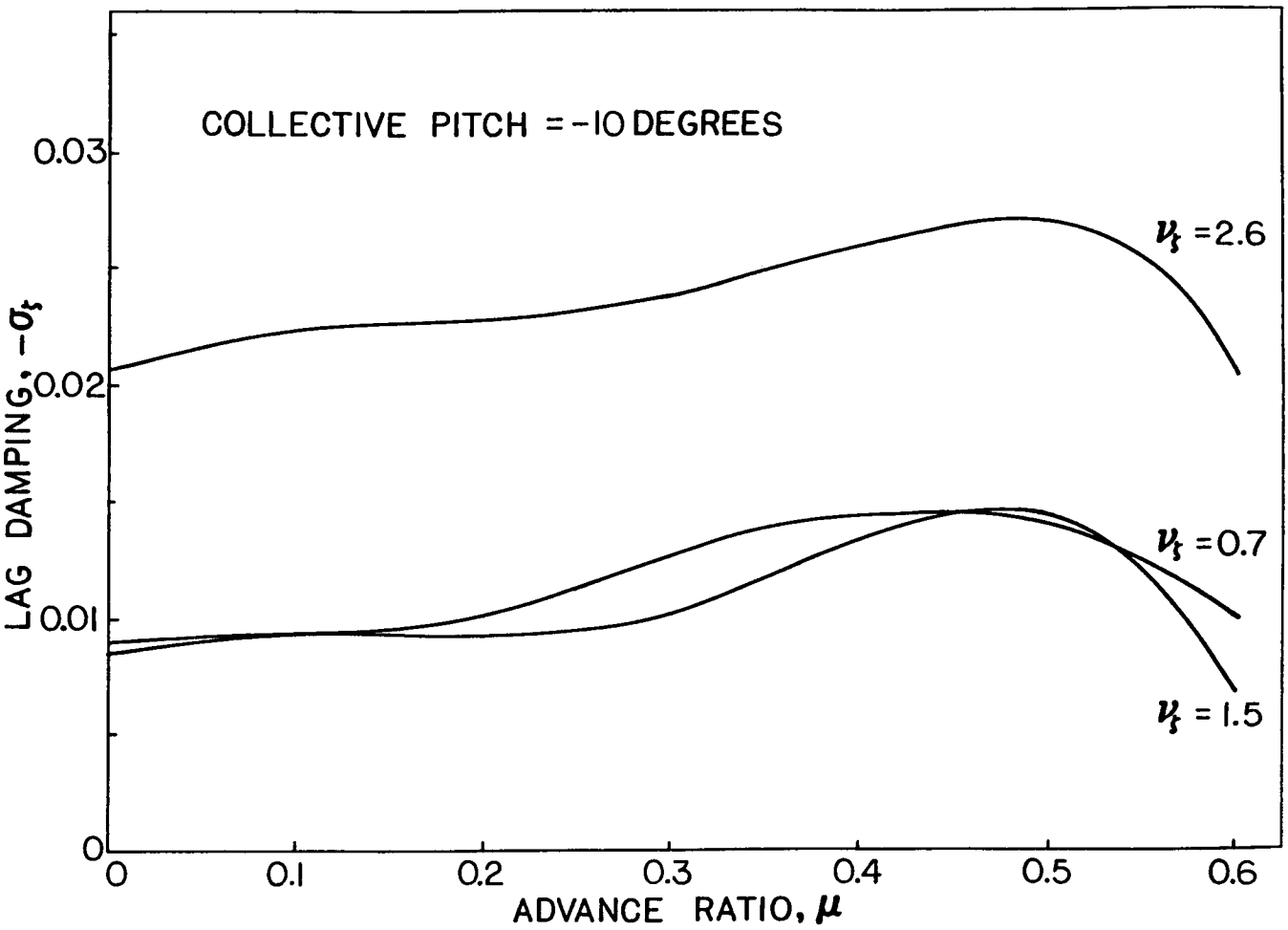

(b) Collective pitch -10 degrees.

Figure 13.- Concluded.

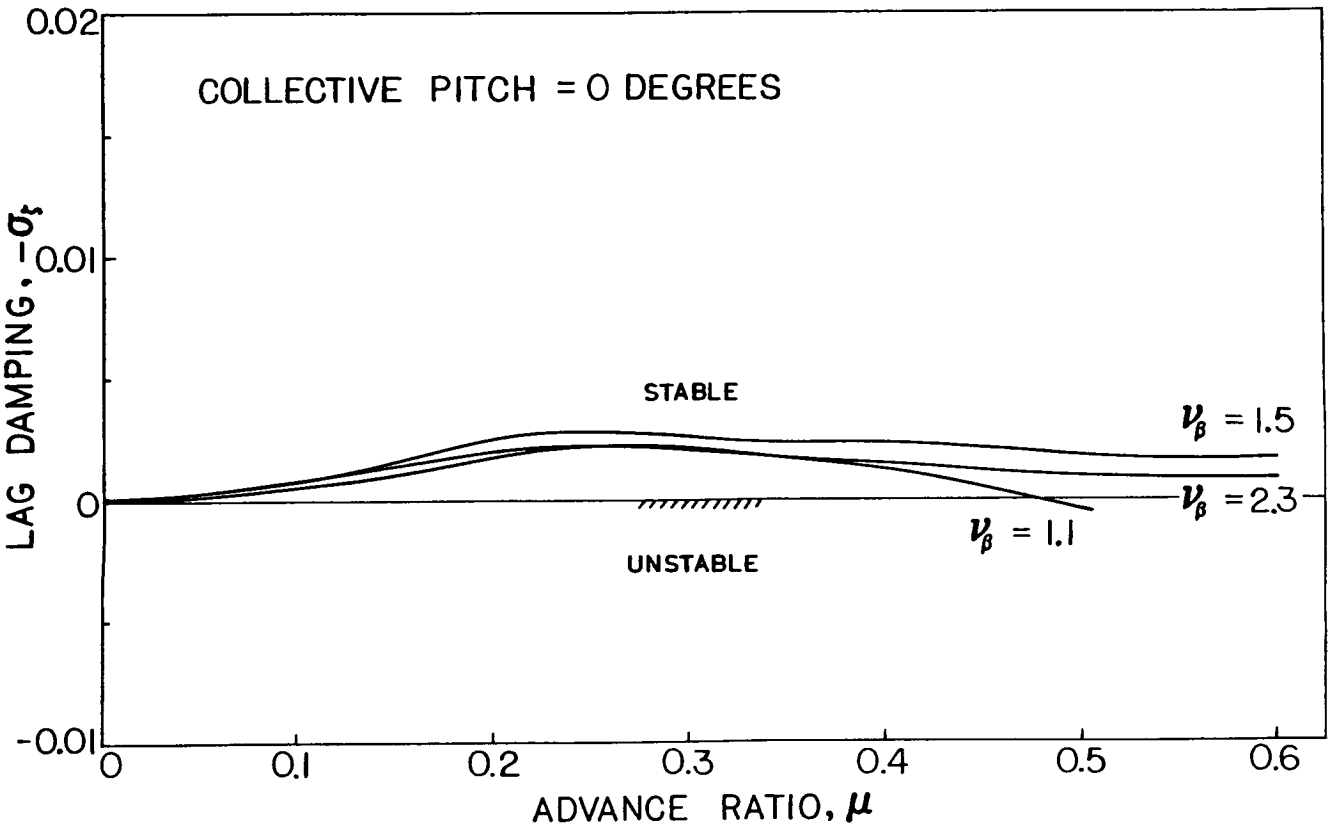

(a) Collective pitch = 0 degrees.

Figure 14. - Effect of flap stiffness on low frequency cyclic lag mode. (C_T/σ = 0.1, ν_ζ = 2.6, ν_θ = 18)

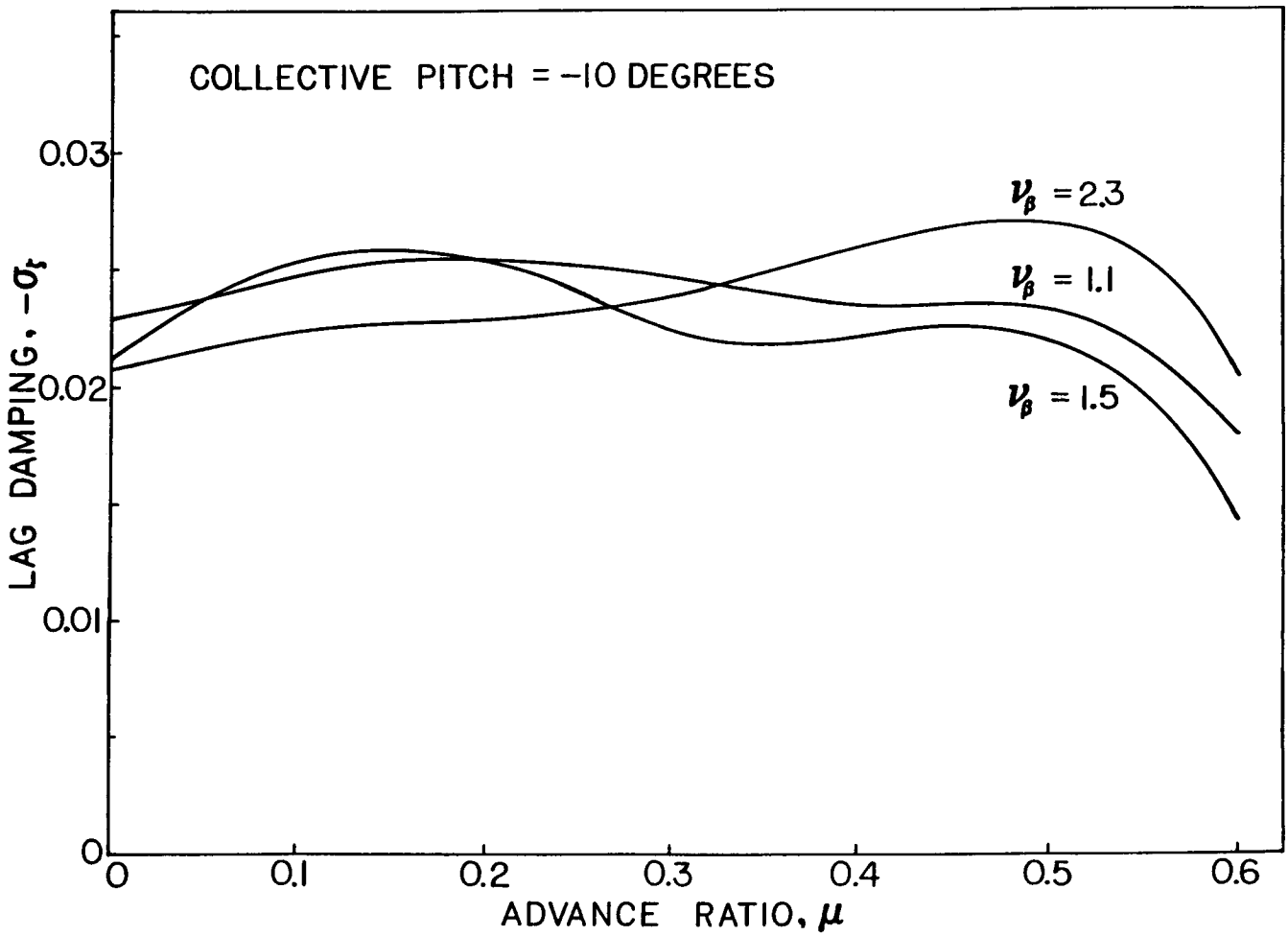

(b) Collective pitch -10 degrees.

Figure 14.- Concluded.

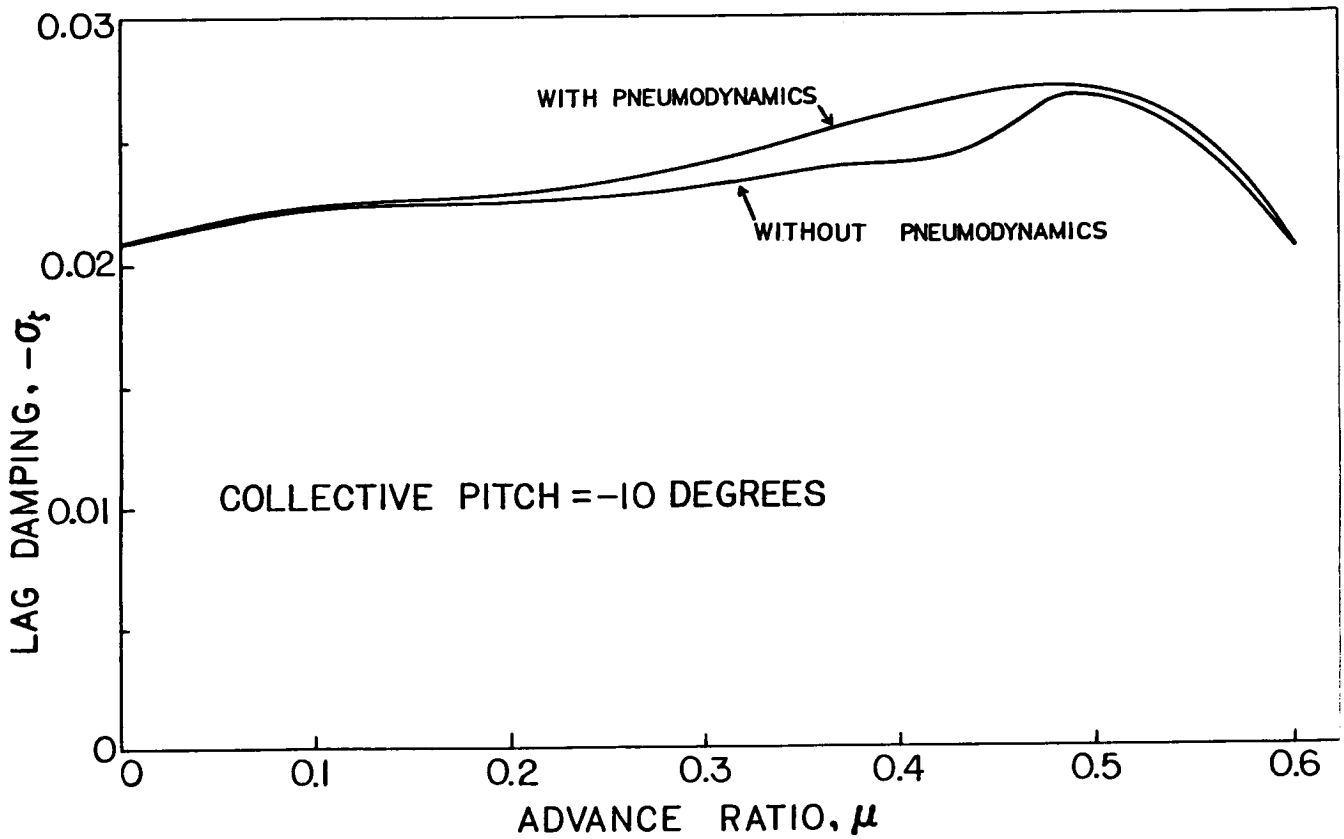

Figure 15. - Effect of pneumodynamics on low frequency cyclic lag mode. ($C_T/\sigma = 0.1$, $\nu_\beta = 2.3$, $\nu_\zeta = 2.6$, $\nu_\theta = 18$)

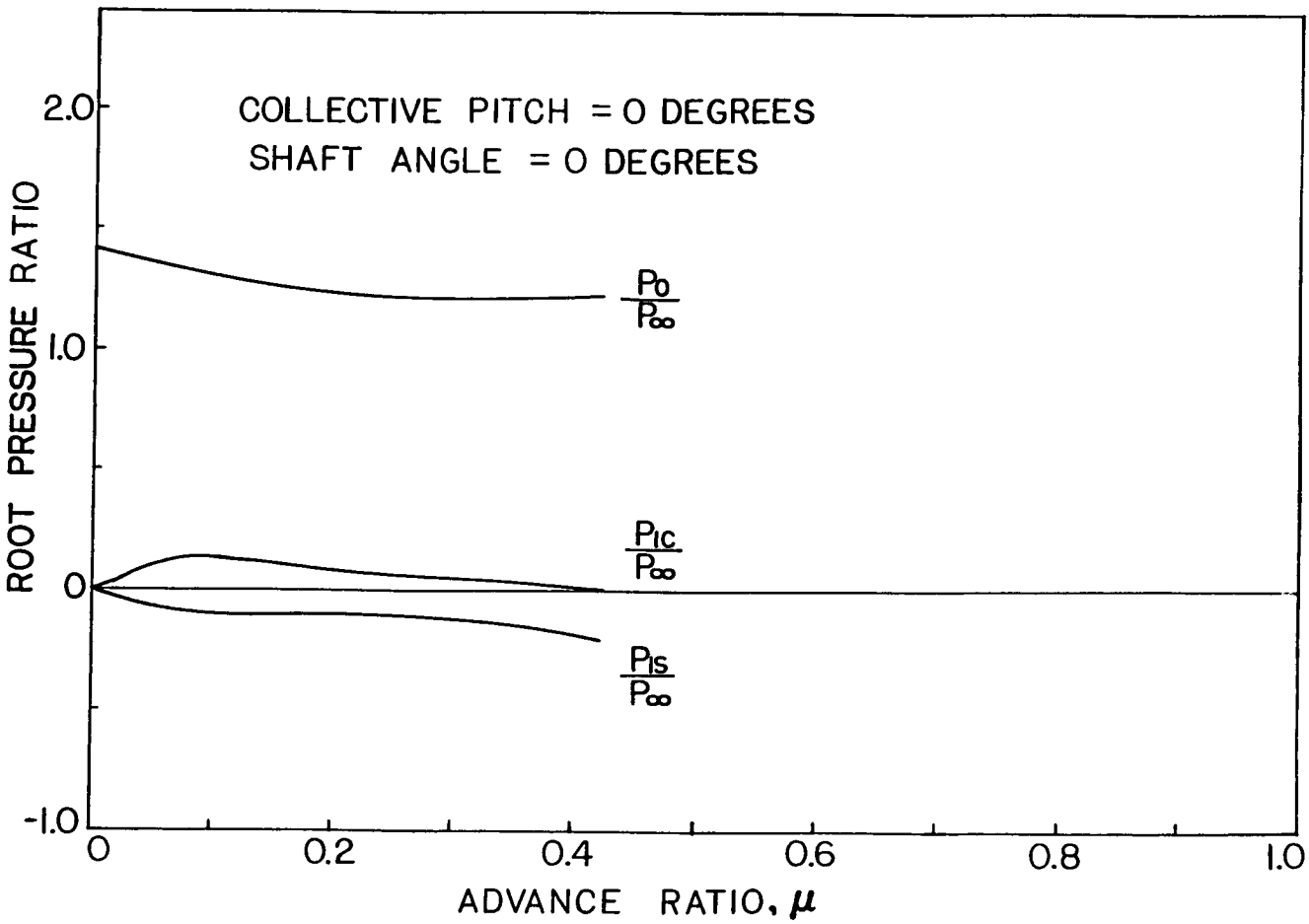

Figure 16. - Blade root blowing pressure requirements for the constrained trim solution. ($C_T/\sigma = 0.1$, $\nu_\beta = 2.3$, $\nu_\zeta = 2.6$, $\nu_\theta = 18$)

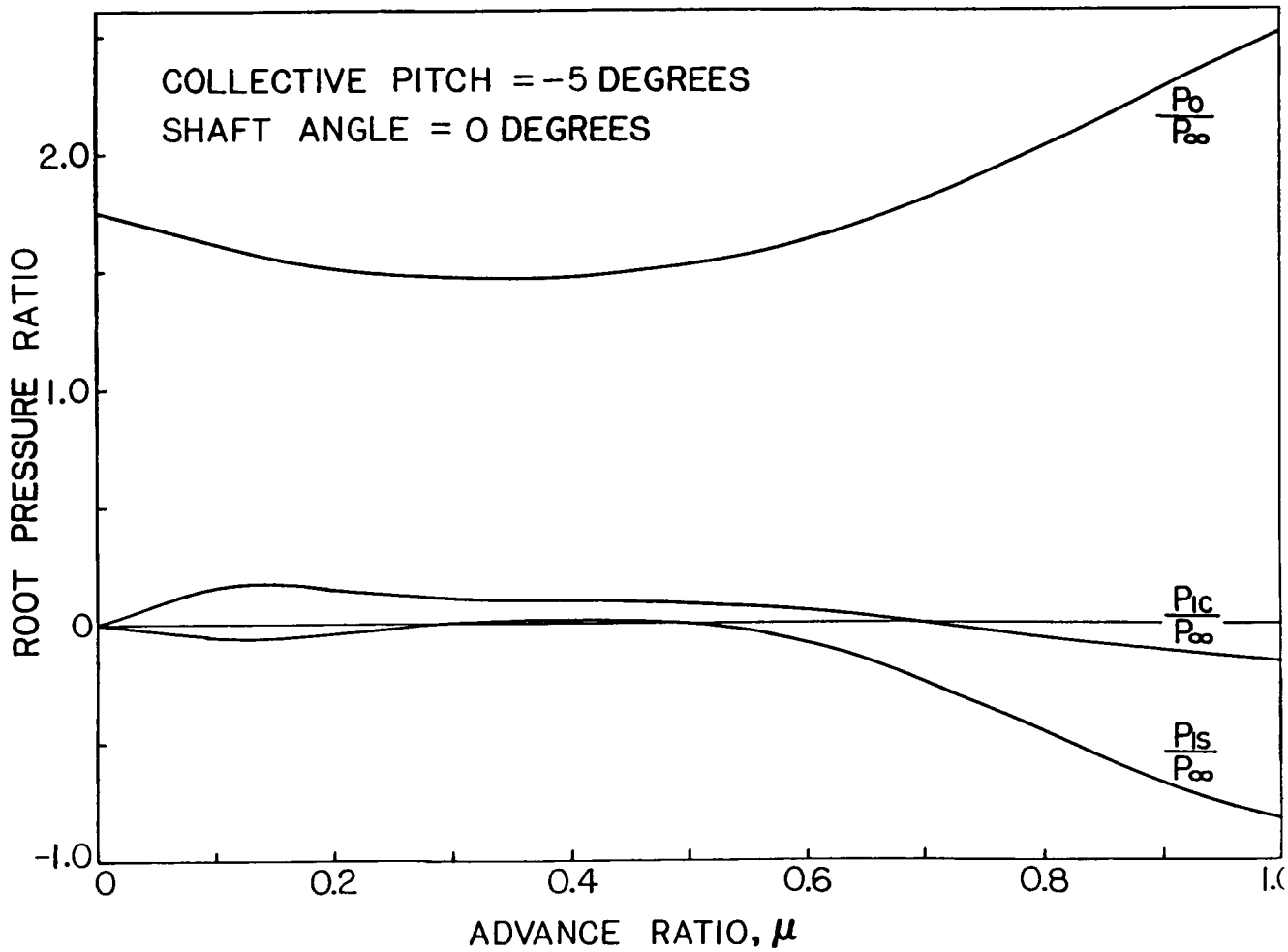

Figure 17. - Blade root blowing pressure requirements for the constrained trim solution. ($C_T/\sigma = 0.1$, $\nu_\beta = 2.3$, $\nu_\zeta = 2.6$, $\nu_\theta = 18$)

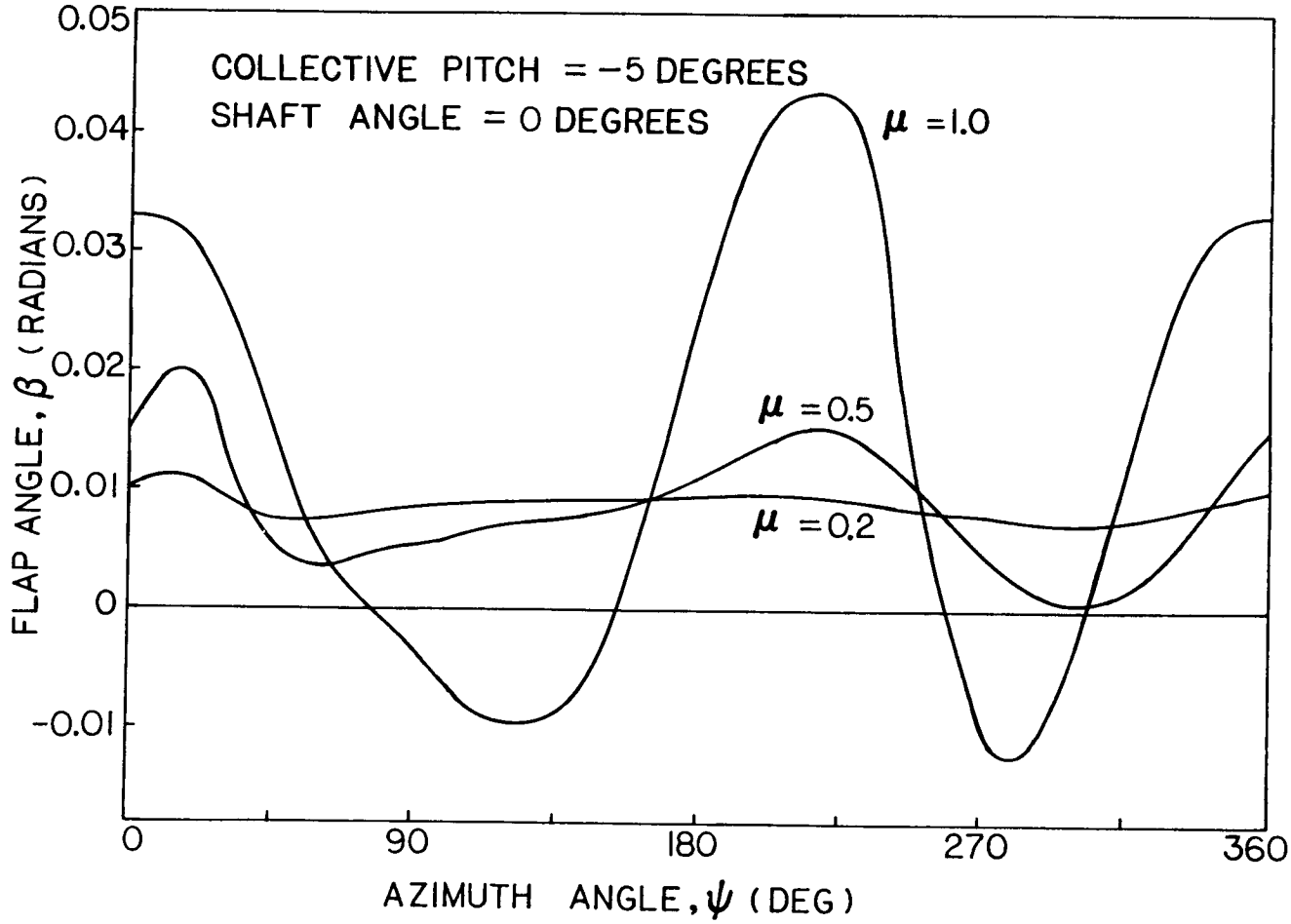

Figure 18. - Blade flap response for various advance ratios. (C_T/σ = 0.1, ν_β = 2.3, ν_ζ = 2.6, ν_θ = 18)

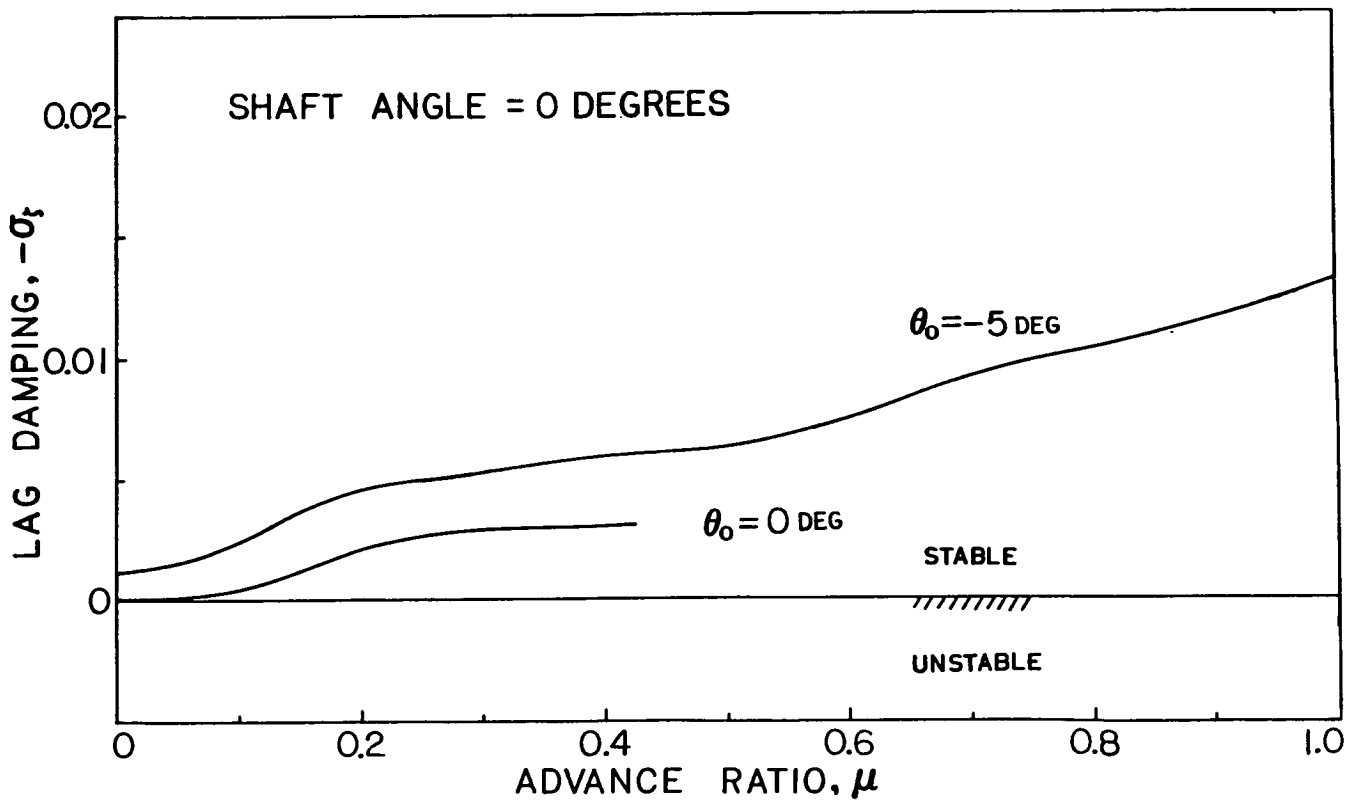

Figure 19. - Effect of collective pitch on low frequency cyclic lag mode. (C_T/σ = 0.1, ν_β = 2.3, ν_ζ = 2.6, ν_θ = 18)

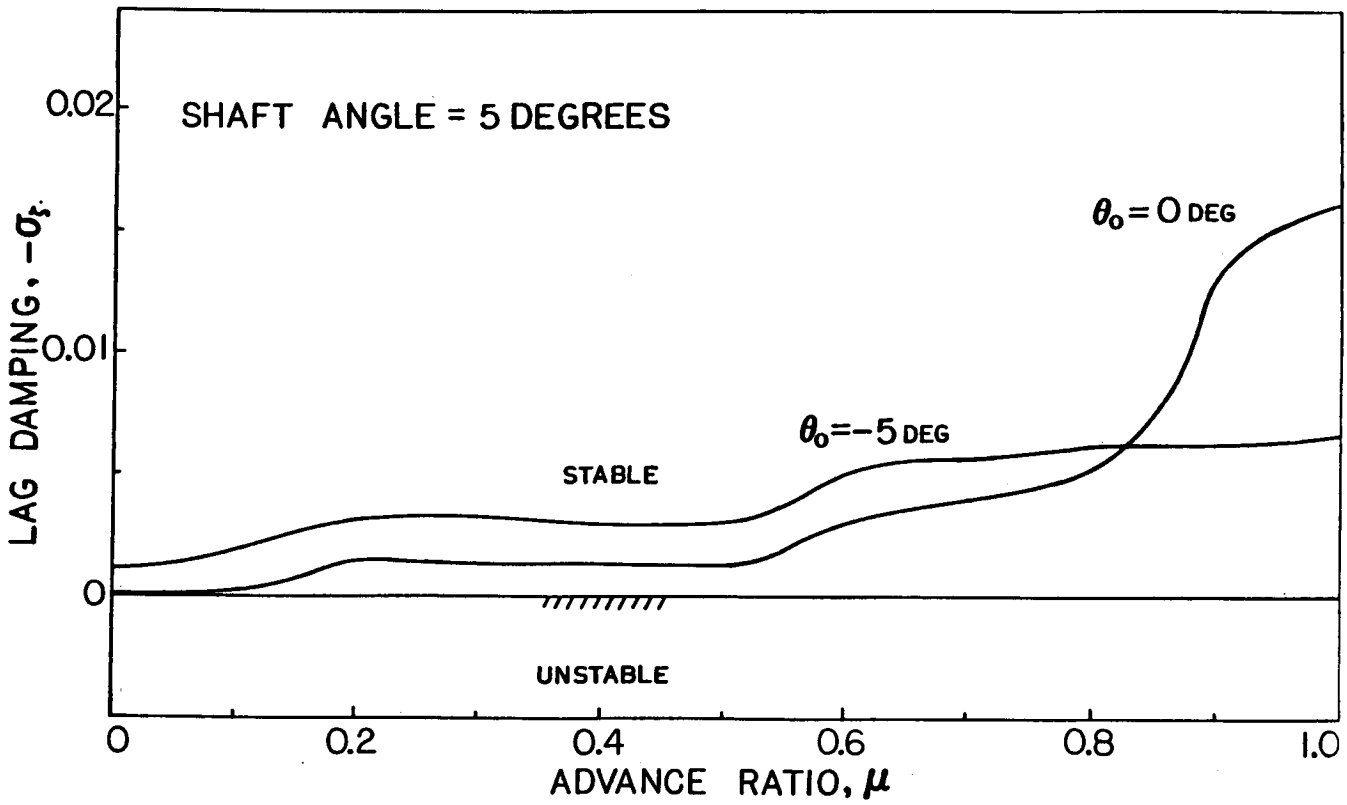

Figure 20. - Effect of collective pitch on low frequency cyclic lag mode. ($C_T/\sigma = 0.1$, $\nu_\beta = 2.3$, $\nu_\zeta = 2.6$, $\nu_\theta = 18$)

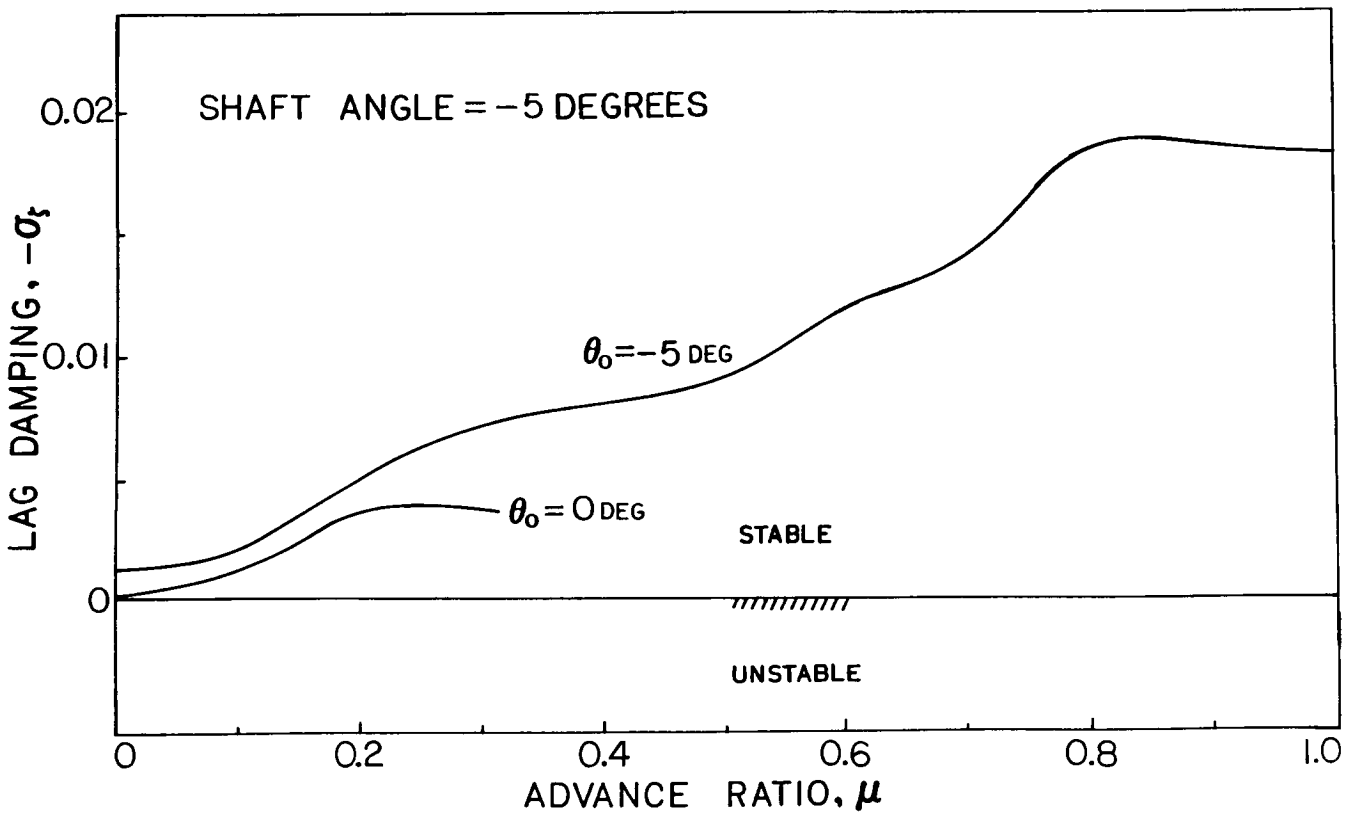

Figure 21. - Effect of collective pitch on low frequency cyclic lag mode. (C_T/σ = 0.1, ν_β = 2.3, ν_ζ = 2.6, ν_θ = 18)

THE IMPACT OF CIRCULATION CONTROL ON ROTARY AIRCRAFT CONTROLS SYSTEMS

BY: R.F. Klingloff and D.E. Cooper
Sikorsky Aircraft Division
United Technologies

Circulation technology for lift augmentation of airfoils has been around for many years. Application of circulation to rotary wing systems is a relative recent development. Substantial efforts to determine experimentally the near and far field flow patterns and to analytically predict those flow patterns have been underway in the fixed wing community for some years.

Rotary wing applications present a new set of challenges in circulation control technology. Rotary wing sections must accommodate substantial Mach number, free stream dynamic pressure and section angle of attack variations at each flight condition within the design envelope. They must also be capable of short term circulation blowing modulation to produce control moments and vibration alleviation in addition to a lift augmentation function. Control system design must provide this primary control moment, vibration alleviation and lift augmentation function. To accomplish this, one must simultaneously control the compressed air source and its distribution. The control law algorithm must therefore address the compressor as the air source, the plenum as the air pressure storage and the pneumatic flow gates or valves that distribute and meter the stored pressure to the rotating blades. Additionally, mechanical collective blade pitch, rotor shaft angle of attack and engine power control must be maintained by the control system.

CONTROL SYSTEM CHALLENGES

The control system design encompasses numerous support subsystem functions not conventionally addressed by control law implementation. These rotor subsystem impacts emanating from the circulation control rotor and its supporting hardware produce numerous challenges to control system design. Listed in Table I are those challenges that are considered to require attention to provide an acceptable control system design for rotary wing flight.

TABLE I. CONTROL SYSTEM DESIGN CHALLENGES

AIR VEHICLE SYSTEM	CHALLENGE DESCRIPTION
Compressor	. Avoid surge and stall
Rotor	. Hub moment feedback trade-offs
Pneumatics	. Valve flow non-linearities . Notable lags
Control	. Limited available range . Angle of attack non-linearities . Higher harmonic control

COMPRESSOR STALL/FLOW RATE/PRESSURE INTERACTIONS

The control system must provide plenum and blade pressure and mass flow required while maintaining the compressor on or below its operating line to avoid compressor stall. To accomplish this the control system employs feed-forward and feedback paths to simultaneously adjust inlet guide vanes, pneumatic control valves and the modulating dump valve to provide the system impedance required to maintain operation on or below the compressor operating line and thus avoid compressor stall. The pressure control loop restricts maximum PCV setting to 80 percent leaving 20 percent margin for high frequency flow demands. Plenum pressure control by IGV setting accommodates low frequency blowing demands. Where 80 percent PCV setting will not provide a low enough impedance to maintain the compressor on its operating line, a modulating dump valve is used to reduce impedance. This occurs any time that the flow demand is less than that produced by the compressor with closed IGV's. These characteristics are apparent in the conceptual compressor map shown in Figure 1.

FIGURE 1

COMPRESSOR STALL/FLOW RATE/PRESSURE INTERACTION

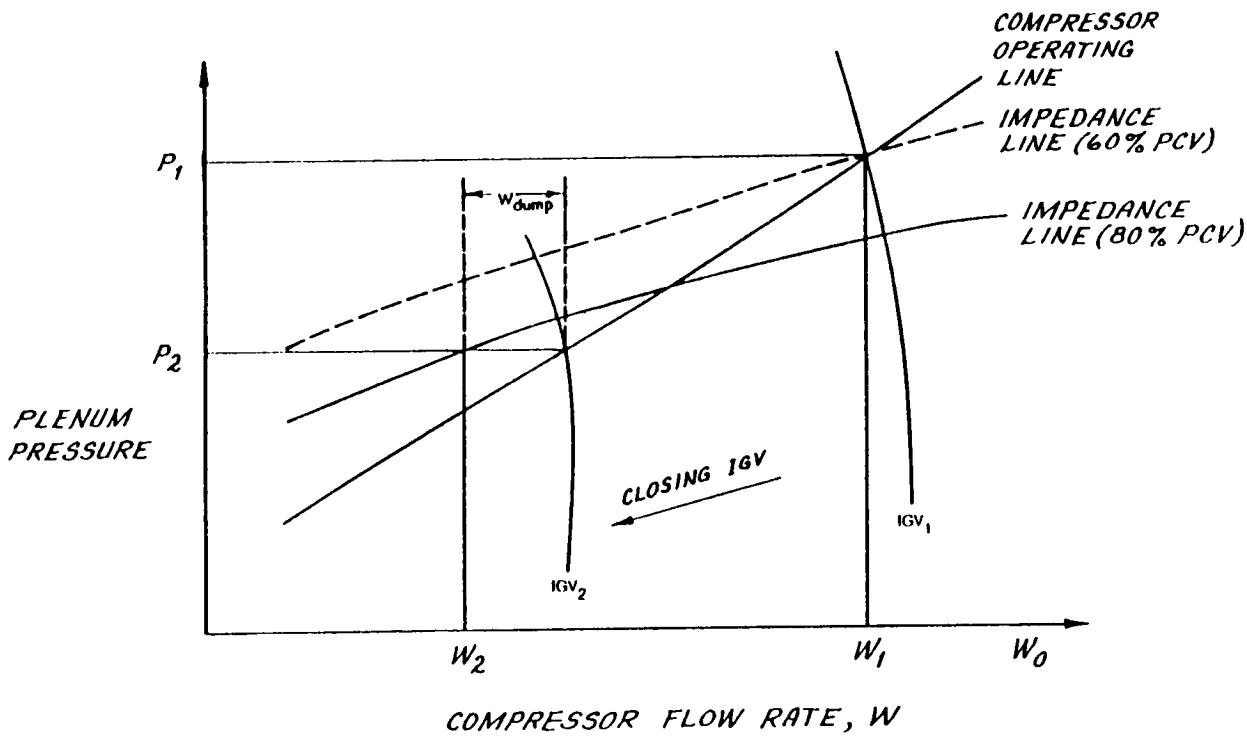

CIRCULATION CONTROL SYSTEM LACKS COLL/CYC "OVERTRAVEL"

Vehicle control with the CCR must be provided with substantially less collective/cyclic range than conventional helicopters enjoy. Modern Helicopters are also provided with "overtravel" to allow full travel of each control independent of the other control setting and provide inner loop stability and outer loop autopilot inputs without infringing on primary flight control travel as shown on the left in Figure 2. The CCR system, shown on the right in the figure without mechanical collective has a very restricted collective/cyclic range. Pneumatic collective settings substantially influence pressure ratio available for cyclic moment control. By addition of mechanical collective control to the CCR system, the nominal center pneumatic collective can be used for lift leaving the full cyclic blowing range for moment control. Rationing the limited pressure ratio range between lift and moment control represents a considerable challenge to the control design.

FIGURE 2

CURRENT SYSTEM LACKS COLL/CYC "OVERTRAVEL"

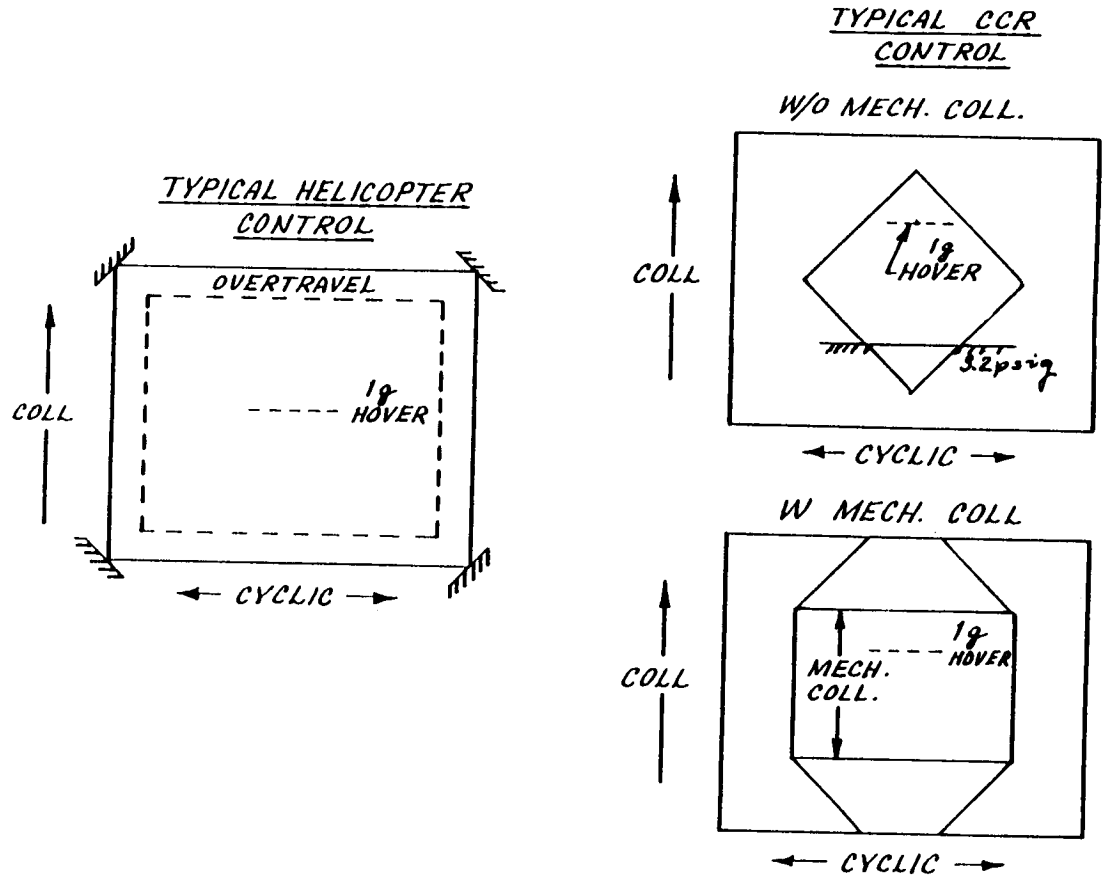

The pressure ratio at which a blade slot will open, increases with pressure altitude as shown in Figure 3. The internal duct pressure for which the slot hold-down spring is set represents higher pressure ratios as the outside ambient pressure gets lower. The limited CCR collective/cycle control range is therefore further reduced as altitude increases. These altitude impacts can be reduced or eliminated completely by providing positive slot control. Both passive and active concepts for slot control are practical and achievable attributes for next and future generation CCR systems.

FIGURE 3
CCR CONTROL RANGE IS LIMITED AT ALTITUDE

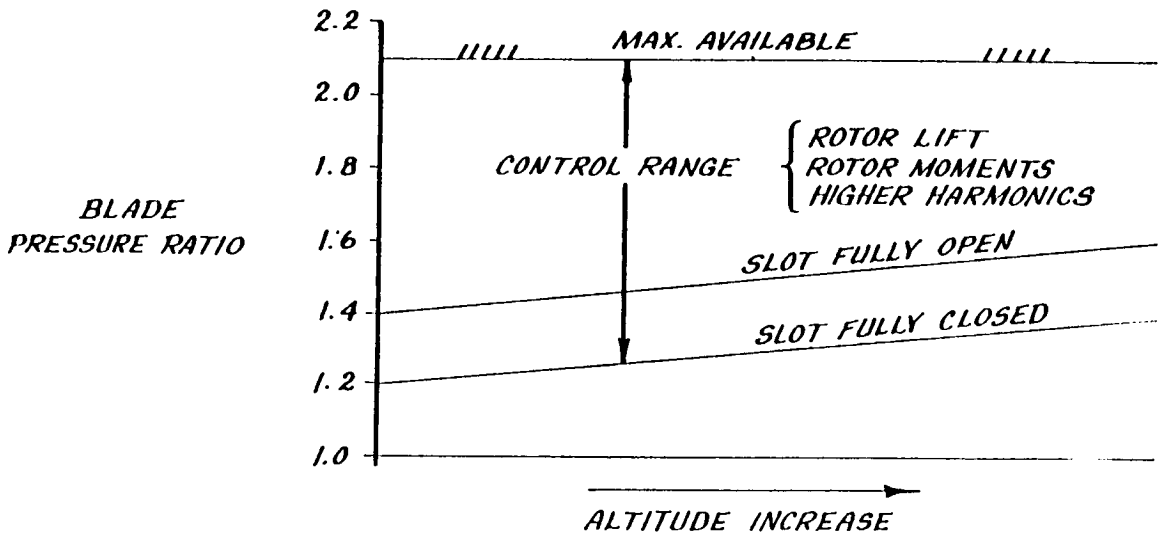

PNEUMATIC MOMENT CONTROL IS NON-LINEAR

Control system design for CCR systems must accommodate the inherent non-linear characteristics of circulation rotors. Conventional aerodynamic rotor systems have a moment producing capability proportional to feathering input magnitude

up to stall encounter. CCR systems do not enjoy this characteristic. The mean control power in foot-pounds per tenth of a pressure ratio reduces rather substantially with the magnitude of the cyclic input as shown in Figure 4. At hover for example, a control power of 115,000 ft-lb per .1 PR cyclic exists if only .1 PR cyclic is applied. If .4 PR cyclic input is applied, however, the control power per .1 PR has a mean value of only 58,500 or essentially one half of that for small cyclic inputs. This non-linear control power characteristic exists to varying degrees over the rotary wing flight envelope. Extreme care must accompany linearization techniques to support linear analyses.

FIGURE 4

PNEUMATIC MOMENT CONTROL IS NON-LINEAR

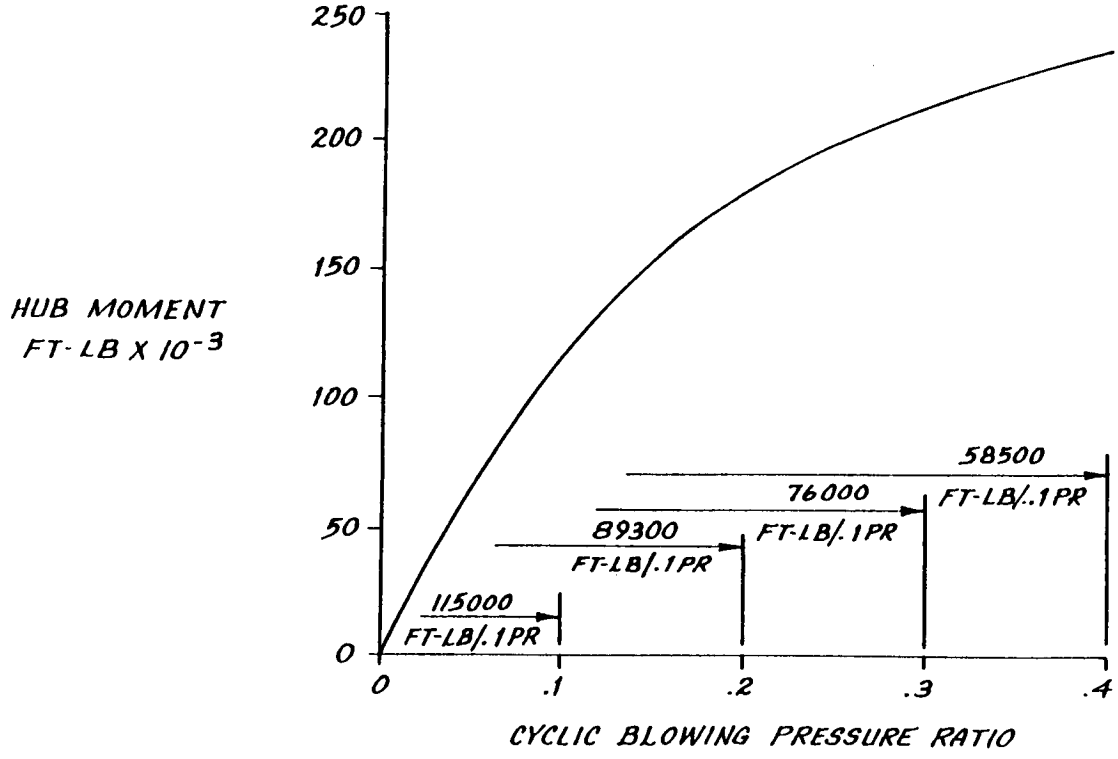

CCR SECTION STALL CHARACTERISTICS ARE UNCONVENTIONAL

Lift coefficient against angle of attack characteristics are presented in Figure 5 for two representative sets of circulation sections. The section on the left is a thick inboard type of airfoil with a slot height to chord ratio of .0013. The section on the right is a relatively thin outboard type section with a slot height to chord ratio of .0020. The inboard type section has a

good circulation lift augmentation ability but stalls at zero angle of attack with any significant blowing applied. The outboard type section provides somewhat less circulation lift augmentation and a somewhat higher stall angle of attack (5 deg). The single most significant characteristic that stands out is the low angle of attack stall of the sections. Control law impact particularly at higher speeds is substantial. Attempts to save pneumatic power by using mechanical collective for roll control must be approached with extreme caution since potential for control reversal is rather apparent. In addition, vehicle angle of attack non-linearities are most probable. Control laws must therefore use combinations of angle of attack and normal load factor feedback algorithms to assure rotor operation be maintained to the maximum extent possible on the positive values of lift curve slope. New airfoil developments underway at Sikorsky and David Taylor NSRDC show promise of substantial extension of stall to higher section angles of attack.

FIGURE 5

CCR SECTION STALL CHARACTERISTICS ARE UNCONVENTIONAL

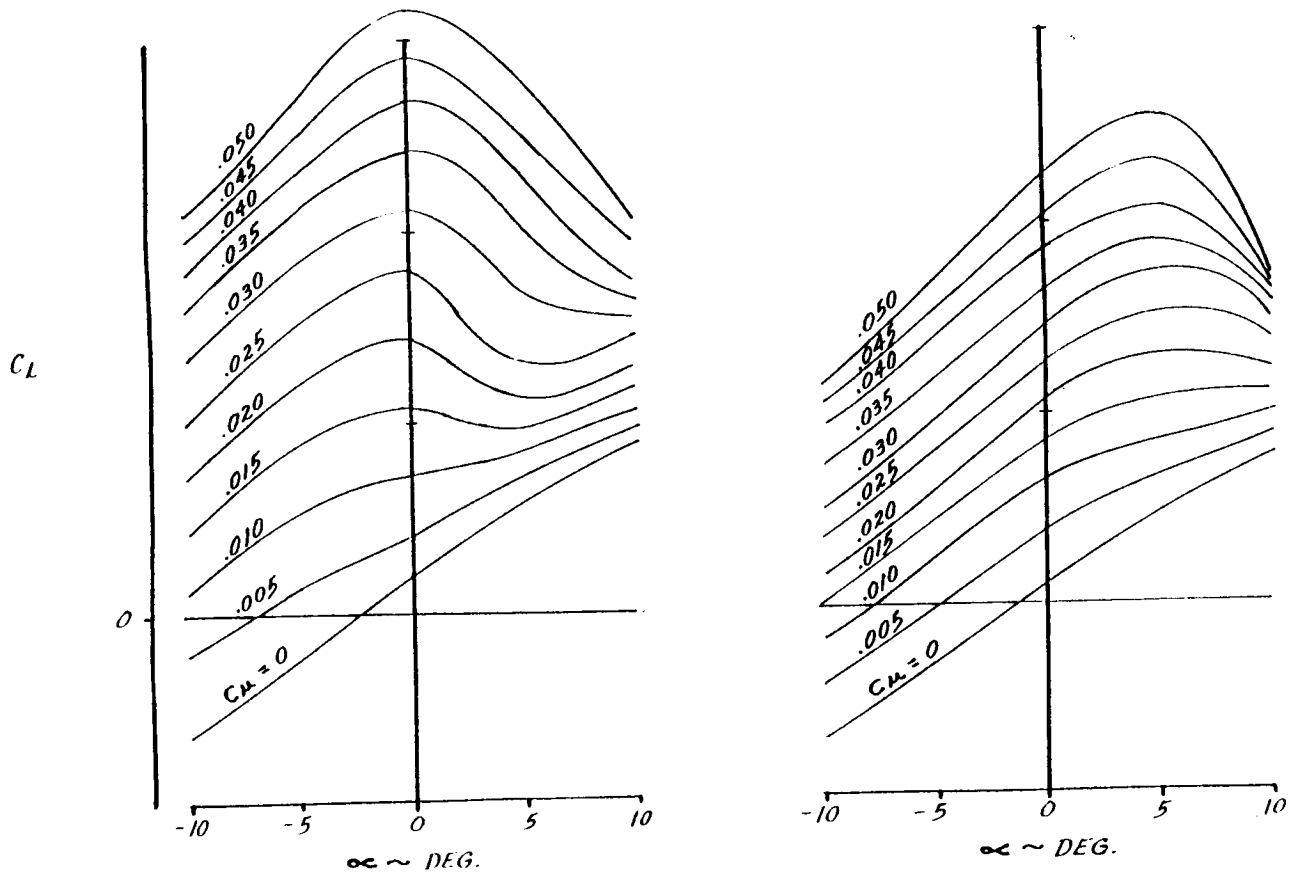

SYSTEM LAGS ADD SERIALLY

Control system design for CCR system applications must be capable of accommodating notable transport and exponential lags. The magnitude of these system lags unique to CCR are shown in Figure 6. Fly-by-wire control through a quad-redundant digital computer together with redundancy management software allows rotor system updates at an 80 Hz rate. Thus the flight control computer represents a 12.5 ms transport lag from input to output. Adding to that is a 25 ms transport lag caused by the sonic pressure wave propagation from the pneumatic control valves (PCV's) to full span slot flow on the blades. Therefore an open loop transport lag of 37.5 ms must be compensated for by the control system design. In addition, two substantial exponential lags exist in the current technology CCR system. The first of these occurs between plenum pressure demand and plenum pressure response as a function of change in the compressor inlet guide vanes. The second exponential lag is associated with the PCV actuators and is also 15 ms. As a result, the control system must accommodate a 30 ms time constant in addition to the 37.5 ms transport lag. This lag compensation must be accomplished by the control algorithms while retaining adequate systems phase margins.

FIGURE 6
SYSTEM LAGS ADD SERIALLY

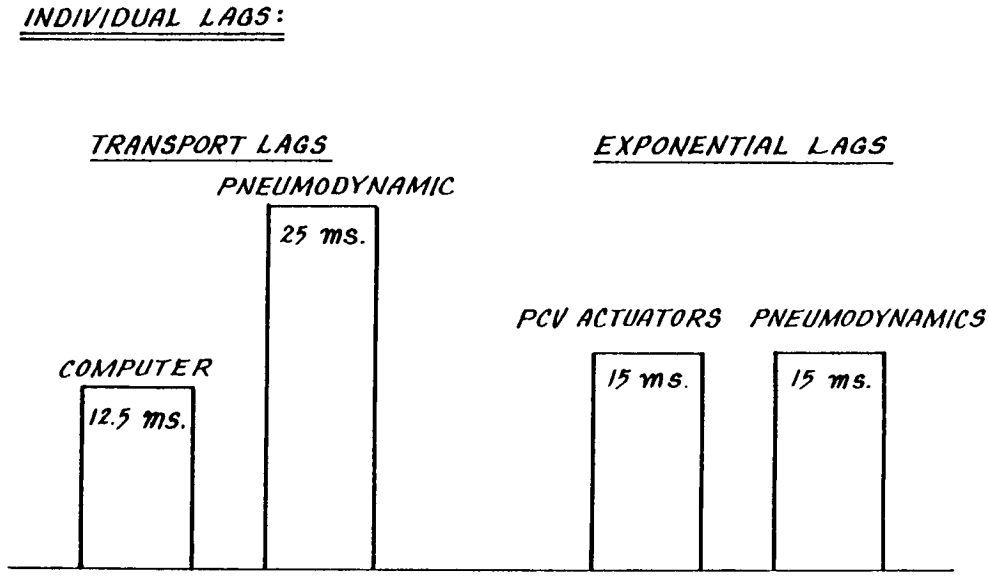

NET OPEN LOOP LAGS:

37.5 ms TRANSPORT
30.0 ms EXPONENTIAL

VALVE POSITION TO MASS FLOW NON-LINEARITIES

Two common types of flow valves have been applied to CCR systems. The two types are gate valves and butterfly valves. There are attributes and deficiencies associated with each type. Flow characteristics as a function of valve position are shown in Figure 7. Gate valves demonstrate the least non-linear flow versus position characteristics but represent a weight and performance penalty solution. Rotor head designs to accommodate vertical travel of trailing edge and leading edge gate valves are rather large and heavy and create excess drag. Design approaches are practical that could make gate valves a future viable solution. Butterly valves on the other hand package in the rotor head very efficiently providing weight and performance benefits. Some additional demand is placed on the control system design to compensate for the substantial non-linear flow versus rotation characteristics of butterfly type valves. Flow characteristics are of a form that basically conforms to a [1-COS(angle)] relation. Pneumatic control valve logic developed for control laws application is effective in compensating for the non-linear characteristic of the butterfly valve system.

FIGURE 7

VALVE POSITION/MASS FLOW NON-LINEARITIES

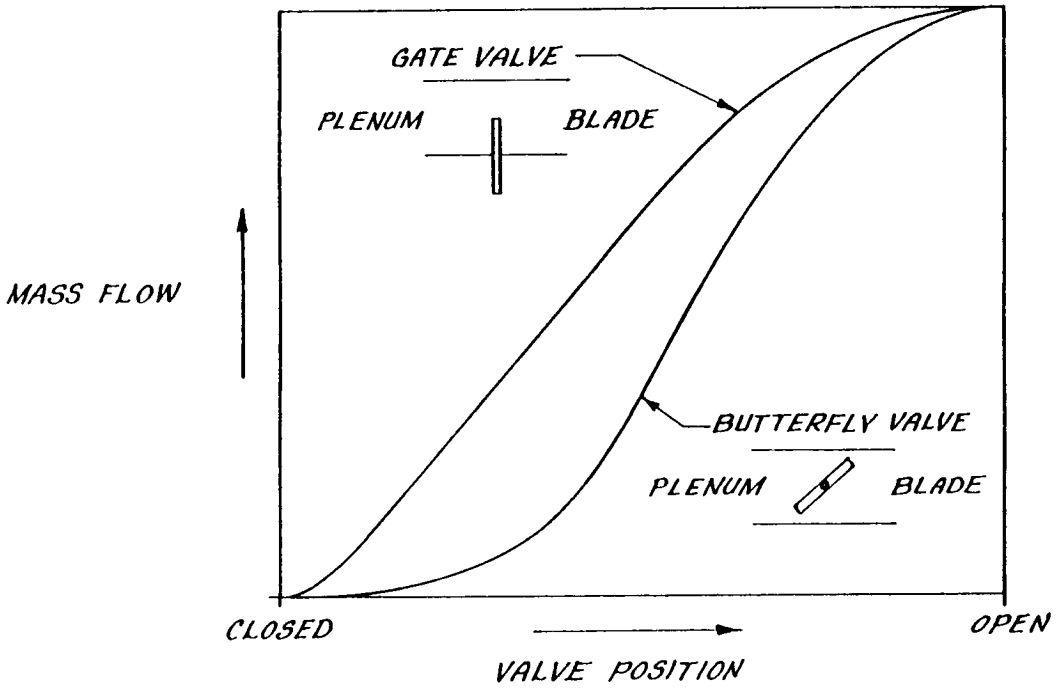

LEADING EDGE BLOWING SCHEDULE

Current technology in slot design requires blowing over the full span or no blowing over the full span of the blades. In addition the slots are spring loaded closed until internal duct pressure of 3.2 psig is present at which

point the slot commences to open. At 5.9 psig the slot is fully open against an internal stop. This is a relatively low risk approach for first generation flight hardware. Possible production variance will only impact blade to blade performance in the elastic slot range between 3.2 and 5.9 psig duct pressure. At higher advance ratios, leading edge blowing is required on the retreating side of the rotor to compensate for the onset of reverse flow. Without the ability to radially adjust slots, a schedule was developed for control of high advance ratio leading edge blowing to maximize lift at these flight conditions. The schedule for high advance ratio dual and leading edge blowing is shown in Figure 8. Dual blowing, trailing edge plus leading edge commences at the 270 degree azimuth location at .5 advance ratio which occurs at 140 KT. Transition to single leading edge blowing occurs at .75 advance ratio. Each of these occurrences spread fore and aft on the retreating side of the disc as advance ratio increases and finally goes to infinity when the rotor stops. At the stopped rotor condition with blades at 225 and 315 degrees azimuth, the valves concerned have only leading edge blowing in accordance with the schedule shown. Leading edge blowing on the retreating side is in fact trailing edge blowing relative to the blade flow.

FIGURE 8

LEADING EDGE BLOWING CONTROL SCHEDULE

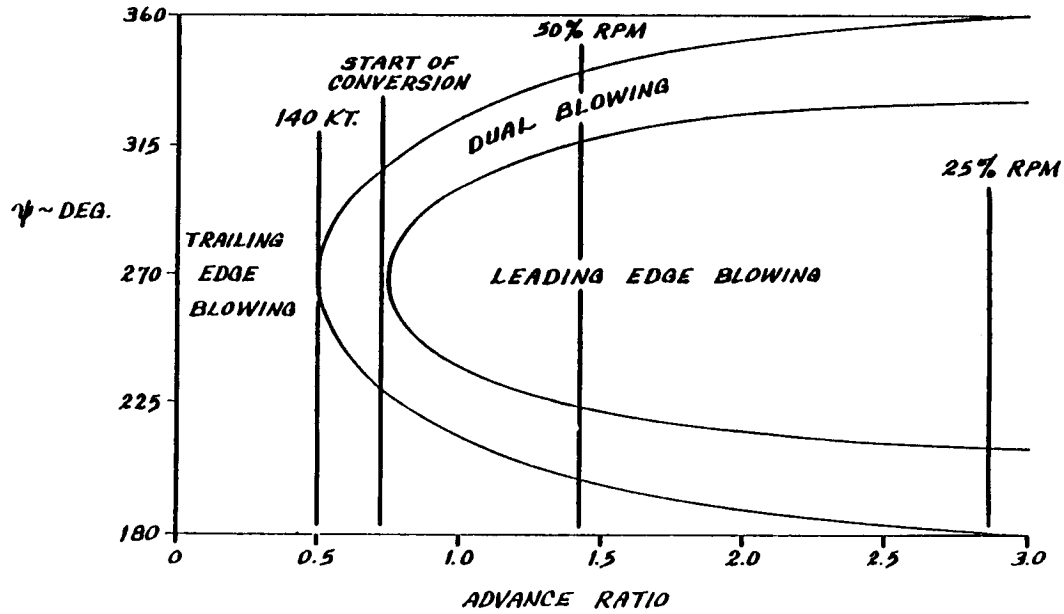

CONCLUSIONS

Current circulation control rotor technology forces some control system design compromises and some control system design challenges. The control system design must accommodate more subsystem functions than encountered in conventional systems. These include:

1. Compressor stall avoidance
2. Pneumatic control valve algorithm
3. Impacts on primary control by HHC blowing
4. Engine power response to rotor and compressor power requirements
5. Adequate lift, moment and vibration control from a limited pneumatic control range
6. Substantial cyclic blowing to control moment nonlinearities
7. Moment trim with pneumatic cyclic when moments are produced by pneumatics plus aerodynamics
8. Substantial non-conventional section stall characteristics
9. Leading edge blowing at higher advance ratios without radial slot control
10. Notable transport and exponential lags not previously encountered in rotary wing control system design
11. Mechanical collective pitch scheduling to enhance system control range characteristics

Circulation control rotor design improvements are under study that will reduce or eliminate many of the above control system design challenges and compromises. Reasonable success in a number of areas can provide substantial performance, maneuverability, stability and handling qualities improvements in next generation rotor designs.

ANALYSIS OF A FIXED-PITCH X-WING ROTOR EMPLOYING LOWER SURFACE BLOWING

Alan W. Schwartz and Ernest O. Rogers
David W. Taylor Naval Ship Research and Development Center

ABSTRACT

Lower surface blowing (LSB) is investigated as an alternative to the variable blade pitch requirement for the X-Wing Circulation Control (CC) rotor concept. Additional trailing edge blowing slots on the lower surfaces of CC airfoils provide a bi-directional lift capability that effectively doubles the control range. The operational requirements (aerodynamic environment) of this rotor system are detailed and compared to the projected performance attributes of LSB airfoils. Analysis shows that, aerodynamically, LSB supplies a fixed-pitch rotor system with the equivalent lift efficiency and rotor control of present CC rotor designs that employ variable blade pitch. Aerodynamic demands of bi-directional lift production are predicted to be within the capabilities of current CC airfoil design methodology. Emphasis in this analysis is given to the high-speed rotary wing flight regime unique to stoppable rotor aircraft. The impact of a fixed-pitch restriction in hover and low-speed (transition) flight is briefly discussed.

INTRODUCTION

Present CC rotor V/STOL designs such as the RSRA/X-Wing rotor (Linden and Biggers, 1985) incorporate a variable mechanical collective blade pitch mechanism primarily to enable lateral moment trim in high-speed rotary flight. This mechanism, together with the additional structural weight associated with controllable pitch, constitutes a significant portion of the lifting system weight. Thus, it is desirable to extend the aerodynamic capabilities of CC rotors to allow a fixed, zero collective pitch rotor design. The work presented is the initial analytical investigation of one proposed route to this design goal; specifically, application of the LSB concept wherein slots are provided on the lower surfaces of the rotor blades for production of negative incremental lift when needed for moment trim.

BACKGROUND

For conventional helicopters, the blade pitch is varied in a cyclic manner about some mean or "collective" value (Θ_c) to effect rotor thrust and moment trim. The pitch angle is cyclically varied inversely to the dynamic pressure (q) with lower pitch and, hence, lower lift coefficients on the advancing side of the rotor disc. Figure 1 illustrates present CC rotor designs that yield comparable cyclic modulation of lift by operating with a low--even negative--collective pitch setting (typically -5 deg at high speed) and by cyclically varying the level of positive augmented (or blowing) lift. The necessity to achieve low C_ℓ's on the advancing side of the rotor disc requires the negative blade pitch, which penalizes the

lifting potential elsewhere on the disc. The advantage of LSB is that low C_ℓ's can be produced in the high q region while operating with a zero collective pitch setting (fig. 1).

A fixed-pitch rotor design would have the advantage of simplified hub design and reduced weight. Weight savings are realized by (1) eliminating the collective pitch actuator hardware, (2) simplifying the rotor head structural design, and (3) integrating the hub fairing with the blade contour. These design changes would also contribute to improved aerodynamic performance by reducing the adverse effects of blade/hub vortices produced by the discontinuity at the blade root/hub fairing interface.

The notion of using dual slotted (upper and lower surfaces) CC airfoils to produce either positive or negative lift is not novel. Kind and Maull demonstrated the application of this concept in 1968. In addition, Ham et al. (1974) applied this airfoil configuration to a gust generator apparatus used in wind tunnel studies.

DESIGN DESCRIPTION

The CC airfoil configuration used in this investigation is shown in figure 2. Here, in addition to the two upper surface blowing (USB) slots commonly associated with high-speed CC rotor designs, a third slot is included on the lower surface trailing edge of the airfoil. For the present study, the elastic properties (slot height versus duct pressure) of the three slots are assumed to be identical. Such an airfoil can optionally have air supplied to the lower duct only, which produces a lift increment in a direction opposite to that of normal CC airfoil operation. There is no requirement for an additional lower surface slot at the leading edge for the purpose of producing roll moment trim in the rotary mode.

The sophistication of representing the pneumatic system with an additional duct and blowing slot required that a simplifying assumption be made in the control philosophy. In the analysis, therefore, the upper and lower surface pneumatic control inputs were coupled so that only one trailing edge slot per blade is blown instantaneously. This is convenient because no changes are required in the current trim control logic, and modeling of the performance behavior of simultaneously blown upper and lower surface slots is avoided. Figure 3a shows the pneumatic control inputs used to trim a representative LSB rotor in conversion at an advance ratio (μ) of 0.85, which is the critical flight condition in terms of rotor lift capability as discussed by Schwartz (1984). The upper surface slot is blown by a sinusoidal control wave with peak pressure truncated at the maximum level of a typical pneumatic supply system. Pressures on the advancing side of the rotor disc descend below the level required to open the flexible slot thereby leaving it closed over a wide azimuth range. The lower surface control wave is also sinusoidal and varies inversely to that of the upper surface. The proximity of the lower surface duct pressure level to that of slot closure is a constant multiple of the proximity of the upper surface pressure to the slot closure value. Thus, strong LSB is used over portions of the disc where the upper surface is unblown; see figure 3a.

The portion of the blade span over which the lower surface slot extends affects the pneumatic control inputs required for trim. Figure 3b shows the

control waves necessary to trim a partial-span LSB rotor design to the same thrust level as that of the full-span design (fig. 3a). In figure 3b, the lower surface slot extends over the outer 30 percent of the blade span. Because LSB is applied over a smaller spanwise range, higher blowing pressures are needed over a wider azimuth range. Note that partial-span LSB leaves a significant portion of the inboard span completely unblown on the advancing side.

EVALUATION APPROACH

The airfoil performance requirements with regard to lift production of an LSB rotor system were not evident at the outset of the investigation. Whether the operational demands of such a system would be conducive to a convergent airfoil design process was uncertain. One objective of this investigation, therefore, is to determine if a given LSB airfoil can be sufficiently effective in producing high positive lift in one aerodynamic environment while providing for sufficient negative lift in another, possibly vastly different, environment. A recursive approach was used to evaluate the suitability of using LSB airfoils in place of variable collective pitch for CC rotor control. In lieu of any relevant LSB airfoil experimental data, an initial conservative representation of LSB airfoil performance was adopted. Use of this representation in the rotor design codes permits identification of the airfoil operating requirements (aerodynamic environment in terms of incidence, Mach number, etc.). The airfoil performance map is then reevaluated with regard to the operational demands of a zero-pitch rotor system to determine the impact of the assumed representation.

AIRFOIL PERFORMANCE REPRESENTATION

Conceptually, the operational lift envelope of an LSB airfoil is greatly extended beyond that of current CC airfoils; see figure 4 for uncambered section. Incremental blowing produces an identical absolute level of incremental lift, if applied in the opposite direction and at an angle of attack of opposite sign. The control range of the LSB airfoil, therefore, is effectively doubled, and high negative C_ℓ's can be produced upon demand.

One limiting factor to this idealized (symmetric) performance is the effect of camber, which is common to all current CC rotor designs. Camber is used to partly shift the chordwise loading distribution to midchord. This is desirable to lessen the effects of steep adverse pressure gradients produced under high loading conditions that can cause stall at relatively low angles of attack. In the case of lower surface blowing, the flat lower surface of a positively cambered airfoil does not provide loading relief to the leading and trailing edges. In fact, the tendency of the loading to be concentrated fore and aft is intensified. Premature stall could result, which would limit the performance envelope.

Theoretical pressure distributions for a typical CC contour at a nominal absolute lift level and zero angle of attack are compared in figure 5 for normal blowing (upper surface) and lower surface blowing. Abramson and Rogers (1983) tentatively established that the limiting criterion for lift due to blowing is the proximity of the trailing edge pressure coefficient level to the value corresponding to sonic velocity (C_p^*) on the Coanda surface. In the normal blowing mode, camber serves to minimize loading in the aft region thereby delaying the occurrence

of C_p^*. Without the redistribution of loading due to camber and because the lift due to camber acts adversely (positively), in the LSB mode a higher level of blowing is required to achieve the same absolute net lift. Also, the loading is concentrated fore and aft, which results in C_p levels that approach the critical value much sooner. The existing X-Wing airfoil series was analyzed in this manner to establish performance boundaries.

Over the full range of operational Mach numbers (fig. 6), the absolute lifting potential of a typical cambered contour is lower when blowing is applied to produce a negative lift increment. However, with regard to the lift increment ($\Delta C_\ell = C_\ell - C_{\ell_{c_\mu=0}}$), the difference is smaller. This variation in lift capability between the two modes of operation was modeled in the rotor design codes. For this study, it is further assumed that incorporation of the lower surface slot does not degrade upper surface blowing characteristics.

A word of caution is appropriate at this point. Results of experimental investigations indicate that if a strong shock wave is present just upstream of a slot, the airfoil capability to augment lift by blowing is substantially reduced. Thus, LSB may not provide the anticipated level of control in those regions of the rotor disc where the local Mach number exceeds approximately 0.75 to 0.80, depending on airfoil geometry. The rotor designs in this study do not experience these speeds; however, it is imperative that experimental LSB airfoil data be obtained in transonic flow conditions to permit high-confidence design of LSB X-Wing rotors intended to convert at high flight speeds (greater than 200 knots).

ROTOR/AIRCRAFT PERFORMANCE

Disc loading distributions for several CC rotor designs operating at the critical advance ratio for the same thrust level are shown in figure 7. These cases are all trimmed to a negligible roll moment. Figure 7a is a typical distribution for a variable collective (without LSB) design. The concentrated loading fore and aft and in the reverse flow region, along with a region of negative loading outboard on the advancing side, are characteristic of high-speed rotary flight. The latter feature is the result of the negative collective pitch setting required to reduce lift on the advancing side for roll moment trim. In this azimuthal range where little blowing is used, lift arises primarily from angle of attack and camber.

Figures 7b through 7d show disc loading distributions for LSB designs in which the lower surface slot extends over varied portions of the blade span. For the full-span LSB case (fig. 7b), a region of negative loading extends from root to tip in the second quadrant. Maximum blowing is applied to the lower surface slot at 90-deg azimuth where it is most effective for lateral moment production. However, as seen by the positive loading over the outboard, high-q region, LSB is not sufficient to completely overcome the basic goemetric (camber plus incidence) lift. (The geometric advancing incidence is +4 deg due to nose-up rotor attitude.) Figure 7b also depicts the steep nature of the azimuthal loading gradient, especially as the blade leaves the negative loading region. Here, the entire span is subjected simultaneously to a rapid change from lowest to highest loading, which may have implications with regard to vibratory forces (no higher harmonic control is used in this study).

As expected, if the lower surface slot is limited to smaller outboard span regions (figs. 7c and 7d), the negative loading becomes concentrated on a small spanwise region near the blade tip. Inboard, an area of high positive lift develops at ψ = 90 deg. This high lift is produced by nonblowing lift forces because neither upper or lower slots are blown in this region.

In addition to comparing LSB rotors with other current CC rotor designs, the benefits of LSB over other methods of achieving fixed-collective incidence designs is of interest. First is consideration of operating current rotor designs (without LSB) at a fixed, zero pitch setting. For a fixed-collective rotor design without LSB, the problem of achieving trimmed flight at high speed becomes a tradeoff between collective pitch and rotor shaft/disc angle settings. The rotor disc angle is crucial for optimized performance in terms of lift-to-power ratio, since the axial component of the high forward speed contributes greatly to the mean incidence experienced at the blades. As the blade pitch setting is increased toward zero deg, the rotor disc angle must be decreased from the typical 4- to 6-deg noseup attitude where the rotor operates in a near auto-gyro state. This trimmed disc angle reaches -2 deg (nosedown) for a zero collective pitch setting. At this rotor attitude, available blowing is not sufficient to overcome the decreased lift due to lower incidence. Figure 8 shows the predicted relative loss of rotor lift capability when this fixed collective pitch restriction is imposed on current CC rotor designs. Moreover, these high-speed V/STOL designs rely on substantial hub/fuselage, incidence-related lift forces, and the fuselage attitude must match the rotor disc angle (within 1 to 2 deg) due to rotor/fuselage proximity. Therefore, an aircraft with a current CC rotor set at zero blade pitch experiences greatly reduced net lift capability.

Conversely, when LSB is applied to a zero collective pitch rotor, the required trim control range is achieved without compromising the efficient rearward tilt of the rotor disc. Not only does the rotor produce equivalent lift, but the nonrotor lifting surfaces also retain their lift capability; see figure 8. Furthermore, as expected, no loss in rotor efficiency is experienced with the LSB design because the power required from the rotor and the compressor is equal to that required by a variable collective pitch rotor at the critical advance ratio.

ALTERNATIVES TO LSB

Other methods of providing cyclically varying control forces for high-speed trim of a fixed-pitch rotor system were briefly investigated. At zero collective pitch, the control forces must be sufficient to counteract a rotor thrust offset equal to approximately 25 percent of the disc radius (offset = moment/thrust/radius). One suggested method uses a modulated high velocity jet at the blade tip to produce a reaction force in opposition to the normal lift direction. Basic calculations show that the airflow requirements for the reaction jet far exceed (by about 400 percent) the output available from a compressor sized for the normal boundary layer control function.

Activation of leading edge (upper blade surface) slot blowing on the advancing side of the rotor often is suggested as a means of spoiling lift. Unfortunately, blowing in opposition to the local flow direction is not effective in producing negative lift increments, as shown in figure 9. The data, which are representative of the performance for the outboard portion of an X-Wing blade, show a negligible

capability of leading edge blowing to degrade lift. Certainly, a mean ΔC_{ℓ} of -0.6, which is needed to produce the required offsetting moment for a zero-pitch configuration cannot be achieved with this technique.

Finally, the use of negative camber was considered as a substitute for a negative pitch setting in conversion. Aerodynamically, 1 deg of incidence is about equal to 1 percent of camber. Therefore, a reduction of the mean camber by approximately 5 percent is required for trim with a fixed zero-collective incidence setting. Such a design would have serious negative implications in hover. Indications are that none of these options are suitable alternatives for production of the required trim moments in high-speed flight.

ROTOR/AIRFOIL DESIGN IMPACT

A statistical analysis of the airfoil local operating environment yields insight to details of the airfoil design requirements for a particular rotor operating condition. By weighting parameters such as angle of attack by the absolute magnitude of the locally generated load, a mean productive value of the parameter can be obtained (Rogers et al., 1985). Figure 10 shows a comparison of the airfoil operating environments for three CC rotor configurations in conversion. For a variable pitch rotor (fig. 10a), the mean load due to blowing is constant along the blade span. Viewed in terms of total (net) load, the inboard section carries substantially more load than the outer regions. The magnitude of the inboard loading highlights the desirability of a blended blade/fairing contour (fixed-pitch design) to minimize the shedding of strong root vortices and improve hub/fuselage lift carryover.

This same rotor design, when forced to operate at a zero collective pitch setting (fig. 10b), operates in an environment of locally lower angle of attack. This is the cause of its inability to produce the required level of net lift with the given air compressor.

The mean local angle-of-attack distribution over the retreating side of an LSB rotor blade (fig. 10c) is quite similar to that of the variable pitch rotor. A majority of the total load is generated in the 0- to -10-deg alpha range. The mean spanwise loading distribution for this full-span LSB configuration is most revealing. Over much of the span, the mean lift due to blowing is negligible because negative incremental lift applied on the advancing side offsets the positive lift from blowing on other portions of the disc. Effectively, the blowing lift forces are being used primarily for cyclic rotor control with the net rotor lift arising from the higher blade incidence possible with LSB. Mean total loading is shifted outboard to resemble that of conventional rotors.

Further investigation of the local aerodynamic environment of an LSB rotor reveals important information concerning the design criteria of LSB airfoils. In figure 11, local airfoil incidence is shown versus local Mach number. Each symbol represents conditions at one of the 180 disc elements used in the analysis. Functional incidence is defined as alpha for conditions of upper surface blowing and as -alpha for LSB conditions. (This convention is used so that LSB operation can be intuitively viewed in the same familiar context as an "upper surface" slot.) The large excursions in angle of attack at low local speed are typical of high-speed rotorcraft operation due to large regions of low speed reversed flow and

numerous tip path crossovers. Within the Mach regime where LSB is applied, the angle-of-attack range is narrow and relatively independent of M_∞. This range also generally coincides with the optimum angle of attack for CC airfoils to produce maximum lift increments. These analytical results suggest airfoil LSB mode design criteria that are quite concise and readily achievable in that the required operating envelope is limited to a narrow angle-of-attack band for all Mach numbers. Upper surface blowing mode operational requirements are similar to those of current variable pitch rotor designs.

The performance requirements of the airfoils for LSB operation and normal blowing are presented in figure 12 for trimmed, high-speed flight. The required lift increment for blowing is shown as a function of local Mach number for the 180 individual disc elements. In the higher speed regimes (0.3 to 0.7 M), where either upper or lower surface blowing may occur, LSB operation requires lift increments with absolute magnitude equal to or slightly greater than that of upper surface blowing. The incremental lift limit ($\Delta C_{\ell_{max}}$), however, is not reached at any disc location.

Tests of a CC airfoil family (the basic contour parameters of the airfoils are the same linear functions of thickness ratio) were recently conducted in a transonic wind tunnel. All of the contours were found to have the same peak value of the lift function ($\Delta C_\ell M_\infty^2$) and to differ only in the Mach number at which the peak occurs; see figure 13.

If an uncambered, LSB equipped airfoil is assumed to have the capability to produce equal absolute lift increments in both positive and negative directions, the empirical results from figure 13 can be compared to the analytically predicted lift requirement. Such a comparison is shown in figure 14, where elements corresponding to the outboard blade location (t/c = 0.15) are isolated from figure 12 and superimposed with the lift limits from figure 13. For USB operation at this span location, the lift limit is approached only at low speed where maximum blowing is applied on the retreating side of the rotor disc. The LSB feature is demanded precisely in the M_∞ regime where the absolute lift capability of the airfoil is maximum. Also, the magnitude of the negative lift increments required is well below the available levels. This match of required and available performance seems to exist over the entire span for this rotor design at the operating conditions examined. Implementation of the LSB concept, therefore, is well suited to the present CC rotor design so that modified, dual-slotted trailing edges can be retrofit to current contours for the purpose of concept demonstration.

OTHER OPERATING CONDITIONS

The relative rotor performance capability in hover, transition, conversion, and fixed-wing flight regimes is a major rotor design issue. While it has been demonstrated analytically that an LSB fixed-pitch design is a viable concept for CC rotor control in high-speed flight, the implications of this design at other operating conditions must also be examined.

Hover

In hover, the variable collective pitch feature of current CC designs is exploited by setting a positive blade pitch angle (typically, 6 deg). This yields optimum efficiency by using lift due to angle of attack generated by the higher mean local incidence to reduce the demand on the compressor. Hovering with a collective pitch setting of zero requires a higher blade pressure and, thus, compromises the rotor efficiency as expressed by the Figure of Merit in figure 15. Assuming that the projected missions of high-speed CC rotorcraft involve relatively short hover durations, it is feasible to accept this reduced hover performance. Note that the alternative of using negative camber for trim in conversion would result in further reductions of hover efficiency through the camber-θ_c equivalence.

Transition

For CC rotors, the available 1P-cyclic control authority is dictated by the proximity of the mean blowing level to the level corresponding to the maximum producible pressure. In transition from hover to rotary wing forward flight (10 to 50 knots), longitudinal moment control is critical. In this environment, a rotor with fixed, zero collective pitch requires a higher mean blowing level. This results in a lower available 1P-cyclic blowing control range than that of a variable pitch design. Analysis of transition flight for the present rotor geometry indicates that the mean pressure level required to maintain rotor lift precludes the use of LSB to augment cyclic control in this flight regime. Therefore, upper surface blowing alone must be capable of both overcoming the effects of reduced mean pitch and providing a sufficient longitudinal control moment. (Applying LSB in a higher harmonic mode to assist in transition flight may be possible, and should be addressed in future investigations.)

Fixed-Wing

Zero collective pitch is the standard control setting for steady, level flight in the fixed-wing mode. Because there is no cyclic control of blade pitch, any non-zero setting results in differential incidence between port and starboard wings. Blowing, then, must be used to trim the laterally unequal forces. Thus, the compressor consumes excess power (at a rate which is linearly proportional to the peak pressure supplied to the wings/blades), which decreases cruise efficiency. The use of differential blowing to achieve trimmed, level flight also diminishes the pneumatic control range available for maneuvering. Yet another inherent benefit of zero-pitch is that both sides of the rotor experience an identical aerodynamic environment. This minimizes the occurrence of roll moment disturbances caused by the differential encounter of nonlinear aerodynamic forces. With regard to these considerations, a fixed, zero-pitch design imposes no disadvantages in this flight regime.

SUMMARY

A fixed-pitch rotor has long been regarded as the ultimate goal of a stoppable rotor aircraft. The fixed collective advantage arises from the control and structural weight savings and from the increased freedom to integrate hub/blade

contours for maximum vehicle aerodynamic performance. Recent advances have been made in understanding and analytically predicting the geometry and Mach number related performance characteristics of CC airfoils. This insight has permitted the adaptation of present CC performance modeling to predict the impact of LSB implementation. This study has shown that dual-action airfoils employing lower surface, trailing edge slots provide an effective means of rotor control thereby eliminating collective pitch control without severely compromising rotor performance. Furthermore, the demands on LSB to produce moderate negative lift increments in a high-speed operating regime are well suited to the airfoil contours of current CC rotors. This indicates that current airfoils, when retrofit with LSB trailing edges, are suitable for an initial experimental investigation of LSB rotor characteristics.

REMARKS

Analytically, LSB offers an attractive alternative to "conventional" CC rotor design. Continued effort is being directed toward design and fabrication of a two-dimensional LSB airfoil model. Of major concern are the Coanda shape and blowing slot locations with regard to the projected operational requirements of both upper and lower surface blowing. The practicability of an LSB rotor system can then be assessed at low cost by modifying the RSRA/X-Wing model rotor pneumatic system and fabricating a set of LSB model blades. A logical extension of these efforts, of course, is to evaluate a full-scale zero-pitch LSB rotor system on the NASA Rotor Systems Research Aircraft.

ADMINISTRATIVE INFORMATION

This work was supported by the David W. Taylor Naval Ship R&D Center (DTNSRDC) Independent Exploratory Development Program sponsored by the Office of Chief of Naval Research, Director of Navy Laboratories (OCNR 300), and administered by the Research Coordinator (DTNSRDC 012.3) under Program Element 62766N, Task Area ZF-66-412-001, DTNSRDC Work Unit 1-1690-107.

REFERENCES

Abramson, J. and Rogers, E.O.: High-Speed Characteristics of Circulation Control Airfoils. Paper AIAA-83-0265 presented at AIAA 21st Aerospace Sciences Meeting, Reno, Nevada, 10-13 Jan 1983.

Ham, N.D., Bauer, P.H. and Lawrence, T.L.: Wind Tunnel Generation of Sinusoidal Lateral and Longitudinal Gusts by Circulation Control of Twin Parallel Airfoils. NASA CR-137547, Aug 1974.

Kind, R.J., and Maull, D.J.: An Experimental Investigation ot a Low-Speed Circulation-Controlled Aerofoil. The Aeronautical Quarterly, May 1968.

Linden, A.W. and Biggers, J.C.: X-Wing Potential For Navy Applications. Paper presented at the 41st Annual Forum of the American Helicopter Society, Fort Worth, Texas, 15-17 May 1985.

Rogers, E.O., Schwartz, A.W. and Abramson, J.S.: Applied Aerodynamics of Circulation Control Airfoils and Rotors. Paper No. 31, Eleventh European Rotorcraft Forum, London, England, Sep 1985.

Schwartz, A.W.: Basic Consideration of the Lifting Capability of Stoppable Rotors. DTNSRDC/ASED-84/10, AD A150 850, Dec 1984.

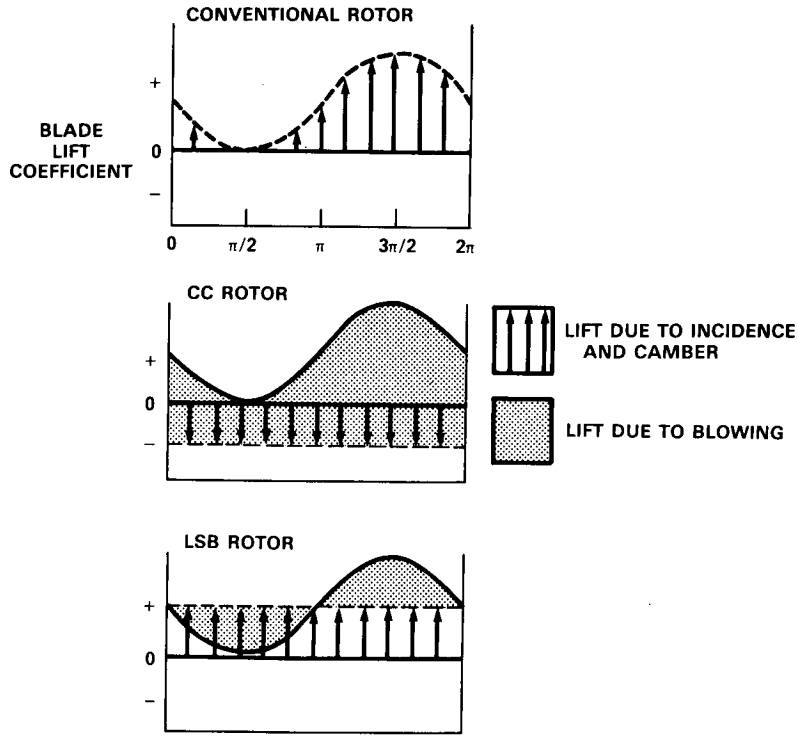

Figure 1.- Conceptual trim control methods for various rotor designs.

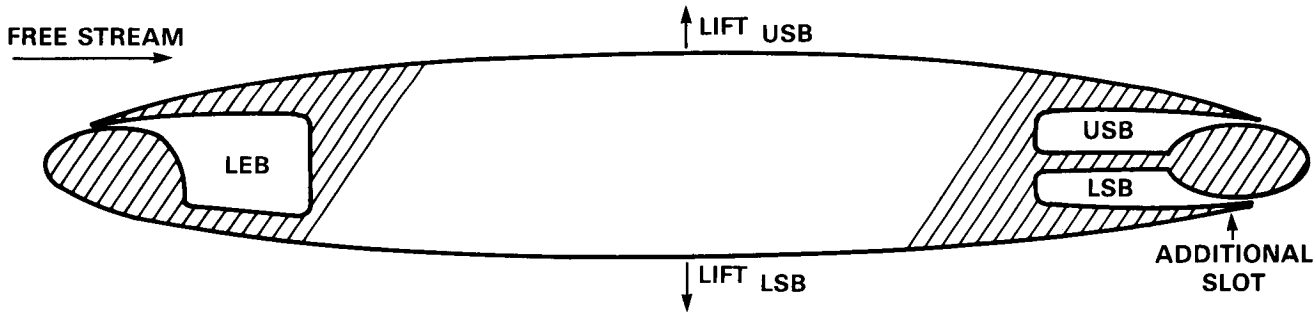

Figure 2.- Airfoil configuration for lower surface blowing.

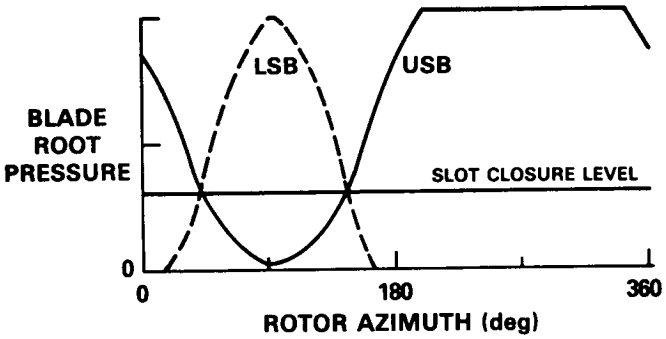

(a) Full-span LSB.

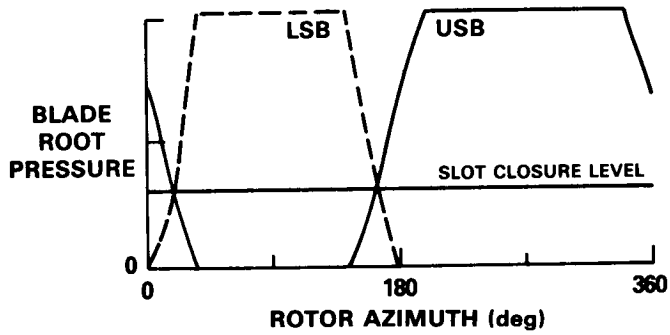

(b) Partial-span LSB.

Figure 3.- Coupled cyclic control pressure waves.

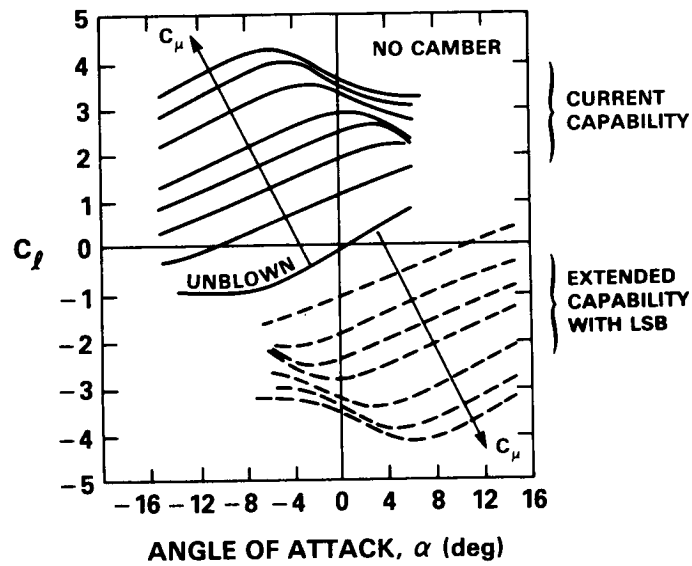

Figure 4.- Idealized lift control range for an LSB airfoil.

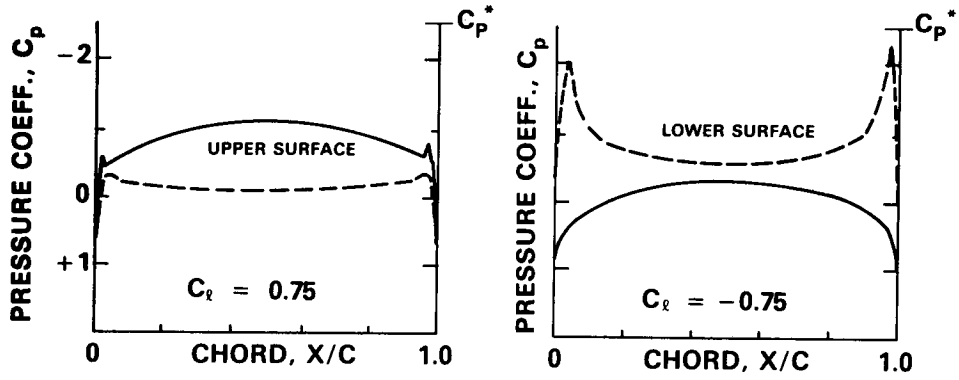

(a) Normal (upper surface) blowing. b) Lower surface blowing.

Figure 5.- Airfoil pressure distributions for absolute lift level (α=0 degrees).

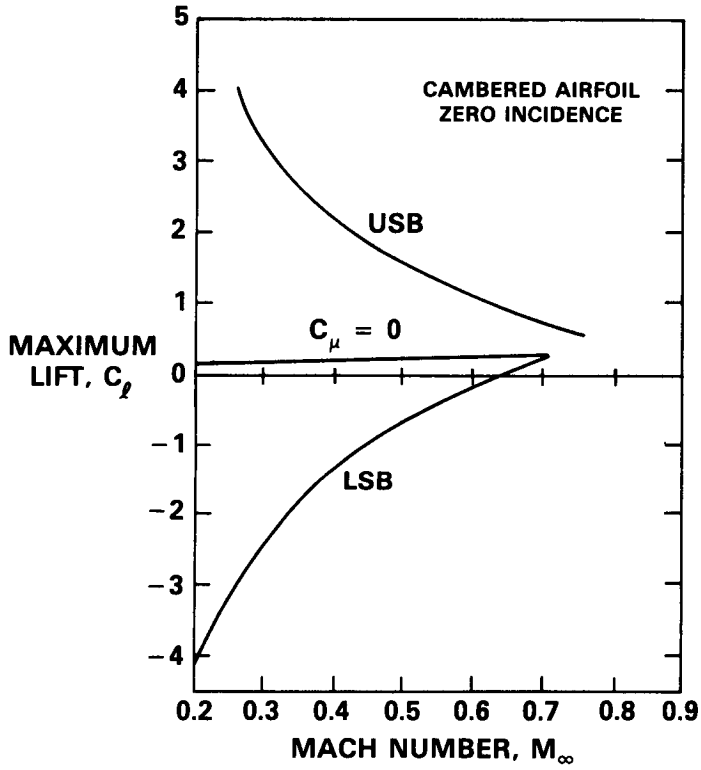

Figure 6.- Comparative influence of Mach number on airfoil theoretical lift capability.

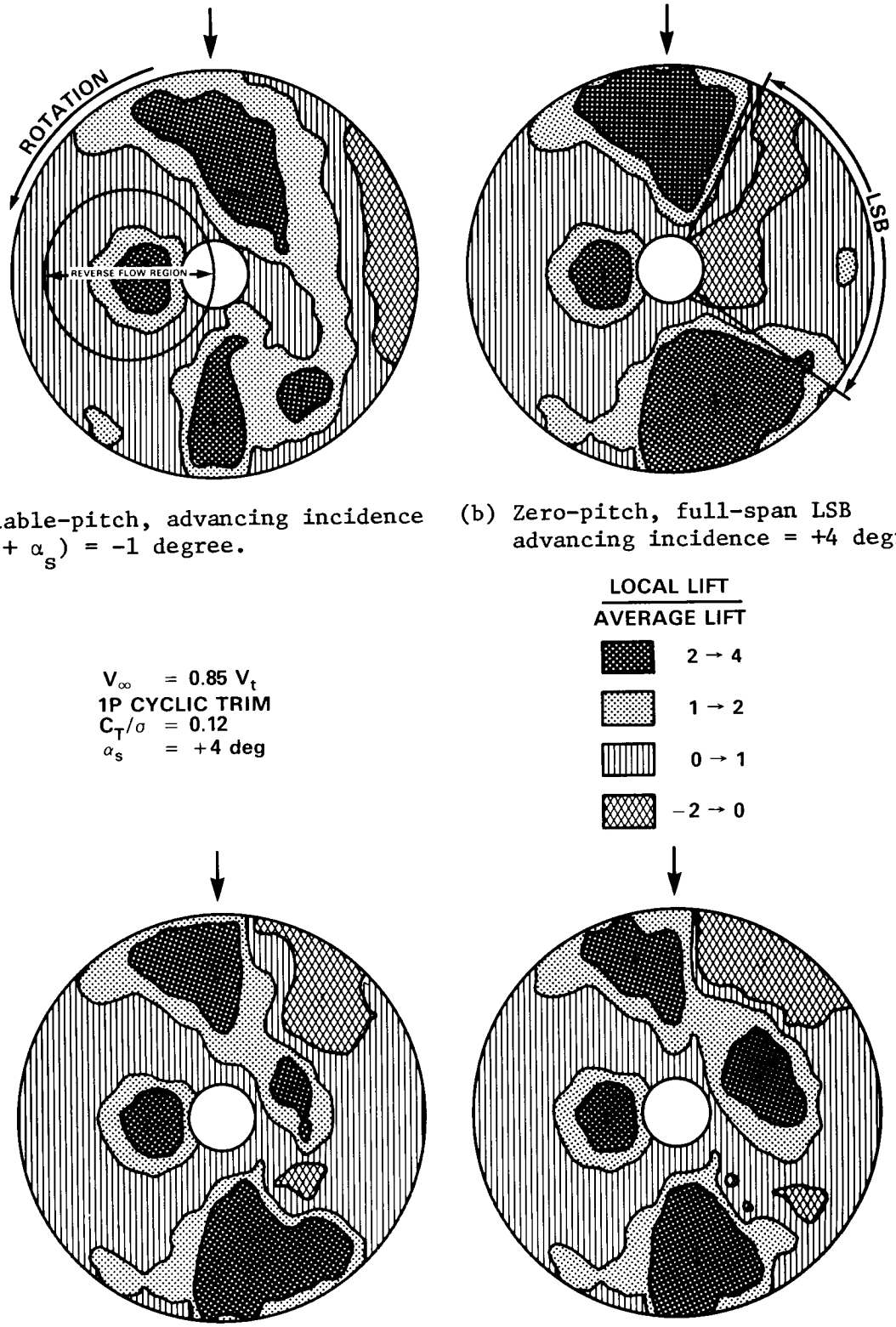

(a) Variable-pitch, advancing incidence $(\theta_c + \alpha_s)$ = -1 degree.

(b) Zero-pitch, full-span LSB advancing incidence = +4 degrees.

(c) Zero-pitch, partial-span LSB (0.5 r/R to tip).

(d) Zero-pitch, partial-span LSB (0.7 r/R to tip).

Figure 7.- Comparison of disc loading distributions for various CC rotor configurations.

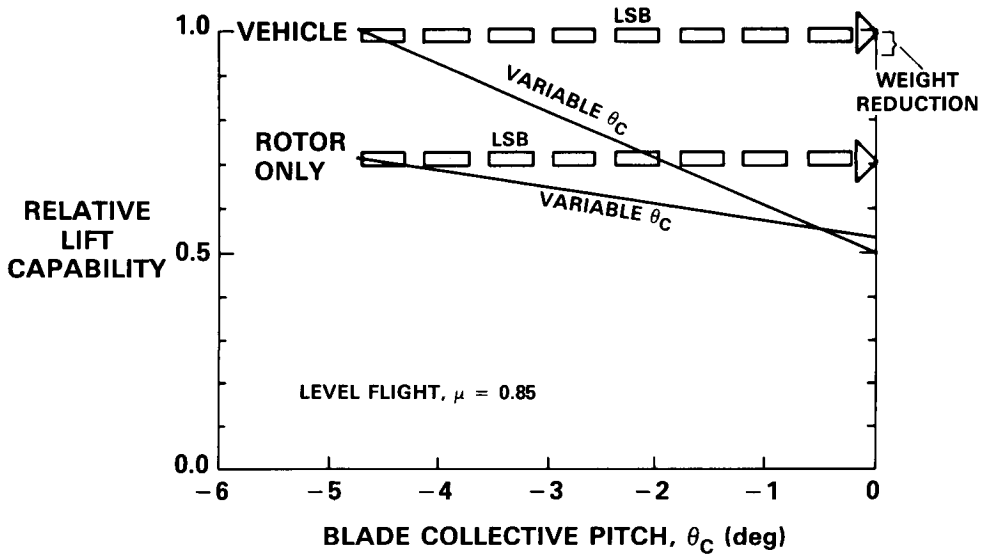

Figure 8.- Lifting performance comparison in conversion with variable collective pitch versus fixed-pitch (θ_c = 0 degrees, LSB).

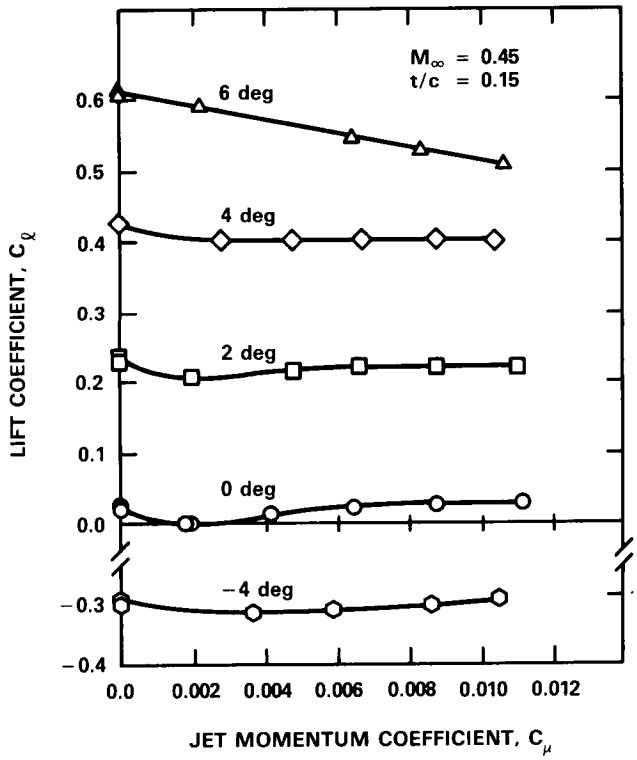

Figure 9.- Airfoil lift response to leading edge only blowing.

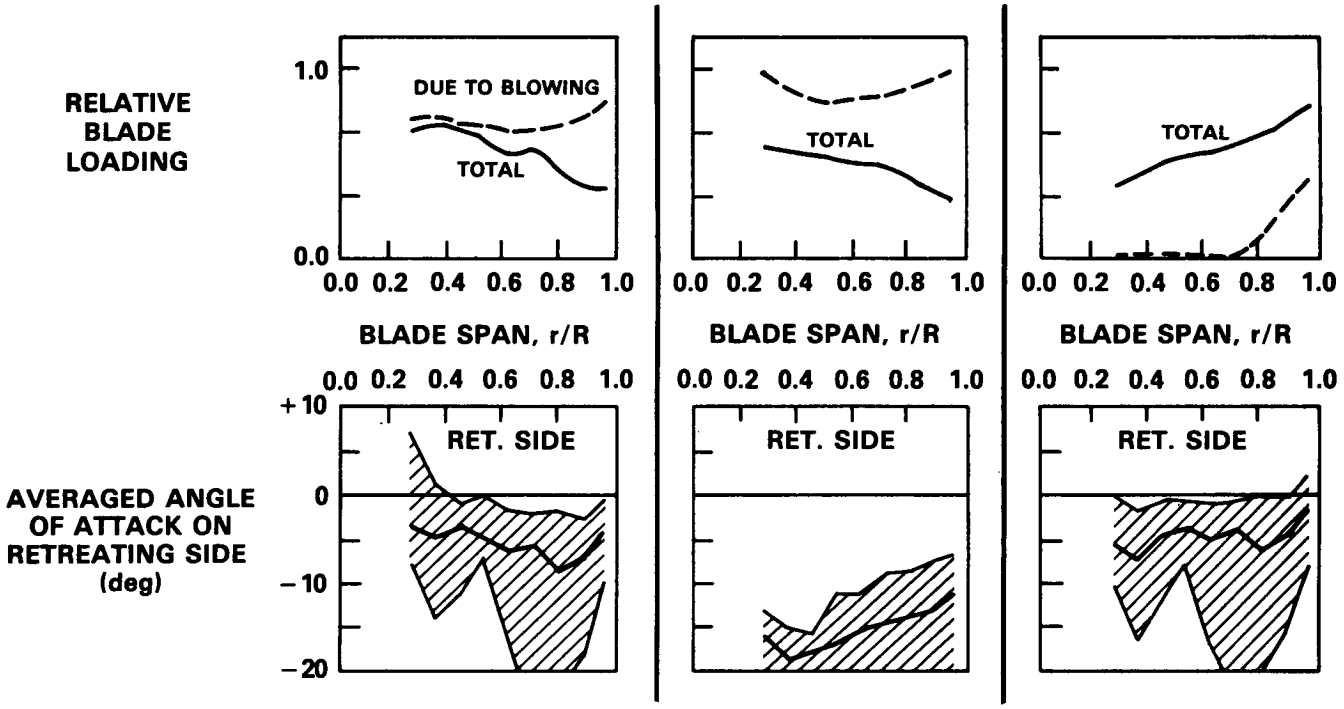

(a) Variable-pitch without LSB.

(b) Zero-pitch without LSB.

(c) Zero-pitch with LSB.

Figure 10.- Airfoil operating environment (azimuthally averaged) for variable pitch and fixed-pitch CC rotor configurations.

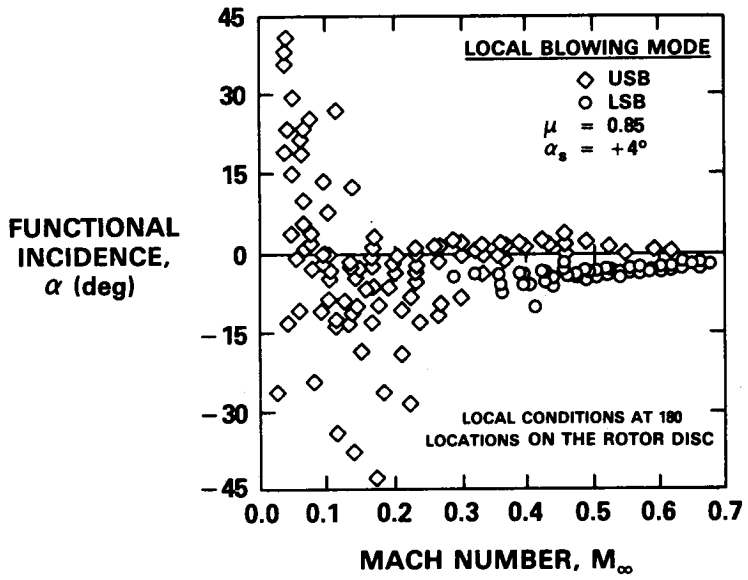

Figure 11.- Airfoil operational angle of attack for LSB rotor in conversion.

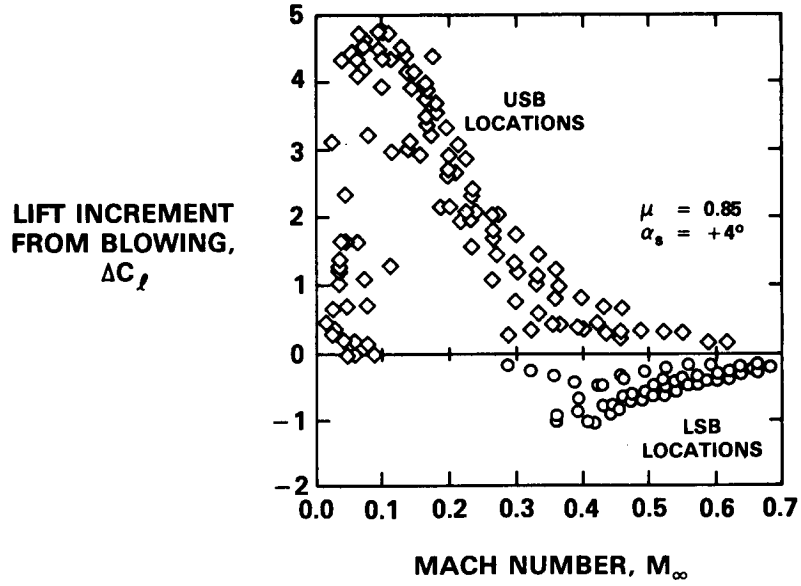

Figure 12.- Airfoil lift performance requirements for LSB rotor in conversion.

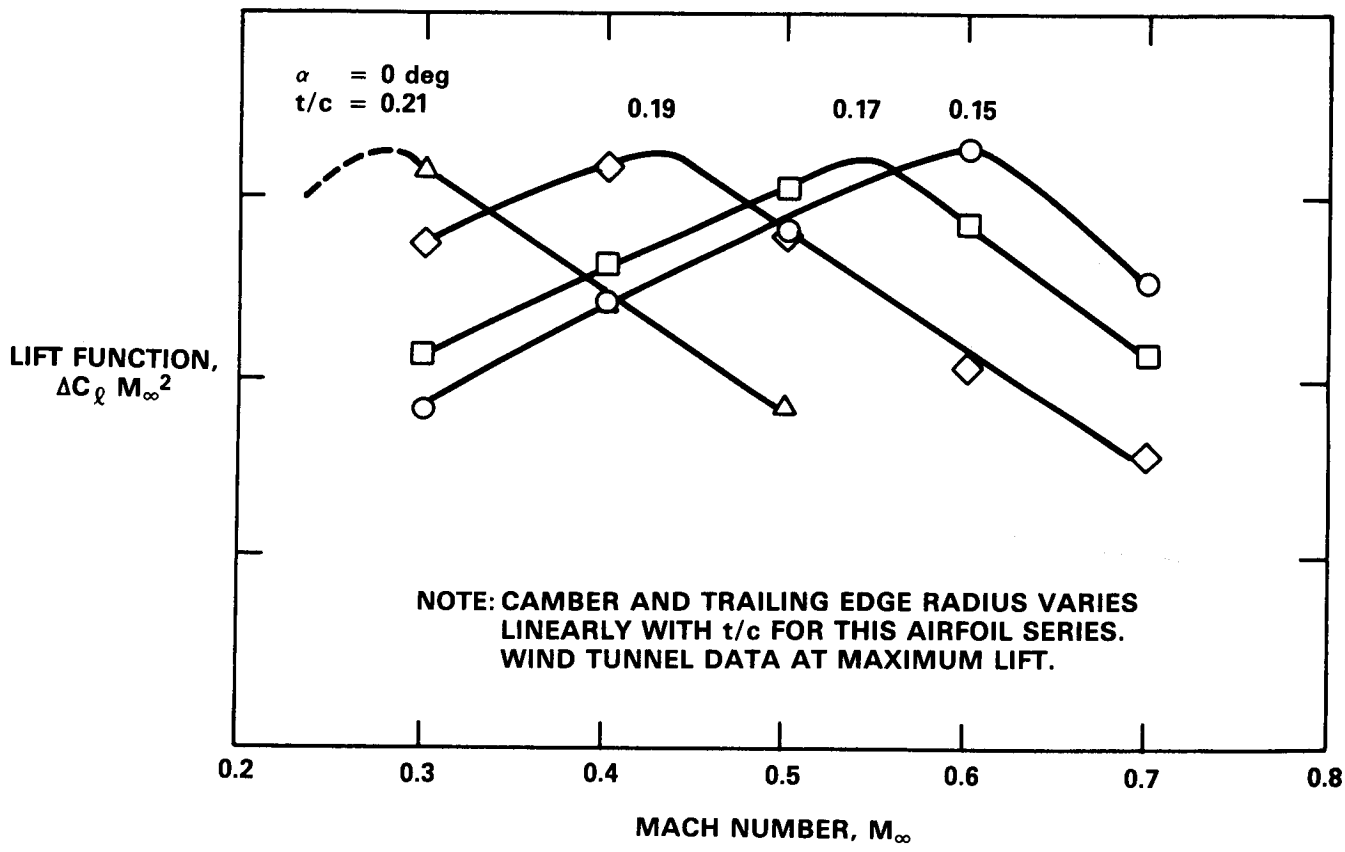

Figure 13.- Airfoil capability to augment loading at zero incidence.

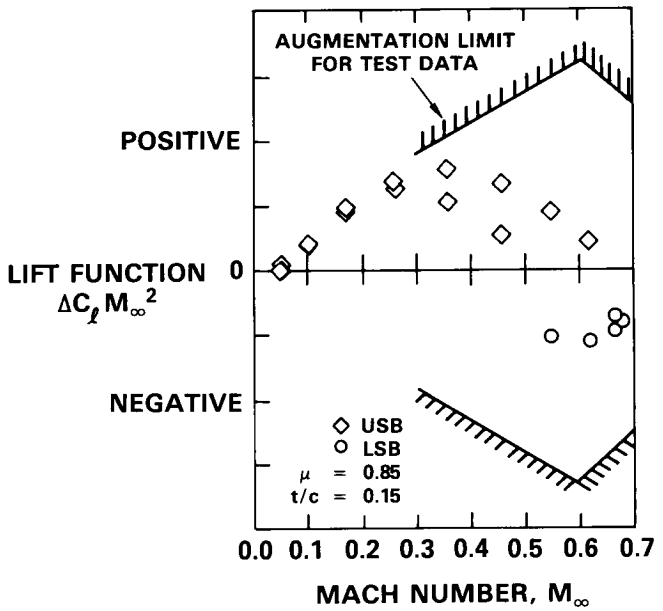

Figure 14.- Comparison of airfoil augmentation requirements and estimated performance limits.

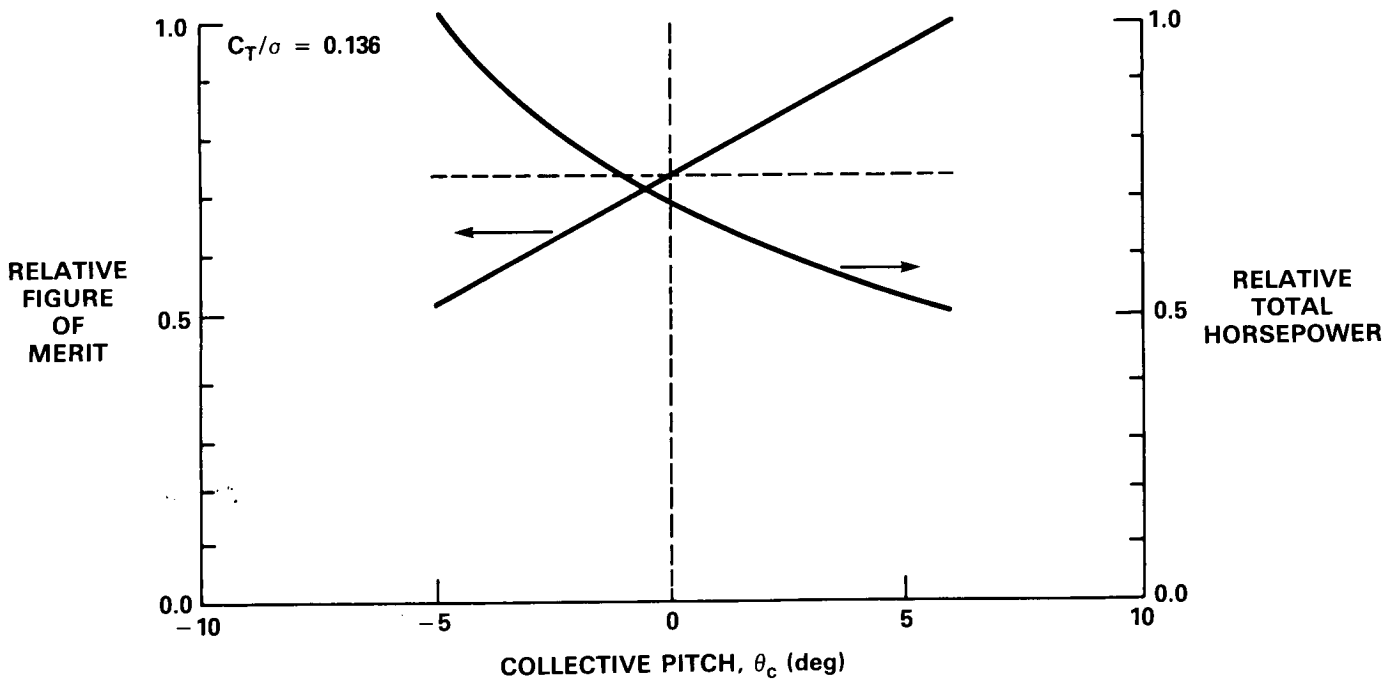

Figure 15.- Influence of collective pitch on CC rotor hover performance.

X-wing Technology

PREDICTION OF AEROELASTIC RESPONSE OF A MODEL X-WING ROTOR*

Robert Sopher

James E. Duh

Sikorsky Aircraft Division
United Technologies Corporation
Stratford, Connecticut

ABSTRACT

The purpose of this paper is to describe comparisons of predictions from an aeroelastic analysis with test data for a model X-Wing rotor to demonstrate the applicability of the analysis to the X-Wing. The analysis is the Rotorcraft Dynamics Analysis (RDYNE), developed by Sikorsky Aircraft, which was modified to incorporate Circulation Control airfoil aerodynamics and a pneumodynamic analysis, developed by the David Taylor Naval Ship Research and Development Center (DTNSRDC). Test data were derived from a representative X-Wing with a 10 ft diameter rotor tested in the Boeing-Vertol Wind Tunnel. A small number of comparisons were also made with data for a 25 ft diameter X-Wing rotor tested in the NASA Ames 40 x 80 ft Wind Tunnel. Several flight regimes were investigated, including hover, transition, and conversion to a fixed wing mode of flight. The comparisons indicate that the analysis is able to give satisfactory predictions of X-Wing behavior. Basic control power effects and the effects of Higher Harmonic Control on vibratory bending moments are predicted accurately. Forward flight vibratory flatwise bending moment and push rod load comparisons were as good as comparisons for conventional rotors. The analysis is able to accurately represent vibratory and steady responses in rotor thrust, blade bending moments, and hub rolling and pitching moments for conversion to a fixed wing flight mode. Refinements which were identified as leading to significant improvements were variable rotor induced flow and acoustic pressure wave delay in the pneumodynamic model.

INTRODUCTION

The X-Wing vehicle is an aircraft which utilizes a rotor to take off (and land) as a helicopter. The aircraft transitions to forward flight and converts to a fixed wing flight mode at a high subsonic flight condition, with the rotor first slowed and then stopped as a fixed wing with an X-planform. Advances in several technologies make more practical the realization of the concept, which has evolved to

---

*Work performed under a NASA contract for the RSRA/X-Wing. Presented at Circulation Control Workshop, NASA Ames Research Center, Moffett Field, California, February 19-21, 1986.

where NASA awarded Sikorsky Aircraft a contract in December 1983 to design, build, and test an X-Wing on the Rotor Systems Research Aircraft (RSRA). The Circulation Control Rotor (CCR) is a key technological solution incorporated in the X-Wing enabling the rotor to behave satisfactorily at high advance ratios and stopped conditions. Jets of air are ejected from slots at leading and trailing edges of the aerodynamically smooth airfoil section to achieve lift augmentation and cyclic control of lift, as well as vibration reduction through Higher Harmonic Control (HHC).

Prior to the Sikorsky contract, small scale and full scale tests were conducted with three models to verify the X-Wing concept and to acquire data (Reader, 1984). Data were obtained on a 6.7 ft. diameter Reverse Blowing Circulation Control Rotor (RBCCR), a Lockheed 25 ft. diameter X-Wing rotor, and a Boeing-Vertol 10 ft. diameter X-Wing rotor. To support the design of the RSRA/X-Wing, Sikorsky modified the Rotorcraft Dynamics Analysis (RDYNE) to model the pneumodynamic and aerodynamic behavior of CCRs, and this was followed by studies to validate the analysis. Comparisons were made with the Boeing-Vertol and Lockheed test data to study the ability of the analysis to predict basic phenomena, consisting of control power relationships, the effects of HHC, and the vibratory response of the rotor in forward flight and conversion to a fixed wing mode. The purpose of the paper is to describe the performance of the RDYNE aeroelastic analysis by comparing predictions from analysis with results from test data in X-Wing regimes of flight.

Acknowledgements are due to Robert H. Blackwell, Sikorsky, and Kenneth R. Reader, DTNSRDC, for their contributions.

AEROELASTIC METHODOLOGY

The methodology utilized to predict the aeroelastic behavior of the X-Wing rotor is the Rotorcraft Dynamics Analysis (RDYNE), developed by Sikorsky Aircraft. This is an analysis which integrates the equations of motion for a dynamical system with respect to time (Sopher and Hallock, 1986). The software is segregated along component lines. Components consist of distinct types of dynamical substructures, aerodynamic representations, trim solutions, and processing capabilities such as table specification and plot variable selection components. The components selected for the application of the analysis to predict the aeroelastic responses of X-Wing rotors were the following:

1) The elastic blade is based on a set of coupled flatwise, edgewise, and torsion equations (Arcidiacono, 1969). Blade mass and stiffness properties are used to calculate uncoupled bending and torsion normal modes, and blade displacements are expressed in terms of these modes to reduce the basis of the blade equations to normal modes coordinates.

2) The section aerodynamic component was developed by the David Taylor Naval Ship Research and Development Center (DTNSRDC) and yields the blade element characteristics of Circulation Control (CC) airfoils for specified values of blowing momentum coefficient, angle-of-attack, and Mach number. Incorporated with this component is a pneumodynamic analysis which calculates blade duct pressures and temperatures, for specified plenum pressure ratios, and allowing for losses and centrifugal pumping in the duct.

There is also a module for calculating the slot deflection height of the flexible slot. The slot height is utilized with duct pressure and temperature to calculate jet velocity and mass flow through the slot, and jet momentum coefficient, which in turn are used to obtain from a set of tables established from tests on CC airfoils the values of C_L, C_D, and C_m applicable to the airfoil state. The effects of acoustic pressure wave delay are represented in RDYNE by calculating the pressure at an orifice at a specified radial station from the pressure at a valve opening in the plenum at an earlier time, by accounting for the time taken for the wave to travel between these points.

The data were derived from tests on two types of CC airfoils consisting of 20% thickness ratio dual slotted cambered airfoil and a 15% thickness ratio uncambered dual slotted airfoil. The 20% thickness ratio airfoil was subsequently used at the root of the Boeing-Vertol X-Wing rotor and the 15% airfoil was used at the tip of the rotor, with intermediate sections obtained from straight line generators extended between root and tip.

3) Rotor induced variable inflow is represented by a procedure which utilizes geometric influence coefficients relating rotor blade circulations to induced velocity, which are calculated by a program external to RDYNE and then transmitted to RDYNE for calculation of the inflow. The geometric influence coefficients are based on the analysis of Landgrebe and Egolf (1976) and are functions of advance ratio and the angle (CHI) assumed between the rotor wake and rotor tip path plane. This angle may be calculated from momentum inflow considerations or may be input to reflect an empirical or arbitrary wake inclination. An iterative procedure is used in RDYNE to ensure that rotor blade circulations, motions, and rotor induced inflow are consistent with each other in the final vibratory state used for the predictions.

DESCRIPTION OF TESTS AND ASSUMPTIONS IN ANALYSIS APPLICATIONS

The objective of the Boeing-Vertol test was to obtain data from the model of an aircraft with a representative X-Wing rotor, for several flight regimes including hover, transition (10 to 100 kn), and high speed rotary wing flight to 200 kn. Fundamental effects of blowing inputs on steady hub moments and vibratory bending and pushrod loads (torsion moments) were studied, including the effects of HHC blowing.

The test was conducted in the Boeing-Vertol Wind Tunnel (BVWT) which has a 20 x 20 foot working section and a conventional closed circuit. The 10 foot diameter rotor is described in table 1. The circulation control airfoils have an aerodynamically smooth contour achieved by means of flexible slots at leading and trailing edges. Leading edge or combined leading edge and trailing edge (dual) blowing is achieved by a blowing system consisting of a plenum to which air is supplied by a

TABLE 1 - BOEING-VERTOL MODEL X-WING ROTOR

- **Rotor**
  - **Diameter** = **10 ft**
  - **Tip Speed (ΩR)** = **600 ft/sec**
  - **Taper ratio** = **0.5**
  - **Solidity** = **0.159**
  - **Airfoil** = **20% t/c at root**
    15% t/c at tip
  - **Slots** = **Dual openings vary with pressure**
  - **Twist** = **0 degrees**
- **Control system**
  - **Pneumodynamic control of leading and trialing edge blowing and**
    - **Mean**
    - **1-5 per rev harmonics**
  - **Mechanical collective**

compressor. The plenum is connected through ducting to leading and trailing edge slots in the blade. Sixteen throttling valves in the nonrotating system control the mean and cyclic variations of trailing edge pressure supplied to the slots, up to the fifth harmonic. Nine valves control the pressure in the leading edge.

The typical rotor loading in comparisons of theory and test in hover was CT/Sigma of .074 at a tip speed of 602 feet per second and a plenum pressure of 14 psig. The RDYNE analysis was run with measured control angles and pressures selected from a station between the 20 to 25 percent radial positions to define input variables for the control power comparisons in hover. Bending moment responses to these inputs were measured at the 29 percent radial position in hover.

To determine the potential of the analysis to predict reductions in vibrations induced by cyclic blowing, comparisons were made of the effects of blowing harmonic excitation (1P to 5P) on the 1/2 peak-to-peak flatwise vibratory bending moment in hover. Flatwise bending moments were compared at the 17 percent radial station, and harmonic pressures were measured at the 25 percent station. In the analysis application, the rotor speed was held at 750 rpm and the harmonic number, n, was varied from 1 to 5. Test data were measured at several different RPMs and harmonic numbers. The normalized frequency used for comparing the results is defined as n.(RPM/60).(1/f) where f is the ratio of flatwise frequency at a specified RPM used in the test or analysis to the flatwise frequency at zero RPM. The nonrotating flatwise natural frequency of the blade is 35 hz.

Comparisons were made in the transition flight regime of 10 to 100 knots to evaluate the ability of the analysis to predict steady rotor lift, torque, and hub rolling and pitching moments. Conditions selected were 20 through 60 knots with

single trailing edge blowing and a plenum pressure of 17 psig. The analysis was run with fixed control angles from the test data and with variable inflow. Three sets of analytical cases were specified to determine the effect of the rotor wake inflow angle (CHI) on correlation of hub steady pitching moment with airspeed. The CHI angle is defined as the uniform inflow (determined by the lift, shaft angle, airspeed and tip speed) divided by the forward airspeed. The theoretical uniform inflow downwash angle and values of this angle reduced to 0.75 and 0.5 of the uniform angle value were specified to study the sensitivities of the predicted results to CHI.

For the comparisons of vibratory loads in forward flight, the tip speed was 602 feet per second, the plenum pressure 14 psig, the rotor loading (CT/Sigma) was .074 and the airfoil had single trailing edge blowing. The analysis was run with specified test control angles, blade pressures from test at 23 percent span, and variable inflow. For all cases the bending moments were compared at the 29 percent blade station.

All analytical cases for the Boeing-Vertol rotor were run with two flatwise, one edgewise and one torsion mode. Figure 1 is a calculated frequency diagram for the blade modes.

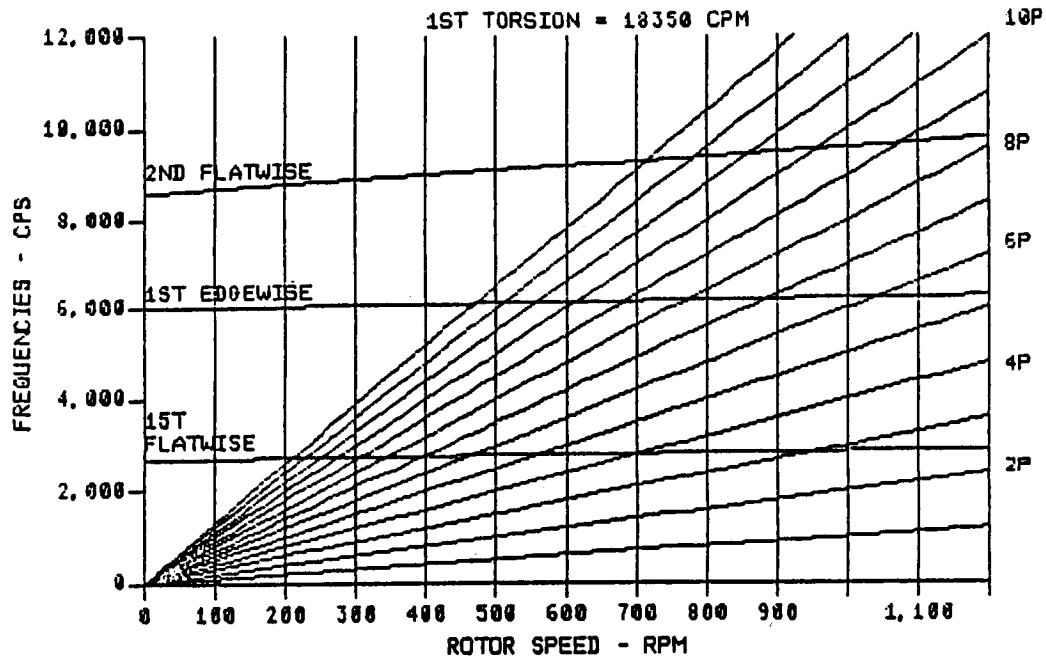

Figure 1 - Frequency Diagram for Modes for Boeing-Vertol Blade

The Lockheed rotor is a dual slotted 25 ft diameter X-Wing rotor which was tested in the NASA Ames 40 x 80 ft Wing Tunnel during the spring of 1979, for flight conditions including conversion, where the rotor was slowed from 90% NR (372 RPM) to a stopped condition at 180 kn. Figure 2 is a frequency diagram for the blade modes for the Lockheed blade.

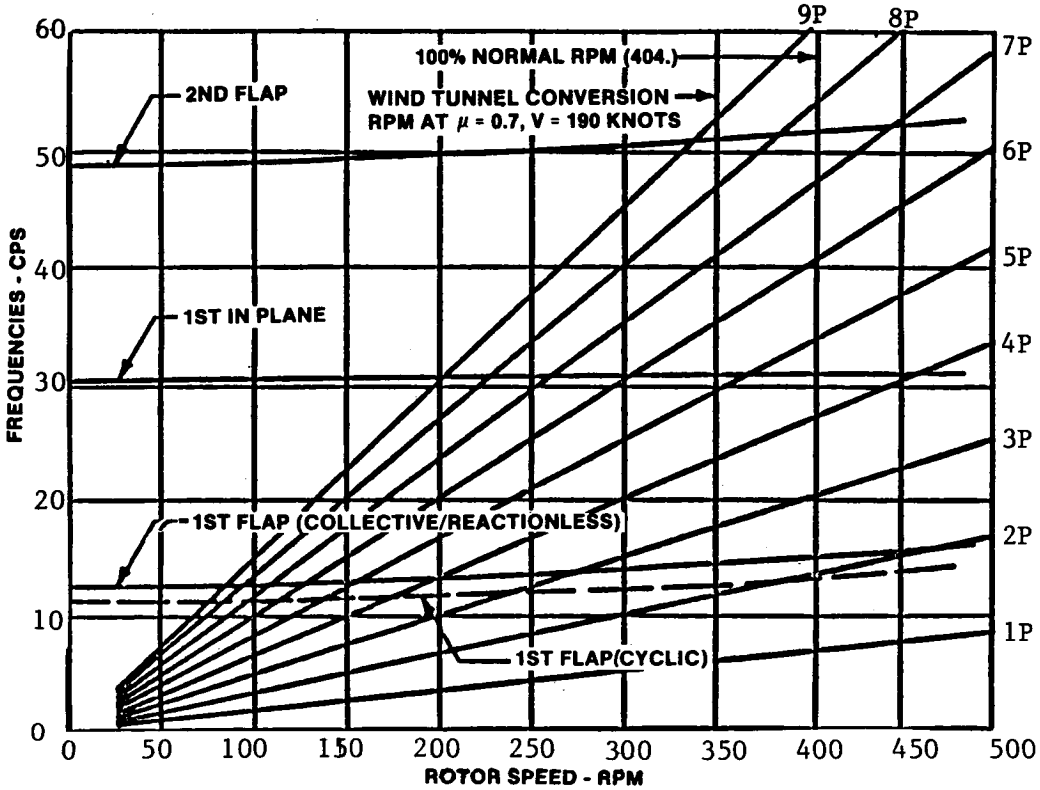

Figure 2 - Frequency Diagram for Modes for Lockheed Blade

The RDYNE analysis was run using uniform inflow to simulate a test conversion. The control angles were fixed at the values measured at the start of the run. The analysis used two flatwise modes and one edgewise mode and varied the blade modal frequencies as functions of rotor speed but used the same mode shapes throughout conversion. The blade torsion mode was omitted to enable the analysis to be run with a large time integration interval. This was felt to be justified based on the very high torsional stiffness and frequency of the Lockheed blade (torsion frequency was on the order of 20P). The test run was made under closed loop hub moment control which continuously adjusted the rotor steady hub moments to zero values. The analysis did not have a feedback hub moment control. Conversion to a stopped rotor condition was performed with blade dual blowing, a plenum pressure of 8.8 psig, 2 degrees shaft angle, and -5 degrees collective (Run 43, point 9).

All comparisons discussed below apply to the Boeing-Vertol X-Wing rotor, unless stated otherwise.

CONTROL POWER AND HIGHER HARMONIC CONTROL IN HOVER

A basic test of the analysis is its ability to predict the effects of once per rev (1P) blowing on hub trimming moments. Figure 3, which shows steady hub moment versus 1P blowing amplitude, demonstrates that the combination of an aeroelastic blade, rotor induced variable inflow, and acoustic pressure wave delay between the pressure source in the plenum and the blade orifices, succeeds in bringing the RDYNE

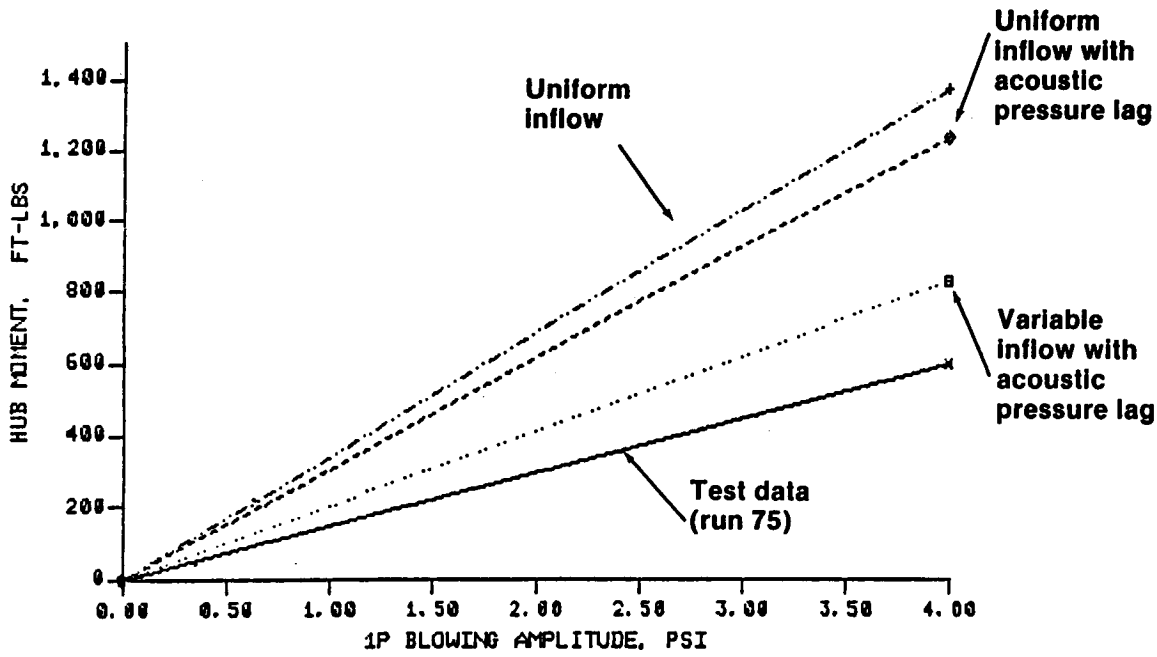

Figure 3 - Effects of 1P Blowing on Steady Hub Moments in Hover

analysis into good agreement with Boeing-Vertol test data. Figures 4 and 5 illustrate the agreement in the blade flatwise bending moment time histories and the harmonically analyzed bending moments. Interestingly, the 1P flatwise blade moment agrees exactly with the test data while the steady hub moment shows the analysis to overpredict the response by approximately twenty percent. This may indicate a slight discrepancy in the test data, since the steady hub moment is only generated from the 1P blade flatwise bending moment.

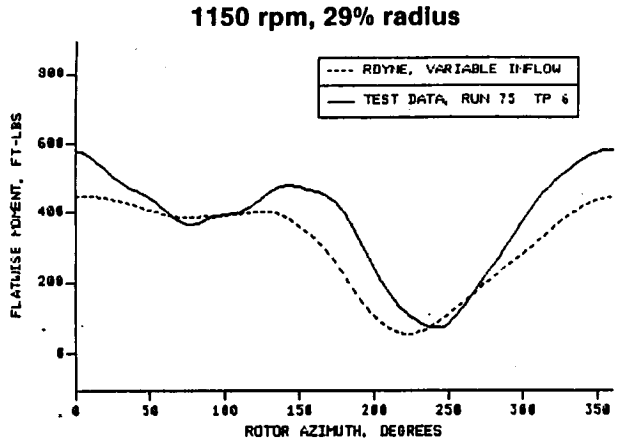

Figure 4 - Effects of 1P Blowing on Flatwise Bending Moment in Hover

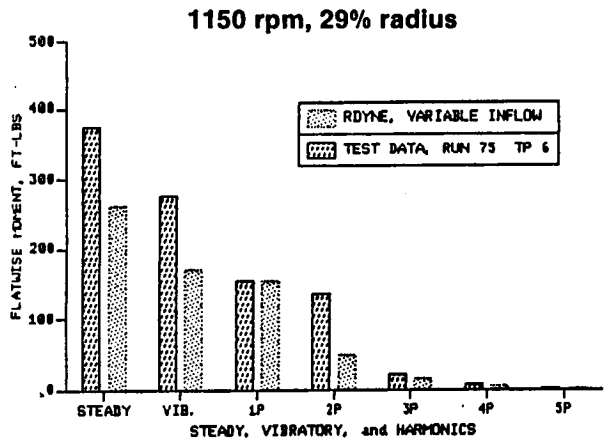

Figure 5 - Harmonic Content of Flatwise Bending Moment Response to 1P Blowing in Hover

Figures 6 and 7 demonstrate that the analysis is able to predict the effects on vibratory bending moments of Higher Harmonic Control of blowing. Variable inflow enables the amplitude to be predicted to within 20 to 30 percent and phase to be predicted almost exactly. Through blade resonance the phase of the response changes 270 degrees instead of the typical 180 degree phase shift associated with a single degree of freedom system. This was demonstrated analytically to be the effect of the acoustic pressure wave delay. Without this wave delay incorporated into the RDYNE analysis, the predicted phase shift approximated 180 degrees (figure 8).

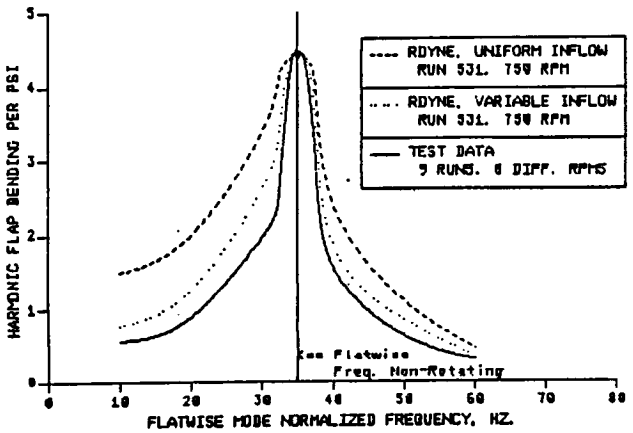

Figure 6 - Effects of Higher Harmonic Blowing on Amplitude of Flatwise Bending Moment in Hover

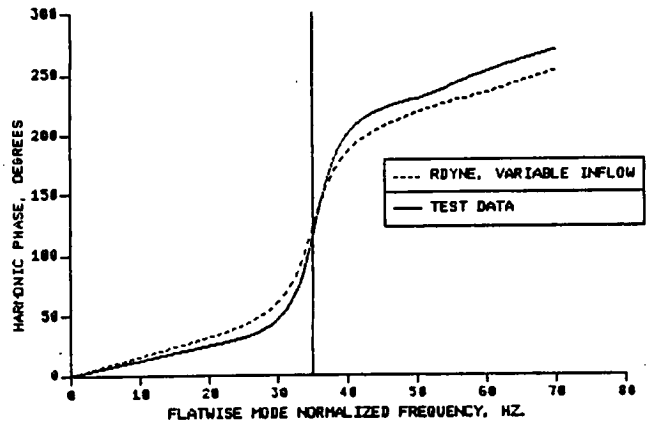

Figure 7 - Effects of Higher Harmonic Blowing on Phase of Flatwise Bending Moment in Hover

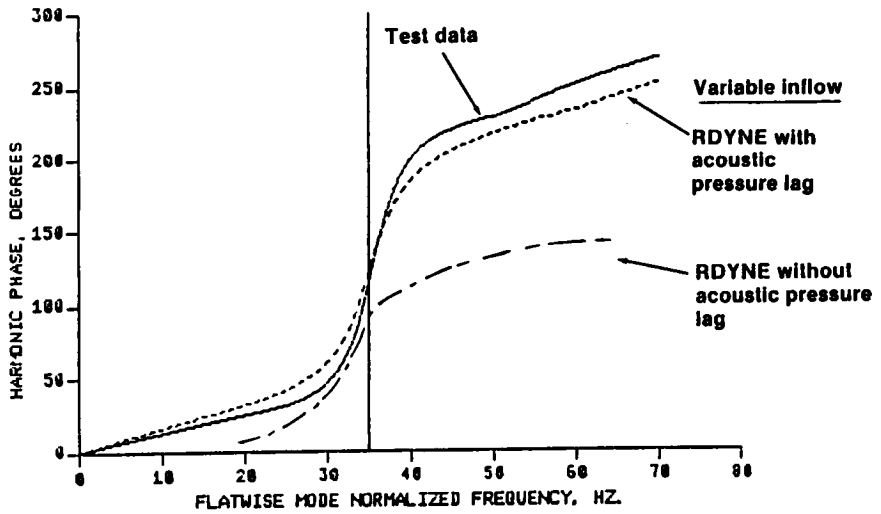

Figure 8 - Effects of Accoustic Pressure Lag on Phase Angle of Flatwise Bending Moment Response to Blowing Harmonic in Hover

TRANSITION FLIGHT

The RDYNE analysis satisfactorily predicts rotor lift (figure 9) and torque (figure 10) in the transition flight region, where the X-Wing has to achieve steady level flight. The CHI angle had little effect on the prediction of rotor lift and rotor torque, but clearly demonstrates that the prediction of the hub steady pitching moment is controlled by the selection of CHI (figure 11). The results showed that good agreement in steady hub pitching moment was obtained by reducing the empirical CHI angle as the airspeed is increased. This reduction brings the rotor wake vertically closer to the rotor, and causes an increase in the downwash in the rear portion of the disc. This in turn increased the hub pitching moment in the nose up direction.

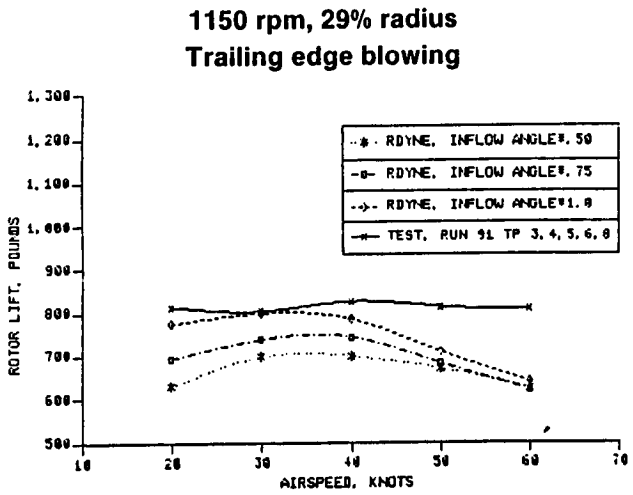

Figure 9 - Variation of Rotor Lift with Transition Airspeed

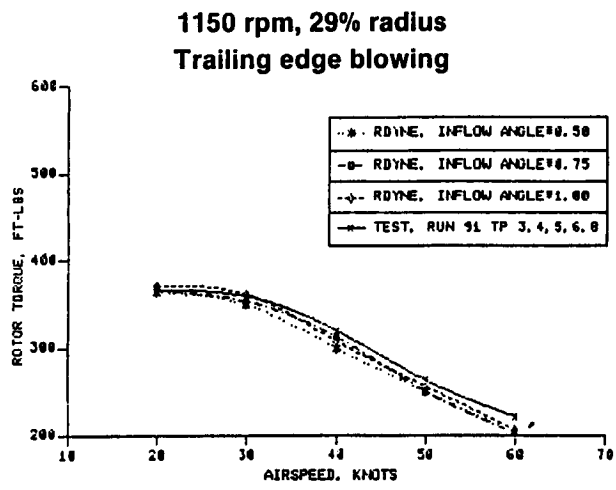

Figure 10 - Variation of Rotor Torque with Transition Airspeed

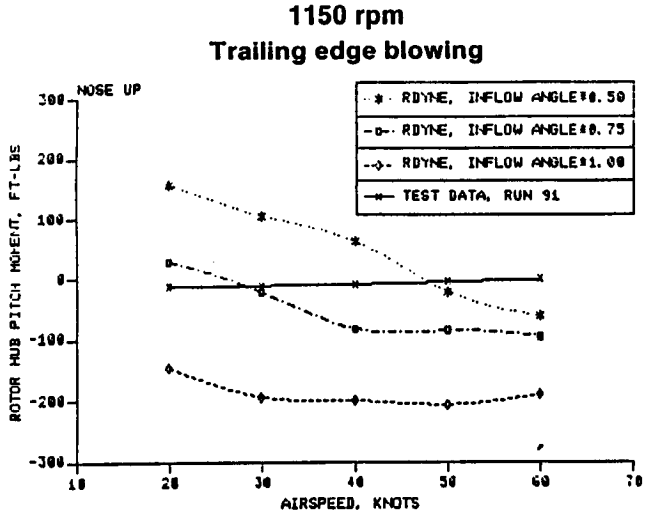

Figure 11 - Variation of Rotor Pitching Moment with Transition Airspeed

VIBRATORY LOADS AT FORWARD SPEED

Many of the comparisons of predicted vibratory loads are as good as comparisons for conventional rotors, and in some cases are better, indicating that a credible tool has been developed for predicting the vibratory loads on X-Wing rotors.

Figures 12 and 13 show the test and predicted blade flatwise bending moment versus blade azimuth at 100 and 120 knots. The overall 1/2 peak-to-peak response agreement is good and in general the time history agreement is fair. At 150 knots (figures 14 and 15) the 1/2 peak-to-peak response agreement is still good and at the same time significant improvement in the predicted harmonics occurred. The bar charts in figure 15 clearly illustrate the excellent prediction achieved at 150 knots with variable inflow. The chart shows steady, vibratory and the first five harmonics of blade flatwise moment. The vibratory and harmonic bending moments matched almost exactly, while the steady prediction is poor. However, this 40 percent underprediction of steady moment may not represent poor predictive ability since the prediction of rotor lift was within ten percent of the measured value. In general, it is normal for measurement of steady blade bending moments to be less reliable than the vibratory moments. Also shown on the bar chart is the RDYNE prediction using uniform inflow. At this airspeed the prediction of vibratory load and all the harmonics improves with incorporation of variable inflow.

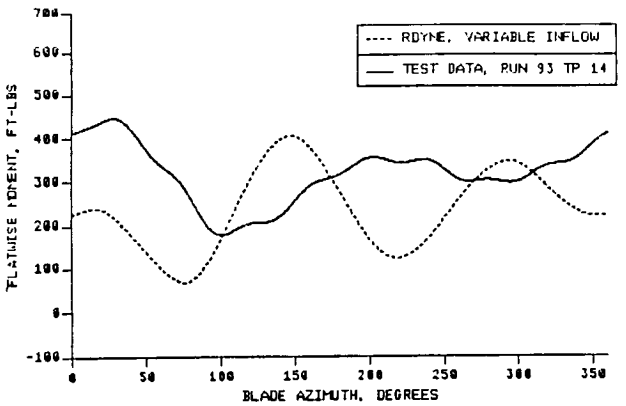

Figure 12 - Effect of Forward Speed on Flatwise Bending Moment at 100 Kn

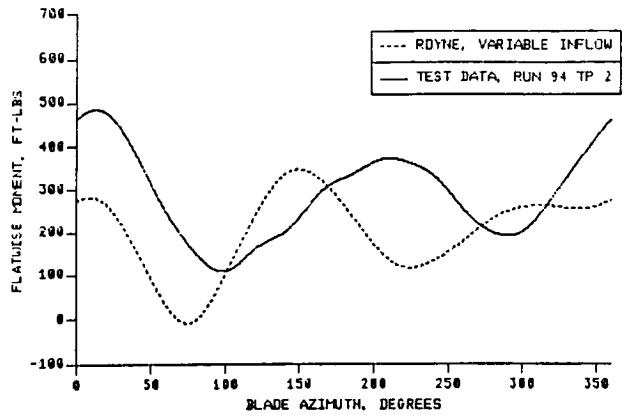

Figure 13 - Effect of Forward Speed on Flatwise Bending Moment at 120 Kn

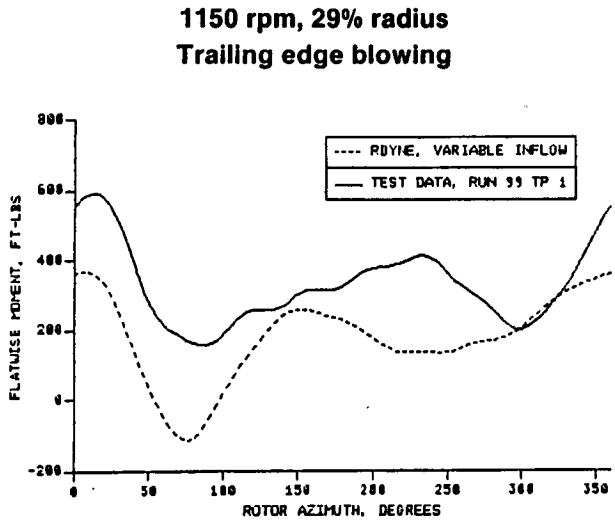

Figure 14 - Effect of Forward Speed on Flatwise Bending Moment at 150 Kn

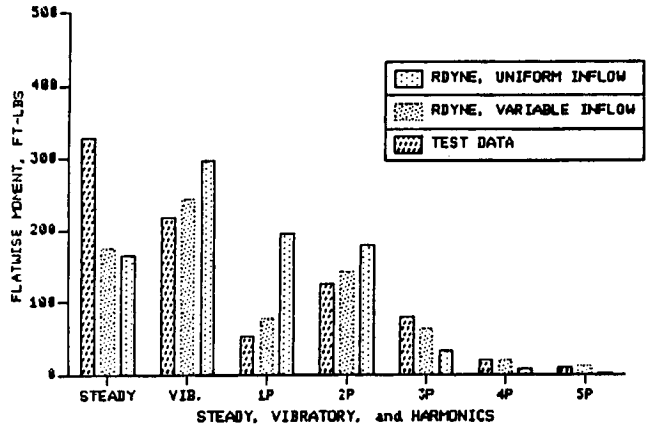

Figure 15 - Harmonic Content of Flatwise Bending Moment at 150 Kn

At the same flight condition of 150 knots, similar time history plots and bar charts are shown for edgewise blade bending moments and push rod loads. Again, both uniform and variable inflow results are shown for comparison. Figures 16 and 17 show that the agreement is quite good. The bar chart demonstrates that the variable inflow compared to the uniform inflow significantly improves the prediction of the vibratory load and all the harmonics of blade edgewise response. In general this edgewise comparison of harmonics is better than a majority of comparisons for conventional rotors.

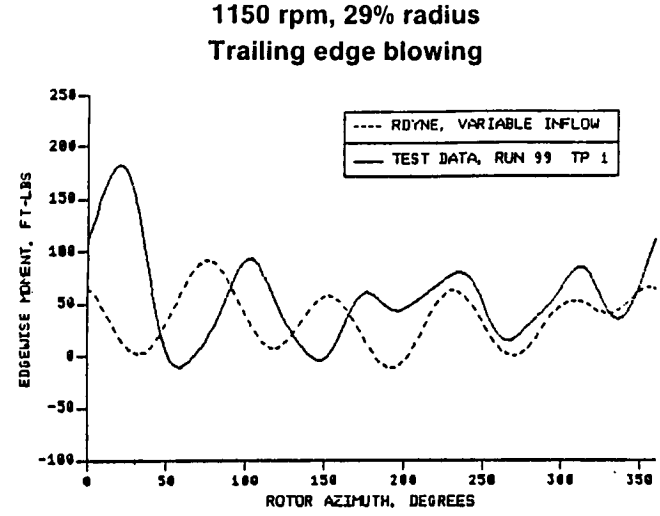

Figure 16 - Edgewise Bending Moment at 150 Kn

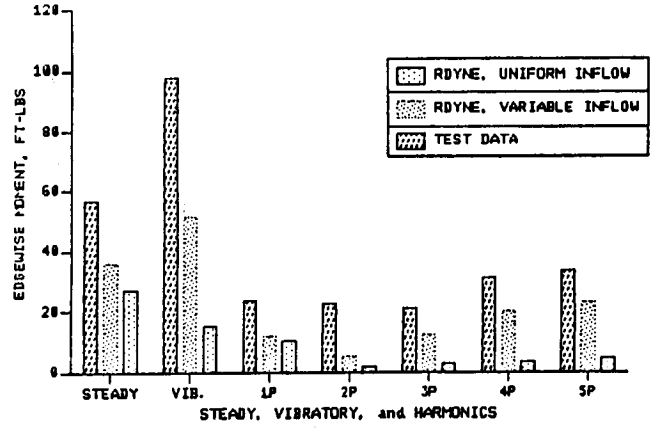

Figure 17 - Harmonic Content of Edgewise Bending Moment at 150 Kn

Figures 18 and 19 show the push rod comparison (derived from the torsional response of the blade). Again, agreement in the time history response and bar chart depicting harmonics of load is quite good. The comparison of variable and uniform inflow shows that both inflows yield good predictions of vibratory and 1P push rod load, with variable inflow improving the prediction of the higher harmonics.

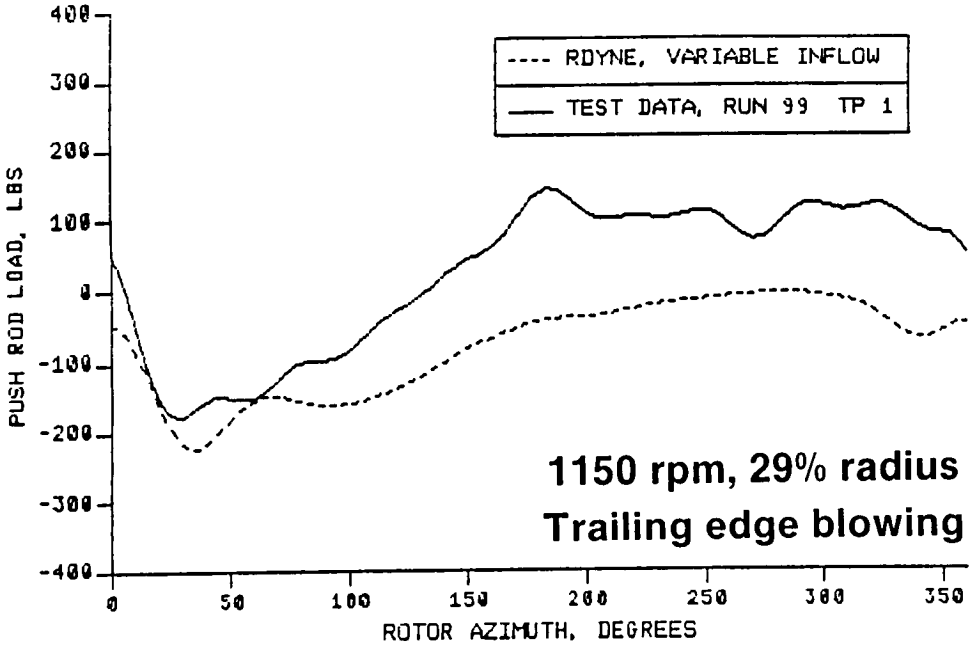

Figure 18 - Push Rod Load at 150 Kn

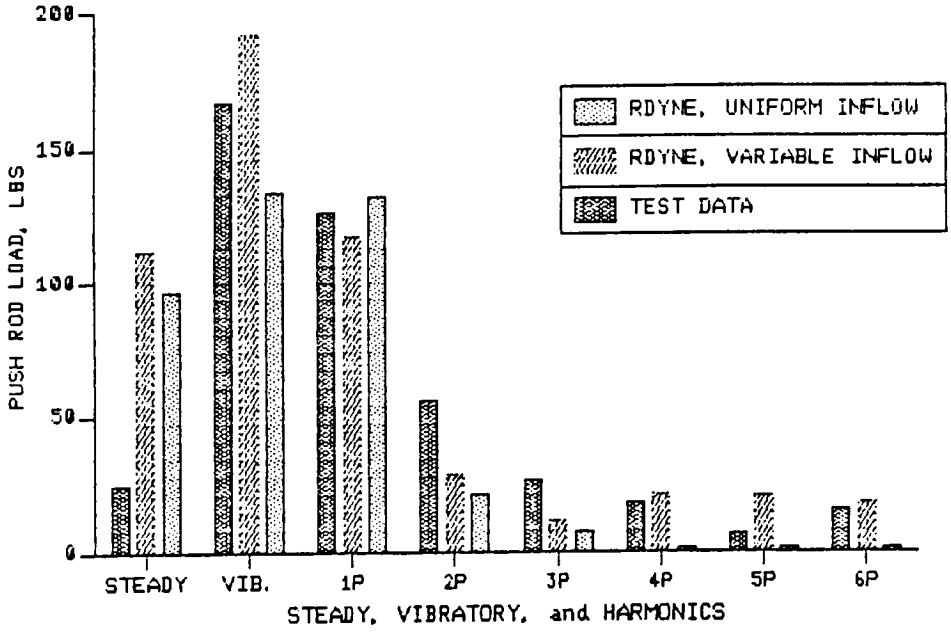

Figure 19 - Harmonic Content of Push Rod Load at 150 Kn

For the above conditions, figures 20 to 22 compare the variation of vibratory blade flatwise bending moments, edgewise bending moments, and vibratory push rod loads with increasing airspeed. Very close agreement was obtained by the RDYNE analysis with variable inflow for the vibratory (1/2 peak to peak) blade flatwise bending moment and the vibratory push rod load. For the edgewise moment, the analysis underpredicts the vibratory component by 50 to 75 percent. In general, the correlation of vibratory flatwise and push rod loads is as good as results obtained for conventional rotors (Arcidiacono and Sopher, 1982; Jepson et al, 1983).

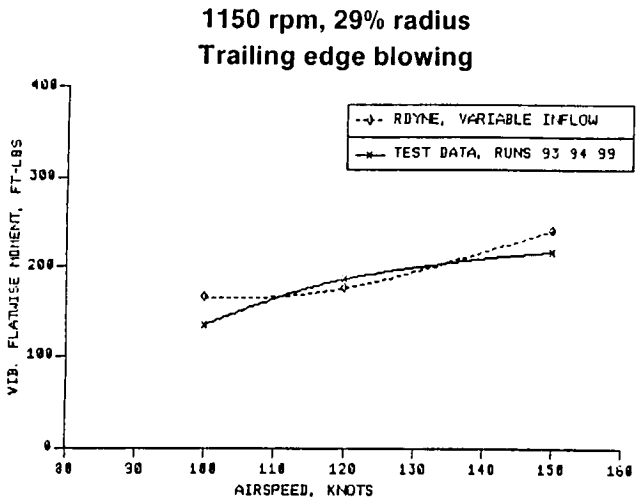

Figure 20 - Variation of Vibratory Flatwise Bending Moment with Airspeed

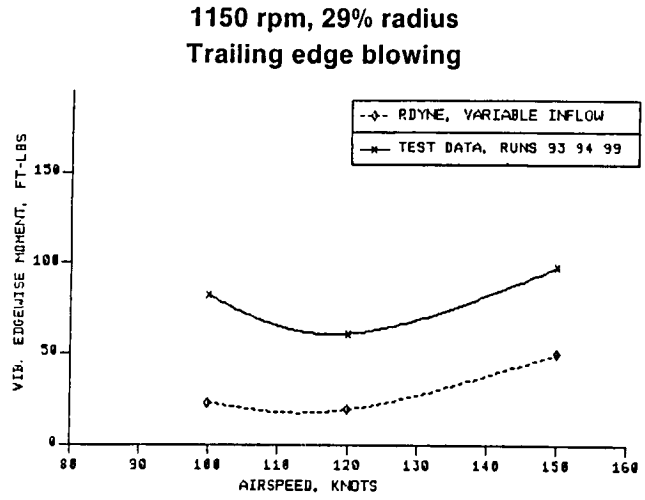

Figure 21 - Variation of Vibratory Edgewise Bending Moment with Airspeed

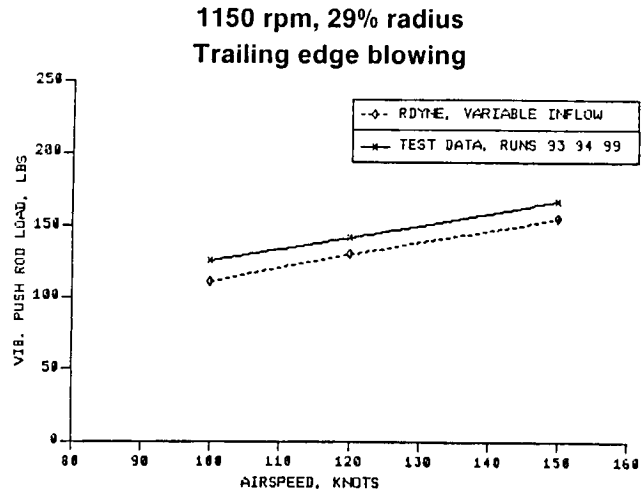

Figure 22 - Variation of Vibratory Push Rod Load with Airspeed

RESPONSES IN CONVERSION

The ability of the RDYNE analysis to predict vibratory blade loads and vibratory hub forces and moments during conversion is important to the design of an X-Wing rotor system. The vibratory levels will be the highest that the rotor will experience because the stopping of the rotor is done at high speed. The rotor system will experience the unique condition of being excited by airloads while the blade bending modes pass through resonance. This is a condition that conventional rotors are designed to avoid to minimize blade and hub loads.

Overall, the agreement in vibratory levels (figures 23 and 24) is good. The predicted thrust shows the same trend in mean values with decreasing rotor speed as the test data. Also the prediction of the mean thrust shows good agreement. The predicted maximum vibratory thrust occurs at approximately the same rotor speed as the test data but its level is underpredicted by 50 percent. The blade flatwise vibratory and steady levels show good agreement but the agreement in rotor speed at the point of maximum blade response cannot be clearly defined since the predicted moment does not show any distinct peaks. These peaks are clearly evident in the time histories of the hub roll and pitch moments for both the test data and the analysis. The predicted peaks are at a lower rotor speed (later time) than the test data. The predicted flatwise blade natural frequency versus rotor speed shown in figure 2 indicates that the test peaks occur at exactly the rotor speed for which the blade mode crosses a harmonic of rotor RPM. However, the analysis shows that the maximum response occurs just after passing through a harmonic of rotor speed (approximately 0.5 second lag) which is typical for a dynamic system being excited by a force with a decreasing frequency. The predicted increase in steady hub roll moment as the rotor slows down was expected due to the lack of an analytical closed loop hub moment control. The predictions of the maximum hub vibratory moments were in close agreement for the pitch direction and showed a slight underprediction for the roll direction.

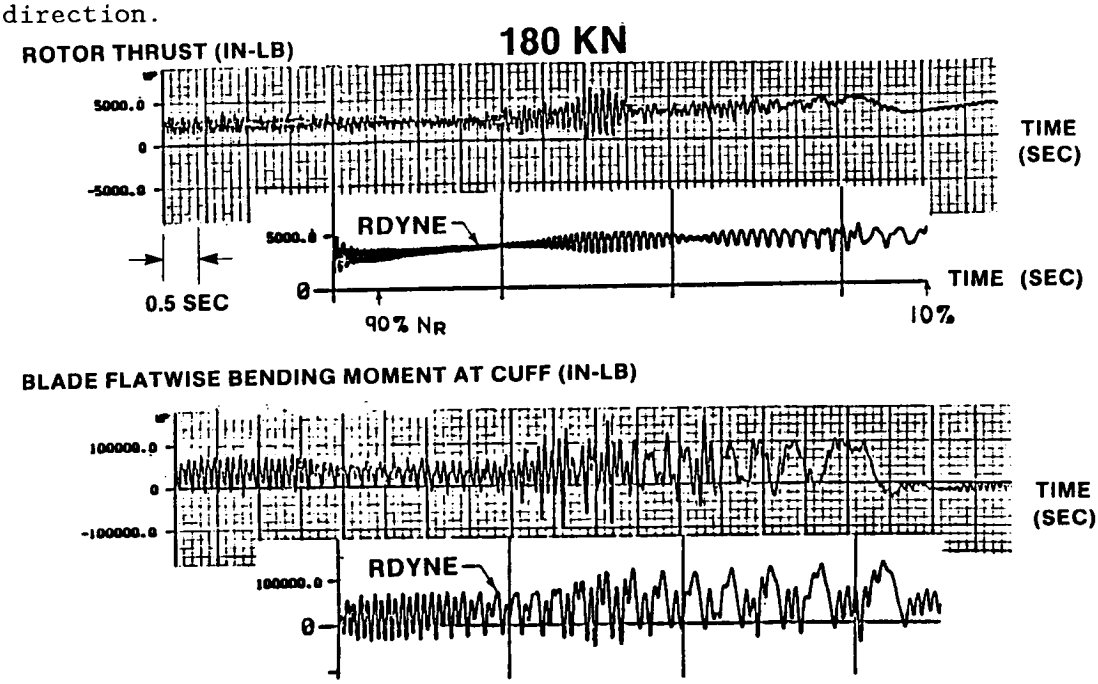

Figure 23 - Variations with Time of Rotor Thrust and Flatwise Bending Moment for Lockheed Rotor in Conversion

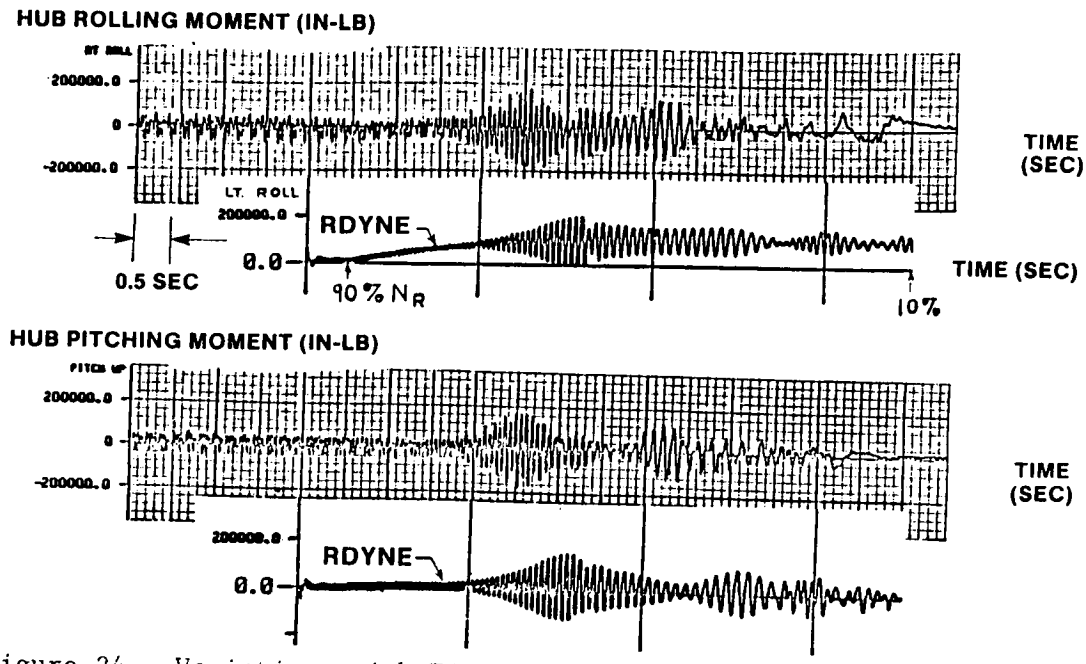

Figure 24 - Variations with Time of Rotor Hub Moments for Lockheed Rotor in Conversion

CONCLUSIONS

The RDYNE analysis was used to predict the aeroelastic responses of a representative X-Wing model with a 10 ft diameter rotor tested in the Boeing-Vertol Wind Tunnel. A small number of predictions were also made for a Lockheed X-Wing with a 25 ft diameter rotor tested in the NASA Ames 40 x 80 ft Wind Tunnel. Comparisons with test results indicate that the analysis is able to give satisfactory predictions of aeroelastic responses in X-Wing flight regimes.

For the Boeing-Vertol model, basic control power effects relating first harmonic blowing control inputs to steady hub loads, analogous to control relationships for mechanically controlled rotors, are predicted accurately in hover. The analysis is able to accurately predict the effects of higher harmonic blowing on blade bending moments, and shows potential for enabling rotors to be designed for reduced vibrations. Forward flight vibratory bending moments showed fairly good agreement with test data, and were as good as comparisons for conventional rotors. The comparisons of vibratory flatwise and push rod loads were better than results obtained for conventional rotors.

Good agreement between analysis and test was achieved for the Lockheed rotor in conversion flight for variations with time of rotor thrust, blade flatwise bending moment, and hub rolling and pitching moments at 180 knots with the rotor slowed from 90% NR to a stopped condition. The correlations establish the ability of the analysis to represent vibratory and steady responses for a mode of flight which is important to the design of the X-Wing.

Refinements which were identified as leading to significant improvements were variable rotor induced flow and acoustic pressure wave delays in the pneumodynamic model. Variable inflow improved the predictions of vibratory loads in forward flight and the amplitudes of vibratory bending moment responses to higher harmonic blowing in hover. Acoustic pressure wave delays significantly improved the predicted phase responses of blade bending moments to higher harmonic blowing in hover.

REFERENCES

Arcidiacono, P.J.: Prediction of Rotor Instability at High Forward Speeds - Volume 1 - Steady Differential Equations of Motion for a Flexible Helicopter Blade with Chordwise Mass Unbalance, USAAVLABS TR 68-18A, February 1969.

Arcidiacono, P.J., and Sopher, R.: Review of Rotor Loads Prediction Methods, AGARD Conference Proceedings No. 334, London, England, May 1982.

Jepson, D., Moffitt, R., Hilzinger, K., and Bissell, J.: Analysis and Correlation of Test Data from an Advanced Technology Rotor System, NASA CR 3714, August 1983.

Landgrebe, A.J., and Egolf, T.A.: Rotorcraft Wake Analysis for Prediction of Induced Velocities, USAAMRDL TR 75-45, 1976.

Reader, K.R., and Dixon, William J., Jr.: Evaluation of a 10-Foot Diameter X-Wing Rotor, Proceedings of the 40th Annual Forum of the American Helicopter Society, Arlington, Virginia, May 1984.

Sopher, R., and Hallock, D.W.: Time-History Analysis for Rotorcraft Dynamics Based on a Component Approach, Journal of the American Helicopter Society, Vol. 31, No. 1, January 1986, pp. 43-51.

X-WING POTENTIAL FOR NAVY APPLICATIONS

Arthur W. Linden
Sikorsky Aircraft

and

James C. Biggers
Department of the Navy

David Taylor Naval Ship Research and Development Center

(No paper received; presentation material only)

SUMMARY

X-Wing Potential For Navy Applications

Arthur W. Linden
Engineering Manager, RSRA/X-Wing
Sikorsky Aircraft Division
United Technologies

James C. Biggers
Head, Rotorcraft Division
David Taylor Navy Ship R&D Center

The X-Wing will provide a VTOL Aircraft which has a low disc loading hover capability, similar to a conventional helicopter, combined with a high subsonic cruise speed capability. As a result, it will hover with low fuel flow rates which make extended hover duration missions practical. Its low hover power requirements also permit hovering and low speed flight on only one engine in a high speed twin-engine aircraft design.

The NASA/DARPA/Sikorsky RSRA/X-Wing program is developing flightworthy X-Wing hardware. The program has now completed all design activity and the majority of its component fabrication. Three key development tests activities are underway: the full size Propulsion System Test Bed, the Vehicle Management Systems Laboratory, and the Powered Wind Tunnel Model. The first flight is scheduled for October 1986.

A design study has been performed on an X-Wing Concept Demonstrator Aircraft which is based on the RSRA/X-Wing components, combined with two MTE engines and a new fuselage. The resulting aircraft has a 51-foot rotor diameter, weights 24000 pounds, and has a cruise speed of 400 knots.

Potential Navy mission take advantage of X-Wing's low disc loading and high speed capability. Missions include ASW, AEW, Forward Pass, and SAR. The logical evolution of the X-Wing concept is from the RSRA program to a Concept Demonstrator Program to a Production Aircraft.

X-WING POTENTIAL FOR NAVY APPLICATIONS

Arthur W. Linden
Engineering Manager, RSRA/X-Wing
Sikorsky Aircraft

James C. Biggers
Head, Rotorcraft Division
David Taylor Naval Ship R&D Center

HOVER DISC LOADING vs. MAX SPEED

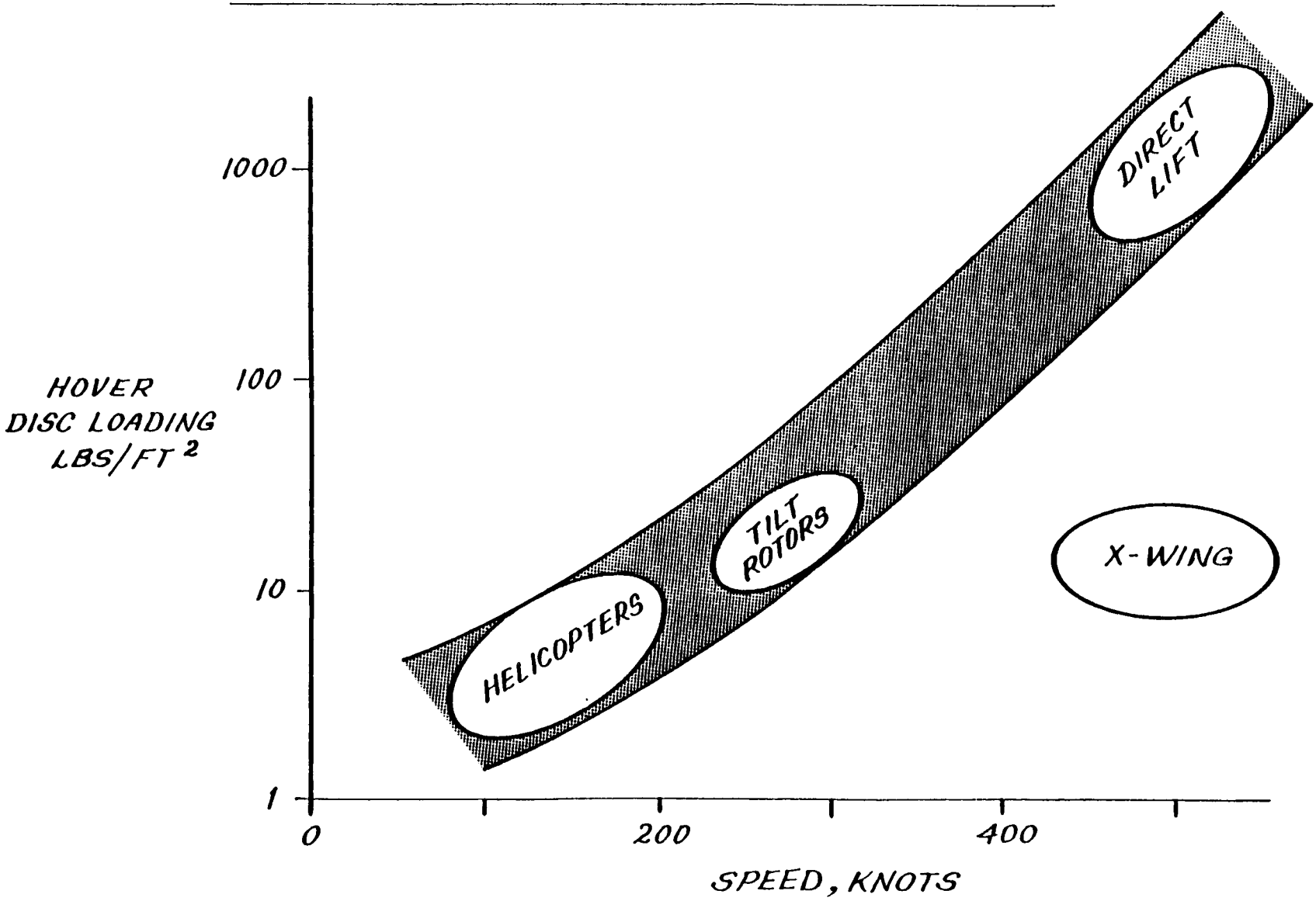

MAXIMUM THRUST PER HORSEPOWER

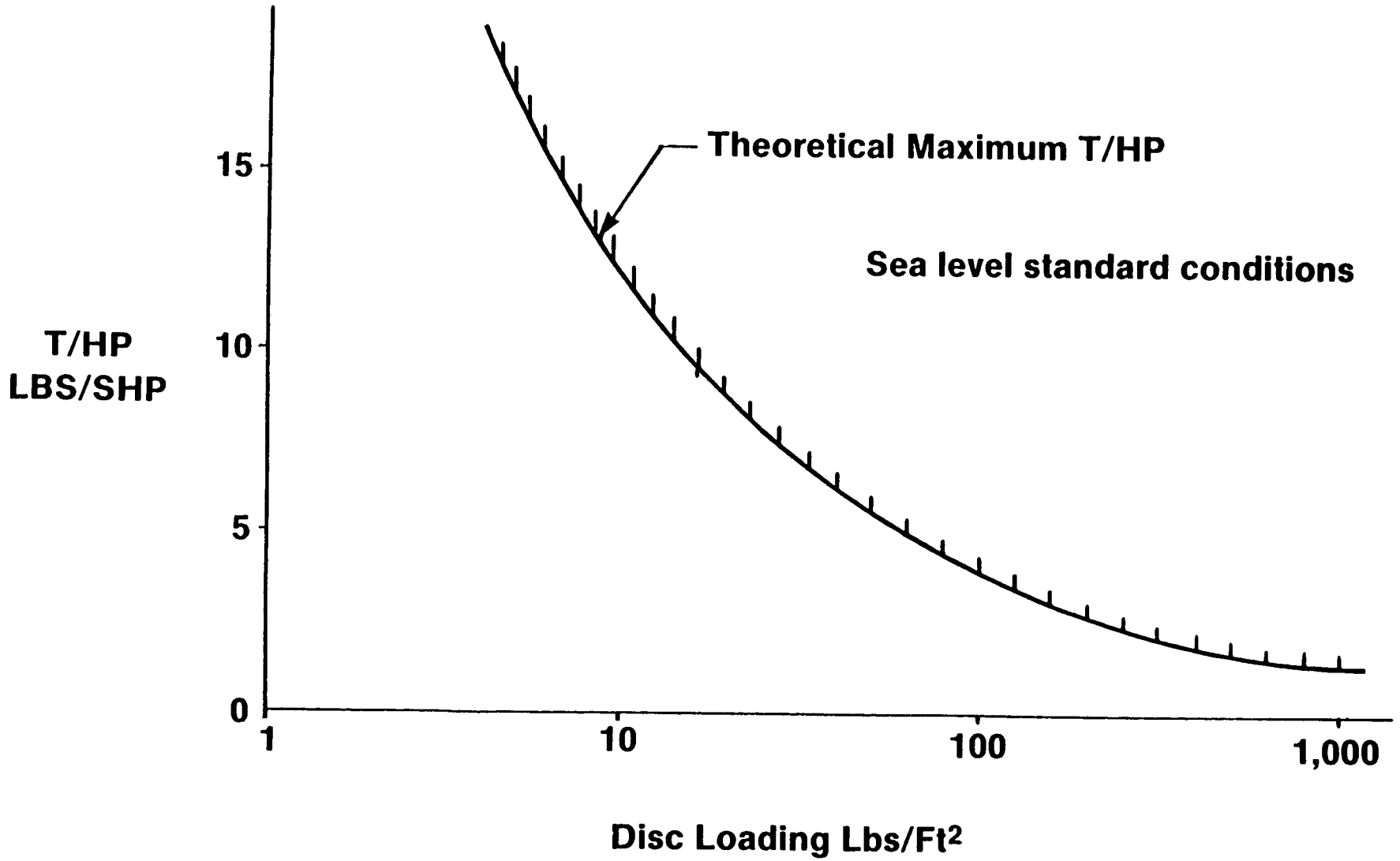

VTOL AIRCRAFT FUEL FLOW

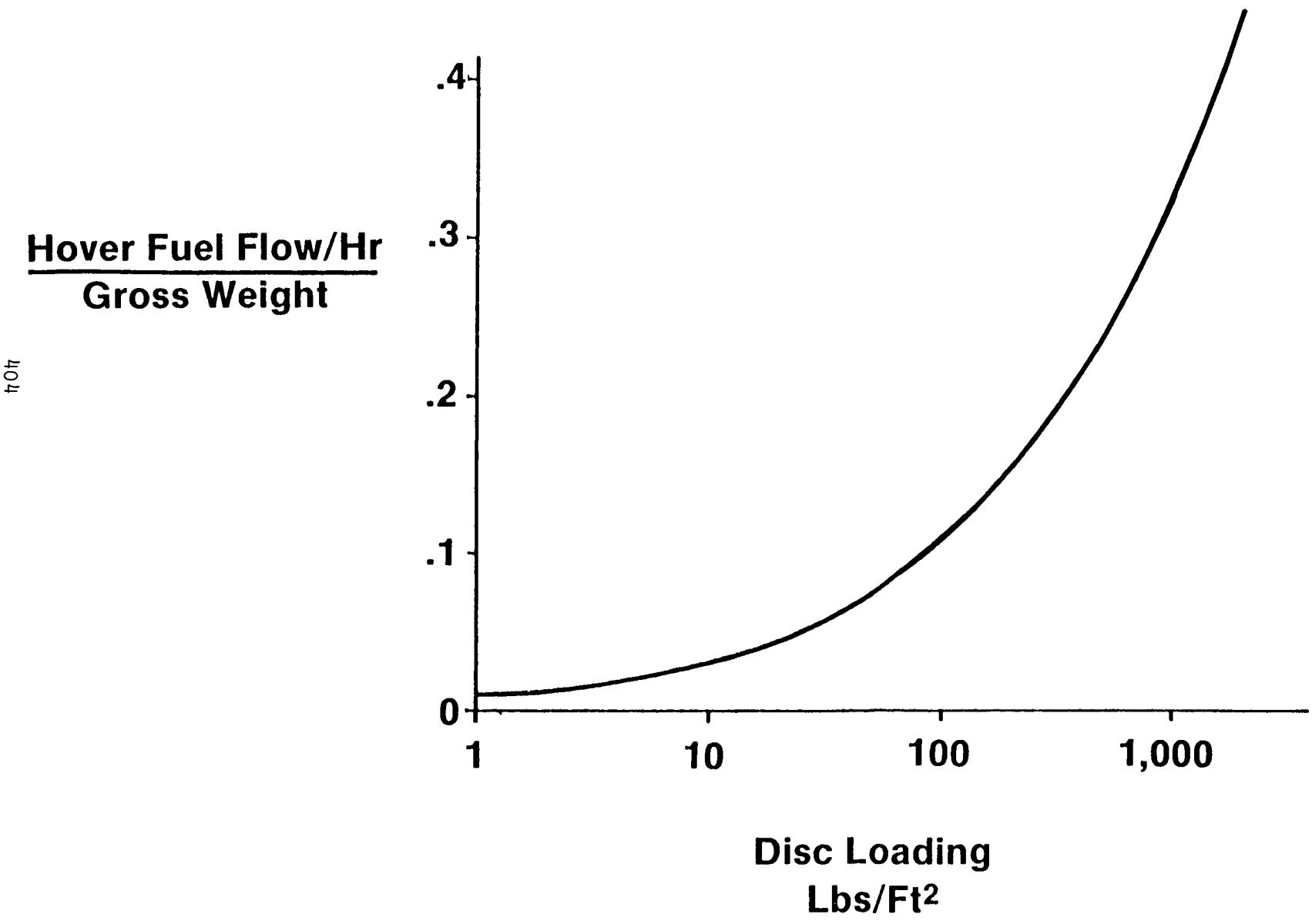

POWER REQUIRED: DIRECT LIFT VTOL

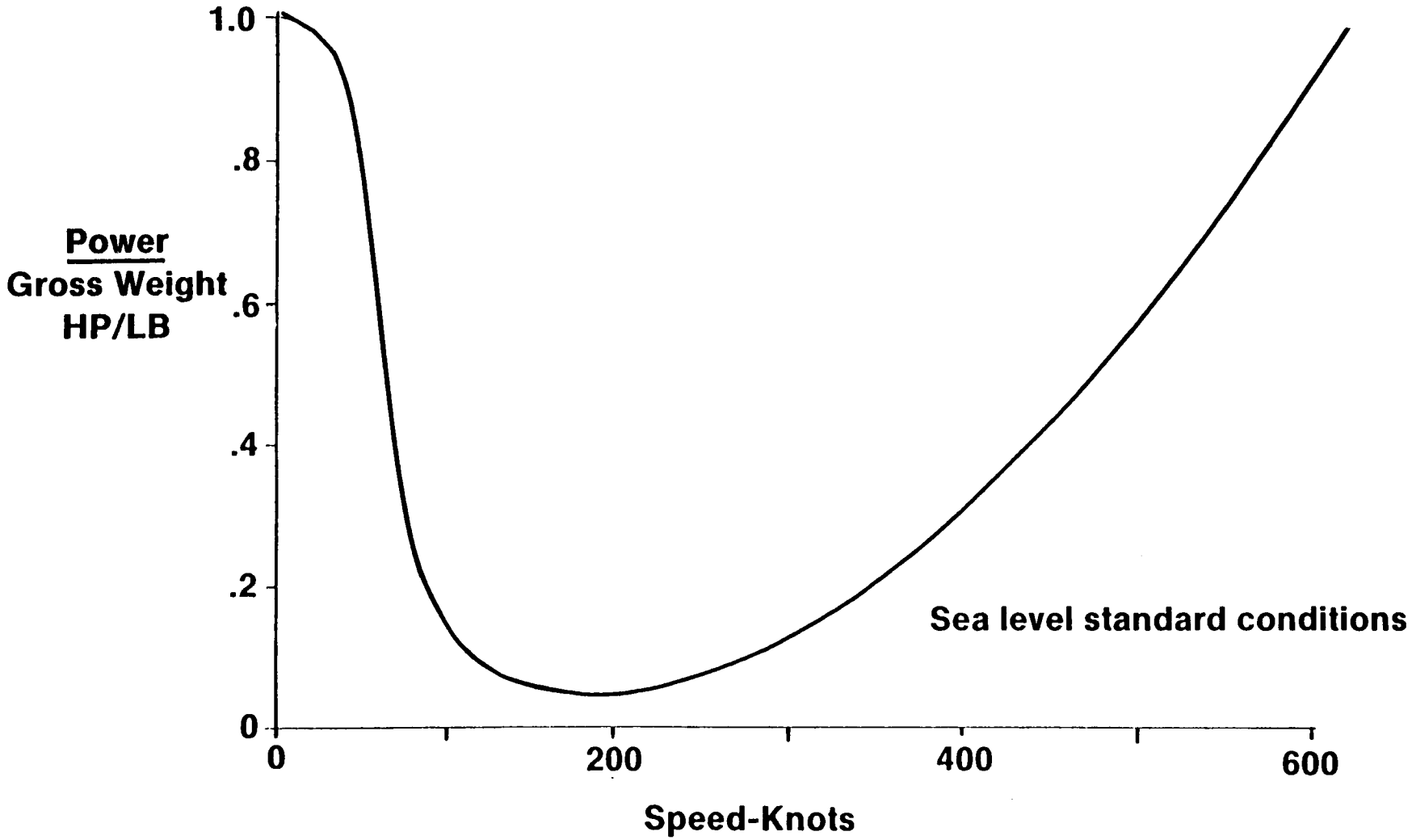

POWER REQUIRED: X-WING

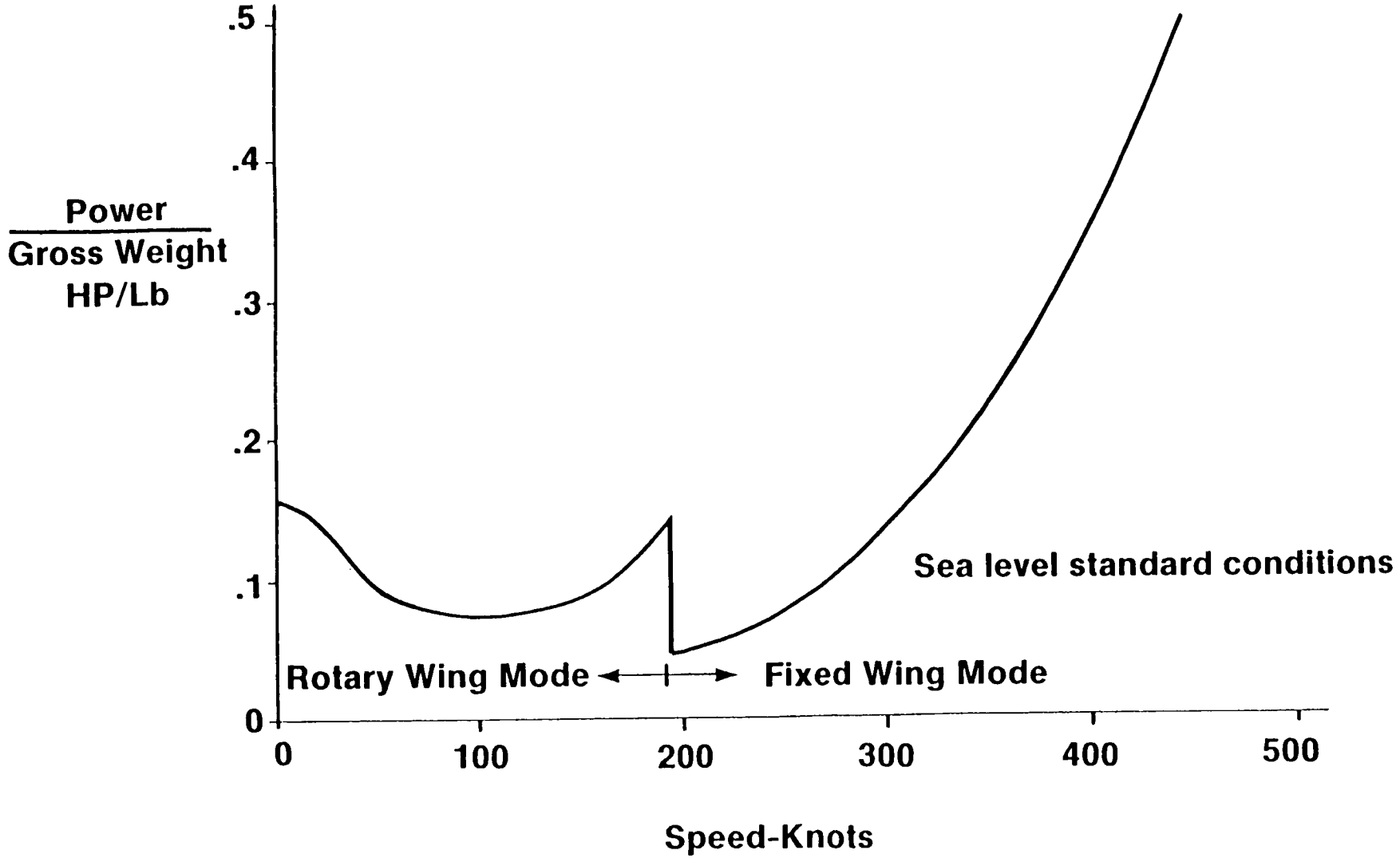

RSRA/X-WING FLIGHT DEMONSTRATOR

Program Objectives

- Demonstrate key advanced X-Wing technologies in flight
  - Stiff, bearingless, stoppable, composite rotor
  - Quad redundant full authority fly-by-wire control system
  - Circulation control rotor and pneumodynamic system
- Low risk approach provided by RSRA
  - RSRA wing shares lift with X-Wing
  - RSRA auxiliary jets provide propulsive force

RSRA/X-WING PROGRAM SCHEDULE

ROTOR/WING

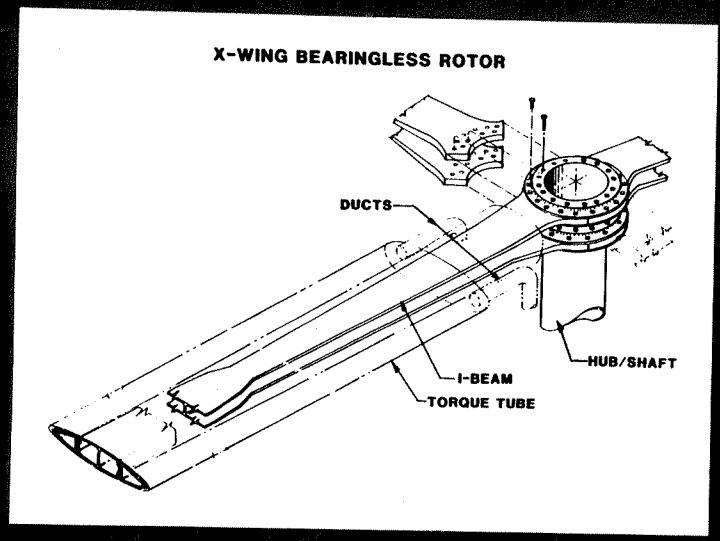

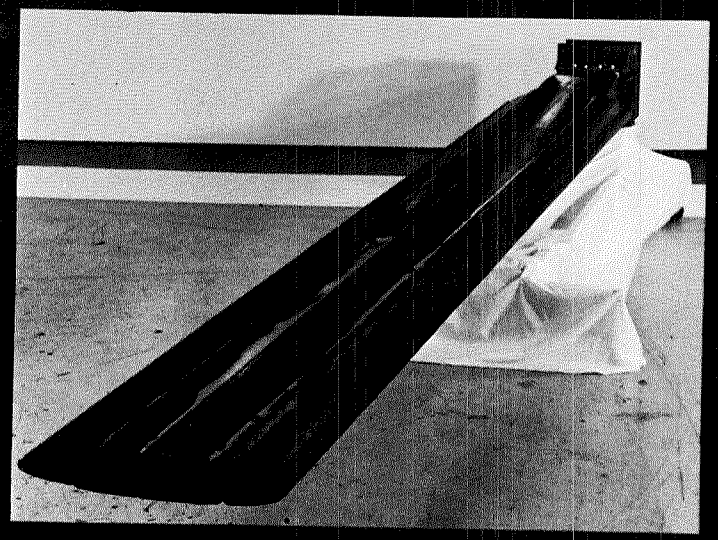

- Stoppable in flight
- Bearingless
- Circulation control aerodynamics
- Composite construction

PNEUMODYNAMIC SYSTEM

- Full rotor cyclic control
- Partial rotor collective control
- Higher harmonic control
- Hub moment feedback

PROPULSION SYSTEM TEST BED

Purpose: Develop full-size flight hardware prior to flight

VEHICLE MANAGEMENT SYSTEM

- Full authority fly-by-wire
- Quad digital with multiprocessors
- Backup software

ORIGINAL PAGE IS
OF POOR QUALITY

VEHICLE MANAGEMENT SYSTEMS LABORATORY

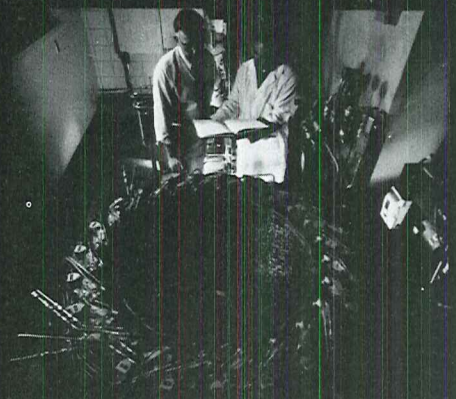

Purpose: Develop full authority fly-by-wire control system prior to flight

POWERED WIND TUNNEL MODEL

Purpose: Develop aerodynamics, dynamics, and pneumodynamics prior to flight.

1985 POINT DESIGN STUDY

- Based on RSRA/X-Wing component evolution
- 24,000 lb gross weight
- Two (2) MTE turboshaft engines

GROWING THREATS TO FLEET

- Quieter submarines
- Longer range anti-ship missiles
- Longer range "smart" torpedoes
- Improved modern surface ships
- New aircraft carriers
- Over-the-Horizon targeting HELOS

POTENTIAL NAVY APPLICATIONS (X-WING ON SMALL SHIPS)

- Anti-submarine warfare
- Airborne electronic warfare
- Forward pass
- Combat search and rescue

ANTI-SUBMARINE WARFARE

- Increase detection range
  - Small ship base ahead of fleet
  - Longer range vehicles
  - Dipping sonar
- Increase kill range
  - Ship-launched weapons
  - Airborne targeting
- Increase protective coverage
  - Operate from small combatants
  - Operate from cargo vessels
  - Operate from small shore bases

AIRBORNE ELECTRONIC WARFARE

- Increase detection
  - Small ship based ahead of fleet
  - Operate at high altitude
- Micro-Awacs with phased array radar
- Sensor suite for intelligence gathering
- Sensor and transmitter suite for jamming
- Common logistics major airframe components

FORWARD PASS

- Ship-launched weapons
  - Large payload
  - Longer range
- X-Wing airborne guidance
  - Mid-course corrections
  - Final guidance/targeting
- Allows lighter, longer-range X-Wing

COMBAT SEARCH AND RESCUE

- Long-range, high speed vehicle
  - Quicker rescue
  - Improved rescue survival
  - Less vulnerable
- Low downwash velocities
  - Low wind load on rescuees
  - Operation into unprepared fields
  - Precision hover over forest
- OEI capable
- Small-ship basing
  - Versatility
  - Further increased range

IMPACT OF NAVY APPLICATIONS

- Better protection of combatant fleet
- New protection for cargo fleet
- Offloads missions from carriers (CVs)
  - Increases space for fighter/attack
  - Reduces aircraft types on CV
    - Fewer shops
    - More space for spares
    - Improves logistics
- Vehicle family approach
  - Common major components
  - Minimum specialized systems

Fixed-Wing Technology and Other Concepts

PRECEDING PAGE BLANK NOT FILMED

REDUCTION OF TILT ROTOR DOWNLOAD USING CIRCULATION CONTROL

Fort F. Felker and Jeffrey S. Light
Aerospace Engineers
NASA Ames Research Center, Moffett Field, California

and

Robert E. Faye
California Polytechnic State University
San Luis Obispo, California

ABSTRACT

The effect of boundary-layer control blowing on the download of a wing in the wake of a hovering rotor was measured in a small-scale experiment. The objective was to evaluate the potential of boundary-layer control blowing for reducing tilt-rotor download. Variations were made in rotor thrust coefficient, blowing pressure ratio, and blowing slot height. The effect of these parameter variations on the wing download and wing surface pressures is presented. The boundary-layer control blowing caused reductions in the wing download of 25 to 55%.

NOMENCLATURE

A	rotor disc area, πR^2, m^2
C_T	rotor thrust coefficient, $T/\rho A V_{tip}^2$
c	wing chord, m
DL	wing download, N
h	blowing slot height, m
P	pressure, N/m^2
P_{atm}	atmospheric pressure, N/m^2
P_p	blowing slot plenum pressure, N/m^2
δP	differential pressure, $P-P_{atm}$, N/m^2

R	rotor radius, m
T	rotor thrust, N
x	wing chordwise location, m
z	distance between rotor and wing, m
ρ	air density, kg/m^3

INTRODUCTION

The hover performance of tilt-rotor aircraft is reduced by the adverse aerodynamic interference on the wing caused by the rotor wake. The wing is immersed in the rotor downwash, and this results in a vertical drag, or "download," on the wing. This download can be as large as 15% of the total rotor thrust (refs. 1 and 2). If this download could be reduced or eliminated, the hover performance of tilt-rotor aircraft could be significantly improved. Since the payload of a tilt rotor is typically 25 to 30% of the aircraft's gross weight, small changes in the wing download can have a large effect on the size of the payload. Some previous investigations of wing download in hover are reported in references 3-7.

Flow visualization studies have shown that the rotor wake separates from the wing at the leading and trailing edges. The separated flow below the wing has a lower pressure than the flow on the top of the wing, and a download results. If a means could be found to reduce or eliminate the flow separation, the pressure below the wing would be increased, and the download would be reduced.

It may be possible to delay or eliminate the flow separation at the wing leading and trailing edges with boundary-layer control technology. The wing used in this investigation had slots for upper-surface boundary-layer control blowing at the wing leading and trailing edges. The jets of air from these slots should remain attached to the airfoil surface because of the Coanda effect. If this high-energy boundary layer, caused by the blowing, delays or prevents the rotor downwash from separating from the wing leading and trailing edges, then the download will be reduced.

The dynamic pressure in the rotor wake is comparable to the disc loading of the aircraft, and is much lower than the free-stream dynamic pressure for typical circulation-control airfoil applications. Therefore, low mass flows will be required to achieve the required blowing momentum coefficients. Thus, the weight of the air supply system, and the power required to drive it, will be small compared to typical circulation-control systems. A net vehicle performance gain will be achieved if the reduction in download is greater than the weight of the air supply system plus the reduction in rotor thrust caused by the power lost to the air supply system.

This paper describes an experimental investigation into the reduction of wing download obtained with leading- and trailing-edge upper-surface blowing. Measurements were made of wing download, wing surface pressures, and boundary-layer control blowing pressure ratio. The effect on the wing download of rotor-thrust coefficient, blowing slot height, and blowing pressure ratio is presented.

DESCRIPTION OF TEST APPARATUS

The test was conducted at the Ames Outdoor Aerodynamic Research Facility, which consists of a 30-m square concrete pad, a below-ground-level frame for attaching model support struts, and an underground control room with a complete data acquisition system. The facility is remotely located from other buildings so that there is no aerodynamic interference (other than with the ground).

The rotor was a 0.16-scale model of the Sikorsky S-76 rotor system (fig. 1). The blades were dynamically and geometrically similar to Sikorsky S-76 blades, except that the model blades had rectangular tips instead of swept-tapered tips. Rotor system characteristics are summarized in table 1. The rotor plane was 2.86 rotor radii above the ground.

The rotor was installed on the Ames rotor test rig (RTR). A six-component, internal strain-gage balance was used to measure steady-state rotor forces and moments. Three single-axis load cells were installed between the RTR and its support stand to provide redundant measurements of the rotor thrust.

The rotor was operated with the rotor thrust down, and the wake of the rotor traveled up into the wing. The wing was mounted upside down on a model support system and balance to allow unobstructed flow between the rotor and the wing. Throughout this paper, references to the upper and lower surfaces of the wing refer to the normal upper and lower surfaces of the wing, and not the test setup (fig. 1). A sketch of the rotor and wing installation is provided in fig. 2. All of the data presented in this paper were obtained with the rotor axis at the center of the wing, and the wing fully immersed in the rotor wake. Thus the test configuration simulated the chordwise flow over the wing of a tilt-rotor aircraft, but did not simulate the spanwise flow or "fountain effect." The distance between the rotor and wing was 0.4 rotor radii throughout the test. This distance is representative of the XV-15 and V-22 tilt-rotor aircraft.

The wing used in this test had an airfoil section (fig. 3) similar to those used on an X-wing aircraft. The airfoil was symmetric about the half-chord line and had 5% camber. Airfoil coordinates from the leading edge to the mid-chord are presented in table 2. The wing had blowing slots at both the leading and trailing edges. The airflow through the slots was varied by either changing the slot height or by changing the air pressure in the two wing plenums. These plenums, one for the leading edge and one for the trailing edge, allowed the effect of differential blowing on the wing download to be tested. Wing forces and moments were measured using a six-component, internal strain-gage task balance. The wing was instrumented

with several rows of chordwise pressure taps. The wing geometry is outlined in table 3.

EFFECT OF BLOWING PRESSURE RATIO ON DOWNLOAD

The effect of the blowing pressure ratio on the wing download is shown in fig. 4. The pressure ratio is defined as the pressure in the blowing slot supply plenum, P_p, divided by atmospheric pressure, P_{atm}. The data shown in fig. 4(a) were obtained with the ratio of slot height to wing chord equal to 0.0014, and in fig. 4(b) the slot height to chord ratio was 0.0010.

Figure 4 shows that the download is steadily reduced by upper surface blowing as the blowing pressure ratio is increased to 1.06. As the pressure ratio is increased past 1.06, there is little further reduction in the download. The reduction in download caused by the upper-surface blowing is greatest at low thrust coefficients, although there is little effect of thrust coefficient on the download at thrust coefficients above 0.005 (fig. 4(b)). The ratio of the velocity in the upper-surface blowing to the rotor downwash velocity is higher at low thrust coefficients than at high thrust coefficients, and this accounts for the greater reduction in download at low thrust coefficients. The reduction in wing download caused by upper-surface blowing ranges from 54% at a thrust coefficient of 0.003 to 25% at a thrust coefficient of 0.009.

EFFECT OF BLOWING SLOT HEIGHT ON DOWNLOAD

For a given pressure ratio, the mass flow of the upper-surface blowing increases linearly with the blowing slot height. The weight of the air supply system, and the power required to operate it, are increased as the blowing mass flow is increased. Therefore, it is desirable to use the minimum slot height that will effectively reduce the download.

The effect of the blowing slot height on the download is shown in fig. 5. The slot heights tested ranged from 0.1% to 0.21% of the wing chord. The data shown in fig. 5 indicate that the slot height had little effect on the download. There was some reduction in the download as the slot height was increased from 0.1% to 0.21% of the wing chord, but the small reduction in download would not be likely to justify the 110% increase in mass flow associated with the larger slot height. Since the slot height does not have a significant effect on the download, future investigations of download reduction using upper-surface blowing should concentrate on slot heights of 0.1% of the wing chord or less, since the lower mass flow associated with the lower slot heights implies lower weight and less power for the wing air supply system.

The fact that the slot height has little effect on the download has some interesting implications. Apparently, the mass flow and momentum of the blowing jet are not important parameters. This is in contrast to what has been observed in other applications of the circulation-control concept (refs. 8 and 9). Normally, the momentum of the blowing jet is of fundamental importance. Also, the fact that the download is primarily controlled by the blowing pressure ratio means that the velocity of the blowing jet is an important parameter, whereas the ratio of the blowing jet velocity to the rotor downwash velocity is relatively unimportant, especially at high thrust coefficients. This effect will be discussed further in the section on wing surface pressures.

COMPARISON OF DOWNLOAD WITH ONE AND TWO BLOWING SLOTS

The wings on the XV-15 and V-22 tilt-rotor aircraft have flaps at the trailing edge, and it would be difficult to modify these aircraft to utilize upper-surface blowing at the trailing edge. However, it would not be difficult to incorporate boundary-layer control blowing at the leading edges of these aircraft, and it is therefore interesting to evaluate the effectiveness of the boundary-layer control blowing when it is applied only to the wing leading edge. This was simulated by blowing out of one slot on the test wing.

A comparison of the download measured with one and two blowing slots is shown in fig. 6. These data were obtained with the rotor thrust coefficient equal to 0.0086. The download was reduced about 26% when both slots were blowing and about 17% when only one slot was blowing. Thus 65% of the reduction in download obtained by blowing with two slots was obtained by blowing with only one slot. The cause of this phenomenon is not known. In any case it is clear that significant reductions in download can be obtained by blowing at the wing leading edge only, while using a conventional flap at the wing trailing edge.

WING SURFACE PRESSURES

Figures 7(a) and 7(b) show the wing surface pressures measured on the circulation-control wing with the upper-surface blowing off and on, respectively. These data were obtained with $z/R = 0.4$, and the slot height equal to 0.1% of the wing chord. Both slots were blowing when the data shown in fig. 7(b) were acquired. The wing surface pressures have been made nondimensional by dividing by the rotor disc loading (T/A).

The data obtained with the blowing off (fig. 7(a)) exhibit a large region on the upper surface of the wing where the pressure is approximately equal to the rotor disc loading, which indicates that the rotor downwash has been stagnated. The entire lower surface of the wing has constant, slightly negative pressure, which is characteristic of separated flow. The rotor downwash has clearly separated from the

wing at the leading and trailing edges. The asymmetry in the pressure distribution is probably caused by the swirl in the rotor wake, which is from the wing leading edge to the wing trailing edge at this wing station.

By comparing the data obtained with the upper-surface blowing on (fig. 7(b)) with that obtained with the blowing off (fig. 7(a)), the aerodynamic phenomena responsible for the reduction in download can be determined. The region of stagnated flow exists on the upper surface of the wing whether the blowing is on or off; however, this region is smaller when the blowing is on. In fact, there is a large region of negative pressure on the wing upper surface near the leading edge when the blowing is on. This negative pressure region extends well aft of the location of the blowing slot, which is located at 2.7% of the wing chord. This indicates that the blowing jet has locally entrained the rotor downwash, thereby reducing the size of the region of stagnated flow on the wing upper surface. The large region of negative pressure on the upper surface of the wing does not exist at the wing trailing edge. This phenomenon was probably caused by the asymmetry induced by the swirl velocity in the rotor wake.

The upper-surface blowing was originally intended to reduce the download by delaying or preventing the rotor wake from separating from the wing leading and trailing edges. The degree to which the blowing has accomplished this objective can be evaluated by comparing the pressures on the wing lower surface when the blowing is on and off. Figure 7 shows that the pressure on the lower surface of the wing was only slightly less negative when the blowing was on than when it was off. Thus, the use of boundary-layer control blowing has not proven very successful in preventing the rotor downwash from separating from the wing leading and trailing edges.

The magnitude of the reduction in download caused by the negative pressure on the upper surface and the increase in pressure on the lower surface was found by integrating the wing surface pressure data. The result was that the negative pressure on the upper surface of the wing was responsible for about two-thirds of the total reduction in download, and the increased pressure on the lower surface caused about one-third of the total reduction in download.

The pressure distribution on the wing when the blowing was off reveals that the attempt to reduce the download by preventing flow separation at the wing leading and trailing edges may have been misguided. About two-thirds of the download is caused by the large region of stagnated flow on the upper surface of the wing, and relatively little download is caused by the negative pressure on the lower surface (caused by flow separation). It seems unlikely that the pressure on the lower surface of the wing could be increased above atmospheric, so the potential for substantially reducing the download by increasing the lower surface pressure for this configuration is small. There is clearly more potential for reducing the download by minimizing the size of the stagnated flow region on the upper surface of the wing. The fact that the boundary-layer control blowing caused a substantial reduction in the pressure on the upper surface of the wing well aft of the blowing slot probably accounts for most of the download reduction caused by the blowing. This may explain why the download was sensitive to the velocity of the blowing jet,

and not to the momentum of the jet or the ratio of blowing jet velocity to rotor downwash velocity.

Future investigations of download reduction using this concept should investigate blowing slot locations on the upper surface of the wing that are farther from the leading or trailing edge than the 2.7% of chord that was tested here. It may be possible to increase the size of the negative pressure region on the wing upper surface caused by the blowing, and thereby obtain further reductions in the download.

CONCLUSIONS

A small-scale experiment was performed to evaluate the potential of upper-surface blowing for reducing the download on tilt-rotor aircraft. The test results have provided new insight into the mechanisms of wing download, and quantitative data on the effect of the upper-surface blowing on the wing download. Specific conclusions are:

1. Wing download is reduced by upper-surface blowing. The reduction in download ranged from 54% at low rotor-thrust coefficients to 25% at high rotor-thrust coefficients.

2. The blowing slot height has little effect on the download.

3. Significant reductions in download are obtained with only one blowing slot operational.

4. The surface pressure data indicated that about two-thirds of the reduction in download with upper surface blowing is caused by suction on the upper surface of the wing, and one-third of the reduction in download is caused by increased pressure on the lower surface of the wing.

REFERENCES

1. Felker, F. F.; and Light, J. S.: Rotor/Wing Aerodynamic Interactions in Hover. Proc. 42nd Annual Forum of the American Helicopter Soc., Washington, June 1986.

2. McCroskey, W. J.; Spalart, P.; Laub, G. H.; and Maisel, M. D.: Airloads on Bluff Bodies, with Application to the Rotor-Induced Downloads on Tilt-Rotor Aircraft. Vertica, vol. 9, no. 1, 1985, pp. 1-11.

3. Makofski, R. A,; and Menkick, G. A.: Investigation of Vertical Drag and Periodic Airloads Acting on Flat Panels in a Rotor Slipstream. NACA TN 3900, 1956.

4. McKee, J. W.; and Naeseth, R. L.: Experimental Investigation of the Drag of Flat Plates and Cylinders in the Slipstream of a Hovering Rotor. NACA TN 4239, 1958.

5. Marr, R. L.; Ford, D. G.; and Ferguson, S. W.: Analysis of the Wind Tunnel Test of a Tilt Rotor Powered Force Model. NASA CR 137529, 1974.

6. Clark, D. R.; and McVeigh, M. A.: Analysis of the Wake Dynamics of a Typical Tilt-Rotor Configuration in Transition Flight, Proc. 11th European Rotorcraft Forum, London, England, September 1985.

7. McVeigh, M. A.: The V-22 Tilt Rotor Large-Scale Rotor Performance/Wing Download Test and Comparison with Theory, Proc. 11th European Rotorcraft Forum, London, England, September 1985.

8. Ottensoser, J.: Two-Dimensional Subsonic Evaluation of a 15-percent Thick Circulation Control Airfoil with Slots at both Leading and Trailing Edges, David Taylor Naval Ship Research and Development Center, Report 4456, July 1974.

9. Wilkerson, J. B.; Reader, K. R.; and Link, D. W.: The Application of Circulation Control Aerodynamics to a Helicopter Rotor Model, Proc. 29th Annual Forum of the American Helicopter Soc. Washington, May 1973.

TABLE 1.- Small-Scale Rotor Characteristics

Radius, m	1.067
Chord, m	0.0629
Airfoils	SC1095/SC1095R8
Number of blades	4
Twist	-10° linear
Solidity	0.0751

TABLE 2.- Wing Airfoil Coordinates

x/c	y/c
Outside of Upper Surface: Starting at Slot	
0.0319	0.0530
0.0531	0.0668
0.0710	0.0716
0.0905	0.0794
0.1115	0.0871
0.1528	0.1002
0.1930	0.1109
0.2306	0.1194
0.2702	0.1269
0.3114	0.1333
0.3727	0.1403
0.4358	0.1447
0.5000	0.1461
Inside of Upper Surface: Starting at Slot	
0.0319	0.0522
0.0505	0.0585
0.0700	0.0615
Outside of Lower Surface: Starting at Leading Edge	
0.0000	0.0000
0.0113	-0.0314
0.0204	-0.0404
0.0324	-0.0472
0.0404	-0.0498
0.0541	-0.0530
0.0748	-0.0558
0.0916	-0.0576
0.1157	-0.0597
0.1550	-0.0621
0.1905	-0.0635
0.2358	-0.0647
0.2918	-0.0656
0.3507	-0.0661
0.4202	-0.0663
0.5000	-0.0664

TABLE 2.- Continued

x/c	y/c
Inside of Lower Surface: Starting at Leading Edge	
0.0000	0.0000
0.0112	0.0340
0.0218	0.0444
0.0324	0.0501
0.0401	0.0518
0.0507	0.0518
0.0613	0.0489
0.0736	0.0379
0.0802	0.0303
0.0934	0.0153

Table 3. Small-Scale Wing Characteristics

Span, m	1.60 m
Chord, m	0.447 m
Thickness/chord	0.2125
Twist, deg	0
Dihedral, deg	0
Camber/chord	0.05
Slot locations, x/c	0.027, 0.973
Leading edge radius, % chord	5.25
Locations of pressure taps, % semispan	13, 27, 53, 80, 93

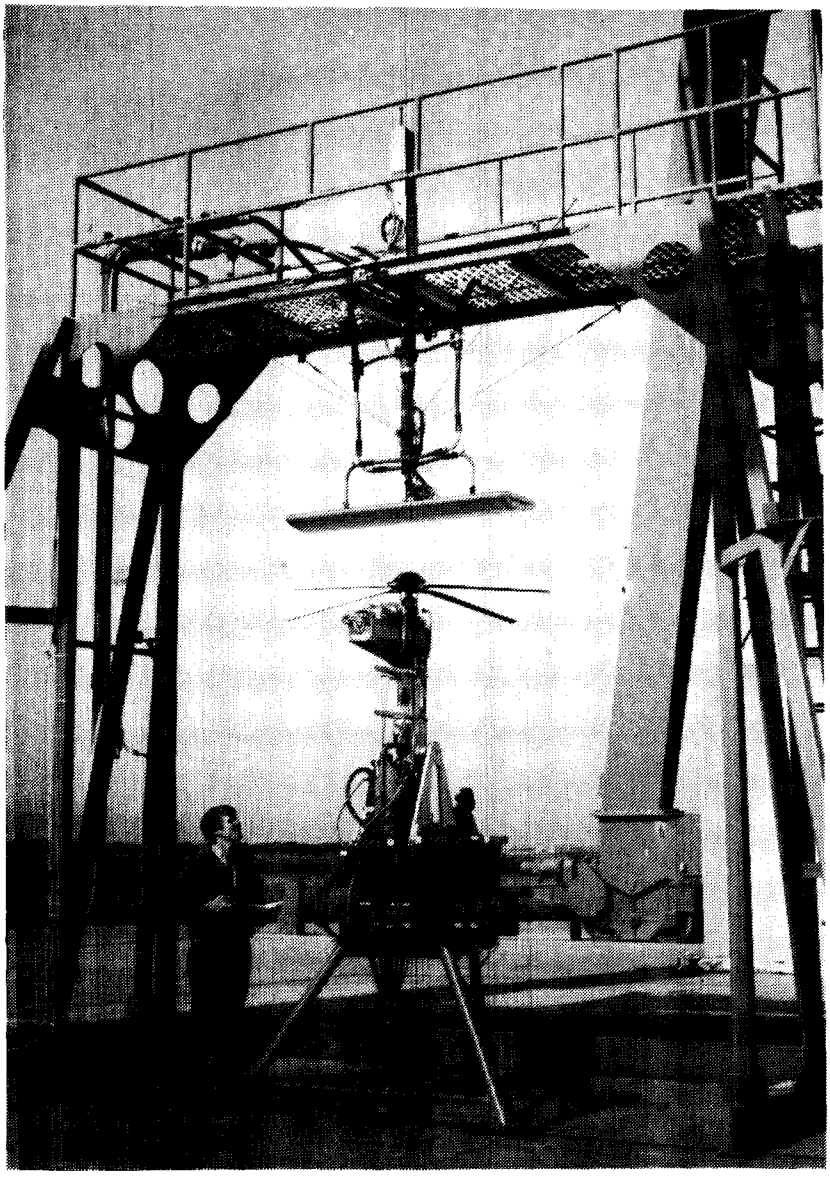

Figure 1.- NASA Ames Rotor Test Rig with circulation control wing.

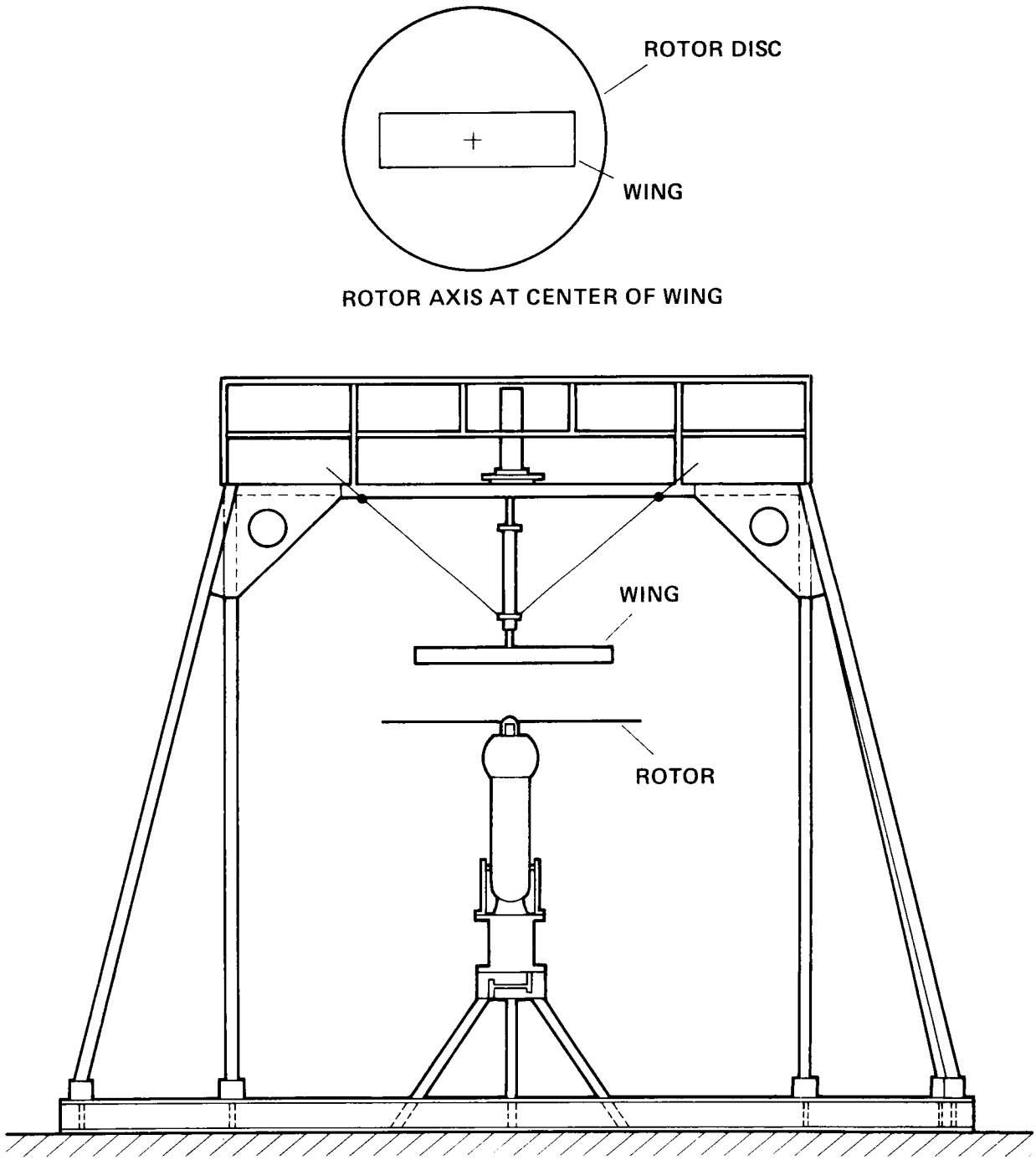

Figure 2.- Small-scale test configuration.

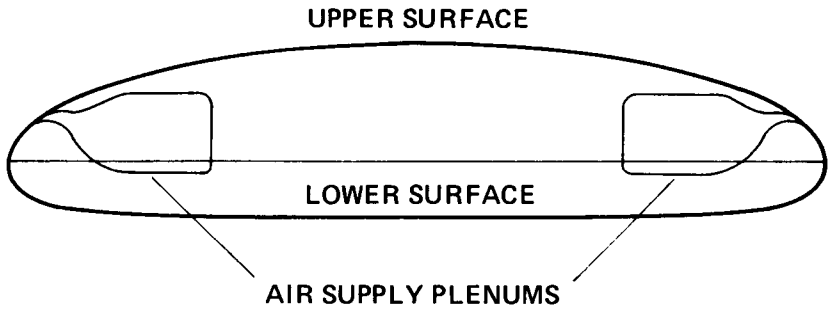

Figure 3.- Circulation control wing airfoil section.

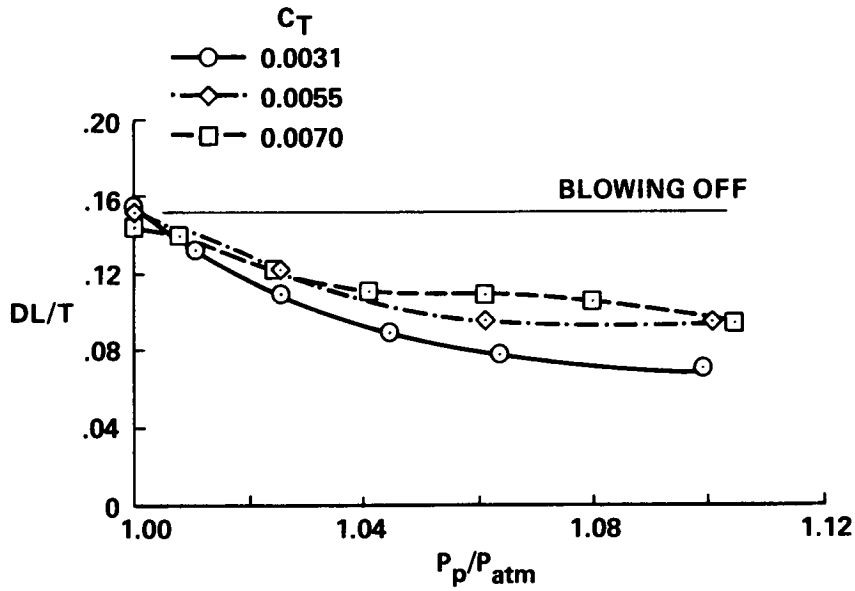

(a) h/c = 0.0014.

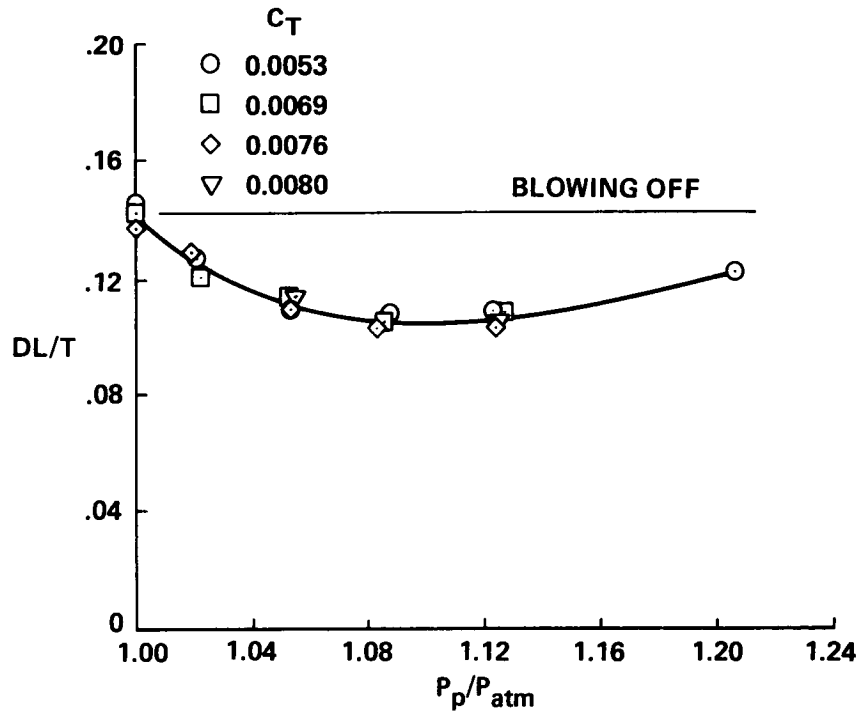

(b) h/c = 0.0010.

Figure 4.- Effect of blowing pressure ratio on download.

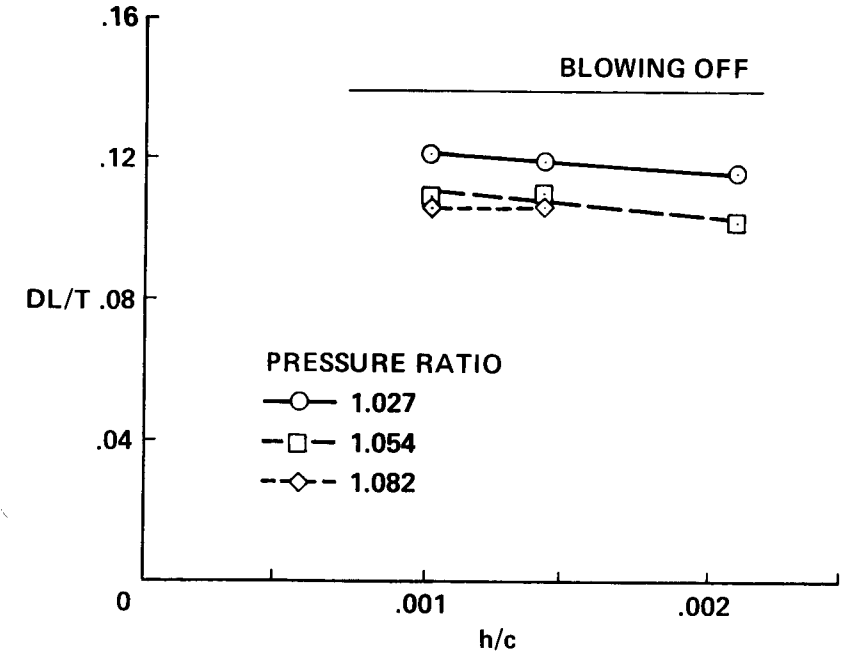

Figure 5.- Effect of blowing slot height on download.

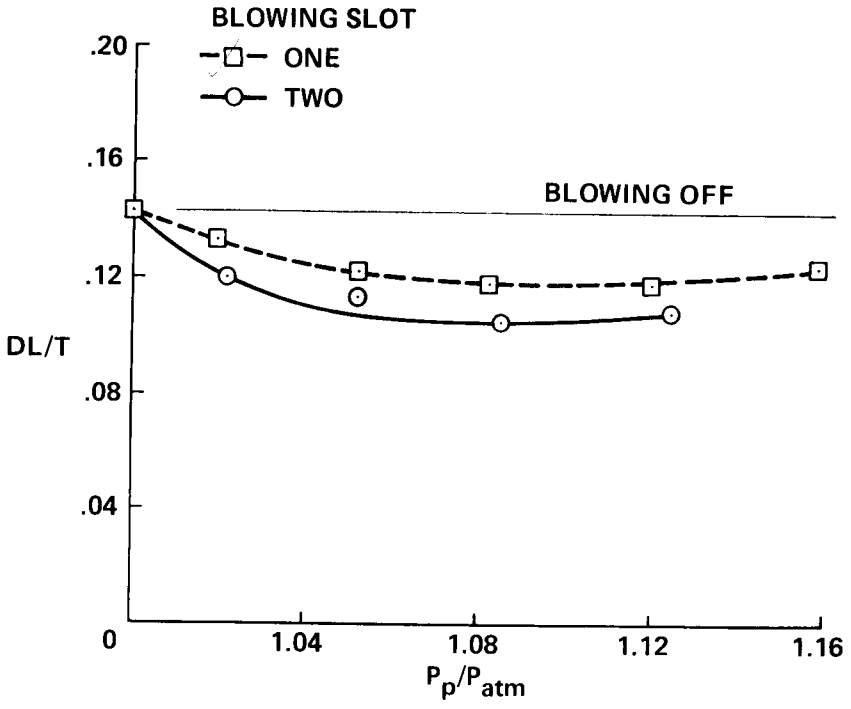

Figure 6.- Comparison of download with one and two blowing slots.

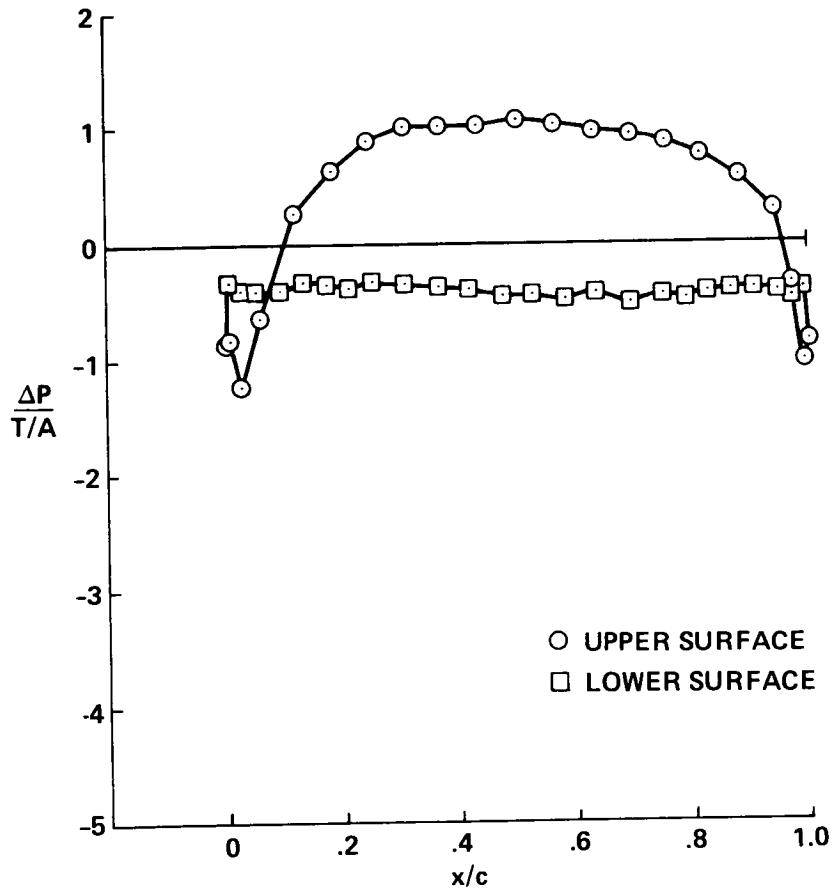

(a) blowing off, P_p/P_{atm} = 1.00.

Figure 7. Circulation control wing surface pressures.

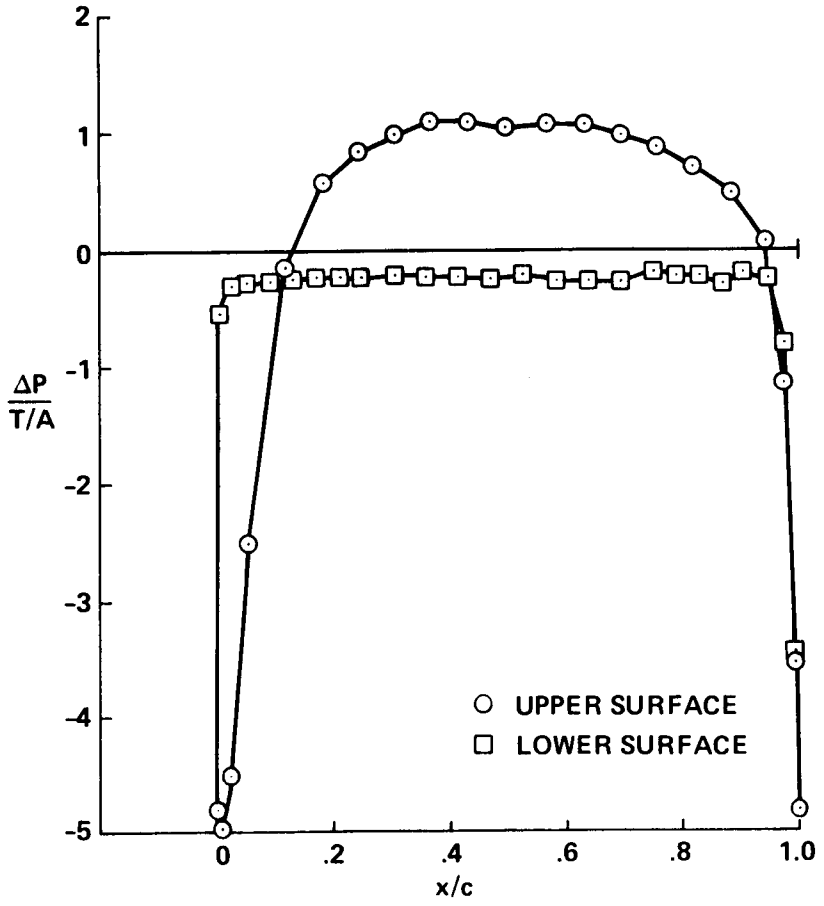

(b) blowing on, P_p/P_{atm} = 1.09.

Figure 7. Concluded.

AN AERODYNAMIC COMPARISON OF BLOWN AND MECHANICAL HIGH LIFT AIRFOILS

John E. Carr
Grumman Aerospace Corporation

ABSTRACT

Short Takeoff and Landing (STOL) performance utilizing a circulation control airfoil was successfully demonstrated on the A-6/CCW in 1978 (Pugliese, 1979). Controlled flight at speeds as slow as 67 knots was demonstrated. Takeoff ground run and liftoff speed reductions in excess of 40 and 20% respectively were achieved. Landing ground roll and approach speeds were similarly reduced. This type of operational capability has been recognized as being advantageous in many future aircraft design studies (Hudson, 1981; Landfield, 1984). The A-6/CCW, however, was intended as a STOL demonstration vehicle only. It was limited by design to low speed flight. In 1981 the Navy accepted a proposal by Grumman Aerospace Corporation to develop and build a new generation of STOL demonstrator. The technology demonstrated was intended to be useable on modern high performance aircraft. STOL performance would be achieved through the combination of a 2-D vectored nozzle and a circulation control type of high lift system. The primary objective of this demonstration effort would be to attain A-6/CCW magnitude reductions in takeoff and landing flight speed and ground distance requirements using practical bleed flow rates from a modern turbofan engine for the blown flap system. Also, cruise performance could not be reduced by the wing high-lift system. The A-6 was again selected as the optimum demonstration vehicle. The goals and further discussion of the A-6 STOL demonstrator were presented by Carr (1984). This paper will document the procedure and findings of a study conducted to select the optimum high-lift wing design. Some findings of a separate study using a supercritical airfoil and a comparison of 2-D and 3-D results will also be described.

NOMENCLATURE

2-D	two dimensional, having an effective aspect ratio approaching infinity
3-D	three dimensional, having span, chord, and thickness
α_g	geometric angle-of-attack
C_ℓ	2-D lift coefficient
C_L	3-D lift coefficient, L/qS
C_d	2-D drag coefficient
C_m	2-D or 3-D pitching moment coefficient (subscript indicates reference location)
C_μ	blowing momentum coefficient, $\dot{m}V_j/qS$ ($\dot{m}V_j/qc$, if $\dot{m}$ is per unit span)
CCW	circulation control wing
c	chord length of original airfoil
c'	chord length with leading and trailing edges deployed
c_F	chord length of the flap
FT	abbreviation for foot
h	blowing slot gap height
GAP	height from flap or slat surface normal to wing surface
in	abbreviation for inch
R	radius of Coanda surface, expressed in percent chord (subscript 1 for dual radius indicates leading radius, 2 indicates aft radius)
t_{TE}	trailing edge thickness of cruise airfoil
q	tunnel dynamic pressure, expressed in pounds per square foot
R_n	Reynolds number
σ_F	trailing edge flap deflection, expressed in degrees
σ_S	leading edge slat deflection, expressed in degrees
σ_V	vane deflection on double slotted flap
C_{ℓ_α}	linear portion of lift curve slope, C_ℓ vs α
$C_{\ell_{max}}$	maximum lift coefficient
α_{stall}	angle of stall, deg
C_{d_o}	minimum drag level
V_{TRUE}	true airspeed, expressed in knots
S, S_{REF}	wing reference area in square feet
S_{BLOWN}	area of 3-D wing with blown trailing edge, ft^2
$\dot{m}$	mass flow through blowing slot in lb_f/sec^2, or $lb_f/ft/sec^2$
V_j	calculated isentropic jet exit velocity in ft/sec^2

INTRODUCTION

Pneumatic augmentation of the fluid surrounding an airfoil section to further amplify lift has received significant attention for several decades. The goal has been to achieve dramatic increases in lift over mechanically reconfigured wings, which changed their camber and/or area through the use of flaps and slats. The development of the jet flap and recognition of the Coanda effect have led to many innovative design concepts, several of which are illustrated in figure 1 along with applications of them. Two basic philosophies are involved. One is to obtain direct lift by exhausting a high momentum flow deflected to the flight path (ground attitude for hover and vertical flight). The jet flap accomplishes this by exhausting a deflected high momentum jet at the trailing edge of an airfoil (Deckert, 1985; Malavard, 1956). Lift is increased by the jet reaction and because the jet effectively extends the wing chord by maintaining a pressure differential above and below it, acting to increase effective wing area and moving the center of pressure rearward. Using the high momentum jet at the trailing edge of a flap, called a jet flap, has the added advantage of inducing increased circulation over the wing (Spence, 1956; Williams, 1962; Mashell, 1959; Schubauer, 1933). Both methods result in increased aerodynamic lift. Jet engine exhaust can also be deflected through rotating nozzles to obtain direct powered lift as on the Harrier (DeMeis, 1985). Deflecting the engine thrust at the wing trailing edge also results in deflected jet lift and increased circulation lift. This can be achieved by the placement of an engine nozzle either over or under the wing or through a properly designed nozzle placed adjacent to the wing trailing edge. This is not as efficient as the jet flap, but eliminates the need for large ducts in the wing and the much larger momentum of the engine has a much higher C_L potential.

Another approach to powered lift augmentation is the blown flap. Unlike the jet flap, the high momentum jet is placed in front of a mechanically deflected flap. This type of augmentation, called chordwise blowing, utilizes the Coanda effect to attach a thin, high momentum sheet of air (or other fluid) to the curved surface of a flap or cylinder. Initially, the sheet of air energizes the boundary layer and keeps the flow attached through large deflection angles due to a balance of centrifugal forces and the pressure differential. This increases wing circulation and entrains more of the freestream air, resulting in a significant increase in lift generated by the wing at low momentum levels. As the amount of blowing is increased, supercirculation of the flow around the airfoil causes the lift to increase

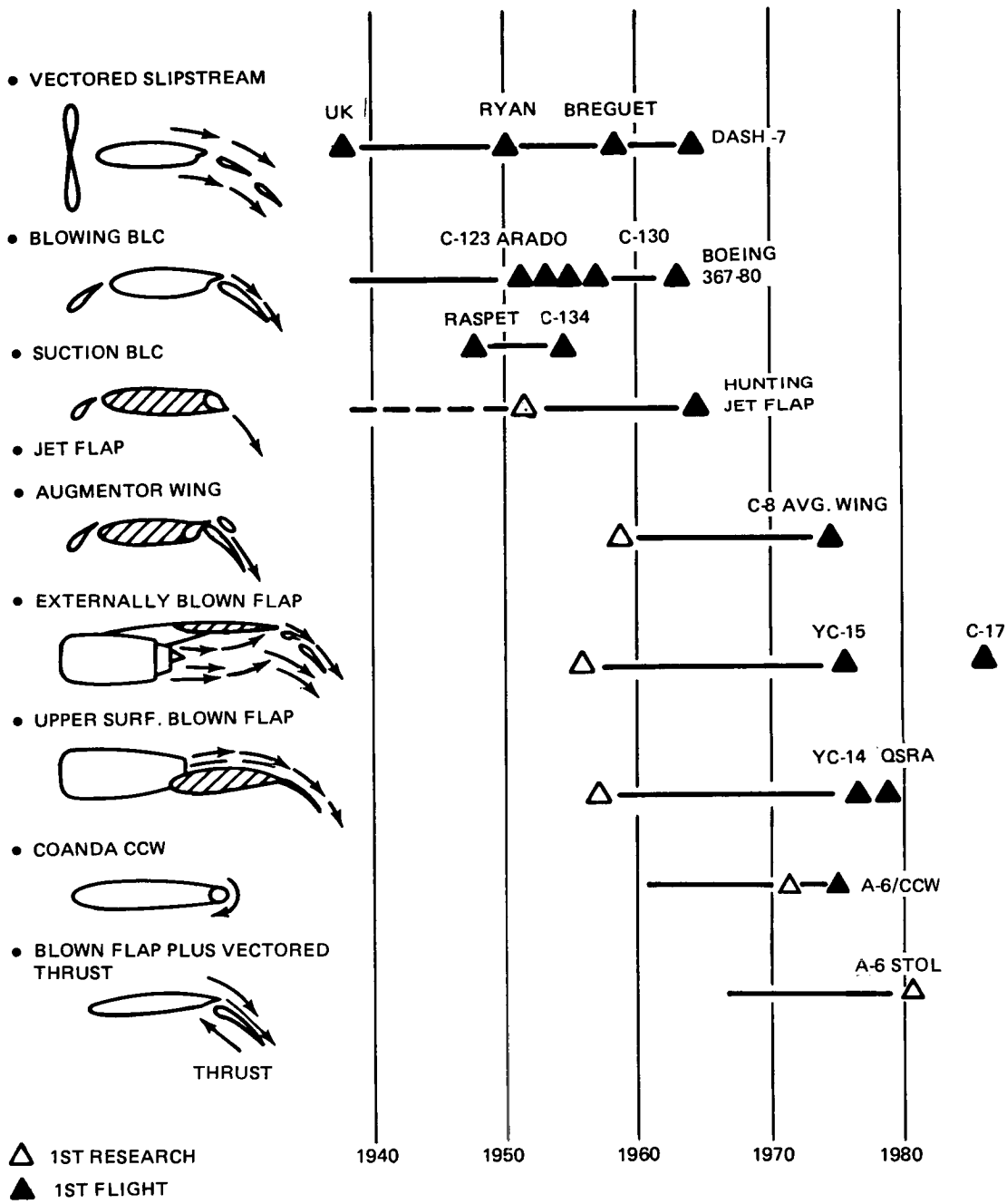

Figure 1. Powered lift chronology.

further. The maximum amount of increased lift is dependent upon the total turn angle of the curved surface and the available momentum. In the case of a 180-deg circular surface, as on the A-6/CCW, the flow can be made to wrap around the airfoil and return on the upper surface (Englar, 1975). The lack of a sharp trailing edge allows control of the stagnation point and greatly increases the circulation around the airfoil. Large increments in $\Delta C_\ell / C_\mu$ can be achieved at relatively low

C_μ values. Tangential and spanwise blowing can be used on leading or trailing edge devices to maintain attached flow and increase lift (Banks, 1984). Suction can also be used to remove the boundary layer to maintain laminar flow and delay separation. The F-4 and other designs have used leading and trailing edge blowing to provide improved takeoff and landing performance.

The NASA Quiet Short-haul Research Aircraft (QSRA), YC-15 and YC-14, used a combination of deflected thrust and the Coanda effect to increase lift. The YC-15, which led to the C-17 (Holt, 1984), uses an externally blown flap where flaps are deflected in the path of the engine exhaust plume. The wing flaps turn the engine thrust downward, resulting in a direct lift component. Slots in the flaps permit a controlled amount of flow to pass onto the upper surface where it acts similiar to a blown flap. The QSRA and YC-14 use upper surface blowing, where the high momentum engine exhaust is vented over the upper surface of the wing (Cochrane, 1981; Queen, 1981). This flow attaches itself to the wing upper surface and is turned by the Coanda effect when a flap is deflected at the wing trailing edge. Both systems have advantages and disadvantages, but are effective powered lift systems (Yen, 1982). While not as efficient as the chordwise blown flap aerodynamically, they have higher momentum levels and avoid the ducting problems of blown flaps. This technique is not easily applied to all aircraft types, however.

Circulation Control Wings (CCW) have been investigated extensively at David Taylor Naval Ship Research Development Center (DTNSRDC) for a number of years (Nichols, 1980; Englar, 1970). This work has been devoted to the idea of developing non-mechanical high-lift systems, which would eliminate conventional mechanical trailing edge devices and all the complexities associated with them. The conventional trailing edge flap is replaced with a fixed curved trailing edge, usually circular. These circulation airfoils rely entirely on the Coanda effect and supercirculation to increase lift above cruise airfoil levels. Lift augmentation ratios of CCWs are much higher than for blown flaps and continue to increase lift through moderate C_μ levels. DTNSRDC proved this concept on the successful A-6/CCW demonstrator aircraft (Englar, 1979a). The A-6/CCW was built and test flown by Grumman under contract with DTNSRDC. STOL performance reductions exceeding 20% in takeoff and approach speed and 40% in takeoff and landing ground distances were demonstrated (Pugliese, 1979). Slow flight was demonstrated down to a speed of 67 knots with a wing C_L of 3.60 at 29-deg angle-of-attack. At this condition the aircraft showed no indication of wing stall. The thick trailing edge and large duct size of the design presented a significant increase in cruise drag. The A-6/CCW was

designed to demonstrate low speed flight and STOL performance only and was not intended for direct application to high performance aircraft design. Improved overall performance has been the subject of subsequent studies with CCW airfoils at DTNSRDC (Englar, 1979b).

Following the completion of the successful A-6/CCW demonstrator program, work continued at Grumman Aerospace Corporation to improve and find applications for this technology. The development of the 2-D ADEN nozzle (Capone, 1979; Doonan, 1983) and the increased engine thrust of modern turbine engines led to the concept of the A-6 STOL demonstrator. The design would use 2-D nozzles deflected 60-deg and a pneumatically augmented wing flap to provide the high C_ℓ's necessary for STOL performance. Each system would provide approximately 50% of the required STOL lift. The wing blowing system would be limited to a practical bleed level, dictated by the capabilities of the engine and allowable thrust losses to meet acceleration requirements. The A-6 nozzle location, at the wing root trailing edge, provides the added benefit of thrust-induced lift on the wing. With a properly designed 2-D nozzle located in this position, the induced lift with deflected thrust would enhance the total lift of the design. The mid-fuselage location of the nozzle also helped to minimize trim requirements of the pitching moment which results from the deflected thrust. Much of the design work is covered by Carr (1984).

A 2-D airfoil wind tunnel test series was planned to evaluate different blown flap systems and arrive at the optimum configuration for the planned engine bleed flow rates. The A-6/CCW airfoil section was capable of turning the flow 180-deg statically, causing a tuft extending behind the blowing slot to wrap itself around the airfoil. However, with a surrounding freestream, the actual turning was less. This was particularly true at low C_μ. Since only a modest amount of bleed flow air was available, the Grumman blown lift designs concentrated on flaps with less total turning arc, but a healthy initial blowing radius. The 2-D test was conducted at DTNSRDC concurrently with a separate DTNSRDC study to define advanced CCW sections. Both of these tests and a test of the A-6 high-lift system were conducted between November 1982 and February 1983. This paper provides the results of the 2-D test series and the evaluation process to select the A-6 STOL high-lift wing configuration. A comparison with results from a separate test on a 13% supercritical airfoil section and with tailoff 3-D wind tunnel data are also provided.

MODEL GEOMETRY

The trailing edge candidates compared in this paper and the 64A008.5 Mod airfoil are shown in figure 2 with some geometric comparisons presented in figure 3. The 64A008.5 Mod airfoil is shown with a 25-deg leading edge slat deflection and a 30% chord semi-Fowler single slotted flap deflected 30-deg. A 30% chord double-slotted Fowler flap was also tested and is presented for comparison with the blown flaps. A 17% chord vane deflected 20-deg and 24% chord flap deflected 40-deg showed maximum high-lift and minimum high-lift drag and was selected for comparison here. This flap retained the original A-6 airfoil shape when retracted. The plain blown flap, which has a large 6% chord leading edge radius blended smoothly into the original airfoil upper surface contour, is shown with 50-deg deflection. This was the maximum deflection possible without modifying the A-6 clean airfoil contour. The primary Grumman candidate, the 13% chord crescent blown flap, consisted of a continuous 8% chord radius upper surface extending from flap leading to trailing edges. A lower surface cusp at the trailing edge permitted a greater total arc and acts to turn the lower surface flow downward. A 6.5% chord crescent flap was also built. However, it was dropped from the test when the larger chord crescent flap failed to produce the expected lift and revealed that much of the achieved lift was due to the flap chord camber. Unlike the single slotted and plain blown flaps which have respectable thin airfoil trailing edges when retracted, the crescent blown flap retains its upper surface contour and has an equivalent trailing edge thickness of 2.8% of the chord. The airfoil also requires thickening beyond the 70% chord to accommodate this section with a maximum deflection of 43-deg. A flat trailing edge was also tested on the crescent flap. This was intended to reduce the retracted trailing edge thickness and provide a tradeoff between maximum high-lift and acceptable cruise drag. Unfortunately, the high-lift results were not impressive, although the clean airfoil drag was reduced. The model design may have affected the results since the flat trailing edge should have done as well as the full arc at low blowing coefficients.

A CCW section proposed by DTNSRDC with a 3.5%c' dual radius flap is also presented here. An analysis of the DTNSRDC CCW sections is contained in Englar's paper (1983). The dual radius configuration extends below the airfoil lower surface when deflected 90-deg by 0.035c'. The blowing surface is provided by two circular surfaces, joined tangentially to form a smooth upper surface curve to the trailing edge. This provides a sharp initial radius for maximum flow acceleration behind the nozzle and a gentler secondary radius to prevent separation and permit a total turn angle of 123-deg from the nozzle centerline. The leading circular surface has a 1.2% chord

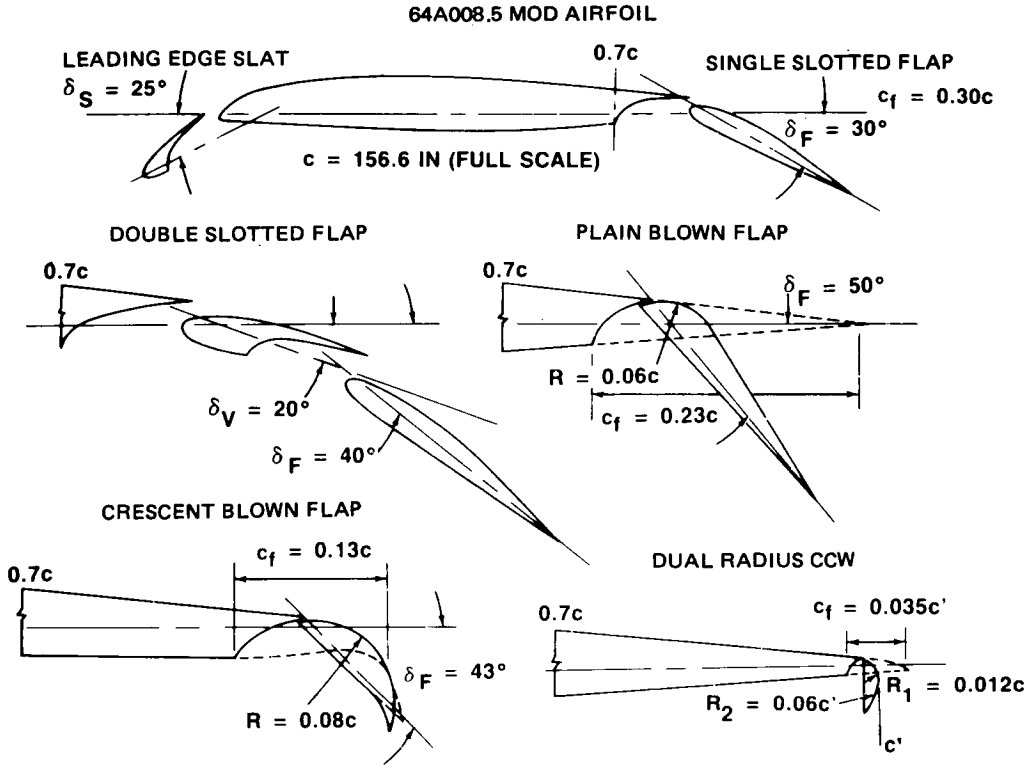

Figure 2. 2-D airfoil sections.

FLAP TYPE	C_f/C	R/C	t_{TE}/C	FLAP ANGLE ~ DEGREES	TOTAL TURNING ARC ~ DEGREES
SINGLE SLOTTED	0.30	—	0.0014	30	—
DOUBLE SLOTTED	0.30 (0.17/0.24)	—	0.0014	30 (20/40)	—
PLAIN BLOWN FLAP	0.23	0.06	0.0014	50	58
CRESCENT BLOWN FLAP	0.13	0.08	0.028	43	110
DUAL RADIUS CCW	0.035	0.012/0.06	0.0014	90	123
A-6/CCW	0.0730	0.0365	0.0730	180	180

Figure 3. Comparison of flap geometries.

radius while the aft surface has a much larger 6% chord radius. This flap is deployed 90-deg for maximum lift, with lesser deflections possible for maneuver and takeoff. Similar to the crescent flap, the dual radius CCW retains its upper surface curvature when retracted to zero deg, although the effective trailing edge thickness is the same as the A-6 airfoil. The impact of the resulting trailing edge camber on cruise lift and drag will be shown later. The A-6/CCW geometry is provided to demonstrate the dramatic reduction in size between it and the dual radius

CCW. The A-6/CCW had a 3.65% chord semi-cylindrical trailing edge with a 180-deg deflection. The effective trailing edge thickness in cruise was 7.3% of the chord.

TEST APPARATUS AND TECHNIQUE

The 2-D test was conducted in the DTNSRDC 8 X 10 ft subsonic wind tunnel between 3 X 8 ft 2-D double wall inserts. A 2-ft chord by 3-ft span 64A008.5 Mod section was installed on rotatable end plates flush to the wall inserts to obtain a 2-D condition. Pressures were recorded on a 144-port scani-valve system through pressure taps located chordwise at the mid-span location. Pressures were also recorded at the 1/4-span locations to check the 2-D spanwise distribution. The mid-span pressures were integrated over the chord to determine 2-D lift and pitching moment. A characteristic pressure distribution for the plain blown flap is shown in figure 4. Drag was measured by use of a drag rake located behind the mid-span station. A comparison of clean airfoil wake profiles is shown in figure 5. The rake pressure taps were spaced closely together to record the detailed variation in the wake pressure. Use of the drag rake resulted in questionable results for the high-lift airfoils, as will be discussed later. Tunnel test conditions were varied between a q of 10 psf for a Reynolds number of 1.2×10^6/ft to a q of 65 psf for a Reynolds number of 2.6×10^6/ft. The low q condition was used to obtain a greater range of C_μ. Most testing was conducted around a q of 35 psf to allow a reasonable C_μ range and Reynolds number compromise. C_μ was calculated by the product of the mass flow into the model per unit span, as measured by a venturimeter in the supply system and the calculated jet velocity using isentropic expansion based on the plenum pressure and static free stream pressure non-dimensionalised by the tunnel q and the deflected wing chord. Blowing momentum was provided through a plenum chamber in the model cavity and exhausted tangentially onto the flap upper surface through a spanwise slot located at the main airfoil section trailing edge. Plenum pressure was varied up to 60 psf. The test apparatus and test technique are described further by Englar (1979b, 1972a, and 1972b).

A leading edge dowel was used on the sharp lower leading edge of the main airfoil, which was exposed with the leading edge slat deflected, to prevent early separation at high-lift conditions. This also helped to improve the Reynolds number characteristics of the leading edge slat. Tests were conducted separately with this dowel in place and removed; without the dowel the leading edge separation was observed to occur early at low tunnel q's, showing a dramatic loss in lift at low

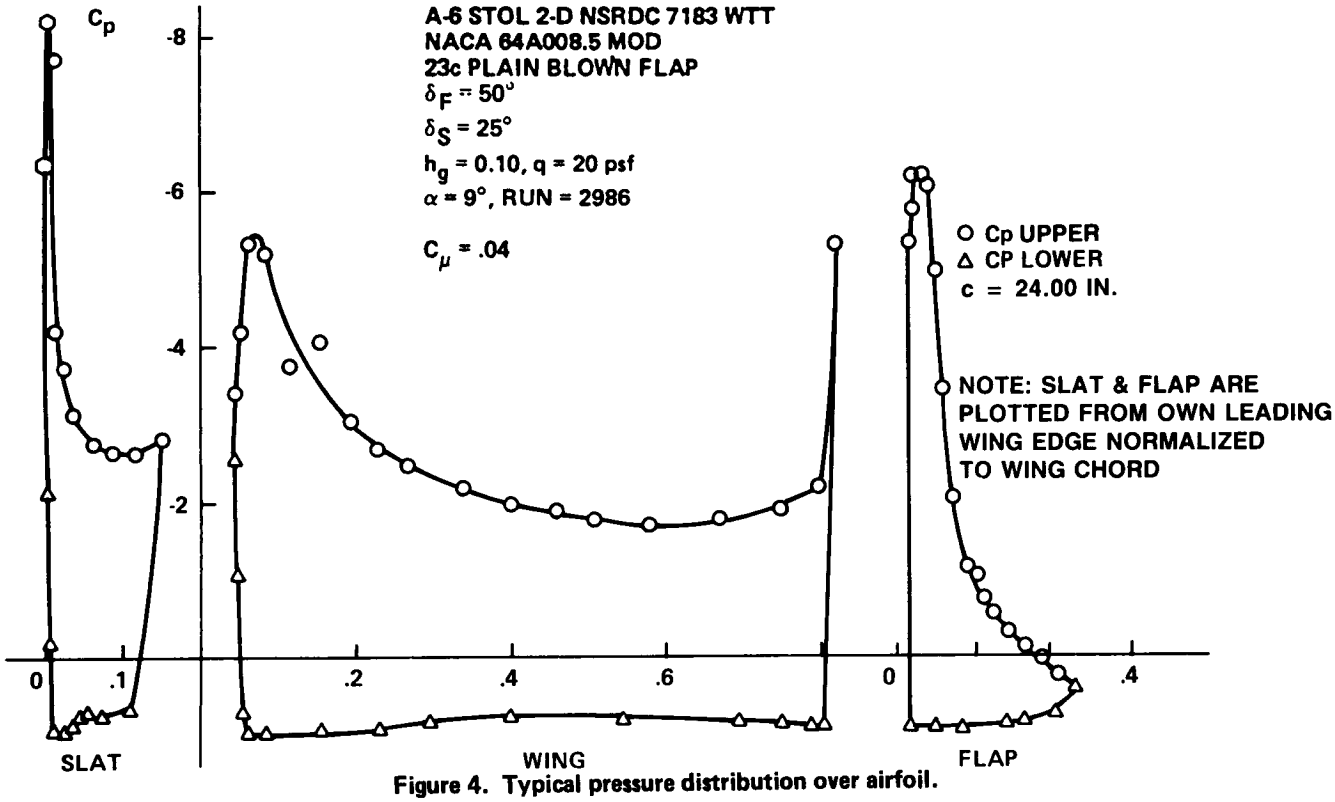

Figure 4. Typical pressure distribution over airfoil.

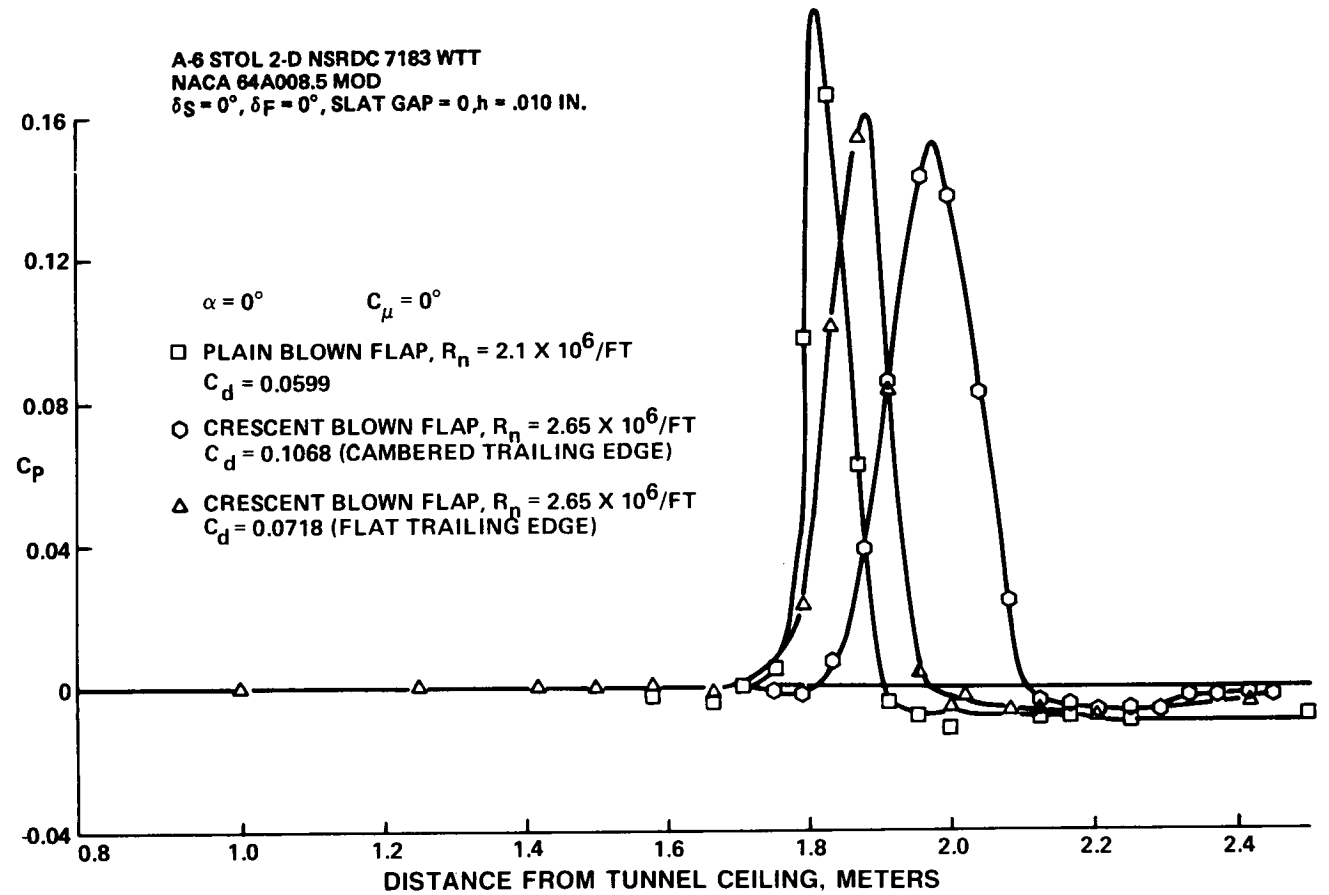

Figure 5. Wake rake drag measurement.

Reynolds numbers. Lift characteristics with the dowel appeared less dependent on Reynolds number. At higher tunnel q, representing a Reynolds number of 2.5×10^6, no difference was found in C_{ℓ_α} or $C_{\ell_{max}}$ with or without the dowel. The dowel was removed for the cruise configuration.

BLOWN FLAP BLC COMPARISON

A comparison of the 2-D blown flap C_ℓ's with blowing momentum coefficient C_μ is shown in figure 6. The data are presented for alpha geometric of 6-deg to avoid apparent stall regions at lower and higher angles-of-attack. The A64A008.5 Mod airfoil lifts with no flap or slat deflection, with the 30% chord semi-Fowler flap deflected 30-deg, and with the double slotted flap, are also shown on the left axis for comparison. Note that the highest lift for low blowing coefficients, C_μ less than 0.04, is obtained by the plain blown flap. This is due largely to the lift generated by the larger 23% chord flap at $C_\mu = 0$. Above $C_\mu = 0.04$ the dual radius achieves greater lift due to its greater turning arc. However, the lift is not significantly greater than the plain blown flap until $C_\mu = 0.08$. The crescent blown flap has nearly the same blowing-off lift as the plain blown flap, but requires substantial C_μ before the total C_ℓ becomes greater than that of the plain blown flap. This is due to the larger turning radius and larger total turning arc of the crescent flap. The data suggest that at even higher C_μ the crescent flap may do as well as the dual radius CCW.

All of the blown flaps produced more lift than the single slotted flap with very little blowing, C_μ less than 0.02. The double slotted flap C_ℓ is higher than the plain blown flap at C_μ below 0.02 and higher than the dual radius CCW at C_μ below 0.03. This indicates that for very low blowing rates, conventional flap design may be equivalent or better than blown flap systems, especially when weight, drag, and thrust loss tradeoffs are considered. To be effective for high performance aircraft, the augmented high-lift system must provide a significant increase in lift relative to the additional weight and complexity of incorporating it instead of a simple mechanical flap. It must also allow reasonable cruise drag levels and minimal thrust drain from the engine to meet acceleration requirements.

Greater total lift is produced by the plain blown flap at C_μ below 0.04 and by the dual radius above 0.04. The dual radius flap always produces a greater lift increment due to blowing, ΔC_ℓ vs. C_μ, as shown in figure 7. The plain blown flap produces equivalent BLC lift up to $C_\mu = 0.01$, but for higher C_μ the

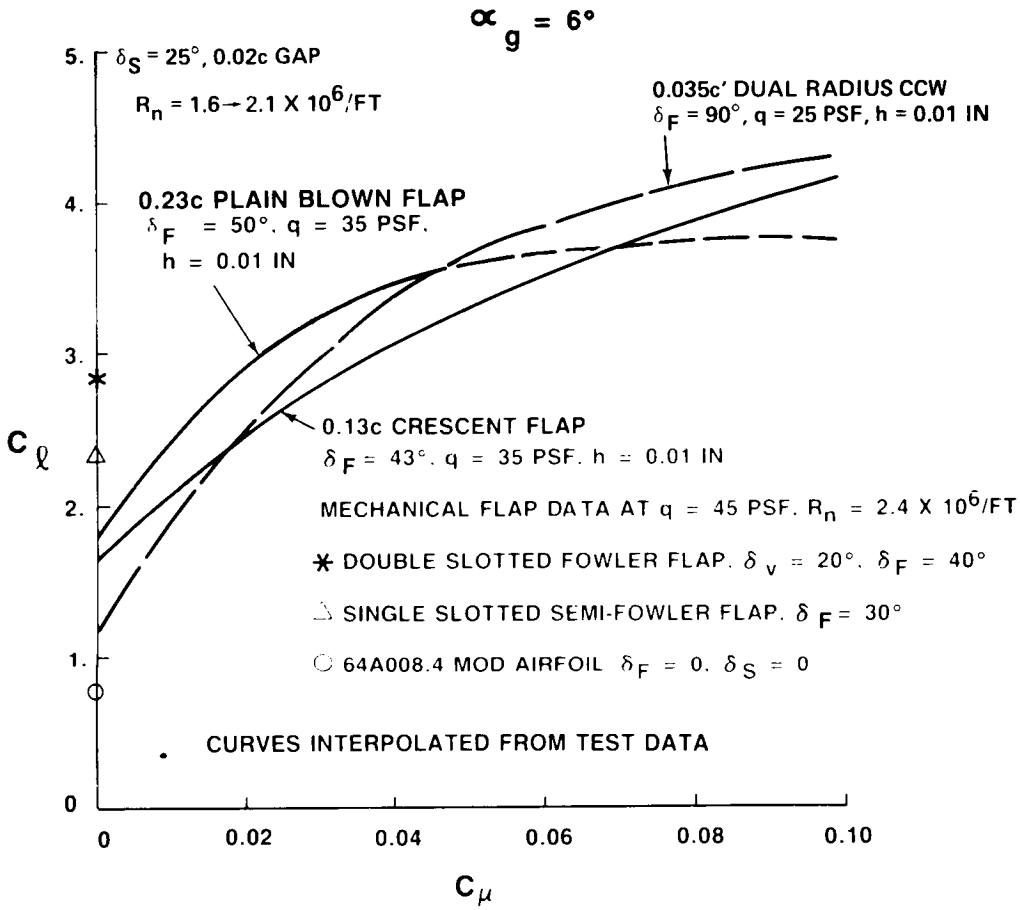

Figure 6. 2-D lift comparison, BLC-on.

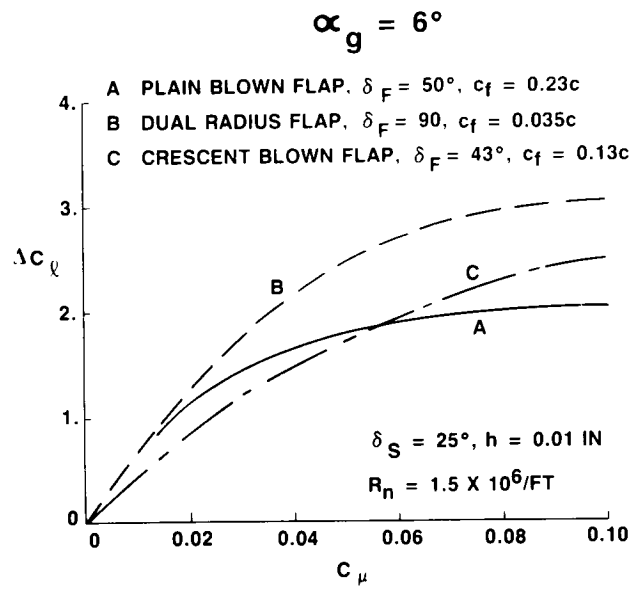

Figure 7. Lift increment due to blowing.

C_ℓ increase tapers off because of the limited turning arc. The plain blown flap shows a flattening in the C_ℓ versus C_μ curve above C_μ = 0.06. This is a familiar characteristic of blown flaps. Figure 8 shows that at alpha geometric = 0 deg, the dual radius CCW achieves an increment in C_ℓ nearly matching Glauert's potential flow theory up to C_μ of 0.02. At higher C_μ the C_ℓ is better than that reported by Lachmann for a 13% thick symmetrical airfoil with a 67.5-deg flap deflection (Lachman, 1961). The plain blown flap does as well as the 3.65% chord CCW at very low C_μ and slightly better at C_μ between 0.02 and 0.04. All of these flaps do significantly better than jet flap theory.

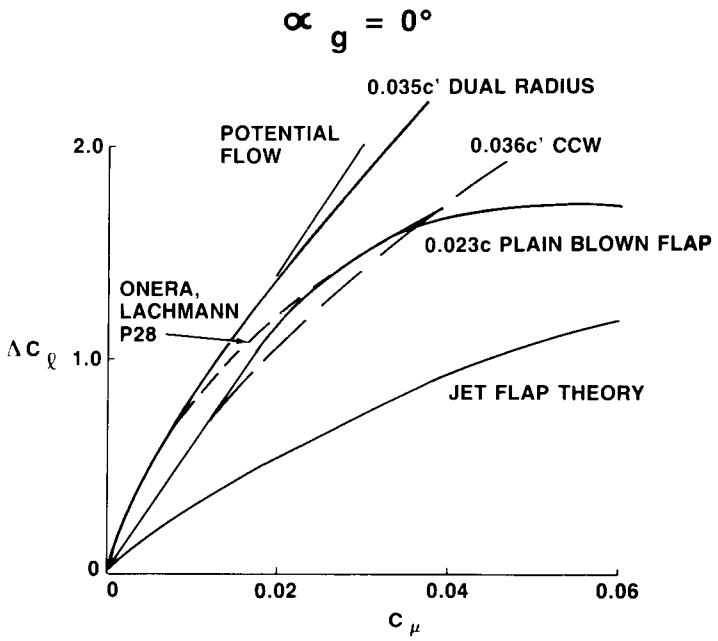

Figure 8. Lift increment comparison.

HIGH-LIFT SYSTEM EVALUATION

The benefits of the blown flap for a given design have been shown to relate directly to the blowing momentum, C_μ. Thus to evaluate the system properly, the aerodynamic characteristics must be compared at the intended operational C_μ, which is limited by the momentum available to the design. Figure 9 shows the A-6/STOL full-scale C_μ variation with velocity based on the amount of bleed air momentum, $\dot{m}V_j$, available from the A-6 STOL powerplants. For designs with large amounts of blowing momentum available to them it may be possible to optimize C_μ to provide maximum performance, as was done on the A-6/CCW. However, where limited amounts of bleed air are available, the available momentum may impose a design C_μ. The 2-D

equivalent C_μ is calculated by multiplying the 3-D C_μ by the ratio of the 3-D blown flap area to reference wing area. Thus at a predicted approach speed of between 82 and 92 knots, the 2-D equivalent C_μ is approximately 0.04. The predicted approach speed is based on estimated aero data and discussions with NAVAIR concerning useable STOL performance improvements. The aerodynamic data was estimated from A-6/CCW flight test results adjusted for configuration differences of this design. Navy personnel indicated that approach speeds below 80 knots would cause pattern congestion when mixed with current carrier aircraft whose typical approach speeds are well in excess of 100 knots. Also, the A-6/CCW demonstrated that aircraft handling characteristics were severely degraded at speeds below 80 knots.

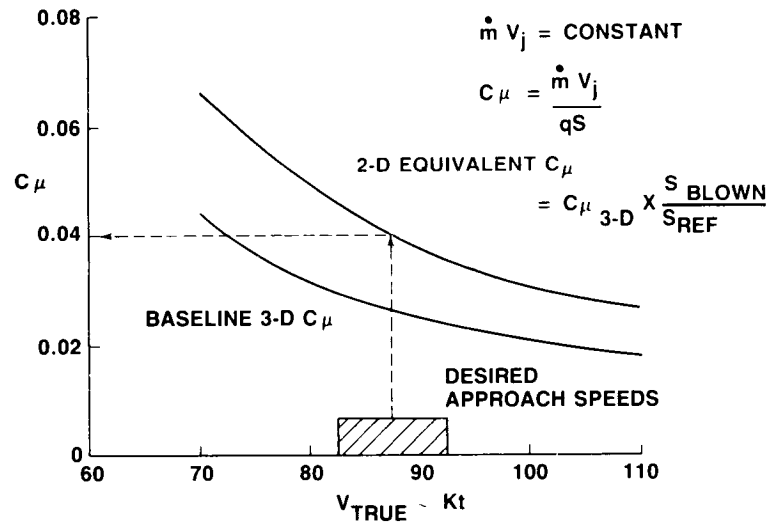

Figure 9. 2-D equivalent C_μ.

A comparison of C_ℓ vs α for C_μ = 0.04 (fig. 10), shows the lift of the plain blown flap and dual radius CCW is nearly equivalent at low alpha. However, the dual radius flap stalls out at alpha of 9-deg and a $C_{\ell_{max}}$ of 3.35; C_{ℓ_α} is also slightly reduced. The plain blown flap stalls at α = 10 deg with a $C_{\ell_{max}}$ of 3.55, increasing the clean airfoil lift three and one-half times. While this is a much lower augmentation ratio than can be achieved by a pure CCW, it is sufficient to meet the desired performance gains. Full scale Reynolds number effects may also increase α stall. The dual radius $C_{\ell_{max}}$ could be increased by some leading edge treatment; however, the stall would have to be delayed to 13-deg α to achieve the same $C_{\ell_{max}}$ as the blown flap. The lift of the single slotted flap is increased by a third with the plain blown flap at C_μ = 0.04. The reduction in α stall indicates that some leading edge treatment would be useful. However, wing mechanical limitations and cruise

performance must also be considered. The crescent blown flap C_ℓ is nearly equivalent to the double slotted flap at this condition, with the crescent flap exhibiting a higher C_{ℓ_α} and a lower α stall, but nearly the same $C_{\ell_{max}}$. Comparing $C_{\ell_{max}}$ at $C_\mu = 0.04$ for the blown high-lift systems, the plain blown flap has the highest $C_{\ell_{max}}$, with the dual radius and crescent blown flap being nearly equal to the double slotted flap.

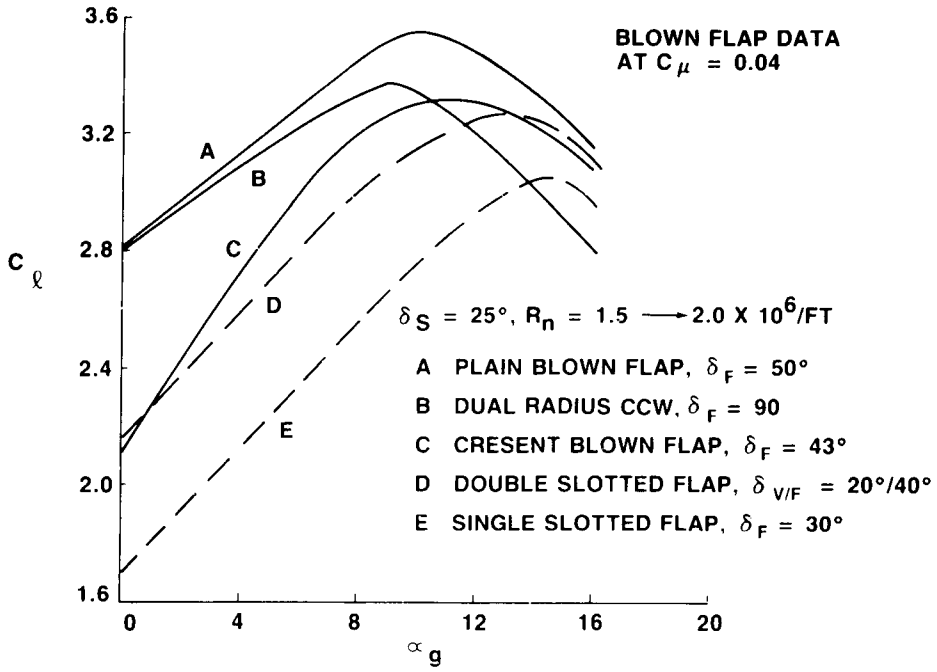

Figure 10. 2-D lift comparison at approach conditions.

The plain blown flap and crescent flap $C_{\ell_{max}}$ are nearly equal at $C_\mu = 0$. The double slotted flap $C_{\ell_{max}}$ is higher than any of the blown flaps, and the lift is nearly triple that of the clean airfoil. At the lower C_ℓ of the blown flaps at $C_\mu = 0$, the flow remains attached on the leading edge slat through higher angles and results in a higher alpha stall than the single or double slotted flaps. The tradeoff between the larger chord plus larger deflection of the plain blown flap, and the upper surface curvature of the crescent flap becomes obvious as both produce about two thirds the lift of the double slotted flap at low alphas. The very small chord dual radius, on the other hand, has half the lift increment of the crescent or plain blown flaps. This impressive result with almost one seventh the chord is due to its curved upper surface and the high flap deflection angle. The baseline airfoil C_ℓ versus alpha is shown for comparison along with the increase in α_{stall} obtained with slat deflection.

Blowing-off lift was important to the demonstrator program (fig. 11). Safety considerations for the demonstrator and for future applications, in case of loss of the blowing system, required a reasonable approach C_ℓ without blowing. Too low a C_ℓ at $C_\mu = 0$ could result in an approach speed that would endanger the aircraft. A part of the test program would be to measure STOL gains using vectored thrust alone and in combination with the blown flap system. Thus, good $C_\mu = 0$ lift is a basic requirement of the design. The C_ℓ level of the plain blown flap at $C_\mu = 0$ and a deflection of 50-deg for approach was deemed acceptable for the demonstrator.

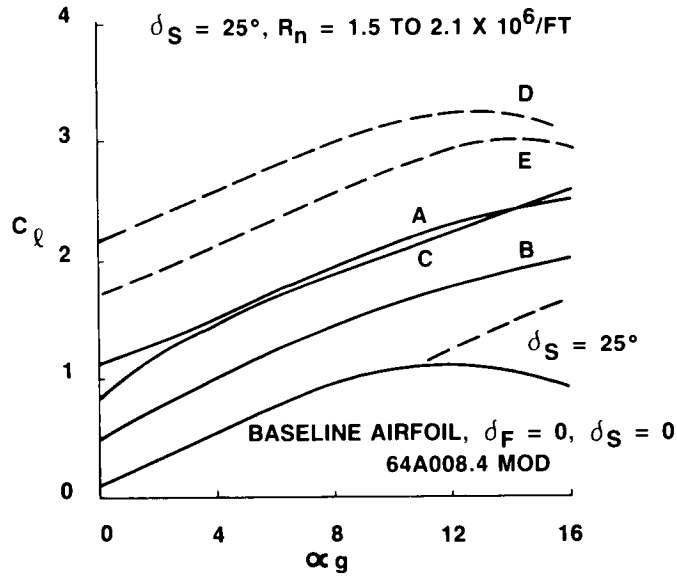

Figure 11. 2-D lift comparison at $C_\mu = 0$.

Another concern in selecting the optimum high-lift system is the amount of pitching moment required to trim. Figure 12 provides a comparison of the 2-D C_m at approach conditions. All of the blown flaps have a more negative C_m than the mechanical flaps due to the amount of lift concentrated at the flap leading edge with very high pressure peaks. The dual radius flap shows over twice the nose-down moment of the mechanical flaps due to the blowing slot and flap pressure peak located at the wing trailing edge, furthest aft of the aerodynamic reference. The increase in C_m also indicates trim lift and downwash would be larger for the blown flaps, resulting in less total lift for some aircraft configurations. The pitching moment for the dual radius is approximately equal to the A-6/CCW moment, which required extensive modification of the horizontal tail to trim. The plain blown flap may also require some horizontal tail redesign for an A-6 configuration, but it would be less extensive than that for the dual radius.

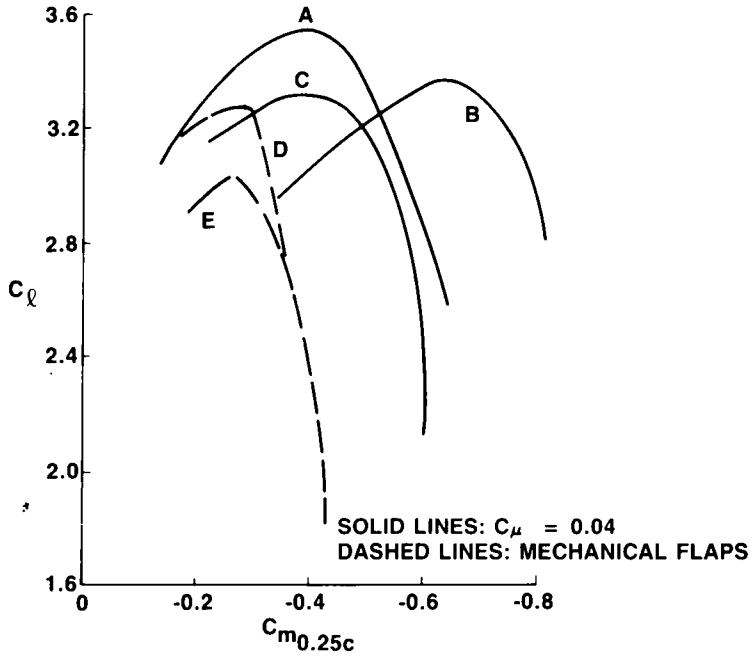

Figure 12. Comparison of C_m.

The clean airfoil drag for the plain, dual radius, and crescent blown flaps is shown in figure 13. To meet the cruise design requirement, the clean airfoil drag must not be increased by the flap system. The retracted plain blown flap which has the same contour as the original airfoil meets this requirement, as do the single and double slotted flaps. The dual radius and crescent blown flap both increase C_{d_o}. The dual radius CCW produces a lower C_d than the original airfoil above $C_\ell = 0.4$, which may improve some point performance. The dual radius C_ℓ for C_{d_o} is higher than for the original airfoil, indicating an increase in C_ℓ at alpha = 0 as well in the retracted position. The crescent flap C_{d_o} represents an unacceptable penalty on the design. Oil flow studies indicated separation on the crescent flap at 72% of the flap chord in the retracted position. Blowing over the retracted crescent flap did result in decreased drag with increased lift. However, stall occurred at a much lower alpha and the thrust drain from the engine would increase engine fuel flow which may not be acceptable. Higher Reynolds number conditions will also move the separation further aft and decrease separation drag somewhat. A flat trailing edge section tested on the crescent flap showed a drag increase about half that of the full crescent flap. C_ℓ vs α and C_μ characteristics for this section were unimpressive, however.

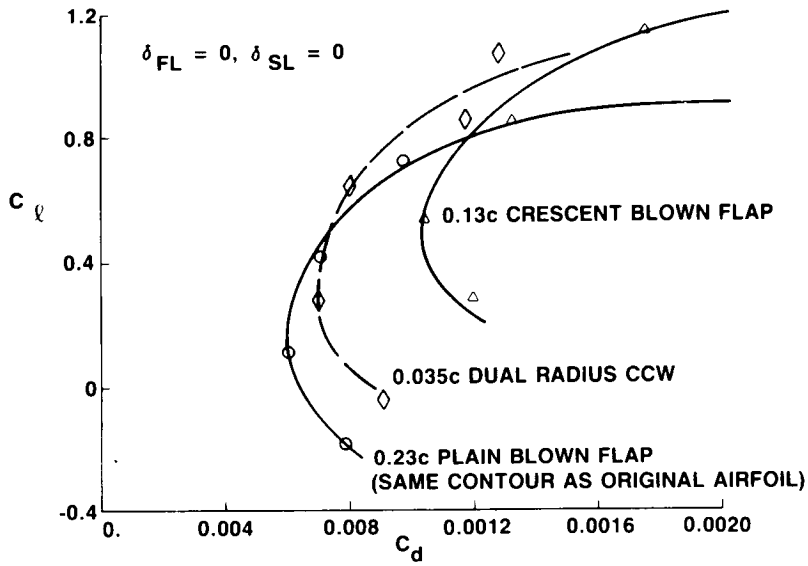

Figure 13. 2-D clean airfoil drag.

A comparison of high-lift system drag would be useful. However, the use of a drag rake to measure blowing-on drag had a questionable result in the view of some Grumman engineers. Figure 14 shows C_d decreases dramatically with increasing C_μ. The dashed $C_d - (-C_\mu)$ line shows that the decrease is much greater than the full value of the forward thrust of the jet at the nozzle exit. This is an optimistic approach that ignores the jet deflection component and flow mixing losses. Typical wake rake pressure profiles that were integrated to obtain the C_d vs C_μ curve on the left are shown on the right. With blowing-off, a nice pressure distribution exists. As blowing is increased, the pressure variation becomes smaller ($C_\mu = 0.02$) until it actually reverses ($C_\mu = 0.04$) and becomes a thrust. The height of the pressure peak relative to the airfoil also increases. Some 2-D drag reduction is expected due to the decreased separation. However, some of the data indicate $C_d + C_\mu$ values less than zero, suggesting negative profile drag. Pope (1966) states, "The wake survey cannot be used to measure drag of the stalled airfoils or of airfoils with flaps down. Under these conditions a large part of drag is caused by rotational losses and does not appear as a drop in linear momentum." Futher study of methods to measure drag with highly rotational flows may be indicated.

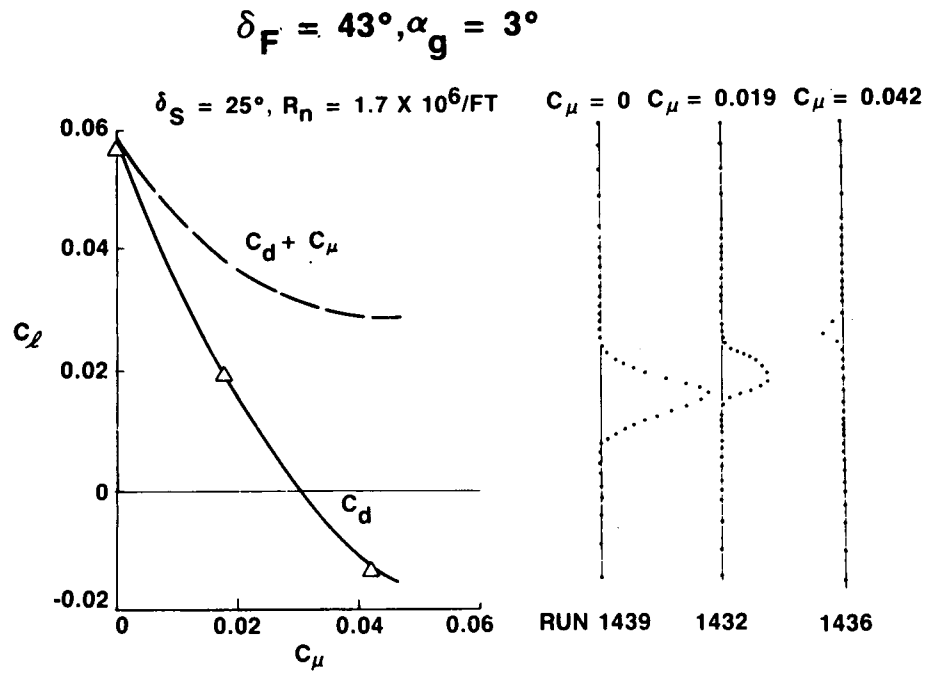

Figure 14. Determination of drag with BLC - on crescent blown flap.

PLAIN BLOWN FLAP RESULTS

This evaluation of lift, drag, and pitching moment for these high-lift systems, in both high-lift and cruise configurations, shows obvious advantages with the plain blown flap for the A-6 STOL demonstrator. The plain blown flap provides higher C_ℓ in the desired C_μ range, has a higher $C_{\ell_{max}}$, higher C_ℓ at $C_\mu = 0$ than the dual radius (its closest competitor), lower trim moment than the dual radius, and a lower C_{d_o} than the other blown flaps. Other test results show that C_ℓ will be even larger with full scale Reynolds number and with increased slot height.

The lift and pitching moments of the plain blown flap are shown in figure 15 as functions of α and C_μ. The increase in lift due to C_μ flattens out above $C_\mu = 0.06$. There is some reduction in α for $C_{\ell_{max}}$ with C_μ suggesting possible leading edge improvements could be made. The C_m curve shows an acceptable nose-down increase in pitching moment with the addition of blowing. Too large an increase in C_m with C_μ could indicate poor transition characteristics that would provide an increased workload for the pilot.

The tests indicated other interesting results as well. All of the data shown earlier used a blowing slot height of 0.01-in. When the slot height was doubled to 0.02-in for the plain blown flap deflected 43-deg (fig. 16), a fair increase in lift resulted. The lift of the plain blown flap with δ_F = 43-deg was increased as much

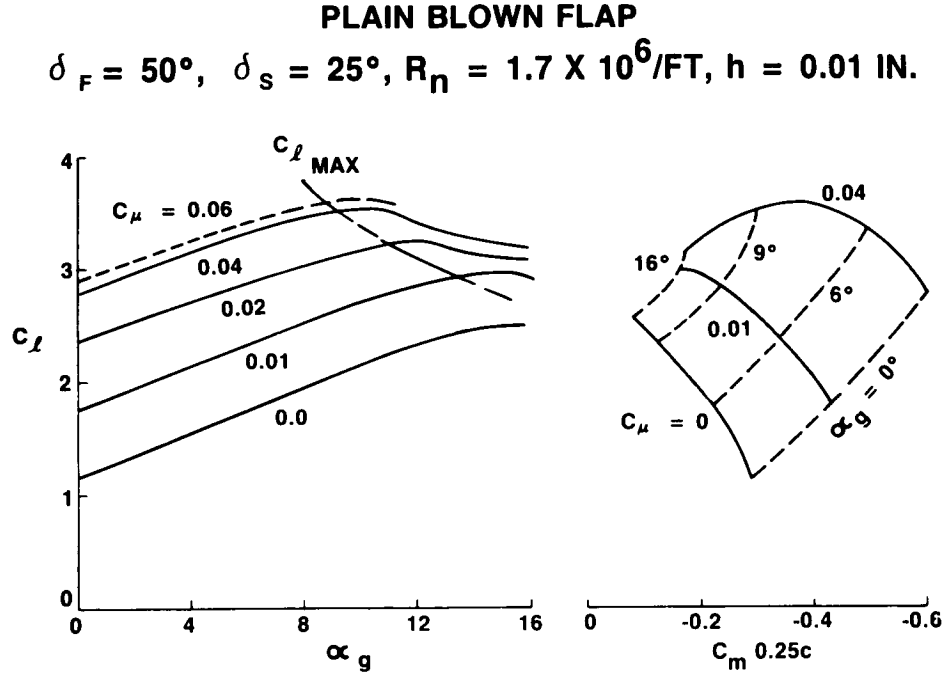

Figure 15. Variation in C_ℓ & C_m with C_μ & α_g.

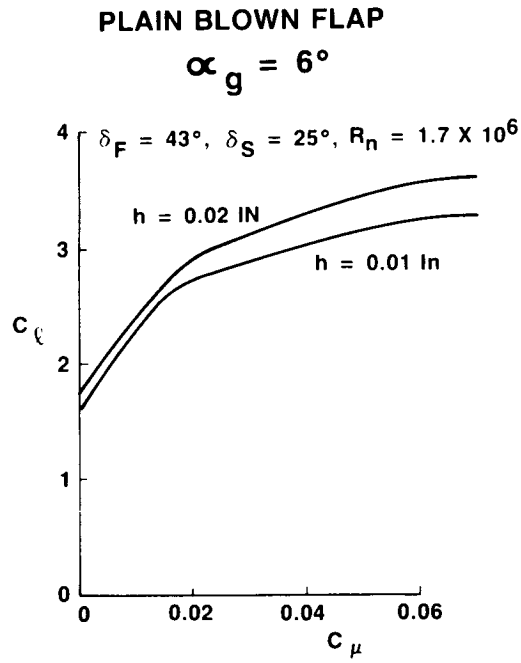

Figure 16. Effect of slot gap height on lift.

by doubling the slot height to 0.02-in as increasing the flap deflection from 43-deg to 50-deg (not shown). These results indicate that even larger lift increments than those shown in the previous curves are possible with increased slot height. The opposite effect was found by increasing slot height on the crescent flap.

The tests were conducted at a q of 35 psf for a Reynolds number of 1.6 x 10^6/ft to obtain data over a reasonable C_μ range. The effect of Reynolds number on the data was checked by increasing tunnel q to 45 psf and 65 psf for Reynolds numbers of 2.1 and 2.6 x 10^6/ft respectively. A significant increase in C_ℓ results with increasing Reynolds number at all C_μ levels (fig. 17).

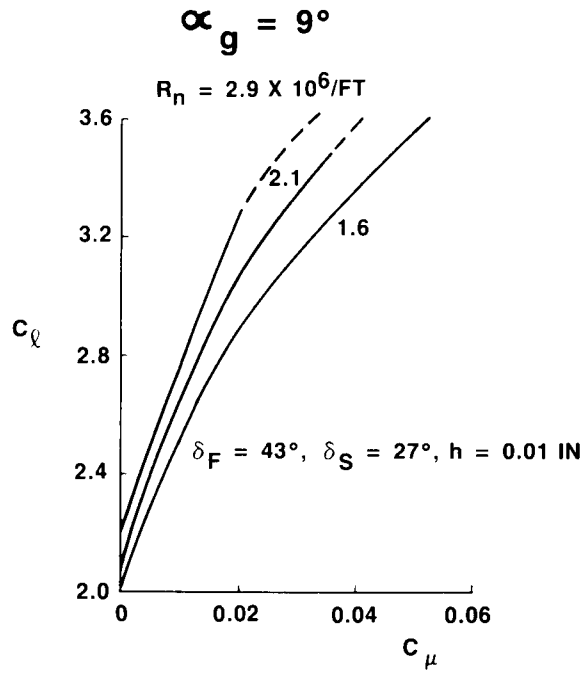

Figure 17. Effect of Reynolds number on C_ℓ.

SUPERCRITICAL SECTION COMPARISON

A separate test was conducted in the Grumman low-speed wind tunnel of a 13% thick airfoil with similar trailing edge high-lift devices. The airfoil and four high-lift devices are shown in figure 18. They are a 30% chord single slotted flap deflected 30-deg, a 30% chord double slotted flap with a 40-deg vane deflection and 50-deg flap deflection, a 23% chord plain blown flap, and a 13% chord crescent blown flap both with deflections of 43-deg.

The plain blown and crescent blown flaps were expected to have better cruise drag and high lift performance with this airfoil since they blend in well with the original airfoil lines. Also, the airfoil has some upper surface trailing edge curvature, which could help the plain blown flap by providing a secondary turning radius with a larger turning angle than the 64 series aft section did.

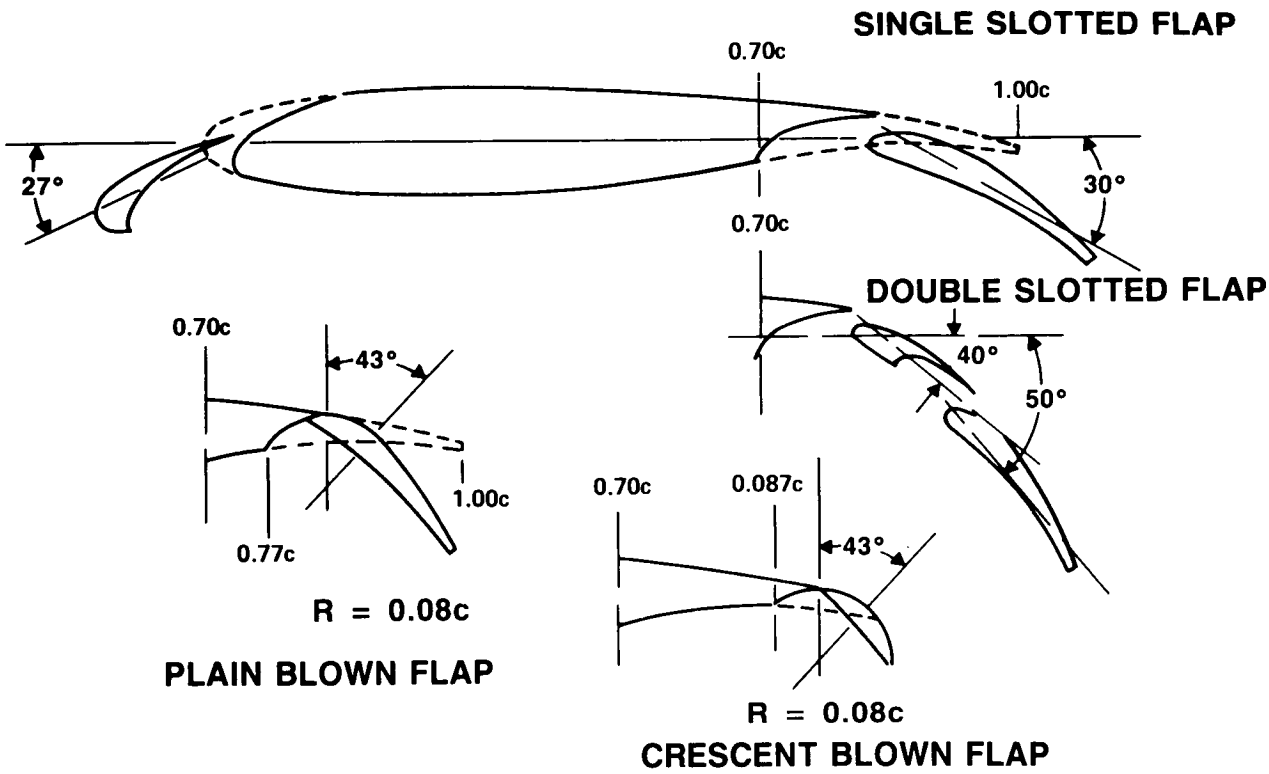

Figure 18. 0.13c supercritical sections.

C_ℓ is shown in figure 19 versus C_μ for alpha = 10-deg and δ_s = 27-deg. The direct lift comparison shown indicates much better performance for the crescent blown flap than was seen for the 64A series airfoil. The double slotted flap also performs quite well, yielding as much lift as the crescent flap up to C_μ = 0.04 and the plain blown flap up to C_μ = 0.055. The characteristic flattening of C_ℓ with increasing C_μ is less evident for the plain blown flap than for the 64A series airfoil. The contour of the supercritical trailing edge apparently works as a secondary radius.

The increase in $C_{\ell_{max}}$ with leading edge slat deflection (fig. 20) is dramatic for the plain blown flap. $C_{\ell_{max}}$ increases by more than ΔC_ℓ = 1.0 with a 27-deg leading edge slot deflection for the whole C_μ range.

Blowing slot height was also investigated. Figure 21 indicates C_ℓ is sensitive to blowing slot height and that an optimum slot height can be found for a given configuration. Here the 0.014-in height always produces the greatest lift. The narrow 0.006-in height becomes more effective as C_μ increases. This may, however, be the result of the slot height increasing under increased plenum pressure as C_μ is increased.

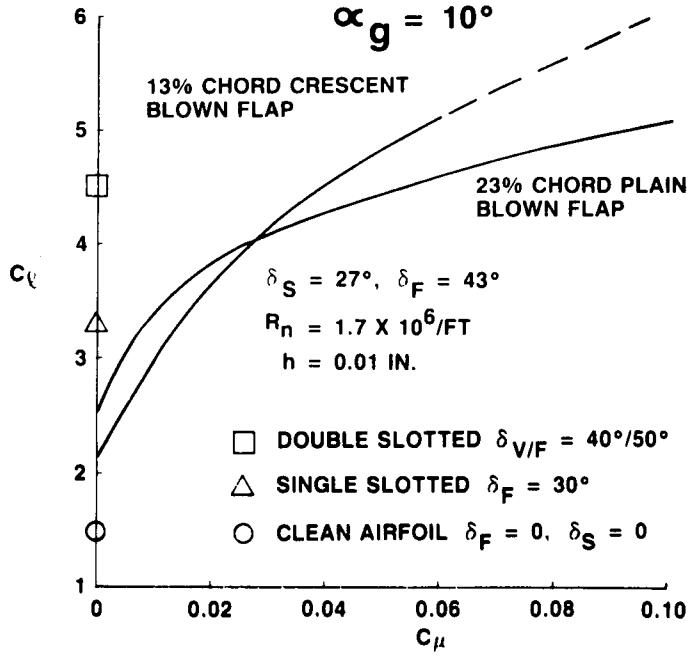

Figure 19. Comparison of C_ℓ for a 13% supercritical airfoil.

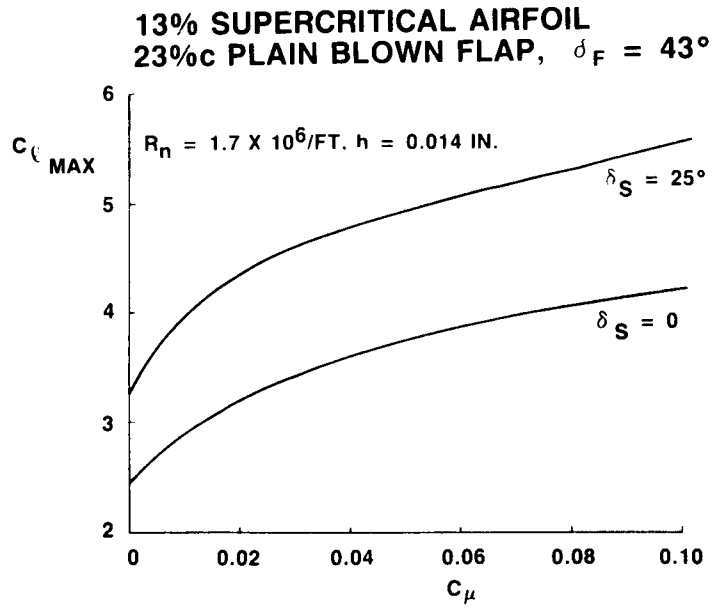

Figure 20. Effect of slat deflection on $C_{\ell_{MAX}}$.

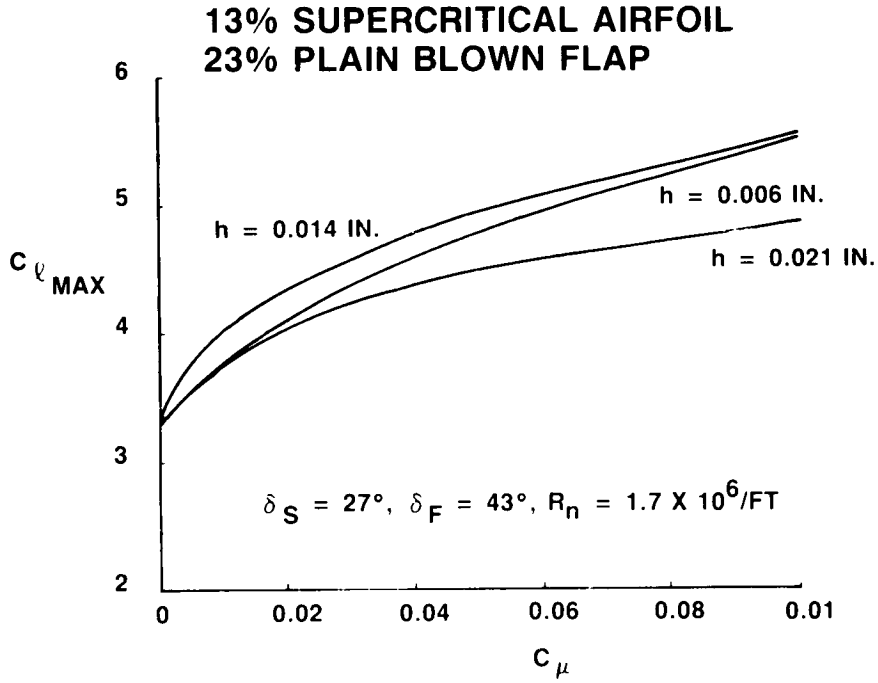

Figure 21. Effect of blowing slot height on $C_{\ell_{MAX}}$.

COMPARISON OF 2-D AND 3-D RESULTS

The plain blown flap was tested on a 1/8.5 scale model of the A-6 in the Grumman low speed wind tunnel. A comparison of the 2-D test results to the 3-D tail-off results is shown in figure 22 for equivalent test conditions. The change in clean airfoil lift is as expected due to the 3-D wing geometry. The change in C_{ℓ_α} and the change in alpha stall is evident for the clean airfoils and with blowing-on. The partial span flap area of the 3-D model results in a 60% decrease from the 2-D lift coefficient due to flap deflection plus BLC lift. The 3-D wing sweep, aspect ratio, and flap characteristics reduce the 2-D flap plus BLC lift coefficient an additional 12%. 2-D and 3-D results are not directly comparable. The lift curves in figure 22 are intended to show how 3-D effects can significantly alter the gains of a blown flap system. The effects shown can be calculated using standard 3-D prediction techniques with 2-D data.

The trimmed lift increment of the 1/8.5 scale model is shown in figure 23 as a function of C_μ. The curve shows that the 3-D test results were superior to the A-6 STOL aerodynamic design C_L's. This data, obtained at low Reynolds number conditions, verifies that the predicted STOL approach speeds of the design are attainable. The data shown indicate superior lift to the A-6/CCW demonstrator at

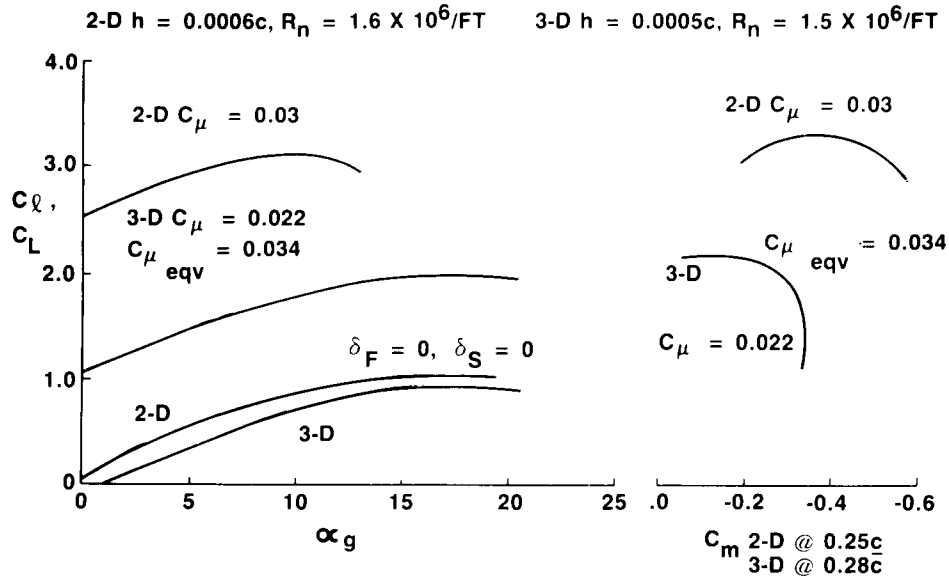

Figure 22. Comparison of 2-D to 3-D.

these low C_μ values. The A-6/CCW attained its STOL performance at C_μ's around 0.1, which is much higher than the C_μ's of the A-6 STOL. The additional lift required to obtain similar STOL performance levels is provided by deflected thrust using vectored 2-D nozzles. The combination of these two high-lift systems promises to be effective in reducing aircraft landing and takeoff speeds. The additional lifting capability can also be used to increase maximum landing weights.

CONCLUSION

The tests conducted revealed a variety of results with many interesting findings. While the data shown here indicated selection of the plain blown flap based on the available momentum, great promise was shown by the dual radius CCW. The DTNSRDC test results reported by Englar (1983) at Danvers show a fair increase in C_ℓ for a dual radius flap with a slight repositioning of the flap and increased chord. Extrapolation of that result indicates that an even larger chord dual radius may result in further increases in C_ℓ. Noting the effectiveness of the tiny chord at C_μ = 0, achieving half the lift increase of flaps with four to six times the chord length, it may be possible for a slightly larger chord dual radius CCW to outperform the plain blown flap at all C_μ levels. Some further work on the flap mechanics may lead to a reduction in the cruise and trim drag penalties of the

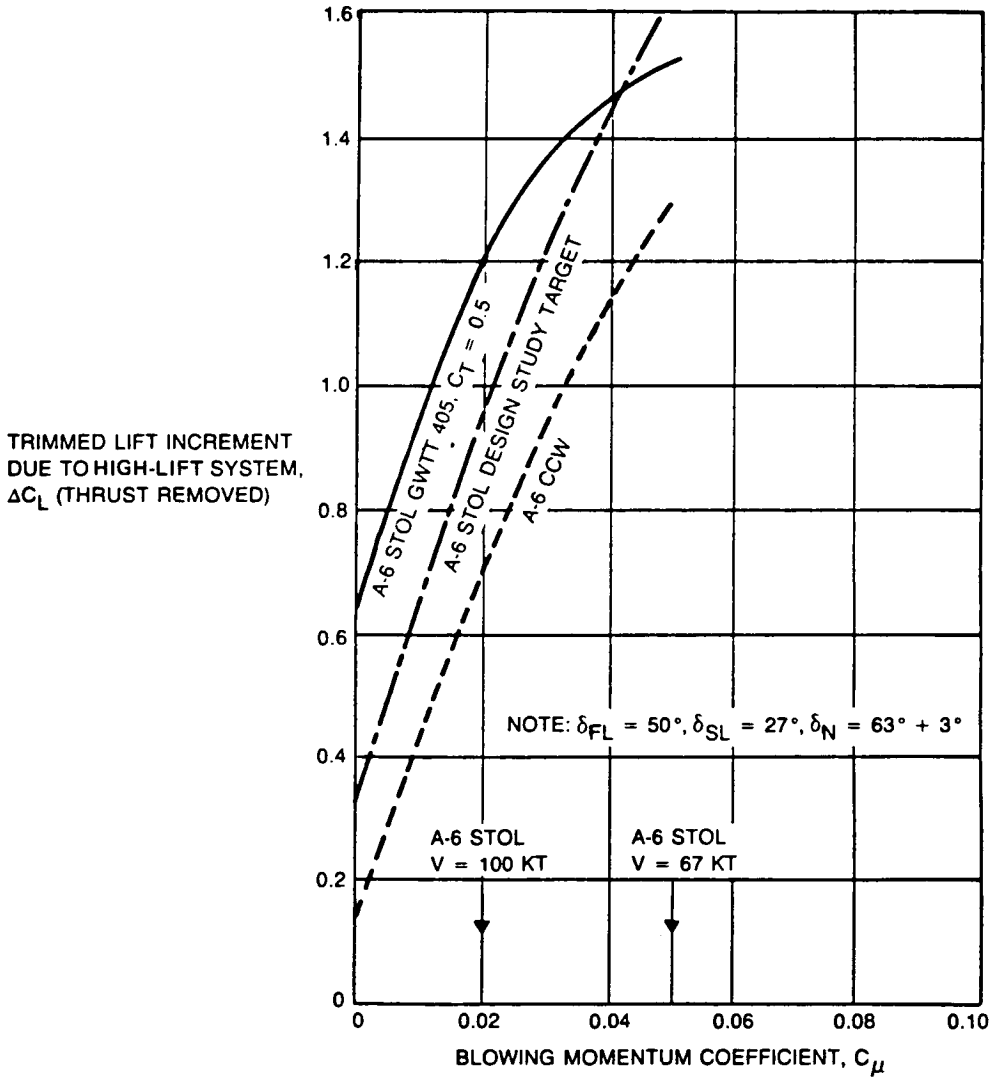

Figure 23. 3-D high-lift system ΔC_L.

trailing edge contour. Blowing over the surface during cruise to reduce C_{d_o} has been suggested; however, this is unlikely due to the high momentum required and the associated engine losses. Research should continue to define flap shape and geometry effects of blown flaps and CCW sections.

The test results also indicate that the pratical bleed levels of modern turbofan engines are the strongest driver in blown flap selection. If two or three times the blowing momentum used here were available, the merits of the dual radius and crescent blown flaps would be much stronger. Although the challenge of negating cruise and trim drag penalties would remain with higher C_μ levels to work with, the promise of these flaps would invite further investigation. The suggestion here is to study engine design to allow more bleed air to be extracted from the engine without inordinate weight penalties and/or thrust loss.

The bleed levels used in the A-6 STOL design are typical of modern turbofan engines. Doubling or tripling the available momentum is desireable to attain the full potential of lift augmentation of blown trailing edge high-lift systems on fixed wing aircraft. While additional challenges remain to be conquered, they may be addressable in an integrated design.

REFERENCES

Banks, D.W.; and Paulson, J.W., Jr.: Approach and Landing Aerodynamic Technologies for Advanced STOL Fighter Configurations. AIAA Paper No. 84-0334, AIAA 22nd Aerospace Sciences Meeting, Reno, NE, Jan. 1984.

Capone, F.J.: The Non-Axisymmetric Nozzle - It is for Real. AIAA Paper No. 79-1810, Aug. 1979.

Carr, J.E.: Aerodynamic Characteristics of a Configuration with Blown Flaps and Vectored Thrust for Low-Speed Flight. AIAA Paper No. 84-2199, AIAA 2nd Applied Aerodynamics Conference, Seattle, WA, Aug. 1984; republished as "Blended Blown Flaps and Vectored Thrust for Low-Speed Flight," AIAA J. Aircraft, vol. 23, no. 1, Jan. 1986, pp 26-31.

Cochrane, J.A.; Riddle, D.W.; and Stevens, V.C.: Quiet Research Aircraft - The First Three Years of Flight Research. AIAA Paper No. 81-2625, AIAA/NASA AMES VSTOL Conference, Palo Alto, CA, Dec. 1981.

Deckert, W.H.; and Franklin, J.A.: Powered Lift Technology on the Threshold. Aerospace America, vol. 23, no. 11, Nov. 1985, pp 34-42.

DeMeis, R.: Designing a V/STOL Fighter: McDonnell's AV-8B Harrier II. Aerospace America, vol. 23, no. 5, May 1985, pp 88-91.

Doonan, J.G.; and Callahan, C.J.: A High Speed Wind Tunnel Test Evaluation of STOL Dedicated Advanced Exhaust Nozzle Concepts. AIAA Paper No. 83-1225, AIAA/SAE/ASME 19th Joint Propulsion Conference, Seattle, WA, June 1983.

Englar, R.J.; and Husen, G.G.: Development of Advanced Circulation Control Wing High Lift Airfoils. AIAA Paper No. 83-1847, AIAA Applied Aerodynamics Conference, Danvers, MA, July 1983.

Englar, R.J.; Seredinsky, V.; et al.: Design of the Circulation Control Wing STOL Demonstrator Aircraft. AIAA Paper No. 79-1842, AIAA Aircraft Systems and Technology Meeting, New York, NY, Aug. 1979(a); republished in AIAA J. Aircraft, vol. 8, no. 1, Jan. 1981, pp 51-58.

Englar, R.J.: Subsonic Two-Dimensional Wind Tunnel Investigations of the High Lift Configuration. DTNSRDC Report ASED-79/01, Jan. 1979(b).

Englar, R.J.: Circulation Control Wing Flight Demonstrator Design Requirements and Aerodynamic Data. DTNSRDC TM-16-76-13, July 1975.

Englar, R.J.; and Williams, R.M.: Test Techniques for High Lift, Two-Dimensional Airfoils with Boundary Layer and Circulation Control For Application to Rotary Wing Aircraft. Canadian Aeronautics and Space J., vol. 19, no. 3, Mar. 1973; also presented at Annual General Meeting in Toronto, May 1972(a).

Englar, R.J.; and Ottensoser, J.: Calibration of Some Subsonic Wind Tunnel Inserts for Two-Dimensional Airfoil Experiments. DTNSRDC Report ASED AL-275, Sept. 1972(b).

Englar, Robert J.: Two-Dimensional Transonic Wind Tunnel Tests of Three 15-Percent-Thick Circulation Control Airfoils. DTNSRDC Technical Note AL-182, AD 882-075, Dec. 1970.

Holt, D.E.: C-17 Transport Employs Externally Blown Flap System. Aerospace Engineering, vol. 4, no. 1, Jan./Feb. 1984, pp 26-30.

Hudson, R.E., Jr.; and Krepski, R.E.: STOL Capability Impact on Advanced Tactical Aircraft Design. AIAA Paper No. 81-2617, AIAA/NASA Ames VSTOL Conference, Palo Alto, CA, Dec. 1981.

Lachman, G.V.: Boundary Layer and Flow Control. Vol. I and II, Pergamon Press, 1961.

Landfield, J.P.: STOL Technology for Conventional Flight Enhancement. AIAA Paper No. 84-2397, AIAA/AHS/ASEE Aircraft Design Systems and Operations Meeting, San Diego, CA, Oct. 1984.

Malavard, L.; Jousserandot, P.; and Poissen-Quinton, Ph.: Jet Induced Circulation Control; Aero Digest, Part I, Sept. 1956, pp 21-27; Part II, Oct. 1956, pp 46-59; Part III, Nov. 1956, pp 34-46.

Mashell, E.C.; and Spence, D.A.: A Theory of the Jet Flap in Three Dimensions. Proc. Royal Society, A, vol. 251, 1959, pp 407-425.

Nichols, J.H., Jr.; and Englar R.J.: Advanced Circulation Control Wing System for Navy STOL Aircraft. AIAA Paper No. 80-1825, AIAA Aircraft Systems Meeting, Anaheim, CA, Aug. 1980.

Pope, Alan; and Harper, John J.: Low-Speed Wind Tunnel Testing. John Wiley & Sons, 1966, p 186.

Pugliese, A.J.; and Englar, R.J.: Flight Testing the Circulation Control Wing STOL Demonstrator Aircraft. AIAA Paper No. 79-1791, AIAA Aircraft Systems and Technology Meeting, New York, NY, Aug. 1979.

Queen, S.; and Cochrane, J.: Quiet Short-Haul Research Aircraft Joint NAVY/NASA Sea Trials. J. Aircraft, vol. 19, no. 8, Aug. 1982, pp 655-660; presented as AIAA Paper No. 81-0152, AIAA 19th Aerospace Sciences Meeting, St. Louis, MO, Jan. 1981.

Schubauer, G.B.: Jet Propulsion with Special Reference to Thrust Augmentations. NACA TN 442, Jan. 1933.

Spence, D.A.: The Lift Coefficient of a Thin Jet-Flapped Wing. Proc. Royal Society, A, vol. 238, 1956, pp 46-68.

Williams, J.; and Butler, S.F.J.: Aerodynamic Aspects of Boundary-Layer Control for High Lift at Low Speeds. Royal Aircraft Establishment, Tech Note Aero 2858, Nov. 1962.

Yen, K.T.: An Analysis of the Flow Turning Characteristics of Upper-Surface Blowing Devices for STOL Aircraft. Report No. NADC-82007-60, Oct. 1982.

FIXED WING CCW AERODYNAMICS WITH AND WITHOUT SUPPLEMENTARY THRUST DEFLECTION

J. H. Nichols and M. J. Harris

Department of the Navy
David Taylor Naval Ship Research and Development Center

(No paper received; presentation material only)

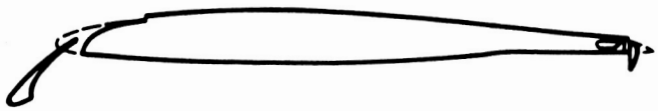

DEVELOPMENT OF ADVANCED HIGH LIFT SYSTEMS

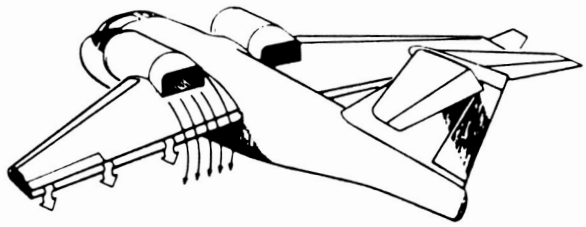

I. Development of high-lift airfoils employing circulation control has been underway at the David Taylor Naval Ship Research and Development Center (DTNSRDC) since 1969. Hybrid systems which combine circulation control with propulsive-lift concepts, like circulation control/upper surface blowing, are also being developed. This presentation will review the highly successful flight demonstration of circulation control on a Navy/Grumman A-6A aircraft and provide an overview of the continuing evolution of circulation control airfoils for fixed-wing applications.

A-6 CIRCULATION CONTROL WING

II. In 1979 a modified A-6A aircraft demonstrated the STOL capability of circulation control. This aircraft is shown as it was modified for this proof-of-concept flight demonstration. Externally the modifications included: a tapered cylindrical wing trailing edge, bleed air cross-over duct under fuselage, Krueger flap on the wing gloves, modified leading edge slats and modified horizontal tail.

CCW TRAILING EDGE APPLIED TO A-6 FLIGHT DEMONSTRATOR WING SECTION

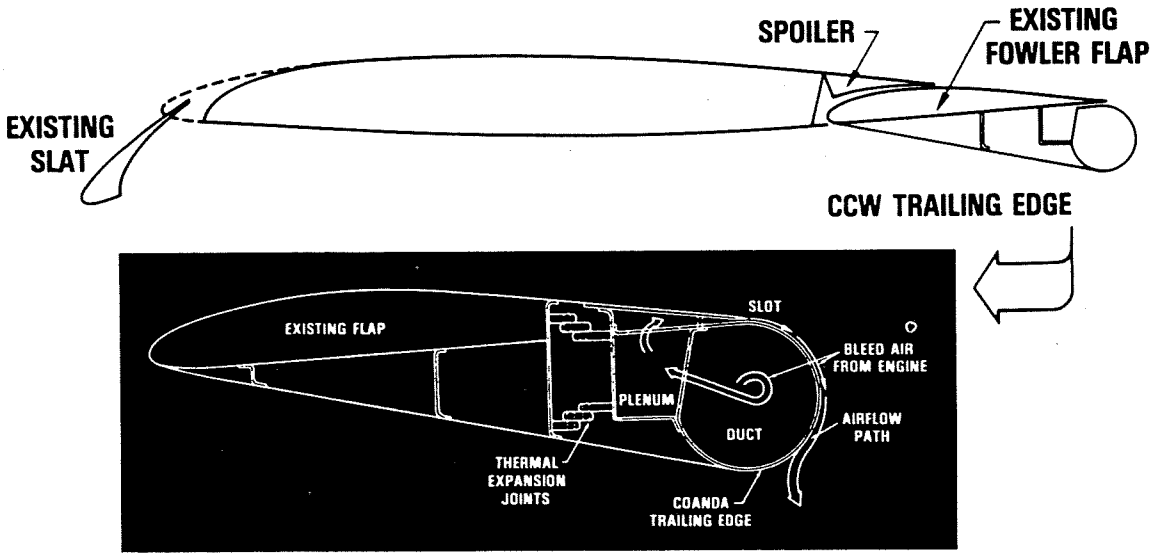

III. The A-6/circulation control airfoil used in the flight demonstration is shown here in cross section. Air bled from the fifth and twelth compressor stages of the two J52-P-8B turbojet engines on the A-6 is ducted along the wing span in the cylindrical trailing edge. The bleed air exits the cylindrical trailing edge, passes through the plenum and is ejected out through a thin slot in the aft upper surface of the airfoil. The thin jet sheet from the slot adheres to the cylindrical trailing edge, due to the Coanda effect, and flows down around this surface. The jet sheet provides boundary layer control and significant augmentation of the lift generated by the wing.

A-6/CCW
STOL PERFORMANCE

	A-6 (30° FLAPS) (REF)	A-6/CCW
85% INCREASE IN $C_{L_{MAX}}$	2.1	3.9 ($C_\mu = 0.30$)
35% REDUCTION IN POWER-ON APPROACH SPEED	118 KTs. ($C_L = 1.49$)	76 KTS (0.75 P_{MAX}, $C_\mu = 0.14$, $C_L = 2.78$)
65% REDUCTION IN LANDING GROUND ROLL	2450 FT	900 FT
30% REDUCTION IN LIFT OFF SPEED	120 KTS ($C_L = 1.41$)	82 KTS (0.6 P_{MAX}, $C_\mu = 0.04$, $C_L = 2.16$)
60% REDUCTION IN TAKEOFF GROUND ROLL	1450 FT	600 FT
75% INCREASE IN PAYLOAD/FUEL AT TYPICAL OPERATING WEIGHT (EW = 28,[illegible]0 LB.)	45,000 LB.	58,000 LB.

BASED ON FLIGHT DEMONSTRATION RESULTS
TOGW = 35,700 LB., LGW = 33,000 LB.
CORRECTED TO SEA LEVEL, STANDARD DAY

IV. Based on results from the flight demonstration, the A-6/circulation control aircraft achieved an 85-percent increase in maximum lift coefficient when compared to a standard A-6 with Fowler flap deflected 30-deg. This increase in lift coefficient was used to reduce the power-on approach velocity by 35-percent which results in a 65-percent reduction in landing ground roll. During takeoff the increase in lift coefficient provides a 30-percent reduction in lift off velocity which results in a 60-percent reduction in takeoff ground roll. Alternatively, at a takeoff velocity of 120 knots the 85-percent increase in maximum lift coefficient can provide a 75-percent increase in payload/fuel weight.

CCW CONFIGURATION DEVELOPMENT

A-6/CCW

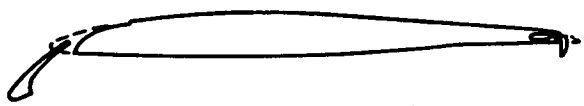

A-6 DUAL RADIUS FLAP

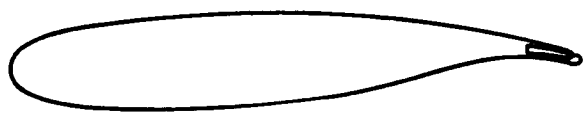

THIN T.E. SUPERCRITICAL/CCW

V. The radius of the cylindrical trailing edge used in the flight demonstration was 3.65-percent of the local wing chord. This relatively large surface could not remain deployed during cruise flight. Several concepts were proposed for converting this airfoil from the high-lift configuration to the cruise configuration. These concepts included: inflatable trailing edges, flaps which rotate nearly 180-deg exposing the cylindrical surface and complex mechanical systems which rotate or translate the cylindrical surface forward into the airfoil

Two mechanically simple alternatives to the large radius trailing edge used in the flight demonstration, which are being developed at DTNSRDC, are the dual radius circulation control flap and circulation control trailing edges with a radius small enough so it can remain deployed and still have minimal impact on cruise flight.

CCW AIRFOIL PERFORMANCE

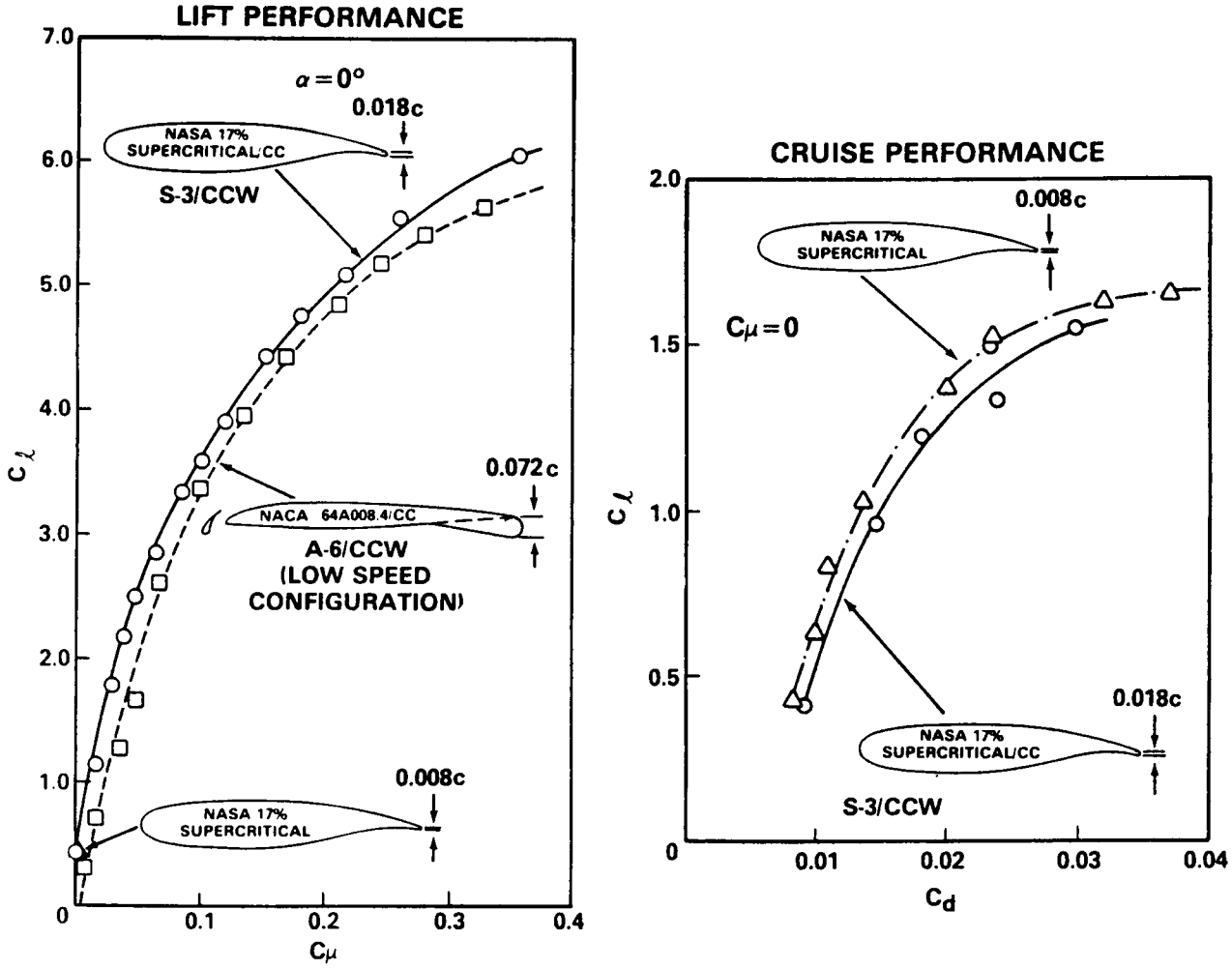

VI. The concept of a circulation control trailing edge which has a base thickness less than two-percent of the wing chord was successfully demonstrated on a supercritical airfoil. Wind tunnel investigations have confirmed the capability of this combination of supercritical airfoil and small radius circulation control trailing edge to achieve, at STOL velocities, lift coefficients equivalent to the lift coefficient achieved in the A-6/circulation control flight demonstration. This combination also results in an airfoil which converts from high-lift configuration to cruise configuration by simply terminating the flow of bleed air to the blowing slot. Since this trailing edge remains deployed during cruise flight no retracting mechanism is needed.

A-6/CCW
CRUISE CONFIGURED AIRFOILS

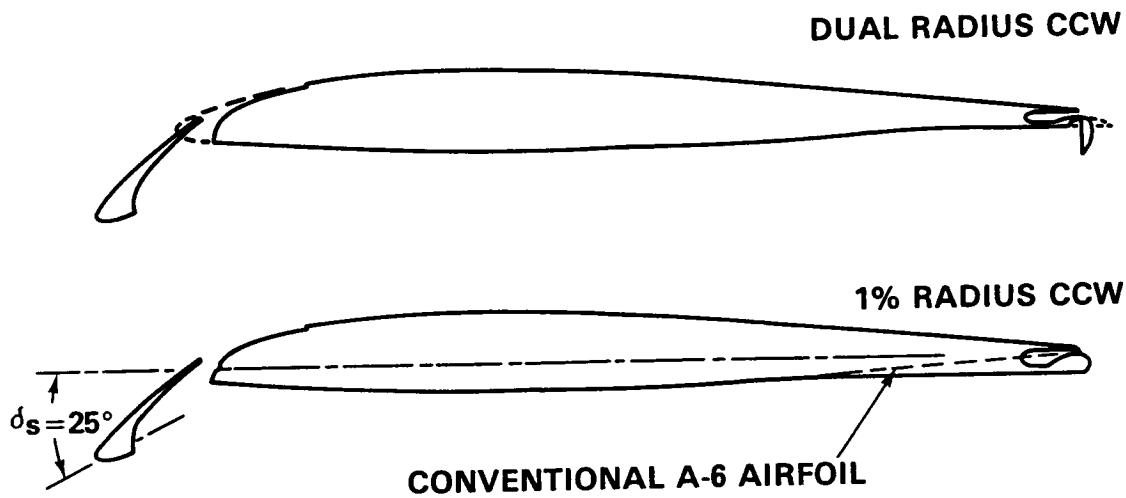

VII. A circulation control trailing edge with a radius of one-percent of the wing chord was also evaluated on the A-6 airfoil along with the dual radius circulation control flap. The dual circulation control flap is a short chord flap which, when rotated from 60 to 90 deg, provides a circulation control trailing edge. The dual radius flap currently being evaluated is 3.5-percent of the wing chord. Dual radius refers to the two arcs which make the upper surface of this flap. In this case the flap leading edge radius is one-percent of the wing chord and the flap trailing edge radius is four-percent of the wing chord.

COMPARISON OF BLOWN LIFT AUGMENTATION

α_g=3 deg
δ_{Slat}=25 deg

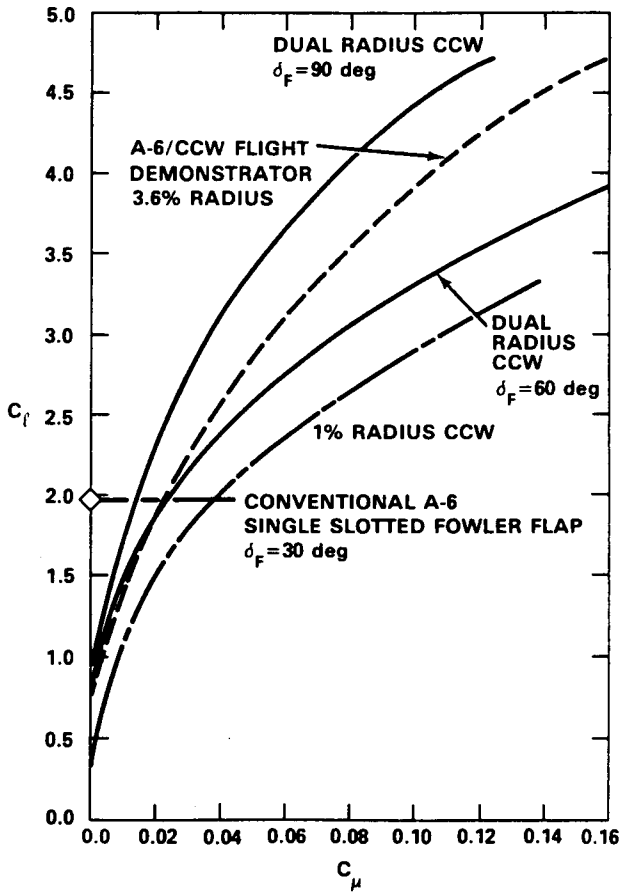

VIII. The A-6 airfoil with either the one-percent radius circulation control trailing edge or the dual radius circulation control flap achieved lift coefficients at relatively low blowing levels which are higher than can be achieved with a single slotted Fowler flap deflected 30 deg. With the dual radius circulation control flap deflected 90 deg, lift coefficients achievable at low to moderate blowing levels are higher than the lift coefficients achievable with the large radius circulation control trailing edge used in the flight demonstration.

CLEAN AIRFOIL COMPARISON (NO BLOWING)

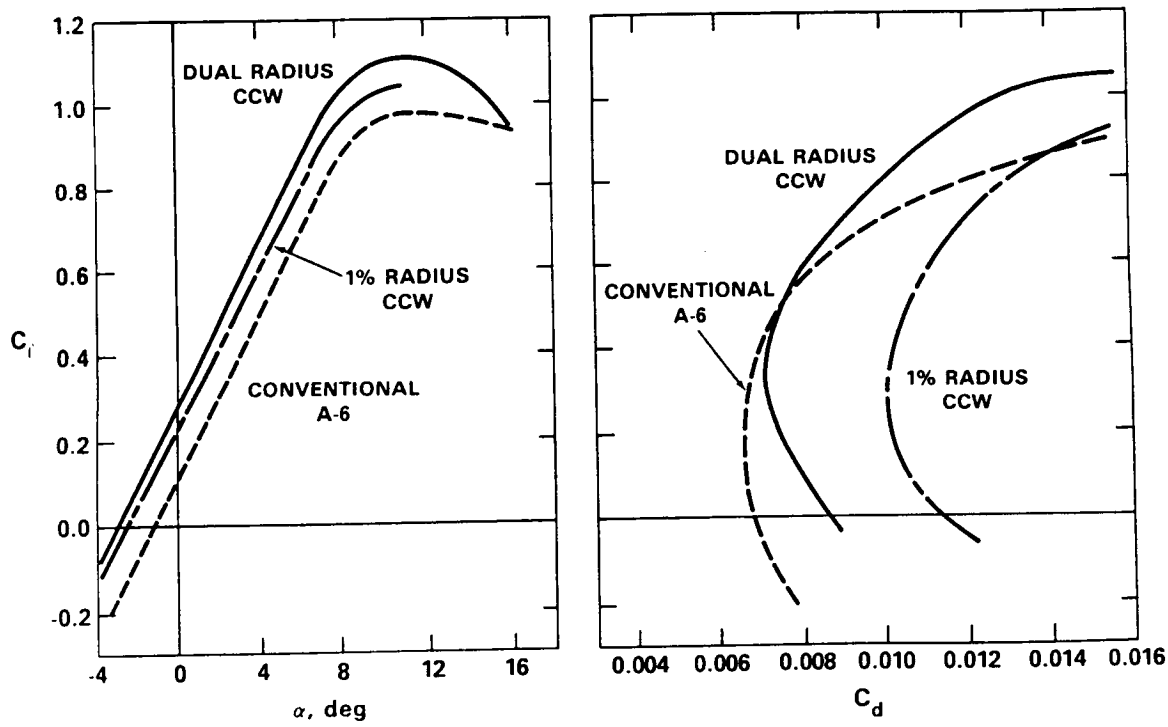

IX. The mechanical system required to rotate the dual radius circulation control flap would be equivalent to the system required for a simple single slotted Fowler flap. The undeflected dual radius circulation control flap would have no significant impact on cruise performance. The dual radius flap provides a means of mechanically varying the wing chamber independent of the circulation control blowing.

The impact of the one-percent radius circulation control trailing edge on cruise performance is significant enough to require that this surface be retracted during cruise flight. Retracting the small radius circulation control trailing edge would be considerably simpler than the large radius surface used in the flight demonstration.

Conclusions:

The concept of circulation control has been successfully demonstrated in flight using an A-6 aircraft.

Circulation control can provide an aircraft with STOL performance of heavy-lift capability.

For ship based Naval aircraft the lower takeoff and landing velocities result in reduced deck gear and wind-over-the-deck requirements.

Circulation control airfoil can be mechanically less complex and light weight compared to multi-element high-lift airfoils.

DEVELOPMENT OF CIRCULATION CONTROL TECHNOLOGY FOR POWERED-LIFT STOL AIRCRAFT

Robert J. Englar
Advanced Flight Sciences Dept.
Lockheed-Georgia Company

SUMMARY

The flow-entraining capabilities of the Circulation Control Wing high-lift system have recently been employed to provide an even stronger STOL potential when synergistically combined with upper-surface-mounted engines. The resulting configurations generate very high supercirculation lift in addition to a vertical component of the pneumatically-deflected engine thrust. The present paper will discuss a series of small-scale wind tunnel tests and full-scale static thrust-deflection tests which provide a sufficient data base confirming the concepts, and show means of improving their STOL and cruise performance. These test results show thrust deflections of greater than 90^{o} produced pneumatically by non-moving aerodynamic surfaces, and the ability to maintain constant high lift while varying the propulsive force from high thrust recovery required for short takeoff to high drag generation required for short low-speed landings. Predicted takeoff and landing performance of a postulated aircraft employing the combined concepts will show their excellent STOL potential, and indicate the need for follow-on research.

INTRODUCTION

The Circulation Control (CC) airfoil has been under development since 1968 (see Ref. 1), with initial application intended for rotary wing vehicles. The underlying principle of operation is shown in Figure 1. Tangential blowing over a round or near-round trailing edge produces a balance between centrifugal force and sub-ambient pressure in the jet, causing the jet to follow the curved surface, generate very high negative pressures in that vicinity and thus strongly entrain the surrounding flowfield. The result is boundary layer entrainment, until the airfoil static pressures return to the inviscid distribution at relatively low momentum coefficient (C_{μ}). Beyond that, additional blowing yields supercirculation and resulting lift greater than that attainable by potential flow. Typical results of early airfoil tests shown in Figure 1 ($C_l > 6.5$ for $C_{\mu} < 0.25$) revealed a very strong potential for CC airfoils beyond application to rotary wing vehicles: fixed wing STOL aircraft using CC airfoils for high lift generation at very low power input. Experimental maximum lift exceeding that predicted by potential flow theory (Fig. 2) has been generated; the minimum blowing required for a given lift increment was far less than that required by traditional blown flaps of similar flap chord. The possibility of obtaining this low required momentum directly from compressor bleed ports of existing jet engines, and

thus supplying excellent STOL capability to high performance aircraft, led to a Navy program to develop the Circulation Control Wing (CCW). Numerous 2-D and 3-D experimental investigations (Refs. 2 and 3 are typical) at David Taylor Naval Ship R&D Center (DTNSRDC) lead to a proof-of-concept flight demonstration program on a Navy A-6 (Ref. 4). The resulting significant STOL capability was confirmed (Ref. 5 and 6), and led to a continuing program at DTNSRDC to develop an operational CCW system for Navy STOL aircraft. This Navy program and advanced developments in CCW configurations are discussed in Reference 7, while an additional flight test program on a propeller-driven CCW aircraft was conducted at West Virginia University (see Ref. 1 for data reports). These two programs very successfully confirmed the CCW potential for fixed wing STOL aircraft, with the capabilities either of operating at very low speeds from short fields (or aircraft carriers) or operating with greatly increased gross weights and lift-off/return payloads.

The flow-entrainment capabilities of the CC trailing edge have recently been proven to provide an even stronger STOL potential when synergistically combined with a powered-lift system such as upper surface blowing (USB). Existing USB aircraft (Ref. 8, for example) entrain and deflect engine exhaust by means of large mechanical flaps, and add both a vertical thrust component $C_T \sin(\alpha+\delta_j)$ and increased wing circulation lift (C_{L_Γ}) to the high-lift capability (Fig. 3). However, CCW alone has virtually no lift component due to vertical thrust recovery, and as Figure 3 shows, obtains most of its high lift due to supercirculation, C_{L_Γ}. Again, this is possible due to the very high suction peaks at the trailing edge and the resulting flow entrainment and negative pressures induced on the airfoil. From Fig. 3 analysis, it appeared quite logical that a synergistic configuration of the two configurations could produce an even more effective and versatile STOL aircraft. Thus, a combination of CCW and USB (Fig. 4) was patented and experimentally confirmed (Refs. 9 and 10) at DTNSRDC. The device exhibited not only very high lift capability but also the ability to interchange drag and thrust at a fixed lift value, and thus provide significant versatility for STOL aircraft on steep approaches or in wave-off maneuvers.

Recent static investigations conducted by DTNSRDC at NASA Ames on the Quiet Short-haul Research Aircraft (QSRA, Ref. 11) have confirmed full-scale static thrust turning greater than 90°. A second series of tests conducted on that aircraft developed improved CCW configurations that required even less blowing to provide usable thrust turning angles. In addition, recent work being conducted at Lockheed-Georgia Company has continued development of the CCW/USB data base and configurations, with specific attention being paid to the cruise mode. With the intention of reducing scrubbing losses due to USB exhaust immersing the wing upper surface in cruise, the Over-The-Wing (OTW) concept previously investigated by NASA (Ref. 12) has been re-evaluated and combined with CCW.

The present paper will elaborate on the above-mentioned developments of the circulation control wing concept integrated with various forms of powered-lift systems. It will provide further details on these recently conducted powered-lift research efforts, both model- and full-scale, and evaluate calculated STOL performance improvements when applied to an existing airframe/engine combination. Primary discussion will center on two recently

conducted series of investigations: a full-scale static development of CCW/USB on the NASA QSRA STOL aircraft, and smaller-scale model tests of CCW/USB and CCW/OTW. A summary of early experimental confirmation of the CCW/USB will precede these.

SYMBOLS

Values are given in SI and U.S. Customary Units, but measurements and calculations were made in the latter.

b_j	blowing jet slot span, cm (in.)
c	airfoil chord, cm (in.)
C_D	wing or aircraft drag coefficient (includes horizontal thrust component if a vectored-thrust configuration)
C_l, C_L	airfoil or wing (aircraft) lift coefficient
C_{L_Γ}	circulation lift coefficient
C_T	thrust coefficient, T/qS
C_μ	blowing momentum coefficient, $\dot{m}V_j/qS$
h, h_j	blowing jet slot height, cm (in.)
h_N	engine exhaust nozzle height, cm (in.)
M_j	blowing jet Mach number
M_{USB}	engine exhaust Mach number
$\dot{m}$	blowing jet mass efflux, kg/sec (slugs/sec)
N_1	engine fan speed, rpm
P_{CCW}, P_{T_d}	blowing plenum total pressure, N/m^2 (lb/ft^2)
q	freestream dynamic pressure, N/m^2 (lb/ft^2)
r	CC trailing edge radius, cm (in.)
S	wing area, m^2 (ft^2)
T	calibrated engine thrust, N(lb)
t/c	airfoil thickness-to-chord ratio
V_{APP}	velocity along approach flight path, m/sec (ft/sec)
V_j	blowing jet velocity, m/sec (ft/sec)
W_N	engine exhaust nozzle width, cm (in.)
α	angle of attack, deg.
α_{geo}	geometric angle of attack, uncorrected for tunnel interference effects, deg.
δ_F	flap deflection, deg.
δ_{USB}	Upper Surface Blowing flap deflection, deg.
θ, δ_j	jet or thrust deflection angle, deg. down from aft horizontal axis

SMALL-SCALE CONFIRMATION OF CCW/USB

The original concept of a CCW/USB combination occurred when the author was at DTNSRDC following the successful A-6/CCW flight test. An initial bench test was conducted on a semi-span CCW model joined with a turbofan engine simulator with a D-nozzle. Flow visualization indicated very large engine thrust deflection angles, and led to the mounting of the model on a tunnel balance frame for static confirmation. Figures 5 and 6 from Ref. 6 present

the results in terms of static jet turning angle (θ) as influenced by CCW blowing pressure and engine thrust level. Large turning angles of 165^{o} are confirmed, as is increased turning corresponding to increased CCW momentum. Two additional trends are also noted. Reduced turning occurs at higher thrust levels because of the additional energy in the engine exhaust that must be entrained by CCW. At constant higher thrust levels, peaks occur beyond which additional blowing yields reduced turning. This could very well be due to a characteristic previously noted for CCW alone (Ref. 13): higher blowing jet velocities, smaller turning radii and increased slot heights can reduce jet turning effectiveness. Figure 6 depicts the efficiency of this form of thrust deflection, with greater than 95 percent of the thrust and blowing momentum being recovered up through 55 degrees of thrust deflection. It also confirms a trend previously unseen in static USB data: thrust deflection of greater than 90^{o}, as well as the generation of both drag and thrust recovery from the same system.

Wind-on investigations, conducted on the same model in the DTNSRDC 8x10-ft. subsonic tunnel, confirm the lift augmentation possible with this system, in two modes of operation (Figure 7). These data, all taken at zero degrees geometric incidence, are for inboard blowing alone ("CC/USB only," solid symbols) and for CCW/USB combined with outboard blowing of a CCW segment ("CCW+CC/USB," open symbols). Inboard blowing alone confirms lift increase with both blowing and thrust increase, due to the increased exhaust deflection and entrained flow. However, the addition of outboard blowing of CCW yields additional lift at the same total C_{μ}. The drag polars confirm the versatility of the system, allowing at constant C_L the generation of either large drag values (for equilibrium approach) or large thrust values (for takeoff or climbout) merely by adjustment of thrust or blowing coefficient. Considerably more developmental work and configuration improvement was conducted at DTNSRDC on this concept, and is reported in detail in References 6, 9, 10, and 14.

LARGE-SCALE QSRA STATIC TESTS - PHASE I

An unknown in the above investigation was the effect of a real mixed-flow turbofan engine with hot exhaust, as well as the effects of scaling to full size. To address these issues, a joint DTNSRDC/NASA Ames full-scale static test was conducted, and is reported in detail in Reference 11. This Phase I test is summarized briefly here to provide a reference data base for the discussion which will follow on a second test series conducted to improve the CCW/USB configuration.

Figure 8 shows the NASA Quiet Short-Haul Research Aircraft (QSRA), a flight-proven Upper Surface Blowing powered-lift STOL aircraft, mounted on static thrust stands during the Phase I static tests conducted at NASA Ames Research Center. A CCW configuration can be seen mounted behind the inboard left engine only. Blowing was supplied using mass flow from standard aircraft ground starter carts, connected to the configuration as shown in Figure 9. The trailing edge radius was 3.62 percent of the average wing chord of the blown wing section, and the blowing slot height was set statically at 0.04 inch. Tufts in Figure 9 confirm the greater-than-90-degree jet turning

produced by the round trailing edge. These curving tufts contrast with a single tuft outboard of the blown section which plots the unaffected exhaust flow exiting aft nearly parallel to the wing upper surface. Static thrust turning resolved from the measured horizontal and vertical static forces is plotted in Figure 10, where trends very similar to the small-scale data of Figure 5 are noted. Actually, the apparently lower thrust turning angles of the full scale test are due solely to the fact that the mass flow output from the ground starter carts was insufficient to match the CCW blowing levels of Figure 5. A comparison between full-scale data and model data from Reference 14, adjusted to match the geometry of the QSRA arrangement, is shown in Figure 11. The agreement was quite good, considering some slight variation in parameters that were not exactly duplicated in the full-scale test (see Ref. 11). The conclusions drawn were that the full-scale hot configuration behaved in a very similar manner to the small-scale cold exhaust tests, jet deflections varied from 43 to 97 degrees at the higher blowing rate, and that additional full-scale jet deflections would result if greater CCW momentum were available. An additional item of interest is shown in Figure 12, where the Figure 10 data are nearly linearized when plotted against Mach number in the engine exhaust measured at the CCW jet slot location, instead of against calibrated engine thrust at the exhaust nozzle.

LARGE-SCALE QSRA STATIC TESTS - PHASE II

The above Phase I investigations revealed some refinements and improvements needed with the CCW/USB system, and suggested means to improve overall system performance and simplicity. Thus, a follow-on Phase II full-scale static investigation was conducted on the QSRA, the results of which will be discussed herein, and compared with the initial tests. Greater detail is found in Reference 15. The objectives of this Phase II series of tests included:

- refinement of CCW trailing edge shape and thickness to reduce cruise drag and determine if configurations other than large circular ones could improve performance,
- increase in blown system span and limitation of losses at the outboard end in order to further entrain more of the engine exhaust sheet,
- variation in blowing slot height to investigate additional entrainment, and
- increase in blowing slot momentum to investigate greater thrust deflection.

Design, Installation and Test Procedure

To investigate the above, two reduced-thickness CCW trailing edges of increased span and different structural arrangement were designed by DTNSRDC and constructed by Micro Craft Inc. of Tullahoma, Tennessee. These are shown in Figure 13 compared to the Phase I fully-circular large radius (r = .0362

chord) trailing edge. The 5-inch diameter 180-degree arc section was intended to reduce trailing edge thickness of the circular CCW device in blowing-off cruise by reducing the radius. The 10-inch diameter 90-degree arc section was intended to do the same, while maintaining the original larger radius of the Phase I configuration. This assumed that a maximum turning angle of 100 degrees from aft horizontal would be satisfactory from a STOL performance standpoint (if thrust reversing were not required). The span of the new configurations was increased to capture the larger spanwise spreading of the engine exhaust that had been exhibited in Phase I, and an outboard fence was installed to limit that spreading to the span of the blown section. Furthermore, variable slot height capability was provided. The five new configurations investigated during Phase II are further compared to the Phase I trailing edge below:

Phase	Config.	Dia., in.	Arc, deg.	Fence	Span, in.	Slot Ht, in.
I	--	10.0	260	Off	75.0	0.040-0.067
II	1	↓	90	↓	88.0	0.070
II	2	↓	↓	On	↓	↓
II	3	↓	↓	↓	↓	0.035
II	4	5.0	180	↓	↓	↓
II	5	↓	↓	↓	↓	0.070

Figures 14 and 15 show closeups of the 90-degree arc and the smaller-radius 180-degree circular arc as installed on the left inboard flap of the QSRA. Trailing edge thickness at the blowing slot location is the same for both, yet the radius of the 90-degree arc is twice as large. This eases the more difficult task for the CCW jet of entraining the high energy of the engine exhaust around a small radius, a phenomenon experienced in several aspects of previous CCW flow investigations (Ref. 13).

Figure 16 shows installation of the removable flow fence located 13" outboard of the separation line between the inboard and outboard mechanical USB flaps, which is where the Phase I trailing edge terminated. This figure also shows the blowing slot, pressure and temperature probes for the engine exhaust, support rod to restrict trailing edge upward deflection under load, and two of three air supply lines connected to the blowing plenum. These lines were connected to three conventional ground air-starter carts to supply the CCW trailing edge blowing; variation in blowing rate was simply by attaching or disconnecting another cart to the plenum. Slot height was pre-set at the values shown in the above chart, and then reset and measured when pressure and temperature had stabilized at each test condition. Since there were no flow meters in the starter cart system, the blowing mass flow ($\dot{m}_j$) and jet velocity (V_j) were calculated using the measured temperatures, pressures, and slot areas in the isentropic equations, just as they were in Phase I (see Ref. 11).

For relative comparison, the 90-degree arc configuration is shown on the QSRA in relation to the undeflected USB mechanical flap behind the outboard engine and the outboard double-slotted flap in Figure 17. On a production aircraft, the trailing edge of the CCW device would align with the conventional trailing edge, not be displaced aft of it as shown here. The

large size of the mechanical devices when deflected is hinted at by the size of the flap mounting brackets and fairings below the wing. A goal of this program was to eliminate the drag and complexity of these mechanisms as required for mechanical high-lift systems.

Results and Discussion, Phase II

Data from References 9, 10, 11 and 14 imply that CCW/USB thrust deflection is primarily a function of engine thrust level and CCW jet characteristics (mainly jet total pressure and momentum), while Reference 13 notes that CCW radius and slot height can strongly influence jet turning, especially at higher blowing pressures. Results of the Phase I test had confirmed some of the above relationships, as did the Phase II results. However, additional trends (such as effects of slot height and blowing span variations) were established during Phase II, and a number of performance improvements were seen.

Thrust Deflection and Recovery - Typical thrust deflection results from Phase II are shown in Figures 18 and 19, which represent two extremes in performance: the excellent turning produced by the larger radius 90-degree arc with a smaller slot height (Config. 3) compared to the considerably reduced turning of the smaller-radius 180-degree circular configuration with a larger slot height (Config. 5). At a typical blowing momentum per unit span of approximately 20 lb/ft at 75%N_1 engine power setting, the 90-degree arc produced 55 degrees of thrust deflection compared to about 37 degrees for the smaller radius 180-degree configuration. Note also for this latter configuration the much higher degree of resultant thrust loss per degree of turning at constant %N_1 (i.e., the more negative slopes of the lines marked constant N_1), a factor which could prove detrimental in climbout or go-around for a STOL aircraft.

An evaluation of the effect of reducing slot height can be made by comparison of Figure 20 with 19, both being for the small-radius 180-degree circular arc configuration. Here, for the same blowing momentum and power setting (say 20 lb/ft and 75%N_1), the smaller slot height yields greater turning compared to the larger slot height (47 degrees versus 37 degrees). This is because, at constant jet momentum, the reduced slot height's exit area must be balanced by increased jet velocity, which (up to certain higher limits on pressure ratio across the slot) produces greater flow entrainment and thrust deflection.

Whereas Figure 19 for the larger slot height confirms the additional thrust turning produced by additional momentum, that test objective was not met for the smaller slot heights. In Figures 18 and 20, the upper two sets of data (higher momenta) represent 2 and 3 ground start carts supplying air to the CCW. These should show the effect of a 50% increase in momentum, yet show little, if any, change in thrust turning. This was due to the fact that higher plenum pressure was required to produce a given momentum with a smaller exit area, and thus a limiting back pressure was reached (approximately 32-34 psig), beyond which the starter carts could produce no additional mass flow. Thus evaluation of the effect of jet momentum greater than about 20 lb/ft at

smaller slot height was not conducted and will require an alternative air supply source to complete.

For the above results, a resultant thrust vector was calculated for each test condition as the vector sum of static forces measured in the horizontal/vertical planes. This vector acted on the aircraft at the thrust deflection angle θ, measured positive downward from the aft horizontal. (No lateral forces are included due to lack of balance components in that direction.) As noted during Phase I (Ref. 11) and previous USB investigations, there is usually some loss in resultant thrust as jet turning increases, due to jet spreading, mixing and viscous losses. In Phase I, at maximum installed power, thrust recovery (resultant/installed thrust) varied from 98% with blowing off to 89% with maximum blowing momentum of 34.3 lb/ft. (Since blowing air came from the external ground starter carts, these recovery values do not include any thrust loss due to engine bleed, which would have to be considered in actual application). For comparison, Figures 21 and 22 present resultant thrust as functions of installed thrust, power setting and blowing rate for both the large- and small-radius CCW trailing edges and a 0.035-inch slot height. Thrust recovery for the 10-inch diameter 90^{o} arc (Fig. 21) is nearly the same as for the Phase I baseline configuration, but the smaller 5-inch circular arc shows considerably less recovery with blowing, down to about 83% at 20.7 lb/ft of blowing at maximum power setting. In general, for similar thrust deflection values, resultant thrust recovery is less with either smaller trailing edge radii or larger jet slot heights. These same trends were noted from the constant N_1 lines of Figures 18, 19, and 20. These trends produce mixed implications in STOL operation, where thrust loss is advantageous on approach along steep glide slopes, but is definitely detrimental on takeoff, climbout or waveoffs (go-arounds).

A typical resolution of measured horizontal and vertical forces and their variation with blowing is shown in Figure 23. Here the versatility of the CCW/USB concept is evident: constant vertical force may be maintained while horizontal force is varied pneumatically. Conversely, constant horizontal force may be held while lift is increased by blowing, again without incidence or mechanical changes. The payoff for STOL aircraft, when the aerodynamic forces are added to these static values, will become more evident in a later section on STOL performance.

Configuration Comparison- A comparison of the effectiveness of the full-scale configurations tested in Phase II with the Phase I baseline is shown in Figures 24 and 25 for values of constant resultant thrust. Resultant thrust levels of 2500 and 5000 pounds represent approximately half- and full-power settings of the engine as installed in this test setup. In Figure 24, blowing momentum is plotted per unit span to offset the effect of additional momentum corresponding to increased slot length. Blowing off, the geometric camber of the Phase I circular configuration increased thrust deflection by 10-11 degrees over the Phase II configurations as well as the basic USB undeflected flap. The 90-degree arc (configuration 3) produced only 1 to 2 degrees incremental turning with blowing off. Large thrust deflection in cruise could prove detrimental because of horizontal thrust loss.

With blowing applied, a number of performance increases were noted. The increased span and endplate of the Phase II 10-in.-diameter configuration 3 nearly doubled the incremental thrust turning due to blowing when compared to the same radius configuration of Phase I. The flow fence alone produced a 2- to 4-degree increase in thrust deflection (Configuration 2 vs. 1). A doubling of the trailing edge radius (Configuration 3 vs. 4) increased thrust turning by 8 to 10 deg, but produced no difference in the blowing-off thrust deflection due to geometric camber. Reducing the slot height by 50 percent (Configuration 3 vs. 2, or 4 vs. 5) added 8 to 15 deg of thrust deflection at the same momentum. These data extend to CCW/USB the Reference 13 findings that flow entrainment over curved surfaces with blowing becomes more difficult with smaller radii, larger slot heights, and higher entrained flow velocity (i.e., greater engine thrust).

Figure 25 supplies useful design data for STOL application of this system, as it provides blowing momentum required for a given thrust deflection as a percentage of installed engine thrust. Since turbofan engine thrust loss can become appreciable when increased bleed is taken from the core, it is desirable to keep the bleed momentum as low as possible for takeoff and climbout. From this viewpoint, it is seen that for a typical thrust deflection of 40 degrees, the 90-degree arc (Config. 3) requires bleed momentum equal to 1.7 percent of the installed thrust, at full power setting. The Phase I configuration required about 4.6 percent to obtain the same turning, while the smaller diameter 180^{o} arc with larger slot height does not appear able to reach that value at all, probably due to the high exhaust energy level and small turning radius. For STOL approaches, where large thrust deflections are desired, the 90-degree arc at half-power setting can produce 60 degrees deflection using 5% of engine thrust as blowing momentum, a value which might typically be bled from the core of the engine; higher values become progressively more difficult to obtain. At the same half-power setting and 5% bleed, the smaller radius 180-degree arc produced 53 degrees jet deflection while the Phase I arc produced 48 degrees. The smaller radius was not as greatly affected by high exhaust velocity at this reduced power setting.

The above results indicate that the most effective trailing edge configuration from a thrust-turning standpoint was found to be the 10-in.-diameter 90-degree circular arc. It provided the same thrust turning as the other configurations while using considerably less momentum, or produced greater thrust turning at the same momentum. Exact comparison with the 10-in.-diameter circular cylinder of Phase I was not possible due to span and other geometry differences, but indications were that additional physical arc greater than 90 degrees performed little useful function. For the range of blowing investigated, a summary performance comparison can best be seen in the following chart of increase in jet deflection due to blowing:

Configuration	$T_{resultant}$, lb.	$\Delta\theta$, deg.
Baseline, Ph.I	2500	26.2
Config. 3, Ph. II	2500	46.0
Baseline, Ph. I	5000	13.8
Config. 3, Ph. II	5000	29.5

Excluding the effects of slightly smaller slot height and better blowing slot lip alignment of the 90-degree circular arc with h_j = 0.035 inch and larger span, that configuration roughly doubled the jet deflection due to blowing of the baseline Phase I configuration. It thus appears that one of the most effective means of increasing jet deflection is to ensure that the entire spread exhaust from the USB engine is captured by the CCW jet. With that provision, very effective pneumatic thrust turning can thus be produced by a much thinner partial arc trailing edge shape, which produces almost no thrust loss in cruise due to camber-induced deflection, and should have considerably reduced base drag. Thus, the performance improvements sought by the Phase II investigation were achieved by configuration improvement, and the new configurations developed should yield not only improved STOL performance, but increased cruise efficiency as well.

STOL APPLICATION AND PREDICTED PERFORMANCE

In order to investigate possible payoffs of the above thrust-vectoring and lift-augmenting technology, a STOL aircraft was postulated, employing the combination of CCW outboard and CCW/USB inboard (Ref. 9). The basic airframe chosen was the Lockheed S-3A Viking, with its existing TF-34 high-bypass turbofan engines retained but re-mounted on the wing in the USB arrangement shown in Figure 26. As the intended mission for this proposed aircraft was STOL operation from small-deck carriers, the original S-3A aspect ratio of 7.73 was reduced to 6.0 to allow flight deck clearance. The CCW/USB data of Figure 7 was used, but adjusted (see Ref. 9) to account for the aspect ratio difference and blowing-off characteristics of the basic S-3. The lift curves of Figure 27 resulted. (The standard S-3A still retains its 7.73 aspect ratio). Since no engine bleed data or thrust turning results were available for this configuration, it was assumed that a C_μ of 0.10 would be obtainable (perhaps from fan rather than core bleed) and that a thrust deflection angle of 38^o was attainable at all thrust settings. A round trailing edge CCW/USB configuration similar to that of the above Phase I test was assumed. In light of the Phase II tests results above, all of these conditions seem to be conservative, and thus the following performance predictions should represent at least a lower level of attainable performance for this type of configuration.

Takeoff Performance

All STOL performance discussed below is based on sea level tropical day ($90^{o}F$) conditions with standard S-3/TF-34 maximum two-engine installed thrust of 13,020 lb total, which include losses due to thrust droop, ram drag at 60 kts, and bleed. Since high thrust/weight ratio can be an important benefit in achieving short takeoff ground rolls, it is important to note that for the S-3A takeoff gross weight range (35,000-40,000 lb), the effective thrust/weight ratio is a relatively low 0.33 - 0.38, as Fig. 28 shows.

For this weight range, conventional S-3A (CTOL) lift-off speeds of 115 knots can be reduced to 60-65 knots by CCW/USB. The implications on reduced requirements for catapult equipment (if, in fact, any is required at all) are significant. The resulting non-catapulted takeoff distances are compared in Fig. 28 for wind-over-deck (WOD) velocities of 0 and 20 knots. Here, the takeoff procedure for the proposed aircraft is to accelerate at maximum thrust (bleed off and no thrust deflection) until the rotation speed is reached. At rotation, blowing is initiated and instantaneous thrust deflection and lift augmentation occur. This procedure was successfully and comfortably used by Grumman test pilots with the A-6/CCW (Ref. 5). For a 20 knot WOD, conventional S-3 takeoff rolls of 1,175 - 1,650 ft will be reduced to 200 - 325 ft. Takeoff distances of 450 - 650 ft are possible if no wind over deck is available.

Landing Performance

Using the conservative assumptions of only 38^{o} thrust deflection and 0.10 blowing coefficient, Fig. 29 compares equilibrium approach speeds at an incidence of 9^{o} or 10^{o} on a 4^{o} glide slope. Since no flare is used in Navy approaches, this glide slope is constant and forces must be in equilibrium along that flight path to avoid acceleration down it. This requires additional drag generation for USB aircraft since high lift is achieved at high thrust settings which normally result in high thrust recovery. This thrust recovery is offset for the CCW + CCW/USB aircraft by the induced drag generated by CCW. Thus all approaches are made along the $C_D = 0$ axis (see Fig. 7) but at the appropriate approach incidence of 10^{o}. For a landing weight of 30,000 - 35,000 lbs, the approach speed is reduced from 95 to 55 knots by the CCW + CCW/USB. For a fixed bleed rate from the engines, available C_μ will not remain constant, but will increase as weight and associated speed decrease. Thus Figure 29 also shows approach speeds at a fixed bleed momentum of 1130 lbs. total, which is felt to be attainable for this configuration. Approach speeds below 50 kts are now possible. These very low approach speeds plus any wind over deck will reduce touchdown speeds, kinetic energy to be dissipated, and landing ground rolls by as much as 70 percent. They also imply the capability for an improved steeper glide slope to minimize flight through carrier-induced turbulence, increased pilot visibility from approach at lower incidence, and increased pilot reaction time due to lower closure rates, all of which contribute to safer carrier operations and thus reduced accident rates.

The above STOL performance predictions indicate significant potential for aircraft operation from small air-capable ships, plus a number of operational

benefits for land-based aircraft as well, resulting from the incorporation of CCW/USB.

SMALL-SCALE ADVANCED CONFIGURATION DEVELOPMENT

While the above developments primarily addressed the high-lift pneumatic STOL configurations, an obvious outgrowth which cannot be overlooked is the associated cruise performance. The immersion of the wing upper surface and trailing edge in the engine exhaust, which is responsible for the thrust-induced lift generated by the CCW/USB configuration, also produces thrust loss due to exhaust scrubbing on these surfaces in the cruise mode. With the intention of reducing these losses without detriment to STOL thrust deflection, the Over-the-Wing (OTW) concept previously investigated by NASA (References 12 and 16) is being re-evaluated and refined at the Lockheed-Georgia Company. As shown schematically in Figure 30, the USB engine is relocated in the OTW configuration onto a pylon above the wing. Reference 16 confirms that this will eliminate the scrubbing drag and, in fact, if the undeflected exhaust nozzle is properly located, can reduce the induced drag in cruise by inducing an upwash on the wing. Recent research conducted at Lockheed-Georgia has focused on developing the high-lift OTW configuration by replacing the mechanical flap system with CCW configurations, and increasing the system's ability to deflect OTW thrust by improving the CCW turning surface geometry.

A generic powered-lift model has been used in these investigations; it is shown in Fig. 31 installed in the Lockheed 30x43-inch Model Test Facility, spanning the 30-inch width of the tunnel in a "quasi 2-D" mode with a chord-to-tunnel height ratio of 5.4. Force data from the floor balance, as well as pressure data from model static taps and a wake rake, were recorded. The model wing could be retracted through the tunnel floor to allow variation in aspect ratio. The same model is shown in Figure 32 as a semi-span aspect ratio 5.5 configuration. The OTW engine as shown was mounted on a wing pylon and employed a nozzle hood to deflect thrust onto the wing surface instead of the mechanical exhaust nozzle shown in the lower portion of Figure 30. For system comparison, the engine was also located on the wing surface and a D-nozzle installed to represent a USB configuration.

Test Results and Discussion

Figure 33 compares lift results for USB and OTW engine arrangements using both CCW and a single-slotted flap to entrain and deflect the thrust. In this "quasi 2-D" mode, as well as in the AR = 5.5 semi-span mode, the wing reference area is considerably larger than that affected by the engine thrust deflection, and thus the thrust coefficients evaluated (C_T = T/qS) are typically lower than would be expected of a STOL aircraft with proportional sizing of wing and engine. For the same trailing edge type, the following trends were noted:

- With the single-slotted mechanical flap, OTW yields greater induced lift and thrust recovery than does USB.

- With moderate thrust and blowing, there is relatively little difference between OTW and USB when combined with CCW. This confirms that CCW is able to entrain the thrust from the OTW engine nacelle which is further above the turning surface than it is for USB. It does however require a nozzle hood device, but the implication is that the two concepts are then equivalent in STOL while OTW should demonstrate reduced thrust loss in cruise.

Cross-plane velocity vectors obtained from 7-hole-probe rake surveys of the wing wake show the effect of the trailing edge high lift device on OTW performance in Figure 34. Clearly, the CCW blowing spreads, deflects and diffuses the exhaust plume, thus enhancing the lift by as much as 75 percent over the OTW/mechanical flap at low incidence, as shown in Figure 33. The engine downwash directly behind the wing is greatly reduced, thus reducing the possibilities of tail stall due to downwash immersion, ground fountain effects in STOL, and large nose-down pitching moments.

In order to generate additional blowing-off lift due to geometric camber, to provide a control device on thrust deflection with blowing, and to provide increased thrust recovery, the round CCW trailing edge used above was converted to a CCW flaplet by addition of an 11.4% plain flap, as shown in Figure 35. This flaplet had straight upper and lower surfaces making 14-degree angles with the chord line, and pivoted about its center on the chordline directly below the blowing slot. The radius exposed as the flap deflected was the same as the original CCW round trailing edge (.031c). A previous series of quasi 2-D investigations at various flaplet angles led to the choice of this 60-degree flap deflection, with the emphasis being on lift augmentation combined with engine and CCW jet thrust recovery.

Resulting lift generated at two CCW blowing levels and two engine thrust levels, as well as data for the plain CCW wing without the engine installed, are shown in Figure 35. An interesting comparison at these lower thrust levels shows that much greater lift augmentation per unit momentum input results from CCW blowing than from thrust deflection. As an example, at C_μ = 0.46, C_L is 2.8 to 3.0 higher than for C_μ = 0, while for C_T = 0.46, C_L is only 0.25 to 0.40 more than for C_T = 0 ("No engine").

The above data were used to extrapolate the CCW/OTW drag polars in Figure 36 to a typical C_T of 2.0. At this thrust level, and over a typical CCW blowing range of C_μ = 0 to 0.4, almost the entire envelope of drag polars lies in the negative drag (positive thrust recovery) region. This is quite desirable for short takeoff, climbout or waveoff, but it can produce a serious problem during a STOL approach: the aircraft cannot generate enough drag to offset the higher engine power level, and thus equilibrium slow-speed approach down a steep glide slope becomes quite difficult, if not impossible.

To generate this required drag, a means of increasing thrust deflection to higher angles is necessary such that little thrust is recovered under approach conditions. The round CCW trailing edge provides a means to do this, as shown by the data from Reference 14 plotted in Figures 35 and 36. As an example, at a C_T = 1.2 and C_L = 3.5, drag coefficient is converted from -0.50 for the 60-degree flaplet to +0.75 for the round CCW.

Although the aspect ratio (AR=4) and the engine arrangement (CCW/USB) of Reference 14 are not exactly comparable with the current model, the similar C_T and C_μ values serve to illustrate the trend: namely, additional turning produced by the round CCW trailing edge can reduce the thrust recovery and increase total drag. Thus, the desired compromise configuration to provide excellent operation in all regions of the STOL flight envelope is one which generates high lift augmentation in all configurations, but at the same time simply and effectively allows high thrust recovery on takeoff and climbout and high drag generation on approach. The further constraint of an efficient clean aircraft cruise configuration is, of course, mandatory.

To pursue these objectives, the CCW Dual Radius configuration developed in References 7 and 17 was combined with OTW. Here the flat upper surface of the short-chord flaplet of Figure 35 was converted to a large secondary radius to yield an additional 36 degrees of turning surface for the CCW jet and engine thrust. Figure 37 shows resulting lift and drag. The dual radius CCW flap alone, when deflected 90^o, generates similar lift and much higher drag than the 60^o flaplet OTW configuration at $C_T = 3.0$. However, when combined with OTW, the dual radius CCW flap increases C_L by as much as 2.5, yet allows thrust to vary from $C_D = -2.0$ to $+ 1.2$ merely by varying C_μ and resulting thrust deflection. Furthermore, tests of the undeflected dual radius CCW alone in a cruise configuration showed drag reduction of 14 percent compared to the undeflected flaplet and 40 percent that of the round CCW ($r = .031c$).

CONCLUSIONS

The above static full-scale and wind-on model-scale results have provided valuable confirmation that CCW can be effectively combined with an above-wing-mounted (USB or OTW) engine system to yield pneumatic thrust deflection and associated lift augmentation. The more important conclusions are:

- CCW flow entrainment can yield pneumatic thrust deflections of 90 degrees or greater from USB-mounted engines, and resulting model-scale maximum lift coefficients of 8-9.

- Improved CCW/USB configurations employing thinner, less-cambered partial arc trailing edges with smaller slot heights and increased blowing spans have yielded improved STOL potential.

- Pneumatic control of lift augmentation and horizontal thrust recovery increases STOL versatility, allowing simple conversion from high drag to high thrust recovery while maintaining a constant lift force. Variation of the combined aerodynamic/propulsive forces is thus seen to be possible without change in angle of attack or deflection/retraction of any external moving parts.

- Advanced versions of CCW and pneumatic thrust deflection can simplify powered-lift systems and improve cruise efficiency by eliminating viscous scrubbing losses. CCW/OTW configurations offer STOL performance similar to CCW/USB, as well as improvements in cruise drag

and efficiency. Both systems make possible few- or no-moving-part powered-lift systems capable of excellent STOL performance.

Small- and large-scale wind tunnel investigations are continuing at Lockheed-Georgia to further develop this technology for useful STOL application. The ultimate test, however, will be a full-scale powered-lift flight program, such as that recommended by Reference 18, where it is proposed to convert the QSRA to a CCW/USB configuration by relatively simple modification to the flaps. This will allow a logical continuation of the above static ground tests and in-flight verification of the indicated STOL potential of these pneumatic thrust-deflecting lift-augmenting concepts.

REFERENCES

1. Englar, R. J. and C. A. Applegate, "Circulation Control - A Bibliography of DTNSRDC Research and Selected Outside References (Jan 1969 through Dec 1983)" DTNSRDC Report 84/052, Sept 1984.

2. Englar, R.J., "Subsonic Two-Dimensional Wind Tunnel Investigations of the High Lift Capability of Circulation Control Wing Sections," DTNSRDC Report ASED-274, April 1975.

3. Englar, R.J., "Development of the A-6/Circulation Control Wing Flight Demonstrator Configuration," DTNSRDC Report ASED-79/01, Jan 1979.

4. Englar, R.J., R. A. Hemmerly, W. H. Moore, V. Seredinsky, ..G. Valckenaere, and J.A. Jackson, "Design of the Circulation Control Wing STOL Demonstrator Aircraft," AIAA Paper No. 79-1842 presented at the AIAA Aircraft Systems and Technology Meeting, New York, Aug 1979. AIAA Journal of Aircraft, Jan 1981, pp. 51-58.

5. Pugliese, A. J. and R. J. Englar, "Flight Testing the Circulation Control Wing," AIAA Paper No. 79-1791 presented at the AIAA Aircraft Systems and Technology Meeting, New York, Aug 1979.

6. Nichols, J.H., Jr. and R.J. Englar, "Advanced Circulation Control Wing System for Navy STOL Aircraft," AIAA Paper No. 80-1825 presented at the AIAA Aircraft Systems Meeting, Anaheim, California, Aug 1980. AIAA Journal of Aircraft, Dec. 1981, pp. 1044 - 1050.

7. Nichols, J. H., Jr. and M. J. Harris, "Fixed Wing CCW Aerodynamics — A Review," NASA Ames Circulation Control Workshop, NASA CP-2432, 1986 (Paper 21).

8. Sleeman, W.C. and W.C. Hohlweg, "Low-Speed Wing-Tunnel Investigation of a Four-Engine Upper Surface Blowing Model Having a Swept Wing and Rectangular and D-Shaped Exhaust Nozzles," NASA TN D-8061, Dec 1975.

9. Nichols, J. H., Jr., R.J. Englar, M.J. Harris, and G.G. Huson, "Experimental Development of an Advanced Circulation Control Wing System for Navy STOL Aircraft," AIAA Paper No. 81-0151 presented at the AIAA 19th Aerospace Sciences Meeting, St. Louis, Missouri, Jan 1981.

10. Harris, M. J., J.H. Nichols, Jr., R.J. Englar, and G.G. Huson, "Development of the Circulation Control Wing/Upper Surface Blowing Powered-Lift System for STOL Aircraft," Paper No. ICAS-82-6.5.1 presented at the 13th Congress of ICAS/AIAA Aircraft Systems and Technology Conference, Seattle, Aug. 1982.

11. Eppel, J. C., M.D. Shovlin, D.N. Jaynes, R.J. Englar, and J.H. Nichols, Jr., "Static Investigation of the Circulation Control Wing/Upper Surface Blowing Concept Applied to the Quiet Short-Haul Research Aircraft," NASA Technical Memo 84232, July 1982.

12. Coe, P. L., Jr., and Fournier, P. G., "Application of Powered Lift Concepts for Improved Cruise Efficiency of Long-Range Aircraft." NASA SP-406, pp. 89-101.

13. Englar, R. J., "Experimental Investigation of the High Velocity Coanda Wall Jet Applied to Bluff Trailing Edge Circulation Control Airfoils," DTNSRDC Report 4708, Sept 1975.

14. Harris, M. J., "Investigation of the Circulation Control Wing/Upper Surface Blowing High Lift System on a Low Aspect Ratio Semispan Model," DTNSRDC Report ASED-81/10, May 1981.

15. Englar, R.J., J.H. Nichols, Jr., M.J. Harris, J.C. Eppel, and M.D. Shovlin, "Development of Pneumatic Thrust Deflecting Powered-Lift Systems," AIAA Paper No. 86-0476, presented at AIAA 24th Aerospace Sciences Meeting, Reno, NV, Jan 1986.

16. Bower, R. E., "Opportunities for Aerodynamic-Drag Reduction." NASA SP-372, 1975, pp. 323-352.

17. Englar, R. J. and G. G. Huson, "Development of Advanced Circulation Control Wing High Lift Airfoils," AIAA Paper No. 83-1847 presented at the AIAA Applied Aerodynamics Conference, Danvers, MA, July 1983; AIAA Journal of Aircraft, July 1984, pp. 476-483.

18. Riddle, D. W. and J. C. Eppel, "A Potential Flight Evaluation of a USB/CCW Concept on the Quiet Short-Haul Research Aircraft," NASA Ames Circulation Control Workshop, NASA CP-2432, 1986 (Paper 23).

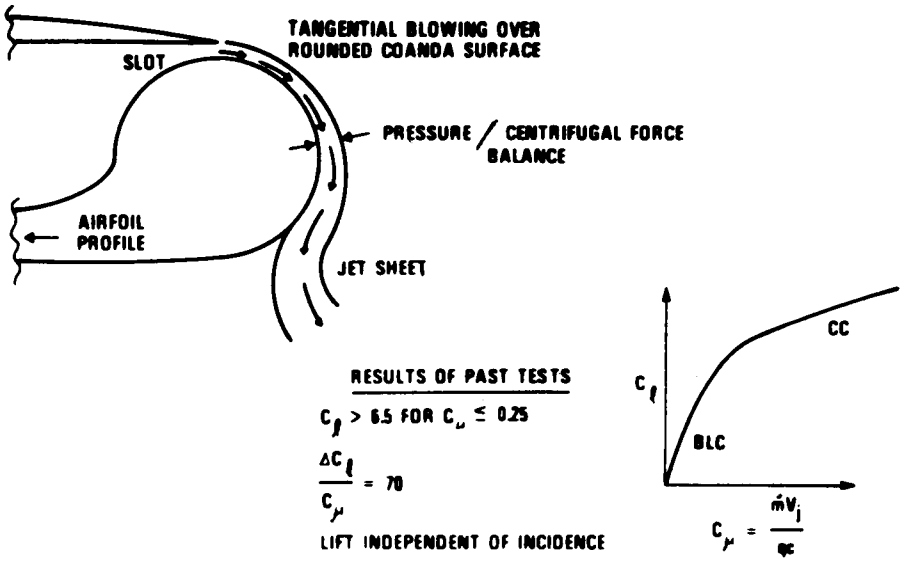

Figure 1. Basic Circulation Control Aerodynamics

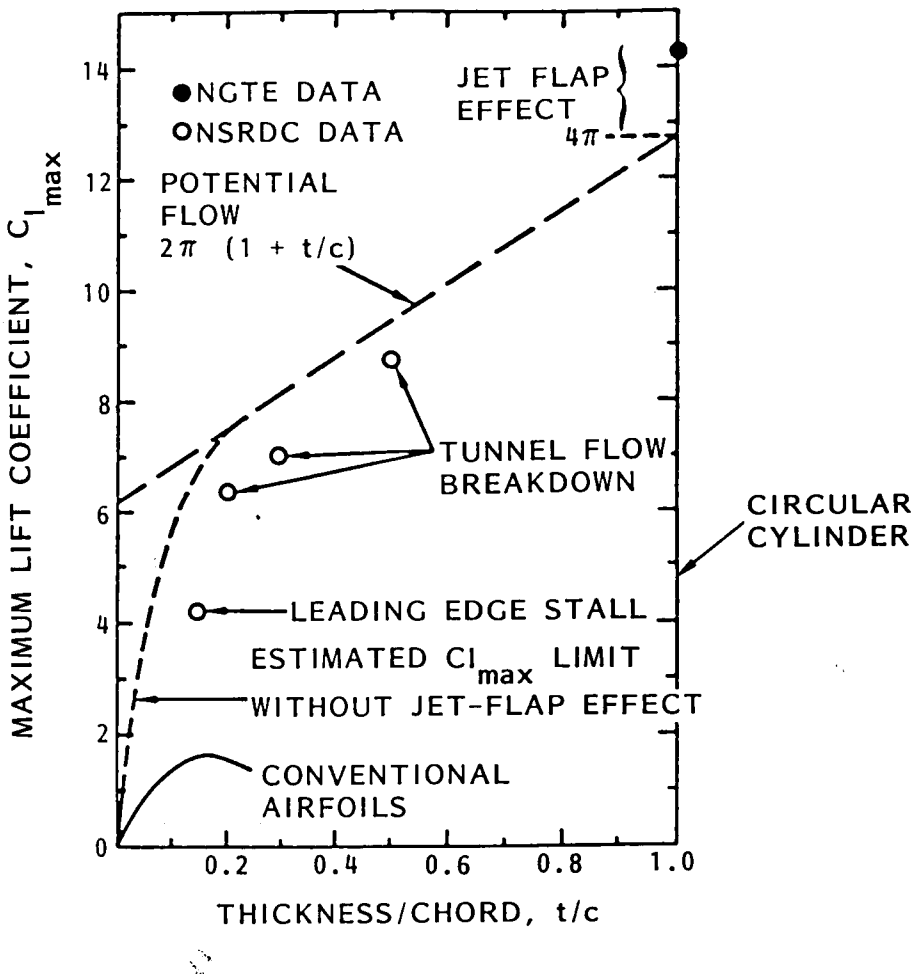

Figure 2. CC Airfoil Maximum Lift Coefficients

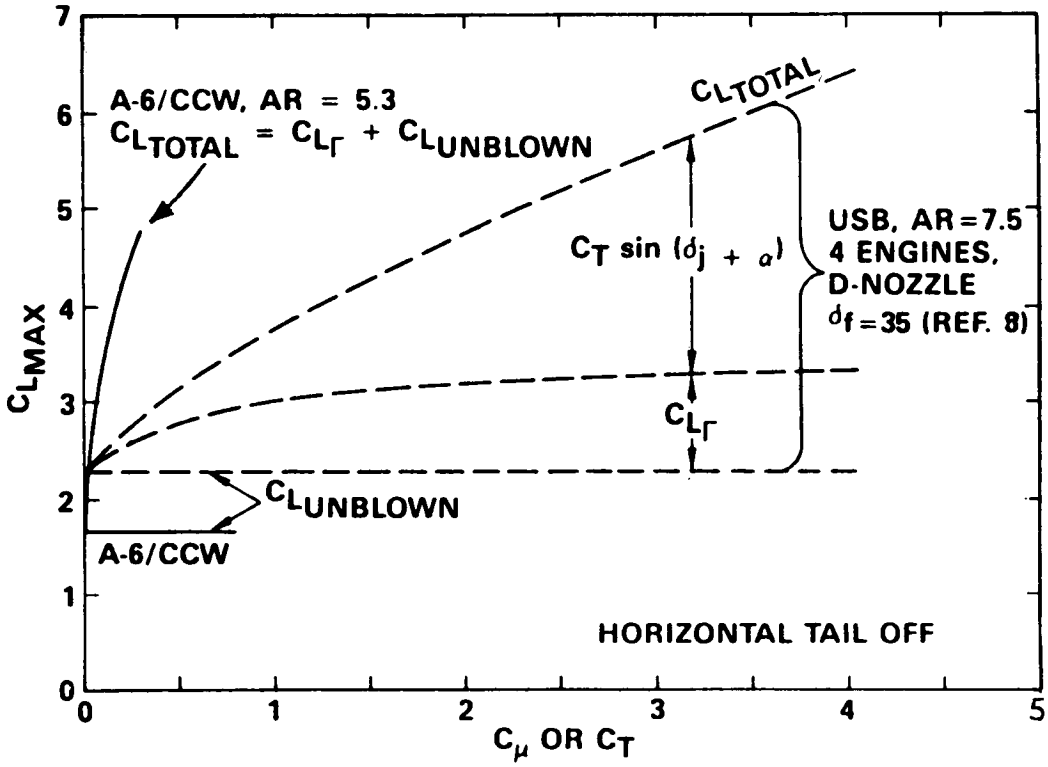

Figure 3. Maximum Lift for Typical CCW and USB Aircraft

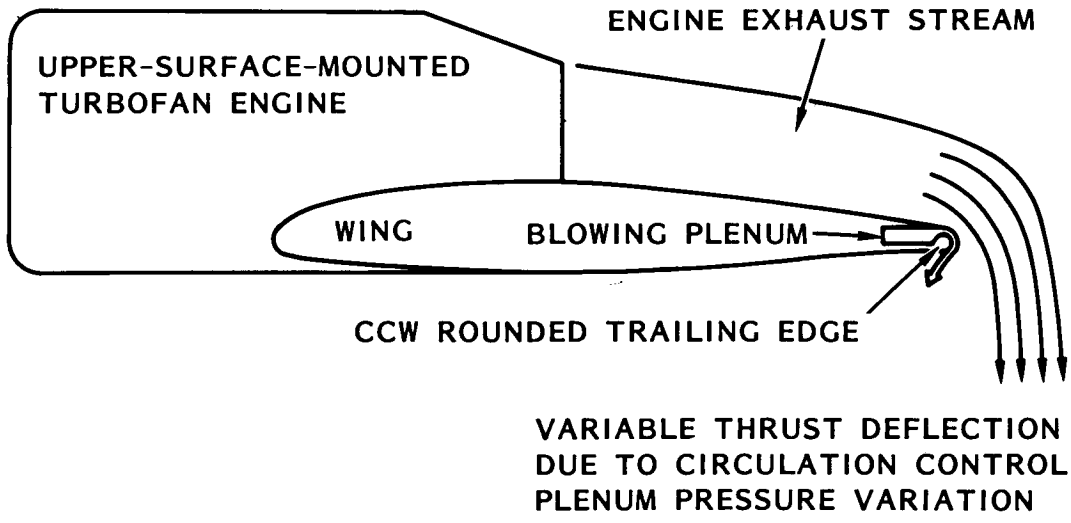

Figure 4. Circulation Control Wing/Upper Surface Blowing Powered-Lift System

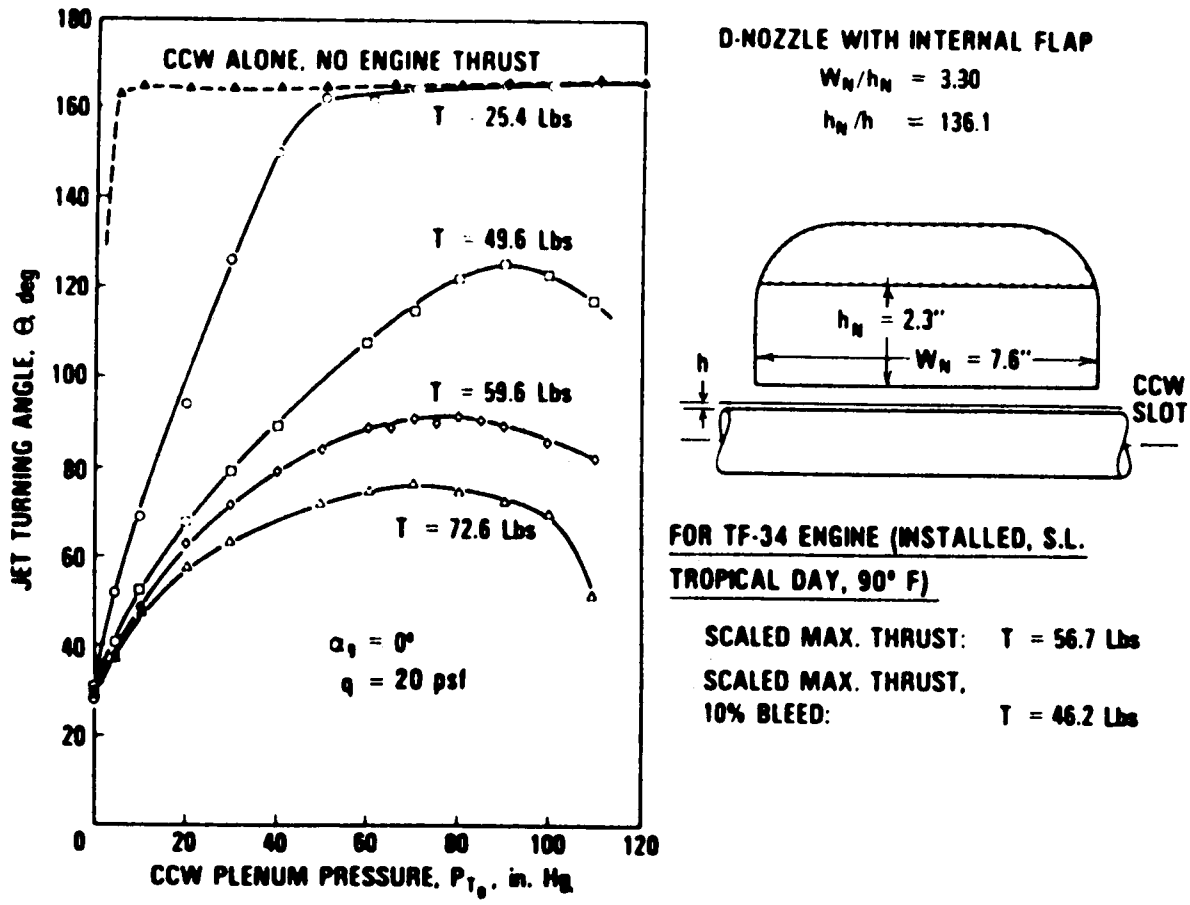

Figure 5. CCW/USB Static Thrust Turning, AR = 4 Semi-Span Model

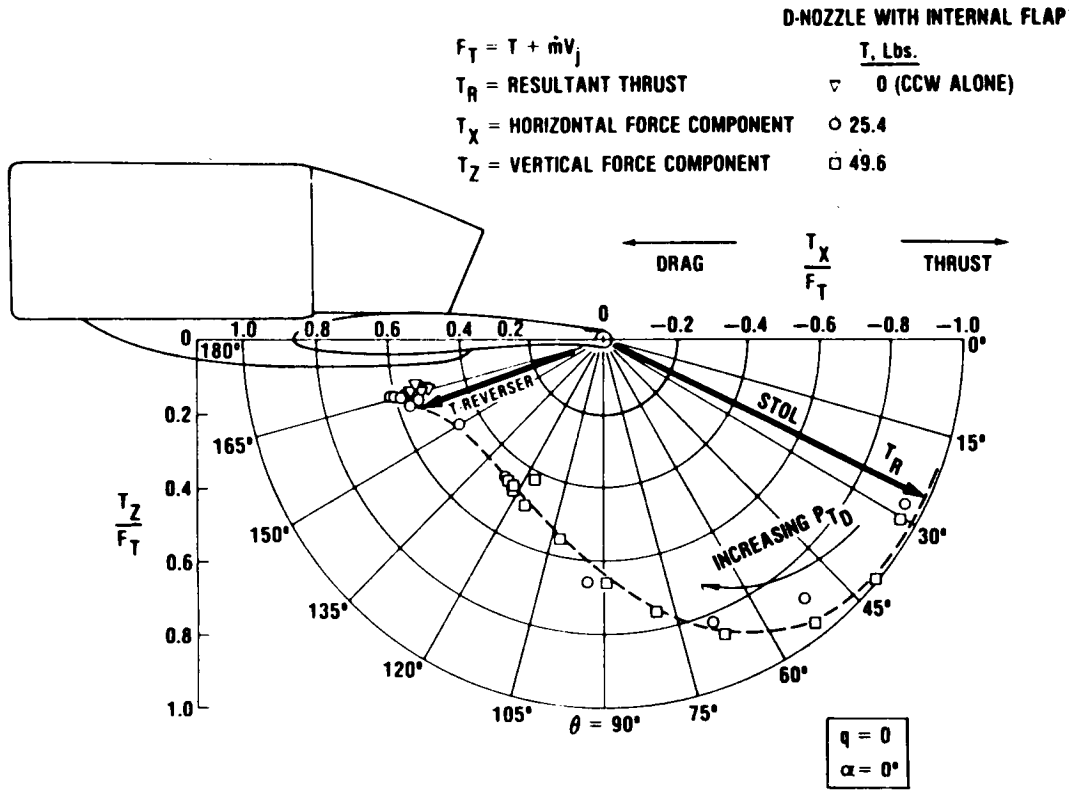

Figure 6. CCW/USB Static Turning Angle and Thrust Recovery Efficiency, AR = 4 Model

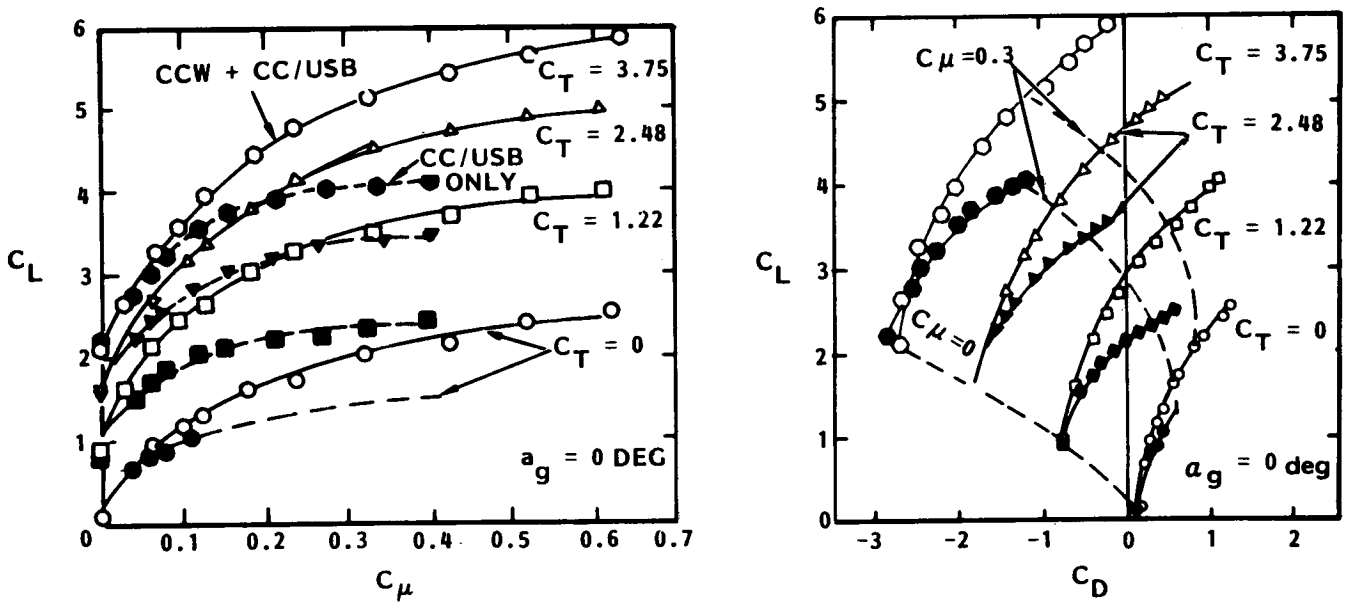

Figure 7. Effect of Blowing and Thrust Deflection on Lift and Drag (Ref. 14 Semi-Span Model)

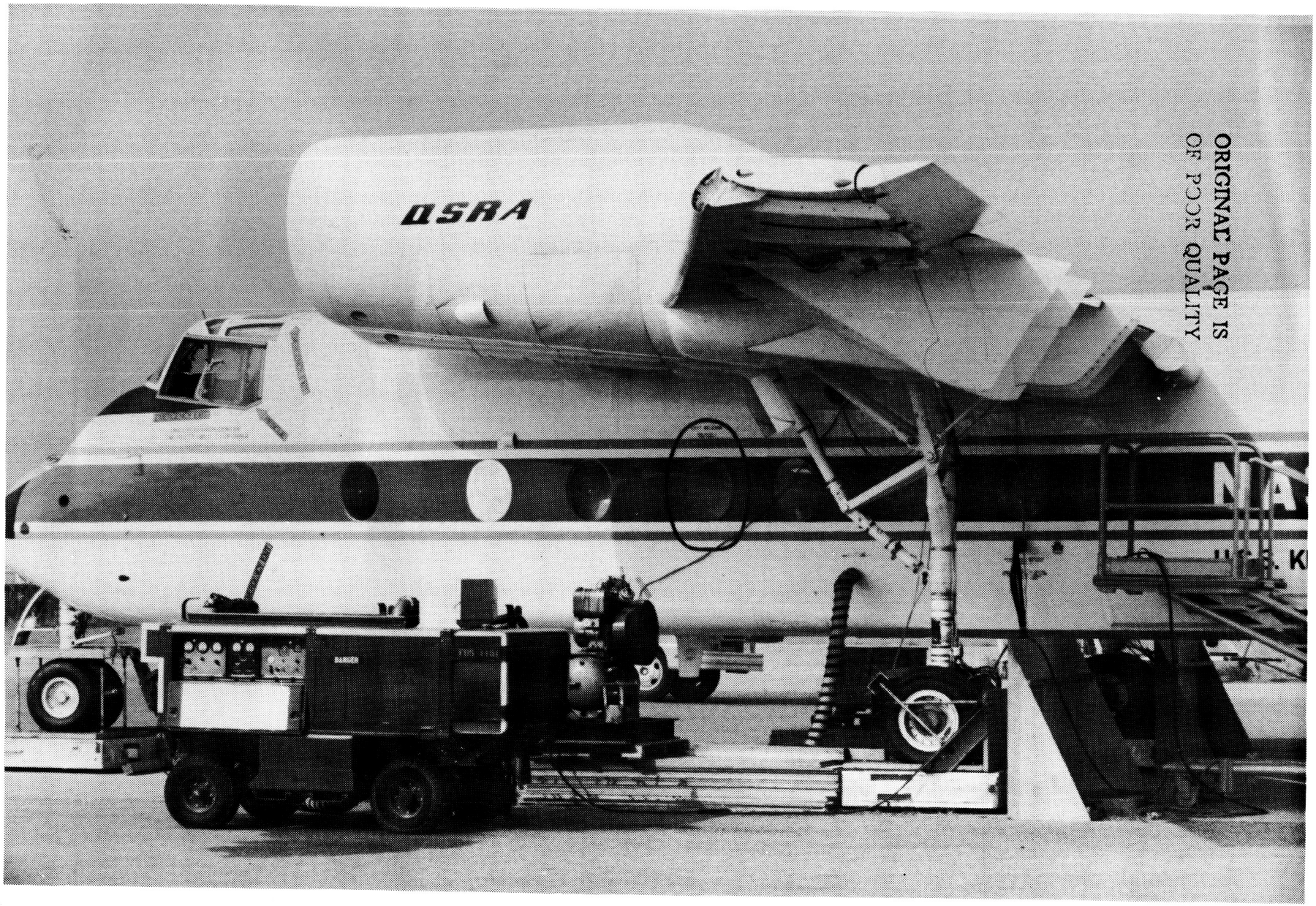

ORIGINAL PAGE IS
OF POOR QUALITY

Figure 8. QSRA CCW/USB Phase I Static Test Setup

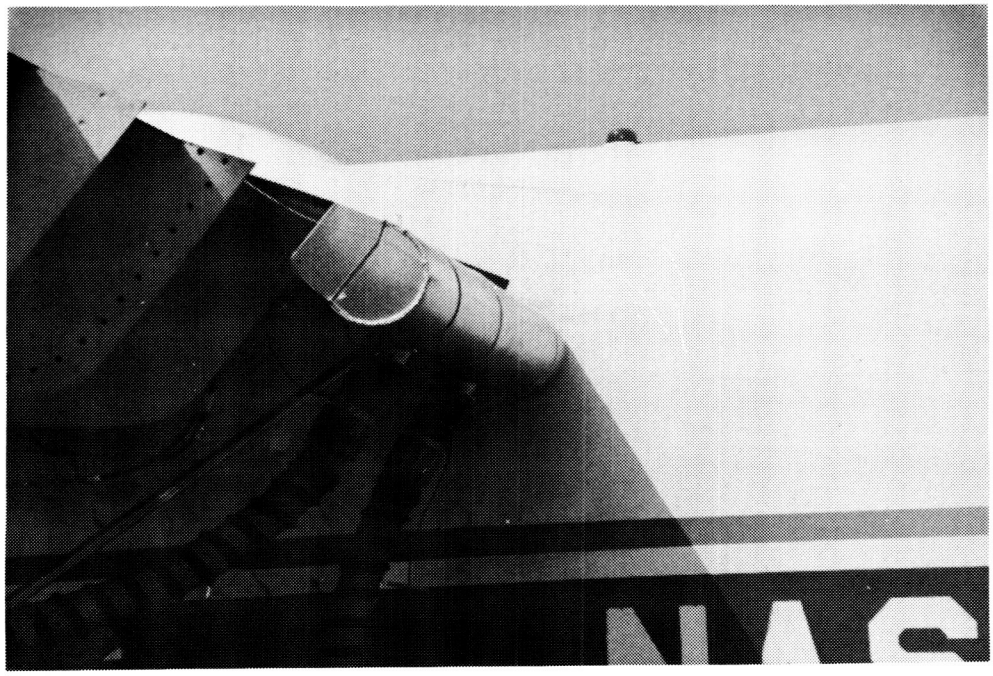

Figure 9. Blowing-On Static Thrust Deflection at the CCW Trailing Edge, Phase I

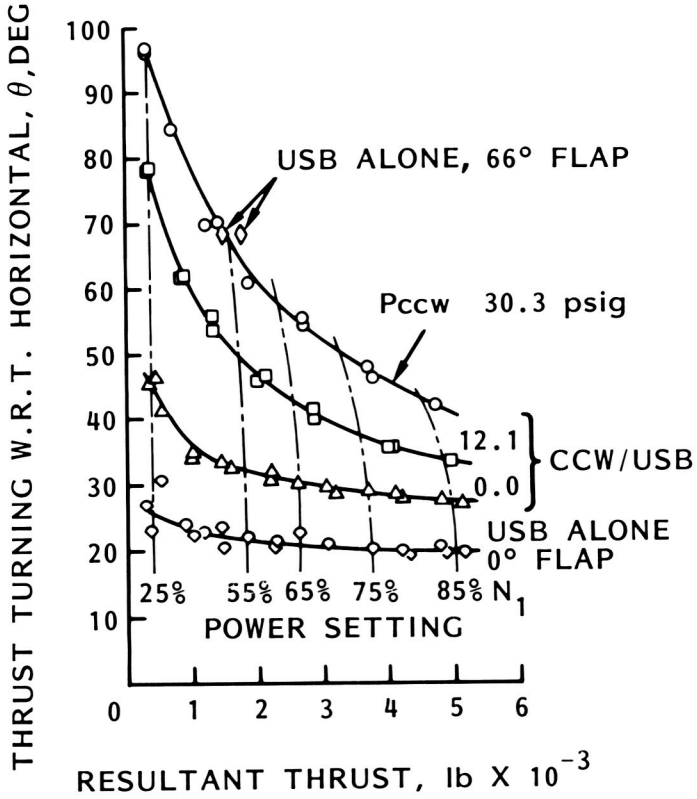

Figure 10. QSRA CCW/USB Phase I Static Thrust Turning

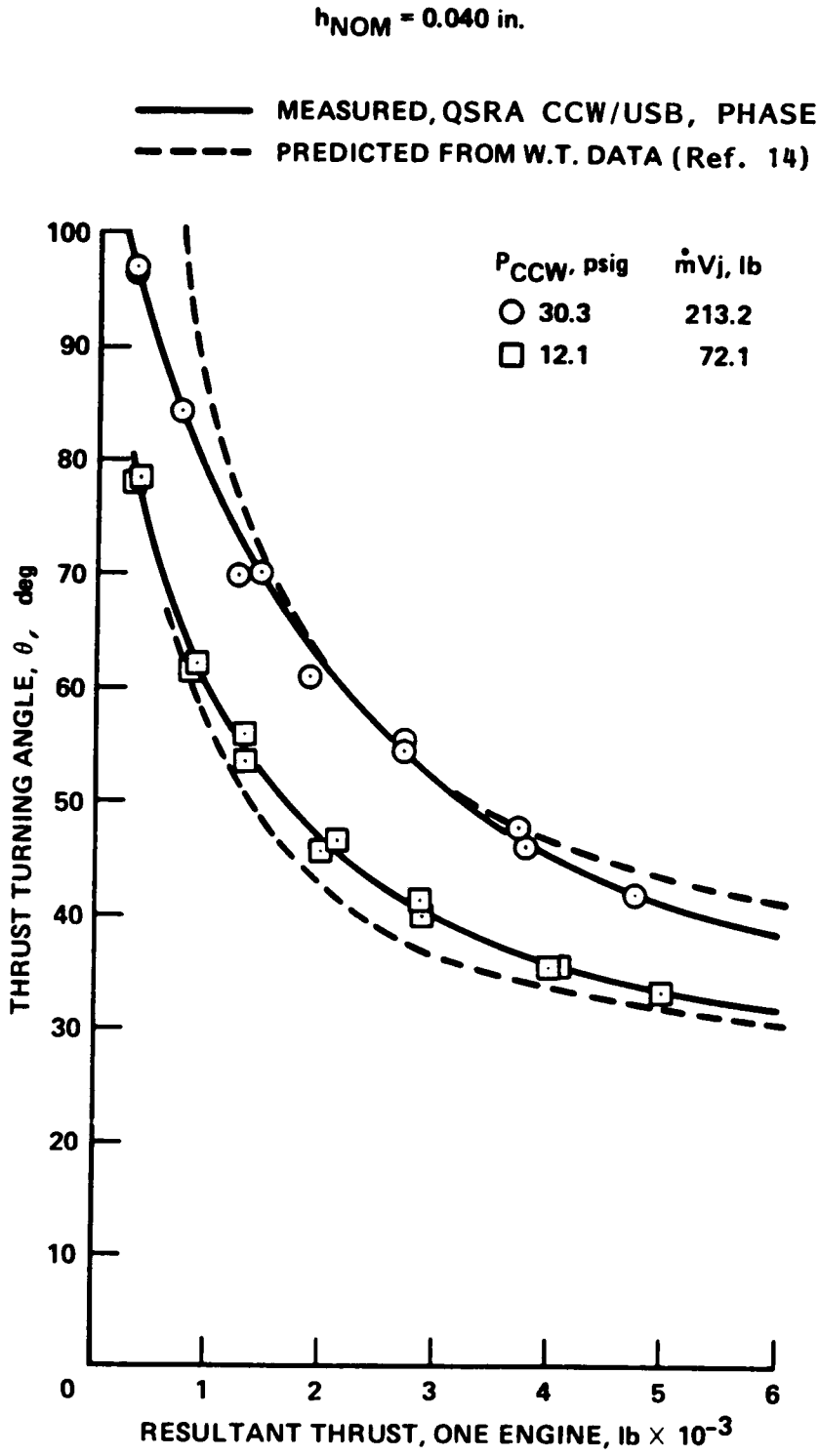

Figure 11. Phase I QSRA CCW/USB Static Thrust Turning, Predicted vs. Measured

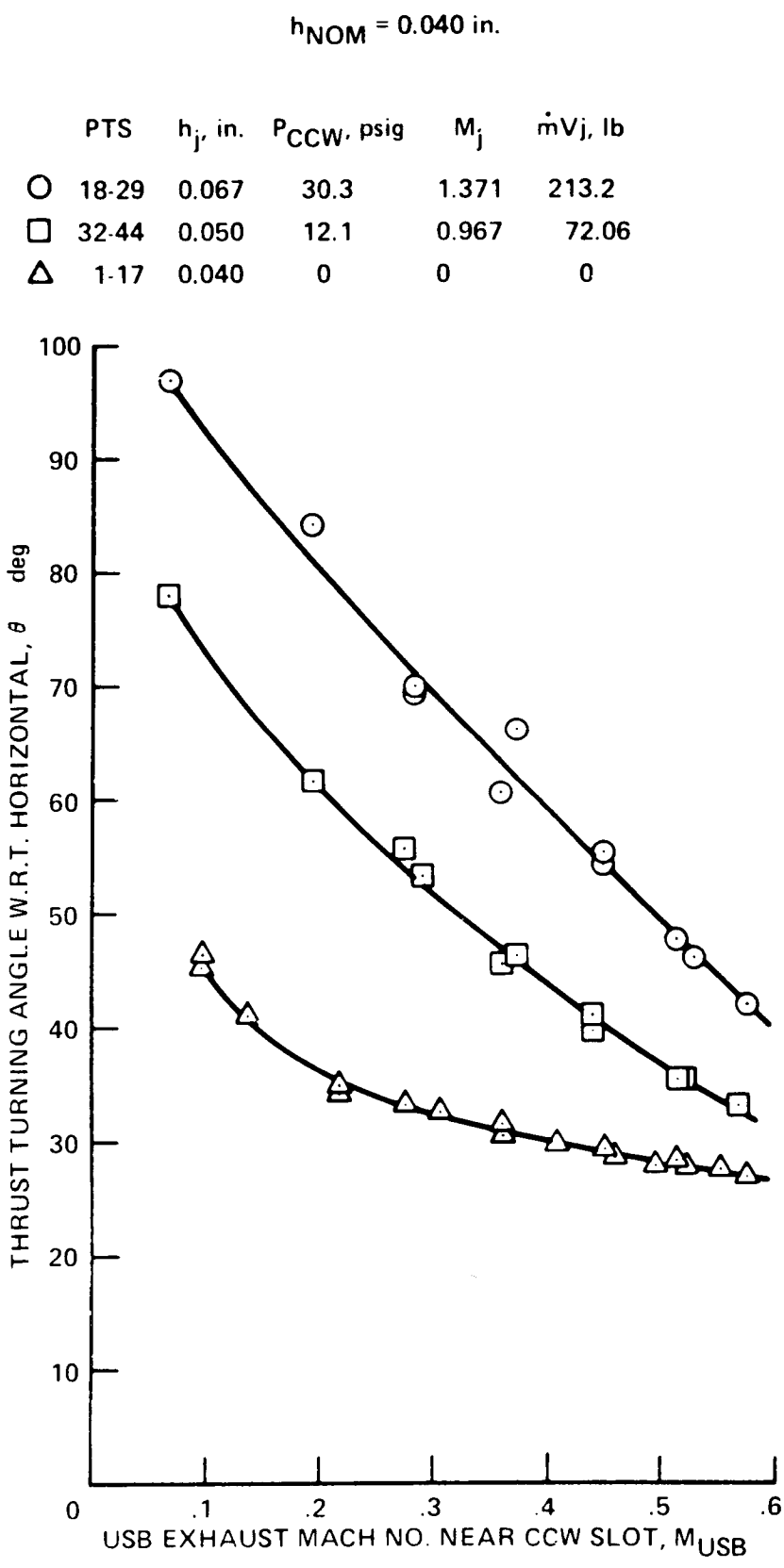

Figure 12. Phase I Static Thrust Turning as a Function of Exhaust Mach Number

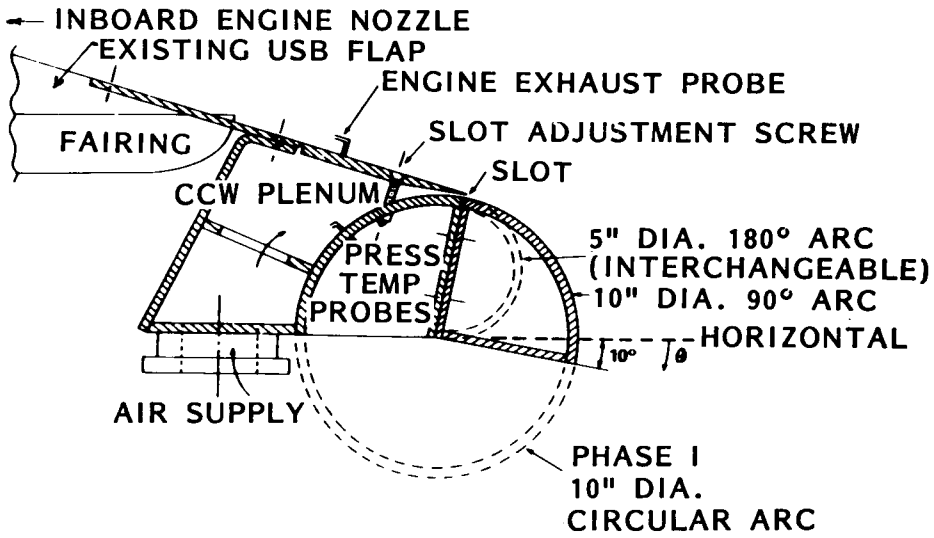

Figure 13. QSRA CCW/USB Phase II Trailing Edge Assembly

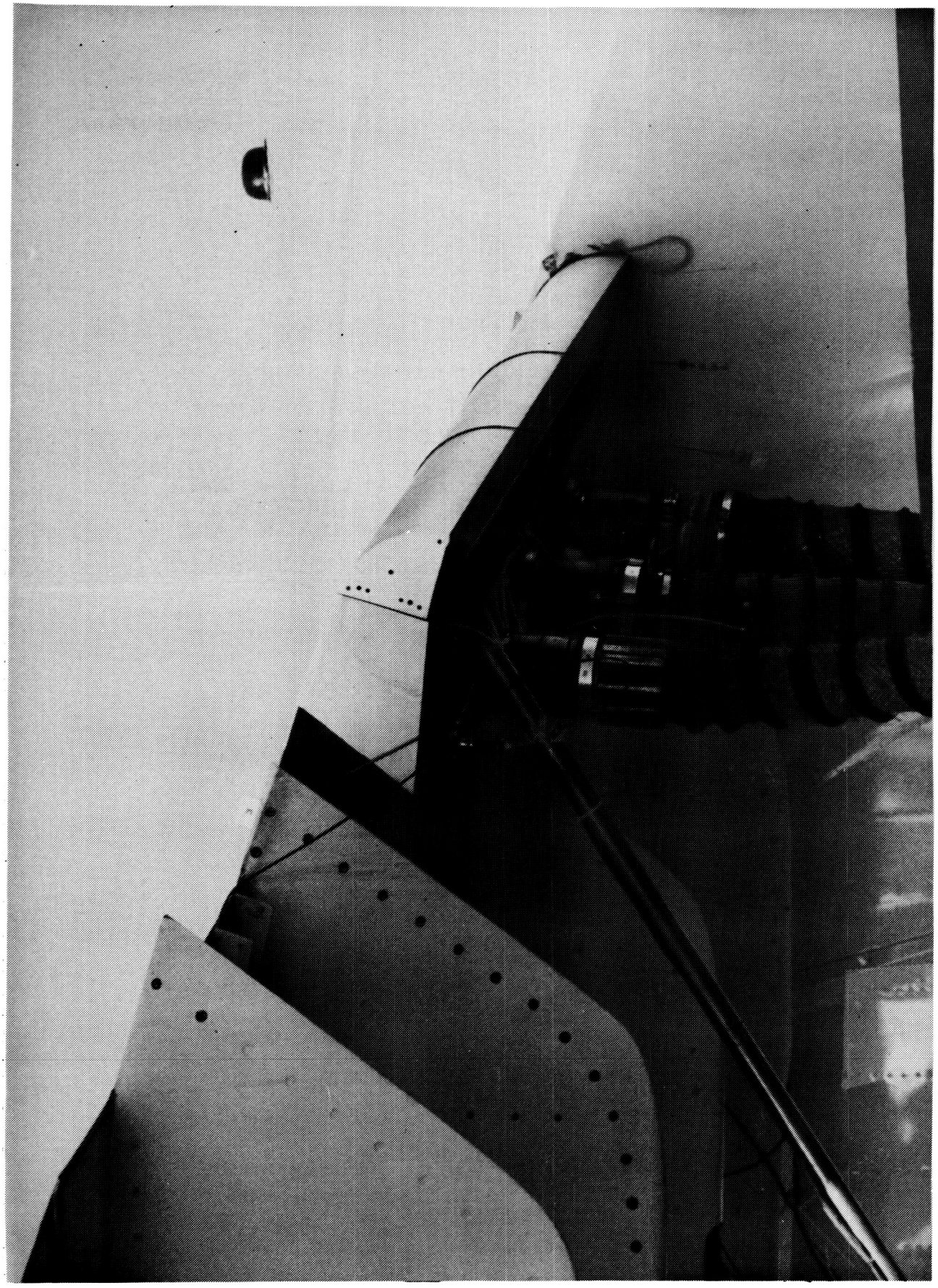

Figure 14. Ten-Inch Diameter, 90° Circular Arc Configuration

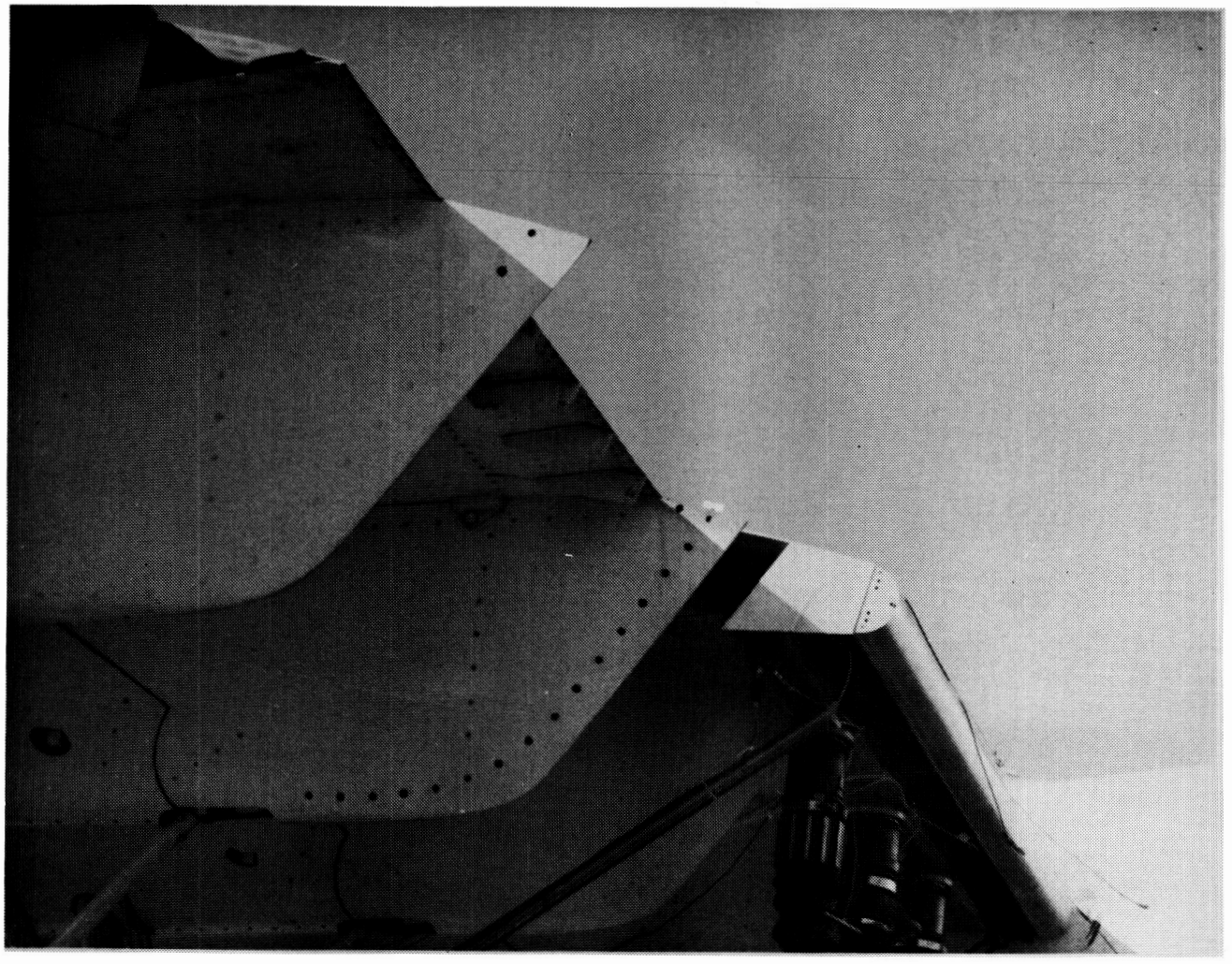

Figure 15. Five-Inch Diameter, 180^{o} Semi-Circular Configuration

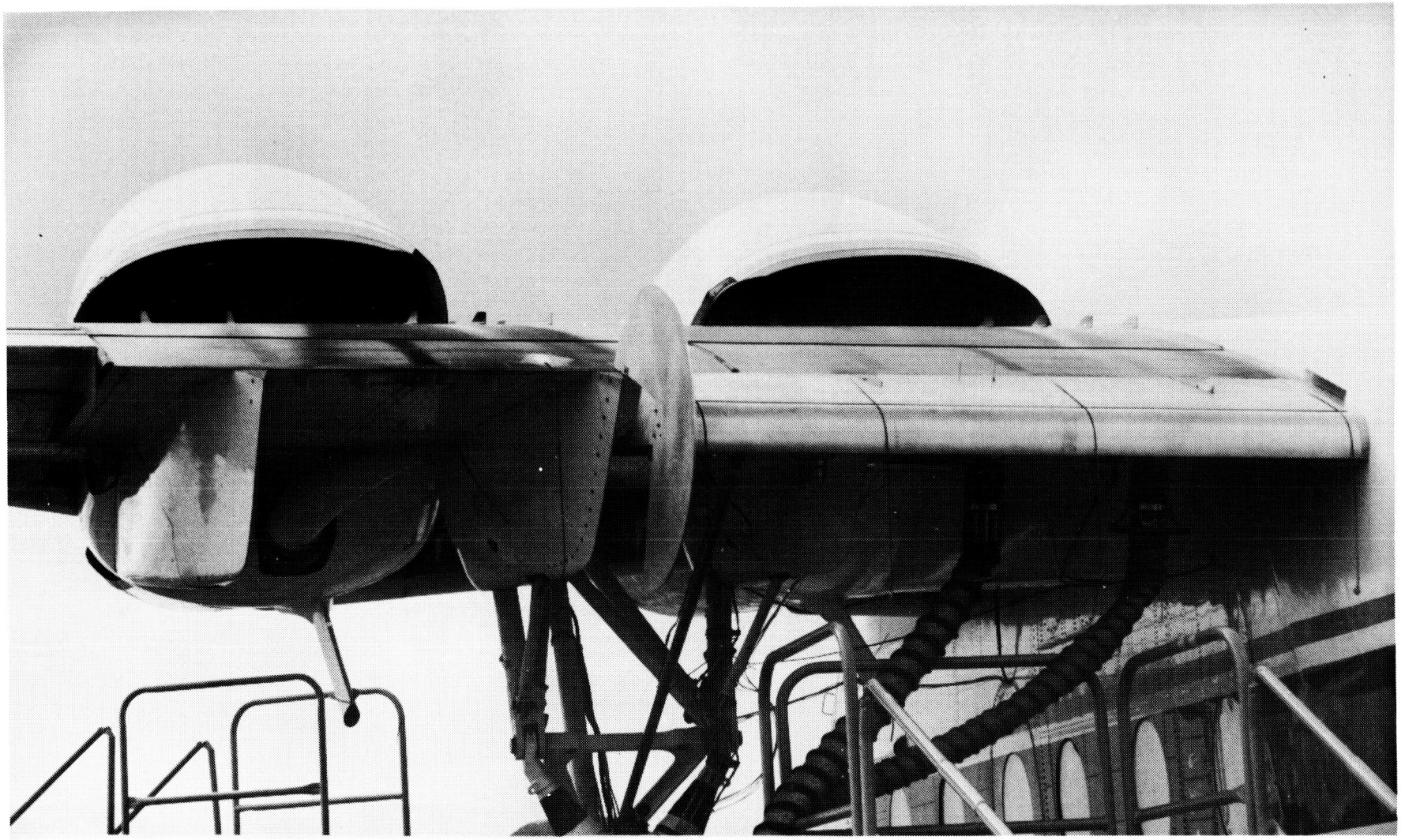

Figure 16. Flow Fence at Outboard End of Increased Span Phase II CCW Trailing Edge

ORIGINAL PAGE IS
OF POOR QUALITY

Figure 17. QSRA Left Wing: CCW, Undeflected USB Flap, and Outboard Double-Slotted Mechanical Flap

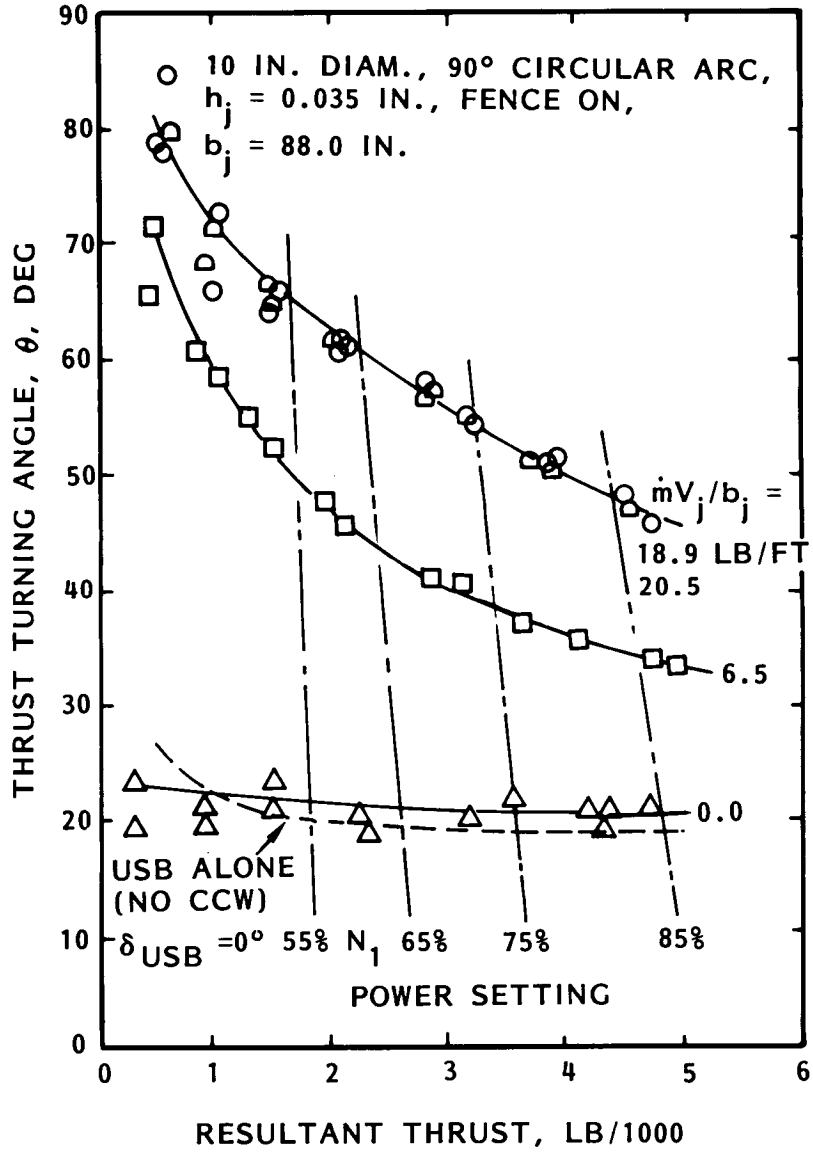

Figure 18. Phase II Static Thrust Turning for Configuration 3

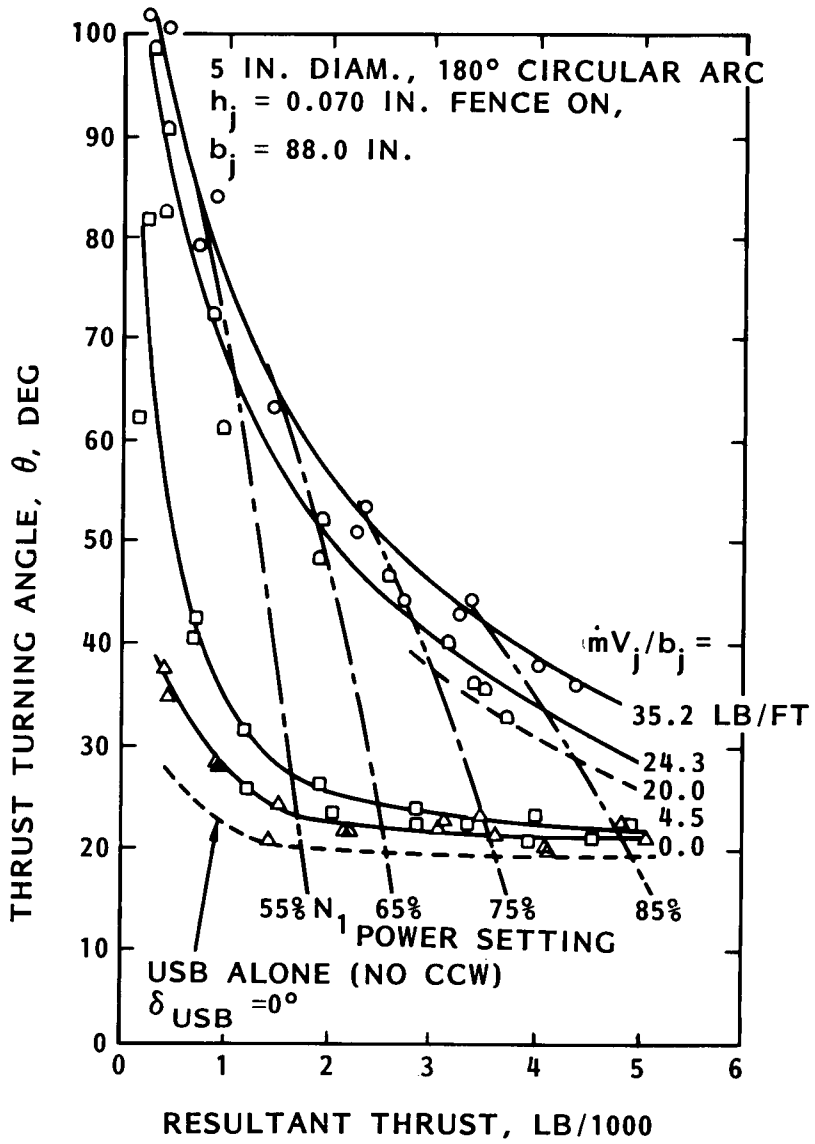

Figure 19. Phase II Static Thrust Turning for Configuration 5

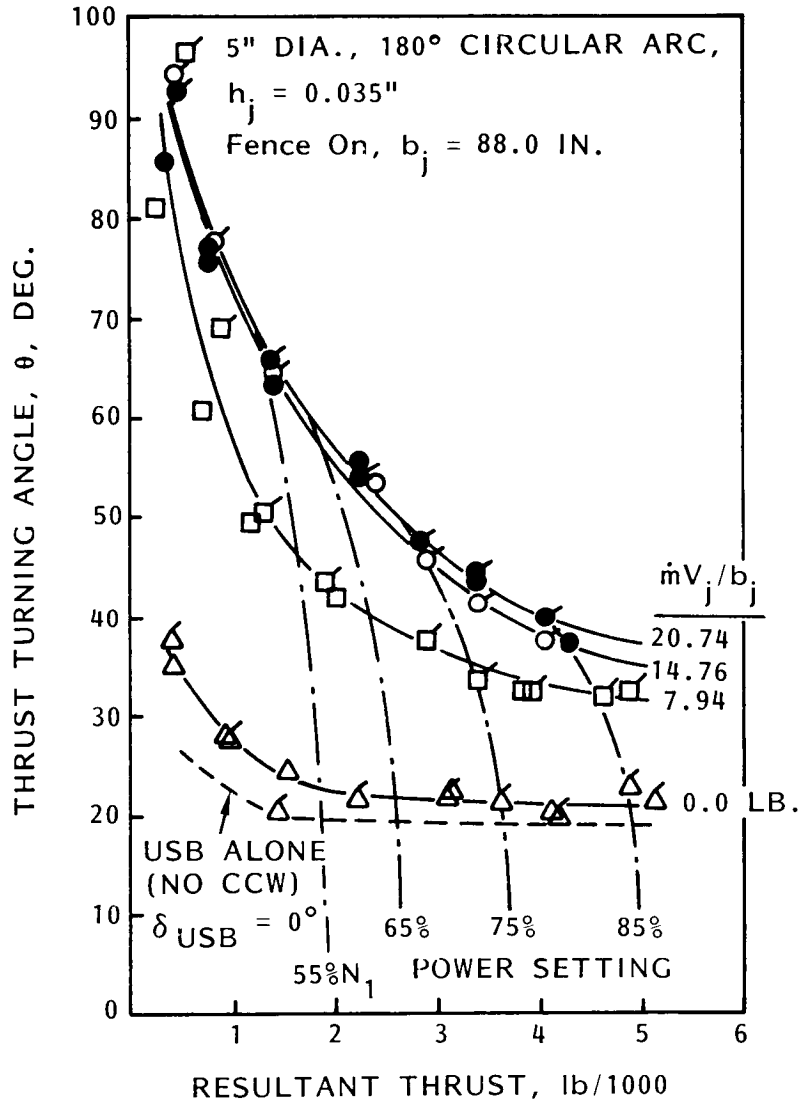

Figure 20. Phase II Static Thrust Turning for Configuration 4

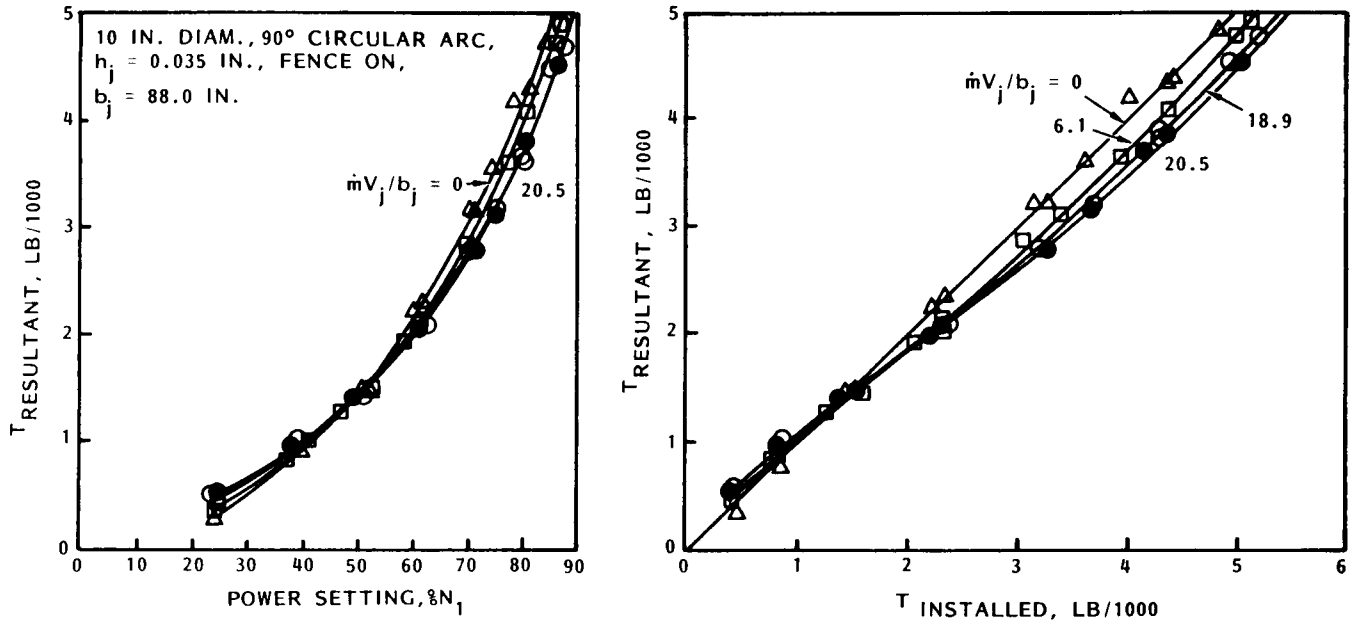

Figure 21. Effect of Blowing on Resultant Engine Thrust, Phase II, Configuration 3

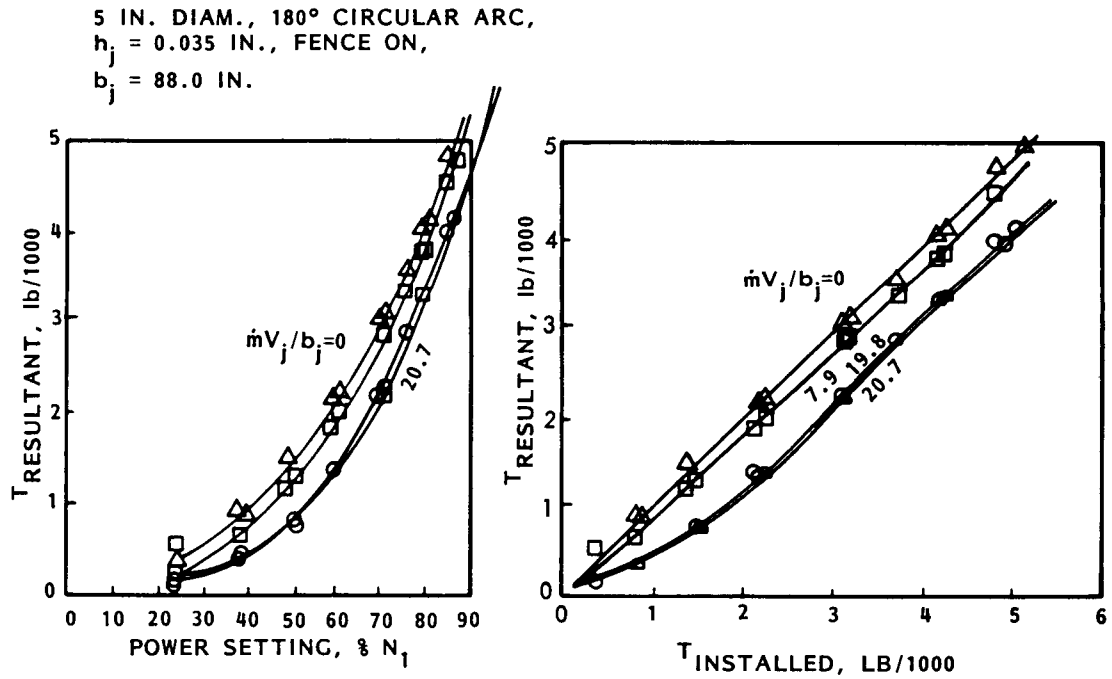

Figure 22. Effect of Blowing on Resultant Engine Thrust, Phase II, Configuration 4

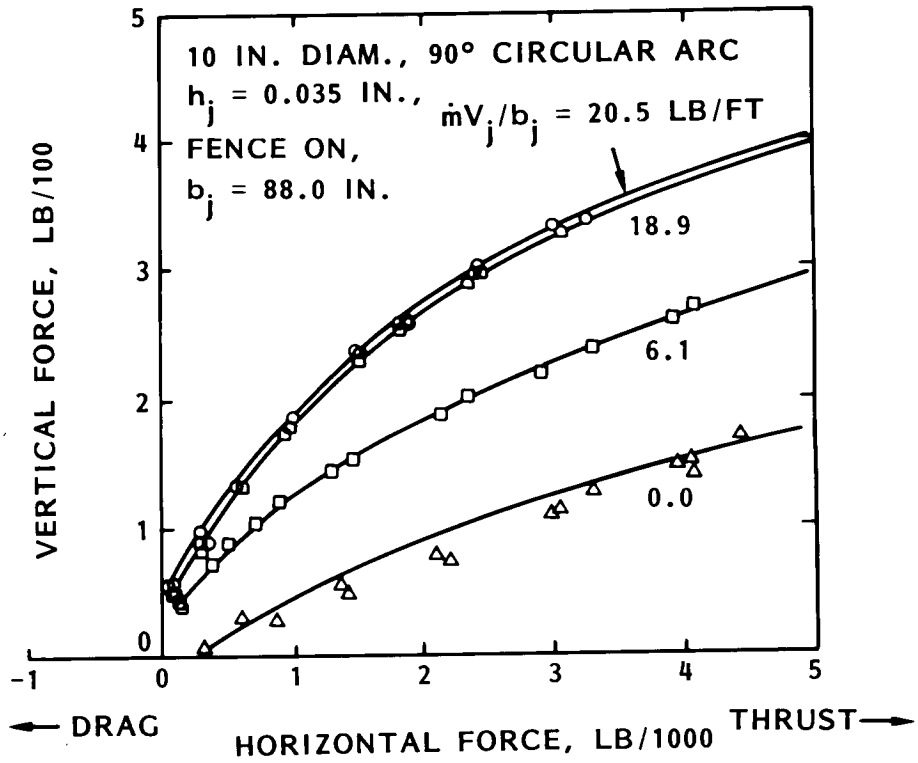

Figure 23. Static Thrust Components Due to Blowing, Phase II, Configuration 3

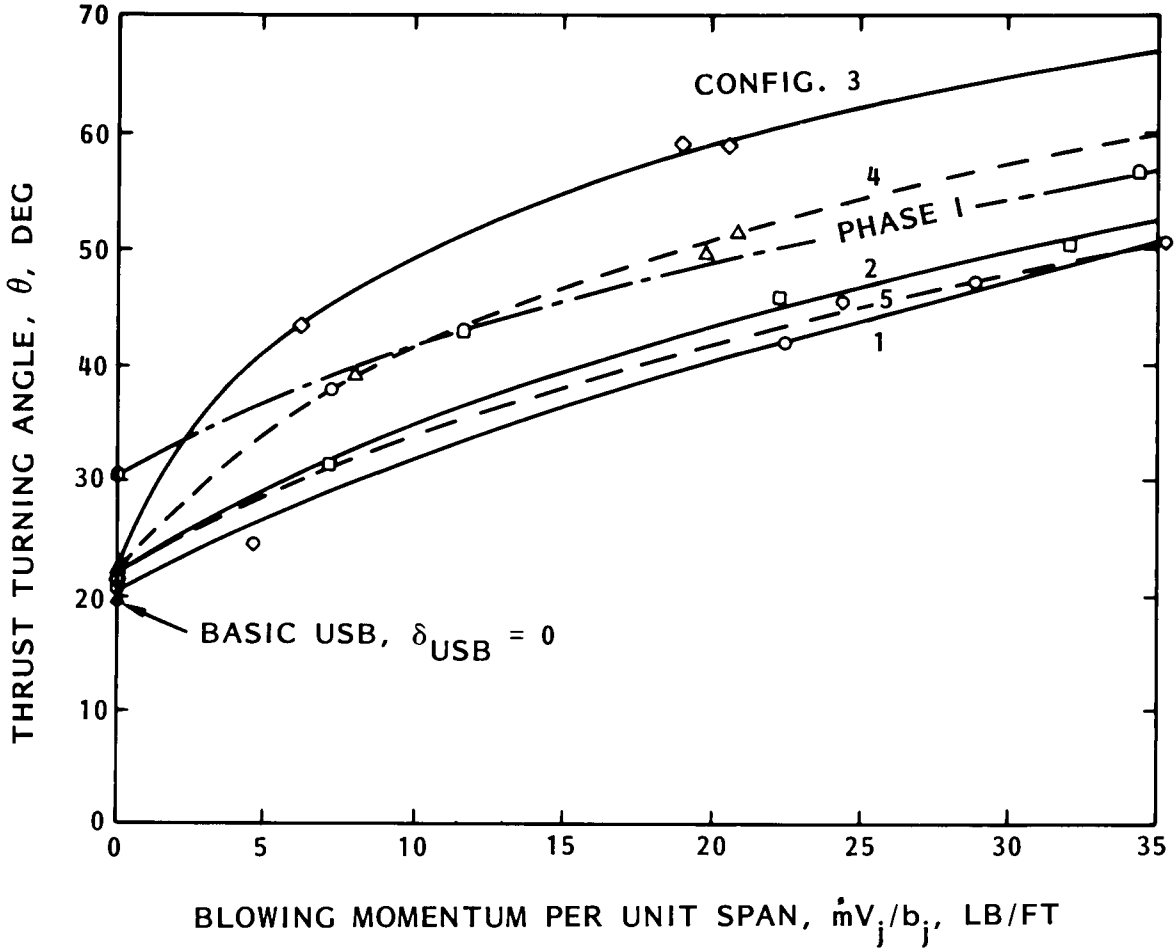

Figure 24. Comparison of Thrust-Deflecting Capability at 2500 lbs. of Resultant Thrust

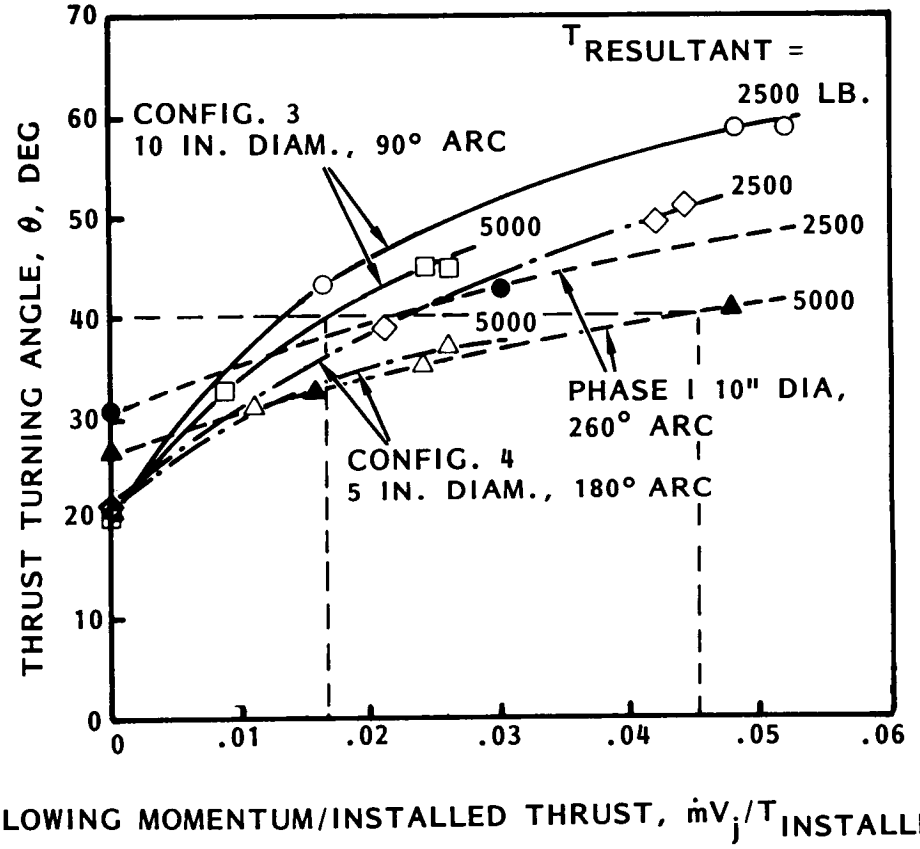

Figure 25. Comparison of CCW Blowing Momentum Required for Thrust Turning

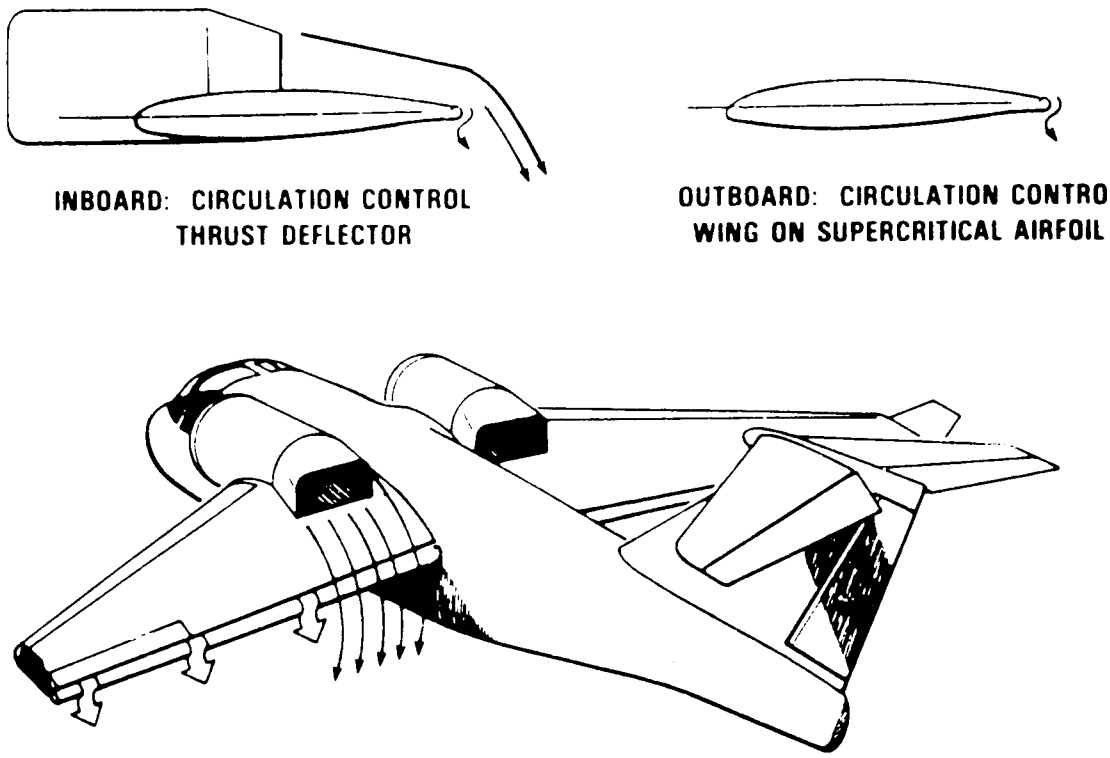

Figure 26. Proposed S-3A-Based CCW/USB STOL Aircraft

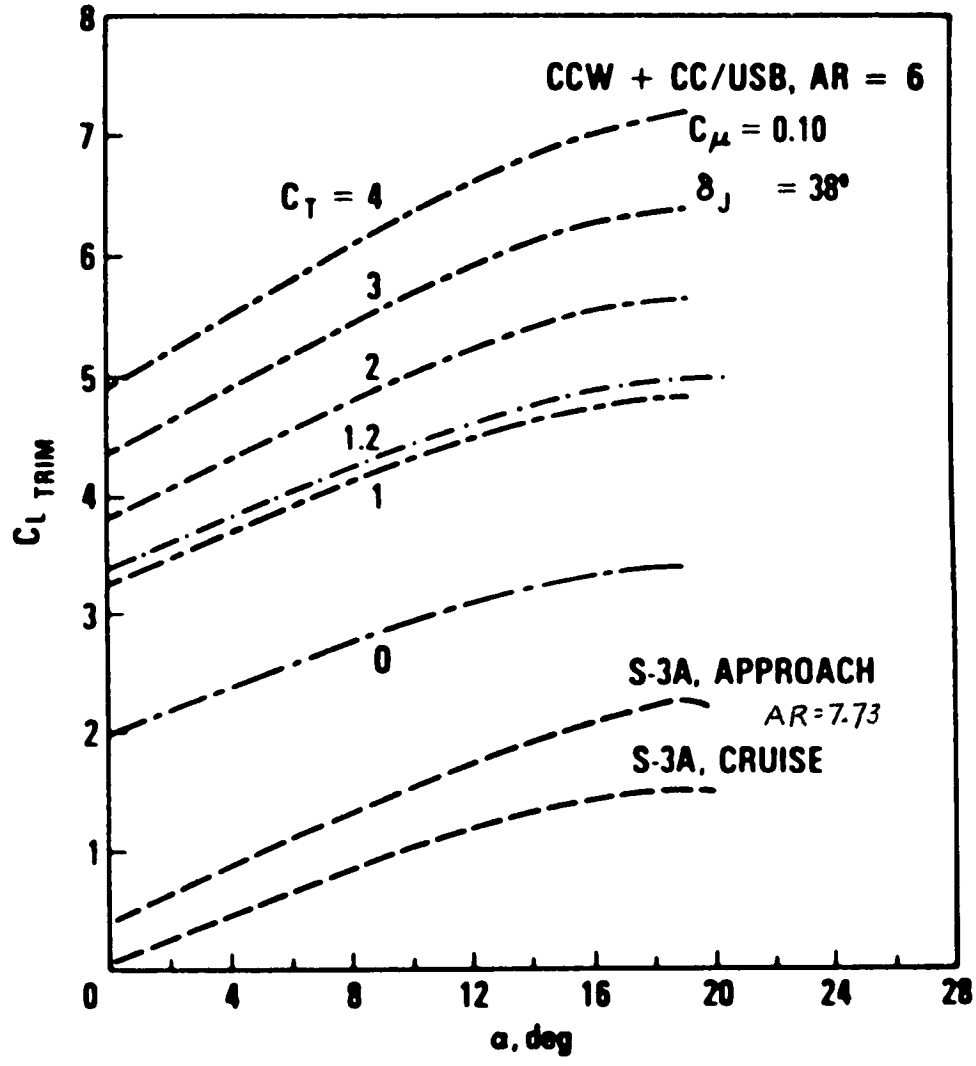

Figure 27. High-Lift Capability of Conventional S-3A and Proposed STOL Aircraft

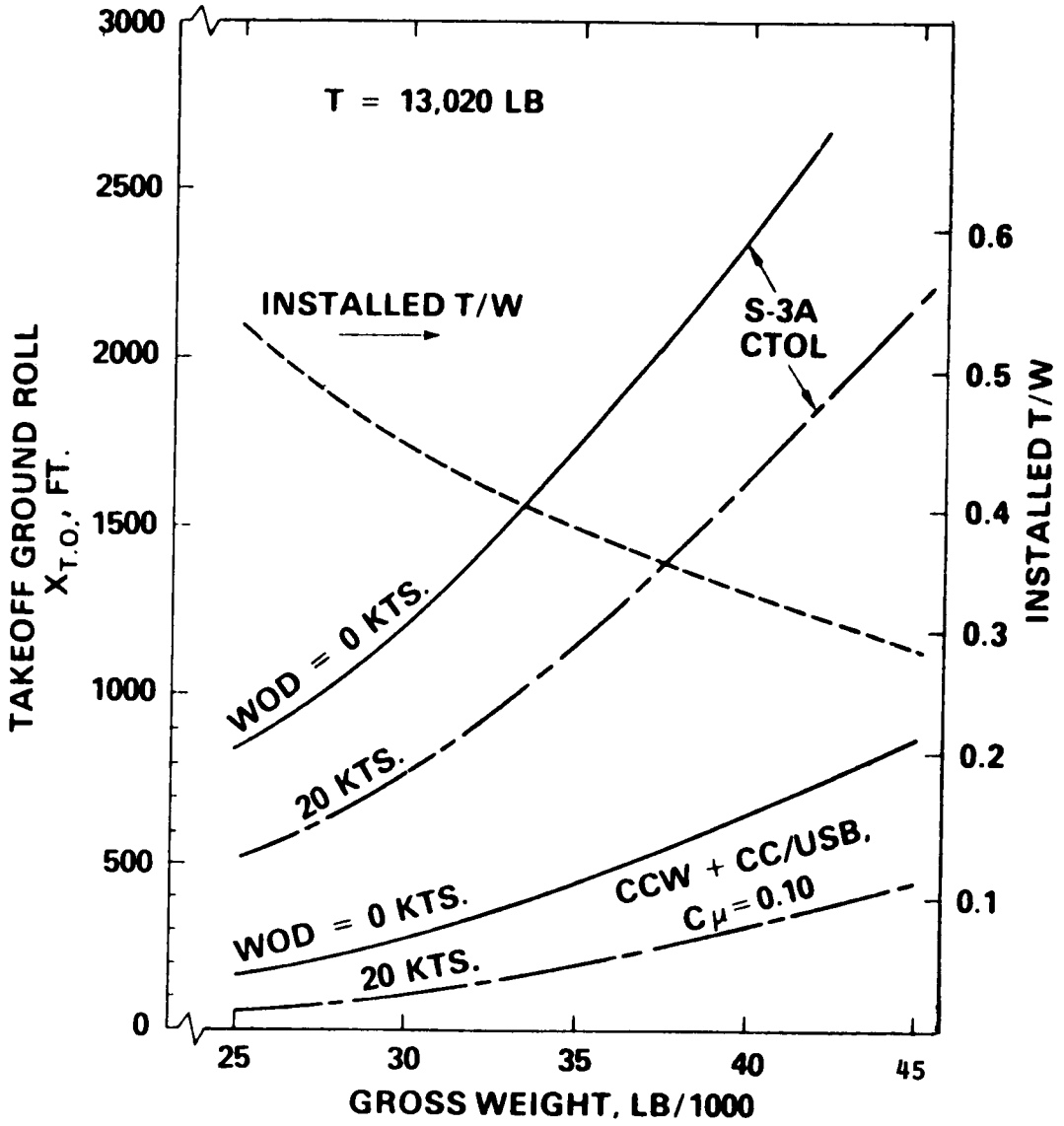

Figure 28. Comparative Unassisted Takeoff Ground Rolls on a Sea-Level Tropical Day

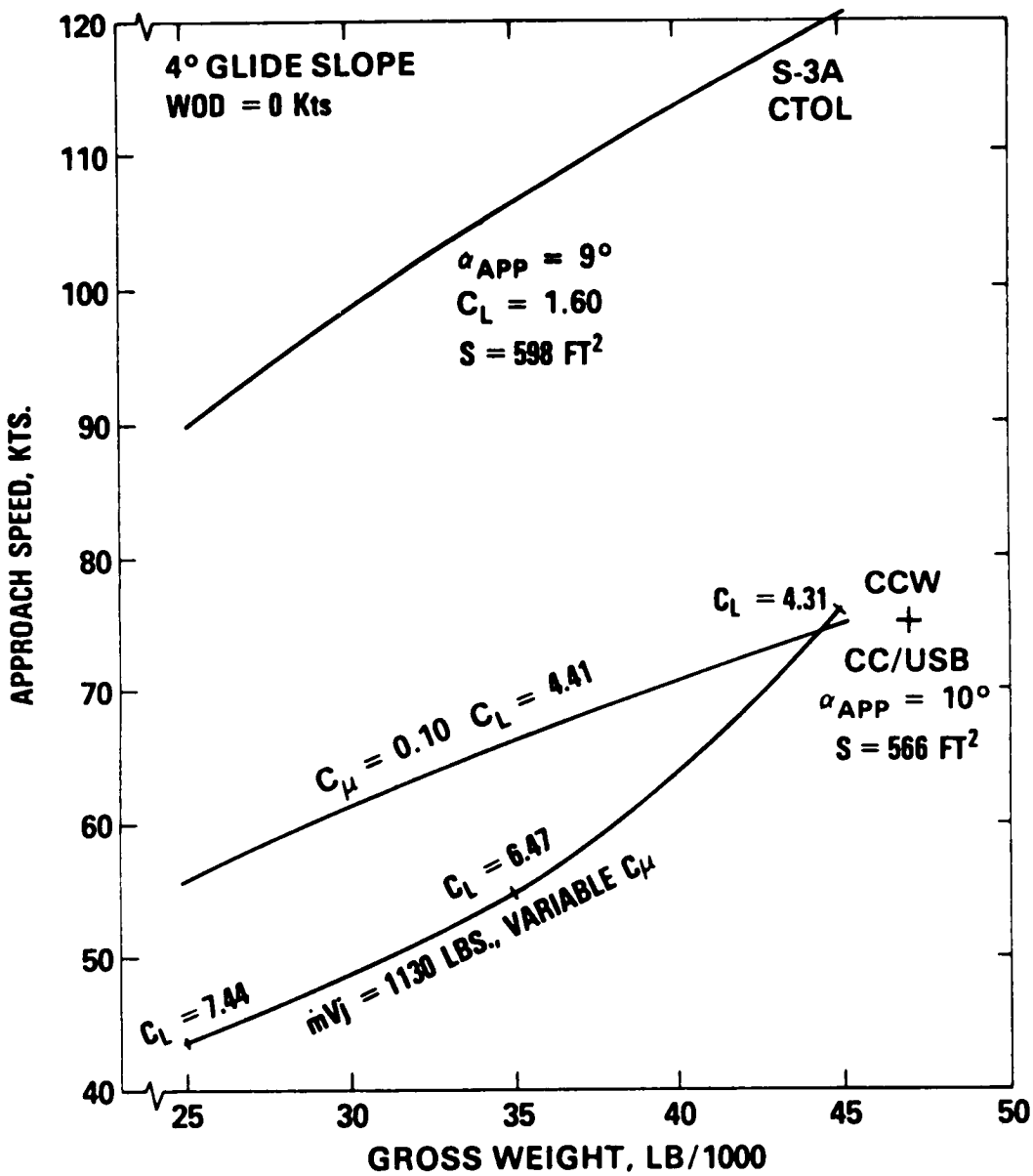

Figure 29. Equilibrium Approach Speeds on a Sea-Level Tropical Day

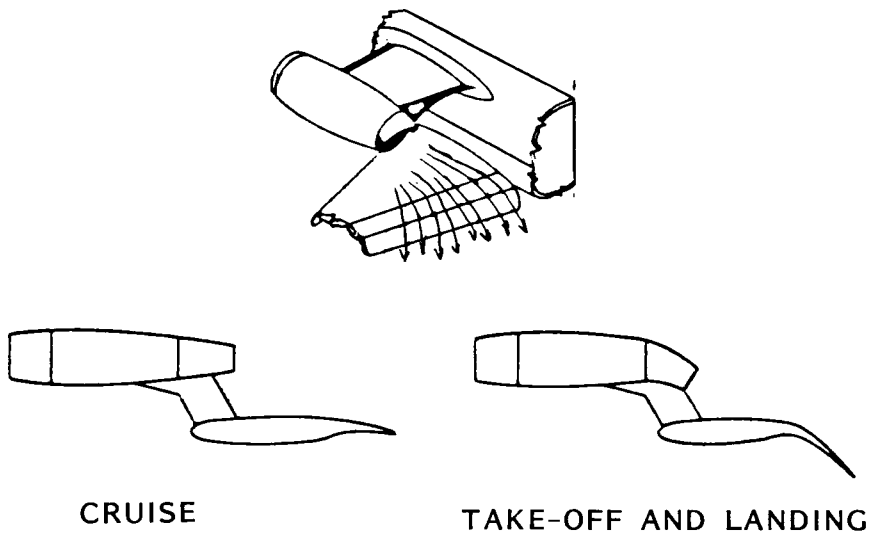

Figure 30. Over-the-Wing (OTW) Blowing Concept Using a Mechanical Flap

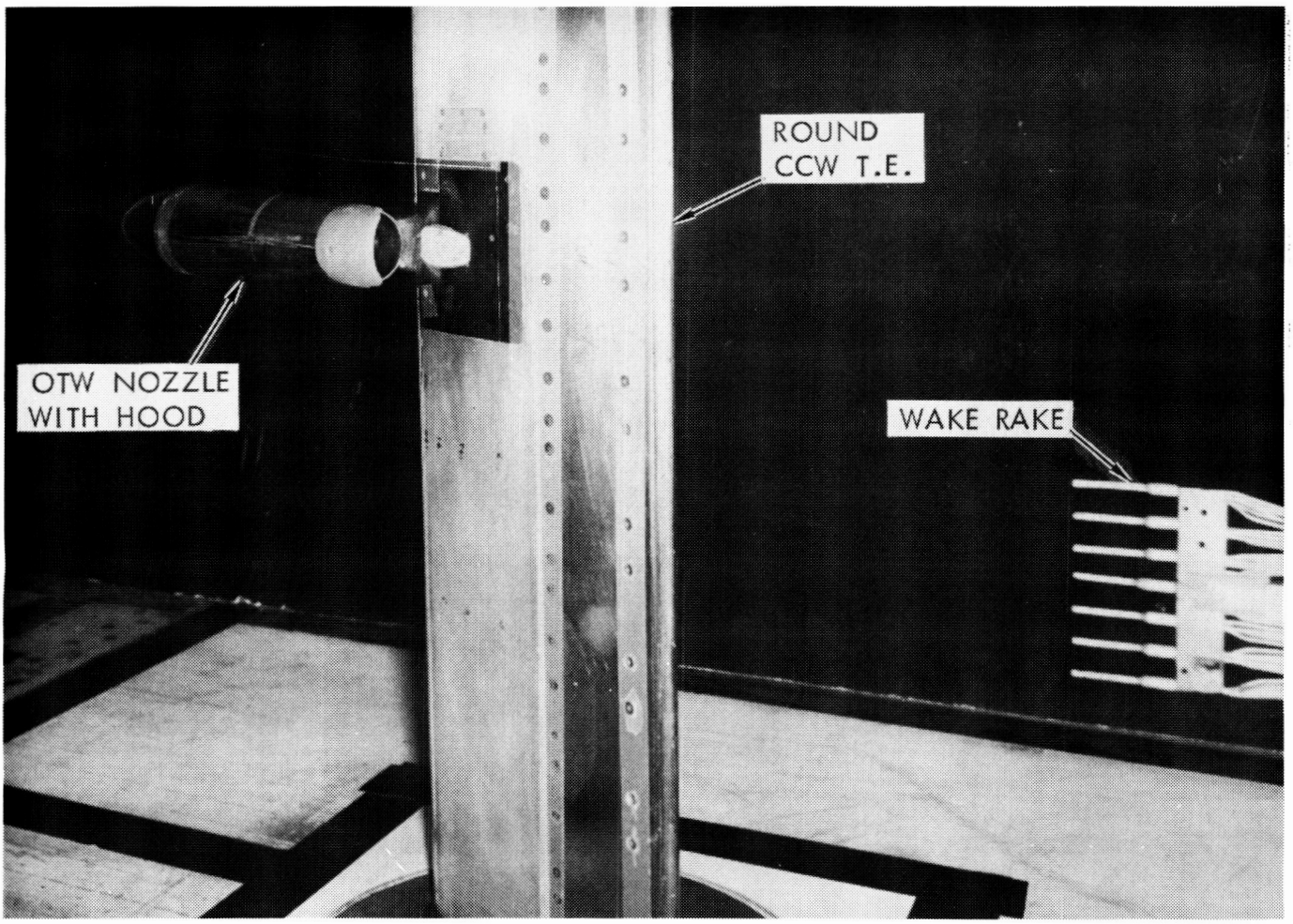

Figure 31. Quasi 2-D CCW/OTW Model in the Lockheed-GA 30-X43-Inch Model Test Facility

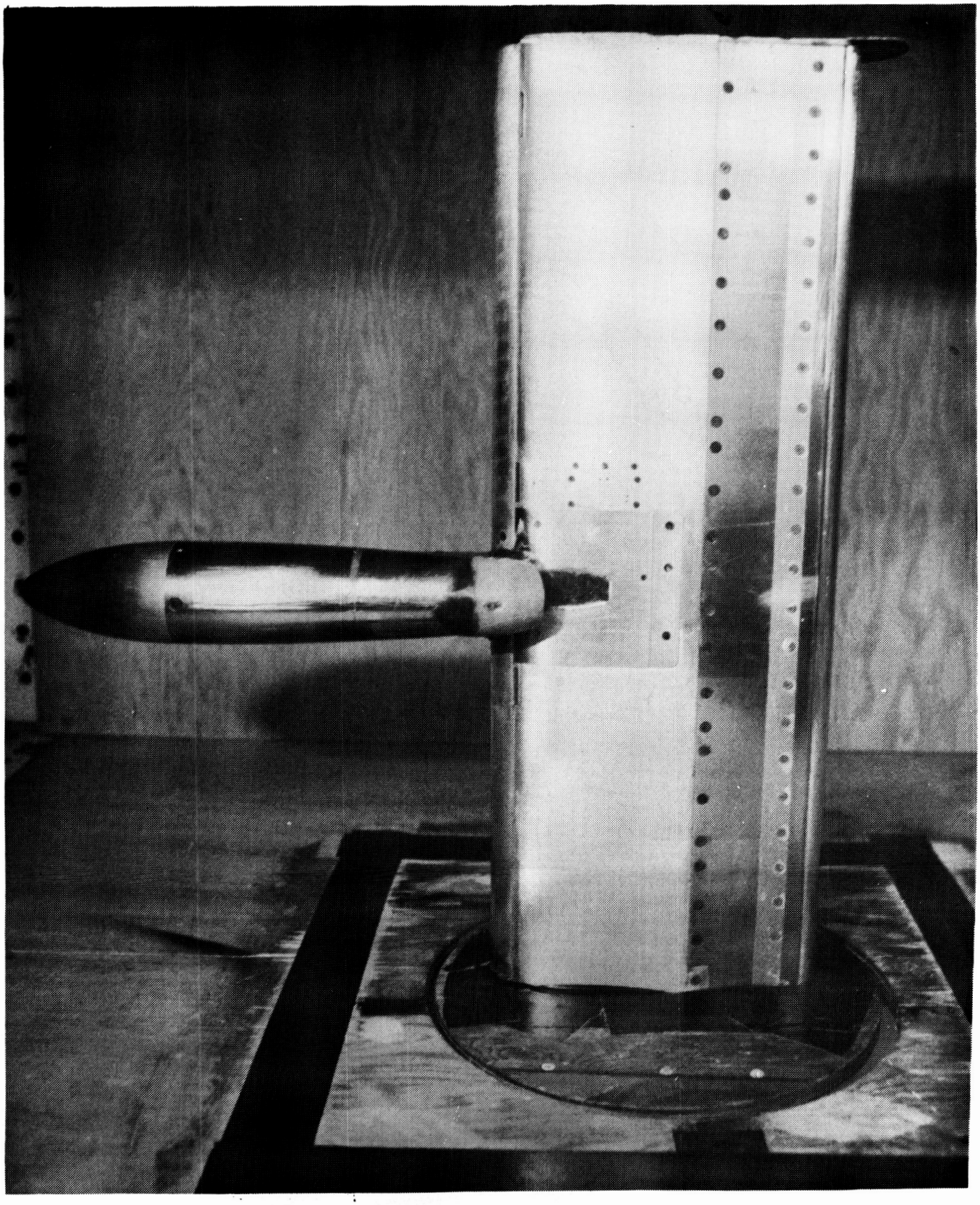

Figure 32. Semi-Span CCW/OTW Aspect-Ratio = 5.5 Model

ORIGINAL PAGE IS
OF POOR QUALITY

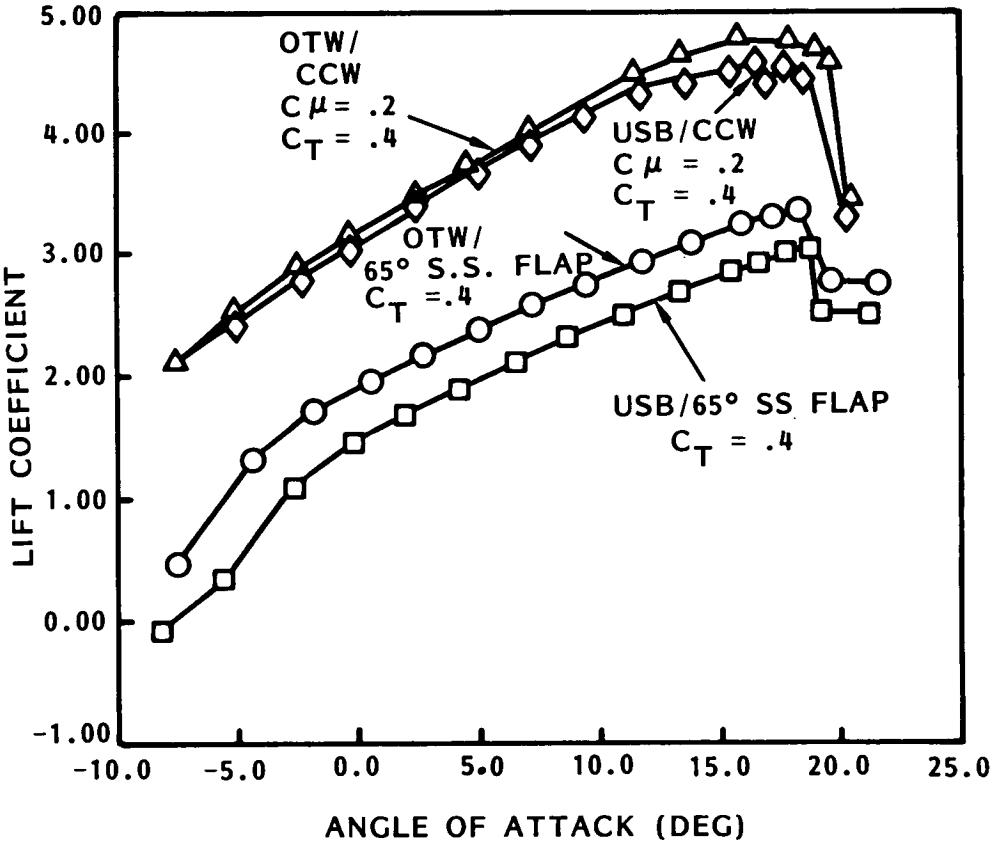

Figure 33. Quasi 2-D Comparison of CCW and Mechanical Flaps on OTW and USB Configurations

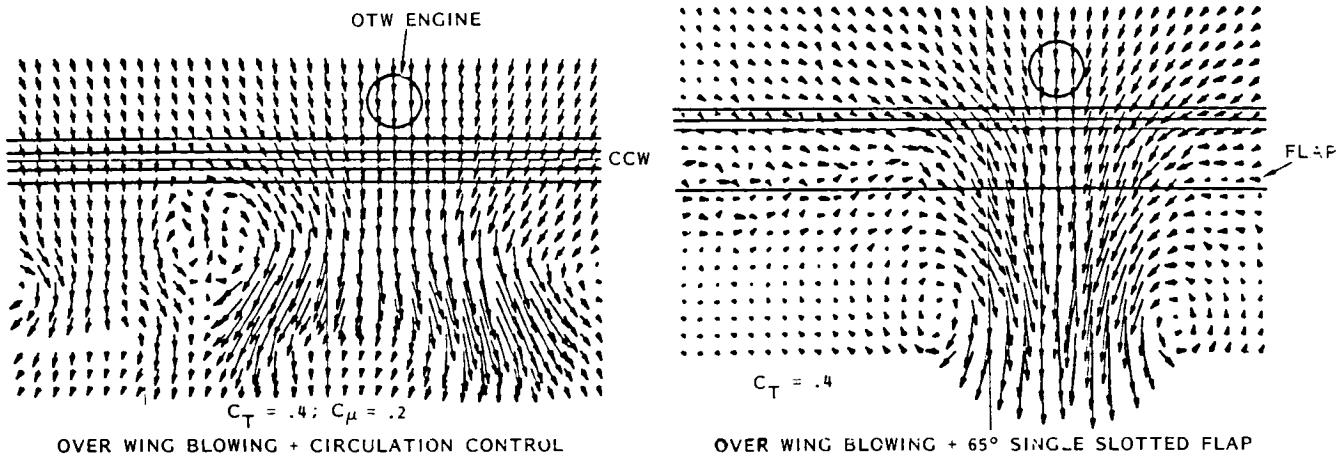

Figure 34. Wake Surveys Comparing the Effect of Trailing Edge Type with OTW Engine Arrangement

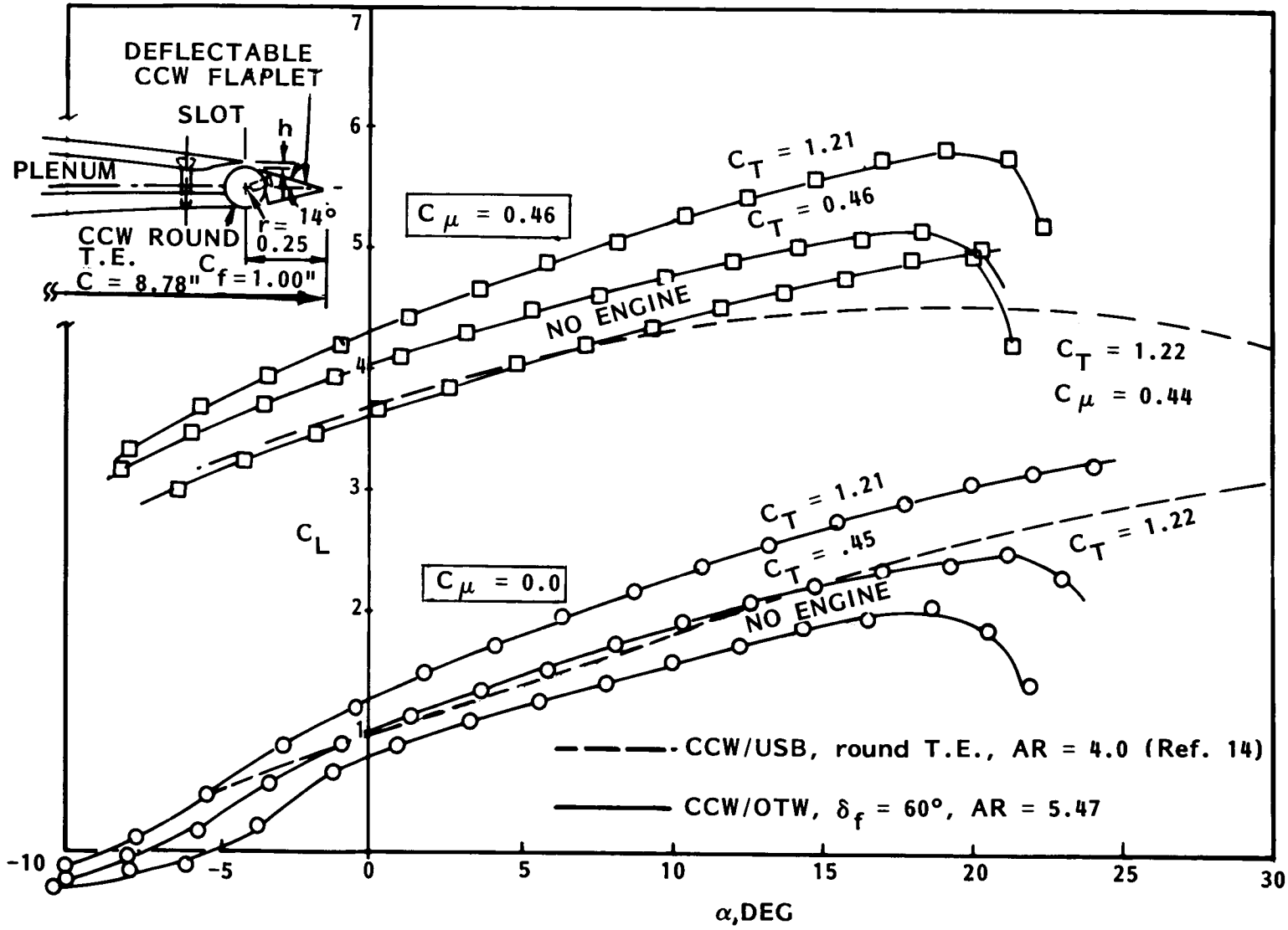

Figure 35. CCW/OTW Semi-Span Model Lift due to Blowing and Thrust Deflection, $\delta_F = 60^o$

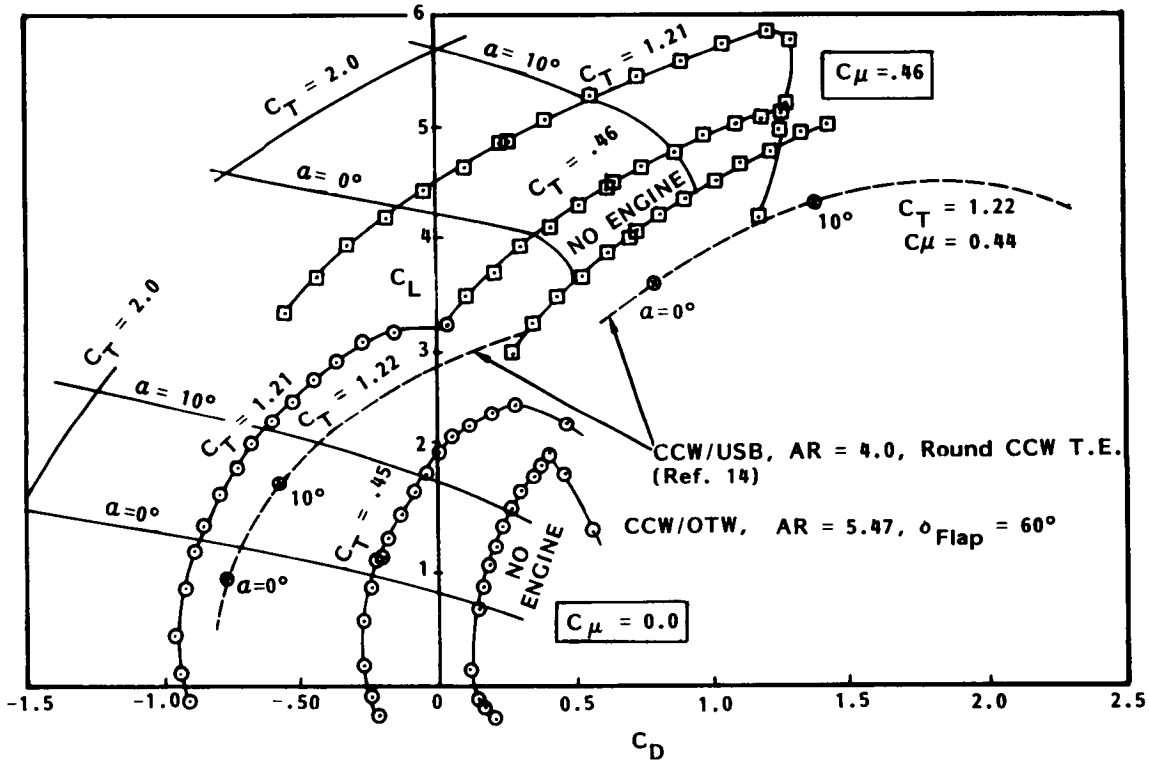

Figure 36. Comparative Drag Polars for CCW/OTW and CCW/USB Semi-Span Models

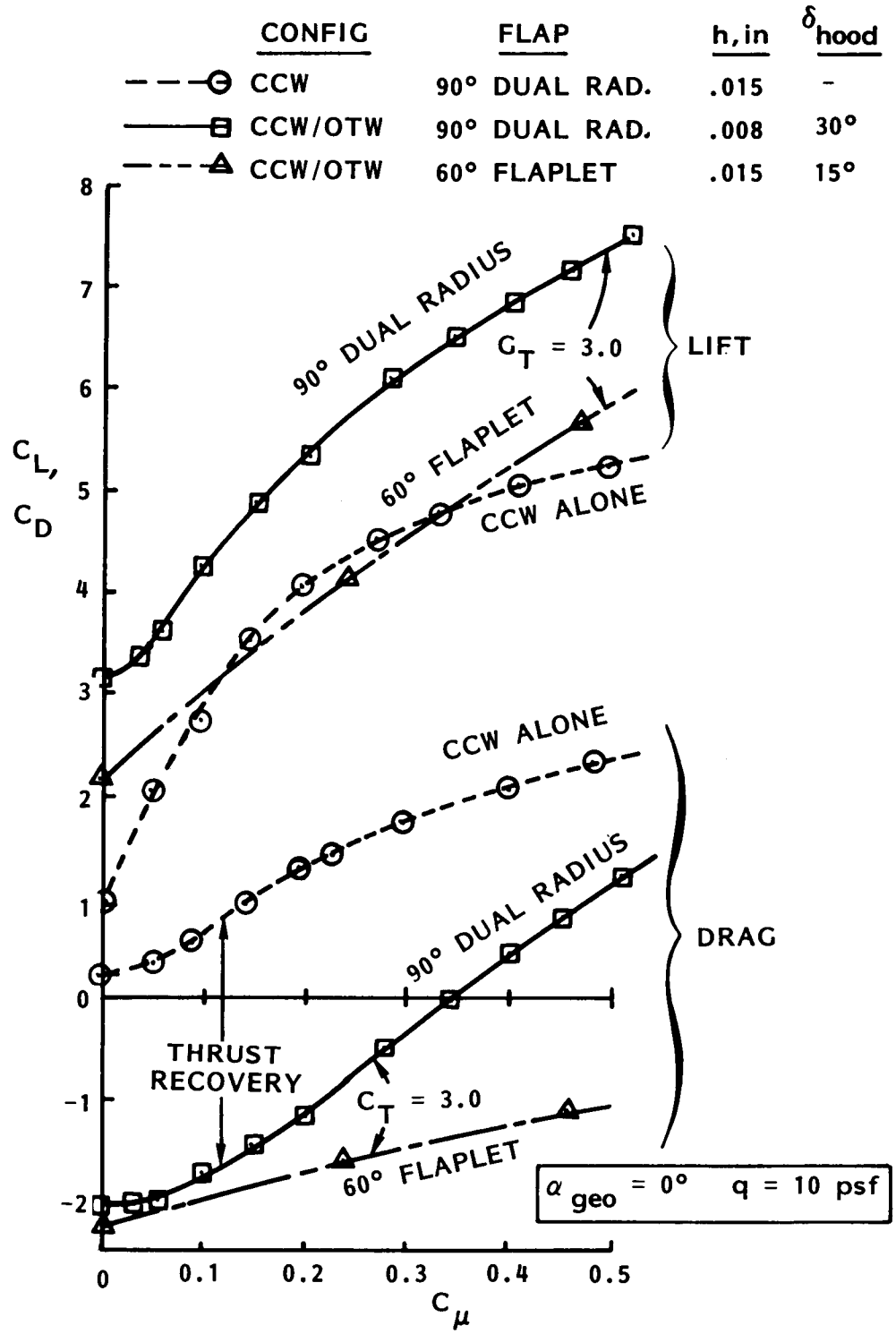

Figure 37. Effect of CCW Configuration on Lift and Drag due to Blowing and Thrust Deflection

A POTENTIAL FLIGHT EVALUATION OF AN UPPER-SURFACE-BLOWING/CIRCULATION-CONTROL-WING CONCEPT

Dennis W. Riddle and Joseph C. Eppel

NASA-Ames Research Center

SUMMARY

The technology data base for powered-lift aircraft design has advanced considerably over the last 15 years. NASA's Quiet Short-Haul Research Aircraft (QSRA) has provided a flight verification of upper surface blowing (USB) technology. The Navy/Grumman A-6 Circulation Control Wing Flight Demonstration Aircraft has provided data for circulation control wing (CCW) technology. Recent small-scale wind-tunnel model tests and full-scale static flow-turning tests have shown the potential of combining USB with CCW technology. A flight research program is deemed necessary to fully explore the performance and control aspects of CCW jet substitution for the mechanical USB Coanda flap. The required hardware design would also address questions about the development of flight-weight ducts and CCW jets and the engine bleed-air capabilities versus requirements. NASA's QSRA would be an optimum flight research vehicle for modification to the USB/CCW configuration. This report discusses the existing QSRA data base, the design simplicity of the QSRA wing trailing edge controls, availability of engine bleed-air, and the low-risk/low-cost potential of the suggested program. Recommendations are made for follow-on efforts to this USB/CCW QSRA modification study.

INTRODUCTION

The requirements for improved lifting, maneuver capability and STOL characteristics for both military and civil aircraft have led to the development of several technology demonstrator aircraft which perform research in powered-lift aerodynamics. Two of these, NASA's QSRA (ref. 1, fig. 1) and the Navy/Grumman A-6 CCW Flight Demonstration Aircraft (ref. 2, fig. 2), have provided extensive data for USB and CCW powered-lift concepts. A powered-lift concept developed at the David Taylor Naval Ship Research and Development Center (DTNSRDC) replaces the mechanical Coanda flap system of the USB airplane with a CCW flap which deflects the USB engine thrust as shown in figure 3. The resulting increase in wing circulation and vertical thrust component augments aerodynamic lift in a manner similar to that

of the Coanda USB flap concept used in the QSRA and the USAF/Boeing YC-14 airplanes. In addition, the full-span CCW system provides circulation lift augmentation over the entire wing. The USB/CCW configuration has the potential for improved performance and versatility for STOL airplanes due to the ability of the CCW pneumatic thrust deflector to rapidly vary horizontal force from thrust to drag while maintaining constant vertical force (ref. 3). Because the circulation lift augmentation is driven by the CCW, the loss of a thrust (USB) engine would create a lower lateral upset than with a Coanda flap, thus requiring less corrective control input. There is a potential for an adequately controllable two-engine USB powered-lift airplane by the combination of USB with CCW.

The ability of this USB/CCW configuration to deflect engine thrust was verified in two QSRA static ground tests conducted for the U.S. Navy in 1981 and 1983 (ref. 4 and 5). The second test series investigated USB/CCW geometries which would be representative of flight configurations where cruise drag is a major consideration. A typical configuration is shown in figure 4. A 90 degree circular arc with a small slot height provided the best performance, demonstrating that adequate thrust turning can be produced by a trailing edge shape which may have minimal cruise performance penalty (ref. 5). Thrust deflections were achieved at considerably lower blowing momentum than was required in the 1981 baseline tests. Small-scale, low-speed wind-tunnel model tests have also shown the ability of the CCW jet, with a small trailing edge flap, to control the thrust deflection of USB engine configurations (ref. 6). This data base was generated by Lockheed-Georgia on an ejector powered model with a twelve foot wing span.

The QSRA, shown in figure 5, is a high performance STOL powered-lift research aircraft which uses the USB technique to achieve maximum lift coefficients of slightly over ten (ref. 1). The QSRA first flew in July 1978 and has logged over 550 flight hours since. The propulsion system consists of four AVCO-Lycoming YF-102 turbofan engines, shown in figure 6, mounted in above-the-wing nacelles (figure 7). These engines, which are prototypes of Lycoming's ALF-502 turbofan, each produce slightly less than 6,000 pounds static sea-level installed thrust. A low-pressure, low-temperature boundary layer control (BLC) air distribution system was designed and built for the QSRA. This system originally provided wing leading edge and aileron BLC blowing from a mix of engine compressor bleed and fan air. The wing leading edge BLC blowing was removed early in the flight research program, having been replaced by a fixed, conventional aerodynamic slat. Thus, a source of engine fan and compressor bleed air exists for blowing a CCW jet. The QSRA fuselage and

empennage is that of a deHavilland C-8 Buffalo. The landing gear is fixed in the down position and has been modified to accommodate gross takeoff weights of 60,000 pounds. The empty weight is approximately 43,000 pounds which includes an extensive onboard data acquisition, recording and telemetry system. An extensive low-speed wind-tunnel, flight simulation and flight research data base exists which fully documents the performance and control characteristics of the QSRA Coanda USB flap configuration.

There are four primary objectives for the proposed USB/CCW flight evaluation program. First would be the assessment of the feasibility of flight-weight, airworthy hardware during the QSRA modification design and fabrication period. Second would be the assessment of the engine bleed air availability versus that required by the CCW jet for a full range of flight conditions. During the detail design phase, the use of an auxiliary air compressor may be deemed necessary, especially as a back-up for single engine-out conditions. Third would be a flight evaluation of the low-speed performance of the USB/CCW configuration. Lift, drag and pitching moment characteristics would be measured and takeoff and landing airspeed and angle-of-attack margins would be determined. Fourth would be a flight evaluation of the STOL control characteristics of the USB/CCW configuration. The ability to maintain high levels of lift (and thus, airspeed and angle-of-attack margins) while varying drag to provide steep STOL landing approach glideslope control would be determined. Performance and control comparisons would be made between the USB/CCW and USB Coanda flap configurations. There is also a potential objective of a wind-tunnel/flight low-speed aerodynamic data correlation. Discussions have been ongoing concerning a wind-tunnel test of the QSRA in the NASA-Ames Research Center 80 by 120 ft. low-speed wind tunnel. This could be timed to be done with the USB/CCW configuration prior to or after the flight tests.

QSRA USB/CCW MODIFICATION POTENTIAL

The existing wing trailing edge controls consist of two USB flap panels, one conventional double-slotted flap, and one aileron on each side of the aircraft as shown on the lower half of the QSRA planform in figure 8. There are also two spoiler panels on each wing which are used in three control modes: 1) asymmetrical deflection for lateral control in conjunction with the ailerons, 2) gross landing approach glideslope control and landing roll lift dump by manual symmetrical deflection, and 3) direct lift control (DLC) for accurate glideslope tracking using symmetrical incremental deflections tied to throttle movements to quicken flight path response. Further details of the flight control systems and characteristics are presented in references 7, 8 and 9.

Structural Modifications

The design of the QSRA basic wing structure is such that all trailing edge control surfaces and fairings can be removed aft of the rear spar, thus providing maximum flexibility for the design and installation of a new CCW trailing edge and associated air ducting. The upper half of the QSRA planform in figure 8 identifies the potential elements of the USB/CCW modification. The existing spoiler panels would be retained to assure adequate lateral control power for the flight research program. Figure 9 provides more detail of the inboard USB segment of the QSRA wing. The upper wing cross-section shows the existing USB Coanda flap and associated hardware. The lower wing cross-section shows a conceptual USB/CCW modification with an identification of new hardware. The trailing edge could be either a small flap as shown or a fixed cylindrical arc as tested in the QSRA static tests in 1983. The existing USB flap support arm, which is attached to the front and rear spars of the wing, would be retained to provide a structural load path to react the CCW trailing edge aerodynamic loads. Figure 10 presents similar wing structure details at the existing double-slotted flap location. Note that the spoiler panels are retained without any modification. CCW trailing edge aerodynamic loads would be reacted through the existing double-slotted flap support arm. Figure 11 details the structure at the ailerons, again showing the ease with which a USB/CCW modification could be made. A potential CCW aileron would be very similar to the existing blown aileron panel except for a shorter chord length. Another possibility would be a cylindrical trailing edge with upper and lower surface blowing for lateral control and a blown base jet for neutral lateral control requirements. The blowing to the proper jet would be controlled by a rotating, slotted cylinder valve within the jet duct. Both of these thoughts are detailed in figure 11.

Control System Modifications

The wing trailing edge flight control system can also be adapted easily to the control of the CCW jet blowing and small aft flap movements. The current lateral control system is shown in figure 12. The ailerons are hydraulically operated with the command coming from the pilots' control wheels via mechanical linkage. There are also lateral trim and lateral stability augmentation system (SAS) electrical commands which are mechanically summed into the aileron command. The summed mechanical command which drives the aileron hydraulic cylinder transfer valve could be made to drive a CCW jet blowing control valve and a CCW aft flap hydraulic transfer valve. Thus, the CCW aileron function would

include pilot wheel inputs, lateral trim inputs and lateral SAS inputs as for the current QSRA system. No change would be made to the electronic pilots' wheel-to-spoiler panel gearing.

The existing USB and double-slotted (or outboard) flaps are hydraulically actuated in response to electrical inputs to the hydraulic transfer valves as shown in figure 13. The electrical driving signals come from flap analog computers which sum pilot control lever, trim and stability and control augmentation system (SCAS) electrical inputs. Essentially, the wing flap system is a "fly-by-wire" configuration in which the electrical commands could be made to drive CCW jet blowing control valves and CCW aft flap hydraulic transfer valves. The current QSRA asymmetric outboard flap lateral trim (for engine-out compensation) and SCAS lift-drag control functions could be maintained with the CCW system.

Engine Fan/Core Bleed Air System

The original QSRA configuration utilized BLC blowing on the entire wing leading edge and on the upper aileron surfaces (ref. 10). The array of ducts, valves and BLC nozzles is shown in figure 14. Currently the QSRA retains the aileron BLC system but the leading edge BLC system has been replaced with a fixed leading edge slat. Removal of the aileron droop, a function of double-slotted flap extension through a mechanical linkage, would negate the need for aileron BLC blowing. Thus, the original BLC system on all four Lycoming YF-102 engines could be used for the CCW jet blowing requirements. Figure 15 shows the mixed flow BLC system components. A fan "S"-duct bleeds approximately 3% of the fan air flow and an engine compressor bleed band allows up to 10% high pressure compressor bleed. A fixed-geometry ejector pump mixes fan and compressor bleed air with an associated pressure rise relative to fan pressure. An ejector bleed air control valve senses and controls exit pressure to a constant value which can be set at the valve. Figure 16 shows the net blowing thrust from the existing aileron BLC nozzles as a function of engine thrust. The ejector bleed air control valve allows a constant 100 pound blowing thrust at a constant BLC pressure of 4.9 psig. The pressure control feature provides for adjustment of BLC levels from 4 to 11 psig on the airplane for research flexibility.

In the event that the required CCW jet blowing requirements cannot be met by the maximum engine bleed air available, it would be plausible to install auxiliary air compressors in underwing pods. A detailed design study would be required to ascertain the capacity, placement and control of such auxiliary compressors.

QSRA: A LOW-RISK USB/CCW PROGRAM

QSRA Performance and Control

The QSRA was designed to have a high level of performance to provide flight research flexibility and safety. The installed thrust-to-weight ratio at 60,000 pounds maximum gross takeoff weight is 0.39; at 45,000 pounds, 0.52. The corresponding wing loadings are 100 psf and 75 psf. Both the STOL and CTOL capabilities of the QSRA have been shown to be superior to other powered-lift aircraft (ref. 11 and 12). Likewise, excess control power, especially in the lateral control axis, was designed into the QSRA to assure safety when performing simulated engine-out flight research. Figure 17 shows the QSRA's lateral control power in terms of roll acceleration versus pilot wheel input. Previous STOL aircraft studies (ref. 13) recommended a minimum roll acceleration capability of 0.4 radians per second squared. The QSRA design team elected to double this goal for the airplane: 0.8 radians per second squared. Figure 17 shows that this goal was exceeded by use of the ailerons and spoilers collectively. The spoilers provide 58% of the maximum lateral control power. These same spoilers, and their use for lateral control, would be maintained for the USB/CCW modification. Therefore, even if CCW lateral control concepts did not prove as effective as the existing ailerons, adequate lateral control would still be available.

Failure Modes Assessment

A very detailed flight simulation was performed during the QSRA design to develop the flight control laws and SCAS and to investigate the risk of various systems failure modes. References 14 and 15 provide the simulation mathematical model and the results of the simulation investigations. The mathematical model used a 40 by 80 ft. wind tunnel, 55% scale QSRA model aerodynamic data base. Failure modes, such as flap and aileron hardovers and asymmetries, were investigated to determine pilot recognition and ability to counter the uncommanded upset.

A USB/CCW aerodynamic performance and control data base has been acquired by the Lockheed-Georgia Company using a 12-foot span model in their low-speed wind tunnel (reference 6). Figure 18 shows how the USB/CCW aerodynamics could be related to the baseline QSRA simulation results. The USB baseline aerodynamic data, combined with the QSRA control laws, provided a failure mode analysis tool. Flap and aileron hardovers and asymmetries

demand sufficient pilot recognition, control power and response times to counter the uncommanded upsets. The baseline USB aerodynamic coefficients can be directly compared to the USB/CCW coefficients. For example, an uncommanded USB flap panel retraction would be expected to generate nearly the same rolling moment coefficient as the loss of CCW jet blowing behind one engine. The pilot reaction and corrective response requirements would be expected to be approximately the same. If certain CCW jet failures caused aerodynamic forces which were found uncontrollable for the baseline configuration, system redundancies would be required to assure a fail safe operation. A new USB/CCW configuration flight simulation would not be required using this analysis technique.

QSRA Instrumentation

The QSRA has a digital data system which processes, records and telemeters approximately 300 discrete items (ref. 7). In conjunction with the NASA ground station many of these parameters can be monitored real-time by the ground test engineer. Real-time computations of items such as corrected lift coefficient can also be monitored. All of the required USB/CCW unique performance, control surface movement, jet blowing and system health monitors can be added to the existing data system for real-time observation and/or post-test analysis.

Phased Modification Program

A phased flight program to study USB/CCW performance and control characteristics would be conducted so as to reduce risk. Three modification phases are shown in figure 19: Phases A, B and C. Phase A would replace the USB Coanda flap panels with the CCW jet/flap configuration behind the turbofan engines. The outboard section of the wing (double-slotted flap, aileron and spoilers) would remain unchanged. Initial takeoffs and landings would be performed in a CTOL configuration, using double-slotted flaps and drooped ailerons as the only lift enhancers, as has been demonstrated numerous times during the QSRA's flight history. Evaluations of performance, control and simulated CCW jet failures (loss of partial blowing) would be performed at a safe altitude. Once the control limitations and airspeed and angle-of-attack margins were firmly established, the USB/CCW system would be employed during takeoffs and landings. A flight data base would be developed which would compare the USB Coanda flap to the USB/CCW configuration for overall performance and control capability.

Phase B would replace the double-slotted flap with the CCW jet/flap configuration. This would increase the percentage of the wing that would be subject to circulation lift augmentation. Initial takeoffs and landings would be performed in a clean-wing CTOL configuration with the CCW jet turned off. As with Phase A, the Phase B modification would be fully explored at a safe altitude before conducting takeoffs and landings.

Phase C would replace the existing aileron with a CCW trailing edge configuration, providing circulation lift augmentation across the entire wing span. Differential CCW jet blowing, in conjunction with the QSRA's lateral control spoiler panel function, would be studied as a means of roll control and engine-out roll trim. Again, the initial assessments would be performed at altitude using conservative CTOL takeoffs and landings. The use of the phased modification approach would not only minimize risk but would provide a three-tiered data base to allow assessment of the gains from each modification phase.

CONCLUSIONS AND RECOMMENDATIONS

The QSRA static USB/CCW ground tests conducted for the U.S. Navy and the low-speed USB/CCW wind-tunnel tests conducted by the Lockheed-Georgia Company have shown the aerodynamic potentials of the combination of USB with CCW. A flight verification is required to assess the overall performance and control characteristics with a fully integrated airframe, propulsion and control system.

The extensive QSRA USB Coanda flap wind-tunnel, flight-simulation and flight research data base can be combined with the USB/CCW wind-tunnel data base to determine and resolve potential performance or control problems during early design. The comparison of the aerodynamics of the two systems will allow, without further wind-tunnel testing or flight simulations, the determination of risks and pilot operational procedures. The phased modification concept will further reduce risks.

The QSRA allows a low-cost approach to USB/CCW flight research by providing a proven, fully instrumented flight facility. The relative simplicity of the QSRA wing structure and flight controls allows maximum modification flexibility. The existence of a fully developed engine air bleed system and associated ducts and valves will further minimize modification costs.

This program will provide a valuable flight data base to assess the USB/CCW performance and STOL control characteristics for comparison to the USB Coanda flap configuration. Many claims

have been made for potential improvement over the mechanical flap system. This program will provide a quantitative evaluation. The USB/CCW concept has a strong potential for two-engine powered lift aircraft. The CCW jet assures the continuance of the circulation lift augmentation following the loss of one engine, thus reducing the lateral upset and required corrective action.

NASA-Ames Research Center has been approached by both the U.S. Navy and the Lockheed-Georgia Company to consider a USB/CCW flight research program using the QSRA facility. At the present time there is no defined funding for such a program. The first step, beyond this feasibility report, would be to develop a cost estimate for the USB/CCW modification. It is recommended that NASA, DOD and industry work together to determine the approximate costs and, if reasonable, then to advocate the funding for the program. A NASA project engineering and technical support team exists for specifying and supervising the QSRA modifications and flight testing.

REFERENCES

1. Cochrane, J. A.; Riddle, D. W.; and Stevens, V. C.: QSRA - The First Three Years of Flight Research. AIAA Paper 81-2625, December 1981.

2. Pugliese, A. J.; and Englar, R. J.: Flight Testing the Circulation Control Wing. AIAA Paper 79-1791, 1979.

3. Nichols, J. H.; and Harris, M. J.: Fixed Wing CCW Aerodynamics With and Without Supplementary Thrust Deflection - A Review. Circulation Control Workshop Proceedings, NASA CP 2432 (Paper 21).

4. Eppel, J. C.; Shovlin, M. D.; Jaynes, D. N.; Englar, R. J.; and Nichols, J. H.: Static Investigation of the Circulation-Control-Wing/Upper-Surface-Blowing Concept Applied to the Quiet Short-Haul Research Aircraft. NASA TM 84,232, 1982.

5. Englar, R. J.; Nichols, J. H.; Harris, M. J.; Eppel, J. C.; and Shovlin, M. D.: Circulation Control Technology Applied to Propulsive High Lift Systems. SAE Paper 841,497, October 1984.

6. Englar, Robert J.: The Application of Circulation Control Technology to Fixed Wing STOL Aircraft. Circulation Control Workshop Proceedings, NASA CP 2432 (Paper 22).

7. Eppel, J. C.: Quiet Short-Haul Research Aircraft Familiarization Document, Revision 1. NASA TM 81,298, 1981.

8. Boeing Commercial Airplane Company Preliminary Design Department: The Development of a Quiet Short-Haul Research Aircraft - Final Report. NASA CR 152,298, 1980.

9. Franklin, J. A.; and Hynes, C. S.: Flight Evaluation of Highly Augmented Controls and Electronic Displays for Precision Approach and Landing of Powered-Lift Aircraft. AIAA Paper 85-1944, August 1985.

10. Shovlin, M. D.; Skavdahl, H.; and Harkonen, D. L.: Design and Performance of the Propulsion System for the Quiet Short-Haul Research Aircraft. AIAA Paper 79-1313, June 1979.

11. Riddle, D. W.; Innis, R. C.; Martin, J. L.; and Cochrane, J. A.: Powered-Lift Takeoff Performance Characteristics Determined from Flight Test of the Quiet Short-Haul Research Aircraft (QSRA). AIAA Paper 81-2409, 1981.

12. Stevens, V. C.; Riddle, D. W.; Martin, J. L.; and Innis R. C.: Powered-Lift Aircraft Shipboard Operations - A Comparison of Simulation, Land-Based and Sea Trial Results for the QSRA. AIAA Paper 81-2480, 1981.

13. Innis, R. C.; Holzhauser, C. A.; and Quigley, H. C.: Airworthiness Considerations for STOL Aircraft. NASA TN D-5594, 1970.

14. Flora, C. C.; Nicol, L. E.; Marley, A. C.; Middleton, R.; Schaer, D. K.; and Vincent, J. H.: Quiet Short-Haul Research Aircraft Phase II Flight Simulation Mathematical Model - Final Report. NASA CR 152,197, 1979.

15. Flora, C. C.; Middleton, R.; and Schaer, D. K.: Quiet Short-Haul Research Aircraft Predicted Flight Characteristics. NASA CR 152,203, 1979.

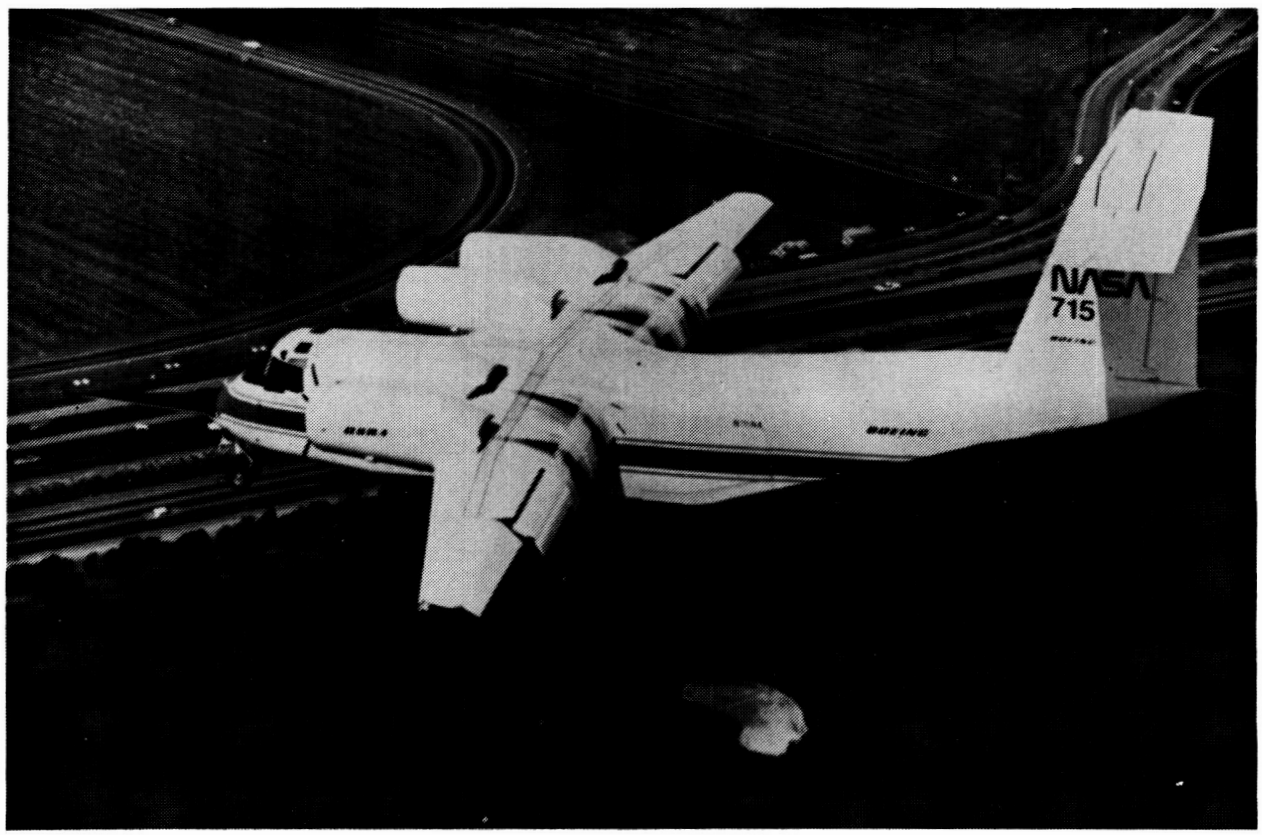

Figure 1. NASA's Quiet Short-Haul Research Aircraft (QSRA).

Figure 2. Navy/Grumman A-6 CCW Flight Demonstration Aircraft.

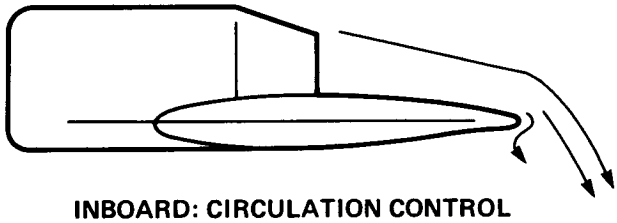

INBOARD: CIRCULATION CONTROL
WING/THRUST DEFLECTOR

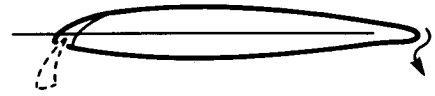

OUTBOARD: CIRCULATION CONTROL
WING ON SUPERCRITICAL AIRFOIL

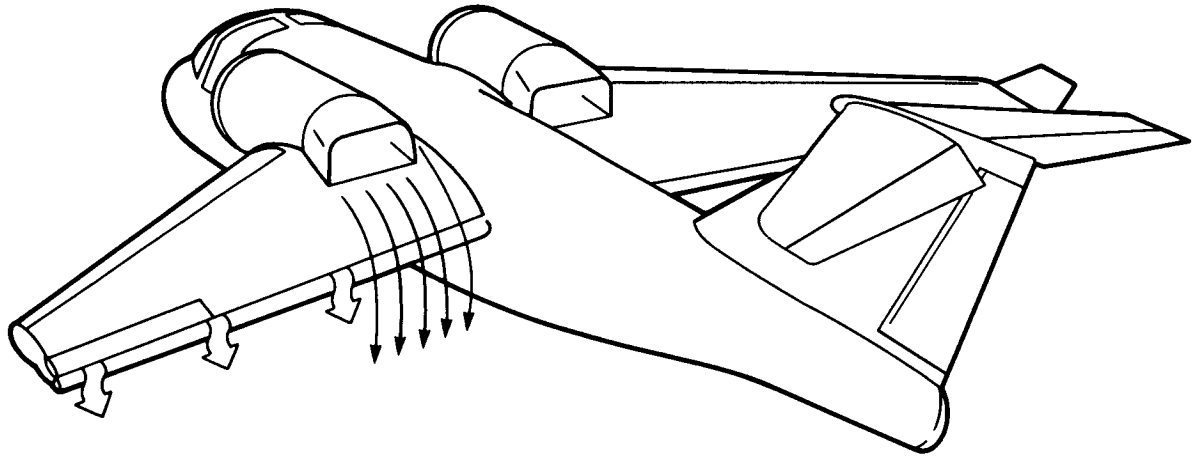

Figure 3. DTNSRDC conceptual USB/CCW aircraft configuration.

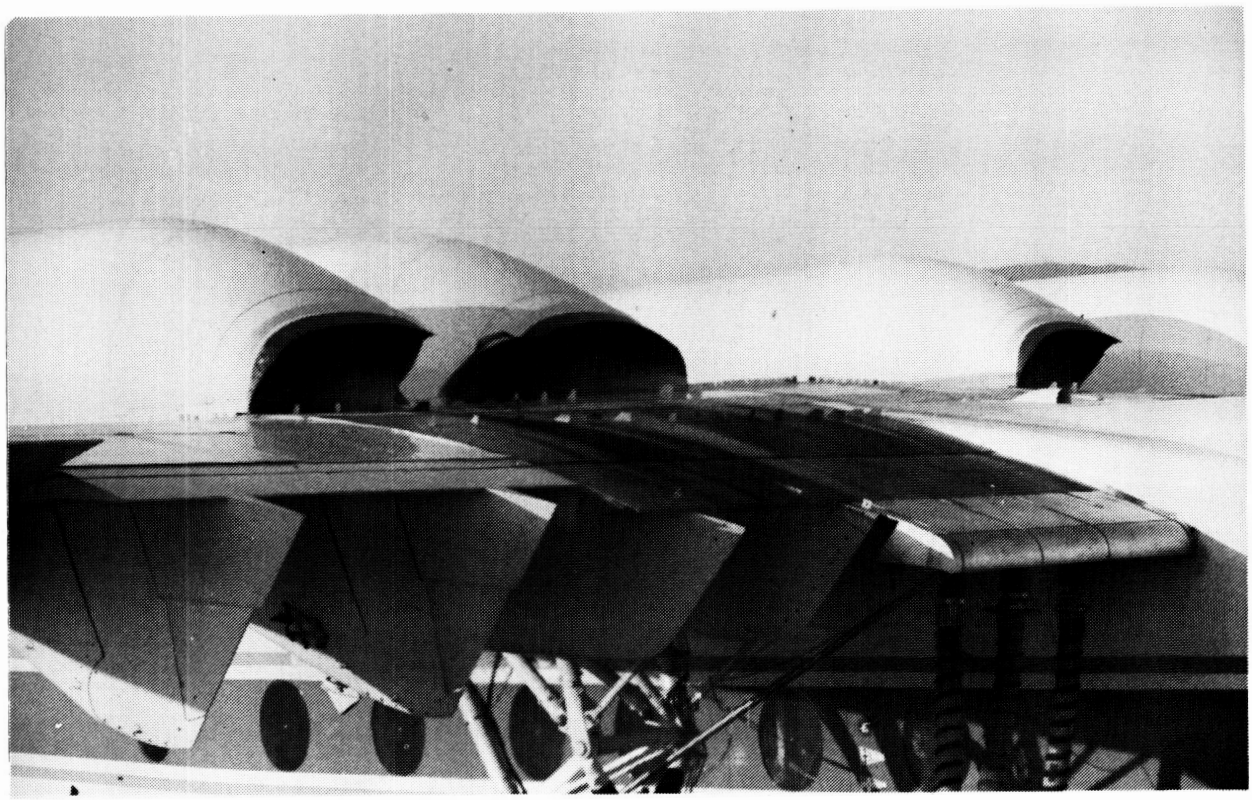

Figure 4. NASA/Navy QSRA USB/CCW static ground test setup.

AERODYNAMIC DATA

	WING	HORIZ	VERT
AREA (TRAP), ft^2	600.0	233.0	152.0
SPAN, ft	73.5	32.0	14.0
ASPECT RATIO	9.0	4.4	1.22
TAPER RATIO	0.30	0.75	0.60
SWEEP, C4, deg	15.0	3.0	18.0
M.A.C., in.	107.4	88.0	137.0
CHORD ROOT, in.	150.7	100.0	168.0
CHORD TIP, in.	45.2	75.0	100.0
T/C BODY SIDE, %	18.54	14.0	14.0
T/C TIP, %	15.12	12.0	14.0
INCIDENCE, deg	4.5	–	–
DIHEDRAL, deg	0.0	–	–
TAIL ARM, in.	–	525.0 in.	488.0 in.
VOL COEFF V	–	1.898	0.1402

CONTROL SURFACES

	ft^2	BLOWN
AILERON	32.2	BLC
FLAPS INBD	105.0	USB
FLAPS OUTBD	40.2	NONE
SPOILERS	33.7	NONE
L.E. FLAPS	54.3	NONE
ELEVATOR	81.6	NONE
RUDDER	60.8	NONE

*THEORETICAL RETRACTED AREA

PROPULSION

ENGINE	LYCOMING YF-102
STATIC THRUST	6225 lb **
FAN P.R.	1.45
BY-PASS RATIO	6.0

**MEASURED THRUST

LANDING GEAR

GEAR	STROKE	TIRE	TIRE O.D.	ROLLING R.
MLG, in.	21.0	11.5-15 NEW DESIGN	32.0	13.5
NLG, in.	17.5	8.90-12.50 TYPE III	27.5	12.0

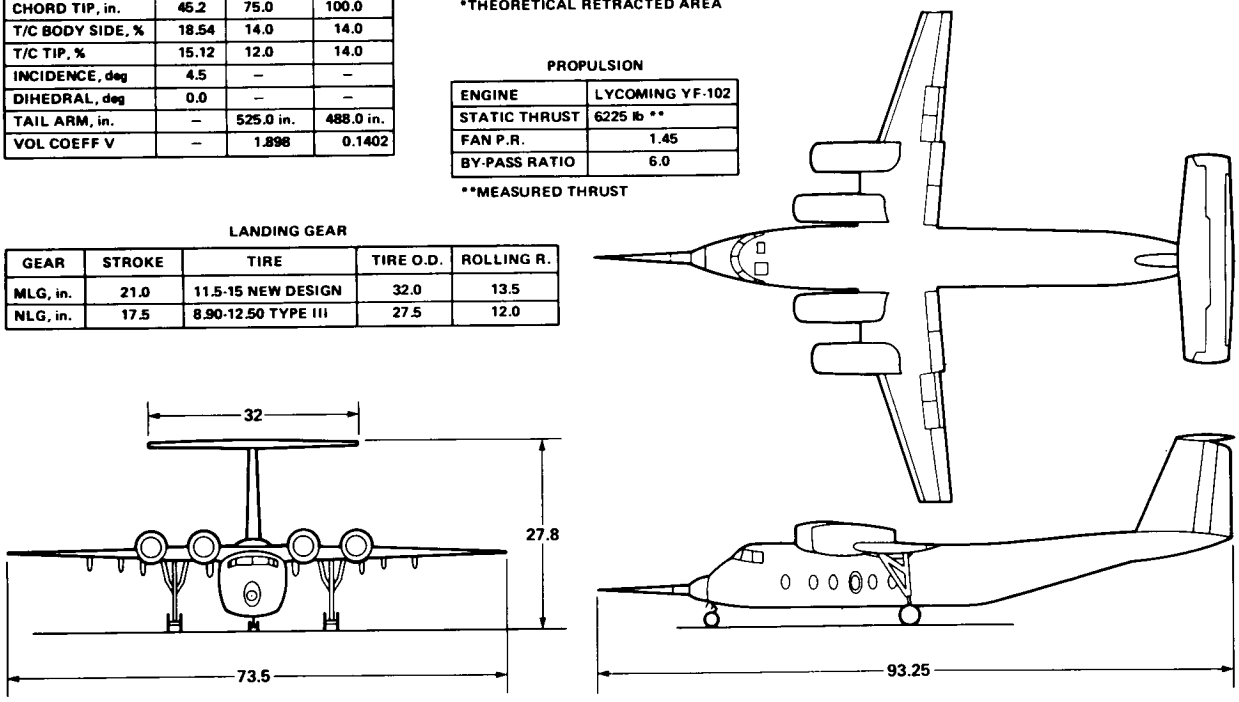

DIMENSIONS IN ft

10/81

Figure 5. QSRA configuration and dimensional details.

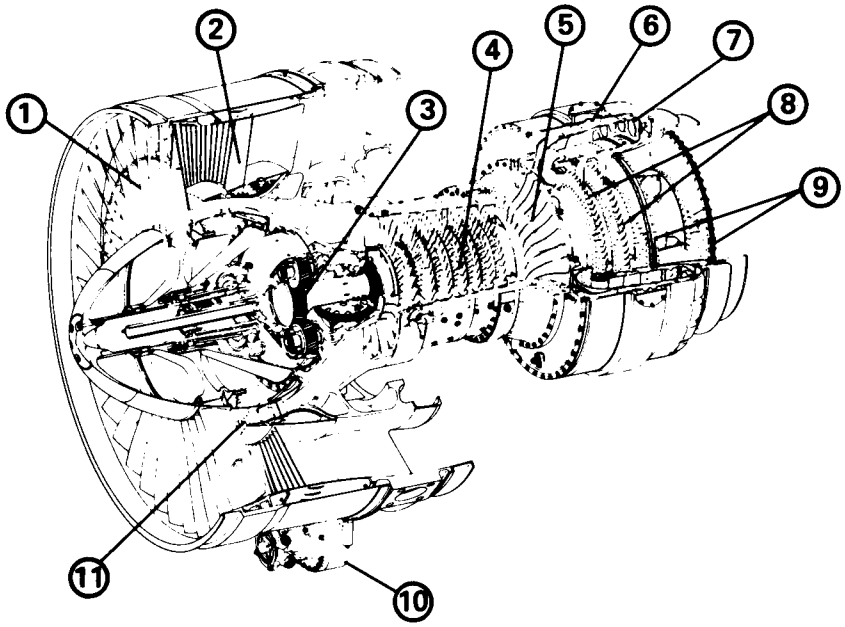

1. FAN STAGE
2. FAN STATOR
3. REDUCTION GEAR ASSEMBLY
4. CORE AXIAL COMPRESSOR
5. CORE CENTRIFUGAL COMPRESSOR
6. CUSTOMER BLEED PORTS
7. COMBUSTOR
8. GAS PRODUCER TURBINES
9. POWER TURBINES
10. ACCESSORY GEARBOX
11. SUPERCHARGER

Figure 6. AVCO-Lycoming YF-102 turbofan engine details.

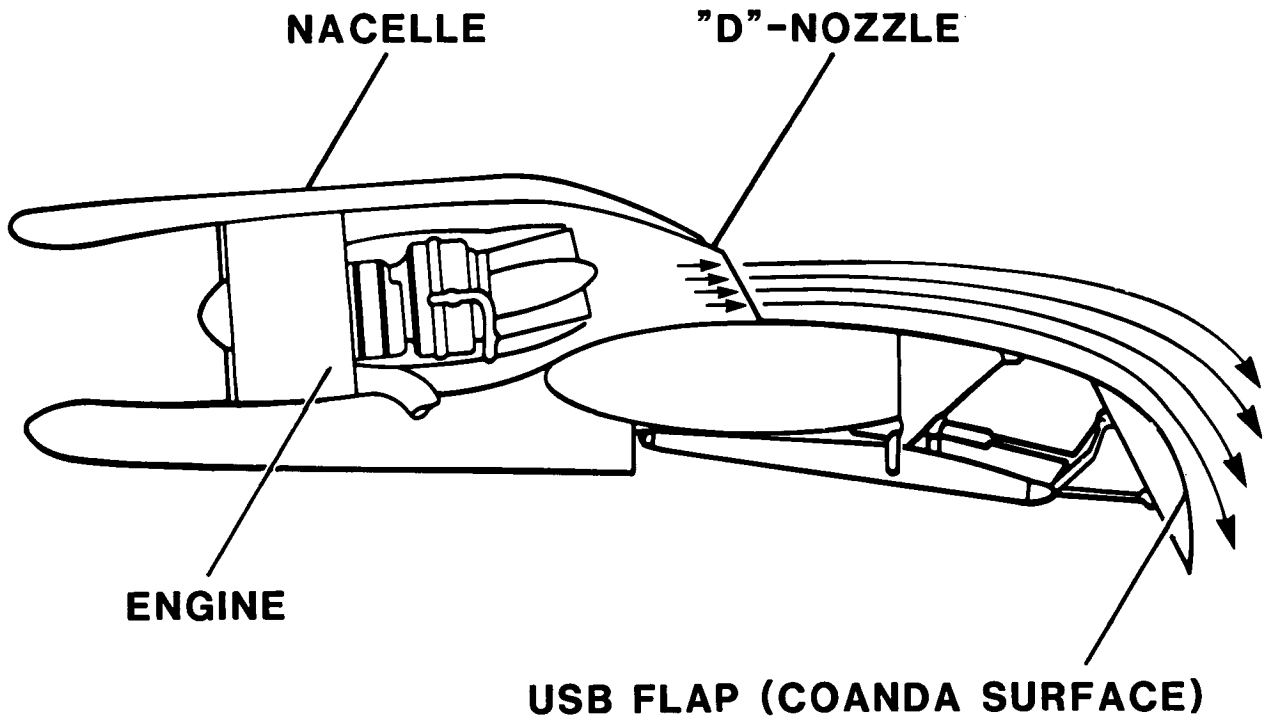

Figure 7. QSRA wing-engine USB configuration.

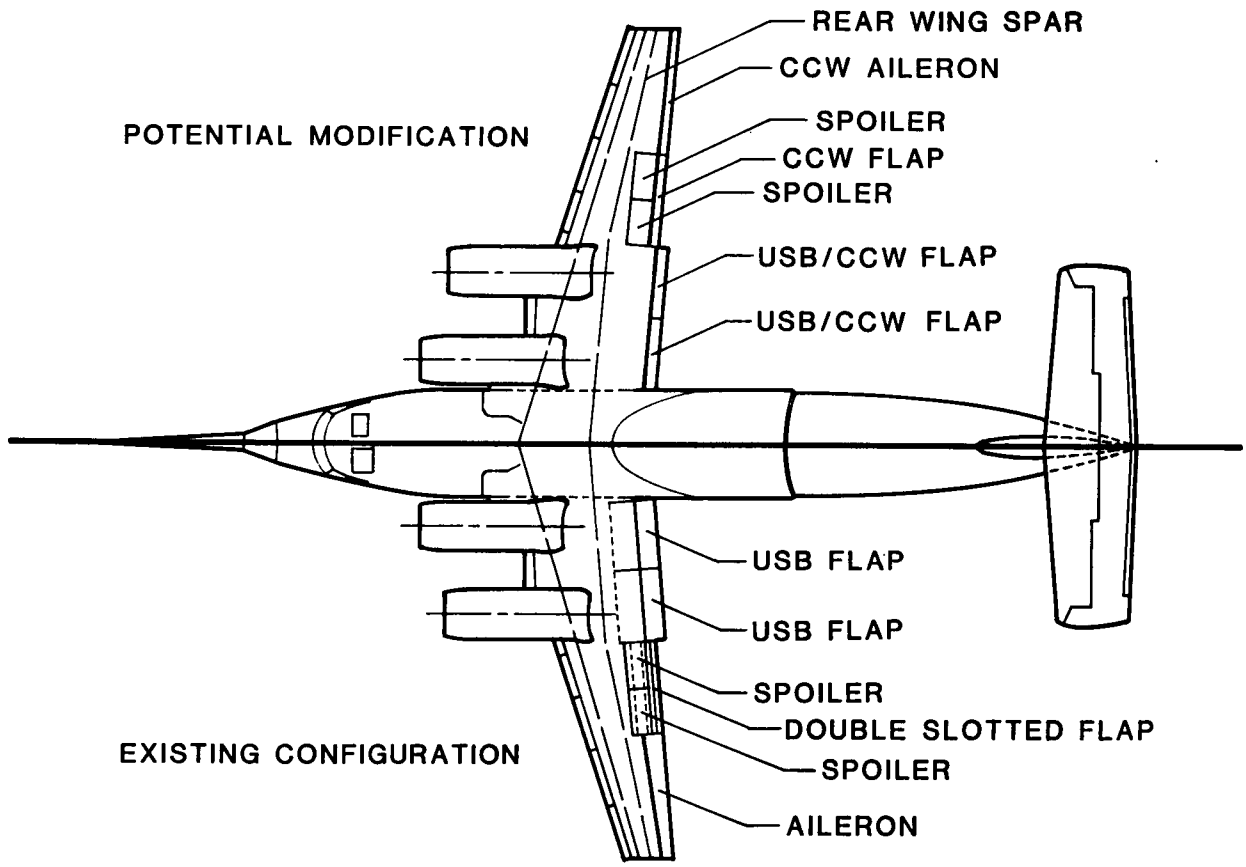

Figure 8. Comparison of existing QSRA wing to a potential USB/CCW modification.

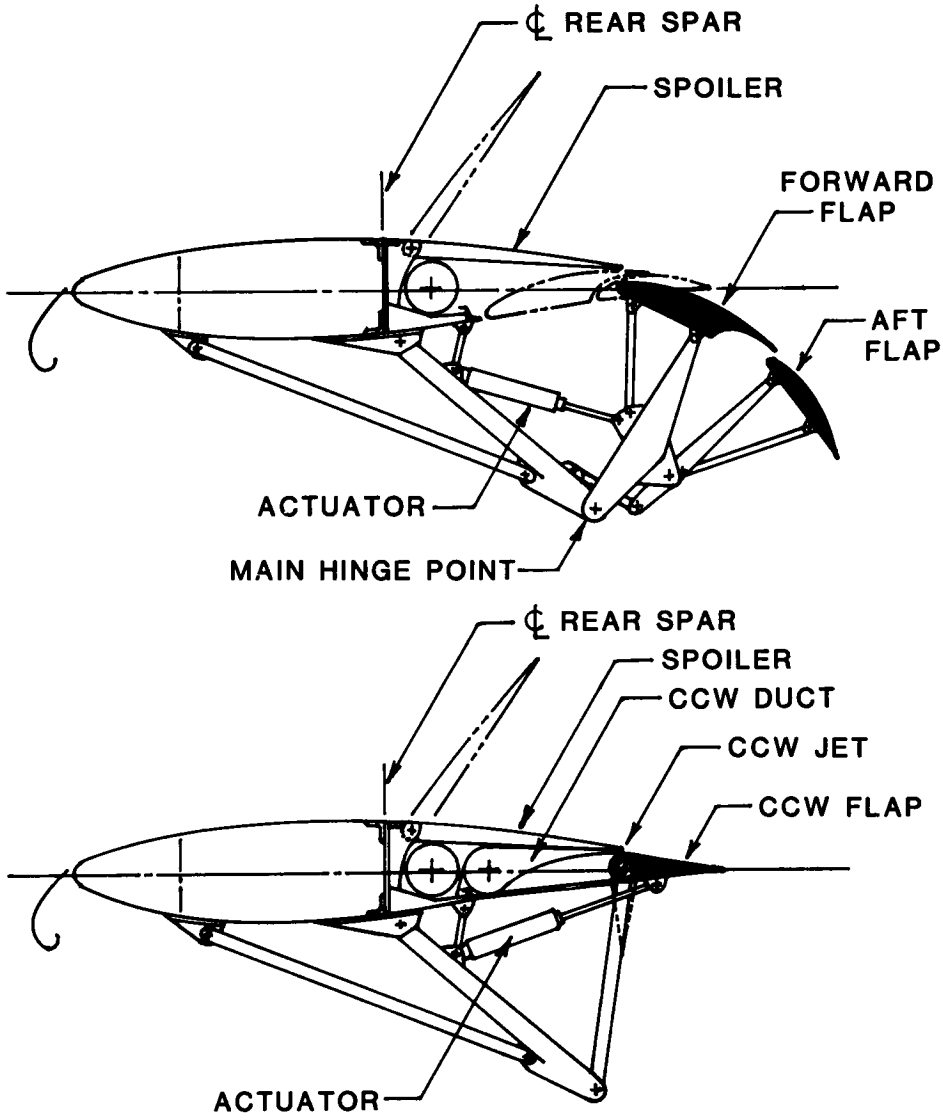

Figure 10. Comparison of existing double-slotted flap to a potential CCW trailing edge modification.

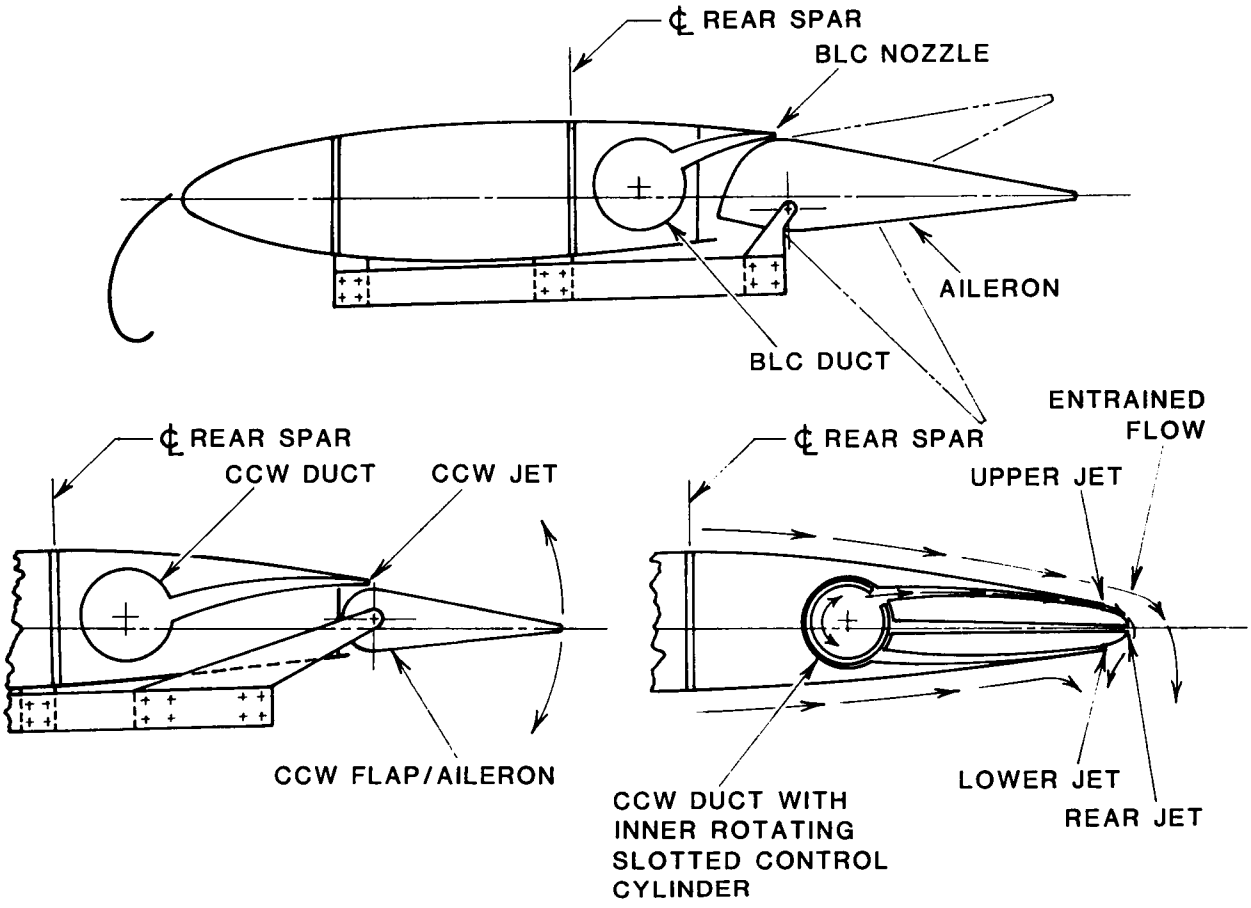

Figure 11. Comparison of existing BLC aileron to two potential CCW trailing edge modifications.

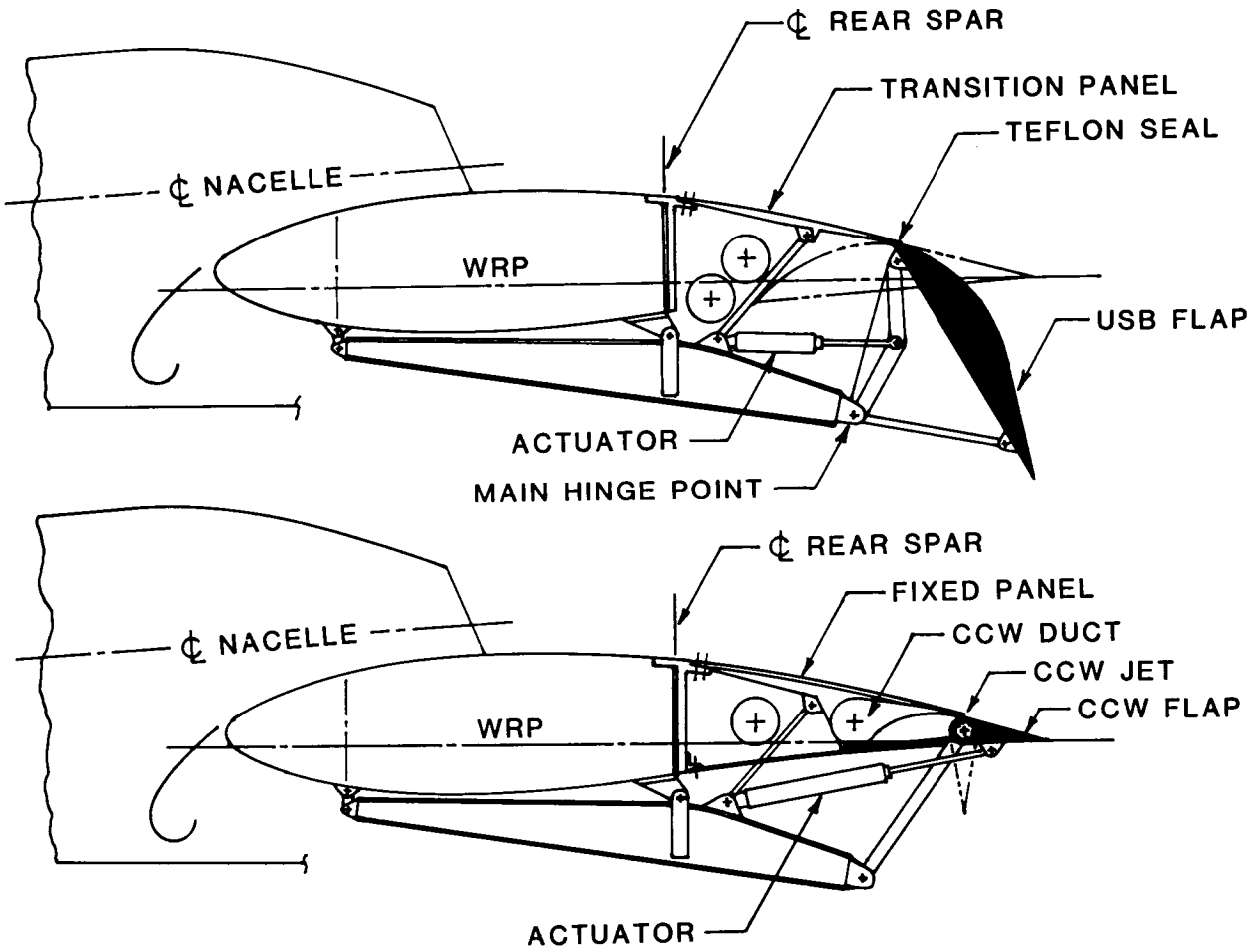

Figure 9. Comparison of existing USB Coanda flap to a potential USB/CCW modification.

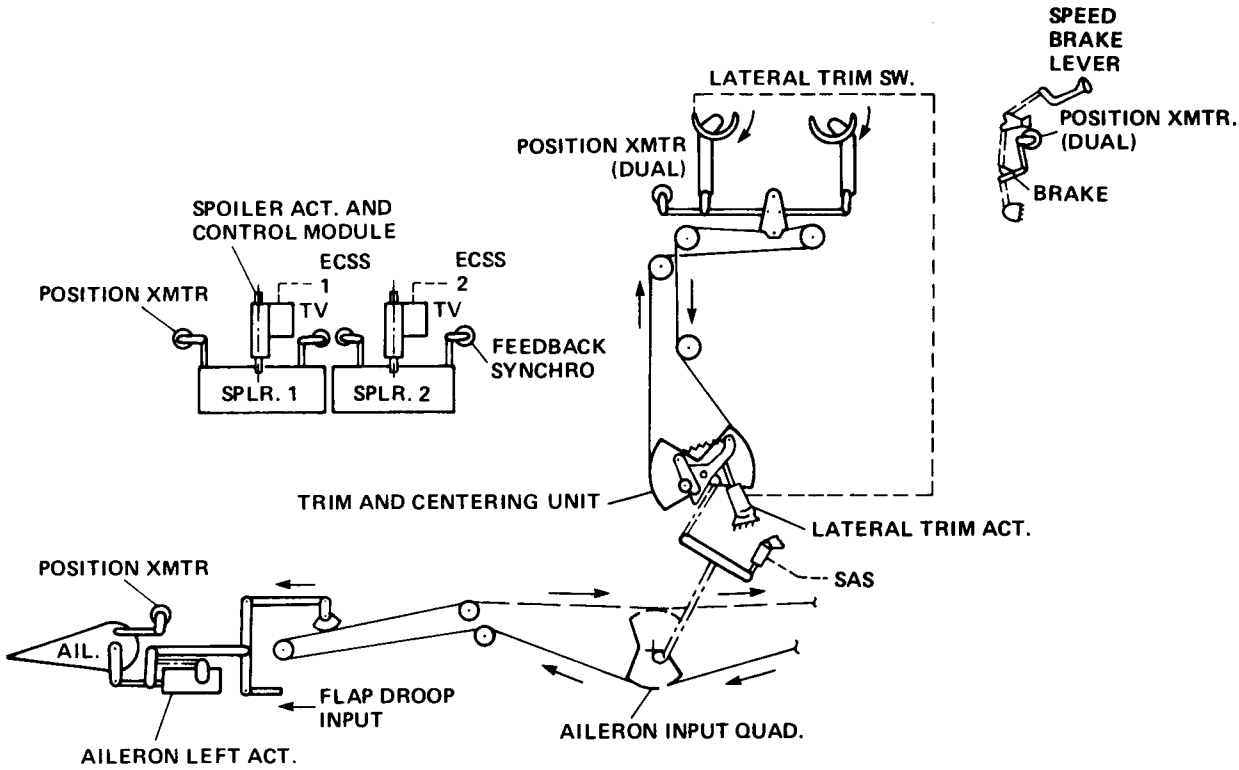

Figure 12. Existing QSRA lateral control system.

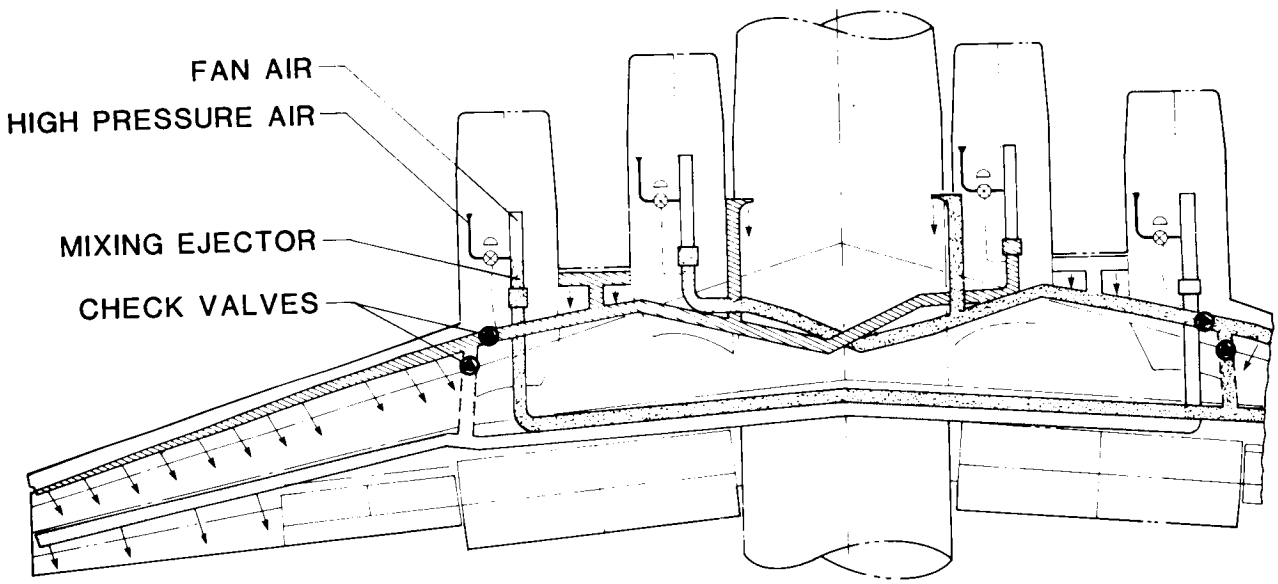

Figure 14. Original QSRA boundary layer control (BLC) system.

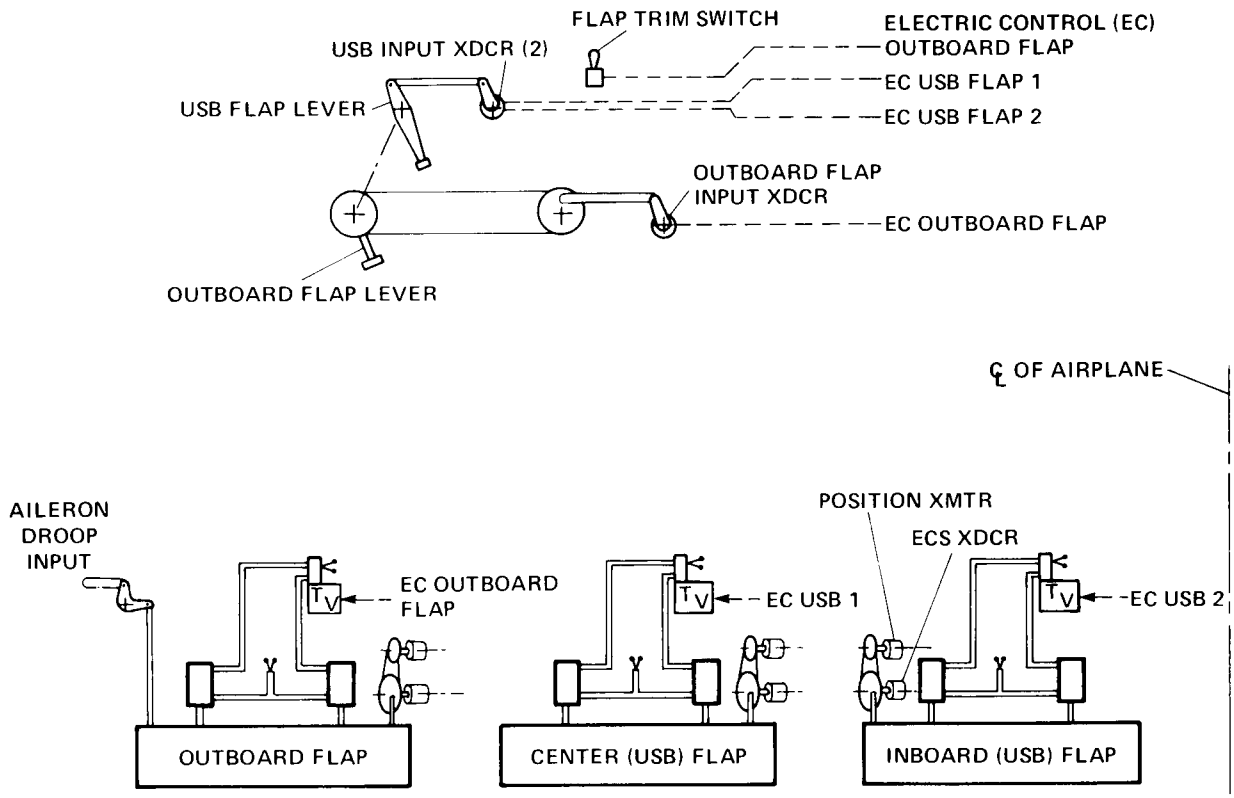

Figure 13. Existing QSRA flap control system.

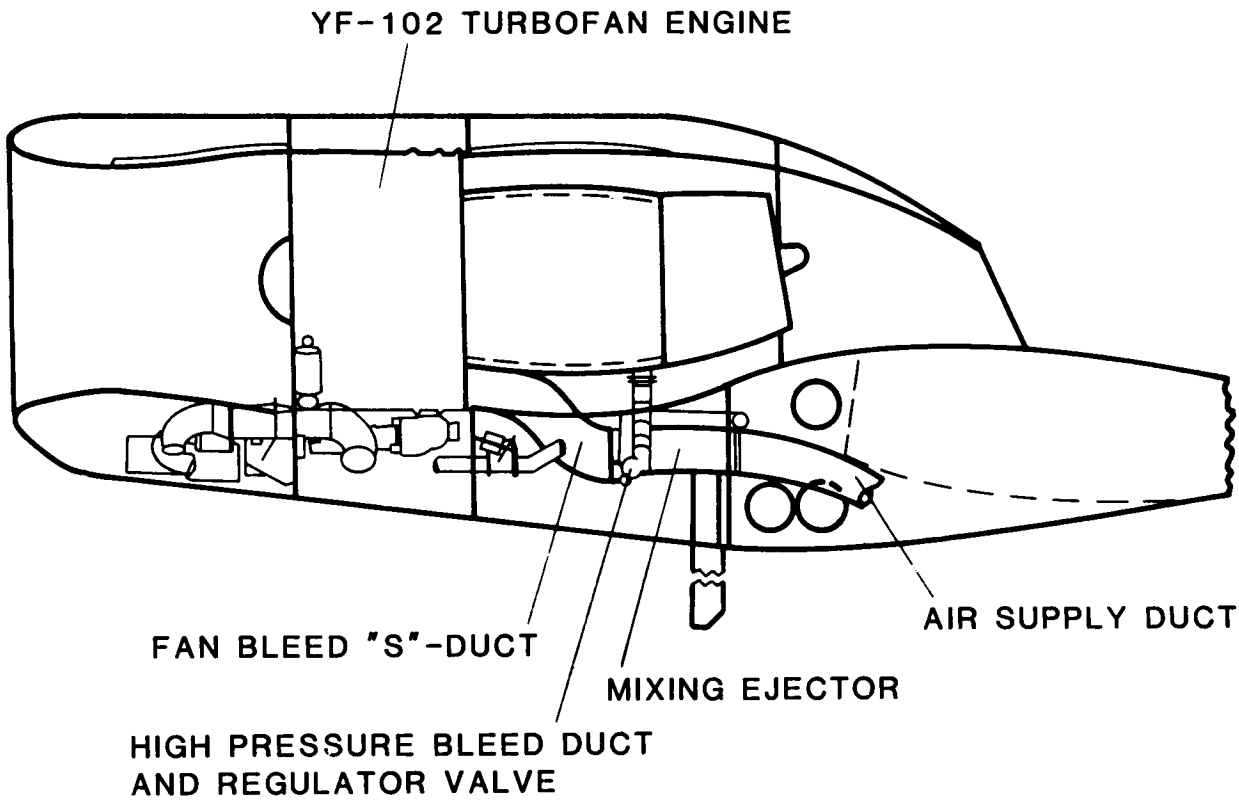

Figure 15. QSRA mixed fan and core bleed air supply system.

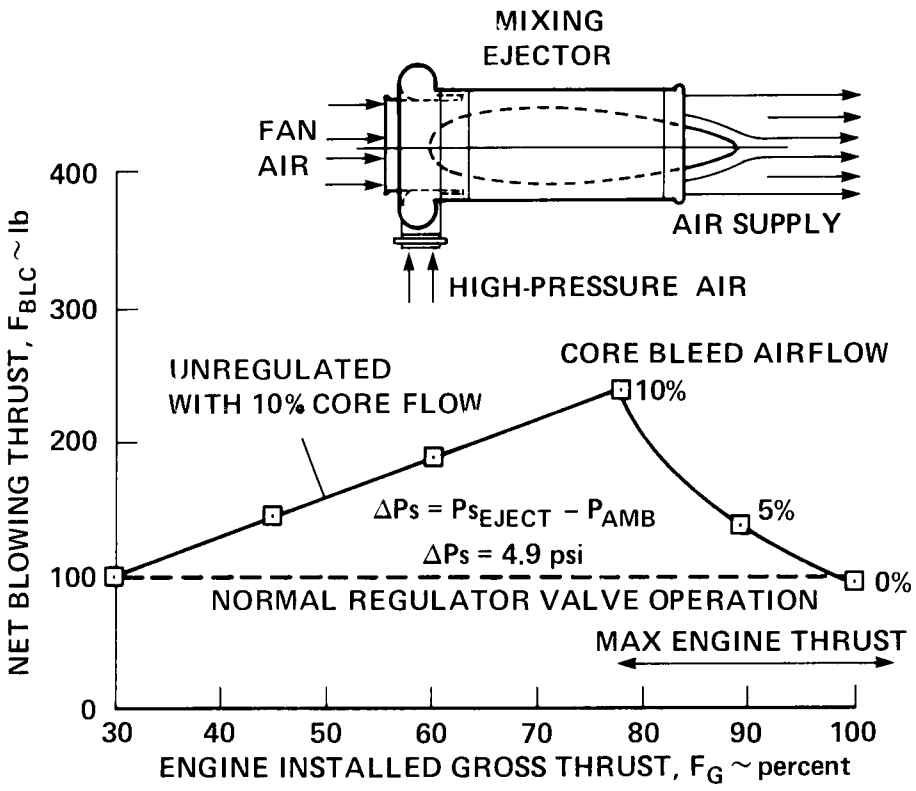

Figure 16. QSRA BLC net blowing momentum characteristics.

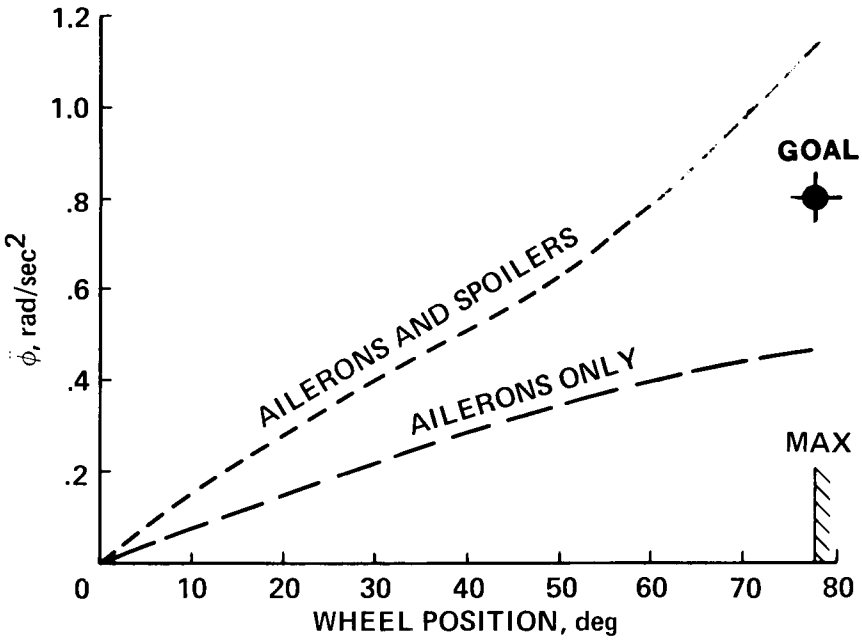

Figure 17. QSRA roll acceleration (C_L=4.6, weight = 48,000 lb).

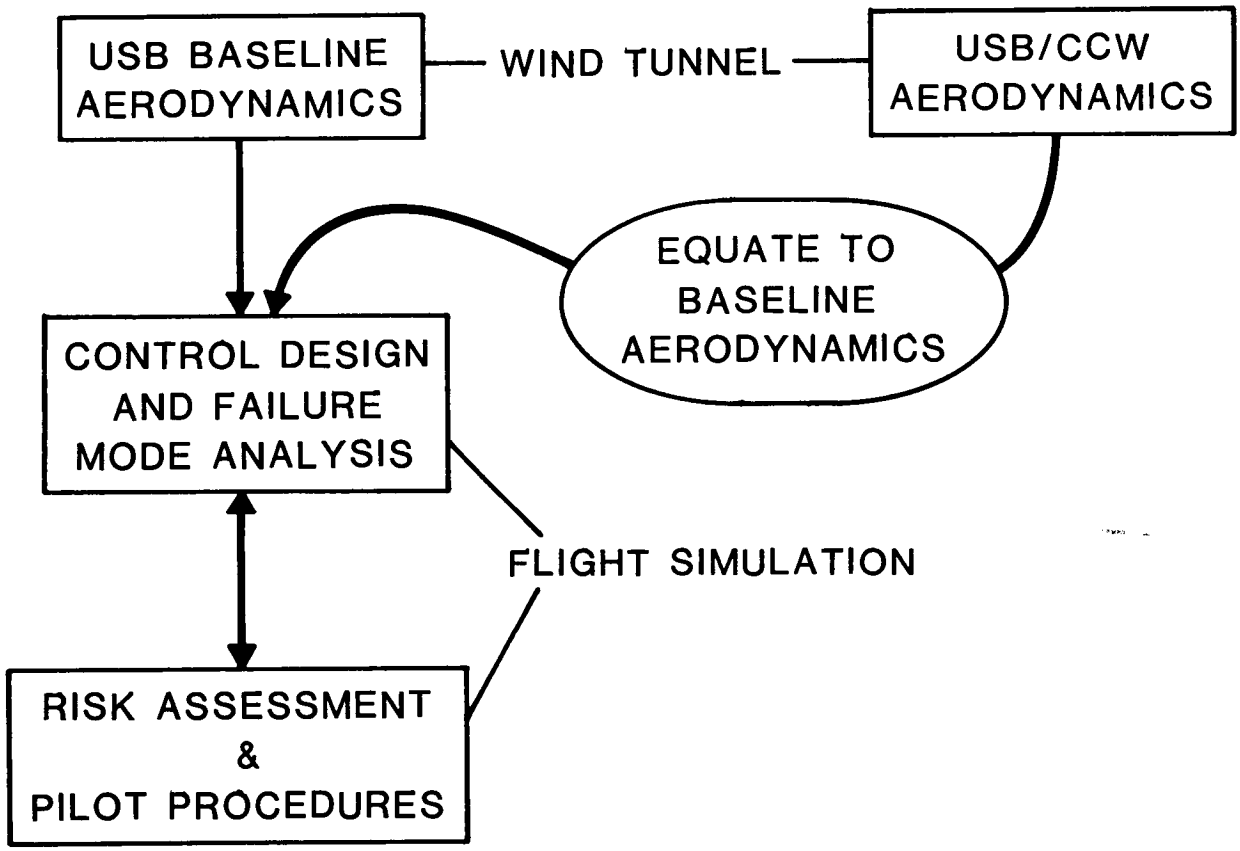

Figure 18. Utilization of USB/CCW aerodynamic data as input to QSRA risk assessment and pilot procedures.

C-7

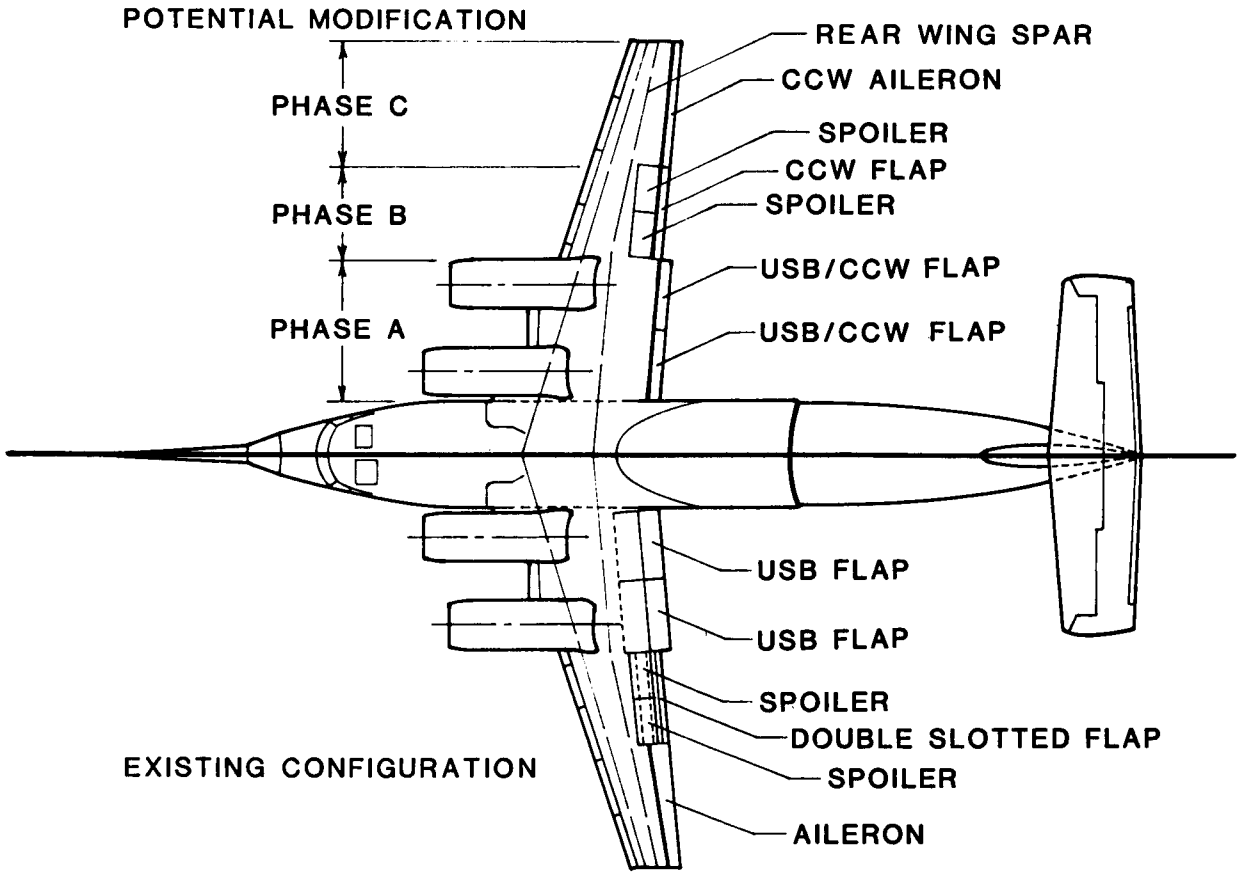

Figure 19. Three phase approach to the potential USB/CCW modification.

CIRCULATION CONTROL STOL AIRCRAFT DESIGN ASPECTS*

John L. Loth

Mechanical and Aerospace Engineering
West Virginia University

Abstract

Since Davidson patented Circulation Control Airfoils in 1960, there have been only two aircraft designed and flown with CC. Designing with CC is complex for the following reasons: the relation between lift increase and blowing momentum is non-linear; for good cruise performance one must change the wing geometry in flight from a round to a sharp trailing edge. The bleed air from the propulsion engines or an auxiliary compressor, must be used efficiently. In designing with CC, the propulsion and control aspects are just as important as aerodynamics. In this paper these design aspects have been examined and linearized equations are presented in order to facilitate a preliminary analysis of the performance potential of CC. The thrust and lift requirements for take-off make the calculated runway lenght very sensitive to the bleed air ratio. Thrust vectoring improves performance and can off-set nose down pitching moments. The choice of blowing jet to free stream velocity ratio determines the efficiency of applying bleed air power.

Introduction

Davidson (1960) patented the Circulation Control concept. The initial application was for cylindrical airfoils. Kind et al (1968) provided experimental data for the elliptical airfoil. The ellipse is desirable for helicopter blade applications because it has some lift generating ability in case of power failure and is structurally rigid. In recent years, it's leading and trailing edges have been modified and camber was added to improve the lift characteristics. More wind tunnel data are available on the basic and modified elliptical shape CC airfoil than all other configurations combined. The elliptical shape with it's maximum thickness near mid-chord has a center of pressure near mid-chord and thus a steeper adverse pressure gradient than conventional airfoils. This thickens the boundary layer upstream of the blowing slot and renders the Coanda turning efficiency very sensitive to geometry, angle of attack, Reynolds number and turbulence level. Various investigators have found significant differences in the lift-to-blowing momentum augmentation ratio for seemingly similar configurations. The non-linearity of this ratio with the blowing coefficient further adds to the complexity of selecting an optimum CC configuration.

* Funded by Lockheed Georgia, Contract No. MDA-53 #108444630

When a CC rounded trailing edge is added to a conventional high lift airfoil, complete with a leading edge modification to prevent separation, it's performance is much more predictable. Such airfoils have their maximum thickness further forward than the ellipse and therefore possess a less steep adverse pressure gradient than the ellipse. The reduced pressure gradient, together with the usually greater chord length and Reynolds number, minimizes the difference in boundary layer shape ahead of the blowing slot for CC modified CTOL wings. Such airfoils can be used for STOL aircraft and provide more comparable lift augmentation ratios and linearity with angle of attack. The greater thickness of a STOL aircraft wing as compared to a helicopter blade, permits incorporating advanced leading edge devices such as Kruger flaps, slats, or drooped leading edges with or without blowing. Large ducts fit inside a STOL wing which permits the power efficient use of blowing air at medium pressure and temperature. An ejector built around the blowing slot can provide boundary layer suction just upstream of the rounded Coanda jet turning surface. For added lift, the chord length may be increased in the CC mode, however the rounded trailing edge must be retracted in order to obtain efficient cruise performance with a sharp trailing edge. The availability of flaps in conjunction with CC is desirable for drag control during descent, adding flexibility and safety in the case of a blowing air failure. Even though the STOL CC airfoil geometry is much more complex than the modified ellipse, it's aerodynamic behavior and linearity is similar to that of the conventional CTOL airfoil. This is evident from the wind tunnel model test data by Englar (1975) on various STOL airfoil configurations. The flight tests on the only two CC STOL aircraft built and tested showed good agreement in lift augmentation ratio and performance, even though these aircraft were significantly different in geometry and wing loading.

Since the CC air mass flow requirements are low they may be provided by a relatively light weight auxiliary turbo-compressor or a compressor driven by shaft power take-off from the thrust engines. In this manner the blowing pressure is independent of the thrust level, thereby simplifying the design and operation with CC. However, the weight, cost, and reliability penalty of an additional compressor makes the use of jet engine bleed air more attractive. The thrust loss associated with compressor bleed air is a complex function of bleed pressure and throttle setting. The bleed mass ratio is one of the most important parameters in determining the effectiveness of CC during the take-off and landing phase. Minimizing the blowing air ducting heat and pressure losses, as well as the throttling loss across the bleed air flow control valve, greatly effects the ratio of blowing thrust generated to engine thrust lost. With CC, the blowing coefficient is in general less than 5% of the lift coefficient, therefore the blowing momentum is a small fraction of the aircraft weight. Most of the momentum is used to energize the boundary layer along the Coanda turning surface. The small fraction remaining in the wall jet after separation is often negligible relative to the take-off thrust coefficient. Even in the high drag landing configuration, the effect of C_μ on the reduction in the drag coefficient can often be ignored.

WVU CC STOL Demonstrator Design Aspects

In 1968, the Office of Naval Research awarded a research contract to West Virginia University to investigate the theoretical and experimental aspects of Circulation Control. This was about the same time that Williams (1970) at NSRDC, started to investigate the performance of elliptical airfoils to be used on a high lift helicopter. As a result, significant improvements were made in the lift-to-blowing momentum augmentation ratio. However, it became apparent that this ratio was very

dependent on the model aspect ratio, slot adjustment mechanism, jet to free stream velocity ratio, tunnel blockage factor, turbulence level and Reynolds number. To eliminate tunnel wall interference and achieve high Reynolds numbers, WVU researchers decided to flight test a CC wing on a light aircraft. The first CC 2-D STOL airfoil built at WVU had a 4 ft chord and incorporated a drooped and blown leading edge. A low pressure blowing slot produced an air jet tangentially to the cylindrical flap hinge. The airfoil could be operated in the blown flap mode or as a CC airfoil after the 15% flap was folded fully forward and flush with the underside of the airfoil. In 1970, this WVU model was tested in the 8 x 10 ft NSRDC tunnel. Even though it performed as anticipated, the following improvements were made. The flap was folded out in the CC mode to increase the chord instead of decreasing it by 15%. The rounded Coanda surface remained stowable in flight, to provide a sharp trailing edge for low drag cruise. A choked flow nozzle was selected for better span-wise blowing uniformity and slot adjustment screws were eliminated. A built in ejector was designed to improve the jet thickness, temperature and Coanda turning of the otherwise supersonic jet. The ejector entrained air provides needed structural cooling and boundary layer suction at the flap hinge. Reducing the boundary layer thickness upstream of the blowing slot greatly improves the Coanda turning. The drooped leading edge was designed by Norio Inumaru, program manager of the Japanese USB QSTOL, and proved to be so effective, that the leading edge blowing could be eliminated. In 1971, the improved CC STOL airfoil (figs. 1 and 2) was tested in the WVU wind tunnel, Loth (1973). At the same time construction was started on the WVU CC STOL Demonstrator Aircraft, using materials from a BEDE 4 home builders kit. A 200 HP GTC 85-72 APU was selected to provide up to 1 kg/sec of air at maximum 2 atm gage, to the CC blowing slot. The blown ailerons could be drooped. Inboard and outboard fences were installed for both aerodynamic and structural reasons (fig. 3). Both chord-wise and span-wise pressure taps were installed on the wing. A sliding blowing air dump valve was installed to provide direct lift control. The DLC valve was actuated by a lever on the throttle quadrant. A splitter valve, linked to the aileron controls, provided optional roll control by differential blowing (fig. 4.)

On April 10, 1974, pilot Shawn Roberts (1974) started 25 hours of flight testing to determine the performance potential and handling qualities of CC. The WVU CC STOL Research program was summarized by Loth and Fanucci (1974). The lift coefficient appeared to increase linearly with angle of attack and with the square root of the blowing coefficient. At high blowing rates, the trim lift coefficient was considerably lower than it was on the CC flap. The loss in lift is due to the download of the stabilator, associated with the large nose down pitching moment. At C_{Lmax}, with thrust power at idle, the CC blowing at $C_\mu = 0.12$ increased the flap lift coefficient from 2.1 to 5.2, or with a lift augmentation ratio: $\Delta C_L/C_\mu = 3.1/0.12 = 25.8$. At the same time the trim C_{Lmax} increased only from 1.98 to 3.8, or with a lift augmentation ratio: $\Delta C_L/C_\mu = 1.82/0.12 = 15.2$ and $C_\mu = 3\%$ of C_{Lmax}. This is considerably lower than the 2-D augmentation ratios obtainable with an elliptical airfoil. CC effectiveness is better described by the proportionality constant $C_B = \Delta C_L/(C_\mu)^{0.5}$, which does not change with C_μ for a given airfoil.

Englar (1978) published wind tunnel data on a three dimensional CC model of a modified A-6A Navy Cruisader. Even though the CC wing configuration was entirely different from the WVU model, the lift augmentation ratio's obtained agree very well. His data shown in figure 5 are nearly linear with angle of attack and with the square root of the blowing coefficient. The solid lines represent an empirical curve fit with $dC_L/d\alpha = 4.74$ and $C_B = 6.1$. In 1979, Englar's efforts resulted in 10 hours of flight testing of a CC modified A-6A Navy Crusader. All the flight test data, Carr

(1986) and wind tunnel model data, appear to have about the same constant of proportionality (C_B), as shown in Table 1.

TABLE 1 COMPARISON OF 3-D STOL WING TEST DATA

SOURCE OF TEST DATA	BLOWING	TAIL-OFF, WING ONLY		TRIMMED AIRCRAFT	
	C_μ	ΔC_L	$C_B = \frac{\Delta C_L}{\sqrt{C_\mu}}$	ΔC_L	$C_B = \frac{\Delta C_L}{\sqrt{C_\mu}}$
1974 WVU CC STOL Aircraft Flight Tests, Loth (1974)					
a) Based on cruise wing area	.12	2.3	6.6	1.8	5.1
b) Based on CC wing area	.10	2.0	6.1	1.5	4.7
1979 Grumman A-6A CC STOL Aircraft Flight Tests, Carr (1986)	0.05			1.3	5.8
	0.025			0.85	5.4
Wind Tunnel A-6A Model Tests Tail-Off, Englar (1978)	0.20	2.75	6.1		
	0.10	2.10	6.6		
	0.05	1.36	6.1		
	0.025	0.90	5.7		

The influence of CC blowing on the lift curve slope ($dC_L/d\alpha$) is negligible. The effect of increasing the wing chord is the CC blowing mode by folding out a flap, is to multiply the lift coefficient by the ratio of the wing area increase. When a flap is used in conjunction with CC blowing, the lift increases as a function of the flap deflection angle (δ_f). This may be estimated from thin airfoil theory as:

$$dC_L/d\delta_f = 2\pi - 2\theta_f + 2 \sin(\theta_f) \tag{1}$$

where the flap hinge locater angle (θ_f) is: $\cos^{-1}(1 - 2\, c_f/c)$. Combining all the factors contributing to the lift coefficient with CC:

$$C_L = \frac{c \text{ (with CC)}}{c \text{ (without)}} \left[\alpha \frac{\partial C_L}{\partial \alpha} + \delta_f \frac{\partial C_L}{\partial \delta_f} + C_B \sqrt{C\mu} \right] \tag{2}$$

Linearized CC Lift Augmentation Ratio.

With a choked flow isentropic CC nozzle, the (2-D) blowing momentum is given by:

$$\dot{m}_j V_j = \rho_j h V_j^2 \quad \text{or} \quad C_\mu = \frac{\dot{m}_j V_j}{q\, c} = \left(\frac{2h}{c}\right) \left[\frac{V_j}{V}\right]^2 \left(\frac{\rho_j}{\rho}\right) \tag{3}$$

For a specified blowing pressure ratio and slot height (h) the momentum is not a function of the temperature (t_j). The reason is that the exit density is proportional to ($1/t_j$), whereas the square of the velocity is proportional to (t_j). In the case of regulated and fixed bleed air flow rate, any heat loss in the duct lowers the nozzle total pressure and therefore the blowing velocity (V_j). Assuming an isentropic

compressor and duct, the jet exit static temperature and density would be identical to the ambient values. In practice, the increase in temperature (t_j) due to compressor inefficiency is approximately off-set by the duct heat and pressure loss, thus the density ratio in the blowing coefficient may often be ignored.

In Figure 6, are wind tunnel test data by Englar (1981), plotted as a function of the lift coefficient versus blowing pressure ratio. The result is highly non-linear. However, when the same data are replotted as a function of velocity ratio (fig. 7), they fall on a straight line! The data appears to fit a single empirical equation with the exception of the data for a very narrow slot operating at high velocity and pressure. The reason may be that the slot deflection under high pressure is more significant at small slot heights. Another explanation may be that at low mass flow rates the expansion becomes more isothermal which would tend to increase the jet velocity, when testing with room temperature compressed air. It is noteworthy that velocity ratios below 1.0 seem to provide no lift augmentation, thus there is a minimum value (C_μ = 2h/c) below which there is no lift augmentation. Such low values, typically below 0.002, are never used and this term becomes negligible at C_μ greater than 0.02. This allows one to linearize the lift augmentation ratio with respect to the square root of the blowing coefficient. In figure 6, the coefficient of proportionality (C_B) equals: 9 for h/c = 0.0003 and 10.9 for h/c = 0.0012. Note that the magnitude of (C_B) for a three dimensional wing is considerably lower and closer to 6 for the conditions shown in Table 1.

Because the engine thrust is reduced when blowing power is extracted, the choice of the blowing velocity to flight velocity ratio, becomes very important. At constant (C_μ), the required blowing power (P_b) decreases in proportion to the reduction in velocity ratio. Then for the linear lift augmentation model, the lift coefficient ratio ($\Delta C_L/P_b$) increases with decreasing velocity ratio, as shown in figure 8. However as (V_j/V) approaches 1.0 the value of ΔC_L reduces to zero, this makes the constant power curve peak at: V_j/V = 2.08. A similar optimum velocity ratio was found with boundary layer energization by tangential blowing to prevent separation in an adverse pressure gradient, Boasson (1985). Note this velocity ratio optimization does not consider blowing air duct characteristics such as: losses, size and weight. When these factors are incorporated the optimum velocity ratio is usually greater than 3.

The effect of duct losses in heat and pressure, are shown in figure 9 in terms of percent blowing momentum recovered at the nozzle. This example is for a typical case where the compressor bleed air is extracted at: 11 atm and 375° C. As can be seen, a 50% loss in air temperature is more detrimental than a 50% duct friction pressure loss. The loss in temperature will be noted by an increase in pressure drop across the valve controlling the bleed air mass flow rate. The reason is that at constant mass flow rate, the loss in temperature results in a reduction of the nozzle total pressure. The reduced nozzle pressure is then transmitted through the subsonic ducting to the control valve.

Thrust Loss Due to CC Blowing Power Extraction

The air power requirements for CC, by blowing over a rounded trailing edge, are greater than for conventional boundary layer control, however less than for any other type of powered lift system such as: the jet flap, augmenter wing, USB, etc. The CC 3-D blowing momentum coefficient, based on the entire wing area rarely exceeds 5% of the lift coefficient, or at C_L = 6 find C_μ < 0.3. Thus even in the

absence of thrust vectoring, the blowing momentum is less than 5% of the weight. For most STOL aircraft this means less than 10% of the thrust. The optimum CC blowing velocity is at least three times higher than the lift-off velocity on take-off and of the same order of magnitude as the cruise velocity. The propulsion system exhaust velocity for a propeller driven aircraft is also of the same order of magnitude as the cruise velocity. Therefore, the jet-kinetic power at the CC nozzle is usually less than 10% of the available thrust power. For jet engine propulsion the exhaust velocity is at least double the cruise speed and the CC jet-kinetic power at the nozzle is usually less than 5% of the thrust power.

An auxiliary compressor for CC blowing can be driven efficiently with a power take-off from propulsion engines driving a propeller. Propeller aircraft suffer a reduction in thrust with forward speed. The power extraction for CC blowing is so low, that the anticipated thrust loss is roughly offset by the associated reduction in lift-off speed, so that lift-off with, or without CC, occurs at about the same thrust to weight ratio! The relative thrust loss due to power take-off can be computed using actuator disk theory and a coefficient of performance (C_p). Without power take-off the static thrust is defined by: (T_o), the induced velocity at the disk by (w_o) and in the wake by ($2\ w_o$). From the change in momentum of the mass flow rate ($\dot{m}$) through disk area (A_d) find:

$$T_o = \dot{m}\ 2\ w_o = 2\ \rho A_d w_o^{\ 2} \tag{4}$$

The ideal power is related to shaft power (P_s) by

$$0.5\ \dot{m}\ (2\ w_o)^2 = 2\ \rho\ A_d w_o^{\ 3} = P_s C_p = T_o w_o \tag{5}$$

$$w_o = \left[\frac{P_s C_p}{2\rho A_d}\right]^{1/3} \sim (P_s)^{1/3} \tag{6a}$$

$$T_o \sim (P_s)^{2/3} \tag{6b}$$

With forward velocity (V), the induced velocity reduces to (w) and the thrust to (T). Assuming constant (P_s) and (C_p) gives:

$$T = \rho\ A_d (V + w)\ (V + 2w) \tag{7a}$$

$$P_s C_p = T\ (V + w) = T_o w_o \tag{7b}$$

solving for (w/V) gives:

$$\frac{w}{V} = 0.5 \sqrt{1 + 4 \left(\frac{T}{T_o}\right)\left(\frac{w_o}{V}\right)^2} \quad -0.5 \tag{8}$$

or the thrust loss with forward speed is:

$$\frac{T}{T_o} = \frac{w_{o/V}}{1 + w/V} = \frac{2\left[\frac{w_o}{V}\right]}{1 + \sqrt{1 + 4\left[\frac{T}{T_o}\right]\left[\frac{w_o}{V}\right]^2}} \tag{9}$$

During take-off and landing at velocities below $3w_o$, [note (w_o) is computed from eq. 6a], the thrust loss can be approximated by:

$$\frac{T}{T_o} = 1 - 0.318\left[\frac{V}{w_o}\right]^{0.678} \tag{10}$$

When the CC blowing power (P_b) is extracted from the propeller shaft by an auxiliary compressor at an overall efficiency (η_b), then the remaining propeller power is reduced to (P_{sb}) and the static induced velocity to (w_{ob}).

$$P_b = 0.5\ \dot{m}_j\ V_j^2 \tag{11}$$

$$P_{sb} = P_s - P_b/\ \eta_b \tag{12}$$

From the dependancy of (w_o) and (T_o) on the available power, the relative change in their magnitude with blowing is found from:

$$\frac{w_{ob}}{w_o} = \left[\frac{P_{sb}}{P_s}\right]^{1/3} \tag{13}$$

$$\frac{T_{ob}}{T_o} = \left[\frac{P_{sb}}{P_s}\right]^{2/3} \tag{14}$$

When the propeller exhaust is vectored, the intake momentum (D_m) is added to the drag and only the outlet momentum is included in the thrust (T_b) or:

$$\frac{D_m}{T_{ob}} = \frac{0.5}{w_{ob}} \tag{15a}$$

$$\frac{T_b}{T_{ob}} = \frac{1 - 0.318\left[\frac{V}{w_{ob}}\right]^{0.678}}{1 - \frac{1}{2w_{ob}}} \tag{15b}$$

The blowing coefficient and CC lift augmentation reduce with increasing compressor pressure ratio and associated velocity (V_j):

$$C_\mu = \frac{T_j}{q\,S} = \frac{2P_b}{q\,V_j S} \tag{16}$$

If flaps are used for speed control then with a constant speed propeller, the compressor rpm, coupled to the propeller shaft, can also remain constant even during landing. This method is lighter and more reliable than using an auxiliary turbo-compressor to obtain constant CC blowing momentum.

For jet aircraft, compressor bleed from either the last, or from an intermediate stage, produces a greater thrust loss than with shaft power extraction in a propeller aircraft. This is due to the loss of mass flow rate through the turbine and nozzle. An additional problem is that jet engine bleed air pressure decreases with RPM or throttle setting. To use this source for CC blowing air, one should be able to maintain a high power setting during approach to landing, which necessitates thrust vectoring. The associated engine thrust loss can be computed from cycle analysis on the T-S diagram. The magnitude of the component efficiencies and the temperature ratio's for the compressor and turbine, determine the thrust loss associated with bleed air and forward speed. For example assume a compressor and turbine efficiency of 80% and 87.5% respectively, a turbine inlet temperature equal five times the ambient temperature and the compressor outlet temperature equals the square root of five times the ambient temperature. This results in a ratio of exhaust velocity to flight velocity given as a function of flight Mach number (M).

$$\frac{V_e}{V} = 2.37\ M \tag{17}$$

The intake density and engine mass flow rate increase by ram compression to about:

$$\frac{\dot{m}}{\dot{m}\ (V = o)} = 1 + 0.5\ M^2 \tag{18}$$

resulting in an exhaust momentum increase with flight Mach number of about:

$$\frac{T}{T_o} = 1 + 0.5\ M^2 \tag{19}$$

The reduced static thrust (T_{ob}) associated with bleed air, can be computed as a function of the bleed mass ratio ($b = \dot{m}_j/\dot{m}$), note: limited to less than 20% for most engines. For example the thrust loss for high pressure bleed with 11 atm at the compressor final stage, is found to be

$$\frac{T_{ob}}{T_o} = (1 - b)^2 \cong (1 - 2b) \tag{20a}$$

With 4 atm at the intermediate compressor stage, the thrust loss is found to be

$$\frac{T_{ob}}{T_o} = (1 - 0.5\ b)\ (1 - b) \cong (1 - 1.5b) \tag{20b}$$

When thrust vectoring is employed the inlet momentum ($\dot{m}\ V = D_m$) is added to the drag, and is about:

$$\frac{D_m}{T_{ob}} = 0.42\ M \tag{21a}$$

The exhaust momentum variation with flight Mach number and bleed air is:

$$\frac{T_b}{T_{ob}} = (1 + 0.5\ M^2)\ (1 - b) \tag{21b}$$

The CC blowing momentum (T_j) obtained with the bleed air, depends on the temperature and pressure losses in the bleed air flow control valve and the ducting. Even when minimal losses are assumed, this results in a ratio of blowing thrust recovered to engine thrust lost of not more than:

$$\frac{T_j}{(T_o - T_{ob})} = 0.4 \text{ at } 11 \text{ atm and } 0.6 \text{ at } 4 \text{ atm} \tag{22}$$

This shows that extracting bleed air at the intermediate compressor stage is more efficient than at the final stage. The cycle analysis can be extended to include the effect of by-pass ratio when a turbofan is used. Experimental jet engine thrust loss data, including the effect of reduced bleed pressure at part throttle, are given by Hemmerly (1977).

Ground Run in Landing and Take-Off

The landing and take-off analysis presented here is based on the treatment by Kohlman (1981). During approach to landing, the descent angle is steep and the required forward component of the thrust is very small. To provide speed control, mechanical drag producing devices are needed unless the thrust can be vectored, for example using Pegasus type nozzles. In equilibrium flight, the minimum decsent velocity can be computed as a function of the available blowing momentum (T_j), from the requirement that the sum of the forces normal and along the direction of flight are zero. For CTOL aircraft with an approach speed equal 1.3 V_{stall} the approach angle of attack is found from

$$\alpha_a = \frac{\alpha_{stall}}{(1.3)^2} \tag{23}$$

For a CC powered STOL aircraft, the same safe approach angle of attack may be specified. If the flap size, deflection angle and effect on C_{Do} are specified then the dynamic pressure (q_a) on approach is found by iteration such that the descent angle (γ_a), isolated from the two equilibrium force equations below, are equal.

$$\gamma_a = \sin^{-1}\left[\frac{q}{(W/S)}\left(C_{Do} + \frac{C_L^2}{\pi e\ AR}\right) + \frac{Dm}{W} - \left[\frac{T_b}{W}\right]\cos\ (\theta_T + \alpha_a)\right] \tag{24}$$

$$\gamma_a = \cos^{-1}\left[\frac{q\ C_L}{(W/S)} + \left[\frac{T_b}{W}\right]\ \sin\ (\theta_T + \alpha_a)\right] \tag{25}$$

The resulting descent angle shall not be too steep, otherwise the pilot's visability is impaired or the vertical component of the approach velocity may exceed 1000 ft/min. If such a problem occurs, then the flap or thrust vector angle must be reduced. An advantage of circulation control over other boundary layer control techniques is that high values of the lift coefficient can be obtained at moderate angles of attack. During a steep descent at an angle (γ_α) greater than the angle of attack, the aircraft attitude will be nose down, providing good pilot visibility. To obtain a flare-out before touch down one must be able to generate extra lift, by either having extra angle of attack or blowing pressure available. If one third of the lift is provided by each: the angle of attack, the CC lift augmentation, and the vectored thrust, then increasing the angle of attack for flare is only one third as effective as it is in a CTOL aircraft! During the optimum performance approach, there is no extra lift available, therefore the flare distance contribution to the landing may be ignored. The FAA specifies that after touch-down the deceleration rate is limited for passenger comfort to dV/dt = -0.5 g. If the deceleration rate is constant then the ground roll (s_q) is directly proportional to the minimum approach dynamic pressure or

$$s_g(\text{landing}) = \frac{q_a}{\rho\left[-\frac{dV}{dt}\right]} \tag{26}$$

For take-off, the above equation shows that the ground run is likely just as sensitive to the minimum lift-off dynamic pressure (q_{lof}) as it is to the acceleration. To minimize the lift-off speed one needs high blowing rates and high thrust angles. However, to maximize acceleration one needs all the obtainable thrust in the horizontal direction. Consequently optimum performance is obtained by delaying CC blowing and thrust vectoring to the moment of lift-off! Such a last minute configuration change increases the pilot's work load and reduces safety. Assuming there are no last minute configuration changes permitted, one finds that the optimum bleed air flow rate and thrust vector angle, become very important parameters in the take-off ground run distance optimization, more so than in the climb distance optimization. During the groundrun, on a low friction, level runway, the ground effect due to CC blowing may be ignored. At the start when q=o find C_μ=∞, and the lift increase due to CC should be ignored till C_μ reduces below 0.3. On the ground, the angle of attack (α_g) is constant prior to rotation and the ground distance is found by integrating the equation for the horizontal acceleration from (q_w) to (q_{lof}). Where (q_w) is the dynamic pressure of the head wind component and (q_{lof}) is the lift-off dynamic pressure. After rotation to (α_{lof}), the sum of the lift and vertical component of the thrust vector equals the weight. The take-off distance (s_g) is:

$$s_g = \frac{1}{\rho g}\int_{q_w}^{q_{lof}} \frac{\left(1-\sqrt{\frac{q_w}{q}}\right)\,dq}{\left(\frac{T_b}{W}\right)\cos(\theta_T+\alpha_g) - f\left(1-\left(\frac{T_b}{W}\right)\sin(\theta_T+\alpha_g)\right) - qC_L/\left(\frac{W}{S}\right)\Big] - qC_D/\left(\frac{W}{S}\right) - \frac{D_m}{W}} \tag{27}$$

Near the end of the ground run, the rotation velocity is reached, and the pilot uses the elevator to increase the angle of attack by at least three degrees per second. Ideally, lift-off is achieved just prior to complete rotation to the maximum safe climb-out angle of attack. This ensures definite lift-off with an upward acceleration. To maintain a safe margin below the stall angle of attack, CTOL aircraft are specified to lift off at 20% above the stall speed or at an angle of attack: $\alpha_{lof} = \alpha$ stall/$(1.2)^2$ = 70% of the stall angle. If the same (α_{lof}) angle of

attack is used on STOL aircraft, with powered lift and thrust vectoring, then the lift-off speed safety margin is less than 20% above the stall speed. When the lift-off angle of attack is specified, the lift-off dynamic pressure can be found from:

$$0 = 1 - \left(\frac{T_b}{W}\right) \sin(\theta_T + \alpha_{lof}) - \frac{q_{lof}}{(W/S)} \left[\alpha_{lof} \frac{\partial C_L}{\partial \alpha} + \delta_f \frac{\partial C_L}{\partial \delta_f} + C_B \sqrt{\frac{(T_j/S)}{q_{lof}}} \right] \quad (28)$$

This is a quadratic equation in $(q_{lof})^{0.5}$ or

$$q_{lof} = \left[\frac{-C_B \sqrt{\left(\frac{T_j}{S}\right)} + \sqrt{C_B^2 \left(\frac{T_j}{S}\right) + 4\left[\left(\frac{W}{S}\right) - \left(\frac{T_b}{S}\right)\sin(\theta_T + \alpha_{lof})\right]\left[\alpha_{lof} \frac{\partial C_L}{\partial \alpha} + \delta_f \frac{\partial C_L}{\partial \delta_f}\right]}}{2\left[\alpha_{lof} \frac{\partial C_L}{\partial \alpha} + \delta_f \frac{\partial C_L}{\partial \delta_f}\right]} \right]^2 \quad (29)$$

Maximum Climb Performance

During the climb period needed to clear an obstacle, the thrust vector angle and the flap angle are not altered for safety reasons. The pilot only modulates the aircraft attitude and thus angle of attack to maximize the rate by which the maximum climb angle is reached. Because of the limited effectiveness of the angle of attack, it should as high as practical, while allowing an assymptotic approach to the maximum climb angle (γ_X) at (α_X). A near optimum performance will be obtained when the angle of attack is reduced in proportion to the available acceleration, but never lower than (α_X).

$$\alpha = \alpha_X + \frac{(\alpha_{lof} - \alpha_x)\left(\frac{dV}{dt}\right)}{\frac{dV}{dt}(\text{at lift-off})} \quad (30)$$

If the climb angle increases sufficiently fast, then the velocity does not overshoot the maximum climb angle value (V_X). In case it does exceed (V_X) the acceleration dV/dt will eventually become negative at which time (α_X) must be held constant. To apply this equation one must first compute the maximum climb angle parameters.

From energy considerations, one may determine the steady state climb angle by equating the excess thrust power to the rate of increase in potential energy or

$$[T_b \cos(\theta_T + \alpha) - D - D_m]V = W.RC \quad (31)$$

The maximum climb angle is reached when: $\sin(\gamma) = \left(\frac{RC}{V}\right)$ is maximum or

$$\sin(\gamma_X) = \left[\left(\frac{T_b}{W}\right) \cos(\theta_T + \alpha) - \left(\frac{D}{W}\right) - \left(\frac{D_m}{W}\right)\right]_{max.} \quad (32)$$

When the engine thrust components are independent of flight speed, then the maximum climb angle occurs when the drag is minimum or $(C_{Do} = C_{Di})$. Without

powered lift (C_L) is proportional to (α) and the induced drag coefficient is related to the lift coefficient squared. Then (C_{Lx}) and (α_x) are found from

$$C_{Lx} = \sqrt{C_{Di}\ \pi\ e\ AR} \quad = \sqrt{C_{Do}\ \pi\ e\ AR} \tag{33}$$

$$\alpha_x = \frac{C_{Lx} - \delta_f \dfrac{\partial C_L}{\partial \delta_f}}{\dfrac{\partial C_L}{\partial \alpha}} \tag{34}$$

The maximum climb angle dynamic pressure (q_x) is obtained when the sum of the forces normal to V are zero or

$$\cos^2(\gamma_x) = \left[\left(\frac{T_b}{W}\right) \sin\ (\theta_T + \alpha_x) + q_x\ C_{Lx} / \left(\frac{W}{S}\right)\right]^2 \tag{35}$$

Eliminate (γ_x) from Eq. 32 and 35 by using:

$$\cos^2(\gamma_x) = 1 - \sin^2(\gamma_x) = 1 - \left[\frac{T_b}{W} \sin\ (\theta_T + \alpha_x) - 2C_{Do} q_x / \left(\frac{W}{S}\right) - \frac{D_m}{W}\right]^2 \tag{36}$$

This gives a quadratic equation from which (q_x) can be determined. In general, the thrust is not constant and the maximum climb angle values are found by iteration. For steady state climb, the sum of the forces parallel and normal to the direction of flight equal zero, they are respectively:

$$o = \left(\frac{T_b}{W}\right) \cos\ (\theta_T + \alpha) - \frac{D}{W} - \frac{Dm}{W} - \sin\ (\gamma) \tag{37}$$

$$o = \left(\frac{T_b}{W}\right) \sin\ (\theta_T + \alpha) + \frac{L}{W} - \cos\ (\gamma) \tag{38}$$

At any flight speed, the tangent of the climb angle is obtained from their ratio.

$$\tan\ (\gamma) = \frac{\left(\dfrac{T_b}{W}\right) \cos\ (\theta_T + \alpha) - \dfrac{D}{W} - \dfrac{D_m}{W}}{\left(\dfrac{T_b}{W}\right) \sin\ (\theta_T + \alpha) + \left(\dfrac{L}{W}\right)} \tag{39}$$

The maximum climb angle (γ_x) is a function of angle of attack and found by iteration. Starting with $V = V_{lof}$ and $\alpha = \alpha_{lof}$, decrease (α) until $\tan(\gamma)$ reaches a peak value, which represents a steady state climb. Higher climb angles can be found at higher velocities. Increment (V) and reduce (α) by a small amount until the next steady state value for $\tan(\gamma)$ is reached. This process is continued until the steady state value of $\tan(\gamma)$ reaches a maximum, at which time the desired magnitudes of: V_x, α_x and γ_x have been obtained. The unsteady climb performance computation can now be performed.

Starting at lift-off with $V=V_{lof}$ and $\gamma = o$, integrate the equations of motion until an obstacle of specified height has been cleared. The corresponding climb distance (s_c) must be added to the ground run to determine the total take-off distance. With powered lift, all the aerodynamic coefficients such as: lift, blowing momentum and drag are functions of the dynamic pressure (q). The second most important parameter is the climb angle (γ) or time (t). In general only time is a montonic increasing variable and both acceleration component equations ($\parallel$ and $\perp$ to V) must be incorporated in the numerical integration.

$$\frac{dV}{dt} = g \left[\left(\frac{T_b}{W}\right) \cos(\theta_T + \alpha) - \frac{D}{W} - \frac{D_m}{W} - \sin(\gamma)\right] \tag{40}$$

$$\frac{V d\gamma}{dt} = g \left[\left(\frac{T_b}{W}\right) \sin(\theta_T + \alpha) + \frac{L}{W} - \cos(\gamma)\right] \tag{41}$$

The initial value of the derivative ($d\gamma/dt$) is zero if the climb-out is started with $\alpha = \alpha_{lof}$. However in practice the lift-off rotation may be continued to start climbing with (α) slightly greater than (α_{lof}) and ($d\gamma/dt$) finite. If (γ) increases monotonically, then the ratio's of the two acceleration equations may be used to eliminate the variable (dt) the result being a single equation in terms of ($d\gamma/dq$):

$$\frac{d\gamma}{dq} = \frac{\left(\frac{T_b}{W}\right) \sin(\theta_T + \alpha) + \frac{L}{W} - \cos(\gamma)}{2q\left[\left(\frac{T_b}{W}\right) \cos(\theta_T + \alpha) - \frac{D}{W} - \frac{D_m}{W} - \sin(\gamma)\right]} \tag{42}$$

This technique is not applicable to a ski-jump take-off where (γ) first decreases before it increases. Then one must integrate Eqs. 40 and 41 with respect to time. Once the values of the (V), (γ) are found at each time increment, the corresponding horizontal and vertical distance increments are found from:

$$dx = dt\ [V \cos(\gamma)]\ \text{(average)} \tag{43}$$

$$dy = dt\ [V \sin(\gamma)]\ \text{(average)} \tag{44}$$

The integration can be terminated as soon as the vertical distance (y) exceeds the obstacle height (h). The corresponding climb-distance is found by interpolation:

$$s_c = x - \left(\frac{dx}{dy}\right)(y - h) \tag{45}$$

and the total take-off distance is

$$s = s_c + s_g \tag{46}$$

Because the dynamic pressure (q) is inversely proportional to the wing loading (W/S), all the distance dimensions can be computed as the ratio s/(W/S), when the the obstacle height is specified in terms of h/(W/S). The velocities are then found in terms of $V/(W/S)0.5$.

For CTOL aircraft the maximum climb angle and the difference between V_X and V_{lof} are small. In such a case the steady state climb is reached quickly and prior to clearing the obstacle. For STOL aircraft, the maximum climb angle as well as the difference between V_X and V_{lof} are large as shown in fig. 10. In that case, the obstacle may be cleared prior to reaching the steady state conditions. Due to the limited rate of increase in the climb angle it is possible to overshoot (V_X) prior to reaching the steady state climb angle (γ_X). When the pilot modulates the angle of attack as suggested in eq. 30, then the time required to reach the steady state climb angle (γ_X) is minimal. Because (γ_X) decreases with bleed air, it is advisable to decrease the blowing rate gradually during climb-out.

Example of a Take-Off Performance

To determine the minimum runway length for a CC STOL aircraft, the designer must compare the performance over a wide range of bleed air mass flow ratio's and thrust vector angles. The associated lift and blowing coefficients vary drastically and should not be used as design input variables. Suitable input parameters are: take-off thrust to weight ratio, thrust vector angle, blowing momentum as a function of bleed air mass ratio, thrust loss as a function of blowing momentum, and lift proportionality constant (C_B). All other input parameters are similar to those needed for a CTOL aircraft. A sample calculation was performed for an aircraft with the following characteristics:

$T_O/W = 0.5$, (e AR) = 5, $\partial C_L/\partial\alpha = 4.74$, $C_B = 5.6$ $\alpha_g = 3°$, $\alpha_{lof} = 11°$, $\delta_f = 0$,

blowing air supplied at 11 atm, and duct momentum loss 20%. The distances for both the ground roll and the climb distance are given as a function of the wing loading (W/S). This requires the obstacle height to be specified in the same units. Here (h = 0.5), this means (h = 35 ft) for a wing loading of 70 psf. The ground run distance is shown in fig. 11 to reach a minimum at 5.5% bleed air and a thrust vector angle of 24 degrees. The minimum ground distance in ft is 15.3 times the wing loading in psf. This is less than half the distance required without CC or thrust vectoring. At this low thrust to weight ratio the effect of thrust vectoring by itself is about 20%. The loss of thrust and acceleration associated with high bleed ratios and thrust vectoring are clearly noticeable. In fig. 12, both the climb distance to clear an obstacle and the total take-off distance are shown. The penalty of not using the optimum bleed air ratio and thrust vector angle is not as critical for the climb distance as for the ground distance. This would be different if the bleed air extraction were delayed till the moment of lift-off. The usual obstacle height is 15 meter or 50 ft. If those distances were used, the climb distance would be closer to the ground distance. The trimmed lift coefficient, shown in fig. 13 varies widely with blowing rate from below 1.0 to above 4.0 and for the minimum take-off distance, it is significantly below the maximum obtainable value. The corresponding blowing coefficient varies with the lift-off dynamic pressure as shown in fig. 14. Like the lift coefficient, it varies over a wide range of values. Practical values are limited to below 0.3, above that value the lift augmentation ratio equal $\Delta CL/(C_\mu)^{0.5}$ becomes less effective.

Conclusions

Designing with CC requires a good insight in CC airfoil aerodynamics, the relation between engine thrust loss as a function of blowing air generation and the lift loss associated with trimming the pitching moments. The large number of design variables involved, necessitates numerous performance calculations were each parameter is varied over a wide range. The linear equations presented in this paper facilitate such an analysis. The thrust loss equations should be modified in accordance with the characteristics of the engine under consideration. Because cost, weight, simplicity and reliability are over-riding factors in the optimization process the minimum achievable take-off and landing distances may not represent the optimum design. The finally selected percent bleed air and duct size are probably lower than those corresponding to the minimum runway length. The partial derivatives of these parameters, such as (ds/db), should be plotted as a function of the high lift system cost or weight, to arrive at an optimum design.

In a comparitive study with other high lift techniques one must realize that even though the power efficiency of CC is very attractive, the magnitude of the locally obtainable lift coefficient, is less than six. Desirable flying aspects are good pilot visability and effective DLC. Undesirable characteristics are sudden wing stall, and required in flight stowing of the rounded trailing edge. From the WVU CC flight test, it was found that drag, with the forward folding CC flap in the downward position, was so large that at full throttle, the sink rate was 1000 ft/min. Because the flap folding maneuver could be completed within four seconds, the change in speed and pitch attitude was acceptable.

An improvement in the stowable flap design was recently patented, see figure 15. Here an independently operating Fowler flap is equipped with a CC rounded trailing edge, when needed. Safety and descent control are enhanced by the availability of conventional flaps in conjunction with CC. A separate air duct, which doubles as a rounded Coanda surface, can be swung in position, like an agricultural airplane spray bar. The available internal ejector suction provides the attachment force between the flap trailing edge and the CC air duct. The duct pivot point can be positioned anywhere to accommodate duct stowing at an optimum location in the wing. The drag associated with stowing only the blowing duct, is much lower than with a forward folding flap.

References

1. Boasson, M., Loth, J.L., "Combination of Suction and Tangential Blowing in Boundary Layer Control" 27th Israel Conf. on Aviation and Astronautics, Feb. 1985.

2. Carr, J.E. "Blended Blown Flaps and Vectored Trust for Low Speed Flight", J. Aircraft, Vol. 23, No. 1 1986 p. 26-31.

3. Davidson, I.M., "Aerofoil Boundary-Layer Control System", British Patent No. 913754, 1960.

4. Englar, R.J., "Circulation Control for High Lift and Drag Generation on STOL Aircraft. Journal of Aircraft. Vol. 12, No. 5, May 1975, pp. 457-463.

5. Englar, R.J., Trobaugh, L.A. and Hemmerly, R.A., "STOL Potential of the Circulation Control Wing for High-Performance Aircraft", J. of Aircraft, Vol. 15, No. 3, March 1978, pp. 175-181.

6. Englar, R.J., "Low-Speed Aerodynamic Characteristics of a Small, Fixed Trailing Edge Circulation Control Wing Configuration Fitted to a Supercritical Airfoil. DTNSRDC/ASED-81/08, March 1981.

7. Hemmerly, R.A., "An Investigation of the Performance of a J52-P-8A Engine Operating Under the Influence of High Bleed Flow Extraction Rates", DT NSRDC ASED-387, August 1977.

8. Kind, R.J. and Maull, D.J., "An Experimental Investigation of a Low-Speed Circulation Controlled Aerofoil", Aeronautical Quarterly, Vol. XIX, May 10, 1968, pp. 170-182.

9. Kohlman, D.L. "VSTOL Airplanes", Iowa State U. Press, 1981.

10. Loth, J.L., "Some Aspects of STOL Aircraft Aerodynamics", SAE Paper No. 730328, Business Aircraft Meeting, April 1973.

11. Loth, J.L., Fanucci, J.B., Roberts, S.C., "Flight Performance of a Circulation Controlled STOL Aircraft", Journal of Aircraft, Vol. 13, No. 3, March 1976, pp. 169-173, also AIAA Paper 74-994, August 1974.

12. Loth, J.L., Boasson, M., "Circulation Controlled STOL Wing Optimization," J. Aircraft, Vol. 21, No. 2, 1984, pp 128-134.

13. Roberts, S.C., "WVU Circulation Controlled STOL Aircraft Flight Tests", WVU Aerospace Technical Report No. 42, July 1974.

14. Williams, R.M. and Howe, H.J., "Two-Dimensional Subsonic Wind Tunnel Tests on a 20 Percent Thick, 5 Percent Combined Circulation Control Airfoil. NSRDC TECH. Note AL-176 (AD877-764) 1970.

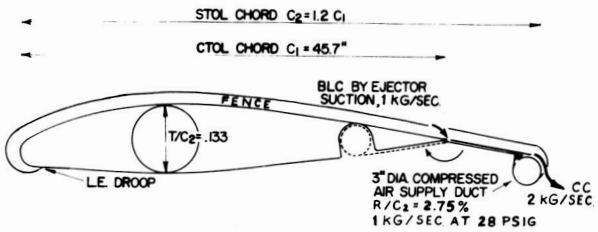

Figure 1 - CC airfoil used on the WVU CC Demonstrator STOL aircraft.

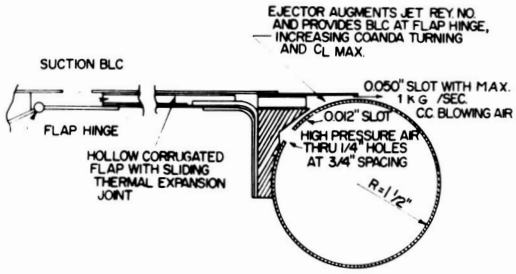

Figure 2 - Hollow flap of the WVU CC wing with supersonic jet ejector.

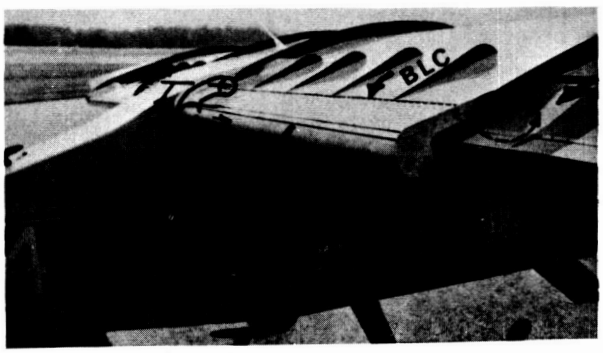

Figure 3 - WVU STOL aircraft with aerodynamic and structural fences needed to transfer loads past the CC duct stowing cavity.

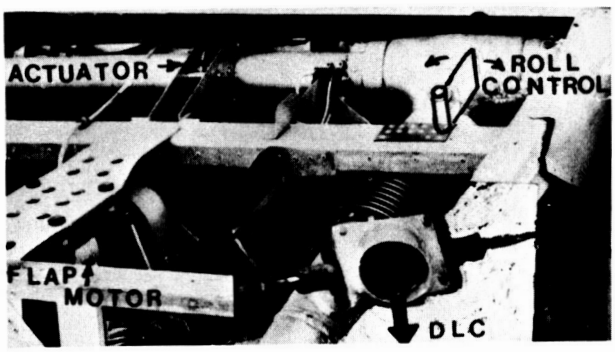

Figure 4 - CC air supply with DLC sliding air dump valve and aileron linked splitter vane for roll control by differential blowing.

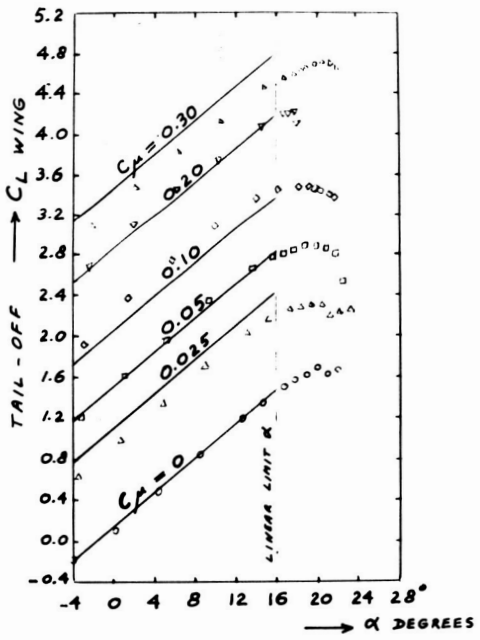

CURVE FIT: $C_{L_{WING}} = 4.74(\alpha + 0.028 \text{ RADIAN}) + 6.1\sqrt{C_\mu}$

Figure 5 - Empirical curve fit with Eq. 2, applied to wind tunnel data on A-6 model with tail-off.

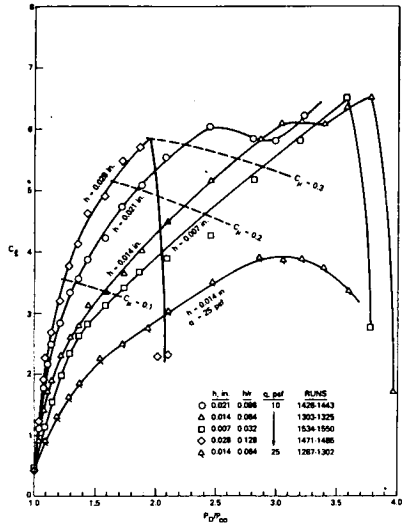

Figure 6 - Non-linear CC airfoil lift versus blowing pressure.

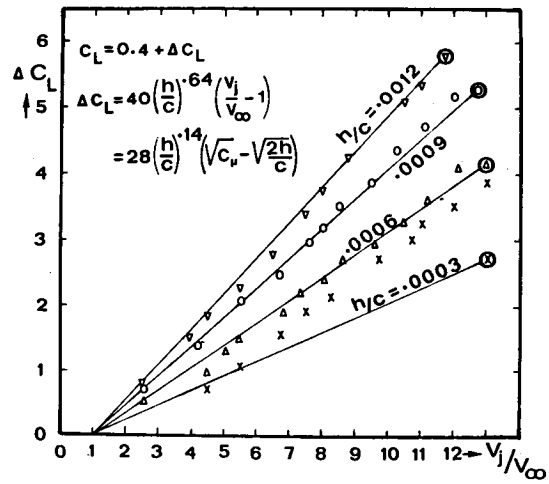

Figure 7 - Linear CC airfoil lift increase versus velocity ratio.

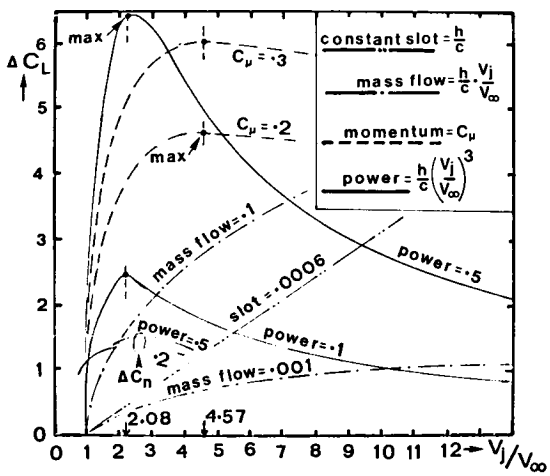

Figure 8 - Effect of velocity ratio on lift increase at constant power.

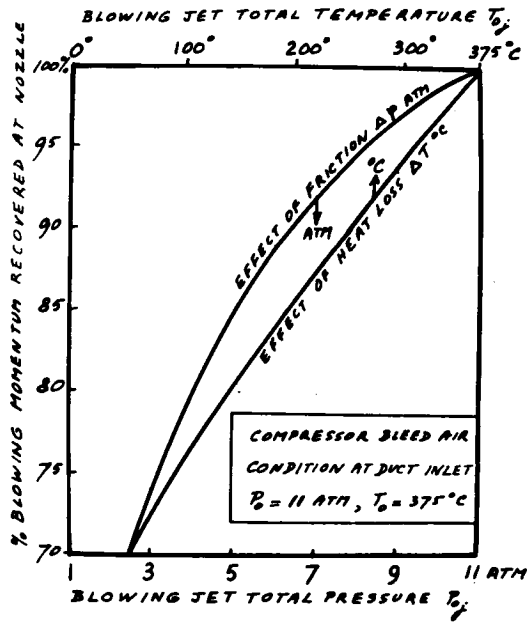

Figure 9 - Example of reduction in blowing momentum due to duct loss.

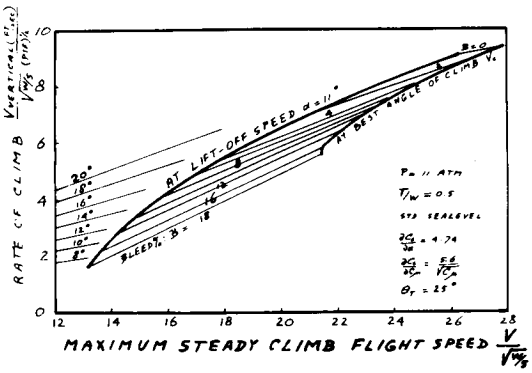

Figure 10 - Reduction in lift-off and best climb angle speed with CC.

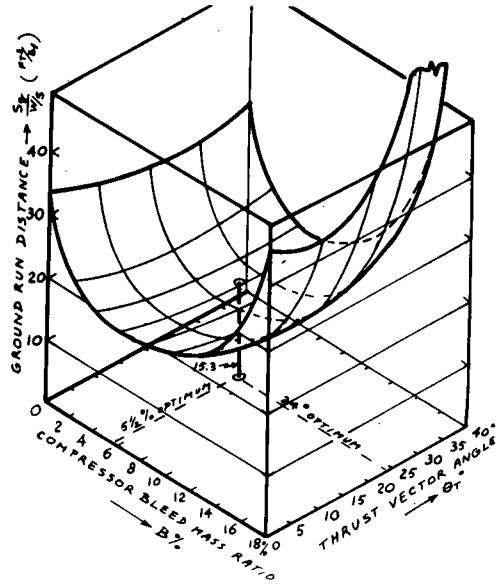

Figure 11 – Example of reduction in take-off ground run with CC.

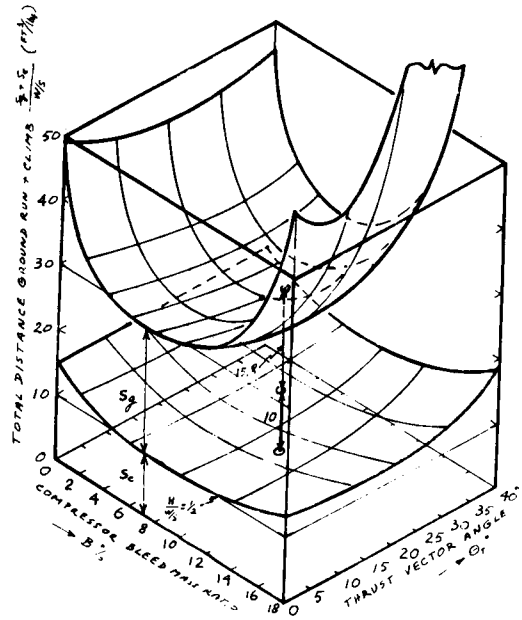

Figure 12 – Example of reduction in climb and ground distance with CC.

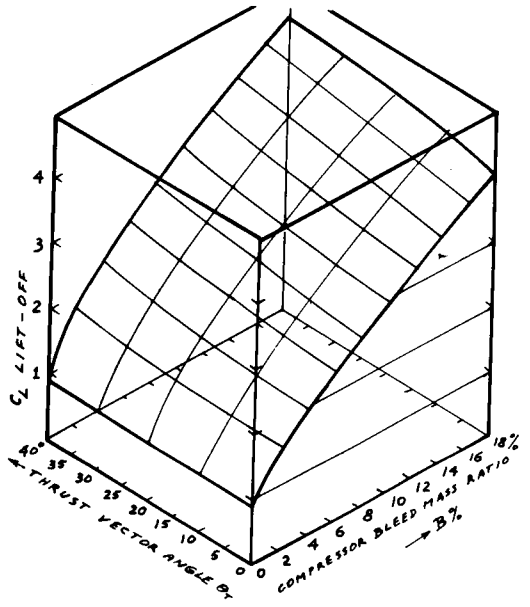

Figure 13 – Example of range in C_L lift-off available with CC.

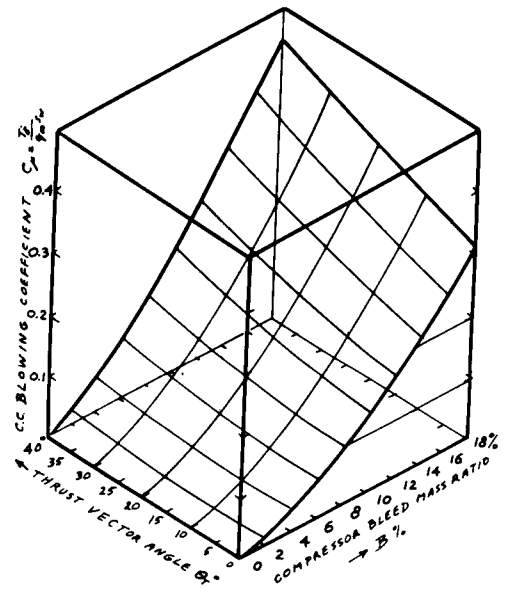

Figure 14 – Example of range in C_μ lift-off available with CC.

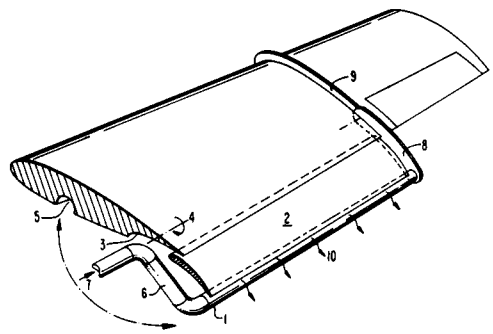

Figure 15 – Patented CC stowable rounded trailing edge in combination with Fowler flaps.

NOMENCLATURE

Ad	=	Propeller disk area
AR	=	Wing aspect ratio
b	=	Ratio of bleed air to jet engine mass flow
C_B	=	Lift proportionality constant for CC
CC	=	Circulation Controlled abbreviation
C_D	=	Total airplane drag coefficient
C_L	=	Lift coefficient
C_p	=	Coefficient of preformance for a propeller
$C\mu$	=	CC blowing coefficient
c	=	Wing chord in cruise mode
D_m	=	Engine inlet air flow momentum
e	=	Span-wise loading efficiency
f	=	Runway friction coefficient
g	=	Acceleration of gravity
h	=	Take-off obstacle height to clear or CC blowing slot height
M	=	Free stream Mach number
m	=	Mass flow rate
P_s	=	Shaft power
q	=	Free stream dynamic pressure
RC	=	Rate of Climb
S	=	Wing area in cruise
s	=	Horizontial take-off or landing distance
t	=	Temperature or time
T	=	Thrust, except with thrust vectoring is only exhaust momentum
V	=	Velocity, without subscript means flight speed
W	=	Aircraft weight
w	=	Velocity increase induced at the propeller disk

Subscripts

a	=	approach related parameter
b	=	parameter with CC blowing
c	=	climb related parameter
e	=	exhaust parameter
g	=	ground distance
i	=	induced drag
j	=	blowing jet parameter
lof	=	parameter related to lift-off speed
o	=	parasite drag or reference static thrust
T	=	thrust related parameter
w	=	head wind component
x	=	maximum angle of climb parameter

Greek

α	=	angle of attack
γ	=	flight path angle
δ_f	=	flap angle
η	=	efficiency
θ	=	thrust vector angle or flap hinge locater angle
ρ	=	air density

Circulation-Control Research Planning

SUMMARY OF SESSION SEVEN: CIRCULATION CONTROL AERODYNAMICS RESEARCH NEEDS

by James C. Biggers

At the 1986 NASA Ames Workshop on Circulation Control Aerodynamics, the last session focused on the needs for research in this new field. A list of such needs was developed and prioritized during the session, with special emphasis given to the needs perceived by contractors who are trying to develop flight systems. The prioritized lists, categorized by application, are presented and discussed. The previous workshop on this subject was hosted by the NASA Ames Research Center in 1982. The overall feeling of the attendees at the 1986 workshop was that significant progress has been made since 1982, but adequate CFD codes for confident aerodynamic design need to be developed for Coanda flows. The important, unique aspects of circulation control need further investigation, with coordinated experiments and theory development. Top priorities for development of the X-wing are new airfoils, extension of the recently documented data base, further development of the lower surface blowing concept, and improved computing for the vibration alleviation system. The fixed-wing developers identified some desires for additional research, but felt ready to develop CC wing vehicles. Some specific needs were discussed to further explore the NOTAR concept, as well as exploring applications of CC to tilt-rotor vehicles.

In the four year period (1982-1986), many studies were undertaken which are still providing researchers with a greater understanding of the CC wing concept. One of these projects, the RSRA/X-wing, led to a greater understanding of the CC concept, as well as the X-wing concept.

During the session, special emphasis was given to the items identified by the manufacturers with experience in developing vehicles using CC aerodynamics. The session began with a review of the CC research needs identified in the 1982 workshop, and a brief discussion of the progress indicated by the participants of this meeting. This list is shown in Table 1 along with an indication of the degree to which progress in these areas was reported at the workshop. A questionnaire was completed by attendees to indicate research needs and how these needs should be addressed. Responses were collected and presented of the session. Manufacturers were then given an opportunity to present their needs and priorities. A list was compiled from these two sources. The open discussion during the session centered on completing and prioritizing the list of research needs. The list was divided into categories of generic CC aerodynamics, X-wing, fixed wing, NOTAR (the no tail rotor CC tail boom of the McDonnell-Douglas helicopter), and Tilt Rotor (CC for reducing the download on the wing).

GENERIC CC AERODYNAMICS

The generic CC aerodynamics list, Table 2, was not prioritized, because it is impossible to schedule scientific breakthroughs and because all of the items listed must be addressed if we are to develop a true design capability in this technology. Also, many of these needs can be addressed simultaneously by different groups. However, all developers agreed that determining the effects of oscillating blowing and developing a simplified "engineering" code

efforts in CFD to develop better turbulence modeling for analysis of the wall-jet area.

The near term rotor-airfoil effort should proceed as soon as possible, with participation including DTNSRDC, Stanford University, Sikorsky Aircraft, and NASA Ames Research Center. When the CFD codes have been fully developed for CC application, including proper turbulence modeling, a third-generation airfoil design effort can begin, with the objective of achieving the full-performance potential of circulation control.

The new data base resulting from the recent series of X-wing airfoil tests at NASA Ames needs to be expanded to include more reliable information in the low-speed, high angle-of-attack regions. Much of the high performance expected of the X-wing (after CC conversion) is in this low-speed, high angle-of-attack regime. Thus these tests are essential to improve the confidence with which such predictions are made. Also, this is the regime where dual-front rear blowing is employed, so more detailed measurements of this operation are needed. These can and should proceed in parallel with other items.

The presentation by Schwartz and Rogers (DTNSRDC) on lower surface blowing as a possible approach to improve X-wing performance and/or reduce lifting system weight was felt to be very important. This concept should be applied to airfoil tests as soon as possible. Such an airfoil model is now under fabrication at DTNSRDC. Additional funding will be necessary to complete the testing of the airfoil and assess its potential for an X-wing application.

The methods for computing higher harmonic blowing for X-wing vibration alleviation are complex and require large throughput in the fly-by-wire computer on the RSRA/X-wing. Analytical studies are needed to identify improved methods for this task. These methods will then need to be implemented in a computer system. When appropriate, the controls laboratory developed at Sikorsky could be used for testing the new algorithms.

The effect of gust encounters with an X-wing needs to be studied. This can be done at universities or at government labs.

Better methods of accounting for three-dimensional effects are needed for the X-wing concept. This includes both fixed- and rotary-wing modes of operation, and the wing-body integration for transonic cruise flight. A scale model with 6-ft span is available at DTNSRDC which may be useful in the cruise-mode investigations.

FIXED WING

The list of needs to develop CC capability for fixed wing aircraft, Table 4, is not prioritized because the manufacturers of fixed-wing vehicles felt there were no urgent research needs to develop vehicles using a CC wing. Indeed, they felt the next step should be development of a CC research vehicle. It was pointed out that feasibility has been proven with the two vehicles already flown. Although very few flight hours were accumulated, no serious problems were encountered when these two vehicles were flown after being equipped with CC.

for analyzing CC airfoils are most urgently needed, hence those items are at the top of the list.

The need for further investigation of basic effects was apparent to all attendees. So far, few of the unique parameters of CC aerodynamics have been adequately explored. The computational fluid dynamics (CFD) codes are promising, but as yet inadequate for a priori modeling of the Coanda flows. The effects listed in the tables must all be better understood if CC aerodynamics technology is to achieve representative application in current aircraft designs. It was felt that very close coordination between theoretical development and carefully planned experiments is essential for the rapid advancement of CC concepts. The theoreticians and experimenters must therefore jointly define the experiments and determine measurements to be made.

To enhance progress, three packages of information should be compiled and given to all parties. First, a list of basic formulas for success should be compiled, listing all information needed to make a CC airfoil which works acceptably. This item was prompted by some of the presentations at the workshop in which the reported performance of the CC elements was disappointing, but could have been greatly improved by using the knowledge of some of the more experienced people in the field. Second, the detailed potential of CC aerodynamics should be compiled for various applications. This would include items such as maximum lift coefficient vs. Mach number, maximum lift augmentation, best slot location, etc. Finally, based on the detailed potential benefits, the system-level potential benefits should be identified for application of CC aerodynamics. This last package would assist researchers in determining the missions and vehicles that would most benefit from this technology.

X-WING

The research needs for the X-wing concept, Table 3, were completed and prioritized quickly by the attendees who are involved in the RSRA/X-wing project. In addition, the X-wing developers reinforced the need for determining the response of a CC airfoil to oscillating blowing. This is especially important with respect to the X-wing because the vibration reduction system to be used requires oscillation of the blowing at frequencies up to 5 per rev.

The need for more advanced X-wing airfoils was emphasized by the Sikorsky representatives in their presentation. The attendees agreed that present CFD codes are not yet adequate to develop a truly new airfoil (including design of the Coanda surface) in the near future but the requirement is too urgent to wait for more accurate CFD codes. However, the ability to shift performance boundaries by altering the camber and thickness distribution upstream of the Coanda trailing edge is within the present state of the art. Therefore, the empirical data base developed by DTNSRDC and recently improved by Sikorsky Aircraft (through airfoil tests), along with the transonic swimilarity principles recently discovered, could be used to develop a follow-on X-wing rotor. Because of the lead time required to design and fabricate a new model rotor, design of airfoils for it must begin immediately. If the CFD codes develop rapidly, they should be used when they become available to achieve further improvements through better Coanda designs. NASA Ames should continue its

Lockheed was very interested in developing a STOL vehicle using a CC wing with jet engines in any of several arrangements. Another presentation pointed out the safety enhancements available with CC wings. However, the attendee who has worked on the Grumman noted that the Navy has concerns about the reliability of blowing systems on the flap.

This suggests that the most important task is to assess the reliability of CC systems for fixed-wing application. Once this reliability is established, the advocacy between industry, academia, and government necessary to develop CC wing flight systems would ensue.

NOTAR

The NOTAR concept involves CC on the tail boom in the downwash of the rotor to generate anti-torque forces. This effect, along with deflection of the remaining air from a fan, allows the tail rotor to be eliminated. This concept is of great interest to developers of the X-wing as an alternative to the fan-in-fin, anti-torque system. Also, elimination of tail rotors from conventional helicopters would greatly reduce the accident rates. The NOTAR uses much lower blowing than other CC concepts and operates at very low Reynolds numbers, so the research needs are unique to this concept. The list of research needs for the NOTAR is in Table 5.

TILT ROTOR

The only developments suggested as necessary for applying CC aerodynamics to tilt-rotor vehicles is the reduction of wing download at hover. Another possible option to explore is to use the high lift coefficients obtainable with CC to reduce the size of the tilt-rotor wing. These needs are listed in Table 6.

Table 1. 1982 Circulation-Control Research Needs

Computational fluid dynamics

- airfoils: Navier-Stokes/Euler, including stall, etc. (1)
- transient rotor wake/inflow (1)
- compare CC rotor wake with conventional rotor wake
- stopped rotor code
  - unsteady aerodynamics
  - front-rear wing interaction (2)
- 3-D pneumodynamics code
- turbulence models for Coanda area (1)
- wing-body integration and interaction

Experiments

- study existing data (basic understanding) (2)
- test CC airfoils (fundamental physics) (1)
- systematic airfoil tests (data base) (2)
- test CC wing, vary sweep, Mach No., blowing, etc. (2)
- transonic tests of vehicle design

Aerodynamic analysis and theory

- CC airfoil prediction (AMI and SAI codes) (1)
- transient rotor wake (empirical)
- upgrade X-wing analytical codes (2)

Aeroelasticity and loads

- nonsteady aero/flutter
- front-wing divergence, including servo feedback (1)
- vibratory loads on rotor (2)
- coupled wing/body flutter (1)
- rotor system aeromechanical stability (2)

Flight dynamics

- pitch/roll rate effects (1)
- ground effects
  - rotors
  - wings
- control and trim aerodynamics
  - transition (1)
  - conversion (2)

(1) Some progress reported in 1986, but that progress not complete or inadequate
(2) Significant progress reported in 1986

Table 2. 1986 Research Needs--Generic Circulation-Control Aerodynamics

What	How	When
develop "engineering" CC airfoil code*	analysis, data base	ASAP
investigate nonsteady effects	test	ASAP
oscillate blowing*		
airfoil motion effects		
investigate basic effects of CC aerodynamics (coordinate experiments and theory)	analysis, 2-D wind tunnel tests	ASAP
turbulence		
local geometry		
compressibility (free-stream and jet)		
external pressure gradient		
off-design effects		
manufacturing defects		
erosion, ice accretion, etc.		
improve/optimize Coanda geometry	analysis, 2-D wind tunnel tests	start now
develop high-speed CC airfoils	analysis, 2-D wind tunnel tests	by 1988
compile information packages		
geometry for success	data base	ASAP
detailed potential of CC*	data base and experience	ASAP
system potential of CC*	analysis	1987

*Identified by manufacturers as very important

Table 3. 1986 Research Needs--X-Wing Concept

What	How	When
extended X-wing airfoil data base to include: low speed and high angle of attack dual front-rear blowing skewed flow oscillating blowing	2-D wind tunnel tests	ASAP (1986)
develop 2nd generation X-wing airfoils with 20% improvement improve low-speed L/D increase drag divergence Mach number extend stall boundaries	data base, analysis, 2-D wind tunnel tests	after extended test above
develop and test lower surface blowing concept	data base, analysis, 2-D wind tunnel tests	1986-1987
improve computing for higher-harmonic control system	analysis	ASAP
improve 3-D predictions rotary wing stopped rotor, including wing-body interaction	analysis	1987
investigate gust response of vehicle	analysis	1986-1987

Table 4. 1986 Research Needs--Fixed Wing

What	How	When
investigate CC control surfaces	test	2-3 yr
use of CC for engine exhaust turning	test	ASAP
effects of CC wing on tail downwash	analysis, test	ASAP
develop small Coanda for high-speed use	analysis, test	ASAP
low drag with zero blowing high augmentation at low speeds use of blowing at high speeds for control		
combine CC with slotted flap	test	2-3 yr
investigate safety and reliability issues*	analysis	ASAP

*Very important for advocacy

Table 5. 1986 Research Needs--NOTAR Concept

What	How	When
investigate effects of variations in external flow	test	ASAP
investigate effects of high-sweep angles (60 deg)	test	ASAP
find best slot heights and slot positions	test	ASAP

Table 6. 1986 Research Needs--Tilt-Rotor Concept

What	How	When
investigate effects of external pressure gradients	test, analysis	1987
investigate use of CC to reduce wing size	analysis	1987-1988

1. Report No.	2. Government Accession No.	3. Recipient's Catalog No.
NASA CP-2432		

4. Title and Subtitle	5. Report Date
Proceedings of the Circulation-Control Workshop - 1986	May 1987
	6. Performing Organization Code
7. Author(s)	8. Performing Organization Report No.
Jack N. Nielsen, Compiler	A-86314
	10. Work Unit No.
9. Performing Organization Name and Address	11. Contract or Grant No.
Ames Research Center Moffett Field, CA 94035	
	13. Type of Report and Period Covered
12. Sponsoring Agency Name and Address	Conference Publication
National Aeronautics and Space Administration Washington, DC 20546	14. Sponsoring Agency Code 505-61-71

15. Supplementary Notes

Point of Contact: Dr. Jack N. Nielsen, Ames Research Center, M/S 200-1A
Moffett Field, CA 94035 (415) 694-5500 or FTS 464-5500

16. Abstract

On February 19-21, 1986, a Circulation-Control Workshop was held at NASA Ames Research Center by representatives of academia, industry, and government. A total of 32 papers were given in six technical sessions covering turbulence, circulation-control airfoil theory, circulation-control airfoil wing experiments, circulation-control rotor theory, X-wing technology, fixed-wing technology, and other concepts. The last session of the workshop was devoted to circulation-control research planning. This publication contains the unclassified and nonproprietary papers of the workshop.

17. Key Words (Suggested by Author(s))	18. Distribution Statement
Circulation control Circulation-control airfoil Circulation-control rotor X-wing airplane Coanda effect	Unclassified-Unlimited Subject Category 02

19. Security Classif. (of this report)	20. Security Classif. (of this page)	21. No. of Pages	22. Price*
Unclassified	Unclassified	607	A99

*For sale by the National Technical Information Service, Springfield, Virginia 22161